THE PHYSICAL REVIEW

VOLUME 95 SECOND SERIES NUMBER 3

AUGUST 1, 1954

Published for the

AMERICAN PHYSICAL SOCIETY

by the

AMERICAN INSTITUTE OF PHYSICS

Lancaster, Pa., and New York, N. Y.

THE PHYSICAL

THE
PHYSICAL REVIEW

A journal of experimental and theoretical physics established by E. L. Nichols in 1893

SECOND SERIES, VOL. 95, NO. 3 AUGUST 1, 1954

Range and Charge of Energetic Nitrogen Ions in Nickel

H. L. REYNOLDS, D. W. SCOTT, AND A. ZUCKER
Oak Ridge National Laboratory, Oak Ridge, Tennessee

(Received April 21, 1954)

The range of nitrogen ions in nickel was measured for energies from 8 to 29 Mev. The rate of energy loss is nearly constant over this range and has a value of 3.7 Mev/(mg cm^{-2}). The average charge of nitrogen ions in nickel was determined as a function of velocity. At a velocity of 1.93×10^9 cm/sec (27.3 Mev), the average charge is 6.2.

A STUDY of the range-energy characteristics of particles heavier than helium has been greatly hampered by the lack of such high-energy particles in the laboratory. The ORNL 63-inch cyclotron provides 29-Mev nitrogen ions which can be used in such an investigation. For ion velocities much greater than the velocity of the particle's most tightly bound electron, the usual range relation,

$$R_Z(V)=(m/Z^2)R_p(V), \qquad (1)$$

where R_p is the range of a proton at velocity V and where m and Z are the nuclear mass and charge, has been successfully applied by cosmic-ray workers and others. However, as the velocity of an ion approaches the velocity of its inner electrons its effective charge decreases as it picks up electrons from the surrounding medium. The proper Z to use in the above relation for medium- and slow-moving ions is unknown.

The range characteristics, in gases, of ions heavier than helium were investigated by Blackett,[1] Blackett and Lees,[2] and Feather,[3] who observed recoil atoms from alpha particles in cloud chambers. The velocities covered were considerably below those that will be discussed here. Knipp and Teller[4] used the early range data to determine the charge behavior of ions as a function of velocity, as will be discussed later. Bohr[5] has given a complete discussion of the information available up to 1948. Bell[6] has treated the problem of the charge of fission fragments in low-pressure gases.

A 2-microampere deflected beam of 29-Mev nitrogen ions is available at the 63-inch cyclotron. This beam was used to determine the range-energy relation of nitrogen ions in nickel, and the charge state of the ions as a function of velocity in nickel. Nickel was chosen as an absorber because it is commercially available in the form of thin, strong, uniform foils which make excellent windows for gas-target chambers. Where a nuclear physics program necessitates the use of such windows a knowledge of the energy lost by nitrogen ions passing through them becomes imperative. Nickel absorbers are also used in investigations of excitation functions.[7]

EXPERIMENTAL METHOD—RANGE-ENERGY RELATION

The energy of the nitrogen ions as a function of nickel absorber thickness was determined by allowing the ions to pass into a chamber of hydrogen and observing the energy of recoil protons at zero degrees to the incoming nitrogen beam. A foil changer, Fig. 1, was placed before the hydrogen chamber to allow nickel foils of various thickness to degrade the energy of the incoming nitrogen ions. The energy of the recoil protons was determined by measuring their range in nuclear emulsions. In order to obtain tracks of a convenient length in the emulsions, aluminum absorbers were interposed between the chamber exit

[1] P. M. S. Blackett, Proc. Roy. Soc. (London) **107**, 349 (1925).
[2] P. M. S. Blackett and D. S. Lees, Proc. Roy. Soc. (London) **134**, 658 (1932).
[3] N. Feather, Proc. Roy. Soc. (London) **141**, 194 (1933).
[4] J. Knipp and E. Teller, Phys. Rev. **59**, 659 (1941).
[5] N. Bohr, Kgl. Danske Videnskab. Selskab, Mat-fys. Medd. **18**, 8 (1948).
[6] G. I. Bell, Phys. Rev. **90**, 548 (1953).
[7] A. Zucker and H. L. Reynolds, Phys. Rev. **94**, 784 (1954); also H. L. Reynolds and A. Zucker, Meeting of the S. E. Section, Am. Phys. Soc., April, 1954.

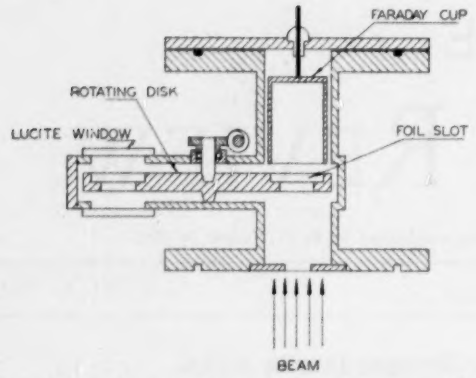

FIG. 1. Foil changer. Schematic drawing of the rotating foil and target changer, with Faraday cup in place. The disk can be readily removed from the chamber by disengaging the center shaft and removing the left end of the chamber.

port and the emulsion. The energy of nitrogen ions is simply related to the energy of recoil protons at zero degrees as follows:

$$E_N = 3.99E_p. \quad (2)$$

The experimental arrangement is shown in Fig. 2. The entrance foil for the hydrogen chamber was 0.025-mil nickel (0.59 mg/cm²). The foil separating the hydrogen from the atmosphere was 0.1-mil nickel (2.38 mg/cm²). The hydrogen pressure was 7.4 mm of mercury. The energy loss of the nitrogen ions in the length of the hydrogen chamber was estimated to be less than 50 kev. Both foils were attached to the brass support plates with Zapon cement. An external collimator allowed only recoil protons making an angle of less than 5 degrees with the incoming nitrogen beam to enter the emulsion. To monitor the beam a small ring

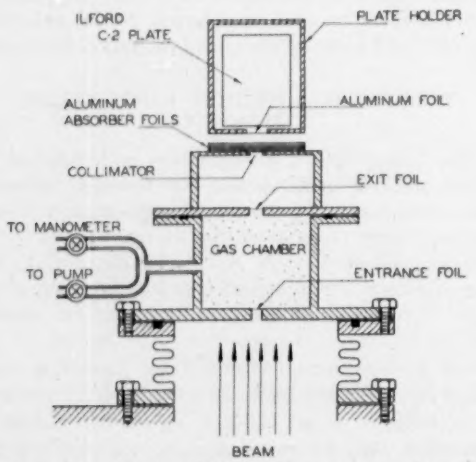

FIG. 2. Gas-scattering chamber. Protons scattered at zero degrees end their range in the emulsion. The aluminum absorbers are used to insure a convenient proton range in the emulsion. Foil changer (Fig. 1) is usually inserted between the gas chamber and bellows.

around the entrance port was painted with Aquadag so that the beam would produce nuclear reactions in the carbon. A Geiger counter was placed close to the port to count gamma rays from these reactions. The monitor served to give a qualitative indication that the beam was entering the scattering chamber.

The emulsions were C-2 Ilford, 50 microns thick. Background protons were negligible as compared with the main recoil proton peak. The exposure time with each nickel absorber was approximately 10 minutes.

EXPERIMENTAL METHOD—CHARGE-VELOCITY RELATION

When the nitrogen ions reach the deflected beam port they have a charge of three, since they have satisfied the cyclotron resonance conditions and have passed through the deflector channel. The charge-velocity experiment consisted of measuring the charge collected in a Faraday cup, Fig. 1, after the beam had passed through a thin nickel foil and comparing it with the charge collected with no nickel foil present. If the beam of nitrogen ions remained constant the charge of the attenuated beam particles could be compared directly with the triply charged particles of the unattenuated beam. The velocity of the particles upon leaving the foils was known from the previously measured range-energy relation.

A foil changer, consisting of a flat disk with twelve 1-inch holes along the periphery, was rotated at a constant velocity through the beam. Nickel foils of various thickness were placed in some of the holes while others were left empty. The nitrogen beam passed through successive holes as the disk was rotated. After passing through a hole or foil the beam current was collected in a Faraday cup 2 inches deep by $1\frac{3}{4}$ inches in diameter, which was spaced about $\frac{1}{4}$ inch from the foils. A $\frac{5}{8}$-inch diameter copper collimator was placed in the path of the beam ahead of the foil changer so that only one hole could be presented to the beam at a time. The rotation of the foil changer disk was adjusted so that the beam passed through each foil or hole for approximately 10 seconds. The current passing through the foil was measured with a vibrating reed electrometer. Comparing the maximum current reading for each foil thickness with the reading for the empty holes gave an average charge as a function of absorber thickness.

The whole apparatus was operated in the 2000-oersted fringing field of the cyclotron. This magnetic field should prevent electrons from migrating into or out of the Faraday cup. To check this possibility, however, a larger Faraday cup approximately 4 inches deep and 4 inches in diameter was placed about $3\frac{1}{2}$ inches beyond the foils. The results obtained with this cup were identical with the results obtained with the smaller cup. A run was performed without the copper collimator; collimation was then effected by just the 1-inch hole under each foil. No difference in the results could be

seen, which indicated that edge effects due to collimation were not important. Calculations indicate that multiple scattering in the foils should not have influenced the results.

RESULTS

The range-energy results are presented in Fig. 3. Because of the absorbers between the hydrogen chamber and the emulsion, consisting principally of the exit foil, the minimum nitrogen energy which could be measured was 8 Mev. The total range of the full-energy (29.1 Mev) beam was found, from the extrapolated charge *versus* absorber thickness curve presented in Fig. 4, to be 7.85 mg/cm² of nickel. The equilibrium charge as a function of ion velocity is given in Fig. 5. It should be pointed out that for velocities below 10^9 cm/sec the curve is based on an extrapolation of the range-energy relation, Fig. 3.

The nickel foils used in these experiments were not tested for uniformity. The majority of the

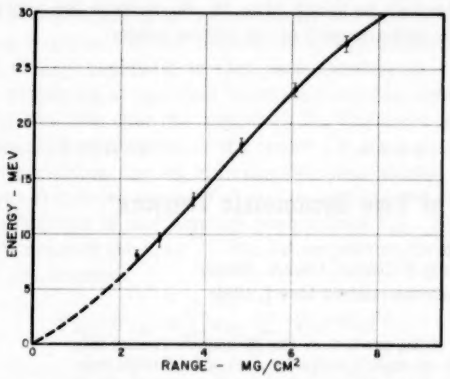

FIG. 3. Energy *vs* range of nitrogen ions in nickel.

absorbers were sandwiches made up of several foils which should average out to some extent the effects of nonuniformity. Replacing foils by others of the same measured surface density did not appear to influence the results.[8] The error in measuring the foil surface density is estimated to be less than one percent. No attempt was made to eliminate occluded gases from the surface of the foils.

The energy spread of the initial beam with the collimating system used for the hydrogen chamber is estimated to be approximately 600 kev, full width at half-maximum. This figure was obtained from the spread in proton energies after correcting for proton straggling and acceptance angles for the protons. The errors shown on the range-energy plot are estimated probable errors.

The errors shown on the charge plot indicate statistical probable errors due to beam intensity fluctuations

[8] Recent measurements [Chilton, Cooper, and Harris, Phys. Rev. **93**, 413 (1954)] on foils purchased from the same vendor (Chromium Corporation of America) indicate the foils are uniform to better than ±1.5 percent.

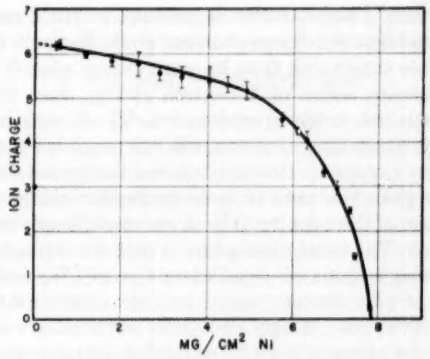

FIG. 4. Average charge of nitrogen ions *vs* nickel absorber thickness.

while the foil changer moved from one hole to the next. Corrections due to electrometer nonlinearity and noncritical damping of the meter have been applied.

DISCUSSION

It has been shown[5] that the range of fission fragments is proportional to their velocity V whereas the range of protons or alpha particles is proportional to V^3. It may be seen from Fig. 2 that the range of nitrogen ions in the velocity region below 2×10^9 cm/sec varies approximately as V^2, less rapidly than alpha particles but more rapidly than fission fragments. Over most of the range of a 29-Mev nitrogen ion the pickup and loss process involves only the K electrons. The K electrons are widely spaced in velocity, and consequently one may expect the effective charge of the nitrogen ion to vary more slowly with velocity than is the case with fission fragments where only outer electrons are involved. This would lead to a larger range-velocity dependence for nitrogen than for fission fragments.

According to Bohr the ratio of electron-loss cross section to capture cross section is proportional to V^5.

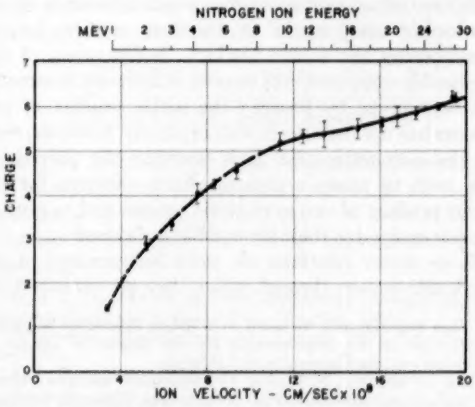

FIG. 5. Average charge of nitrogen ions *vs* energy and velocity in nickel. Region below 6 Mev is based on an extrapolation of range-energy curve, Fig. 3.

With such a high-velocity dependence it would not be expected that the charge of an ion would fluctuate more than one charge unit from its mean charge when it is in the velocity region of K-electron pickup, since the K electrons are widely spaced in velocity. If such is the case, it is meaningful to compare our measured charge-velocity curve with the calculation of Knipp and Teller[4] which gives the ratio of ionic to nuclear charge as a function of the velocity (V_e) of the most loosely bound electron. The usual assumption is that the capture and loss cross sections are equal when $V_e=\gamma V$. We find the value of γ for nitrogen ions to be approximately 0.65 at 1.8×10^9 cm/sec. Knipp and Teller obtained a γ value of 1.1 for nitrogen in air by analyzing the range data of Blackett and Lees.[2] However, the data fall in the velocity region below 5×10^8 cm/sec. The value of γ appears to decrease with increasing velocity.

By using relation 1 and the experimentally determined dE/dx relations for protons given by Allison and Warshaw[9] in combination with our charge-energy curve, one can calculate the range-energy relation for nitrogen in nickel. We have done this by normalizing the calculation to the experimental curve at 8 Mev to avoid the necessity of calculating nuclear stopping effects. In so doing, we find that the calculated curve falls about 2.4 Mev below the experimental curve for particles with a range of 7.5 mg/cm². The increased energy loss for nitrogen over that of equivalent protons can be attributed to several effects. The charge exchange process itself leads to an energy loss since energy is required to remove electrons from the moving ion. The magnitude of this energy loss depends, of course, upon the magnitudes of the capture and loss cross sections. Also, the charge of the ion is not necessarily the charge that contributes to energy loss. For close collisions the screening of the nucleus is not complete. If the whole 2.4-Mev discrepancy is attributed to the latter effect, the effective charge which contributes to energy loss would be about 6 percent larger than that shown in Fig. 5.

We wish to thank Mrs. W. R. Bowelle for assisting in the measurement of the proton ranges.

[9] S. K. Allison and S. D. Warshaw, Revs. Modern Phys. **25**, 784 (1953).

PHYSICAL REVIEW VOLUME 95, NUMBER 3 AUGUST 1, 1954

Decomposition of the Scalar Product of Two Symmetric Tensors*

M. H. COHEN
Institute for the Study of Metals, The University of Chicago, Chicago, Illinois
(Received February 10, 1954; revised manuscript received May 5, 1954)

A simple method is given for the decomposition of the scalar product of two symmetric tensors into products of their irreducible components, which leads also to an explicit recipe for a set of irreducible components of a symmetric tensor. Applications to dipole-dipole interaction and electrostatic multipole interaction are discussed.

IN many problems of physics one begins with a scalar product of two Cartesian tensors and one is faced with the task of expressing that product in terms of the irreducible components[1] of the two tensors, i.e., of decomposing the scalar product. A discussion of the irreducible components of tensors of arbitrary symmetry has been given by Racah;[2] the scalar product of two tensors has not been dealt with explicitly, however, even for the symmetric case. It is therefore the purpose of this note to prove a decomposition theorem for the scalar product of two symmetric tensors and to give an explicit recipe for their irreducible components.

Since tensor relations are valid independent of the particular tensors through which they are exhibited, we shall work with the simple symmetric tensors,

$$X^n{}_{\alpha\beta\ldots}=x_\alpha x_\beta\cdots \tag{1}$$

and $Y^n{}_{\alpha\beta\ldots}$, formed by the n-fold direct product of the vector **x**, or **y**, with itself. Their scalar product is

$$S=X^n{}_{\alpha\beta\ldots}Y^n{}_{\alpha\beta\ldots}=x^n y^n(\cos\theta)^n, \tag{2}$$

where θ is the angle between **x** and **y** and where x and y are the magnitudes of **x** and **y**. Expand $(\cos\theta)^n$ in Legendre polynomials[3]

$$(\cos\theta)^n=\sum_{l=0}^{n}a_{nl}P_l^0(\cos\theta), \tag{3}$$

where

$$a_{nl}=\frac{(2l+1)2^l n!(\frac{1}{2}n+\frac{1}{2}l)!}{(\frac{1}{2}n-\frac{1}{2}l)!(n+l+1)!};\quad n-l\geqslant 0 \text{ and even};$$
$$=0;\quad n-l\leqslant 0,\quad \text{or } n-l\geqslant 0 \text{ and odd}. \tag{4}$$

* This material was included in a thesis submitted in partial satisfaction of the requirements for the degree of Doctor of Philosophy at the University of California.

[1] See, for example, E. Wigner, *Gruppentheorie und ihre anwendung auf die quantenmechanik der atomspektren* (Edwards Brothers, Inc., Ann Arbor, 1944), pp. 263, 264; G. Racah, Phys. Rev. **62**, 438 (1942).

[2] G. Racah, Revs. Modern Phys. **21**, 494 (1949).

[3] E. T. Whittaker and G. N. Watson, *A Course of Modern Analysis* (The University Press, Cambridge, 1952), fourth edition, pp. 310, 311.

Using the addition formula for spherical harmonics,[4]

$$P_l^0(\cos\theta)=\sum_{m=-l}^{l}\mathcal{Y}_l^m(\theta_1,\phi_1)\mathcal{Y}_l^{-m}(\theta_2,\phi_2), \tag{5}$$

$$\mathcal{Y}_l^m(\theta,\phi)=\left[\frac{(l-|m|)!}{(l+|m|)!}\right]^{\frac{1}{2}}P_l^{|m|}(\cos\theta)e^{im\phi},$$

where θ_1 and ϕ_1 are the polar angles of $\mathbf{x}$ and θ_2, ϕ_2 those of $\mathbf{y}$, one obtains

$$S=\sum_{l=0}^{n}a_{nl}\sum_{m=-l}^{l}\Pi_{nl}^m(\mathbf{x})\Pi_{nl}^{-m}(\mathbf{y}), \tag{6}$$

where

$$\Pi_{nl}^m(\mathbf{x})=x^n\mathcal{Y}_l^m(\theta_1,\phi_1). \tag{7}$$

In Eq. (7), S is expressed in terms of the $\frac{1}{2}(n+1)(n+2)$ quantities $\Pi_{nl}^m(\mathbf{x})$ which are linear combinations of the Cartesian components $X^n{}_{\alpha\beta\ldots}$. They are formed by contracting $X^n{}_{\alpha\beta\ldots}$ $(n-l)/2$ times and then taking linear combinations of the remaining products of components of $\mathbf{x}$ so that they become the spherical harmonics $x^l\mathcal{Y}_l^m(\theta_1,\phi_1)$ expressed in Cartesian coordinates. From the properties of spherical harmonics one can immediately conclude that the quantities $\Pi_{nl}^m(\mathbf{x})$ are a set of irreducible components of the tensor $X^n{}_{\alpha\beta\ldots}$.

Generalizing, the set of irreducible components T_{nl}^m of any symmetric tensor T of rank n are the same linear combinations of its Cartesian components $T_{\alpha\beta\ldots}$ as the $\Pi_{nl}^m(\mathbf{x})$ are of the $x_\alpha x_\beta\cdots$. The decomposition formula, Eq. (6), becomes

$$T_{\alpha\beta\ldots}U_{\alpha\beta\ldots}=\sum_{l=0}^{n}a_{nl}\sum_{m=-l}^{l}T_{nl}^mU_{nl}^{-m}. \tag{8}$$

Although the T_{nl}^m form a particular set of irreducible components of T, the decomposition formula, Eq. (8), is valid for any arbitrary set of irreducible components, which, of course, must be related to the T_{nl}^m by a unitary transformation leaving the l's unmixed.

The foregoing results apply also to the scalar product of a symmetric tensor with a tensor of arbitrary symmetry, since symmetrization of the latter before contraction leaves the scalar product unchanged.

The theorem expressed in Eq. (8) facilitates many otherwise tedious calculations in direct application to tensor products. An elementary example is the expression of the dipole-dipole interaction in terms of the raising and lowering operators $I^\pm$, a problem which occurs in the theory of ferromagnetism,[5] in the theory of magnetic-resonance line widths,[6] and elsewhere. If $\mathbf{I}_1$ and $\mathbf{I}_2$ are the angular momenta of two non-overlapping charge distributions with centers separated by $\mathbf{R}$, then their dipole-dipole interaction energy is proportional to

$$W=(\mathbf{I}_1\cdot\mathbf{I}_2)R^{-3}-3(\mathbf{I}_1\cdot\mathbf{R})(\mathbf{I}_2\cdot\mathbf{R})R^{-5}.$$

Observing that W is the scalar product of the tensors $\frac{1}{2}(I_1{}^iI_2{}^j+I_1{}^jI_2{}^i)$, $R^{-5}[R^2\delta_{ij}-3R_iR_j]$ and that the irreducible components of the former involve only $I^\pm$ and I^z, one may effect the required transformation by inspection.

Another illustration is afforded by the electrostatic multipole interaction of a localized system, with angular momentum $\mathbf{I}$, in interaction with an external potential. Expanding the latter in a Taylor's series about its value at the center of the charge distribution, one obtains an infinite sum of scalar products of two symmetric tensors. Applying Eq. (8) to express these in terms of irreducible tensor components, one can then relate the resulting operators to the angular momentum and obtain for the Hamiltonian:

$$\mathcal{H}=\sum_{l=0}^{2I}\mathcal{H}_l, \tag{9}$$

$$\mathcal{H}_l=\sum_{m=-l}^{l}C_l{}^{-m}\Pi_{ll}^m(\mathbf{I}), \tag{10}$$

$$C_l{}^{-m}=\sum_{n\geq l}^{\infty}(a_{nl}/n!)Q_{nl}\Pi_{nl}{}^{-m}(\boldsymbol{\nabla})V(0), \tag{11}$$

$$Q_{nl}=\frac{\langle I|\sum_i q_i\Pi_{nl}^0(\mathbf{r}_i)|I\rangle}{[I(I+1)]^{l/2}P_l^0(I^z(I+1)^{-1})}. \tag{12}$$

In Eq. (12), q_i is the charge of the ith particle of the system. Note that Q_{nl} vanishes for l odd.

For nuclei, the usual procedure[7] yields only the leading term $(n=l)$ in the coupling constant C_l^m by neglect of overlap of the interacting systems. Examination of Eq. (11) shows that the overlap terms $(n>l)$ can cause a chemical shift in the quadrupole-moment ratio of two spin-$\frac{3}{2}$ isotopes[8] of at most one part in 10^7. On the other hand, the convergence of these overlap terms is much slower for the case of a paramagnetic ion interacting with a crystalline field, where $(p=n+2)$:

$$\frac{Q_{pl}\Pi_{pl}^m(\boldsymbol{\nabla})V(0)}{Q_{nl}\Pi_{nl}^m(\boldsymbol{\nabla})V(0)}\sim\left[\frac{\text{ionic radius}}{\text{ionic separation}}\right]^2.$$

Hence the customary practice of neglecting overlap in the interpretation[9] of measured values of C_l^m could easily lead to errors of more than 10 percent in an attempt to calculate C_l^m from approximate wave functions.

[4] See reference 3, pp. 326 ff., pp. 393 ff.
[5] T. Holstein and H. Primakoff, Phys. Rev. **58**, 1098 (1940).
[6] J. H. Van Vleck, Phys. Rev. **74**, 1168 (1948).
[7] H. B. G. Casimir, *On the Interaction between Atomic Nuclei and Electrons* (De Erven F. Bohn, N.V., Haarlem, 1936).
[8] Geschwind, Gunther-Mohr, and Townes, Phys. Rev. **81**, 288, 289 (1951).
[9] R. J. Elliot, Revs. Modern Phys. **25**, 167 (1953).

Spherical Model of an Antiferromagnet*

BARRY S. GOURARY AND ROBERT W. HART
Applied Physics Laboratory, The Johns Hopkins University, Silver Spring, Maryland
(Received March 31, 1954)

The sphericalization technique is adapted to the calculation of the partition function of a body-centered cubic lattice of spins with isotropic antiferromagnetic interactions between nearest neighbors and between second-nearest neighbors. Two transition points may be obtained. The usual Curie point transition from the paramagnetic state to the antiferromagnetic state (caused by the sticking of the saddle point) leads to an antiferromagnetic state with ordering either of the first kind or of the second kind, depending on the value of the ratio of the second-nearest neighbor interaction to the nearest-neighbor interaction. In addition a first-order transition from one kind of ordering to the other can occur if the ratio of the interactions varies with the specific volume in such a way that it moves through a critical value. Mathematically, this transition occurs because the largest eigenvalue of the interaction matrix becomes triply degenerate at the temperature at which the ratio of the interactions attains the critical value.

The long-range order is measured in terms of long-range order parameters, which are closely related to the sublattice magnetizations. The analog of the perpendicular susceptibility is also calculated.

Qualitative agreement with the molecular field theory is obtained for all those properties of the model which depend on the long-range order. In contrast to the molecular field theory, this model should give valid predictions for quantities depending on short-range order.

INTRODUCTION

In recent years, interest in the study of antiferromagnetism has grown steadily. Extensive experimental investigations have been paralleled by attempts to develop a theory of antiferromagnetism.[1–4] Considerable success has been achieved at very low temperatures, where the spin wave theory provides the necessary mathematical framework.[5–7] At higher temperatures, particularly in the vicinity of the critical points, the situation is far less satisfactory. While the phenomenological molecular field theory serves a useful heuristic purpose, it fails to give a consistent and reliable description of magnetic phenomena near the Curie point.

The Van Vleck molecular field theory starts out from the well-known physical result that short-range forces are responsible for antiferromagnetism. Physically, this clearly implies that the local field acting on each spin is determined by the local magnetic order. The molecular field theory, however, proceeds to set the local field proportional to the magnetization of a sublattice—a magnetization existing only when long-range order is present. This approximation has a measure of validity well below the Curie temperature, where long-range order is actually present; but it fails completely just above the Curie temperature, where local order persists even though long-range order is absent. In the entire region of the transition temperature, it is not always clear which predictions of the theory are consequences of the model and which are due to the approximations.

The purpose of this paper is to adapt the recently developed "sphericalization" technique to the study of antiferromagnetism.[8–12] This is a method which can be applied to a well-defined mathematical model, the "spherical" model of an antiferromagnet, and which permits the calculation of pertinent physical quantities without approximations other than that of letting the number of spins tend to infinity. The results of these calculations will, therefore, be rigorously true for the spherical model. The question still remains whether the spherical model is a good approximation to the physical antiferromagnet. We believe that it merits careful study because of its success in the treatment of ferromagnetism.

THE SPHERICAL MODEL

Let us define our model. Consider a body-centered[13] cubic lattice of N spins, each of which is a classical vector fixed at a point in space but free to rotate about it. We shall assume that there are isotropic antiferromagnetic interactions both between nearest neighbors and between next nearest neighbors. The spins will be required to obey the spherical condition

$$\sum_j \mathbf{S}_j^2 = NS(S+1), \tag{1}$$

where the summation extends over the N spins. This condition will be imposed rather than the more usual quantum condition,

$$\mathbf{S}_j^2 = S(S+1), \quad j=0, 1, 2, \cdots N-1, \tag{2}$$

in order to render the model tractable. The substitution

* This work was supported by the Bureau of Ordnance, Department of the Navy.

[1] J. H. Van Vleck, J. Chem. Phys. **9**, 85–90 (1941).
[2] P. W. Anderson, Phys. Rev. **79**, 705–710 (1950).
[3] J. H. Van Vleck, J. phys. radium **12**, 262 (1951).
[4] J. S. Smart, Phys. Rev. **90**, 55 (1953).
[5] P. W. Anderson, Phys. Rev. **86**, 694 (1952).
[6] Keffer, Kaplan, and Yafet, Am. J. Phys. **21**, 250 (1953).
[7] J. R. Tessman, Phys. Rev. **88**, 1132 (1952).
[8] T. H. Berlin and M. Kac, Phys. Rev. **86**, 821 (1952).
[9] E. W. Montroll, Nuovo cimento **6**, Supplement No. 2, 265 (1949).
[10] M. Lax, J. Chem. Phys. **20**, 1351 (1952).
[11] T. H. Berlin and J. S. Thomsen, J. Chem. Phys. **20**, 1368 (1952).
[12] An entirely different approach to the problem has been adopted by Y. Y. Li, Phys. Rev. **84**, 721 (1951). He uses the cluster method of Bethe, Peierls, and Weiss.
[13] The body-centered cubic lattice appeared to be somewhat easier to handle analytically than the more interesting case of the face-centered cubic.

of the continuum model (1) for the more conventional discrete model (2) leads to spurious effects at very low temperatures. Berlin and Kac[5] have shown, however, that at higher temperatures the spherical model (1) closely approximates the discrete model (2). It should, therefore, be no worse an approximation to the physical situation than is the discrete model (2).

The Hamiltonian of our system is of the form

$$H=-\sum_{jk} B_{jk}\mathbf{S}_j\cdot\mathbf{S}_k-g\beta_0\mathbf{H}\cdot\sum_j \mathbf{S}_j. \tag{3}$$

Here, $\mathbf{S}_j$ is the classical spin vector at the jth lattice point, B_{jk} the interaction coefficient between the jth and the kth spins, g the spectroscopic splitting factor, β_0 the Bohr magneton, and $\mathbf{H}$ the externally applied, uniform, static magnetic field.

Two types of properties of the model are of interest to us: the thermodynamic quantities, and the long-range magnetic order parameters. The former can be obtained from the partition function. The latter are closely related to the magnetizations of the sublattices, and are obtained from the expectation value of the absolute magnitude of a certain linear function of the $\mathbf{S}_j$.

The partition function can be written as

$$Z=\int d^3S_0\int d^3S_1\cdots\int d^3S_{N-1}\times\exp[\sum_{ij} A_{ij}\mathbf{S}_i\cdot\mathbf{S}_j+\mathfrak{K}\cdot\sum_j \mathbf{S}_j]\cdot\delta[\sum_j \mathbf{S}_j^2-NS(S+1)], \tag{4}$$

where

$$A_{ij}=(B_{ij}/kT),\quad \mathfrak{K}=(g\beta_0/kT)\mathbf{H}, \tag{5}$$

the integration is extended over all spin space, and constraint (1) is imposed by the introduction of the Dirac delta function under the integral sign. The multiple integral of (4) can be reduced to a single integral over an auxiliary variable t in the following steps.

(a) Replace the delta function by its Fourier integral representation,

$$\delta\{\textstyle\sum_j S_j^2-NS(S+1)\}=\frac{1}{2\pi i}\int_{\gamma-i\infty}^{\gamma+i\infty} dt\exp\{-t[\textstyle\sum_j S_j^2-NS(S+1)]\}, \tag{6}$$

choose γ large and positive, and interchange the order of integrations.

(b) Introduce the new variables

$$\mathbf{S}_j=\boldsymbol{\sigma}_j+\mathbf{C},\quad \mathbf{C}=\mathbf{C}(t), \tag{7}$$

where $\mathbf{C}$ is chosen so as to eliminate the linear terms from the exponent. The explicit expression for $\mathbf{C}$ is given in Eq. (25).

(c) Then diagonalize the interaction matrix A_{ij} (which will be shown to be symmetric and cyclic) by the real orthogonal transformation T_{jk}. The partition function now becomes

$$Z=\frac{1}{2\pi i}\int_{\gamma-i\infty}^{\gamma+i\infty} dt\varphi(t)\exp[NH^2G(t)+NS(S+1)t], \tag{8}$$

where

$$\varphi(t)=\int d^3u_0\int d^3u_1\cdots\int d^3u_{N-1}\times\exp\{-[\textstyle\sum_j (t-\Lambda_j)u_j^2]\} \tag{9}$$
$$=\pi^{(3N/2)}\prod_{j=0}^{N-1}(t-\Lambda_j)^{-3/2},\quad \gamma>\mathrm{Max}(\Lambda_j).$$

Here, the $\mathbf{u}_j$ are related to the $\boldsymbol{\sigma}_k$ by the transformation equations:

$$\mathbf{u}_j=\textstyle\sum_k T_{kj}\boldsymbol{\sigma}_k. \tag{10}$$

They are the eigenvectors of A_{ij}. The Λ_j are the eigenvalues of A_{ij} and are given by

$$\Lambda_j=(\tilde{T}AT)_{jj}. \tag{11}$$

$G(t)$ is a function of t only, arising from the transformation of (b). Its explicit form will be given later [see Eq. (26)].

One major task of this paper is the evaluation of (8). The other is the calculation of the expectation value of the absolute magnitude of a Cartesian component of the eigenvector $\mathbf{u}_j$. It will be shown later that this expectation value is closely related to the magnetizations of the sublattices.

The actual evaluation of (8) is performed by a saddle point method. In order to be able to investigate the existence and location of the saddle point, we must know the explicit form of the eigenvalues. We shall proceed to deduce them presently.

THE INTERACTION MATRIX

In order to facilitate the interpretation of our results in terms of the sublattice picture, the following scheme is adopted for numbering the spins. The original body centered cubic lattice is divided into two simple cubic sublattices, the A and B sublattices.[3] Then the nearest neighbors of a spin on A are on sublattice B, and *vice versa*. Sublattice A is further subdivided into two face centered cubic sublattices A_1 and A_2, so that all the second nearest neighbors of a spin on A_1 are found on sublattice A_2 and *vice versa*. A similar subdivision is carried out on the B sublattice.

Analytically this subdivision is effected as follows. Assume a set of rectangular axes along the cube edges, and consider the three families of planes (see Fig. 1):

$$\begin{aligned} &-x+y+z=p, \quad p=0,1,2\cdots 2n_1-1;\\ &+x-y+z=q, \quad q=0,1,2\cdots 2n_2-1;\\ &+x+y-z=s, \quad s=0,1,2\cdots 2n_3-1. \end{aligned} \tag{12}$$

It is clear that the position of each spin can be specified by the triad of numbers (p,q,s) as well as by the Car-

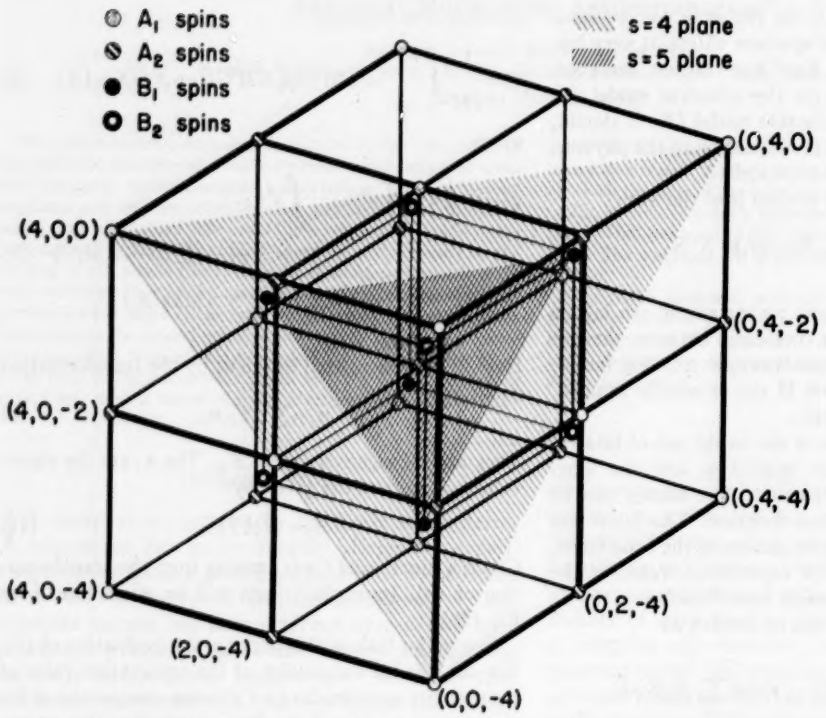

FIG. 1. Some of the $x+y-z=s$ planes.

tesian coordinates (x,y,z). In fact,

$$x=\tfrac{1}{2}(q+s), \quad y=\tfrac{1}{2}(s+p), \quad z=\tfrac{1}{2}(p+q). \tag{13}$$

In order that the Cartesian coordinates of each spin be integers, p,q, and s must be either all odd or all even. It is then possible to choose the sublattices so that

$$\begin{aligned} &s=4m && \text{for the } A_1 \text{ sublattice,}\\ &s=4m+1 && \text{for the } B_1 \text{ sublattice,}\\ &s=4m+2 && \text{for the } A_2 \text{ sublattice,}\\ &s=4m+3 && \text{for the } B_2 \text{ sublattice,} \end{aligned} \tag{14}$$

where m is an integer or zero. The total number of spins in the crystal is evidently

$$2n_1n_2n_3=N. \tag{15}$$

The position of each spin can also be designated by the single number j, where

$$\begin{aligned} &j=s+n_3q+n_2n_3p,\\ &j=0,\ 2,\ \cdots N-2 \text{ for even } p,\ q, \text{ and } s;\\ &j=1+(n_3+n_2n_3),\ 3+(n_3+n_2n_3),\ \cdots\\ &\qquad N-1+(n_3+n_2n_3) \text{ for odd } p,\ q, \text{ and } s. \end{aligned} \tag{16}$$

It is convenient to assume that n_3 is a multiple of 4. Then

$$\begin{aligned} &j=4m && \text{for } A_1,\\ &j=4m+1 && \text{for } B_1,\\ &j=4m+2 && \text{for } A_2,\\ &j=4m+3 && \text{for } B_2. \end{aligned} \tag{17}$$

Since the matrix A_{ij} is defined as the matrix of interactions between nearest neighbors and next-nearest neighbors, it must be symmetric and invariant under a translation of coordinates. Consequently,

$$A_{(i+k)(j+k)}=A_{ij}, \tag{18}$$

$$A_{ij}=A_{ji}. \tag{19}$$

In order to simplify the calculations, we also impose periodic boundary conditions on the crystal lattice by requiring

$$A_{(i+N)j}=A_{ij}. \tag{20}$$

The periodicity condition (20) permits us to change the range of j from the one given in (16) to

$$j=0,\ 1,\ 2,\ \cdots N-1. \tag{21}$$

This merely rearranges the order of appearance of the various terms, but does not affect their value. The resulting matrix has the form

$$A_{ij}=c_{j-i}=c_{i-j}=c_{j-i+N}. \tag{22}$$

The problem of determining the interaction matrix now reduces to that of finding $(j-i)$ for nearest and next-nearest neighbors. Let one spin be situated at (x,y,z) and have the index i, and let the other spin be at (x',y',z') and have the index j. Then Table I gives $(j-i)$ for nearest neighbors and for next-nearest neighbors. For nearest neighbors

$$c_{j-i}=-(J/kT)=-K, \tag{23}$$

and for next-nearest neighbors

$$c_{j-i}=-(J'/kT)=-K'. \tag{24}$$

J and J' are interaction coefficients given by the appropriate superexchange theory (in principle at least). From this table it is clear that the nearest neighbors of a spin on A_1 are distributed equally between B_1 and B_2. The next nearest neighbors of a spin on A_1 are all on A_2. Analogous statements hold for the other sublattices.

Digressing from our subject for a moment, we note that it is now evident that $\mathbf{C}$ in Eq. (7) is

$$\mathbf{C}=\mathfrak{C}/[2(t+8K+6K')], \tag{25}$$

and that $G(t)$ is given by

$$G(t)=\left(\frac{g\beta_0}{2kT}\right)^2\frac{1}{t+8K+6K'}. \tag{26}$$

When the external field is zero, $\mathbf{S}_k=\boldsymbol{\sigma}_k$.

We now return to the determination of the eigenvalues of the interaction matrix. It is shown in the literature[8] that the cyclic, symmetric matrix A_{ij} can be diagonalized by the real orthogonal transformation T_{jk}, where the T_{jk} are given by

$$T_{jk}=(2/N)^{\frac{1}{2}}\cos[(2\pi jk/N)+\tfrac{1}{4}\pi]. \tag{27}$$

The eigenvalues become

$$\Lambda_m=\sum_{k=0}^{N-1}c_k\cos(2\pi km/N)=\Lambda_{N-m}. \tag{28}$$

It is evident from Eq. (28) that all but two of the eigenvalues are doubly degenerate. The two nondegenerate eigenvalues are Λ_0 and $\Lambda_{N/2}$. The degeneracy derives from the symmetry and periodicity of the matrix (A_{ij}). Substituting the values of the c_k, we obtain the explicit form of the eigenvalues.

$$\begin{aligned}\Lambda_m=&-2K[\cos(\Omega_1+\Omega_2+\Omega_3)+\cos(-\Omega_1+\Omega_2+\Omega_3)\\&+\cos(+\Omega_1-\Omega_2+\Omega_3)+\cos(+\Omega_1+\Omega_2-\Omega_3)]\\&-2K'(\cos2\Omega_1+\cos2\Omega_2+\cos2\Omega_3)\\=&-8K\cos\Omega_1\cos\Omega_2\cos\Omega_3\\&-2K'(\cos2\Omega_1+\cos2\Omega_2+\cos2\Omega_3),\end{aligned} \tag{29}$$

$$\begin{aligned}\Omega_1&=(2\pi m/N)(n_2n_3-n_3-1),\\\Omega_2&=(2\pi m/N)(n_2n_3+n_3-1),\\\Omega_3&=(2\pi m/N)(n_2n_3-n_3+1).\end{aligned} \tag{30}$$

THE PARTITION FUNCTION

It will be convenient to define

$$z=t/2K, \tag{31}$$

$$\rho=K'/K=J'/J, \tag{32}$$

$$\lambda_m=\Lambda_m/2K. \tag{33}$$

In this notation, the partition function becomes

$$\begin{aligned}Z=\frac{K}{\pi i}\int_{\gamma'-i\infty}^{\gamma'+i\infty}dz\exp\{&N[H^2G(2Kz)\\&+S(S+1)2Kz]\}\varphi(2Kz),\quad \gamma'>\mathrm{Max}(\lambda_m).\end{aligned} \tag{34}$$

TABLE I. Values of $(j-i)$ for nearest neighbors and next-nearest neighbors.

$x'-x$	$y'-y$	$z'-z$	$p'-p$	$q'-q$	$z'-z$	$(j-i)$
			Nearest neighbors			
1	1	1	1	1	1	$1+n_3+n_2n_3$
−1	1	1	3	−1	−1	$-1-n_3+3n_2n_3$
1	−1	1	−1	3	−1	$-1+3n_3-n_2n_3$
1	1	−1	−1	−1	3	$+3-n_3-n_2n_3$
−1	−1	1	1	1	−3	$-3+n_3+n_2n_3$
−1	1	−1	1	−3	1	$1-3n_3+n_2n_3$
1	−1	−1	−3	1	1	$1+n_3-3n_2n_3$
−1	−1	−1	−1	−1	−1	$-1-n_3-n_2n_3$
			Next-nearest neighbors			
2	0	0	−2	2	2	$+2+2n_3-2n_2n_3$
−2	0	0	2	−2	−2	$-2-2n_3+2n_2n_3$
0	2	0	2	−2	2	$2-2n_3+2n_2n_3$
0	−2	0	−2	2	−2	$-2+2n_3-2n_2n_3$
0	0	2	2	2	−2	$-2+2n_3+2n_2n_3$
0	0	−2	−2	−2	2	$2-2n_3-2n_2n_3$

In order to perform the saddle point integration, it will be necessary to obtain a more manageable expression for $\varphi(t)$ than the one given by Eq. (9). This is done in Appendix I. A tractable expression is obtained for the product in Eq. (9), after first factoring out the terms containing the largest eigenvalue. Let

$$\begin{aligned}\lambda(\omega_1,\omega_2,\omega_3)=&-\cos(\omega_1+\omega_2+\omega_3)-\cos(-3\omega_1+\omega_2+\omega_3)\\&-\cos(\omega_1-3\omega_2+\omega_3)-\cos(\omega_1+\omega_2-3\omega_3)\\&-\rho[\cos2(-\omega_1+\omega_2+\omega_3)+\cos2(\omega_1-\omega_2+\omega_3)\\&+\cos2(\omega_1+\omega_2-\omega_3)],\end{aligned} \tag{35}$$

and

$$\lambda_M=\mathrm{Max}(\lambda_m). \tag{36}$$

Note that $\mathrm{Max}(\lambda_m)=\mathrm{Max}[\lambda(\omega_1,\omega_2,\omega_3)]$. The expression for $\varphi(2Kz)$ can take on one of two forms, depending on the value of ρ. Case I: $\rho<\frac{2}{3}$.

$$\lambda_M=4-3\rho=\lambda', \tag{37}$$

corresponding to

$$m=N/2\quad\text{or}\quad\omega_1=\omega_2=0,\quad\omega_3=\pi. \tag{38}$$

Then

$$\begin{aligned}&\exp[NS(S+1)2Kz]\varphi(2Kz)\\&\quad=(\pi/2K)^{3N/2}\exp[Nf(z)]/(z-\lambda')^{\frac{1}{2}},\end{aligned} \tag{39}$$

where

$$\begin{aligned}f(z)=&S(S+1)2Kz-\tfrac{3}{2}(1/2\pi)^3\\&\times\int_0^{2\pi}d\omega_1\int_0^{2\pi}d\omega_2\int_0^{2\pi}d\omega_3\ln[z-\lambda(\omega_1,\omega_2,\omega_3)].\end{aligned} \tag{40}$$

Case II: $\rho>\frac{2}{3}$.

$$\lambda_M=3\rho=\lambda'', \tag{41}$$

corresponding to

$$\begin{aligned}&m=N/2\quad\text{or}\quad 3N/2,\quad\text{or}\quad\omega_1=\omega_2=0,\\&\omega_3=\pi/2\quad\text{or}\quad 3\pi/2.\end{aligned} \tag{42}$$

The largest eigenvalue is doubly degenerate in this case.

$$\begin{aligned}&\exp[NS(S+1)2Kz]\varphi(2Kz)\\&\quad=(\pi/2K)^{3N/2}\exp[Nf(z)]/(z-\lambda'')^3.\end{aligned} \tag{43}$$

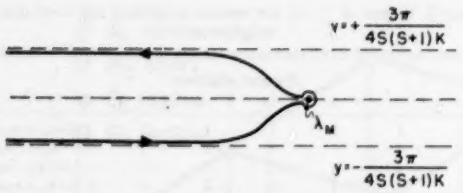

FIG. 2. Path of integration above T_c.

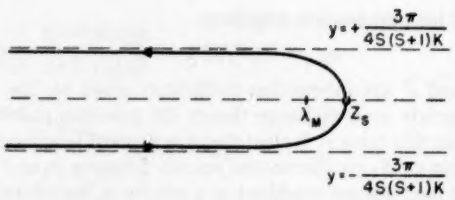

FIG. 3. Path of integration below T_c.

The expression for the partition function becomes, therefore,

$$Z=(1/2i)(\pi/2K)^{3N/2-1}$$
$$\times\int dz\,\exp[NH^2G(2Kz)+Nf(z)]/(z-\lambda_M)^r, \quad (44)$$

where $r=\frac{3}{2}$ in case I and $r=3$ in case II.

At the point $\rho=\frac{2}{3}$, $\lambda'=\lambda''$. The largest eigenvalue becomes triply degenerate. We shall later show that a transition from one kind of antiferromagnetic ordering to another can take place at this point.

The susceptibility per spin at zero field is given by

$$\chi=\frac{kT}{H}\frac{\partial}{\partial H}\left(\frac{\ln Z}{N}\right)$$
$$=2kT\frac{\int dz(z-\lambda_M)^{-r}G(2Kz)\exp[Nf(z)]}{\int dz(z-\lambda_M)^{-r}\exp[Nf(z)]}. \quad (45)$$

We shall be interested in the properties of our model in an infinitesimal applied field. A finite external field may shift the position of the Curie point, or, if the applied field is strong enough to saturate the material, it may prevent the transition from taking place. Most of these effects, however, cannot be observed except when a material with a very low Curie point is placed in a strong field. The influence of a finite field may be calculated by the methods used by Berlin and Thomsen[11] and by Lax.[10] In this paper, however, we shall evaluate (44) and (45) only in the limit of vanishing external field.

The existence and location of the saddle point are determined by the equation

$$f'(z)=0=S(S+1)2K-\tfrac{3}{2}(1/2\pi)^3$$
$$\times\int d\omega_1\int d\omega_2\int d\omega_3[z-\lambda(\omega_1,\omega_2,\omega_3)]^{-1}. \quad (46)$$

Since the integral converges for all values of z, this equation can have a solution z_s only for $K<K_c$, where

$$K_c=\frac{3}{4S(S+1)}(1/2\pi)^3\int d\omega_1\int d\omega_2\int d\omega_3$$
$$\times[\lambda_M-\lambda(\omega_1,\omega_2,\omega_3)]^{-1}. \quad (47)$$

In this temperature region, $T>T_c$; there exists one normal saddle point. It lies on the real axis, to the right of λ_M. The path of integration is deformed into the path of steepest descent given by $\mathrm{Im}[f(z)]=0$ (see Fig. 2). The saddle point integration is carried through in the usual manner, giving

$$Z=\frac{1}{2}\left(\frac{\pi}{2K}\right)^{3N/2-1}\left[\frac{2\pi}{Nf''(z_s)}\right]^{\frac{1}{2}}\frac{\exp[Nf(z_s)]}{(z_s-\lambda_M)^r}. \quad (48)$$

If $K>K_c(T<T_c)$, on the other hand, the saddle point equation has no solution, and no normal saddle point exists. A path of steepest descent can still be found, however, by setting $\mathrm{Im}[f(z)]=0$. Somewhere along this path (which is shown in Fig. 3), $f'(z)$ must have a branch point. This is the point which now replaces the saddle point and from whose vicinity come most of the contributions to the integral. In Appendix II it is shown that in the vicinity of the point λ_M, $f'(z)$ takes the form

$$f'(z)=2S(S+1)(K-K_c)+(z-\lambda_M)^{\frac{1}{2}}F(0),\ F(0)>0; \quad (49)$$

and

$$f(z)=f(\lambda_M)+2S(S+1)(K-K_c)(z-\lambda_M)$$
$$+\tfrac{2}{3}(z-\lambda_M)^{\frac{1}{2}}F(0). \quad (50)$$

Using the first two terms of (50) and remembering the contour integral representation of the gamma function, one obtains

$$Z=\pi\left(\frac{\pi}{2K}\right)^{3N/2-1}\frac{[2S(S+1)(K-K_c)N]^{r-1}}{\Gamma(r)}$$
$$\times\exp[Nf(\lambda_M)]. \quad (51)$$

The evaluation of (45) is carried out in the same manner, remembering that $G(2Kz)$ is a slowly varying function in the region of the saddle point (or the branch point). The result is

$$\chi=2kTG(2Kz_s), \quad \text{above the Curie point,} \quad (52)$$

and

$$\chi=2kTG(2K\lambda_M), \quad \text{below.} \quad (53)$$

THE THERMODYNAMIC PROPERTIES AND THE NATURE OF THE PHASE TRANSITIONS

We shall define F and U, respectively, as limiting values of the Helmholtz free energy and the internal

energy per spin as N approaches infinity. Then,

$$-F/kT=\tfrac{3}{2}\ln(\pi/2K)+f(z'), \tag{54}$$

where $z'=z_s$ above the Curie point and $z'=\lambda_M$ below.

Before proceeding with the calculation, we must note that J and J' are functions of the interatomic distances in the solid. They are, therefore, functions of the specific volume, and possibly also explicit functions of the temperature. In the following, the calculation will be simplified by the assumption that J and J' are explicit functions of the specific volume only. The specific volume itself, of course, is a function of the temperature and pressure. The implicit dependence of ρ on the temperature gives rise to the possibility of transition from one kind of antiferromagnetic ordering to another. It has been demonstrated already that the analytical form of λ_M changes at $\rho=\frac{2}{3}$. This will be shown to lead to a transition of the first order at $\rho=\frac{2}{3}$. Such a transition can occur in a given substance only if the interaction coefficients J and J' vary with the specific volume in such a way that ρ passes through the value $\frac{2}{3}$ for some temperature below the Curie point. In this section, we shall study the thermodynamic characteristics of the transitions. In the next section, we shall investigate the changes in magnetic order which occur at the transition temperatures.

The internal energy is

$$U=T^2\left[\frac{d}{dT}\left(-\frac{F}{T}\right)\right]_v=\tfrac{3}{2}kT-2S(S+1)Jz', \tag{55}$$

where we have made use of the fact that above the Curie point $f'(z_s)=0$,[14] because of the existence of the saddle point; and below the Curie point,

$$(d\lambda_M/dT)_v=0. \tag{56}$$

From (54) we obtain for the pressure

$$\frac{p}{kT}=\left[\frac{\partial}{\partial v}\left(\frac{-F}{kT}\right)\right]_T=\frac{\partial f(z')}{\partial z'}\left(\frac{\partial z'}{\partial v}\right)_T+\frac{\partial f(z')}{\partial \rho}\left(\frac{\partial \rho}{\partial v}\right)_T+\left(\frac{\partial J}{\partial v}\right)_T\left[\frac{2S(S+1)z'}{kT}-\frac{3}{2J}\right]. \tag{57}$$

The order of the Curie point transition is now readily established. We note that the right-hand member of (57) and its first partial derivatives are continuous through the Curie point. From (54) and (55), we can easily obtain the entropy and show that it and its first partials are also continuous through the Curie point. The second partials are discontinuous, however. Thus the Curie point transition is of the third order. It is clear, therefore, that the inclusion of the next-nearest neighbor interaction in the Hamiltonian has not changed the order of the Curie point transition.

The other transition point (whenever it occurs), however, exhibits quite different characteristics. Here the first term on the right-hand side of (57) is not zero at the transition temperature, for no saddle point exists in this temperature region. It is now easy to show that this transition is of the first order by demonstrating that p, v, and T cannot all be continuous through the transition. This is established by supposing that p, v, T are all continuous in Eq. (57) and considering the increment in the right-hand member as we pass through the transition temperature. Since this increment must be zero, we have

$$0=\left[2KS(S+1)-\frac{3}{2}\left(\frac{1}{2\pi}\right)^3\int_0^{2\pi}d\omega_1\int_0^{2\pi}d\omega_2\times\int_0^{2\pi}\frac{d\omega_3}{z'-\lambda(\omega_1,\omega_2,\omega_3)}\right]_{\rho=2/3}\left(\frac{d\rho}{dv}\right)_{\rho=2/3}. \tag{58}$$

Since no saddle point exists in this region, the term in the bracket cannot vanish. We have, therefore,

$$(d\rho/dv)_{\rho=2/3}=0. \tag{59}$$

This is obviously a condition which cannot be expected to hold in all materials under all circumstances. Thus it is clear that, in general, p, v, and T cannot all remain constant through this order-order transition. The transition is, therefore, a first order transition.

One other macroscopic property of the model which can be readily obtained is the susceptibility corresponding to the equilibrium configuration of the spin system in a vanishingly small external field. Since no anisotropy has been introduced into the model, the spins tend to assume fixed orientations with respect to each other, but not with respect to a fixed direction in space. When a vanishingly small external magnetic field is applied, the intrinsic magnetizations retain their orientation with respect to each other, but the entire configuration rotates to assume minimum energy. In the molecular field theory, this corresponds to the perpendicular susceptibility. From (52), (53), and (26),

$$\chi=2kTG(2Kz')=\frac{g^2\beta_0^2}{4J}\frac{1}{(z'+4+3\rho)}. \tag{60}$$

From (46), it is clear that far above the Curie point,

$$T=4S(S+1)Jz'/3k. \tag{61}$$

We write, therefore,

$$\chi=\frac{S(S+1)g^2\beta_0^2}{3k}\cdot\frac{1}{\tau+\theta}, \tag{62}$$

where

$$\tau=4S(S+1)Jz'/3k, \tag{63}$$

and

$$\theta=4S(S+1)(4J+3J')/3k. \tag{64}$$

At very high temperatures, $\tau\to T$. Below the Curie point, τ and θ depend on the temperature only through

[14] We shall continue to use the notation $f'(z)$ for $(df/dz)_{\rho,K}$.

the temperature dependence of J and J'. At $\rho=\frac{2}{3}$, the susceptibility at constant pressure suffers a discontinuous change because of the jump in z'.

LONG-RANGE ORDER PARAMETERS AND SUBLATTICE MAGNETIZATIONS

The commonly used measure of long-range order is the sublattice magnetization per spin, defined by the equation

$$\mathfrak{y}(p)=\frac{4\beta_0 g}{N}\sum_j \mathbf{S}_j, \quad p=A_1, B_1, A_2, B_2, \tag{65}$$

j summed over the p'th sublattice.

The expectation values of these sublattice magnetizations are obviously zero, for our model is spherically symmetric. The calculation of the expectation values of the absolute magnitudes of the $\mathfrak{y}(p)$ is not feasible. Consequently, it is inconvenient to use the sublattice magnetizations directly as a measure of long-range order.

Below the Curie point, the model is predominantly in one eigenstate, the eigenstate of lowest energy, which determines the prevailing long-range magnetic order. The corresponding eigenvector may be expressed as a linear combination of the sublattice magnetizations. It is a simple matter to calculate the expectation value of the absolute magnitude of a Cartesian component of an eigenvector of the interaction matrix. These quantities are also easily obtainable from molecular field theory, and we shall therefore use them as our long-range order parameters.

Our first task is, then, to express some of the eigenvectors in terms of the sublattice magnetizations. Clearly,

$$\frac{\mathbf{u}_0}{\sqrt{N}}=\frac{1}{N}\sum_{l=0}^{N-1}\boldsymbol{\sigma}_l$$

$$=\frac{1}{4g\beta_0}[\mathfrak{y}(A_1)+\mathfrak{y}(A_2)+\mathfrak{y}(B_1)+\mathfrak{y}(B_2)], \tag{66}$$

$$\frac{\mathbf{u}_{N/2}}{\sqrt{N}}=\frac{1}{N}\sum_{l=0}^{N-1}\boldsymbol{\sigma}_l\cos(\pi l)$$

$$=\frac{1}{4g\beta_0}[\{\mathfrak{y}(A_1)+\mathfrak{y}(A_2)\}-\{\mathfrak{y}(B_1)+\mathfrak{y}(B_2)\}]. \tag{67}$$

From (28) we recall that the two eigenvalues $\lambda_{N/4}$ and $\lambda_{3N/4}$ are degenerate. Thus, any linear combination of the eigenvectors $\mathbf{u}_{N/4}$ and $\mathbf{u}_{3N/4}$ is an eigenvector of the interaction matrix. We use, therefore, the linear combinations

$$\frac{1}{\sqrt{N}}\mathbf{v}_{N/4}\equiv\frac{1}{\sqrt{(2N)}}(\mathbf{u}_{3N/4}+\mathbf{u}_{N/4})$$

$$=\frac{\sqrt{2}}{N}\sum_{l=0}^{N-1}\boldsymbol{\sigma}_l\cos\left(\frac{\pi l}{2}\right)=\frac{\sqrt{2}}{4\beta_0 g}[\mathfrak{y}(A_1)-\mathfrak{y}(A)_2], \tag{68}$$

$$\frac{1}{\sqrt{N}}\mathbf{v}_{2N/4}=\frac{1}{\sqrt{(2N)}}(\mathbf{u}_{3N/4}-\mathbf{u}_{N/4})$$

$$=\frac{\sqrt{2}}{N}\sum_{l=0}^{N-1}\boldsymbol{\sigma}_l\sin\left(\frac{\pi l}{2}\right)=\frac{\sqrt{2}}{4\beta_0 g}[\mathfrak{y}(B_1)-\mathfrak{y}(B_2)] \tag{69}$$

which have a simple meaning in terms of the sublattice magnetizations. Defining $\mathbf{v}_0=\mathbf{u}_0$ and $\mathbf{v}_{N/2}=\mathbf{u}_{N/2}$, we introduce the long-range order parameters L_i ($i=0$, $N/4$, $N/2$, $3N/4$), where

$$L_i=\frac{\int d^3\sigma_0\cdots\int d^3\sigma_{N-1}\left|\frac{1}{\sqrt{N}}v_{ix}\right|\delta(\sum_j \boldsymbol{\sigma}_j{}^2-NS(S+1))\exp(\sum_{jk}A_{jk}\boldsymbol{\sigma}_j\cdot\boldsymbol{\sigma}_k)}{\int d^3\sigma_0\cdots\int d^3\sigma_{N-1}\delta(\sum_j \boldsymbol{\sigma}_j{}^2-NS(S+1))\exp(\sum_{jk}A_{jk}\boldsymbol{\sigma}_j\cdot\boldsymbol{\sigma}_k)}=\left\langle\left|\frac{1}{\sqrt{N}}v_{ix}\right|\right\rangle. \tag{70}$$

Note that we are considering the case where no external field is applied.

By methods similar to those used in the evaluation of the partition function,[8] we reduce (70) to the form

$$L_i(2\pi K)^{\frac{1}{2}}\int_{\gamma'-i\infty}^{\gamma'+i\infty}dz(z-\lambda_M)^{-\tau}\exp[Nf(z)]$$

$$=\frac{1}{\sqrt{N}}\int_{\gamma'-i\infty}^{\gamma'+i\infty}dz(z-\lambda_M)^{-\tau}(z-\lambda_i)^{-1/2}\exp[Nf(z)]. \tag{71}$$

It is now easy to show that above the Curie point, L_i goes to zero as N tends toward infinity. Below the Curie point, there are two cases to be considered. If $i\neq M$,

$$L_i=\lim_{N\to\infty}[2\pi KN(\lambda_M-\lambda_i)]^{-1/2}, \tag{72}$$

this quantity vanishes in the limit. On the other hand, if $i=M$,

$$L_M=\frac{\Gamma(\tau)}{\Gamma(\tau+\frac{1}{2})}\left[\frac{S(S+1)}{\pi}\left(1-\frac{T}{T_c}\right)\right]^{\frac{1}{2}}. \tag{73}$$

Above the Curie temperature there is no long-range order. This follows from the fact that the L_i are all zero.

$$L_0=0=\frac{1}{4g\beta_0}\langle|\mu_x(A_1)+\mu_x(A_2)+\mu_x(B_1)+\mu_x(B_2)|\rangle,$$

$$L_{N/2}=0=\frac{1}{4g\beta_0}\langle|\mu_x(A_1)+\mu_x(A_2)-\mu_x(B_1)-\mu_x(B_2)|\rangle, \tag{74}$$

$$L_{N/4}=0=\frac{\sqrt{2}}{4g\beta_0}\langle|\mu_x(A_1)-\mu_x(A_2)|\rangle;$$

$$L_{3N/4}=0=\frac{\sqrt{2}}{4g\beta_0}\langle|\mu_x(B_1)-\mu_x(B_2)|\rangle.$$

According to the sublattice picture, this implies that all the sublattice magnetizations vanish.

Below the Curie temperature, there are two cases to be distinguished. In Case I, $\rho<\frac{2}{3}$, and only $L_{N/2}\neq 0$.

$$L_0=L_{N/4}=L_{3N/4}=0,$$

$$L_{N/2}=\frac{1}{2}\left[S(S+1)\left(1-\frac{T}{T_c}\right)\right]^{\frac{1}{2}}$$

$$=\frac{1}{4g\beta_0}\langle|\mu_x(A_1)+\mu_x(A_2)-\mu_x(B_1)-\mu_x(B_2)|\rangle. \tag{75}$$

In terms of the sublattice picture, this implies antiferromagnetic ordering of the first kind. This means that most of the spins on the A sublattice are parallel and most of the spins on the B sublattice are parallel, but the A spins are antiparallel to the B spins. In Case II, on the other hand, $\rho>\frac{2}{3}$ and $L_{N/4}=L_{3N/4}\neq 0$. In fact,

$$L_0=L_{N/2}=0,$$

$$L_{N/4}=\frac{16}{15\pi}\left[S(S+1)\left(1-\frac{T}{T_c}\right)\right]^{\frac{1}{2}}$$

$$=\frac{\sqrt{2}}{4g\beta_0}\langle|\mu_x(A_1)-\mu_x(A_2)|\rangle, \tag{76}$$

$$L_{3N/4}=\frac{16}{15\pi}\left[S(S+1)\left(1-\frac{T}{T_c}\right)\right]^{\frac{1}{2}}$$

$$=\frac{\sqrt{2}}{4g\beta_0}\langle|\mu_x(B_1)-\mu_x(B_2)|\rangle.$$

The interpretation is that ordering of the second kind prevails. The net magnetization of the A sublattice and the net magnetization of the B sublattice vanish. The magnetization of the A_1 sublattice is equal and opposite to the magnetization of the A_2 sublattice, and similarly for the B_1 and B_2 sublattices. The magnetizations of A_1 and B_1 (or B_2) appear to be completely uncorrelated.

DISCUSSION

The range of validity of the classical spherical model of the antiferromagnet is bounded at the low temperature end by the omission of quantum effects. The quantum conditions have been violated in two ways: On the one hand, the operator $\mathbf{S}_i\cdot\mathbf{S}_j$ has been treated as a c number; on the other hand, the use of the spherical condition means that the quantization of each $\mathbf{S}_j^2$ has been relaxed. Practically, this limitation is probably less serious in the case of antiferromagnetism than it is in ferromagnetism. In ferromagnetism, interest is usually centered on the behavior of the saturation magnetization, a quantity best observed at very low temperatures where quantum effects are paramount. In antiferromagnetism, on the other hand, interest is usually centered on the behavior of the susceptibility in the vicinity of the transition temperature where quantum effects are probably less important and the sphericalization procedure may be expected to hold.

The spherical model combines into one formalism many of the advantages of the molecular field theory and the Bethe-Peierls-Weiss-Li (B.P.W.L.) cluster theory. It retains much of the simplicity of the molecular field theory below the Curie point and yet it holds in the region of the transition temperature and above. It predicts a transition of higher order at the Curie point, the local order smoothing the way for the onset of long-range order. A more thorough investigation of the local order can be easily performed by calculating the correlation function $\langle\mathbf{S}_i\cdot\mathbf{S}_j\rangle$. The onset of local order well above the Curie point is predicted by the spherical model and the B.P.W.L. theory, and is confirmed by experiment, but is not envisaged by the molecular field theory.

Below the Curie point, long-range order parameters L_i are introduced to furnish a quantitative measure of long-range order. The L_i are expressed in terms of the sublattice magnetizations for convenience in comparison with molecular field theory. It should be noted, of course, that the sublattice concept facilitates interpretation, but is not essential to the spherical model.

Two kinds of antiferromagnetic ordering can occur below the Curie point. A first-order transition between the two kinds of order is predicted, in agreement with the thermodynamic theory of Smart.[4]

The susceptibility corresponding to the equilibrium configuration of the spin system in a vanishingly small external field has been calculated on the spherical model. It agrees qualitatively with the perpendicular susceptibility of the molecular field theory, to which it corresponds. Below the Curie temperature it assumes a constant value for a given kind of long-range order, if the interaction coefficients J and J' do not vary with the volume. Above the Curie temperature, it follows a modified Curie-Weiss law. The analog of the parallel susceptibility cannot be calculated from an isotropic model with a single spherical constraint.

The qualitative features of the sphericalized antiferromagnet agree well with the available experimental information.[1,3,4] A quantitative comparison with the experimental data was not attempted because the authors are not aware of any data on body-centered antiferromagnets. For the same reason we have not carried through the discussion of the case of one ferromagnetic and one antiferromagnetic interaction, or the evaluation of the integral for K_c. The latter quantity is required for the numerical calculation of (θ/T_c), a ratio convenient for the quantitative comparison of theory and experiment. The present theory appears to be easily adaptable to the somewhat more complicated case of a face-centered cubic lattice, for which experimental data are available.

ACKNOWLEDGMENTS

We are indebted to Professor T. H. Berlin and Professor E. W. Montroll and to Dr. J. S. Smart and Dr. R. K. Wangsness for informative and stimulating discussions. This research would not have been accomplished without the encouragement of Dr. F. T. McClure and Dr. C. K. Jen.

APPENDIX I

In part I of this appendix, we shall obtain the maximum eigenvalues of the interaction matrix. In part II, we derive a tractable expression for $\varphi(t)$.

Part I. It is clear from part II that the Ω's may be regarded as independent variables. We therefore determine λ_{max}[15] by regarding the Ω's as continuous variables, and verify that λ_{max} actually occurs for an integral m. It is now clear from Eq. (29) that the equations $\partial\lambda/\partial\Omega_r=0$, $(r=1,2,3)$, become

$$\begin{aligned}
&\sin\Omega_1[\cos\Omega_2\cos\Omega_3+\rho\cos\Omega_1]=0,\\
&\sin\Omega_2[\cos\Omega_3\cos\Omega_1+\rho\cos\Omega_2]=0,\\
&\sin\Omega_3[\cos\Omega_1\cos\Omega_2+\rho\cos\Omega_3]-0.
\end{aligned} \tag{A-I-1}$$

The two roots which can be absolute maxima correspond to the following two cases:

Case I

$$\cos\Omega_1=\cos\Omega_2=\cos\Omega_3=-1.$$

The maximum eigenvalue for this case (λ') is given by

$$\lambda'=4-3\rho. \tag{A-I-2}$$

To determine the value of m corresponding to this case, note that each Ω is an odd multiple of π, i.e., $\Omega_1=(2\nu_1+1)\pi$, $\Omega_2=(2\nu_2+1)\pi$, $\Omega_3=(2\nu_3+1)\pi$ where ν_1, ν_2, ν_3, are integers or zero. From Eq. (30),

$$m=(N/4\pi)(\Omega_3-\Omega_1). \tag{A-I-3}$$

For this case, the above equation can be rewritten in terms of the ν's as

$$m=(N/2)(\nu_3-\nu_1). \tag{A-I-4}$$

It is evident that the two possible values of $\nu_3-\nu_1$ which are consistent with $0\leq m\leq N-1$ are the values 0 and 1. The unique value of m for which the three conditions $(\cos\Omega_1=\cos\Omega_2=\cos\Omega_3=-1)$ are satisfied is readily determined by substituting the above possibilities into Eq. (30). The result is that the value of m corresponding to $\lambda'=4-3\rho$ is

$$m=N/2. \tag{A-I-5}$$

Case II

$$\cos\Omega_1=\cos\Omega_2=\cos\Omega_3=0.$$

The maximum eigenvalue for this case (λ'') is given by

$$\lambda''=3\rho. \tag{A-I-6}$$

To determine the value of m for which these conditions on $\cos\Omega$ are satisfied, note that each Ω must be an odd half-integer multiple of π, i.e.,

$$\Omega_1=(\nu_1+\tfrac{1}{2})\pi,\quad \Omega_2=(\nu_2+\tfrac{1}{2})\pi,$$

and

$$\Omega_3=(\nu_3+\tfrac{1}{2})\pi.$$

It follows from Eq. (A-I-3) that

$$m=\frac{N}{4}(\nu_3-\nu_1), \tag{A-1-7}$$

which limits $(\nu_3-\nu_1)$ to the possible values 0, 1, 2, 3. It follows from Eq. (30) that only the values $\nu_3-\nu_1=1$, 3 are consistent with (A-I-6), so that the values of m corresponding to case II are

$$m=N/4, \tag{A-I-8}$$

and

$$m=3N/4. \tag{A-I-9}$$

The two roots are plotted in Fig. 4. From this plot it is clear that for $\rho<\frac{2}{3}$, λ' is the largest eigenvalue while for $\rho>\frac{2}{3}$, λ'' is the largest. The two eigenvalues are degenerate when $\rho=\frac{2}{3}$.

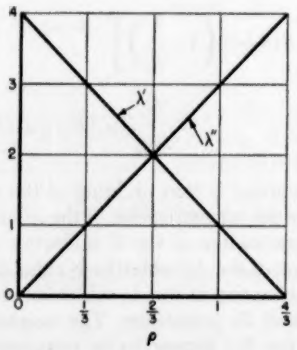

FIG. 4. The roots.

[15] See Eq. (36).

Part II

For the purpose of performing the saddle point integration in the text, it is convenient to put the rapidly varying part of the integrand into the exponent. Consider the product

$$\prod_{m=0}^{N-1}(t-\Lambda_m)^{-3/2}=(2K)^{-3N/2}(z-\lambda_M)^{-r}\times\exp\left(\frac{-3}{2}\sum_{m=0}^{N-1}{}'\ln[z-\lambda_m]\right), \quad \text{(A-I-10)}$$

where the prime on the sum indicates that the maximum eigenvalue(s) is (are) omitted from the summand. The reason for treating the term(s) containing the maximum eigenvalue separately is that the summation in the exponent will be replaced by an integration. In this limiting process, each term in the sum loses its identity: the density of terms is what counts. Consequently, this replacement can be legitimate only if the summand does not contain terms whose singularities lie arbitrarily close to the path of integration. Since (as is readily shown) the separation between adjacent eigenvalues near λ_M is of order $N^{-2/3}$, the path of steepest descents can not come arbitrarily close to any singularity except λ_M, and this term(s) is (are), therefore, removed from the summand before converting it to an integral.

We write m in the form

$$m=p_1+n_1p_2+n_1n_2p_3, \quad p_1=0,\,1,\,2\cdots 2n_1-1,\quad p_2=0,\,1,\,2\cdots 2n_2-1,\quad p_3=0,\,1,\,2\cdots 2n_3-1,\quad \text{(all } p\text{'s even or all odd)}; \quad \text{(A-I-11)}$$

and introduce the variables

$$\omega_r=\pi p_r/n_r, \quad r=1,\,2,\,3, \quad \text{(A-I-12)}$$

which will become continuous as N approaches infinity. It is clear that since the p's are independent, the ω's, too, are independent variables.

For convenience, we shall let n_2 be even. Then

$$\Omega_1=\omega_1-\omega_2-\omega_3+\pi(n_2p_3+p_2-p_3)-\frac{\omega_1}{n_2}-\frac{\omega_2}{n_3}-\frac{\omega_1}{n_2n_3},$$

$$\Omega_2=\omega_1+\omega_2-\omega_3+\pi(n_2p_3+p_2+p_3)+\frac{\omega_1}{n_2}-\frac{\omega_2}{n_3}-\frac{\omega_1}{n_2n_3}, \quad \text{(A-I-13)}$$

$$\Omega_3=\omega_1-\omega_2+\omega_3+\pi(n_2p_3+p_2-p_3)-\frac{\omega_1}{n_2}+\frac{\omega_2}{n_3}+\frac{\omega_1}{n_2n_3}.$$

The sum in the exponent can now be rewritten in the form

$$\frac{1}{N}\sum_{m=0}^{N-1}{}'\ln(z-\lambda_m)=\frac{1}{2n_1n_2n_3}\sum_{p_1=0}^{2n_1-2}\sum_{p_2=0}^{2n_2-2}\sum_{p_3=0}^{2n_3-2}{}'\ln[z-\lambda(\omega_1,\omega_2,\omega_3)]_{\text{even } p\text{'s only}}+\frac{1}{2n_1n_2n_3}\sum_{p_1=1}^{2n_1-1}\sum_{p_2=1}^{2n_2-1}\sum_{p_3=1}^{2n_3-1}\ln[z-\lambda(\omega_1,\omega_2,\omega_3)]_{\text{odd } p\text{'s only}}. \quad \text{(A-I-14)}$$

As $n_1\to\infty$, $n_2\to\infty$, $n_3\to\infty$, this becomes

$$\left(\frac{1}{2\pi}\right)^3\int_0^{2\pi}d\omega_1\int_0^{2\pi}d\omega_2\int_0^{2\pi}d\omega_3\ln[z-\lambda(\omega_1,\omega_2,\omega_3)], \quad \text{(A-I-15)}$$

where

$$\lambda(\omega_1,\omega_2,\omega_3)=-\cos(\omega_1+\omega_2+\omega_3)-\cos(-3\omega_1+\omega_2+\omega_3)-\cos(\omega_1-3\omega_2+\omega_3)-\cos(\omega_1+\omega_2-3\omega_3)-\rho[\cos2(-\omega_1+\omega_2+\omega_3)+\cos2(\omega_1-\omega_2+\omega_3)+\cos2(\omega_1+\omega_2-\omega_3)]. \quad \text{(A-I-16)}$$

Thus,

$$e^{NS(S+1)2Kz}\varphi(2Kz)=\left(\frac{\pi}{2K}\right)^{3N/2}\frac{e^{Nf(z)}}{(z-\lambda_M)^r}, \quad \text{(A-I-17)}$$

where

$$f(z)=S(S+1)2Kz-\frac{3}{2}\left(\frac{1}{2\pi}\right)^3\int_0^{2\pi}d\omega_1\int_0^{2\pi}d\omega_2\int_0^{2\pi}d\omega_3\times\ln[z-\lambda(\omega_1,\omega_2,\omega_3)]. \quad \text{(A-I-18)}$$

APPENDIX II

Our problem is to determine the behavior of $f(z)$ in the neighborhood of the point $z=+\lambda_M$. This can be done without actually evaluating the integral. We shall introduce the notation

$$\Delta=(z-\lambda_M)^{\frac{1}{2}}, \quad \text{(A-II-1)}$$

positive and real for $z-\lambda_M>0$.

$$D(\omega_1,\omega_2,\omega_3)=[\lambda_M-\lambda(\omega_1,\omega_2,\omega_3)]^{\frac{1}{2}}.$$

Then

$$\frac{1}{z-\lambda}=\frac{1}{\Delta^2+D^2}=\frac{1}{D^2}+\frac{i\Delta}{2}\left\{\frac{1}{D^2(D-i\Delta)}-\frac{1}{D^2(D+i\Delta)}\right\}=\frac{1}{\lambda_M-\lambda}+\frac{i\Delta}{2}\left\{\frac{1}{D^2(D-i\Delta)}-\frac{1}{D^2(D+i\Delta)}\right\}, \quad \text{(A-II-2)}$$

$$f'(z)=2S(S+1)K-\frac{3}{2}\left(\frac{1}{2\pi}\right)^3\int_0^{2\pi}d\omega_1\int_0^{2\pi}d\omega_2 \times\int_0^{2\pi}d\omega_3\frac{1}{\lambda_M-\lambda(\omega_1,\omega_2,\omega_3)} -\frac{3i\Delta}{4}\left(\frac{1}{2\pi}\right)^3\int_0^{2\pi}d\omega_1\int_0^{2\pi}d\omega_2\int_0^{2\pi}d\omega_3 \times\left[\frac{1}{D^2(D-i\Delta)}-\frac{1}{D^2(D+i\Delta)}\right] =2S(S+1)(K-K_c)+\Delta F(\Delta). \quad \text{(A-II-3)}$$

Here,

$$F(\Delta)=\frac{3}{4}\left(\frac{1}{2\pi}\right)^3(-i)\int d\omega_1\int d\omega_2\int d\omega_3 \times\left[\frac{1}{D^2(D-i\Delta)}-\frac{1}{D^2(D+i\Delta)}\right]. \quad \text{(A-II-4)}$$

We can readily show that $F(0)\equiv\lim_{\Delta\to 0^+}F(\Delta)\neq 0$, and we can also determine its sign. This will suffice to indicate that $f'(z)$ has a branch point at $+\lambda_M$, and also to show the direction of the path of integration.

We note that the largest contribution to the integral in (A-II-4) will come from the region where D^2 is very small. Since the zero of D^2 is also its minimum value, we expand D^2 about this point in a Taylor's series in $(\omega_1-\omega_1^0)$, $(\omega_2-\omega_2^0)$, and $(\omega_3-\omega_3^0)$, retaining only the first terms, which give a positive definite quadratic form in the $(\omega_i-\omega_i^0)$'s. We now introduce the spherical coordinates R, θ, and φ, defined by the equations

$$\begin{aligned}\omega_1-\omega_1^0&=R\sin\theta\cos\varphi,\\ \omega_2-\omega_2^0&=R\sin\theta\sin\varphi,\\ \omega_3-\omega_3^0&=R\cos\theta.\end{aligned} \quad \text{(A-II-5)}$$

The quadratic form now factors into

$$D^2=R^2\Phi^2(\theta,\varphi), \quad \text{(A-II-6)}$$

where Φ is positive for all values of θ and φ. We first perform the integration over R. This gives

$$F(\Delta)\doteq\frac{-3i}{4}\left(\frac{1}{2\pi}\right)^3\int_0^{\pi}d\theta\sin\theta\int_0^{2\pi}d\varphi\Phi^{-3}(\theta,\varphi) \times\int_0^{R_0}R^2dR\cdot\left[\frac{1}{R^2(R-i\Delta/\Phi)}-\frac{1}{R^2(R+i\Delta/\Phi)}\right] =-\frac{3i}{4}\left(\frac{1}{2\pi}\right)^3\int_0^{\pi}d\theta\sin\theta\int_0^{2\pi}d\varphi\Phi^{-3}(\theta,\varphi) \times\left[\ln\left(\frac{R_0-i\Delta/\Phi}{R_0+i\Delta/\Phi}\right)+\pi i\right], \quad \text{(A-II-7)}$$

where R_0 is the upper limit of the validity of the approximate expansion. If we now let $\Delta\to 0$, we obtain

$$F(0)=\frac{3\pi}{4}\left(\frac{1}{2\pi}\right)^3\int_0^{2\pi}d\varphi\int_0^{\pi}d\theta\frac{\sin\theta}{\Phi^3(\theta,\varphi)}>0. \quad \text{(A-II-8)}$$

The first three terms in the expansion of $f(z)$ about $+\lambda_M$ are, therefore,

$$f(z)=f(+\lambda_M)+2S(S+1)(K-K_c)(z-\lambda_M) +\tfrac{2}{3}(z-\lambda_M)^{\frac{3}{2}}F(0), \quad \text{(A-II-9)}$$

where $F(0)>0$.

Setting $\mathrm{Im}[f(z)]=0$, we can now find the path of integration near the branch point of the integrand of Eq. (44).

Periodic Impurities in a Periodic Lattice

EDWARD H. KERNER
Physics Department, University of Buffalo, Buffalo, New York
(Received March 5, 1954; revised manuscript received April 20, 1954)

Because binary delta-function lattices of the Kronig-Penney type which have been previously studied are incapable of describing several important features of real crystals, the eigenvalue problem for a periodic linear chain $\cdots A(BB\cdots BB)A(BB\cdots BB)\cdots$ of arbitrary square-well, A and B atoms of an arbitrary concentration is taken up and solved. The methods used are generalizable to other binary or multi-nary chains. It is shown that a theorem of Saxon and Hutner and of Luttinger relating to the preservation of the common forbidden energies of pure A and pure B lattices in a mixed A, B lattice is peculiar to their delta-function representations of A and B, and is without general validity.

THE problem of the band structure of a one-dimensional binary alloy of A and B atoms has been treated by Saxon and Hutner[1] and Luttinger[2] using a Kronig-Penney model in which A and B are represented by delta-function potentials of different strengths. Hoffman[3] also has discussed some of the properties of the linear binary alloy using another model. As has been remarked by Allen,[4] a delta-function lattice (as well as even a sinusoidal lattice) lacks important qualitative characteristics found in real crystals, while square-well lattices possess these characteristics. In this note we solve (by techniques essentially different from those that have been previously used) the eigenvalue problem for a periodic chain $\cdots A(BB\cdots BB)A(BB\cdots BB)\cdots$ of arbitrary "impurity" square wells A and "purity" wells B in the arbitrary ratio $B/A=\nu$, toward the end of supplying as realistic a picture of binary solid solutions as a one-dimensional model will permit. The methods used will be seen to be applicable to more general binary mixtures than the one treated, and to multi-nary mixtures of any specified type. An interesting consequence of the results is that the theorem of Saxon-Hutner-Luttinger—to the effect that the forbidden energies common to pure A and pure B lattices are forbidden also in any substitutional alloy of A's and B's—has no general validity, but is peculiar to delta-function A's and B's.

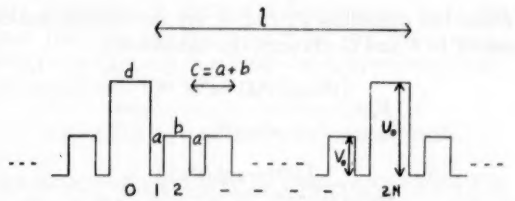

FIG. 1. Generalized one-dimensional Kronig-Penney type of lattice for the chain $\cdots A(BB\cdots BB)A(BB\cdots BB)\cdots$ of ν purity (B) atoms (potential hills of height V_0) between successive impurity (A) atoms (potential hills of height U_0). The numbers 0, 1, $\cdots$, $2N$ label the regions in which the wave function is specified in the first equation in the text. The origin of x coordinates is at the juncture of regions 0 and 1.

Consider the motion of an electron in the lattice illustrated in Fig. 1. This lattice has the periodicity l of the impurities, so that by Floquet's theorem we look for solutions of the wave equation of the form $\psi=\varphi(x)\exp(ikx)$ with $\varphi(x+l)=\varphi(x)$. In region s we have

$$\varphi(x)=a_s\exp(\alpha_s x)+b_s\exp(\beta_s x),$$

where

$$\begin{matrix}\alpha_s=i(\epsilon_0-k)\\ \beta_s=-i(\epsilon_0+k)\end{matrix}\quad\text{odd } s;\qquad \begin{matrix}\alpha_s=\epsilon_1-ik\\ \beta_s=-(\epsilon_1+ik)\end{matrix}\quad\text{even } s,$$

$$\text{but}\quad \begin{matrix}\alpha_0=\alpha_{2N}=\epsilon_2-ik;\\ \beta_0=\beta_{2N}=-(\epsilon_2+ik)\end{matrix}$$

$$\epsilon_0=\left(\frac{2mE}{\hbar^2}\right)^{\frac{1}{2}};\quad \epsilon_1=\left(\frac{2m(V_0-E)}{\hbar^2}\right)^{\frac{1}{2}};\quad \epsilon_2=\left(\frac{2m(U_0-E)}{\hbar^2}\right)^{\frac{1}{2}}.$$

If the vector $\begin{bmatrix}a_j\\ b_j\end{bmatrix}$ is denoted by A_j, the matching of ψ and ψ' at the boundary between regions j and $j-1$ is accomplished by writing $A_j=T_jA_{j-1}$, where

$$T_j=-\frac{1}{2\epsilon_1}s[a+\tfrac{1}{2}(j-2)c];\quad T_j=-\frac{1}{2i\epsilon_0}t[\tfrac{1}{2}(j-1)c];$$

$$j\text{ even, but }\neq 2N\qquad j\text{ odd, but }\neq 1$$

$$s(x)=\begin{pmatrix}p(x) & p^*(x)\\ q(x) & q^*(x)\end{pmatrix};\quad t(x)=\begin{pmatrix}q^*(x) & -p^*(x)\\ -q(x) & p(x)\end{pmatrix};$$

$$p(x)=u\exp(-u^*x),\quad q(x)=u^*e^{ux},\quad u=\epsilon_1+i\epsilon_0.$$

For $j=1, 2N$, T_j is defined similarly with ϵ_1 replaced by ϵ_2 and, for convenience, u by $v=\epsilon_2+i\epsilon_0$. The last and first vectors A_{2N} and A_0 are connected now by

$$A_{2N}=\Big(\prod_{j=2N}^{1}T_j\Big)A_0=TA_0.$$

[1] D. S. Saxon and R. A. Hutner, Philips Research Repts. **4**, 82 (1949).
[2] J. M. Luttinger, Philips Research Repts. **6**, 303 (1951).
[3] T. A. Hoffman, Acta Phys. Acad. Sci. Hung. **1**, 175 (1951).
[4] G. Allen, Phys. Rev. **91**, 531 (1953).

At the same time the periodicity of $\varphi(x)$ requires

$$A_{2N}=\begin{pmatrix} e^{-\alpha_0 l} & 0 \\ 0 & e^{-\beta_0 l} \end{pmatrix} A_0 = FA_0.$$

Hence we must have $|T-F|=0$. This is the characteristic equation for the allowed values of E. It may be written more conveniently as

$$\begin{aligned} |T-F| &= |T|+|F|-F_{11}T_{22}-F_{22}T_{11} \\ &= |T|+|F|-\mathrm{Tr}(TF') \\ &= 1+e^{2ikl}-\mathrm{Tr}(TF')=0, \end{aligned}$$

where F' stands for the "anti-transpose" of F, i.e.,

$$F_{11}'=F_{22}, \quad F_{22}'=F_{11}, \quad F_{12}'=F_{21}'=0.$$

The evaluation of T is performed as follows. First group the interior T's in pairs:

$$\begin{aligned} T &= T_{2N}(T_{2N-1}T_{2N-2})\cdots(T_3T_2)T_1 \\ &= T_{2N}F_\nu\cdots F_1T_1, \end{aligned}$$

where $\nu=N-1$ is the number of purity atoms B between impurities. Then it is found that

$$F_n=\frac{1}{4i\epsilon_0\epsilon_1}\begin{pmatrix} f(b) & g(-b)e^{-2in\epsilon_0 c} \\ g(b)e^{2in\epsilon_0 c} & f(-b) \end{pmatrix},$$

$$f(b)=u^3\exp(u^*b)-u^{*2}e^{-ub},$$

$$g(b)=|u|^2[e^{-ub}-\exp(u^*b)].$$

Upon writing F_n as the sum of diagonal and "anti-diagonal" matrices, it will be seen that

$$S=\begin{pmatrix} e^{-i\epsilon_0 c} & 0 \\ 0 & e^{i\epsilon_0 c} \end{pmatrix}$$

has the property that F_{n+1} is the similarity transform of F_n with S as transformation matrix: $F_{n+1}=SF_nS^{-1}$. Therefore T may be written as

$$\begin{aligned} T &= T_{2N}S^\nu(S^{-1}F_1)^\nu T_1 \\ &= T_{2N}S^\nu H^\nu T_1. \end{aligned}$$

The matrix H is explicitly

$$H=\frac{1}{4i\epsilon_0\epsilon_1}\begin{pmatrix} f(b)e^{i\epsilon_0 c} & g(-b)e^{-i\epsilon_0 c} \\ g(b)e^{i\epsilon_0 c} & f(-b)e^{-i\epsilon_0 c} \end{pmatrix}$$

or

$$H=\begin{pmatrix} F & G^* \\ G & F^* \end{pmatrix},$$

with

$$F=\frac{f(b)e^{i\epsilon_0 c}}{u^2-u^{*2}}, \quad G=\frac{g(b)e^{i\epsilon_0 c}}{u^2-u^{*2}}.$$

Now the eigenvalues λ of H are

$$\lambda=B\pm(B^2-1)^{\frac{1}{2}},$$

B standing for

$$B=\tfrac{1}{2}(F+F^*)=\cosh\epsilon_1 b\cos\epsilon_0 a+\frac{\epsilon_1^2-\epsilon_0^2}{2\epsilon_0\epsilon_1}\sinh\epsilon_1 b\sin\epsilon_0 a.$$

This is the quantity which, in the Kronig-Penney model for only purity atoms, gives the E eigenvalues according to $B=\cos kc$.

For convenience, put

$$\cos\beta=\tfrac{1}{2}(F+F^*),$$

so that the eigenvalues of H are $e^{i\beta}$ and $e^{-i\beta}$; we shall treat β as real, though actually it need not be so. The similarity transformation which diagonalizes H is

$$WHW^{-1}=\begin{pmatrix} e^{i\beta} & 0 \\ 0 & e^{-i\beta} \end{pmatrix}=L,$$

say;

$$W=\begin{pmatrix} G & e^{i\beta}-F \\ G & e^{-i\beta}-F \end{pmatrix}, \quad W^{-1}=\frac{1}{|W|}\begin{pmatrix} e^{-i\beta}-F & F-e^{i\beta} \\ -G & G \end{pmatrix},$$

$$|W|=-G(e^{i\beta}-e^{-i\beta})=-2iG\sin\beta.$$

The $\mathrm{Tr}(TF')$ needed in the eigenvalue equation is now

$$\mathrm{Tr}(TF')=\mathrm{Tr}(T_1F'T_{2N}S^\nu W^{-1}L^\nu W),$$

and this may be explicitly evaluated. For this purpose it turns out to be helpful to use the equalities

$$-|G|^2=(e^{-i\beta}-F)(e^{i\beta}-F), \quad e^{-i\beta}-F=F^*-e^{i\beta},$$

$$|F|^2-|G|^2=|F_\nu|^2-|G_\nu|^2=1,$$

where the quantities F_ν and G_ν are introduced, analogously to F and G, through the definitions:

$$F_\nu=\frac{[v^2\exp(v^*d)-v^{*2}e^{-vd}]}{v^2-v^{*2}}e^{i\epsilon_0 l}$$

$$G_\nu=|v|^2\frac{[e^{-vd}-\exp(v^*d)]}{v^2-v^{*2}}e^{i\epsilon_0 l}.$$

The direct evaluation of $\mathrm{Tr}(TF')$ gives, upon grouping terms properly,

$$\begin{aligned} \mathrm{Tr}(TF') &= \frac{e^{ikl}}{\sin\beta} \\ &\times\{-\sin\nu\beta[(e^{-i\nu\epsilon_0 c}F_\nu F^*-e^{-i\nu\epsilon_0 c}G_\nu G^*)+\text{c.c.}] \\ &+\sin(\nu+1)\beta[F_\nu e^{-i\nu\epsilon_0 c}+\text{c.c.}]\}. \quad (1) \end{aligned}$$

After further algebraic reduction, the eigenvalue equation reads finally

$$\cos kl=\frac{1}{\sin\beta}\Big\{\sin(\nu+1)\beta\Big[\cosh\epsilon_2 d\cos\epsilon_0 a+\frac{1}{2}\frac{\epsilon_2^2-\epsilon_0^2}{\epsilon_2\epsilon_0}\sinh\epsilon_2 d\sin\epsilon_0 a\Big]-\sin\nu\beta\Big[\frac{(\epsilon_1+\epsilon_2)^2}{4\epsilon_1\epsilon_2}\cosh(\epsilon_2 d-\epsilon_1 b)-\frac{(\epsilon_1-\epsilon_2)^2}{4\epsilon_1\epsilon_2}\cosh(\epsilon_2 d+\epsilon_1 b)\Big]\Big\}. \quad (2)$$

The last square bracket may be written also as

$$\cos\beta_m=\cosh\epsilon_2 d\cosh\epsilon_1 b-\frac{\epsilon_1^2+\epsilon_2^2}{2\epsilon_1\epsilon_2}\sinh\epsilon_2 d\sinh\epsilon_1 b.$$

The allowed energy bands are specified in (2) through the requirement that the right-hand side be of modulus not exceeding unity. The restriction that the separation a between A and the neighboring B atoms be the same as that between adjacent B atoms has been introduced for the sake of some gain in simplicity, but it may be removed by obvious modifications in the analysis.

Several limiting cases of the final results provide an instructive check on the calculation; of these the simplest are the limits $\nu\to 0$ and impurities$\to$purities. For the first of these we have $l=d+a+\nu c\to d+a=l'$. In this case, by (1) and (2),

$$\cos kl'=\tfrac{1}{2}(F_\nu+F_\nu^*)=\cos\beta_\nu=\cosh\epsilon_2 d\cos\epsilon_0 a+\frac{1}{2}\frac{\epsilon_2^2-\epsilon_0^2}{\epsilon_2\epsilon_0}\sinh\epsilon_2 d\sin\epsilon_0 a,$$

which is the Kronig-Penney result for the lattice of only impurities of width d and separation a. In the limit that the impurities$\to$purities, we have $\epsilon_2=\epsilon_1$, $d=b, l=(\nu+1)c$, and $F_\nu=F\exp(i\nu\epsilon_0 c)$, $G_\nu=G\exp(i\nu\epsilon_0 c)$; and now, either by (1) or (2),

$$\cos(\nu+1)kc=[\cos\beta\sin(\nu+1)\beta-\sin\nu\beta]/\sin\beta.$$

This is satisfied identically by $\cos kc=\cos\beta=\tfrac{1}{2}(F+F^*)$, the Kronig-Penney result for only purity atoms.

It is easy now to fabricate an example violating the Saxon-Hutner-Luttinger theorem mentioned earlier. By choosing $\nu=1$ and writing Eq. (2) in the form

$$\cos kl=2\cos\beta\cos\beta_\nu-\cos\beta_m, \quad (3)$$

it is only necessary to require $|\cos\beta|>1$, $|\cos\beta_\nu|>1$, while insuring $|\cos kl|<1$. Let $E<U_0, V_0$, so that ϵ_1 and ϵ_2 are real, and suppose $\epsilon_0 a=\pi/2$. Then

$$\cos\beta=\sinh\eta_1\sinh\epsilon_1 b,\quad \cos\beta_\nu=\sinh\eta_2\sinh\epsilon_2 d,$$
$$\cos\beta_m=\cosh\epsilon_2 d\cosh\epsilon_1 b-\cosh(\eta_1-\eta_2)\sinh\epsilon_2 d\sinh\epsilon_1 b,$$

where for short

$$\sinh\eta_1=\frac{1}{2}\left(\frac{\epsilon_1}{\epsilon_0}-\frac{\epsilon_0}{\epsilon_1}\right),\quad \sinh\eta_2=\frac{1}{2}\left(\frac{\epsilon_2}{\epsilon_0}-\frac{\epsilon_0}{\epsilon_2}\right).$$

Equation (3) is now expressible as

$$\cos kl=\cos\beta\cos\beta_\nu-(1+\sinh^2\epsilon_1 b)^{\frac{1}{2}}(1+\sinh^2\epsilon_2 d)^{\frac{1}{2}}+(\sinh^2\epsilon_1 b+\cos^2\beta)^{\frac{1}{2}}(\sinh^2\epsilon_2 d+\cos^2\beta_\nu)^{\frac{1}{2}}.$$

If both $\cos\beta, \cos\beta_\nu$ exceed 1 or if both are less than -1, $\cos kl$ must >1. But if $\cos\beta$ and $\cos\beta_\nu$ are of opposite sign and of modulus greater than unity, they, and $\sinh\epsilon_1 b$ and $\sinh\epsilon_2 d$ may be so chosen that $|\cos kl|<1$; and then $\sinh\eta_1$ and $\sinh\eta_2$, which may assume any real values, are determined. For instance, $\sinh\epsilon_1 b=\sinh\epsilon_2 d=1$ and $\cos\beta=2$, $\cos\beta_\nu=-3$ give $\cos kl=-8+\sqrt{(50)}$; this case corresponds to tall, thin B wells and fat, short A wells.

If it be required that the periods of the pure A and pure B lattices be the same, i.e., that $b=d$, the consistency condition,

$$\frac{\epsilon_1}{\epsilon_2}=\frac{\epsilon_1}{\epsilon_0}\Big/\frac{\epsilon_2}{\epsilon_0}=\frac{\sinh\epsilon_2 b}{\sinh\epsilon_1 b}\,\frac{\cos\beta+(\cos^2\beta+\sinh^2\epsilon_1 b)^{\frac{1}{2}}}{\cos\beta_\nu+(\cos^2\beta_\nu+\sinh^2\epsilon_2 b)^{\frac{1}{2}}},$$

must be fulfilled while still enforcing $|\cos kl|<1$, $|\cos\beta|>1$, $|\cos\beta_\nu|>1$. These conditions all together are not incompatible; for example, $\sinh\epsilon_1 b=1$, $\sinh\epsilon_2 b=10$, $\cos\beta_\nu=1.5$, $\cos\beta=-1.295$, $\cos kl=0.389$ satisfy them.

These examples would seem to hint at the conclusion that only those common forbidden energies of pure A and pure B lattices having the same "polarity" (i.e., giving $\cos\beta$ and $\cos\beta_\nu$ of the same sign) are the ones that survive as forbidden in a mixed A,B lattice; in this case the Saxon-Hutner-Luttinger theorem would be a consequence of the fact that for delta-function A and B all common forbidden energies of the pure lattices (both having the same periodicity) are of the same polarity. However, an investigation in progress on the exact conditions under which pure-lattice common forbidden regions remain forbidden in the mixed lattice shows this conclusion not to be correct in general, a consideration of more than just relative polarities being involved in these conditions.

Domain Formation and Domain Wall Motions in Ferroelectric $BaTiO_3$ Single Crystals

WALTER J. MERZ
Bell Telephone Laboratories, Murray Hill, New Jersey
(Received April 19, 1954)

The nucleation and growth of ferroelectric domains in barium titanate have been studied as a function of applied electric field and temperature. The optical and electrical measurements were made on thin single-crystal plates normal to c, the polar direction. When the electric field applied along this direction is reversed, new domains with opposite polarization are formed. The manner of growth of these domains is very different from that of domain growth in ferromagnetic materials. The sidewise motion of the 180° side walls (walls between domains with antiparallel polarization) which is common in ferromagnetic crystals is almost never found in barium titanate. Instead its polarization is changed by the formation of very many new antiparallel domains which are extremely thin (10^{-4} cm) and appear to grow only in the forward direction. The explanation of this behavior is found in the weak coupling between the dipoles perpendicular to the dipole direction. The wall thickness is small, of the order of one to a few lattice constants; the wall energy in $BaTiO_3$ is of the order of 10 erg/cm^2. Electrical pulsing experiments substantiate the optical observations very clearly. Pulsing the samples at different temperatures shows that the nucleation rate of new domains is accelerated at elevated temperatures. Furthermore, the growth of the new domains is faster at higher temperatures. Experimental results are presented showing how the switching current and the switching time depend on applied electrical field, on temperature, and on the size of the sample.

I. INTRODUCTION

THE ferroelectric domains in $BaTiO_3$ single crystals have been studied by a number of authors, especially by Forsbergh.[1] All these investigations showed that the sometimes very complex domain arrangements can be explained by twinning of crystals along {011} planes. However, the formation and movement of antiparallel domains (domains with opposite polarization) have not been discussed extensively up to now. One difficulty is that without special means one cannot see the antiparallel domains very easily. We became interested in these antiparallel domains because they are very important in the process of reversing the dipoles with an electric field. Questions such as how long it takes to reverse the polarization, how fast the domain walls move, how large the current is which flows, and how these properties depend on the applied electrical field, temperature, and size of the sample can be answered by the study of the formation of the antiparallel domains and the movement of the walls between them. Besides the theoretical interest in the switching mechanism of electrical dipoles, all the above-mentioned questions are of prime importance when $BaTiO_3$ single crystals are used as memory devices.

II. OPTICAL OBSERVATIONS ON DOMAINS

We can distinguish among three types of domain boundaries (walls) in $BaTiO_3$. The first one is the boundary between a domain in which all the dipoles are aligned perpendicular to the crystal plate under investigation (c domain) and a domain in which all the dipoles are aligned in a direction parallel to the crystal plate surface (a domain). Since the c axis of the tetragonal crystal is the optic axis, the c domain looks dark through a microscope between crossed nicols. The a domain is bright when viewed between crossed nicols except in two special positions where the direction of electric polarization is parallel or perpendicular to the direction of polarization of the light. We call this type of boundary a 90° wall because the two domains are polarized at 90° to each other. The 90° wall goes through the crystal at an angle of 45° to the major surfaces (Fig. 1), so that no surface charges can build up on the wall, as will be discussed later.

In the second case, the boundary is also a 90° wall, but the polarization on both sides of the wall lies parallel to the major surfaces of the crystal plate (a domains). In contrast to the first case these walls go straight through the crystal at 90° to the major surfaces. Because of total reflection of the light at the boundary, one can see this type of 90° wall very easily (Fig. 2). The direction of polarization of the two domains can be determined with a quarter-wave plate.

The third type of boundary is the 180° wall, that is, a boundary between domains with antiparallel polarization. As shown in a previous paper,[2] we can see these antiparallel domains only when the crystal is strained (by external or internal stresses or by an external electrical dc field). In Fig. 3 an edge of a c domain crystal is shown. The dark and bright lines represent the domains with parallel and antiparallel polarization. In other words the c domain, usually thought of as a single domain, consists of very many domains with antiparallel polarization. The width of these domains is of the order of 10^{-4} cm. In Fig. 4 a similar case is shown. The 45° lines are 90° walls, as shown before in Fig. 2. However, when the crystal is strained we can see that every supposedly single domain splits up into many domains with antiparallel polarization. They arrange themselves in such a way that no surface charges are

[1] P. W. Forsbergh, Jr., Phys. Rev. **76**, 1187 (1949).

[2] W. J. Merz, Phys. Rev. **88**, 421 (1952).

built up on the 90° walls: head-to-tail zig-zag arrangement, as shown in Fig. 4.

When an electrical field is applied to the crystal, we can, of course, move the domain walls and align the domains.[2] The most interesting experiment, however, is the one in which we can observe the formation of new domains with opposite polarization. If one applies an ac voltage to a *c*-domain crystal and watches the edge of it, using a stroboscopic light source whose frequency is close to the ac frequency, it is possible to see how the new domains with opposite polarization are formed and how they grow. The new domains are created at the surface and at imperfections in the form of needles which then grow in the forward direction through the crystal. Two important conclusions are drawn from these observations. First there are very many new domains, and second there is practically no sidewise growth of the new domains. In other words the nuclei which have the shape of needles grow only in the forward direction. This behavior is quite different from the ferromagnetics and will be discussed later. Figure 5 shows a few of the needles as observed with stroboscopic light. In order to facilitate the observations of this

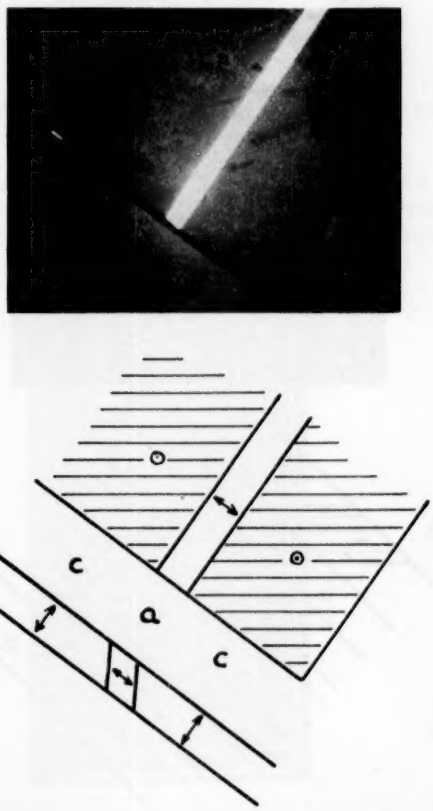

FIG. 1. Photo and schematic sketch of 90° walls between an *a* domain and two *c* domains in $BaTiO_3$. (×50).

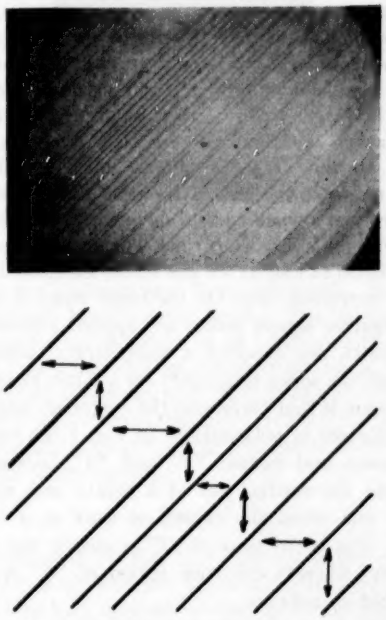

FIG. 2. 90° walls between *a* domains in $BaTiO_3$. (×50).

effect, the crystal was highly strained. In some cases where this strain was excessive small cracks and thus *a* domains and 90° walls were produced (see the 45° lines in Fig. 5). The width of the new domains is also of the order of 10^{-4} cm, like the antiparallel domains in Figs. 3 and 4.

III. ELECTRICAL PULSING EXPERIMENTS

Both optical and electrical investigations were performed on single crystals grown by Remeika[3] of this laboratory. Experiments showed that reproducible results can only be obtained if one uses very strain-free crystals with extremely clean surfaces and electrodes which adhere to the crystal very uniformly without straining it. Since the dielectric constant of $BaTiO_3$ is very high (10^5 to 10^6 for the steep part of the hysteresis loop[4]), one has to be sure that no impurities are between the crystal and the electrode. Evaporated films of noble metals on extremely clean crystal surfaces gave good results. A photograph of the ferroelectric 60-cycle hysteresis loop of a $BaTiO_3$ single crystal is shown in Fig. 6. Some characteristic data of this loop were given in a previous paper.[4] ($E_c \sim 500$ volts/cm; $P_s = 26 \times 10^{-6}$ coulomb/cm^2; ratio of two slopes $\sim 10^3$.)

The domain formation and domain wall motions as described in Chapter II were also investigated electrically by the following pulsing experiments. Square pulses are applied to a crystal (thickness $d = 5 \times 10^{-3}$ cm;

[3] J. P. Remeika, J. Am. Chem. Soc. **76**, 940 (1954).
[4] W. J. Merz, Phys. Rev. **91**, 513 (1953).

electrode area $A = 10^{-4}$ cm^2) in series with a resistance. The rise time of the pulses has to be short compared to the time required for the field to reverse the polarization of the sample. Furthermore, the length of the pulses has to be longer than the time required to reverse the polarization. We applied pulses of 1 to 10 μsec length with a rise time of about 0.02 μsec. If repeated square pulses of just one sign are applied to the crystal, one observes just a small current flowing through the series resistance for a very short time. The change in polarization is small as long as we just travel along the flat part of the hysteresis loop. On the other hand, if positive and negative square pulses are applied alternately to the crystal, one observes a much larger current flow (through the series resistance) for a much longer time. The reason is that traversing the hysteresis loop causes large changes in polarization. In Fig. 7 the two cases are shown and named "0" and "1" because they represent the reading out of a binary zero and of a binary one when the crystal is used as a memory device. The initial peak of "1" is mostly due to lead capacity, whereas the wide region of "1" is due to switching of domains.

In Fig. 8 we plot the measured peak current i_{max} (shown in Fig. 7) *versus* the applied field E of the pulse. Figure 9 is a plot of switching time t_s *versus* applied field E. The higher the applied field E, the faster the dipoles switch and thus the larger the peak current i_{max}.

Figure 8 shows that the plot of switching current *versus* applied field can be divided into two parts, a curved low-field strength part and a linear high-field strength part. At high fields the crystal thus behaves like an ohmic resistance in series with a voltage bias. We can calculate this switching resistance R in the following way. From Fig. 9 we know that the switching time t_s is proportional to $1/(E-E'')$, where E'' is a kind of coercive field strength. Since the new domains have to grow from one side of the crystal to the other side (Fig. 5), t_s must also be proportional to the thickness d of the sample; thus

$$t_s \cong \beta d/(E-E''), \tag{1}$$

with β = constant. Furthermore,

$$i_{max} \cdot t_s = \text{constant (total charge)} = 2 \cdot P_s \cdot A \cdot q \tag{2}$$

with P_s = spontaneous polarization (coulombs/cm^2); A = area of the crystal (cm^2); and q = constant of order of about 2 which takes care of the shape of the $i(t)$ curve (Fig. 7). We then get

$$R = \frac{\Delta V}{\Delta i} = \frac{d(E-E') \cdot \beta d}{2 \cdot P_s \cdot A \cdot q(E-E'')} \cong \frac{\beta d^2}{2 \cdot q \cdot A \cdot P_s}, \tag{3}$$

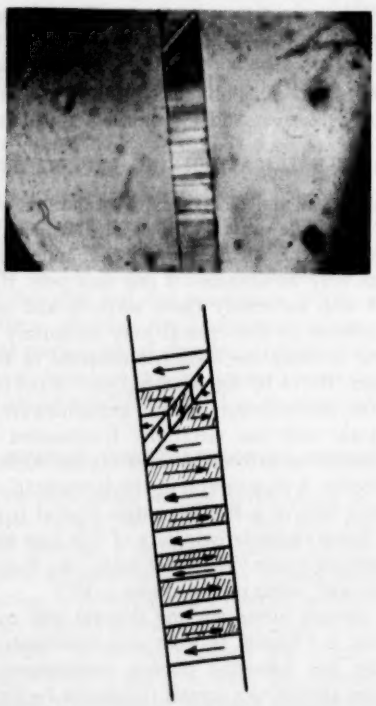

FIG. 3. 180° walls (antiparallel domains) at the edge of a crystal. (×50).

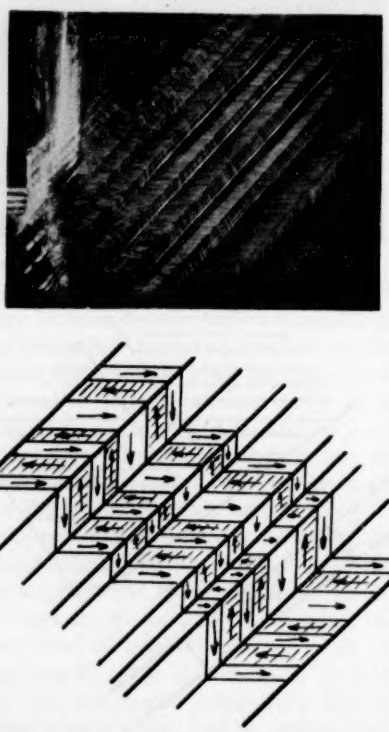

FIG. 4. 180° and 90° walls in a $BaTiO_3$ crystal surface. (×50).

FIG. 5. New antiparallel domains observed with stroboscopic light. (×50).

if E' is close to E''; that is, the switching resistance R of the linear part in Fig. 8 is proportional to the square of the thickness d of the sample and inversely proportional to the electrode area A of the sample. This has experimentally been found to be true. The resistance of the electrodes has of course to be subtracted from the measured resistance. All the curves shown in this paper were obtained on samples with the following dimensions: thickness $d=5\times10^{-3}$ cm, electrode area $A=10^{-4}$ cm².

FIG. 6. 60-cycle hysteresis loop of $BaTiO_3$.

The low field strength part of Fig. 8 can be expressed best in the following way:

$$i_{max}\sim e^{-\alpha/E}, \tag{4}$$

with $\alpha=$constant. In Fig. 10 a logarithmic plot of i_{max} *versus* $1/E$ is shown. We get a straight line over 5 decades. One very interesting result of this is that even at field strengths below the 60-cycle coercive force we get switching if we wait long enough. The apparent coercive force increases when the frequency of the applied field is increased.

Measurements at different temperatures show that at higher temperatures the switching time becomes shorter and thus the switching current increases considerably. But the general shape of the curves $i(E)$ (Fig. 7) stays the same. Figure 11 shows the plots of current i *versus* field E for different temperatures. It can be seen that

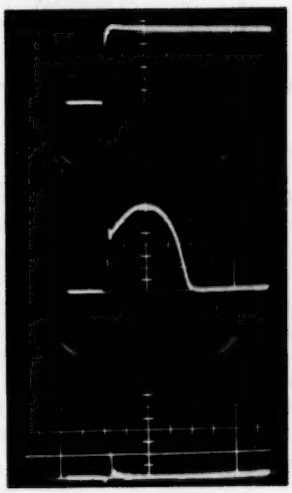

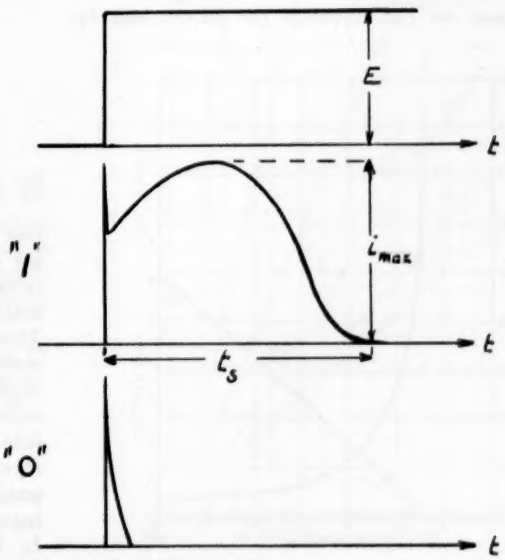

FIG. 7. Pulsing current and pulsing field *versus* time.

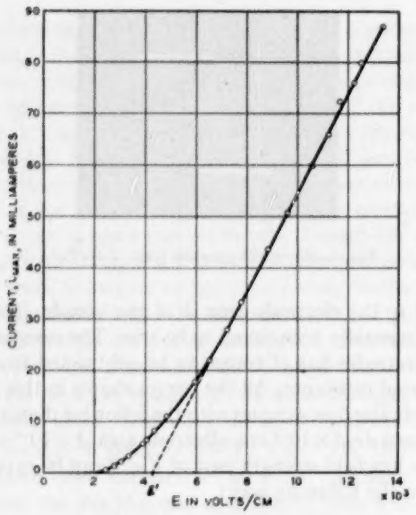

FIG. 8. Pulsing current i_{max} *versus* applied field E.

the resistance R (inverse slope of the linear part) decreases with increasing temperature as shown in Fig. 12. In a similar way, the switching time t_s drops with increasing temperature for the same applied field strength as shown in Fig. 13. The constant β from Eq. (1), which is proportional to the slope of the lines in Fig. 13, is plotted as a function of temperature in Fig. 14. The behavior is very similar to $R(T)$ (Fig. 12), as is to be expected since R is proportional to β [Eq. (3)] and the only other temperature dependent quantity, P_s, does not change rapidly with temperature.

The low field strength part is shown in Fig. 15. At all temperatures we can represent the curves best by writing

$$i_{max} \sim e^{-\alpha(T)/E}. \tag{5}$$

The value of the coefficient $\alpha(T)$ is plotted *versus* temperature in Fig. 16. We will discuss these experiments in the next chapter.

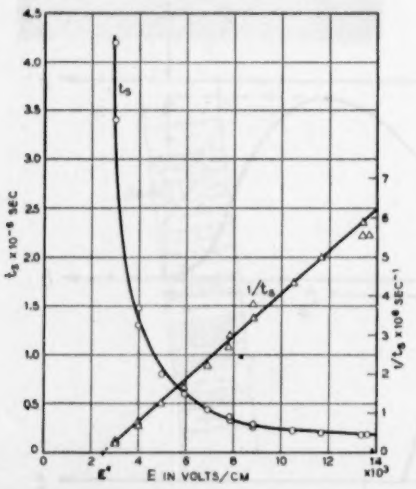

FIG. 9. Switching time t_s and $1/t_s$ *versus* applied field E.

IV. DISCUSSION

The most interesting result obtained from our domain observations is that by reversing the applied electric field very many new domains are created. Furthermore, the polarization in $BaTiO_3$ does not change by a sidewise motion of the side walls of those domains which are already polarized in the right direction. $BaTiO_3$ prefers to create many new small domains instead of making an existing properly polarized domain grow. This is in contrast to ferromagnetics, where from the work of Williams and Shockley[8] we know that in good single crystals of iron we can observe only a few domain walls and that these move sidewise when a magnetic field is applied. Figures 3 and 4 illustrate the case of crystals where about half of the domains have a polarization pointing in one direction whereas the other half have a polarization pointing in the opposite direction. In Fig. 5 we have shown the situation where the

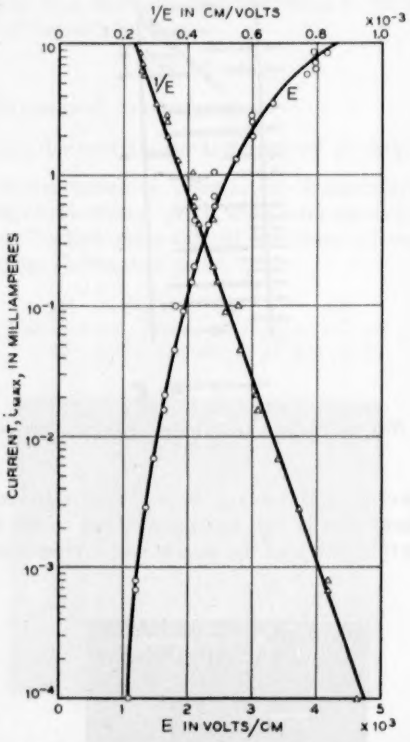

FIG. 10. Switching current *versus* applied field E and *versus* $1/E$.

[8] H. J. Williams and W. Shockley, Phys. Rev. **75**, 178 (1949).

domains are in the process of reversing and only a few of them have the direction of the reversed electric field. The boundaries of the antiparallel domains are not as sharp as the 90° walls because what we see are only changes in birefringence due to strains. However, we get a good idea of the size and shape of the domains with antiparallel polarization. The question is "why do the 180° side walls not move sidewise in contrast to the magnetic case?"

We think the explanation is as follows. The forward coupling of the electric dipoles is large so that the growth of the nuclei in the forward direction is fast. The coupling sidewise, however, is very small. In other words, an electric dipole does not care too much whether the neighboring dipoles on the side are parallel or antiparallel. Of course, the parallel alignment is usually

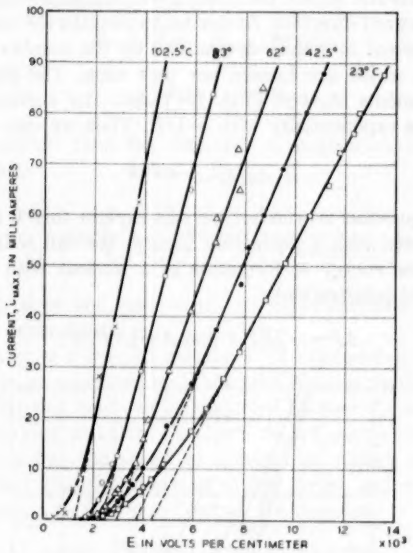

FIG. 11. Switching current *versus* applied field at different temperatures.

preferred because the crystal is ferroelectric. On the other hand, we know from the work of Kittel[6] that an antiferroelectric arrangement is energetically almost as likely as a ferroelectric one. Furthermore, crystals similar to $BaTiO_3$ are known where the antiparallel arrangement is preferred ($PbZrO_3$, for example).[7]

Furthermore, we can also explain this behavior by investigating the wall thickness and the wall energy. The energy of the wall per cm² can be represented as

$$\sigma_w = \sigma_{dip} + \sigma_{anis}, \tag{6}$$

where σ_{dip} is the contribution from dipole-dipole interaction and σ_{anis} is the contribution from anisotropy.

[6] C. Kittel, Phys. Rev. **82**, 729 (1951).
[7] Shirane, Sawaguchi, and Takagi, Phys. Rev. **84**, 476 (1951).

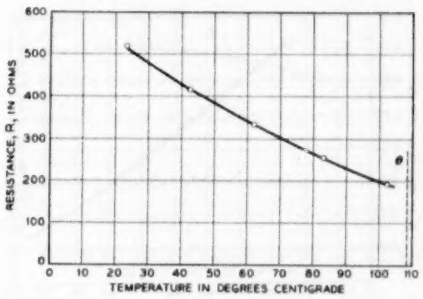

FIG. 12. Switching resistance R *versus* temperature.

In the ferromagnetic case one replaces σ_{dip} by $\sigma_{exchange}$ because the exchange interaction is much larger than the dipole-dipole interaction. Here the dipole energy is the important one and may be estimated from calculations of dipolar interactions.[8] The result is roughly

$$\sigma_{dip} \cong 10^{-14}/Na^2 \text{ erg/cm}^2, \tag{7}$$

where N is the thickness of the wall in atomic separations and a is the lattice constant. The energy due to anisotropy we can calculate in the following way. The elastic energy per cm³ which is stored when we deform the unit cell from tetragonal to cubic is of the order of

$$\epsilon_{elast} \cong \tfrac{1}{2} c_{33} z_s^2 \text{ erg/cm}^3, \tag{8}$$

where c_{33} is an elastic constant and z_s is the spontaneous strain in $BaTiO_3$ at room temperature because of elec-

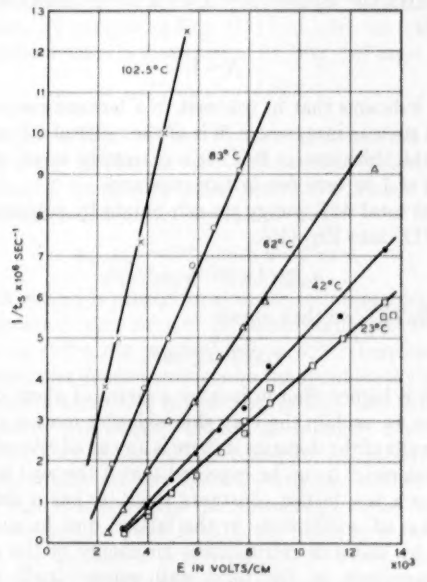

FIG. 13. Reciprocal switching time *versus* field at different temperatures.

[8] P. W. Anderson (private communication); see also W. Kinase, Busseiron Kenkyu **69**, 145 (1953).

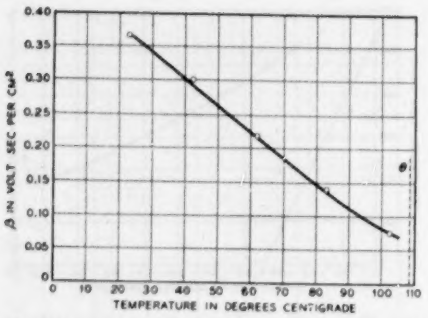

FIG. 14. β (reciprocal mobility) *versus* temperature.

tromechanical effects. Thus, the wall energy per cm² due to anisotropy becomes

$$\sigma_{\text{anis}} \cong \tfrac{1}{2} c_{33} z_s^2 N a \text{ erg/cm}^2. \tag{9}$$

From (7) and (9) we get for the total wall energy density

$$\sigma_w \cong (10^{-14}/Na^2) + \tfrac{1}{2} c_{33} z_s^2 N a \text{ erg/cm}^2. \tag{10}$$

The minimum wall energy is obtained when

$$\partial \sigma_w / \partial N = 0 = -(10^{-14}/N^2 a^2) + \tfrac{1}{2} c_{33} z_s^2 a, \tag{11}$$

or when

$$N \cong (2 \times 10^{-14}/c_{33} z_s^2 a^3)^{\frac{1}{2}}. \tag{12}$$

It is clear that N (wall thickness expressed in atomic separations) must be small in $BaTiO_3$ because the dipole-dipole interaction is small and the anisotropy large. We obtain for N at room temperature with $c_{33} = 2.0 \times 10^{12}$ dynes/cm²,[9] $z_s = 7 \times 10^{-3}$,[10] $a = 4.0 \times 10^{-8}$ cm [11]:

$$N \sim 1. \tag{13}$$

This indicates that in contrast to a ferromagnetic material such as iron, where N is of the order of 10^2 to 10^3, the wall thickness in $BaTiO_3$ is extremely small, of the order of 1 to very few lattice constants.

The total wall energy we can obtain by substituting Eq. (12) into Eq. (10),

$$\sigma_w \cong (2 \times 10^{-14} c_{33} z_s^2 / a)^{\frac{1}{2}}. \tag{14}$$

For $BaTiO_3$ we then obtain

$$\sigma_w \cong 7 \text{ erg/cm}^2, \tag{15}$$

which is higher than in iron by a factor of about 5.

Can we explain the very slow sidewise motion of the side walls of the domains if there is any at all? According to Anderson[12] it can be expected that if the wall is only one or a few lattice constants thick, it has a definite position of equilibrium in the lattice, and to move it over by one unit cell requires an energy of the order of magnitude of the total wall energy itself (~10 erg/cm²). In the magnetic case, however, where the wall is a few hundred lattice constants thick, the energy required to move the wall one lattice constant is very small because the total wall energy is spread out over a much larger region. Since the energy gained by moving the wall one lattice constant to the side is only about

$$EP = 1/10 \text{ erg/cm}^2, \tag{16}$$

with $E \sim 10^4$ volts/cm, which is much smaller than the wall energy [Eq. (15)], it is obvious that it is very unlikely that the side walls can move sidewise. The crystal thus prefers to create many new nuclei with the reversed polarization as we can see optically so clearly.

Both the optical and the electrical pulsing experiments show that the reversing of the polarization in $BaTiO_3$ occurs in two steps, first the nucleation of new domains and second the linear growth of these nuclei in the forward direction. At low field strengths the switching current is mainly determined by the number n of nuclei which are formed per unit time. The pulsing experiments showed [Eq. (5)] that the current increases exponentially with $-1/E$. Thus we can write that

$$i \sim dn/dt \sim e^{-\alpha(T)/E}. \tag{17}$$

The question is whether we can explain this $1/E$ dependence with a nucleation theory. We can write for the free energy of formation of a nucleus with antiparallel polarization[13]:

$$\Delta F = -2EP_s V + \sigma_w A + \tfrac{1}{2} N P_s^2 V, \tag{18}$$

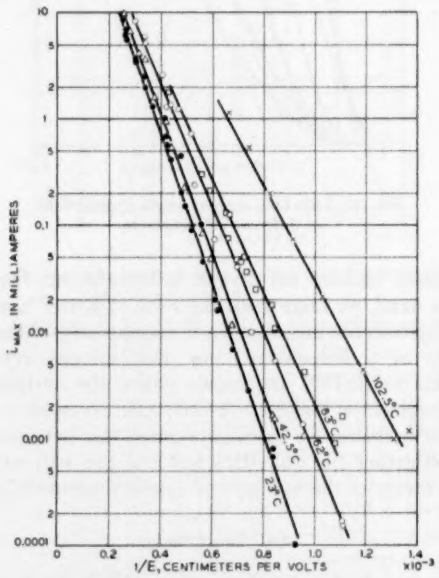

FIG. 15. Switching current *versus* reciprocal field at different temperatures.

[9] Bond, Mason, and McSkimin, Phys. Rev. **82**, 442 (1951).
[10] W. J. Merz, Phys. Rev. **76**, 1221 (1949).
[11] Helen B. Megaw, Proc. Roy. Soc. (London) **A189**, 261 (1947).
[12] P. W. Anderson (private communication).
[13] R. Becker and W. Doering, *Ferromagnetismus* (Springer, Berlin, 1939).

where the first term represents the electrostatic energy, which is gained by the formation of a nucleus, the second term represents the surface energy, and the third term the field energy of the depolarizing field. In Eq. (18), V is the volume and A is wall area of the nucleus; σ_w is the wall energy/cm² and N is the depolarizing factor; P_s is the spontaneous polarization and E is the applied electric field.

If we assume for the shape of the nucleus something like a thin long cone or ellipsoid as optical observations indicate, we can write

$$V=a\cdot r^2 l, \quad A=brl, \quad N=cr^2/l^2, \tag{19}$$

where r is the radius of the base, l is the length of the nucleus, and a, b, c are constants. The minimum of ΔF can be found by differentiating Eq. (18) with respect to r and l and equating to zero. We then find for the critical dimensions:

$$r^*\sim 1/EP, \quad l^*\sim 1/E^{3/2}P^{1/2}, \tag{20}$$

and thus

$$\Delta F^*\sim 1/E^{5/2}P^{3/2}. \tag{21}$$

We obtain then for the rate of nucleation of new domains

$$\frac{dn}{dt}\sim\exp\left(-\frac{\Delta F^*}{kT}\right)\sim\exp\left(-\frac{\text{constant}}{E^{5/2}P^{3/2}kT}\right), \tag{22}$$

which does not agree with the experimentally found $e^{-1/E}$ dependence.

There is a way to get the $e^{-1/E}$ dependence of the current as suggested by Wannier.[14] We assume that the depolarizing field can be neglected because the nucleus is very long and thin. Furthermore, we assume that the nucleus has the shape of a long flat dagger with a length l (in the direction of the field) and a cross dimension $t\times w$, where $l\gg w>t$. We then get

$$\Delta F=-2EPlwt+\sigma_w'(wl+tl)+\sigma_w''wt, \tag{23}$$

and, since $w>t$,

$$\Delta F=-2EPlwt+\sigma_w'wl+\sigma_w''wt, \tag{24}$$

where the width w can be considered as a constant but still $w\ll l$ and $w>t$. We then find for the critical dimensions:

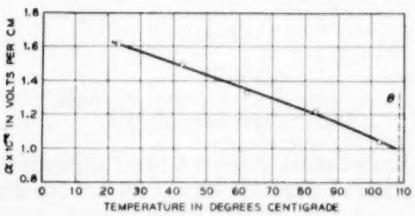

FIG. 16. Activation energy α *versus* temperature.

[14] G. H. Wannier (private communication).

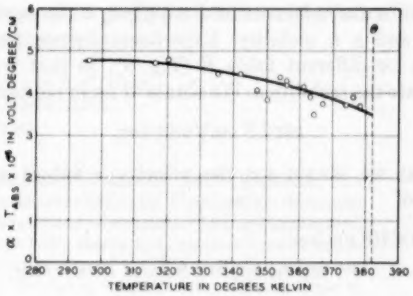

FIG. 17. Activation energy α times temperature T *versus* temperature.

sions:

$$l^*\sim\sigma_w'/EP, \quad l^*\sim\sigma_w''/EP, \tag{25}$$

and thus

$$\Delta F^*\sim\sigma_w'\sigma_w''/EP; \qquad dn/dt\sim\exp(-\sigma_w'\sigma_w''/EPkT), \tag{26}$$

which gives the experimentally observed $e^{-1/E}$ dependence of the current. Since $l^*\gg t^*$, Eq. (25) says that $\sigma_w''\gg\sigma_w'$, which means that the wall energy/cm² of the front wall is much higher than the wall energy/cm² of the side walls of the nucleus. This is to be expected because on the front wall we find an electric charge.

However, we have no direct proof for the fact that w should be larger than t. The strain patterns we see in Figs. 3, 4, and 5 indicate a value of about 10^{-4} cm for the width w of the antiparallel domains so that t would not be observable if the above-mentioned assumption is correct. By comparing Eqs. (17) and (26), we find that the experimentally measured $\alpha(T)$ (Fig. 16) must be

$$\alpha(T)\sim\sigma_w'\sigma_w''/PkT. \tag{27}$$

If we plot $\alpha(T)\times T$ (Fig. 17), we notice that this curve looks very similar to the spontaneous polarization P_s *versus* T curve[4] or a higher power of P_s *versus* T. We are therefore led to the conclusion that

$$\sigma_w'\cdot\sigma_w''\sim P^n \quad \text{with } n\sim 2 \text{ to } 4, \tag{28}$$

which in turn is proportional to the spontaneous lattice deformation $x_s^{n/2}$ or $z_s^{n/2}$ or some similar expression, since x_s and z_s are proportional to P_s^2.[4] Therefore, the wall energies depend strongly on the spontaneous lattice deformations, as also can be seen in Eq. (14). Whether the nuclei are dagger-shaped, as assumed above, or whether they are needle- or cone-like, as optical observations might indicate, cannot yet be determined.

At high field strengths the current i_{max} varies linearly with the applied field E (Fig. 8). Since at these high fields the nucleation is extremely fast, we can assume that the peak current is determined only by the velocity v with which the nuclei grow in the forward direction.

$$i_{max}\sim v=d/t_s=\mu(E-E''), \tag{29}$$

where d is the thickness of the sample, t_s the switching time, and μ a mobility. Experimentally we know d and t_s for different fields E (Fig. 9), so that we can calculate the mobility μ. We obtain at room temperature

$$\mu \cong 2.5 \text{ cm}^2/\text{volt sec}, \tag{30}$$

so that we obtain for the velocity v values of the order of

$$v = 0.5 \times 10^4 \text{ cm/sec}$$

for an applied field of 2000 v/cm,

or (31)

$$v = 3.5 \times 10^4 \text{ cm/sec}$$

for an applied field of 14 000 v/cm.

These are average values because they were obtained from the total switching time t_s of the whole crystal. It is quite possible that the velocity with which one single domain grows is larger because the nucleation time, though small, is finite. However, it is reasonable to assume that the average velocity of one domain at applied field strengths of the order of 10^4 volts/cm is of the order of 10^4 to 5×10^4 cm/sec, which is comparable to the wall velocity in ferromagnetic crystals. However, it is interesting to note that it is smaller than the velocity of sound in $BaTiO_3$. An accurate direct measurement of v by measuring the velocity with which the end point of a new antiparallel domain (Fig. 5) moves through the crystal, was not possible because of stability problems.

Since the mobility μ is equal to $1/\beta$ as defined in Eq. (1), we can see from Fig. 14 that μ increases strongly with temperature. This is to be expected because the switching certainly is easier to perform when the crystal is less anisotropic. (The ratio c/a approaches 1 when we approach the Curie point.)

V. CONCLUSIONS AND SUMMARY

Though we do not understand all the details of the switching mechanism in ferroelectric $BaTiO_3$, we can observe quite clearly the following fundamental differences between the switching in a ferromagnetic crystal such as iron and a ferroelectric crystal such as $BaTiO_3$. The wall thickness in $BaTiO_3$ is very much smaller than in iron; probably just one or very few lattice constants thick. A similar result was obtained for ferroelectric rochelle salt by Mitsui and Furuichi[15] and for ferroelectric KH_2PO_4 by Kaenzig and Sommerhalder.[16] The wall energy per cm^2 seems to be somewhat larger than in iron. $BaTiO_3$ reverses its polarization by forming very many new domains whereas in iron the magnetization is reversed mostly by wall motion. The nucleation problem thus becomes very important in $BaTiO_3$. This can be seen very clearly in Figs. 8 and 11 where one observes a very large curved part in the plot of the switching current *versus* applied electric field. In the magnetic case, on the other hand, a linear behavior is found between magnetic flux change and magnetic field even at very low field strengths.[17] Since there is practically no sidewise motion of the side walls, there is no interference (crosstalk) between one set of electrodes to another on the same crystal plate even when they are very closely spaced (10^{-2} cm or less). This is, of course, of great importance when $BaTiO_3$ crystals are used in a matrix-type memory.

Further studies on the nucleation time, the dielectric relaxation time, and the switching losses especially near the transitions are under way and will be reported later.

VI. ACKNOWLEDGMENT

I would like to thank many of my colleagues without whose help the present work would not have been possible. In particular I would like to thank J. P. Remeika for the preparation of the very excellent crystals; P. W. Anderson, J. R. Anderson, G. H. Wannier, and J. K. Galt for very many helpful discussions; R. Nelson for helping with some experiments; and E. M. Kelly and J. Andrus for help in the preparation of samples.

[15] T. Mitsui and J. Furuichi, Phys. Rev. **90**, 193 (1953).
[16] W. Kaenzig and R. Sommerhalder, Helv. Phys. Acta **26**, 603 (1953).
[17] Galt, Andrus, and Hopper, Revs. Modern Phys. **25**, 93 (1953).

Analysis of Magnetoresistance and Hall Coefficient in p-Type Indium-Antimonide and p-Type Germanium

T. C. HARMAN, R. K. WILLARDSON, AND A. C. BEER
Battelle Memorial Institute, Columbus, Ohio
(Received April 26, 1954)

Existing theory on the variation of resistivity and Hall coefficient with magnetic field in semiconductors has been extended to the case of arbitrary concentrations of the electrons and holes. Equations are developed for the magnetoresistance $\Delta\rho/\rho_H$ and the Hall coefficient R_H, as functions of parameters such as temperature, magnetic-field strength, and impurity concentration. For p-type InSb, theory and experiment are in agreement on the following observations: (1) a shift to higher temperatures of the Hall coefficient crossover, magnetoresistance maxima, and Hall coefficient maxima with increasing magnetic field, (2) a decrease in magnitude of the Hall coefficient maxima with increasing magnetic field, (3) the occurrence of the largest effects in the transition region between extrinsic and intrinsic conductivity, (4) magnetoresistance maxima occurring at about the same temperature as Hall coefficient maxima.

For p-type germanium, however, the effects are not even qualitatively explained. The observed magnetic-field dependence of the Hall coefficient in the temperature region of the crossover is opposite to that predicted by the theory. Furthermore, no magnetoresistance maximum has been observed in the temperature region of the Hall coefficient maximum. Hence, it appears that a basic revision of existing treatments of p-type germanium is necessary.

INTRODUCTION

THERE has been an increasing amount of interest in the effects of magnetic field on the resistivity and Hall coefficient of semiconductors. There have been numerous contributors to the development of both the theoretical and experimental aspects. Recently, Johnson and Whitesell[1] have extended the theory by considering (1) scattering of charge carriers by impurity ions as well as by the lattice and (2) conduction by both electrons and holes of equal concentrations. Considering lattice scattering only, Madelung[2] has extended their work to include arbitrary concentrations of the electrons and holes, while Appel[3] has obtained analytical expressions for the weak and strong magnetic field of (1) above, as well as generalizing (2). The treatment presented here is also an extension of the earlier work. It is, however, presented in a somewhat different form, which we find readily adaptable to the analysis of our experimental results.

DEVELOPMENT OF EQUATIONS

The conductivity σ_H and Hall coefficient R_H of a two-carrier semiconductor in the presence of an external magnetic field can be written as[1]

$$\sigma_H=\frac{(A_1+A_2)^2+(B_1-B_2)^2}{A_1+A_2}, \tag{1}$$

$$R_H=\frac{-(B_1-B_2)}{H\{(A_1+A_2)^2+(B_1-B_2)^2\}}, \tag{2}$$

where subscripts 1 and 2 apply to electrons and holes, respectively. For the case of (1) mean free path independent of energy, (2) an arbitrary transverse magnetic field, (3) classical statistics, and (4) spherical energy surfaces,

$$A_j=n_j e\mu_j K_1(\gamma_j), \quad j=1, 2, \tag{3}$$

$$B_j=n_j e\mu_j\gamma_j^{\frac{1}{2}}K_2(\gamma_j), \tag{4}$$

$$\gamma_j=1.77\mu_j^2H^2, \tag{5}$$

where n_j is the concentration of the electrons and holes and μ_j is the lattice mobility of the electrons and holes in zero magnetic field. All electrical quantities are in electromagnetic units. The K's can be expressed in terms of tabulated functions[4] as follows:

$$K_1(\gamma)=1-\gamma+\gamma^2e^\gamma\{-\mathrm{Ei}(-\gamma)\}, \tag{6}$$

$$K_2(\gamma)=\tfrac{1}{2}\pi^{\frac{1}{2}}(1-2\gamma)+\pi\gamma^{\frac{1}{2}}e^\gamma[1-\Phi(\gamma^{\frac{1}{2}})]. \tag{7}$$

For large values of γ, the asymptotic expressions are

$$K_1(\gamma)=\frac{2!}{\gamma}-\frac{3!}{\gamma^2}+\frac{4!}{\gamma^3}-\cdots, \tag{8}$$

$$K_2(\gamma)=\pi^{\frac{1}{2}}\left(\frac{1\cdot3}{2^2\gamma}-\frac{1\cdot3\cdot5}{2^3\gamma^2}+\frac{1\cdot3\cdot5\cdot7}{2^4\gamma^3}-\cdots\right). \tag{9}$$

For $H=0$,

$$A_j^0=n_j e\mu_j, \tag{10}$$

and

$$\frac{\sigma_0-\sigma_H}{\sigma_0}=\frac{\Delta\rho}{\rho_H}=1-\frac{A_1+A_2}{A_1^0+A_2^0}=\frac{(B_1-B_2)^2}{(A_1+A_2)(A_1^0+A_2^0)}. \tag{11}$$

Substituting Eqs. (3), (4), and (10), in Eq. (11), and

[1] V. A. Johnson and W. J. Whitesell, Phys. Rev. **89**, 941 (1953).
[2] O. Madelung, Z. Naturforsch. **8a**, 791 (1953).
[3] J. Appel, Z. Naturforsch. **9a**, 167 (1954).
[4] See Jahnke-Emde, *Tables of Functions* (Dover Publications, New York, 1945).

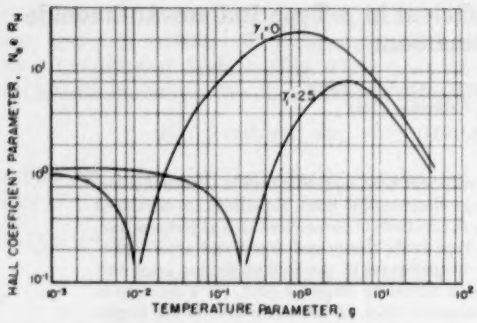

FIG. 1. Hall coefficient parameter $N_a e R_H$ as a function of the temperature parameter g for $c=85$, $\gamma_1=0$, 25.

defining $g\equiv n_1\mu_1/n_2\mu_2$, $c\equiv\mu_1/\mu_2$, one obtains

$$\frac{\Delta\rho}{\rho_H}=1-\frac{gK_1(\gamma_1)+K_1(\gamma_2)}{g+1}\cdot\frac{\gamma_2\{gcK_2(\gamma_1)-K_2(\gamma_2)\}^2}{(g+1)\{gK_1(\gamma_1)+K_1(\gamma_2)\}}, \tag{12}$$

and

$$R_H=-3\pi^{\frac{1}{2}}/4n_2e \cdot\frac{\{gcK_2(\gamma_1)-K_2(\gamma_2)\}}{\{gK_1(\gamma_1)+K_1(\gamma_2)\}^2+\gamma_2\{gcK_2(\gamma_1)-K_2(\gamma_2)\}^2}. \tag{13}$$

For a p-type semiconductor with an acceptor density N_a, assumed completely ionized, one has

$$n_2=n_1+N_a, \tag{14}$$

$$n_1n_2\equiv n_i^2=4\left[2\pi(m_1m_2)^{\frac{1}{2}}kT/h^2\right]^3e^{-W/kT}. \tag{15}$$

Hence,

$$g=c\left\{\frac{-N_a+(N_a^2+4n_i^2)^{\frac{1}{2}}}{+N_a+(N_a^2+4n_i^2)^{\frac{1}{2}}}\right\}. \tag{16}$$

Also, Eq. (13) may be written

$$R_H=-\frac{3\pi}{8N_ae}\cdot\frac{2}{\pi^{\frac{1}{2}}} \cdot\frac{\{gcK_2(\gamma_1)-K_2(\gamma_2)\}\{1-g/c\}}{\{gK_1(\gamma_1)+K_1(\gamma_2)\}^2+\gamma_2\{gcK_2(\gamma_1)-K_2(\gamma_2)\}^2}. \tag{17}$$

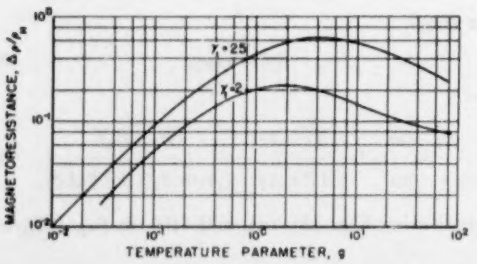

FIG. 2. Magnetoresistance $\Delta\rho/\rho_H$ as a function of the temperature parameter g for $c=85$, $\gamma_1=2$, 25.

The preceding relationships are sufficient to determine $\Delta\rho/\rho_H$ and R_H as functions of temperature, impurity concentration, and magnetic-field strength for those cases where the conditions previously enunciated are satisfied.

DISCUSSION OF THE THEORETICAL RESULTS

Assuming for a particular specimen of germanium or InSb that the lattice mobility ratio and the density of ionized impurities can be considered constant throughout the temperature interval investigated, then the Hall coefficient and the magnetoresistance are functions of only two independent variables, namely, g and γ_1. Since g is a monotonic function of temperature, plots of $\Delta\rho/\rho_H$ or R_H as functions of g for various values of γ_1 reveal the essential temperature-dependent characteristics of the magnetoresistance and Hall effects. A representation of this type gives a good portrayal of the temperature dependence of the effects since g varies much more rapidly over the temperature interval of interest than does γ_1.

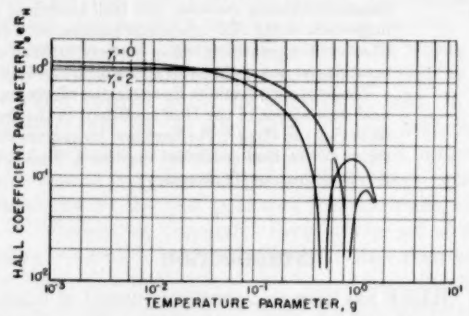

FIG. 3. Hall coefficient parameter as a function of the temperature parameter g for $c=2$, $\gamma_1=0$, 2.

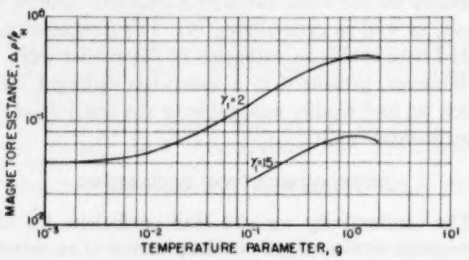

FIG. 4. Magnetoresistance $\Delta\rho/\rho_H$ as a function of the temperature parameter g for $c=2$, $\gamma_1=0.15$, 2.

Such a plot for the Hall effect is shown in Fig. 1. A mobility ratio value 85, representative of InSb,[5] was used. It is readily seen that (1) the Hall coefficient maxima shift to larger values of g (thus to higher temperatures) with increasing magnetic-field strength, (2) the magnitudes of the Hall coefficient maxima decrease

[5] M. Tannenbaum and J. P. Maita, Phys. Rev. **91**, 1009 (1953).

with increasing field, (3) the temperature at which the Hall coefficient crossover occurs increases with increasing field, (4) the variation in Hall coefficient with field in the extrinsic and intrinsic regions are small. A similar presentation for magnetoresistance is shown in Fig. 2. The following points are obvious: (1) the magnetoresistance maxima shift to higher temperature with increasing field, (2) the magnetoresistance maxima occur at approximately the same temperature as the Hall coefficient maxima, (3) at a given temperature, the magnetoresistance increases with magnetic field, (4) as $g \to 0$, corresponding to the extrinsic region, all carrier-density parameters vanish, leaving Eq. (12) a function only of μ_2. This suggests the occurrence of a minimum at low temperatures in those specimens where lattice scattering still predominates in the extrinsic region so that μ_2 rises with decreasing temperature.

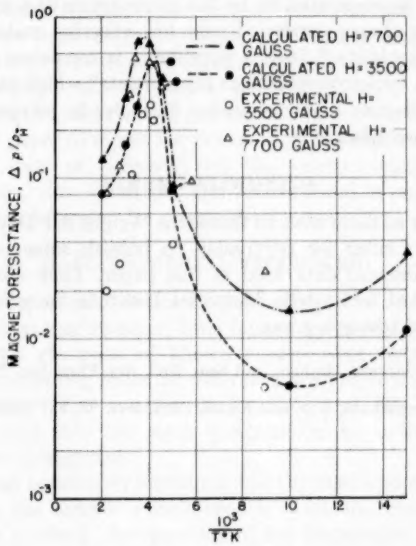

FIG. 5. Calculated and experimental Hall coefficient of a p-type InSb specimen as a function of inverse absolute temperature.

Figures 3 and 4 present similar curves computed for a mobility ratio characteristic of germanium. There is little difference in shape between these curves and the InSb curves. Consequently, this treatment indicates the variation of resistivity and Hall coefficient with magnetic field to be qualitatively the same for the two materials.

COMPARISON OF THEORY AND EXPERIMENT

The magnetoresistance[6] and Hall coefficient[7] of an InSb specimen with 2×10^{16} ionized impurities has been measured as a function of temperature for two magnetic-field strengths. In Fig. 5 and Fig. 6, these experimental data are shown, along with the calculated[8] values. It is obvious that the theory describes the essential behavior of $\Delta\rho/\rho_H$ and R_H as functions of temperature. As to actual magnitudes, however, discrepancies do exist. At the lower temperatures, this might, in part, be accounted for by impurity scattering. At the higher temperatures, there are indications that degeneracy is

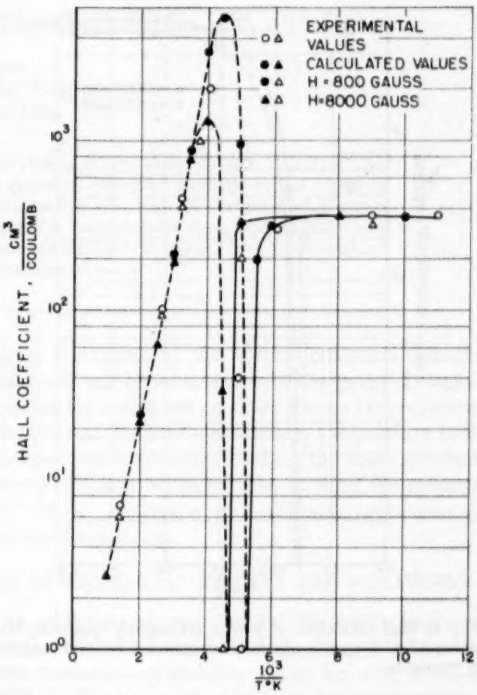

FIG. 6. Calculated and experimental magnetoresistance of a p-type InSb specimen as a function of inverse absolute temperature.

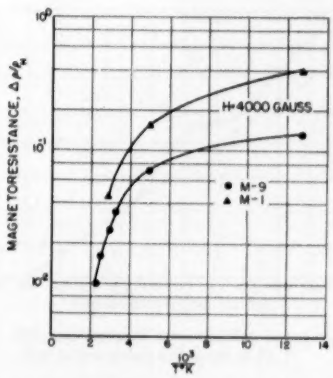

FIG. 7. Magnetoresistance of two p-type germanium specimens, $M-1$ ($\rho_{300°K}=55$ ohm-cm) and $M-9$ ($\rho_{300°K}=2.2$ ohm-cm), as a function of inverse absolute temperature.

[6] Harman, Willardson, and Beer, Phys. Rev. **93**, 912 (1954).
[7] Willardson, Beer, and Middleton, Phys. Rev. **93**, 912 (1954).

[8] The values of n_i^2 and of lattice mobilities used in the calculations are given in reference 5.

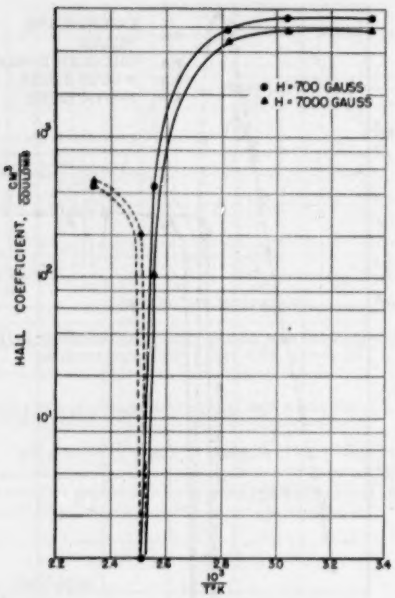

FIG. 8. Hall coefficient of p-type germanium specimen $M-9$ as a function of inverse absolute temperature for two magnetic-field strengths.

significant[9] even in p-type InSb. Finally, there is also the possibility that the mobility ratio might vary over the relatively large temperature over which the data were taken.

The results of measurements of the transverse magnetoresistance as a function of temperature in two germanium specimens are shown in Fig. 7. Unlike InSb and contrary to the theoretical predications, no magnetoresistance maxima were observed in the vicinity of the Hall coefficient maxima. A second salient feature is shown in Fig. 8, where it is seen that the variation of the Hall coefficient with magnetic field in the temperature region of the crossover is in the opposite direction to that predicted by the theory and to that observed in InSb. This radical disagreement with the theory for p-type germanium is basic and does not appear explicable by considerations of such obvious effects as impurity scattering, degeneracy, temperature dependence of mobility ratio, etc. It appears that a more fundamental modification of the theory is necessary.

Our recent investigations have shown that this anomalous behavior in p-type germanium can effectively be accounted for by the introduction of a second p-type charge carrier of very low effective mass and large mobility.[10] Such a hypothesis is consistent with recent cyclotron resonance experiments[11] which yielded two effective mass values for the holes in p-type germanium specimens.

ACKNOWLEDGMENTS

The authors wish to thank the Wright Air Development Center for permission to publish some of the experimental data used in this paper. They are also indebted to Battelle Memorial Institute for a fundamental research grant.

[9] Beer, Willardson, and Middleton, Phys. Rev. **93**, 912 (1954).

[10] Willardson, Harman, and Beer, Bull. Am. Phys. Soc. **29**, 4, 9 (1954).

[11] Dresselhaus, Kip, and Kittel, Phys. Rev. **92**, 827 (1953).

Ionization Probability Curves Near Threshold for Zn, Cd, and Hg

W. M. HICKAM
Westinghouse Research Laboratories, East Pittsburgh, Pennsylvania
(Received April 26, 1954)

The ionization probability curves near threshold of the closely related elements zinc, cadmium, and mercury have been obtained using nearly monoenergetic electrons. Structure observed in the curves is interpreted as the result of autoionization of states of the atom which arise from the excitation of a single inner shell electron. In the analysis of the results, it is necessary to consider both the optically allowed and forbidden excited states. The energy levels of the optically allowed states of this system have been identified by Beutler, but the locations of the optically forbidden states are unknown.

I. INTRODUCTION

SINCE the work of Lawrence,[1] many investigations have been made of the structure in the ionization probability curve for Hg by electron impact.[2] Of these results, the most precise measurements are probably reported by Nottingham.[3] Using a magnetic analyzer to provide electrons of a narrow energy spread, he obtained the ionization probability curve near threshold for mercury in great detail. It is the purpose of this paper to report the curves obtained within some three volts of threshold for the closely associated elements, zinc, cadmium, and mercury and to suggest an explanation for the observed structure.

II. EXPERIMENTAL PROCEDURE

The experiment was carried out using a 90° sectored type mass spectrometer. Ions formed by nearly monoenergetic electrons of known energy were obtained by the retarding potential difference method previously described.[4] The samples of Zn, Cd, and Hg were introduced into the mass spectrometer by a simple furnace arrangement.

It was possible to introduce into the mass spectrometer a gas sample simultaneously with the metallic vapors to check the operation of the instrument. The ability to reproduce the previously reported curves of krypton and xenon[5] was considered an indication of satisfactory performance. Mercury could be introduced simultaneously with either cadmium or zinc for direct comparison of the curves under similar conditions. The relative absence of any structure in the mercury curve at electron energies which resulted in pronounced structure in the cadmium and zinc curves is further evidence that the reported structure is truly associated with the ionization probability and is not instrumental.

Measurements of the mercury pressure using an ion gauge located outside the ionization chamber indicated that the mercury pressure in the ionization chamber was approximately 10^{-5} mm Hg. Since the vapor pressure of zinc and cadmium was appreciable only in the region of the heated ionization chamber, these could not be measured with the gauge. However, assuming the ionization cross section for these elements to be the same as that for mercury, the pressure in the ionization chamber determined by the mass spectrometer was of this same magnitude. At these low pressures only single electron-atom collision processes are considered significant.

III. EXPERIMENTAL RESULTS AND DISCUSSION

We shall present and discuss the results beginning with the simplest case, that of Zn. The initial portion of the ionization probability curve for zinc is shown in Fig. 1. The curve rises linearly for approximately 1.4 ev. Pronounced structure is then observed over a region of one electron volt. This is followed by an approximately linear rise. The voltage scale on this and other curves to be presented was adjusted so that the measured appearance potential agreed with the spectroscopic ionization potential.[6] The necessary adjustment was 0.2 volt or less.

The curve for zinc is interpreted in a similar manner to that suggested in previous work.[5,7,8] There it was possible to attribute the deviations from linearity in

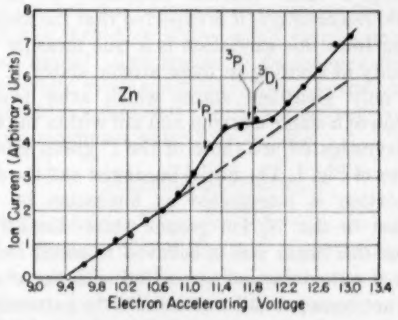

FIG. 1. Relative ionization probability curve for Zn. The states noted are those of Zn I[6].

[1] E. O. Lawrence, Phys. Rev. **28**, 947 (1926).
[2] O. M. White, Proc. Phys. Soc. (London) **66**, 641 (1953).
[3] W. B. Nottingham, Phys. Rev. **55**, 203 (1939).
[4] Fox, Hickam, Kjeldaas, and Grove, Phys. Rev. **84**, 859 (1951).
[5] Fox, Hickam, and Kjeldaas, Phys. Rev. **89**, 555 (1953).
[6] Atomic Energy Levels, National Bureau of Standards Circular 467 (1950), Vol. 2, and Landolt-Börnstein, *Zahlenwerte und Funktionen* (Springer-Verlag, Berlin, 1950), Vol. 1. The conversion factor used is 8066.8 cm^{-1} per volt from J. W. M. Du Mond and E. R. Cohen, Phys. Rev. **82**, 555 (1951).
[7] Hickam, Fox, and Kjeldaas, Phys. Rev. **90**, 386 (1953).
[8] Kjeldaas, Hickam, and Fox, Phys. Rev. **90**, 386 (1953).

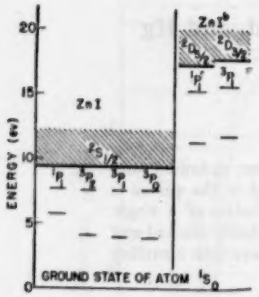

FIG. 2. Simplified energy level diagram for zinc atom. The states arise from the excitation of either a single valence electron (Zn I) or a single inner (d) shell electron (Zn I^b).

the ionization probability curves near threshold to the presence of excited states of either the atom or the ion. Excitation to such states may introduce a mechanism for ionization in addition to direct excitation to the ion ground state. When this occurs, one must consider the ionization probability curve as the summation of a number of ionization processes, each of which has a definite threshold energy.

We shall now consider the energy levels of zinc as a basis for such an interpretation. A simplified energy level diagram for the zinc atom is shown in Fig. 2. The electronic configuration of the $^1S_0$ ground state is $3d^{10}4s^2$. The states associated with Zn I arise from the excitation of a single valence (s) electron. The states all converge to the $^2S_{\frac{1}{2}}$ state of the ion at 9.39 ev. The Zn I^b states are those identified by Beutler[9] from absorption spectroscopy as arising from the excitation of a single inner (d) shell electron. An example of this type transition is $3d^{10}4s^2\ {}^1S_0 \rightarrow 3d^9 4s^2 4p\ {}^1P_1$. These states are observed only in absorption spectra because of autoionization, i.e., atoms excited to such levels undergo radiationless transitions to the ground state of the ion with the ejection of an electron. The absorption lines resulting from optical excitation to some of the states of Zn I^b are very diffuse (half-width $\sim$0.05 ev) indicating a short lifetime compared to radiative lifetimes. Accordingly, it is expected that the ionization resulting from this excitation is a true measure of the probability of exciting to these atomic states.

The only identified states which arise from the excitation of a single electron and fall within the energy range investigated are those of the I^b group shown on the curve of Fig. 1. The initial linear rise and the dashed extrapolation is interpreted as ionization by direct excitation to the $^2S_{\frac{1}{2}}$ ion ground state. Ionization in excess of this linear rise is believed to result from the process of autoionization associated with the I^b states. It does not seem possible to attribute the autoionization threshold to the $^1P_1$ state which is located approximately 0.5 volt higher. We propose that this threshold indicates the presence of states which are not observed in absorption spectroscopy because of forbidden transitions. In particular, to be included in the optically forbidden states are those of J value 0 and 2. Since the autoionization curve may be a composite of excitation curves associated with several states, it is difficult to obtain much information on the excitation for the individual states. However, the curve does show that a maximum excitation probability must occur for one or more of the states close to threshold. The shape of excitation curves associated with different states will be discussed later.

The discussion of the zinc ionization probability curve is equally applicable to cadmium (Fig. 3). The structural details of the autoionization curve can be related in an identical manner to the Cd I^b states identified by Beutler[10] and here also an additional state is required to explain the autoionization threshold.[10] Only the energy displacement of the structure from the ionization threshold is significantly different in the two curves.

In the case of mercury the relative location of the I^b states[11] with respect to the $^2S_{\frac{1}{2}}$ ground state of the ion should be particularly noted (Fig. 4). The lowest-lying $^1P_1$ state of this group falls below the $^2S_{\frac{1}{2}}$ state and so is not capable of contributing to the ionization. Furthermore, the lowest-lying $^3P_1$ state is only some 0.6 ev above the $^2S_{\frac{1}{2}}$ ion ground state.

The ionization probability curve for mercury (Fig. 5) is in satisfactory agreement with that of Nottingham[3] and can be analyzed in an identical fashion to that just discussed. The pronounced structure near threshold is interpreted as autoionization superimposed on a linearly rising excitation curve associated with the $^2S_{\frac{1}{2}}$ ion ground state. In this particular case there is no interference from the $^1P_1$ state and so the pronounced maximum is believed to be associated with the optically forbidden levels of the I^b group. The experimental data indicate that the state in question is located very close to the $^2S_{\frac{1}{2}}$ ion ground state. The location of the $^3D_1$ state on a linear portion of the curve suggests that the probability of exciting to this particular state is relatively small.

The interpretation of the structure of the ionization probability curves given above requires that the excita-

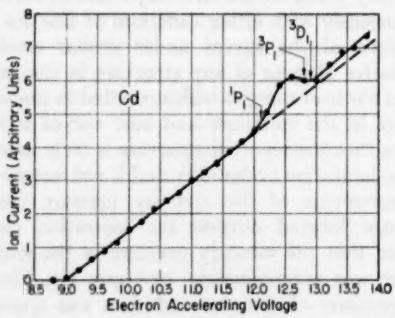

FIG. 3. Relative ionization probability curve for Cd. The states noted are those of Cd I^b.

[9] H. Beutler, Z. Physik **87**, 176 (1933).

[10] H. Beutler, Z. Physik **87**, 19 (1933).

[11] H. Beutler, Z. Physik **86**, 710 (1933).

tion function for the optically forbidden state has a maximum within approximately one electron volt of threshold. Investigations on the cross section for excitation of spectral lines by electron impact have been carried out for zinc, cadmium, and mercury by a number of workers.[12] In general, the excitation function associated with the lowest-lying partially forbidden $^3P_1$ state of the normal spectrum reveals a pronounced maximum near onset while the maximum observed for the optically allowed $^1P_1$ state is many electron volts above threshold. These results are in agreement with the theoretical calculations of Penny[13] on mercury, which in addition show a maximum near threshold for the optically forbidden $^3P_0$ and $^3P_2$ states.

The interpretations of Lawrence[1] and Nottingham[3] of the structure in the mercury curve are difficult to extend to the curves for zinc and cadmium. Lawrence inferred that the probability of exciting any type of atomic transition involving ionization by a slow electron reached a maximum when the electron had just enough energy to excite the process. Nottingham based his interpretation on the shapes of the excitation curves of the lowest-lying $^1P_1$ and $^3P_1$ states of Hg I which have been discussed. He suggested that the observed ionization probability curve is the sum of two curves. The peak at 10.8 volts was to be associated with the triplet system and the broad maximum at 32 volts was characteristic of the singlet mode of ionization. Since the excitation curves of the $^3P_1$ state for zinc and cadmium resemble closely that of mercury, Nottingham's explanation implies that such structure would appear within one volt of threshold in the ionization probability curve of these elements.

Another interpretation considered was that the structure resulted from states[6] associated with the excitation of both valence electrons. Since these states

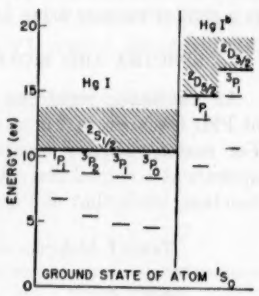

FIG. 4. Simplified energy level diagram for mercury atom. The states arise from the excitation of either a single valence electron (Hg I) or a single inner (d) shell electron (Hg I^b).

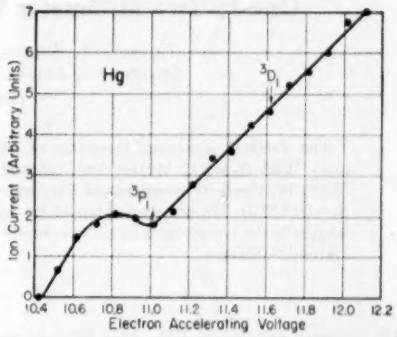

FIG. 5. Relative ionization probability curve for Hg. The states noted are those of Hg I^b.

are identified by emission spectra, it is doubtful that they would contribute significantly by the autoionization process. In the experimental results this is evidenced by the fact that these states fall on a linear portion of the curves and reveal no pronounced peaks.

Of the interpretations advanced, it appears that the one proposed in this paper is most consistent in explaining the observed structure.

SUMMARY

Zinc, cadmium, and mercury ionization probability curves near threshold have been obtained using nearly monoenergetic electrons. As in a number of previous gases, it has been shown that where ionization by excitation to the ionic ground state is the only process which can occur, a linear threshold law is observed. Structure in the three curves is closely correlated with the optically allowed states of the atom arising from the excitation of a single inner (d) shell electron. The states contribute by the process of autoionization. In order to account for details of the observed structure by this process, it is necessary to postulate the presence of optically forbidden states which can be excited by electron impact. This results in the proposed location of a new state which most likely has a J value of 0 or 2 and further suggests that the excitation to such a state reaches a maximum very close to onset.

ACKNOWLEDGMENT

I wish to acknowledge the help and advice of my many colleagues in the Physics Department during these investigations. In particular, I wish to thank T. Kjeldaas, Jr., A. V. Phelps, M. A. Biondi, and R. E. Fox for their valuable counsel in the interpretation of the results and critical review of the manuscript.

[12] H. S. W. Massey and E. H. S. Burhop, *Electronic and Ionic Impact Phenomena* (Oxford University Press, London, 1952), p. 55.

[13] W. G. Penny, Phys. Rev. **39**, 467 (1932).

One-to-Two Millimeter Wave Spectroscopy. V. PH_3 and PD_3†

CHARLES A. BURRUS,* ALBERT JACHE, AND WALTER GORDY
Department of Physics, Duke University, Durham, North Carolina

(Received April 19, 1954)

The $J=0\rightarrow1$ rotational transition of PH_3 has been measured at $\nu_0=266\,944.0\pm1.0$ Mc/sec ($\lambda=1.12$ mm). With $D_J=3.15$ Mc/sec from infrared spectroscopy, this measurement yields $B_0=133\,478.3$ Mc/sec. Similarly, the $0\rightarrow1$ transition of PD_3 was measured at $\nu_0=138\,937.98\pm0.30$ Mc/sec ($\lambda=2.16$ mm) and $B_0=69\,470.41$ Mc/sec was obtained by using $D_J=0.71$ Mc/sec from infrared spectroscopy. The bond lengths in the two isotopic forms were found to be slightly different with $d_{PH}=1.4206\pm0.005$ A and $d_{PD}=1.4166\pm0.005$ A.

THE present paper on PH_3 and PD_3 is one of a series[1] reporting measurements in the newly opened one-to-two millimeter wave region on molecules which do not have rotational transitions occuring at the lower microwave frequencies. The first rotational line ($J=0\rightarrow1$ transition) of PH_3, observed in the present work, occurs at 1.12-mm wavelength, and thus the second (the $J=1\rightarrow2$ not yet measured) should fall at 0.556 mm (556 microns) in what can be appropriately called the infrared region.

As early as 1933 pure rotational lines of PH_3 down to the $J=9\rightarrow10$ transition were measured by Wright and Randall[2] with purely infrared-optical methods. More recently these measurements have been extended by Stroup, Oetjen, and Bell[3] to the $J=5\rightarrow6$ transition. Thus the rotational spectrum of PH_3 has now been measured by both microwave-electronic and infrared-optical methods. Although it has not yet been achieved, it seems probable that soon the same transition can be measured by both methods. It is an evidence of careful work by Wright and Randall that the $0\rightarrow1$ transition was found to occur within 220 Mc/sec of the frequency predicted from their infrared measurements made some 21 years ago.

The mixed isotopic forms of phosphine PHD_2 and PH_2D are asymmetric rotors, and these have rotational transitions occurring in the lower-frequency microwave region. Certain of these have been investigated by Loomis and Strandberg[4] and by Sirvetz and Weston.[5] The infrared rotational vibration spectrum of phosphine has been studied by Fung and Barker[6] and by McConaghie and Nielsen.[7]

EXPERIMENTAL ASPECTS

The millimeter wave components employed are those already described by King and Gordy[1] (Parts I and IV of this series). For PD_3 measurements the cell was of K-band guide of one meter length with electroformed tapered sections to match to the smaller guide of the multiplier and detector. For PH_3 a cell of G-band guide of length 15 centimeters and total volume of 0.2 cubic centimeter was employed.

Lines of both PH_3 and PD_3 were observed on the cathode-ray scope with a simple video spectrometer having 60-cps sweep and a P amplifier of 5 kc/sec band width. However, it was found that an improvement in signal-to-noise ratio of about 25 times that of the video signal could be obtained with automatic recording with a phase lock-in detector as described elsewhere.[1] In the present work the receiver was tuned to the second harmonic of the modulation frequency, so that for sufficiently small modulation amplitudes the signal appears as a second derivative of the actual line shape function. The line frequencies were measured in the usual manner with a frequency standard monitored by Station WWV. The PH_3 was prepared by the action of H_2O on Mg_3P_2, while the PD_3 was made in a similar manner using D_2O instead of H_2O.

SPECTRA AND MOLECULAR STRUCTURE

An automatic recording of the $J=0\rightarrow1$ transition of PH_3 is shown in Fig. 1 and that of PD_3 in Fig. 2. For reasons already mentioned, the signal of Fig. 1 appears as a second derivative of the actual line shape function, while that of Fig. 2, because of the different

TABLE I. Molecular constants of phosphine.

PD_3	PH_3
$\nu_0(J=0\rightarrow1)=138\,937.98\pm0.30$ Mc/sec	$\nu_0(J=0\rightarrow1)=266\,944.0\pm1.0$ Mc/sec
$B_0=69\,470.41$ Mc/sec	$B_0=133\,478.3$ Mc/sec
$D_J=0.710$ Mc/sec (from infrared data[a])	$D_J=3.15$ Mc/sec (from infrared data[a])
$I_b=12.0758_0\times10^{-40}$ g cm²	$I_b=6.28499_7\times10^{-40}$ g cm²
$\angle DPD=93°10'$ (assumed)	$\angle HPH=93°27'$ (assumed)
$d_{PD}=1.4166\pm0.005$A	$d_{PH}=1.4206\pm0.005$A

[a] See reference 3.

† This research was supported by the U. S. Air Force under a contract monitored by the Office of Scientific Research, Air Research and Development Command.

* Shell Company Fellow.

[1] W. C. King and W. Gordy, Phys Rev. **90**, 319 (1953); **93**, 407 (1954). Charles A. Burrus and W. Gordy, Phys. Rev. **92**, 274 (1953); **92**, 1437 (1953). W. Gordy and Charles A. Burrus, Phys. Rev. **93**, 419 (1954).

[2] N. Wright and H. M. Randall, Phys. Rev. **44**, 391 (1933).

[3] Stroup, Oetjen, and Bell, J. Opt. Soc. Am. **43**, 1096 (1953).

[4] C. C. Loomis and M. W. P. Strandberg, Phys. Rev. **81**, 798 (1951).

[5] M. H. Sirvetz and R. E. Weston, Jr., J. Chem. Phys. **21**, 898 (1953).

[6] L. W. Fung and E. F. Barker, Phys. Rev. **45**, 238 (1934).

[7] V. M. McConaghie and H. H. Nielsen, J. Chem. Phys. **21**, 1836 (1953).

modulation employed, represents approximately a first derivative of the line shape. The line frequencies and other constants are listed in Table I.

The rotational lines of a symmetric top molecule are given by the formula

$$\nu_0 = 2B_0(J+1) - 2D_{JK}(J+1)K^2 - 4D_J(J+1)^3,$$

where J represents the lower rotational quantum number of the transition. Since only the 0→1 transitions were observed, D_{JK} and D_J cannot be obtained from the present measurements. In the infrared region, where the second term on the right becomes large, it is possible to obtain D_J with sufficient accuracy to correct for the small stretching effects on the 0→1 frequency to the degree of accuracy of our microwave measurements. Stroup, Oetjen, and Bell[3] give for PH_3, $4D_J = 421 \times 10^{-6}$ cm^{-1} and for PD_3, $4D_J = 95 \times 10^{-6}$. When converted to Mc/sec, these become 12.6 and 2.85, respectively, and with our 0→1 frequencies yield the B_0 values listed in Table I.

Because the zero-point vibration causes the effective ground-state values of the bond angles and bond lengths to be slightly different for the different isotopic forms, a simultaneous solution of the isotopic equation for PH_3 and PD_3 gives unreliable values for these parameters. For this reason we use information obtained by others on mixed isotopic forms in combination with our data to deduce values of the PH and PD distances. Since the mixed isotopic forms PH_2D and PHD_2 are asymmetric tops, more than one independent spectral constant can be obtained from microwave measurements for each form. Hence, a bond angle and a bond-length value for each species can be calculated if it is assumed that the PH and PD distances and the angle between the three bonds in each species are the same. Such solutions have been obtained by Sirvetz and Weston.[5] These solutions are shown in Table II. They indicate that the PH and PD distances, as well as the HPH and DPD angles, are measurably different. Although the values given by Sirvetz and Weston are averaged values for the mixed forms, we can assume that those for PH_2D are nearer to the correct values for PH_3 than are those of PHD_2, and similarly those obtained for PHD_2 are nearer to the correct values for PD_3 than are those of PH_2D. Furthermore, it is evident that the percentage variation for the bond angle in passing from one species to the other is much less than the percentage variation in the distances. For these reasons we assume that a change from PH_2D to PH_3 would cause the same increase in the effective angle as that of PHD_2 to PH_2D, and likewise that the change from PD_3 to PD_2H would cause the same increase as that from PD_2H to PH_2D. Thus are the angles listed for PH_3 and PD_3 in Table II obtained. With these assumed angles we calculated the PH and PD distances given in the same table. They are seen to differ by 0.004 A. The error limits given for the PH and PD lengths are based on the assumption that the total difference in the bond angles of PH_2D and PHD_2 gives the maximum errors in the "guessed" bond angles for PH_3 and PD_3.

Because the $K=0$ line is not split, no information could be obtained about the interesting possibility of low-frequency inversion splitting in PH_3. We are hoping that further development of our generators and detectors may soon make it possible to observe the second rotational transition of PH_3 at 0.55-mm wavelength for which the $K=1$ line should be split

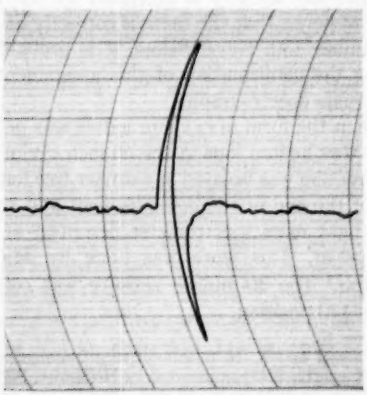

FIG. 1. Recorder tracing of the $J=0\rightarrow1$ transition of PH_3 at 1.12-mm wavelength.

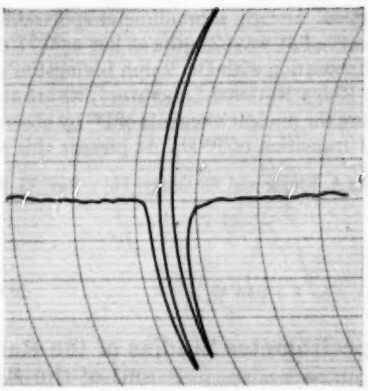

FIG. 2. Recorder tracing of the $J=0\rightarrow1$ transition of PD_3 at 2.16-mm wavelength.

TABLE II. Molecular dimensions of phosphine.

	Bond angle	Bond length	Reference
PH_2D	93°21.6′	1.4177A	Sirvetz and Weston[a]
PD_2H	93°15.4′	1.4116A	Sirvetz and Weston[a]
PH_3	93°27′±6′ (assumed)	1.4206±0.005A	Present work
PD_3	93°10′±6′ (assumed)	1.4166±0.005A	Present work

[a] See reference 5.

by inversion. Already submillimeter spectral lines have been observed at wavelengths as low as 0.77 mm.[8]

In collaboration with Dr. Ralph Livingston's group of the Oak Ridge National Laboratory, we are attempting to measure the nuclear moments of P^{32} by observation on the 0→1 transition of $P^{32}D_3$. At present this rotational line is being used as an analytical indicator by Dr. Livingston and Dr. Benjamin in the development of the microchemistry for the radioactive compound. The advantages of the shorter millimeter wave region for the study of moments of radioactive nuclei is obvious from the small cell volume of 0.2 cc employed for observations on PH_3 in the present work.

[8] Charles A. Burrus and W. Gordy, Phys. Rev. **93**, 897 (1954).

PHYSICAL REVIEW VOLUME 95, NUMBER 3 AUGUST 1, 1954

Spectrometer Studies of the Radiations of Neutron Deficient Isotopes of Cesium and of the *E*3 Isomers, Xe^{127m} and Xe^{125m}†

HIRDAYA B. MATHUR* AND EARL K. HYDE
Radiation Laboratory and Department of Chemistry, University of California, Berkeley, California

(Received February 4, 1954; revised manuscript received April 27, 1954)

Cesium isotopes produced by $I^{127}(\alpha,xn)$ type reactions in the 60-inch and 184-inch cyclotrons were studied in Geiger counters, a mass spectrometer, beta-ray spectrometers, a sodium iodide crystal scintillation spectrometer, and a gamma-gamma coincidence spectrometer. The mass assignment of 30-minute Cs^{130} was verified. The 6.25-hour Cs^{127} was shown to decay predominantly by electron capture but also by the emission of positrons of 1.063-Mev and 0.685-Mev energy. Prominent gamma rays of 125 and 406 kev are observed. Cs^{127} exhibits branching decay to 75-second Xe^{127m} in about one disintegration in 10^4. This isomer was isolated and studied in a scintillation spectrometer. *E*3 radiation of 175 kev connecting $h_{11/2}$ and $d_{3/2}$ levels is followed by 125-kev *M*1 radiation corresponding to a $d_{3/2}-d_{3/2}$ transition to the ground state. Forty-five minute Cs^{125} is shown to decay predominantly by electron capture and also by the emission of positrons of 2.05-Mev energy. Other lower energy positron groups are present. A prominent gamma ray of 112 kev is observed. In one disintegration in about 10^6, Cs^{125} decays to a 55-second Xe^{125m}. This isomer emits gamma rays of 75 and 110 kev which are believed to be *E*3 $h_{11/2}-d_{3/2}$ and *M*1 $d_{3/2}-d_{3/2}$ transitions, respectively. An incomplete study of Cs^{123} shows it to be a 6-minute positron emitter.

I. INTRODUCTION

THIS report concerns a study of some neutron-deficient isotopes of cesium prepared by bombardment of iodine with high-energy helium ions. The principal emphasis is on Cs^{127} and Cs^{125}, although some preliminary data on Cs^{123} and a confirmation of the mass assignment of Cs^{130} are also reported. The work on Cs^{127} represents a considerable extension of the previous studies of Fink, Reynolds, and Templeton,[1] while that on Cs^{125} and Cs^{123} represents completely new work. This report also describes a study of some short-lived isomers of Xe^{127} and Xe^{125} which appear in the decay of the cesium activities. The data on Xe^{127m} confirm and extend previous data on this isomer, while Xe^{125m} has not been reported before. Both isomers are probably of the *E*3 type.

The experimental results are presented and discussed first, following which a brief account is given of our chemical methods and of the various instruments used to study the radiations.

II. MASS ASSIGNMENT OF Cs^{130}

Following the preliminary studies of Risser and Smith[2] and of Fink, Reynolds, and Templeton[1] on a 30-minute cesium activity produced in bombardments of iodine with low-energy helium ions a careful study of the radiations emitted by this activity was carried out by Smith, Mitchell, and Caird.[3] There is little doubt that the activity is produced by the (α,n) reaction and hence that the mass is correctly assigned to mass number 130. Nevertheless, it is probably worth recording the confirmation of this assignment by the use of a mass spectrograph.

Iodine in the form of calcium iodide was bombarded with 20-Mev helium ions in the 60-inch cyclotron. The cesium fraction was isolated in a carrier-free form within 1 hour of the end of the bombardment and run in the time-of-flight mass spectrometer described at the end of the paper. This work was done by Michel and Templeton.[4] The 30-minute activity was collected in the mass-130 position.

† This work was carried out with the support of the U. S. Atomic Energy Commission.

* On leave of absence, Department of Chemistry, University of Delhi, Delhi, India.

[1] Fink, Reynolds, and Templeton, Phys. Rev. **77**, 614 (1950).

[2] J. R. Risser and R. N. Smith (private communication from K. Lark-Horowitz, 1948) as reported by Hollander, Perlman, and Seaborg, Revs. Modern Phys. **25**, 469 (1953).

[3] Smith, Mitchell, and Caird, Phys. Rev. **87**, 454 (1952).

[4] M. C. Michel and D. H. Templeton, Phys. Rev. **93**, 1422 (1954).

III. THE RADIATIONS OF Cs^{127} AND THE ISOMER, Xe^{127m}

Fink, Reynolds, and Templeton[1] reported Cs^{127} to be a positron activity with a half-life of 5.5 hours. The mass assignment was made by the identification of the 34-day Xe^{127} daughter. More recently Wapstra, Verster, and Boelhouwer[5] have studied the gamma rays of Cs^{127} by scintillation spectrometric methods and have reported gamma rays of 410±20 and 125±5 kev.[6]

In our experiments we noted that the cesium fraction of a calcium iodide target bombarded with 60-Mev helium ions in the 184-inch cyclotron was a mixture of 30-minute Cs^{130}, 6.25-hour Cs^{127}, and 31-hour Cs^{129}. Even immediately after bombardment the major activity was Cs^{127} and if the isolation of the cesium were delayed a few hours past the end of the bombardment more than 90 percent of the G-M activity was Cs^{127}.

The mass assignment was checked directly by a run in the time-of-flight mass spectrometer.[4] Decay curves

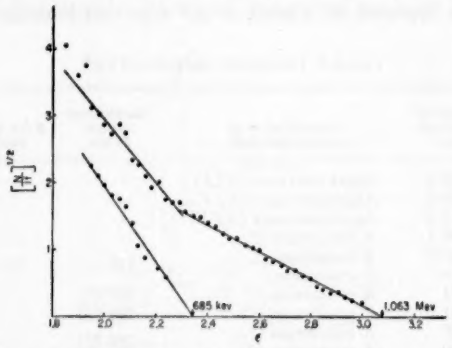

FIG. 1. Fermi-Kurie plot of high energy portion of Cs^{127} positron spectrum. Resolution of a second component after correction for conversion electrons is shown.

taken with a G-M counter using mass separated Cs^{127} showed no deviation from a half-life of 6.25±0.1 hours in more than 4 half-lives. This half-life is somewhat longer than that given by Fink *et al.*[1] Negligible 6.25-hour activity was collected at neighboring mass positions.

The positrons of Cs^{127} were studied in the beta-ray spectrometers briefly described at the end of this report. The runs were not made with mass-separated activity since sources of sufficient intensity could not be prepared. However, the presence of a small amount of Cs^{129} caused no difficulty in the interpretation of data taken on unseparated cesium fractions isolated a few hours after bombardment. Our best runs were obtained on the lens spectrometer. Figure 1 shows the Fermi-Kurie plot of the positron spectrum. The most energetic component has an energy of 1.063±0.010 Mev. The

[5] Wapstra, Verster, and Boelhouwer, Physica **19**, 138 (1953).

[6] A study of Cs^{127} and Cs^{129} has recently been carried out by Nijgh, Ornstein, Haaf, and Wapstra (private communication from A. H. Wapstra).

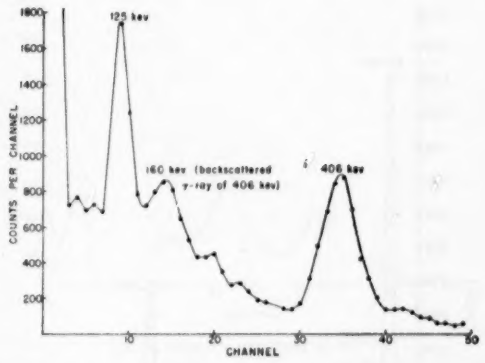

FIG. 2. Gamma spectrum of mass-separated Cs^{127} determined in scintillation spectrometer. Sample mounted on aluminum.

presence of numerous conversion electrons complicates the resolution of the second component and the value of 685 kev (378 kev lower in energy than the first component) is uncertain to perhaps 25 kev. This leaves unresolved the question whether the prominent 406-kev gamma ray observed in the scintillation spectrometer (see below) connects the Xe^{127} energy levels reached by these two positron groups.

Figures 2 and 3 show the gamma spectrum of Cs^{127} as determined in the scintillation spectrometer. There are prominent gamma rays of energies 125 and 406 kev as well as a large 30-kev peak of xenon x-radiation from the electron-capture (*EC*) decay of Cs^{127}. The small amount of 510-kev annihilation radiation by comparison to this peak indicates a low β^+/EC ratio ($<1/15$). The ratio of the 406- to 125-kev gamma radiation after correction for counting efficiency is about 8.

Figures 4 and 5 show the conversion electron spectrum of Cs^{127} as studied on the magnetic double-focusing spectrometer and the lens spectrometer, respectively. In Table I the energies of the electrons, the conversion shell and the energy of the corresponding gamma rays are given. The *K* and *L* lines of the 125- and 406-kev gamma rays are identified. Conversion

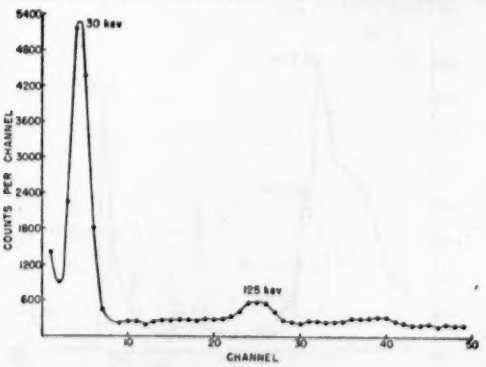

FIG. 3. Gamma spectrum of mass-separated Cs^{127} in 0–200-kev region showing prominent x-ray peak. Sample mounted on aluminum.

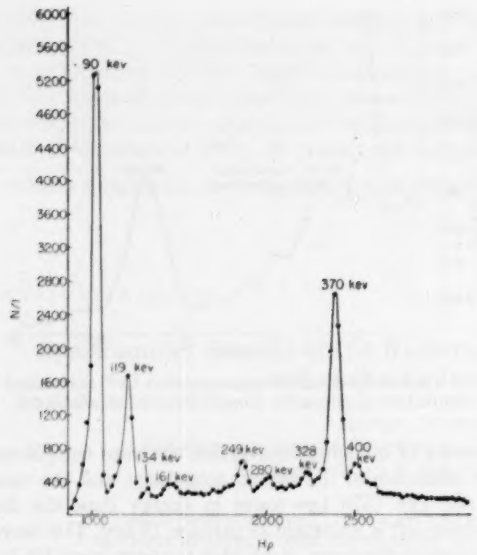

FIG. 4. Conversion electron spectrum of Cs^{127} in 80–450-kev region determined in lens spectrometer.

electrons of 3 or more gamma rays of lower intensity are present but the assignment of K and L lines is uncertain. Nothing further was learned about this group since their intensity was so low that no further data was obtained in the scintillation spectrometer or the coincidence spectrometer.

Mr. Frank Stephens has assisted us in carrying out gamma-gamma coincidence studies on our Cs^{127} preparations with the following results: the 125-kev radiation is not in coincidence with the 406-kev radiation. It is in coincidence with 30-kev x-radiation and with 440-kev gamma radiation. The intensity of this latter was low enough to explain why it was not seen in the straight gamma spectrum runs. The 406-kev radiation was not in coincidence with 125-kev radiation, but was in coincidence with 30-kev x-radiation. In coincidence experiments in which annihilation radiation was selected

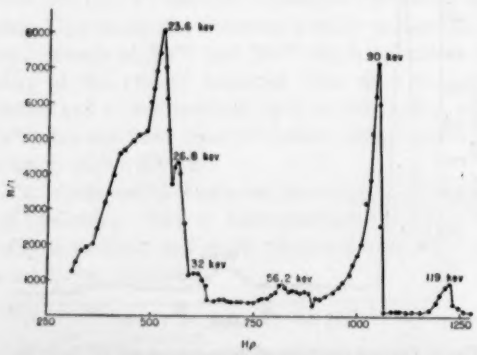

FIG. 5. Conversion electron spectrum of Cs^{127} in 0–120-kev region determined in double-focusing spectrometer.

by the gate crystal, coincidence peaks were observed at 125 and 406 kev.

These findings in connection with the information derived from the isomer studies to be described next were employed in the construction of the proposed decay scheme shown in Fig. 8. Following Wapstra,[7] we designate the ground state of Cs^{127} as $d_{5/2}$. We have included a 280-kev gamma ray in Fig. 8 to connect the $g_{7/2}$ and $d_{5/2}$ levels. The electron lines at 249 and 280 (see Table I and Fig. 4) may be the conversion electrons of this transition but the gamma intensity was too low for resolution from the scintillation spectrometer curves. In the coincidence studies the 125–280 kev coincidence to be expected from Fig. 8 was looked for, but unfortunately it was completely obscured by a large spurious 125–280 kev coincidence resulting from Compton scattering of the 406-kev gamma ray.

A number of preliminary experiments made it evident that the decay of Cs^{127} to the 75-second isomeric state of Xe^{127} was slight if it took place at all. This isomer had been reported by Creutz *et al.*[8] who had bombarded

TABLE I. Conversion electrons of Cs^{127}.

Energy of electrons in kev	Identification of conversion shell	Gamma-ray energy in kev	$K/(L+M)$ ratio
23.6	Auger electrons (KLL)	...	...
26.8	Auger electrons (KLY)	...	...
32.0	Auger electrons (KXY)	...	...
56.2	K conversion (?)	...	...
90.0	K conversion	125	7.9
119	L conversion		
134	K conversion (?)	169 (?)	...
161	K conversion (?)	196 (?)	...
249	K conversion (?)	285 (?)	...
280	L conversion (?)		
328	K conversion (?)	363 (?)	...
370	K conversion	406	6.3
400	L conversion		

iodide targets with 5–6 Mev protons to make Xe^{127} by the (p,n) reaction. In the volatile fraction removed from the target these workers had found two activities of 34 ± 2 days and 75 ± 1 seconds, respectively, and assigned both to Xe^{127}.

Studies of the conversion electrons emitted by the 75-second isomer using a permanent magnet spectrometer with photographic emulsion detection had shown 3 groups of 91.4, 140, and 170 kev, respectively. The first was interpreted as the K line of a 125-kev gamma ray and the last two as the K and L lines, respectively, of a 175-kev gamma ray. Xenon x-radiation resulting from the conversion of these gamma rays was also observed.

We were able to observe this isomer in the decay of Cs^{127} in the following manner. An active sample of carrier-free Cs^{127} was evaporated on a metal disk and

[7] A. H. Wapstra, Physica **19**, 671 (1953).
[8] Creutz, Delasasso, Sutton, White, and Barkas, Phys. Rev. **58**, 481 (1940).

placed in the depression of the slide of the apparatus diagrammed in Fig. 6. The greased tight-fitting slide was pushed in until the cesium sample was located in the 1.5-inch diameter chamber 0.25 inch deep drilled in from the top of the block. This chamber was covered with a 0.1-mil foil of aluminum to prevent loss of xenon. After a growth period of 3 minutes the Cs^{127} sample was withdrawn. Recoil daughter atoms of Xe^{127} and Xe^{127m} ejected from the cesium source plate during the growth period remained in the closed chamber and their radiations were examined with the sodium iodide crystal mounted immediately above the chamber. The whole assembly was housed in a 2-inch thick lead castle. The gamma spectrum was determined with the 50-channel analyzer making runs at about 1-minute intervals for 10 or 15 minutes.

Figure 7 shows the spectrum of the recoil activity obtained immediately after the growth period. Two gamma rays of 125- and 175-kev energy are to be noted as well as xenon K x-rays. Since the decay of all three peaks followed a 75-second decay line, we have little

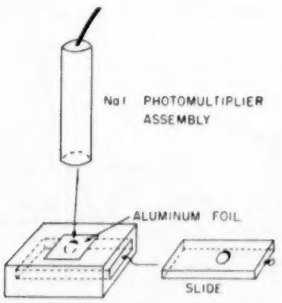

FIG. 6. Apparatus for the collection and study of the gamma spectrum of short-lived xenon daughter activity from Cs^{127} or Cs^{125} samples.

doubt that this is the same activity observed by Creutz *et al.*[8] It was established more securely that this isomer was the product of the decay of Cs^{127} by plotting the yield of the isomer in a 3-minute growth period as a function of the time at which the "milking" took place. The half-life of 6.1 hours obtained as the result of a series of 5 milkings over an 18-hour period confirms the genetic relationship.

A small amount of long-lived recoil activity remains after decay of the 75-second Xe^{127m}. If we assign all of this to 34-day Xe^{127} we can estimate the branching of Cs^{127} to 34-day Xe^{127} and to 75-second Xe^{127m} to be in the ratio of $\sim 10^4/1$.

In their summary of nuclear isomers Goldhaber and Sunyar[9] listed Xe^{127m} as an $E3$ isomer with the 175-kev gamma ray indicated as an $h_{11/2}-d_{5/2}$ transition. They preferred to reinterpret tentatively the 91-kev electrons observed originally by Creutz *et al.*[8] as L electrons of a 96-kev $d_{5/2}-s_{1/2}$ $E2$ transition rather than as K electrons of a 125-kev transition. Their reason for this reassignment was the non-observation of L electrons of the 125-kev gamma ray which should have been prominent (K/L ratio ~ 1–2) for a 125-kev $E2$ transition. More recently Wapstra, Verster, and Boelhouwer,[5] in discussing the 125-kev radiation prominent in the decay of Cs^{127}, stated that it was probably identical with the second transition in the decay of 75-second Xe^{127m} and that the 125-kev gamma ray represents an $M1$ transition going to a $d_{3/2}$ ground state in Xe^{127}. Our results appear to confirm this interpretation. The $K/(L+M)$ ratio of 7.9 obtained by us for the 125-kev gamma ray in the decay of Cs^{127} is of the correct magnitude for $M1$ and much too high for $E2$ radiation.

[9] M. Goldhaber and A. W. Sunyar, Phys. Rev. **83**, 906 (1951).

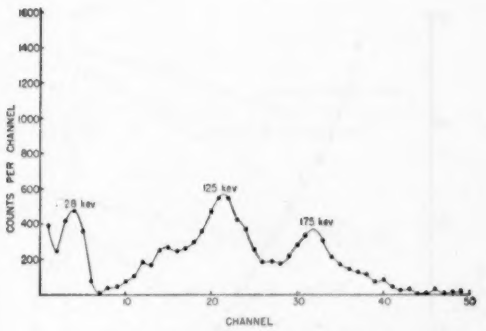

FIG. 7. Gamma spectrum of Xe^{127m}.

The Xe^{127m} results have been incorporated in the decay scheme of Fig. 8.

IV. THE RADIATIONS OF Cs^{125} AND THE ISOMER Xe^{125m}

In the bombardments of calcium iodide with helium ions a new positron activity of 45-minute half-life appeared in the cesium fraction when the energy of the bombarding helium ions was raised to 100 Mev. One hour after the end of the bombardment this new isotope accounted for more than 80 percent of the G-M activity in the cesium fraction, most of the rest being 6.25-hour

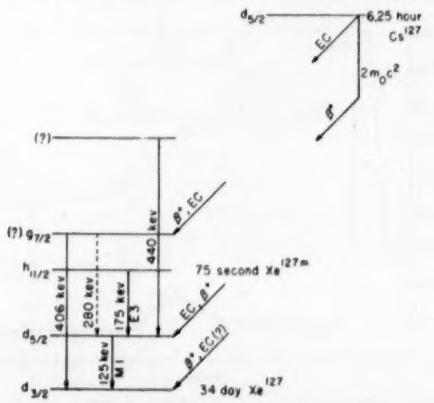

FIG. 8. Proposed decay scheme for Cs^{127}.

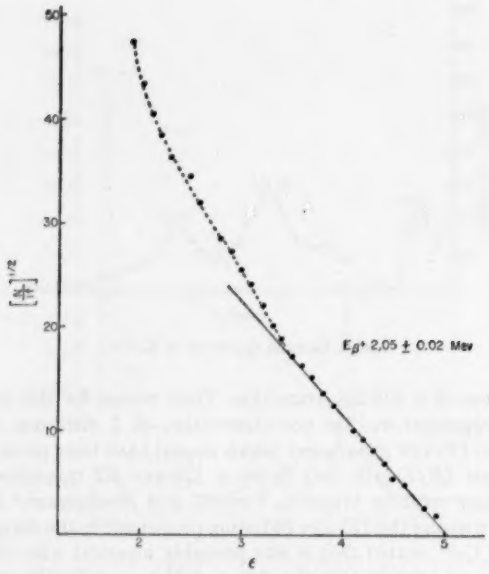

FIG. 9. Fermi-Kurie plot showing endpoint energy of the most energetic positron in Cs^{125}.

Cs^{127} and a small amount of 31-hour Cs^{129}. When the xenon daughter activity was separated and deposited on metallic counting foils by the methods described below, decay curves taken on a G-M counter showed a mixture of 18-hour Xe^{125} and 34-day Xe^{127}. This suggested that the 45-minute activity was Cs^{125} and the assignment was confirmed by mass separation. A G-M decay curve of the mass-125 fraction isolated with the help of Michel and Templeton[4] in the time-of-flight mass separator showed a straight line decay of 45±1 minutes from an initial counting rate of 18 000 to less than 10 counts per minute. The counting efficiency of the 18-hour electron capture daughter Xe^{125} was very low in the G-M tube but when the sample was placed in a "nucleometer" windowless methane flow proportional counter a decay line of 18-hour half-life was observed.

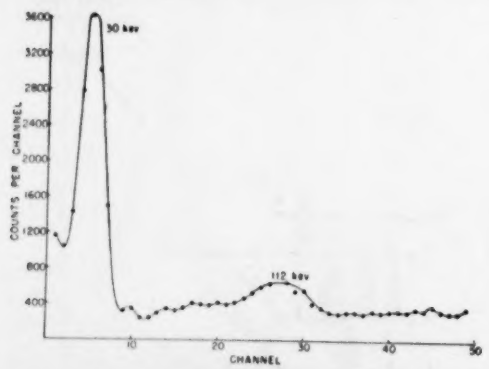

FIG. 10. Gamma spectrum of Cs^{125} in 0–200-kev region. Sample mounted on aluminum.

It was possible to determine the energy of the most energetic positron group of Cs^{125} by running a cesium sample in the double-focusing beta-ray spectrometer starting about 1 hour after bombardment because this positron energy was greater than that of Cs^{127}. Figure 9 which shows a Fermi plot of the high-energy region indicates that the energy of the Cs^{125} positrons is 2.05±0.02 Mev. Because of the presence of Cs^{127} no attempt was made to resolve out lower-energy components.

The gamma spectrum of Cs^{125} (see Figs. 10 and 11) shows a gamma ray of 112 kev in addition to annihilation radiation and 30-kev xenon x-rays. No gamma rays of higher energy were observed. The large abundance of x-rays as compared to the gamma rays suggests that Cs^{125} decays prominently by electron capture but the EC/β^+ branching ratio was not determined. As in the case of Cs^{127}, gamma-gamma coincidence studies were carried out on Cs^{125}. It was observed that the 112-kev gamma ray was in coincidence with K x-radiation and also with annihilation radiation.

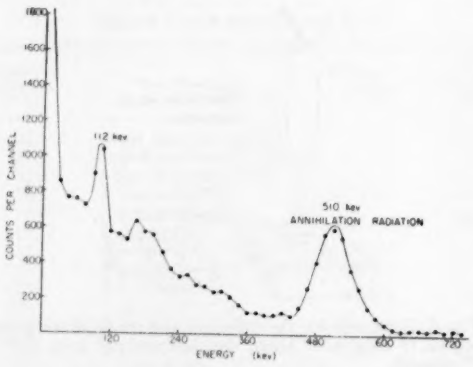

FIG. 11. Gamma spectrum of mass-separated Cs^{125} in 0–600-kev region.

The conversion electron spectrum was not studied in detail but the energy of the 112-kev gamma ray was checked by measurement of the K and L conversion lines. The K/L ratio was determined as 3.6. This may be somewhat in error since the time spent in obtaining the data made necessary rather large half-life corrections. It is believed that the 112-kev transition is the $d_{5/2}-d_{3/2}$ transition in Xe^{125} analogous to the 125-kev transition in Xe^{127}. From Goldhaber and Sunyar's[9] empirical curves, one would expect a K/L ratio of 7–8 for an $M1$ transition of this energy

At the suggestion of Dr. Ingmar Bergström we made a search for an isomer of Xe^{125} since his study of the systematics of the odd-mass xenon isotopes,[10] as well as those of Goldhaber and Hill,[11] indicated the probability of a short-lived $E3$ isomer in Xe^{125} very similar

[10] I. Bergström, Arkiv Fysik **5**, 191 (1952).
[11] M. Goldhaber and R. D. Hill, Revs. Modern Phys. **24**, 179 (1952).

to that in Xe^{127}. By performing experiments analogous to those described above in the Xe^{127m} case, we have been successful in the search for this isomer but, because the interference from 18-hour Xe^{125} was much greater than that from 34-day Xe^{127} in the earlier study, the results are not quite as clean-cut.

Carrier-free cesium samples isolated within an hour of the end of bombardment from calcium iodide targets bombarded with 100-Mev protons were inserted in the depression of the slide of Fig. 6 and pushed into the inner recoil collection chamber for 1-minute growth periods. Immediately after the cesium source was removed the gamma spectrum of the xenon daughter recoil activity was studied with the sodium iodide 50-channel analyzer. The registers were photographed with a Leica camera at 12-second intervals over a period of several minutes without disturbing the count switch. By subtraction of the dial readings of one negative from that of the next the spectrum during any particular 12-second period could be reconstructed. The upper curve of Fig. 12 shows the spectrum integrated over the first 1 minute while the lower curve shows the spectrum of the second minute's run. It is seen that gamma rays of 75, 110, 187, and 245 kev as well as 30-kev x-radiation are present.

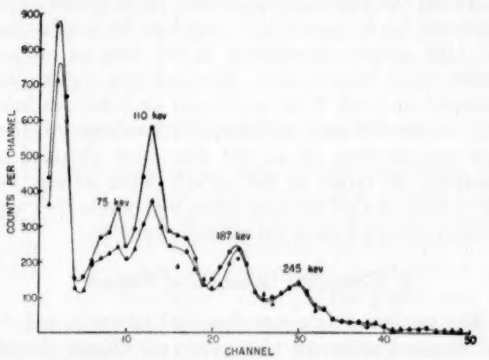

FIG. 12. Gamma spectrum of $Xe^{125m}+Xe^{125}$ daughter activity collected in apparatus of Fig. 6 during one-minute growth period. Upper curve is spectrum recorded for first minute after collection; lower curve is for second minute.

As shown in Fig. 13 the areas under the x-ray peak, the 75-kev peak, and the 110-kev peak decay initially with a half-life of 50–60 seconds and this decay in all likelihood is correctly assigned to Xe^{125m}. (The longer-lived component in the curves of Fig. 13 is based on points not shown.) Part of the radiation at these energies and most or all of it at 187 and 245 kev is due to 18-hour Xe^{125}, as will be discussed a little further on.

We are inclined to the view that the 110-kev peak is identical with the 112-kev peak of Figs. 10 and 11 and represents the $M1$ transition, $d_{5/2}-d_{3/2}$, following a 55-second $E3$ transition, $h_{11/2}-d_{5/2}$. The 75-kev radiation may be this $E3$ radiation as indicated in Fig. 14, but we cannot entirely exclude the possibility that this is

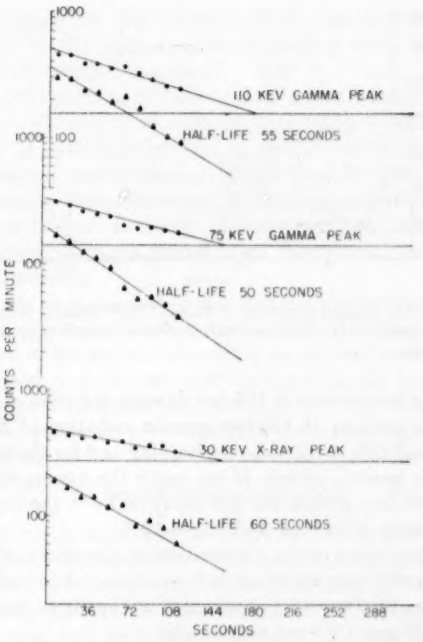

FIG. 13. Decay of gamma rays recorded in 30, 75, and 110 kev peaks during 12 second runs on $Xe^{125m}+Xe^{125}$ daughter activity collected from Cs^{125} source. Resolution shows 55-second decay of Xe^{125m}.

fluorescent radiation from the lead shielding and that the true $E3$ radiation is hidden in the region above 110 kev.

One difficulty in the further study of the isomer is the low branching ratio for its production in the decay of Cs^{125}. This branching ratio was estimated by com-

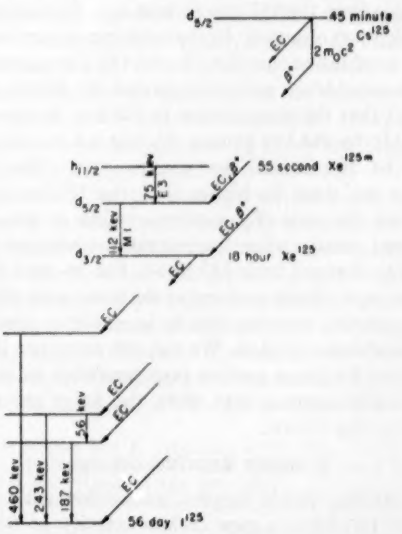

FIG. 14. Proposed decay scheme for Cs^{125}.

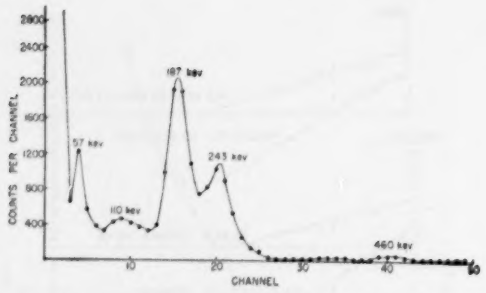

FIG. 15. Gamma spectrum of 18-hour Xe^{125} isolated from Cs^{125} and deposited on aluminum foil. Purity of sample was checked by decay.

paring the amount of 187-kev gamma radiation of Xe^{125} to the amount of 110-kev gamma radiation of Xe^{125m} with suitable corrections for half-life and for the length of the growth period. If we make the assumption of one 187-kev gamma ray per decay of Xe^{125}, the branching decay of Cs^{125} to Xe^{125m} is $\sim 10^{-3}$.

A good part of the information on the decay of Cs^{125} and Xe^{125m} is summarized in the proposed decay scheme of Fig. 14. It can be observed that the decay schemes of Cs^{125} and Cs^{127} are very similar.

The longer-lived Xe^{125} formed in the decay of Cs^{125} is identical with the 18-hour activity mass-separated and characterized by Bergström.[10,12] We repeated Bergström's scintillation spectrometer studies (but not his conversion electron studies) using Xe^{125} samples isolated by the glow discharge method from decayed Cs^{125} samples.

Figure 15 shows the gamma spectrum determined in the scintillation spectrometer. Definite photopeaks were observed at 56, 187, and 243 kev in agreement with Bergström. The small peak at 110 is probably Compton radiation from the 187-kev gamma ray. No annihilation radiation was observed. In the coincidence spectrometer it was established that the 56- and 187-kev gamma rays are in coincidence as was suggested by Bergström by the fact that the energies sum to 243 kev. In agreement with this the 243-kev gamma ray was not in coincidence with the 56- or 187-kev gamma rays. The 56-kev gamma ray must lie higher than the 187-kev gamma ray since the ratio of coincidence pulses to gate pulses increased greatly when the gamma ray selected by the gate was changed from 187 to 56. The 96- and 106-kev gamma rays whose conversion electrons were observed by Bergström were too low in intensity to observe in our coincidence studies. We can set an upper limit of 2 percent for these gamma rays compared to the 187- and 243-kev gamma rays when the latter are applied to the gating circuit.

V. BRIEF REPORT ON Cs^{123}

In calcium iodide targets bombarded with helium ions of 130 Mev, a new cesium activity of 6-minute half-life was produced along with 45-minute Cs^{125} and 6.25-hour Cs^{127}. When the xenon daughter activity grown in during a 5-minute period was isolated and deposited on thin metallic counting foils by the glow discharge method described below and followed for decay in a G-M counter, a mixture of 1.8-hour Xe^{123}, 13-hour I^{123}, and 18-hour Xe^{125} was observed. When this procedure was repeated after complete decay of the 6-minute cesium parent, no 1.8-hour Xe^{123} was isolated. This identifies the 6-minute cesium activity as Cs^{123}. Annihilation radiation of 6-minute half-life was prominent in scintillation spectrometer curves taken on the cesium fraction shortly after the bombardment, indicating that Cs^{123} decays by positron emission. No detailed study of Cs^{123} was carried out.

VI. EXPERIMENTAL PART

1. Cyclotron Targets

During the course of this work cesium isotopes were produced by $I^{127}(\alpha,xn)Cs^{<131}$ reactions by bombarding I^{127} (100 percent abundance) in the form of calcium iodide with helium ions. The calcium iodide was wrapped in 1-mil thick aluminum or ½-mil platinum foil. In the 184-inch cyclotron bombardments helium ions ranging from 60 to 150 Mev were obtained by inserting the target to the correct radial setting. For the studies of Cs^{130} calcium iodide was bombarded with 20-Mev helium ions in the 60-inch cyclotron.

2. Chemical Isolation of Cesium

The calcium iodide was dissolved in water and the solution was saturated with gaseous hydrogen chloride while being cooled with ice water. Several drops of 0.4 molar silicotungstic acid was added to precipitate free silicotungstic acid. This precipitate was centrifuged from the solution carrying cesium activity. The silicotungstic acid was dissolved in 2 drops of water and reprecipitated by the addition of cold saturated hydrochloric acid for more purification. Finally the silicotungstic acid dissolved in 0.5 ml water was passed through a 1 cm×4 mm column of Dowex-50 cation exchange resin. The cesium adsorbed on the resin while the silicotungstic acid passed through. The resin column was washed free of silicotungstic acid with distilled water following which the cesium activity was quickly desorbed from the column with a few drops of 6 *M* hydrochloric acid. The cesium so obtained was carrier-free. This procedure is described more fully elsewhere.[13]

3. Preparation of Xenon Counting Foils

Samples of daughter xenon activity produced in the decay of the cesium isotopes were deposited on thin metallic foils by the method developed and used extensively by Momyer and Hyde for the study of isotopes

[12] I. Bergström, Phys. Rev. 82, 111 (1951).

[13] E. K. Hyde, J. Am. Chem. Soc. 74 4181 (1952).

of emanation.[14] This method makes use of a glow discharge tube of the type shown in Fig. 16. Xenon was swept out of the cesium solution in a closed glass vacuum system and after crude fractionation from less volatile impurities was transferred by condensation at the temperature of liquid air into the glow discharge tube together with sufficient inert gas to raise the total pressure in the tube to the region of 100–1000 microns when the stopcock leading to the tube was closed and the gas was allowed to warm up. When a dc potential of 400–600 volts was placed across the electrodes with a 50 000-ohm resistor in the circuit, a glow discharge was produced. The discharge served to ionize the xenon atoms and the resulting ions were accelerated into the cathode with sufficient velocity that they remained affixed to the plate when the discharge was terminated. In a run of 5–10 minutes about 5 percent of the xenon activity could be deposited. The xenon was collected either on 1-mil platinum disks or on 0.1-mil aluminum foil. At room temperature the xenon activity remained affixed to the foils indefinitely. A more complete description of this method will be given in a forthcoming paper describing our studies on Xe^{121}, Xe^{122}, and Xe^{123}.

4. Time-of-Flight Mass Spectrometer

The mass assignment and isotopic separation reported in this report were done on a time-of-flight isotope separator in use in this laboratory. An unpublished account of this instrument has been given by Glenn[15] and a full description will be published by Michel and Templeton[16] shortly. The instrument is a medium-resolution, high-transmission time-of-flight mass separator which is used to collect samples of radioactive isotopes in the mass region 65 to 270. The overlapping of one mass on adjacent masses is less than 1 percent of peak intensity.

In the case of cesium isotopes, the ion source was a tungsten ribbon surface on which carrier-free Cs_2SO_4 was evaporated. The tungsten ribbon was heated electrically in the source region to produce thermal ions with a low spread in energy.

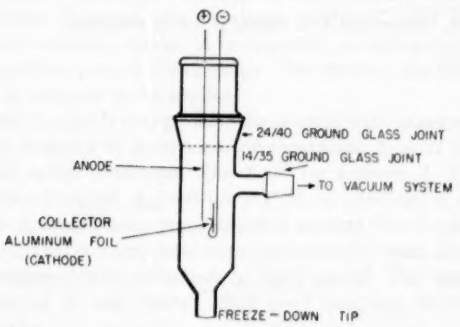

FIG. 16. Glow discharge tube used for collection of xenon activities.

For the purpose of collection of active isotopes, the ions are discharged on a platinum counting plate introduced in the collection end at ground potential. The majority of ions formed are of the type M^+ which are nonvolatile when discharged and remain as a thin uniform covering on the metal surface exposed to the beam. The metal plate can thus be used directly for counting measurements.

It was thus possible to get separated single isotopes of purity greater than 99 percent with a yield from 5–10 percent of the activity placed on the source filament as compared to 1 percent yield obtained by the conventional magnetic mass spectrometer.

It is possible to work rapidly in order to assign short half-lives.

5. Beta-Ray Spectrometers

Two precision beta-ray spectrometers were used. The first was a 25-cm radius-of-curvature spectrometer of the double-focusing type proposed by Svartholm and Siegbahn[17] and by Shull and Dennison.[18] A side-window G-M tube was used as a detector. This tube had a 0.005-inch platinum central wire; a thin window of vinyl plastic supported on a grid of 0.001-inch tungsten wires was filled to a regulated pressure of 8.8 cm with a gas mixture 90 percent argon and 10 percent ethylene. A more complete description of the instrument is given in an unpublished report by O'Kelley.[19]

The calibration for negative electrons was checked with the K line of the 662-kev gamma ray of Cs^{137}, and the K line of the 80.1-kev gamma ray of I^{131}. The transmission of the spectrometer under the conditions used was ~0.3 percent. For the study of the positrons the calibration was checked with the 1.97-Mev positron of Cs^{130}. We are indebted to Dr. Thomas O. Passell for major assistance in the use of this instrument.

Cesium samples for the spectrometer were prepared by evaporating the carrier-free activity dissolved in hydrochloric acid on gold leaf of 87 $\mu g/cm^2$ thickness. The gold leaf was supported on a brass ring.

For the study of the positrons and electrons of Cs^{127} the results on the double-focusing spectrometer were supplemented by studies carried out on a magnetic-lens-type spectrometer with somewhat lower resolution but considerably higher transmission (about 1 percent). This instrument was made available to us through the kindness of the chemistry division of the California Research and Development Corporation and we are particularly indebted to Mr. James Olson and Dr. G.

[14] F. F. Momyer, University of California Radiation Laboratory Report UCRL-2060, 1953 (unpublished).
[15] W. E. Glenn, University of California Radiation Laboratory Report UCRL-1628, January 1952 (unpublished).
[16] M. C. Michel and D. H. Templeton (to be published).
[17] N. Svartholm and K. Siegbahn, Arkiv. Mat. Astron. Fysik **A33**, No. 21 (1946); see also Hedgran, Siegbahn, and Svartholm, Proc. Phys. Soc. (London) **A63**, 960 (1950).
[18] F. Shull and D. Dennison, Phys. Rev. **71**, 681 (1947); **72**, 256 (1947).
[19] G. D. O'Kelley, University of California Radiation Laboratory Report UCRL-1243, March 1951 (unpublished).

D. O'Kelley for assistance in its use. The cesium samples used in this instrument were mounted on a single layer of Tygon film ($\sim$20 μg/cm^2) supported by a plastic ring.

6. Scintillation Spectrometer

The gamma-ray scintillation spectrometer used in this work was assembled by A. Ghiorso and A. E. Larsh of this laboratory. The gamma detection initially occurred in a 1.5-inch diameter by 1-inch thick crystal of sodium iodide (thallium activated) procured from Harshaw Chemical Company. The photomultiplier coupled to the crystal was a Dumont 6292 tube. The mounting of the crystal followed methods described by Borkowski.[20] On the side of the crystal facing the photomultiplier tube was affixed a quartz disk; a layer of oil between quartz and outside surface of the tube provided optical coupling. The other surfaces of the tube were packed into a reflecting layer of magnesium oxide. The whole assembly was mounted in an aluminum-lined lead shield on top of a standard G-M counter 5-position shelf assembly. Incident gamma rays penetrated a thin foil of beryllium ($\sim$150 mg/cm^2) and a thin layer of magnesium oxide (about $\frac{1}{8}$ inch) before entering the crystal.

The output pulse from the photomultiplier was amplified in a preamplifier, then in a linear amplifier. The final pulse is introduced to a 50-channel differential pulse-height analyzer. The analyzer based on a novel use of 6BN6 as one arm of a gated univibrator, is a new design of Ghiorso and Larsh. After proper alignment the channel-width stability (operating at a 5-volt channel width) was better than 1 percent and remained so for a period of weeks. Gain and bias controls permitted the inspection of any predetermined energy intervals with the full 50 channels. In order to calibrate the apparatus at any particular gain and bias settings, use was made of the known energies in the gamma spectrum of various standards such as annihilation radiation from Na^{22}, 662-kev radiation from Cs^{137}, 60-kev radiation from Am^{241}, 184-kev radiation from U^{235}, etc. Further details of this equipment will be obtainable in a forthcoming publication of Ghiorso and Larsh.[21]

The gamma-gamma coincidence spectrometer incorporated the above equipment in combination with a second single-channel pulse-height analyzer. The sample was mounted between two sodium iodide photomultiplier tube detectors. Pulses resulting from events in the gate crystal were fed to the single-channel analyzer and those corresponding to a selected gamma-energy interval were used to gate a coincidence circuit. Pulses arriving from the second crystal in coincidence with these were fed to the 50-channel analyzer. Hence they gamma spectrum in coincidence with a particular gamma ray could be determined quickly.

[20] C. J. Borkowski, Oak Ridge National Laboratory Report ORNL-1336, September, 1952 (unpublished).

[21] A. Ghiorso and A. E. Larsh, Jr. (to be published).

VII. ACKNOWLEDGMENTS

The authors wish to express their thanks to Dr. A. H. Wapstra and to Dr. Ingmar Bergström for helpful criticism of an earlier unpublished version (University of California Radiation Laboratory Report UCRL-2469) of this work. Statements in this report concerning 60–66 kev radiation in Cs^{125} and Cs^{127} are erroneous.

The authors also wish to express their thanks to James T. Vale, Lloyd Houser, and members of the 184-inch cyclotron crew for the numerous 184-inch cyclotron bombardments. Similarly, acknowledgment is made to G. B. Rossi, W. B. Jones, and members of the 60-inch cyclotron crew. We acknowledge the indispensable assistance of Dr. M. C. Michel and Dr. D. H. Templeton in the mass separations, and of Dr. T. O. Passell for the beta-ray spectroscopy studies, and Mr. F. S. Stephens for the coincidence studies. The work with the lens spectrometer was carried out with the assistance of Mr. J. L. Olson and Dr. G. D. O'Kelley of the California Research and Development Corporation, Livermore, California.

Coulomb Energies of Light Nuclei*

D. C. PEASLEE
Columbia University, New York, New York

(Received April 27, 1954)

The Coulomb energy differences of light nuclei, determined mostly from β decay, are fitted to a formula $\Delta E_c = a(Z/A^{\frac{1}{3}}) + b$, where b is an exchange term. With modern data, the nuclear series $A = 4n$, $4n+1$, $4n+2$, $4n+3$ all yield surprisingly consistent values: $a = 1.46$ Mev, $b = -1.11$ Mev. The data very clearly exhibit the presence of the exchange term; the value of a corresponds to a square well radius, $R = 1.18A^{\frac{1}{3}} \times 10^{-13}$ cm. The ΔE_c formula is combined with β-decay energies to determine the spacing $\Delta_{TT'}$ of the lowest-lying states of isotopic spins T, T' for a given A. The observed behavior of the Δ provides qualitative evidence for dominant supermultiplet structure in light nuclei.

1. INTRODUCTION AND SUMMARY

IN the expression for the Coulomb energy of a nucleus, the exchange term is interpreted as the electrostatic self-energy of a proton that cannot be precisely located. The necessary autocorrelation function $\rho(x,y)$ can then be specified on the basis of physical plausibility, and an order of magnitude value for the exchange term obtained. This simplified treatment leads at once to a $Z^{4/3}$ dependence for the exchange term. The Coulomb energy difference for mirror nuclei is then expected to have the form $\Delta E_c = a(Z/A^{1/3}) + b$.

This form is fitted to recent data in Sec. 3. For $A = 4n+1, 4n+2, 4n+3$, the fit is remarkably uniform,† yielding $a = 1.46$ Mev, $b = -1.11$ Mev. Data for the $A = 4n$ series are not so precise but appear to agree well with these values. The general validity of the formula for nuclei of all series indicates that certain superallowed positron decays will frequently be masked by others that are easier to produce and of extremely similar character.

The empirical value of a corresponds to a square well radius $R = 1.18A^{1/3} \times 10^{-13}$ cm, in agreement with recent direct electromagnetic measurements of nuclear size. The exchange term is unequivocally indicated by the data and seems larger than previously estimated. The difference between the Coulomb radius R and the nuclear reaction radius is interpreted as indicating a nonuniform proton distribution; the neutron distribution is assumed to be similar.

The Coulomb energy formula is used with observed decay energies to determine the separation $\Delta_{TT'}$ of the lowest levels of isotopic spin T, T' for a given A. For $A = 4n+2$ nuclei, $\Delta_{10}' \approx 0$ for $A \gtrsim 30$, in contrast to all other Δ, which have magnitudes of several Mev in this region. This is interpreted as evidence for the dominance of supermultiplet structure in light nuclei. The same curves of Δ also reveal some $j-j$ coupling effects, however.

* This work performed under the research program of the U. S. Atomic Energy Commission.

† To within a standard error of ± 0.15 Mev. The possibility of significant even-odd differences [I. Talmi and B. C. Carlson, Bull. Am. Phys. Soc. **29** (4), 18 (1954)] has been neglected here as a second-order effect in comparison with the first-order uniformity for all families.

2. FORMULATION

The Coulomb energy is conveniently computed without recourse to the isotopic spin formalism: protons and neutrons are regarded as two separate species of particle, each type satisfying exclusion statistics only with itself. A properly antisymmetrized wave function for the protons can be written in determinantal form:

$$\Psi = \frac{1}{(Z!)^{\frac{1}{2}}} \begin{vmatrix} \psi_1(1) \cdots \psi_1(Z) \\ \cdot \quad\quad \cdot \\ \cdot \quad\quad \cdot \\ \psi_Z(1) \cdots \psi_Z(Z) \end{vmatrix}, \tag{1}$$

where the ψ's are all normalized to unity. The Coulomb energy operator is

$$C = \sum_{i>j=1}^{Z} e^2/R_{ij}, \tag{2}$$

and its expectation value is the Coulomb energy of the nuclear state:

$$E_c = \int \Psi^* C \Psi dV_{12\cdots Z}$$

$$= e^2 \left[\int \rho(1)\rho(2)/r_{12} dV_{12} - \int |\rho(12)|^2/r_{12} dV_{12} \right]. \tag{3}$$

Here the first term is the direct Coulomb potential, the second the "exchange term," and

$$\rho(x,y) = \sum_{q=1}^{Z} \psi_q^*(x)\psi_q(y),$$
$$\rho(x) = \rho(x,x). \tag{4}$$

The quantity $\rho(x)$ is just the proton density at position x. To gain some physical picture of the mixed density $\rho(x,y)$, note that

$$\int |\rho(x,y)|^2 dV_x = \rho(y), \quad \int |\rho(x,y)|^2 dV_y = \rho(x). \tag{5}$$

From this we infer that $|\rho(x,y)|^2$ is the joint probability of finding a proton simultaneously at x and at y in the

TABLE I. Coulomb energies, $A=4n+1$.

A	Z'	ΔE_c (Mev)	Accuracy[a]
9	4	1.85	A
13	6	3.00	A
17	8	3.55	A
21	10	4.30	A
29	14	5.75	A[b]

[a] For accuracy classification see text.
[b] See reference 4.

nucleus. Furthermore, it must be the *same* proton at both points according to the following argument: let $Z\rightarrow\infty$ while the volume of the nucleus remains finite. On a physical picture the joint probability of finding two distinct protons at $x\neq y$ should also become infinite under these conditions. This is in contradiction with the mathematical fact that

$$\sum_{q=1}^{Z}\psi_q^*(x)\psi_q(y)\rightarrow\delta(x-y)\text{ as }Z\rightarrow\infty. \tag{6}$$

On the other hand, if $\rho(x,y)$ refers to the same proton, it represents physically the narrowest wave packet that can be formed from the available wave functions ψ_q ($q=1$ to Z). As $Z\rightarrow\infty$, this wave packet should become infinitesimally narrow, which is in accord with (6).

We thus come to regard the exchange term in (3) as the electrostatic self-energy of the protons. This energy is finite because the protons cannot be precisely localized, since the wave functions describing them are limited to the incomplete set ψ_q with $q=1$ to Z. This is in contrast to electrodynamic problems where the virtual intermediate states ψ_q span a complete set, so that the charged particle is point-localizable, and an infinite electrostatic self-energy results.[1]

It is perhaps of interest to relate these considerations to the classical formula,

$$E_c=Z(Z-1)e^2\int P(1)P(2)/r_{12}dV_{12}. \tag{7}$$

Here $P(x)$ is the average probability distribution of the protons, normalized to unity; and the factor $Z(Z-1)$ occurs because there are just Z point charges e, none of which can interact with itself. Now, suppose we keep the exchange term in Eq. (3) but relax the exclusion principle to the extent of letting all the protons have the same (lowest state) wave function ψ_1. The narrowest wave packet now has the dimensions of the whole nucleus; and

$$|\rho(x,y)|^2\sim\rho(x)\rho(y)\sim P(x)P(y). \tag{8}$$

The constants of proportionality are determined by (5) to be

$$\begin{aligned}\rho(x)&=ZP(x),\\ |\rho(x,y)|^2&=ZP(x)P(y),\end{aligned} \tag{9}$$

whence (3) becomes

$$E_c=(Z^2e^2-Ze^2)\int P(1)P(2)/r_{12}dV_{12}. \tag{10}$$

Here Z^2e^2 represents the direct interaction and $-Ze^2$ is the exchange term.

Actually the protons must be considerably more localized than allowed by (8). The $-Ze^2$ term in (10) and (7) may be regarded as a minimum estimate of the exchange effect. It is only a minimum estimate and can never be literally correct, because it is obtained by relaxing the exclusion principle at one point of the argument and retaining it at another. Thus, the classical formula (7) appears basically inconsistent from a quantum-mechanical point of view.

According to the arguments above, we can write

$$\begin{aligned}|\rho(x,y)|^2&=\rho(x)P(x-y),\\ \int P(s)dV_s&=1,\end{aligned} \tag{11}$$

where $P(s)$ is an autocorrelation function. The second term in (3) involves the quantity

$$\int s^{-1}P(s)dV=C_1/S\approx 1/S. \tag{12}$$

Here S is a characteristic radius of the function P; the constant C_1 must be of order unity, but its exact value will vary with the functional form of P and the definition of S. When S is the root-mean-square radius, $C_1=0.7$, 1.2, and 1.7 when P is, respectively, Gaussian, square, and exponential in shape. Taking these as representative values leads to

$$C_1=1.2\pm 0.5. \tag{13}$$

If the proton density is not uniform, S will vary with position throughout the nucleus:

$$(\rho/2)^{1/3}S=C_2\approx 1. \tag{14}$$

TABLE II. Coulomb energies, $A=4n+2$.

A	Z'	ΔE_c (Mev)	Accuracy[a]
6	2	0.84	A
10	4	1.96	A
10	5	2.88	B
14	6	2.93	A
14	7	3.63	B[b]
18	8.5	3.73	B[c]
22	10	4.23	B[d]
26	12	4.95	C
30	14	5.88	C[e]
34	16	6.25	B
38	18	6.86	B

[a] For accuracy classification see text.
[b] See reference 5.
[c] See reference 6.
[d] See reference 7.
[e] See reference 8.

[1] V. Weisskopf, Z. Physik 89, 27 (1934).

Here C_2 is another constant of order unity; the factor $1/2$ in $\rho/2$ accounts for the two proton spin states. The constant C_2 is uncertain by a factor $(4\pi/3)^{\pm 1/3}$, depending on whether S is regarded as the "effective radius" of the proton, or whether $S=1/K$ with K the maximum wave number of the occupied states. If this factor gives representative limits for the uncertainty in C_2,

$$C_2=1.1\pm 0.5. \tag{15}$$

The exchange term of (3) now becomes

$$e^2 2^{-1/3} Z^{4/3} C_0 \int \sigma^{4/3} dV, \tag{16}$$

where $C_0=C_1/C_2$ and $\sigma=\rho/Z$ is the proton density normalized to unity. The total Coulomb energy is

$$E_c=e^2 J[Z^2-2^{-1/3}Z^{4/3}C_0K], \tag{17}$$
$$J=\int \sigma(1)\sigma(2)/r_{12}dV_{12}, \quad K=J^{-1}\int \sigma^{4/3}dV.$$

For a transition $Z\rightarrow Z'=Z-1$ in which σ remains unchanged, the Coulomb energy difference is

$$\Delta E_c=2e^2JA^{1/3}\left[\frac{(Z'+\frac{1}{2})}{A^{1/3}}-\frac{2^{2/3}}{3}\left(\frac{Z'+\frac{1}{2}}{A}\right)^{1/3}C_0K\right]. \tag{18}$$

The parameter K depends on the shape of the proton distribution in the nucleus:

$$\begin{aligned} K&=1.5 \text{ (Gaussian)}\\ &=1.0 \text{ (square)}\\ &=0.9 \text{ (exponential).}\end{aligned} \tag{19}$$

The exponential distribution is unrealistic, since it does not have $d\sigma/dr\rightarrow 0$ as $r\rightarrow 0$; but a suitably modified exponential form like $(1+\mu r)e^{-\mu r}$ yields the same value of K to the accuracy of (19).

3. SURVEY OF EXPERIMENTAL DATA

The experimental ΔE_c for comparison with (18) may be obtained from the positron decay energies of mirror nuclei (odd A), and from the known positions of corresponding $T=1$ levels in the $A=4n+2$ series. Data for this latter series extend through $A=38$ because of the fortunate circumstance that in the odd-odd members of the series, the lowest $T=1$ and $T=0$ states tend to have about the same energy. For positron decay with endpoint E_{β^+} between corresponding states,

$$\Delta E_c=E_{\beta^+}+1.80 \text{ Mev}. \tag{20}$$

For negatron decay between noncorresponding states (as in He^6),

$$\Delta E=E_{\beta^-}-0.78 \text{ Mev}. \tag{21}$$

The data[2-8] for the $4n+1$, $4n+2$, $4n+3$ series are summarized in Tables I–III. All values are taken from references 2 and 3 unless otherwise noted. None of the old cloud-chamber values are included, since they frequently are in serious disagreement with recent scintillation spectrometer measurements. The assignments A, B, C indicate estimated accuracies of ≤ 0.05, ~ 0.1, ≥ 0.2 Mev, respectively. The value Z' is listed for the product nucleus in β^+ decay between corresponding states (hypothetical for the lightest $A=4n+2$ nuclei). In some $A=4n+2$ cases, it has been possible to include two transitions for a given A. At $A=18$, the sum of the two E_{β^+} from Ne^{18} to O^{18} is known, although the corresponding state in F^{18} is not: the average E_{β^+} and Z' are used. Figures 1–3 show plots of ΔE_c against $(Z'+\frac{1}{2})A^{-1/3}$. The straight lines are least-squares fits to the form

$$\Delta E_c=a\left(\frac{Z'+\frac{1}{2}}{A^{1/3}}\right)+b \tag{22}$$

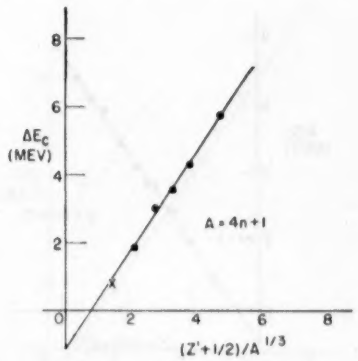

FIG. 1. Coulomb energies, $A=4n+1$. The crossed point at $A=5$ was not used to determine the fitted line.

TABLE III. Coulomb energies, $A=4n+3$.

A	Z'	ΔE_c (Mev)	Accuracy*
7	3	1.64	A
11	5	2.77	A
15	7	3.50	C
19	9	4.00	A
23	11	4.75	B
27	13	5.56	B
31	15	6.30	B
39	19	7.90	C

* For accuracy classification see text.

[2] F. Ajzenberg and T. Lauritsen, Revs. Modern Phys. **24**, 321 (1952).
[3] W. A. Hunt, thesis, Iowa State College, 1954 (unpublished); Hunt, Kline, and Zaffarano, Bull. Am. Phys. Soc. **29** (4), 23 (1954).
[4] H. Roderick and C. Wong, Phys. Rev. **92**, 204 (1953).
[5] J. R. Penning and F. H. Schmidt, Phys. Rev. **94**, 779 (1954).
[6] J. D. Gow and L. W. Alvarez, Phys. Rev. **94**, 365 (1954).
[7] N. P. Heydenburg and G. M. Temmer, Phys. Rev. **94**, 1252 (1954).
[8] Mandeville, Swann, Chatterjee, and van Patter, Phys. Rev. **85**, 193 (1952).

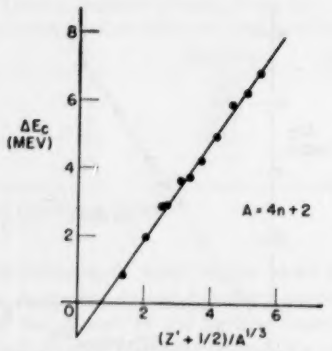

FIG. 2. Coulomb energies, $A=4n+2$.

in which the points of classes A, B, and C are weighted 10, 3, and 1, respectively. The results are

$a=1.48$ Mev	$b=-1.27$ Mev	$\sigma=0.12$ Mev	$A=4n+1$
1.45	−1.06	0.12	$4n+2$
1.46	−1.00	0.17	$4n+3$.

(23)

The σ are root-mean-square deviations of the observed ΔE_c from the values calculated with (22) and (23). The average of (23) is

$$a=1.46 \text{ Mev}, \quad b=-1.11 \text{ Mev}, \quad \sigma=0.15 \text{ Mev}. \quad (24)$$

Within this average deviation of about 150 kev, Eq. (24) fits all the subcases in (23) over the range of light nuclei, $1<Z/A^{1/3}\lesssim 6$.

The rather sizable magnitude of b is clear empirical evidence for the exchange effect. The data give no consistent evidence for the presence of any further terms in (22), since both high and low Z' fit the straight line about equally well. It is of interest to note that even the points at $A=5$ and $A=3$ do not deviate greatly from the fitted lines. These points are plotted in Figs. 1 and 3, although they were not used to determine a and b.

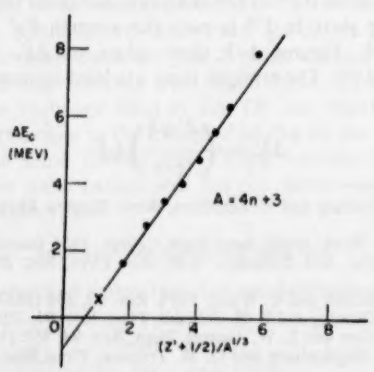

FIG. 3. Coulomb energies, $A=4n+3$. The crossed point at $A=3$ was not used to determine the fitted line.

There is some indication that ΔE_c is slightly lower for the $A=4n+1$ series than for the others, although the difference is not larger than the statistical error. This could be interpreted[9] in terms of a tendency for these nuclei to have a core-plus-outside-nucleon structure. The effect, if present, is of second order and will be neglected in the discussion below.

The general validity of (24) for $A=4n+1$, $4n+2$, and $4n+3$ implies that certain β^+ decays of mirror nuclei will be difficult to observe because of masking by very similar decays of isotopes with different A values. For example, according to (24), the decay energies of Al^{25} and the $0-0$ Al^{26} transition should differ by only about $\frac{1}{2}\Delta A/A\approx 2$ percent <0.1 Mev, which is less than the uncertainty in (23), (24). They are both superallowed transitions and will have very similar lifetimes. Thus, the lighter isotope can be observed with certainty only when produced by itself; this precludes reactions that involve multiple emission of particles, such as $Al^{27}(\gamma,2n)Al^{25}$. This difficulty also affects Cl^{33} and K^{37} and the $A=4n+2$, $Z=N+2$, series: Mg^{22}, Si^{26}, (S^{30}), A^{34}, Ca^{38}.

We can also use β-decay energies to estimate ΔE_c for the series $A=4n$. In these nuclei, the $T=1$ levels are of order 10 Mev above the $T=0$ ground state, so that both β^- and β^+ decays occur up to $A=40$. Let E_{β^-}, E_{β^+} be the end points of the decays leading to the $T=0$ ground state of the $N=Z=2n$ nucleus, and Δ_{01} the (positive) energy difference between this ground state and the lowest $T=1$ state of the same nucleus. Then

$$\begin{aligned} E_{\beta^-}-0.78 \text{ Mev}&=\Delta_{01}-\Delta E_c^1, \\ E_{\beta^+}+1.80 \text{ Mev}&=\Delta_{01}+\Delta E_c^2, \end{aligned} \quad (25)$$

and the average Coulomb energy difference is

$$\Delta E_c=\tfrac{1}{2}(\Delta E_c^1+\Delta E_c^2)=\tfrac{1}{2}(E_{\beta^+}-E_{\beta^-})+1.29. \quad (26)$$

Table IV presents the ΔE_c obtained in this way, with the corresponding average Z'; E_{β^+} is frequently taken from (p,n) threshold measurements. At $A=24$, two independent determinations of ΔE_c are possible, since measurement[10] of the decay of Al^{24} has located the corresponding $T=1$ state in Mg^{24} at $\Delta_{01}=9.4$ Mev. Since these ΔE_c are generally of class C accuracy, no attempt is made to deduce values of a and b from them. They are instead plotted (Fig. 4) with a line representing (24). The agreement is within experimental error, so that (24) appears valid for all types of light nuclei. All data in Table IV are from references 2 and 9, except where noted.

The β-decay energies given by (22), (24) tend substantially to exceed some of the older measured values for the heavy mirror nuclei. This implies that the ft value for these transitions (e.g., A^{35}, K^{37}) should be

[9] H. A. Bethe, Phys. Rev. **54**, 436 (1938).

[10] Glass, Jensen, and Richardson, Phys. Rev. **90**, 320 (1953); also, H. Morinaga and S. A. Moszkowski (private communications).

increased. This in turn has the tendency to increase the estimate of the inverse coupling constant $B\sim 1/g^2$ that is determined from a survey of such transitions.[11]

4. THE NUCLEAR RADIUS

Comparison of (18) and (24) yields

$$(JA^{1/3})^{-1}=1.96\times 10^{-13}\text{ cm}. \tag{27}$$

For a square well of radius R, this means

$$R=1.18A^{1/3}\times 10^{-13}\text{ cm} \tag{28}$$

in accordance with other observations.[12-15] For other proton distributions, the corresponding parameters are, in units of 10^{-13} cm,

$$\begin{aligned}&\text{Gaussian:} && \sim\exp(-\gamma^2r^2), && \gamma^{-1}=0.39A^{1/3},\\ &\text{experimental:} && \sim\exp(-\alpha r), && \alpha^{-1}=0.30A^{1/3},\\ &\text{parabolic:} && \sim 1-(r/R)^2, && R=1.40A^{1/3}.\end{aligned} \tag{29}$$

The observed magnitude of the exchange term may be specified by

$$-b/a=0.75=(2^{1/3}/3)C_0K,\quad C_0K=1.8, \tag{30}$$

where we have put $[(Z'+\frac{1}{2})/A]\approx\frac{1}{2}$ for all transitions considered. The "plane wave approximation"[16] yields $C_0K\approx 1.0$. Because of the large uncertainty attendant upon C_0 in the present discussion, the value in Eq. (30) cannot be given a very positive interpretation.

The nuclear reaction radius for protons on these same light nuclei appears[17] to be of order $a_r\approx 1.5A^{1/3}\times 10^{-13}$ cm, in contrast to (28). The most straightforward interpretation of this difference is that a nuclear reaction is initiated in the outside tail of the distribution at much lower nuclear densities than the average. This was already apparent in the large fluctuation among neighboring isotopes sometimes observed for the effective radius a_r in (p,n) excitation functions.[18]

The discussion above concerns only the distribution of protons in the nucleus, but there is no reason to suppose that the neutron distribution is substantially different. For $A\lesssim 40$ the β-stable nuclei are generally within one or two units of $N=Z$, so that there cannot be a very thick shell of extra neutrons surrounding the proton core, as has been suggested for heavier nuclei.[19] Nevertheless, these light nuclei display exactly the difficulty that the model of reference 19 is supposed to eliminate; namely, a relatively large nuclear reaction radius as compared to the "Coulomb radius." The explanation for light nuclei, at least, seems to be in an appreciably nonuniform density that is about the same for neutrons and protons.

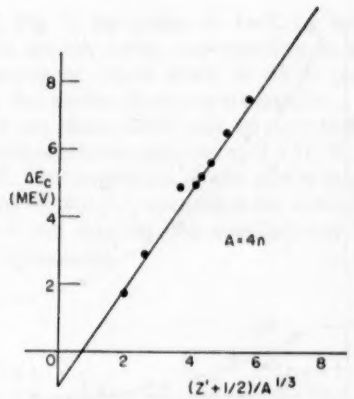

FIG. 4. Coulomb energies, $A=4n$. The line is not fitted to the points but represents Eq. (24).

5. SUPERMULTIPLET STRUCTURE IN LIGHT NUCLEI

Equations (22) and (24) may be applied to deduce the separations of certain levels in light nuclei. We assume that all the levels discussed here have a dominant isotopic spin T, by which they may be characterized. Let $\Delta_{TT'}$ with $T'<T$ be the energy difference between the lowest levels of isotopic spin T and T' for a given mass number. This quantity can be obtained from the end-point energy E_{β^-} of the appropriate negatron decay:

$$\begin{aligned}\Delta_{TT'}&=E_{\beta^-}+\Delta E_c-0.78\text{ Mev}\\ &=E_{\beta^-}+1.46\left(\frac{Z'+\frac{1}{2}}{A^{1/3}}\right)-1.89\text{ Mev},\end{aligned} \tag{31}$$

TABLE IV. Coulomb energies for $A=4n$.

A	Z' (Mev)	E_{β^-} Mev	E_{β^+} (Mev)	ΔE_c (Mev)
8	3.5	16.0	16.8	1.7
12	5.5	13.4	16.7	2.9
20	9.5	7.0	14.3	4.9
24	11.5	5.5	12.9	5.0
24	12	$\Delta_{01}=9.4$		5.2
28	13.5	4.6	13.2	5.6
32	15.5	1.7	12.1	6.5
40	19.5	1.3	14.1	7.5[a]

[a] N. W. Glass and J. R. Richardson, Phys. Rev. **93**, 942 (1954).

[11] O. Kofoed-Hansen and A. Winther, Phys. Rev. **86**, 428 (1952).
[12] V. L. Fitch and L. J. Rainwater, Phys. Rev. **92**, 789 (1953).
[13] L. N. Cooper and E. M. Henley, Phys. Rev. **92**, 801 (1953). These authors have emphasized the importance of the exchange term in fitting ΔE_c for light nuclei.
[14] Hofstadter, Fechter, and McIntyre, Phys. Rev. **92**, 978 (1953); Yennie, Wilson, and Ravenhall, Phys. Rev. **92**, 1325 (1953).
[15] A. E. S. Green and N. A. Engler, Phys. Rev. **91**, 40 (1953). In this reference, the coefficient $2a_3=1.50$ mMU$=1.40$ Mev is equivalent to the coefficient of a of Eq. (22); no account is taken of exchange effects.
[16] H. A. Bethe and R. F. Bacher, Revs. Modern Phys. **8**, 162 (1936).
[17] E.g., R. G. Thomas, Phys. Rev. **88**, 1109 (1952).
[18] Blaser, Boehn, and Marmier, Helv. Phys. Acta **24**, 3, 441 (1951).
[19] M. H. Johnson and E. Teller, Phys. Rev. **93**, 357 (1954).

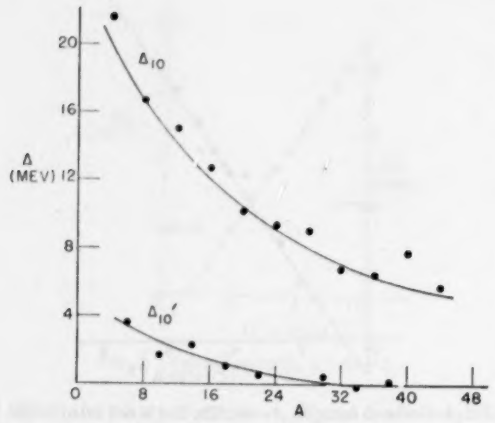

FIG. 5. Δ_{10} for $A=4n$ and Δ_{10}' for $A=4n+2$.

where Z' refers to the parent nucleus. The values of $\Delta_{TT'}$ thus obtained are shown in Figs. 5–7. For even A it is necessary to distinguish two curves, one for $A=4n$, the other for $A=4n+2$. For odd A no significant distinction appears between $A=4n+1$ and $A=4n+3$, so that only a single curve is drawn.

The most striking feature of these curves is the qualitative difference between Δ_{10} for $A=4n$ and Δ_{10}' for $A=4n+2$. All curves of Δ decrease monotonically with increasing A, but Δ_{10} is always of order 5–10 Mev, while $\Delta_{10}'\approx 0$ for $A\gtrsim 30$; and for all A, $\Delta_{10}'\ll\Delta_{10}$. This behavior is consistent with a dominant supermultiplet $L-S$ structure for light nuclei and appears inconsistent with dominant $j-j$ coupling.

As an example, consider Cl^{34} in the simplest approximation where the low-lying states comprise an inactive S^{32} core ($J=T=0$) plus an external neutron and proton in d states. In $L-S$ coupling, the exclusion principle requires the exchange operation on the two extra nucleons to satisfy

$$P_L P_S P_T=-1. \tag{32}$$

For two nucleons $P_S=(-1)^{S+1}$, $P_T=(-1)^{T+1}$, so that the space exchange operator P_L can be the same for $T=1$ and $T=0$ states provided that S is different. Thus, $\Delta_{10}'\approx 0$ is consistent with interaction forces that

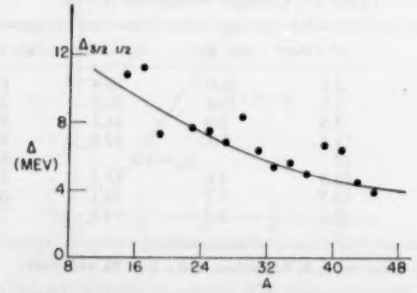

FIG. 6. Δ_{11} for $A=4n+1$ and $A=4n+3$.

do not depend strongly on S but do depend strongly on the space symmetry as specified by P_L.

For $j-j$ coupling on the other hand, L and S do not appear separately, and we have only

$$P_J P_T=-1, \tag{33}$$

where P_J is the exchange of two nucleons in space-spin state j. Thus $\Delta_{10}'\approx 0$ means that the nuclear interaction is indeed independent of the nucleon exchange symmetry (P_J).

The difference between the extremes of $L-S$ and $j-j$ coupling appears where more than two equivalent nucleons are considered. In $L-S$ coupling three equivalent neutrons ($T=3/2$) cannot satisfy exclusion with complete symmetry under P_L because their spin components cannot assume three different values but have only $s_z=\pm 1/2$. For two equivalent neutrons and a proton ($T=1/2$), symmetry under P_L is possible because only the neutrons must have different s_z. Then $T=3/2$ and $T=1/2$ must have different P_L, and $\Delta_{3/2\ 1/2}$ may be large. Similarly Δ_{10} for $A=4n$ depends on different P_L and may be large.

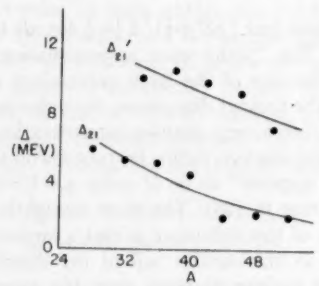

FIG. 7. Δ_{21} for $A=4n$ and Δ_{21}' for $A=4n+2$.

In $j-j$ coupling, however, any number of equivalent neutrons up to $(2j+1)(T=j+\frac{1}{2})$ can have different spin components j_z. The possible symmetries under P_J do not change if some of the neutrons are replaced by protons; besides, $\Delta_{10}'\approx 0$ implies that the energy of the total state does not depend much on the symmetry under P_J. Thus on strict $j-j$ coupling

$$\Delta_{TT'}\approx 0 \quad \text{for} \quad j+1/2\geq T>T'. \tag{34}$$

The experimental evidence in Figs. 5–7 uniformly contradicts (34), suggesting the dominance of supermultiplet structure.[20]

For even A the simplest supermultiplet symmetries can be pictured in terms of an α-particle model. The large Δ_{10} arises from the difficulty of breaking up an α particle, the small Δ_{10}' from the relative ease of breaking a deuteron. Extending this picture to $T=2$ states, Δ_{21}' should be large because it involves breaking

[20] The importance of supermultiplet structure in understanding the "unfavored" ft values of light nuclei has also been emphasized. I. Talmi, Phys. Rev. **91**, 122 (1953).

up an α particle in the core of an $A=4n+2$ nucleus, but Δ_{21} involves no new α-particle destruction and should be smaller. This expectation is borne out in Fig. 7. Over the small range for which data exist ($A\approx 32$ to 40) it is roughly true that

$$\Delta_{20}\approx\Delta_{20}'. \tag{35}$$

The curves of Δ show that supermultiplet structure is dominant; at the same time, they provide some indication that $j-j$ coupling effects are not negligibly small. In Fig. 5, the points at $A=4$, 16, and 40 are above the smooth curve, corresponding to especially tight binding of closed shells in $L-S$ (and $j-j$) coupling. But similar effects are apparent at $A=12$ and 28, which are closed shells only on $j-j$ coupling. In Fig. 6, shell effects are apparent at $A=17$, 41, but also at $A=29$. The magnitude of the effects at the $j-j$ shells suggests that $j-j$ coupling is not so much weaker than $L-S$ and that the true situation may be intermediate in character.

PHYSICAL REVIEW VOLUME 95, NUMBER 3 AUGUST 1, 1954

Angular Distribution of Photoelectrons Produced by 0.4–0.8-Mev Polarized Photons*

WILLIAM H. MCMASTER† AND FRANK L. HEREFORD
Department of Physics, University of Virginia, Charlottesville, Virginia
(Received April 5, 1954)

The angular distribution of high-energy (0.4 to 0.8 Mev) photoelectrons produced in Pb and Au foils by linearly polarized photons has been investigated using scintillation counting and pulse-height analysis techniques. A Compton-scattered photon beam from Co^{60} provided a source of partially polarized radiation. Experimental results confirm the theoretical prediction of predominate photoemission orthogonal to the electric vector of the incident photon for photoelectron energies greater than 0.5 Mev.

INTRODUCTION

THE theory of the azimuthal distribution of photoelectrons produced by linearly polarized photons requires the application of Dirac's relativistic wave equation. Several workers have performed relativistic calculations of the photoelectric cross section. Hall and Oppenheimer[1] carried through a Born approximation calculation of the total cross section for transitions to plane wave states of the ejected photoelectrons. Hall[2] later modified this to the extent that extreme relativistic Coulomb continuum functions were used for the final electron states. Hulme[3] and his co-workers did an exact numerical calculation of the total cross section for a few elements. However, none of these workers obtained a differential cross section exhibiting the angular distribution of the photoelectrons.

Prior to this work Sauter[4] obtained a differential cross section for linearly polarized incident photons using Coulomb continuum functions correct in the limit $\alpha Z\ll 1$. His integrated cross section agreed quite well with the numerical results of Hulme. Sommerfeld[5] obtained the same cross section by a slightly different and independent method.

The differential cross section for ejection from the K shell obtained by Sauter and Sommerfeld is

$$\frac{d\sigma_K}{d\Omega}\sim\left(\frac{1}{\epsilon}\right)^4(1-\beta^2)^{\frac{1}{2}}\frac{\beta^2\sin^2\theta}{(1-\beta\cos\theta)^4}\left[\frac{\epsilon^2}{4}(1-\beta\cos\theta)+\left\{(1-\beta^2)^{\frac{1}{2}}-\frac{\epsilon}{2}(1-\beta\cos\theta)\right\}\cos^2\varphi\right],$$

where β is the photoelectron velocity in units of c, and ϵ is the kinetic energy of the photoelectrons in units of mc^2. The angles involved are shown in Fig. 1.

In simplified notation the relativistic cross section is of the form

$$d\sigma_K\sim[A(\epsilon,\theta)+B(\epsilon,\theta)\cos^2\varphi]d\theta d\varphi.$$

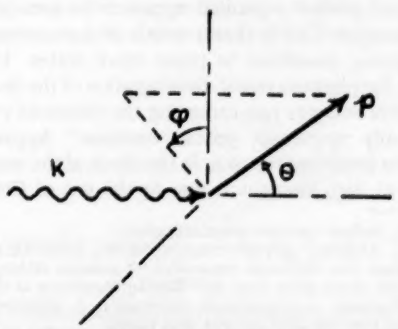

FIG. 1. Angles involved in the photoelectric cross section. **k** is the incident polarized photon with electric vector in the plane of the diagram.

* Sponsored by Office of Ordnance Research, U. S. Army.
† Present address: Los Alamos Scientific Laboratory, Los Alamos, New Mexico.
[1] H. Hall and J. R. Oppenheimer, Phys. Rev. **35**, 71 (1931).
[2] H. Hall, Revs. Modern Phys. **8**, 358 (1936).
[3] H. R. Hulme *et al.*, Proc. Roy. Soc. (London) **149**, 131 (1935).
[4] P. Sauter, Ann. Physik **11**, 454 (1931).
[5] A. Sommerfeld, *Atombau und Spektrallinien* (F. Vieweg und Sohn, Braunschweig, 1939), Vol. 2, p. 482.

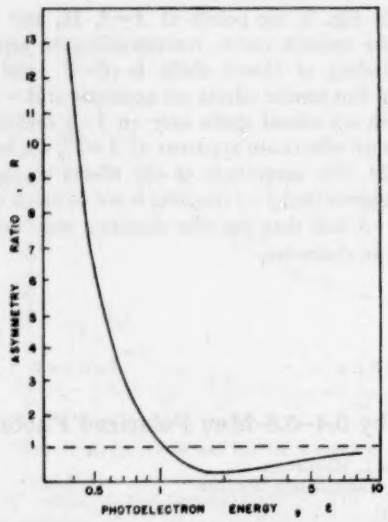

FIG. 2. Asymmetry ratio for photoelectrons ejected from the K shell by linearly polarized photons for $\theta=\pi/2$.

Let us now define an asymmetry ratio,

$$R=d\sigma_0/d\sigma_{\pi/2}=(A+B)/A,$$

that is, the ratio of the differential cross sections for ejection coplanar with, and orthogonal to, the electric vector of the incident photon. This asymmetry ratio is plotted against the photoelectron energy for $\theta=\pi/2$ in Fig. 2. It is seen that in the nonrelativistic limit the familiar emission in the plane of the electric vector of the incident photon is preferred. However, for energies greater than mc^2 the preferred emission is orthogonal to the electric vector. This phenomenon will henceforth be referred to as the "crossover" of the asymmetry ratio.

No classical model of the electron as a charged particle possessing a magnetic moment predicts such an effect. Relativistic calculations of both Jackson[6] and Archibald[7] using transitions to plane wave states also fail to show the crossover feature in the asymmetry ratio and predict a gradual approach to symmetry at high energies. This is characteristic of a photomagnetic spinflipping transition to plane wave states. For example, the photomagnetic disintegration of the deuteron at photon energies just exceeding the threshold yields a spherically symmetric proton emission.[8] Apparently, then, the preferred emission in the plane of the magnetic vector at high energies is due to the use of Coulomb functions for the final electron states. Some interference effect among subwaves in the outgoing photoelectron current is probably involved.

The present experiment was designed to investigate the asymmetry ratio in the region of the crossover point. As a source of polarized photons, Compton scattered gamma rays from a one-Curie Co^{60} source were used. By changing the angle of Compton scattering, various energies and degrees of polarization were available.

THE EXPERIMENT

The Co^{60} source used provided an unpolarized beam of photons of energies 1.17 and 1.33 Mev. This beam was partially polarized by Compton scattering in a small copper cylinder into an angle θ_1. After collimation by six inches of lead, this beam impinged upon a target of two thin foils located inside a thin wall polystyrene vacuum chamber. This target could be moved out of the beam to determine the background. The photoelectrons ejected from this target were then detected by an uncovered NaI(Tl) scintillation crystal using a RCA-5819 photomultiplier tube. The pulses from the photomultiplier were amplified and then analyzed by a single-channel pulse-height analyzer. The vacuum chamber was mounted so that it could be rotated in a plane perpendicular to the incident partially polarized beam. A schematic diagram of the experimental arrangement is shown in Fig. 3.

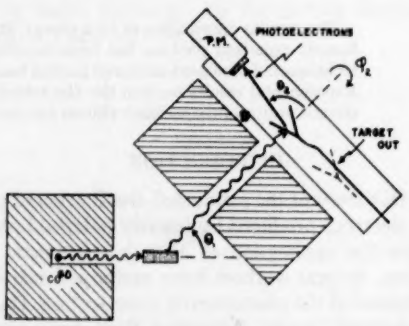

FIG. 3. Experimental arrangement for the investigation of the photoelectric asymmetry ratio. Dotted lines show position of target when withdrawn from the photon beam.

For each set of runs a freshly cleaned sodium iodide crystal (4.5 mm thick) was mounted on the face of a Lucite light pipe inside the vacuum chamber, and the scintillation detector was then calibrated using the photoelectric peaks of the gamma radiation of Cs^{137} (0.66 Mev) and Na^{22} (0.51 and 1.28 Mev). The calibration was checked in both a horizontal and a vertical position to verify that there was no shift in calibration due to the orientation of the photomultiplier.

Once the calibration of the crystal was determined, the energy dial and the window width of the analyzer

[6] J. D. Jackson (private communication).
[7] W. J. Archibald (private communication). Archibald's calculations show that the terms responsible for emission orthogonal to the electric vector arise from spin flipping transitions of the electrons. However, a symmetrical distribution is obtained upon averaging over the final electron spin states.
[8] F. E. Myers and L. C. Van Atta, Phys. Rev. **61**, 19 (1942); G. Graham and H. Halban, Revs. Modern Phys. **17**, 297 (1945); E. P. Meiners, Phys. Rev. **76**, 259 (1949).

were set to accept pulses originating in the crystal due to energy losses in the range calculated for the photoelectrons. Background effects due to the target, such as the Compton recoil electrons and Compton scattered photons, were not detected, since their energies were well below the energy region accepted by the analyzer.

The photoelectron rate was measured as the difference in the counting rates with the target in and out of the Compton scattered photon beam. The difference rate was observed at four orientations of the target chamber corresponding to values of ϕ_2 of 0°, 90°, 180°, and 270°, in order to average out any possible effect of a noncylindrical geometry about the direction of the scattered photon.

As an additional check on geometrical asymmetry, the hole in the Co^{60} container was plugged; and the copper scatterer was replaced by a radioactive source emitting unpolarized photons of energy comparable to the scattered photons. The asymmetry ratio measured in this way for unpolarized photons was unity in each case.

THEORY

We now consider the expected results of these measurements. All references to angles will be in terms of Fig. 4 which depicts the interactions involved.

The degree of polarization of an unpolarized incident beam resulting from Compton scattering is dependent upon the angle of scattering and is given from the Klein-Nishina formula by

$$P=\frac{d\sigma_\perp}{d\sigma_{11}}=\frac{(k_0-k)(1-\cos\theta_1)+2}{(k_0-k)(1-\cos\theta_1)+2\cos^2\theta_1},$$

with $d\sigma_\perp$ and $d\sigma_{11}$ referring to photons scattered through an angle θ_1 which are polarized perpendicular to the plane of scattering and in the plane of scattering, respectively. The energy of the partially polarized beam is also a function of the scattering angle and is readily calculated.

We next seek the expected probability of photoelectron ejection at the various values of ϕ_2 [measured from a direction parallel to the electric vector; i.e., $\phi_2=0$ is orthogonal to the $(\mathbf{k}_0,\mathbf{k})$ plane]. The Sauter K-shell cross section is used to compute the probability of photoejection after correction for non-K-shell ejection. At the energies involved about 20 percent of the total photoelectron intensity comes from higher levels.[9] No relativistic calculations have been performed bearing upon ejection from these higher levels. In the absence of such information we have assumed a symmetrical distribution for non-K electron emission. Thus the total differential cross section is obtained by adding to the K-shell cross section a symmetrical term equal to one-fourth the K-shell cross section for unpolarized photons (obtained by averaging over ϕ_2), yielding

$$d\sigma\sim[\tfrac{1}{8}(10A+B)+B\cos^2\varphi]d\theta_2 d\varphi_2.$$

By analyzing photon k into two orthogonal states of polarization, one can compute and add the contribution of each state to the differential probability of photoelectron ejection, making use of the degree of polarization as computed above. This yields

$$dP(\theta_1,\varphi_1,\theta_2,\varphi_2)=[f_1(\theta_1,\theta_2)+f_2(\theta_1,\theta_2)\cos^2\varphi_2]d\theta_1 d\varphi_1 d\theta_2 d\varphi_2.$$

This expression can then be integrated over the finite geometry of the detector and scatterers. The most tedious integration involved is that over θ_1. In this experiment the spread of θ_1 was only 10°. Fortunately, one can show that it is of negligible consequence. The more forward scattering angles yield a smaller degree of polarization weighted with an increased photon intensity, which is compensated for at the more backward angles by a greater degree of polarization weighted with a decreased photon intensity. The spread in ϕ_1 was 10°, and integration over this variable can also be omitted, since it does not appear in dP. Hence, one need only integrate over θ_2 and ϕ_2 to obtain the desired probability of photoelectron detection at fixed θ_2 and variable ϕ_2. The integrated probability of photoelectron ejection into the solid angles around θ_2 and ϕ_2 is of the form

$$P(\varphi_2)=F_1+F_2\cos^2\varphi_2.$$

From this expression we form the asymmetry ratio for a given θ_2:

$$R_{\theta_2}=P(0)/P(\pi/2)=C_\perp(\mathbf{E})/C_{11}(\mathbf{H}),$$

where $C_\perp$ and C_{11} represent the expected counting rates in the two positions corresponding to predominate ejection in the electric and magnetic planes. Measurement of this ratio at different scattering angles θ_1 provides an experimental test of the Sauter cross section at different energies.

RESULTS

The photoelectric asymmetry ratio was investigated in the energy regions determined by the three angles of

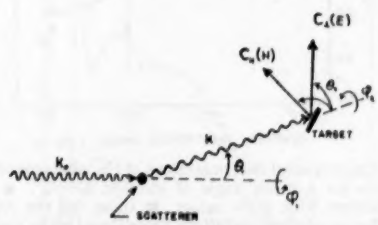

FIG. 4. Compton scattering and photoelectron ejection angles involved in the experiment. $\mathbf{k}_0$ is the unpolarized γ ray from the Co^{60} source, $\mathbf{k}$ is the partially polarized photon after Compton scattering. $C_\perp(\mathbf{E})$ and $C_{11}(\mathbf{H})$ represent, respectively, directions orthogonal to and coplanar with the (k_0,k) plane (see text).

[9] G. D. Latyshev, Revs. Modern Phys. **19**, 132 (1947).

Compton scattering, $\theta_1=40°$, 50°, and 65°, corresponding to mean photon energies of 0.79, 0.67, and 0.52 Mev, respectively. These settings were chosen to show the crossover feature of the asymmetry ratio.

The choice of the photoelectron ejection angle θ_2 is dependent upon two factors: (1) the asymmetry is greater for large angles, but (2) the cross section decreases rapidly with an increase of θ_2. The mean angle of $\theta_2=85°$ for the two foils used in the target was chosen as giving the optimum counting efficiency as determined for the $\theta_1=40°$ setting.

The asymmetry ratio was determined in the three energy ranges using thin lead foils. Because of the energy selection by the analyzer, only those photoelectrons originating in a thin layer of the foil were detected. As an experimental check to determine if multiple scattering effects were being detected, an extremely thin (1-mg/cm²) gold foil was used at the $\theta_1=40°$ setting. The asymmetry ratio as determined with this foil agrees satisfactorily with that obtained using the lead foil. A separate experimental investigation using the gold foil and a monoenergetic source showed that the photoelectrons detected had suffered negligible energy loss in leaving the foil.

The results which have been obtained are shown in Fig. 5 where the asymmetry ratio is plotted against the Compton scattering angle θ_1 and the corresponding mean K-shell photoelectron energy (photon energy k minus the K-shell binding energy). The curve was computed as described above, and the significance of the various experimental points is indicated in the caption. Each experimental point was the result of a large number of independent measurements of the asymmetry ratio. The experimental data clearly confirm the crossover feature of the Sauter cross section.

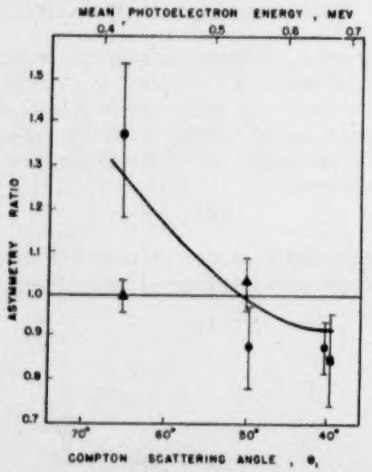

FIG. 5. Experimental determinations of the photoelectric asymmetry ratio for a mean angle of ejection $\theta_2=85°$. ● signifies values obtained with a Pb target, ■ those for the Au target, ▲ values for unpolarized radiation. The values for the unpolarized photons are seen to be unity as would be expected.

Previous experiments at this laboratory[10,11] have been carried out to determine the photoelectric asymmetry ratio below the crossover. It is particularly helpful to have this check on the results presented above, since they do confirm an effect which is difficult to reconcile with our intuitive notions of electromagnetic interactions. These previous investigations have employed electron-positron annihilation quanta to obtain a beam of polarized photons. As a consequence, results were obtained for a single incident photon energy of 0.51 Mev. These previous results, together with the determinations of this experiment, are presented in Table I.

From the experimental results we note that the observed asymmetry is, in all cases, greater than the theoretical prediction (i.e., farther from symmetry). If this feature of the data is considered significant, there is an immediately obvious explanation. It will be recalled that the non-K-shell electron emission was assumed to be symmetric in the absence of relativistic calculations on this point. The probabilities of ejection from the K, $L_{\rm I}$, $L_{\rm II}$, etc., levels should be approximately in the ratios 1, 1/8, 1/27, etc. (the probabilities of the electrons being near the nucleus). Thus most of the ejected non-K electrons come from the $L_{\rm I}$ level. Nonrelativistic calculations by Schur[12] yield an azimuthal distribution for ejection from the $L_{\rm I}$ level which is similar to the nonrelativistic K-shell distribution. Both, of course, are S states. If one now assumes that the relativistically computed distributions are also similar, then the expected asymmetry will be increased both below and above the cross over point. The experimental data support this inference.

TABLE I. Summary of results.

Photon energy (Mev)	θ_2	Asymmetry ratio Theoretical	Observed	Target
0.51	75°	1.43	1.54±0.09[10]	Pb
0.51	90°	1.30	1.46±0.11[11]	Pb
0.52	85°	1.28	1.37±0.18	Pb
0.67	85°	0.99	0.88±0.10	Pb
0.79	85°	0.91	0.88±0.06	Pb
0.79	85°	0.91	0.85±0.11	Au

The authors are indebted to Dr. Stephan Berko, Dr. William J. Archibald, and Dr. U. Fano for many helpful and stimulating discussions concerning the physical origin of the preferred ejection in the magnetic plane.

[10] A. Stevenson, dissertation, University of Virginia, 1953 (unpublished).
[11] F. L. Hereford and J. P. Keuper, Phys. Rev. **90**, 1043 (1953).
[12] G. Schur, Ann. Physik **4**, 433 (1930).

Disintegration of Ba^{139}†

ALLAN C. G. MITCHELL AND ELIZABETH HEBB
Indiana University, Bloomington, Indiana
(Received April 5, 1954)

The nuclear radiations from Ba^{139} have been investigated with the help of a magnetic lens spectrograph and scintillation counters in coincidence. Beta rays of energy 2.380, 2.227, and 0.822 Mev have been found together with an internal conversion line from a gamma ray of energy 0.163 Mev. The photoelectron spectrum, taken in the lens, showed gamma rays of energies 0.163 and 1.43 Mev. Beta-gamma coincidence experiments, performed with scintillation counters, showed that the 2.23-Mev beta-ray group is in coincidence with the 0.163-Mev gamma ray. The 0.163-Mev line has a $K/(L+M)$ ratio of 7.0 and an internal conversion coefficient α_K of 0.22, both of which correspond to an $M1$ transition. The connection with the shell model is discussed.

1. INTRODUCTION

A NUMBER of investigations of the radiations from Ba^{139} (85 min) have been carried out in the last few years, but none has led to a complete understanding of the disintegration scheme. Shepperd and Hill[1] used a magnetic lens spectrometer to measure the particle spectrum. They found a beta-ray distribution having an end-point energy of 2.27±0.02 Mev together with a K and an L internal conversion line for a gamma ray of energy 0.163 Mev. In addition they found a weak gamma ray of higher energy. Using a counter and absorption methods they estimated the energy of this gamma ray to be approximately 1.05±0.1 Mev. Shepperd and Hill made a Fermi plot of their data which appeared to support the idea of a single beta-ray group.

In the meantime, this element had been under investigation in this laboratory off and on, since 1948. The high-energy gamma ray was measured in a magnetic lens spectrometer, using the photoelectrons from a lead converter, and an energy of 1.46 Mev was found. The internal conversion line at 0.163 Mev was found in the investigation of the beta-ray spectrum. However, the Fermi plot of the beta rays did not give a straight line and it was surmised that there were several groups present. Coincidence work, done with ordinary counters, appeared to show that there were no gamma-gamma coincidences but that there were beta-gamma coincidences dependent on energy. In order to clear up these various difficulties it was decided to reinvestigate the spectrum of Ba^{139}.

2. EXPERIMENTAL RESULTS

Sources were prepared by bombarding barium metal with 11.5-Mev deuterons in the Indiana University cyclotron. The material was purified chemically, was separated, and used as $BaCrO_4$.

The beta-ray spectrum was investigated in a magnetic lens spectrometer. Since the half-life is 85 minutes the entire spectrum could not be investigated with one source. A number of separate runs were therefore taken and each was monitored to some convenient point on the beta-ray spectrum. The results of the investigation are shown in Fig. 1. A casual inspection of the beta-ray spectrum shows that it must be complex.

A Fermi analysis of the data was then made, and the results are shown in Fig. 2. The analysis suggests that there are two beta-ray groups having end-point energies around 2.3 Mev and differing by something of the order of magnitude of 0.150 Mev. In addition there is a group of considerably lower energy. The end-point energies, relative agundances, and values of log ft for the various groups are given in Table I.

The internal conversion line was measured carefully. Figure 3, in which the number of counts/min is plotted against the current in the lens, shows the profile of the line. The energy of the gamma ray responsible for the line is 0.163±0.001 Mev. From a plot of N/I *versus* I the value of $K/(L+M)$ was found to be 7.0±0.3. The

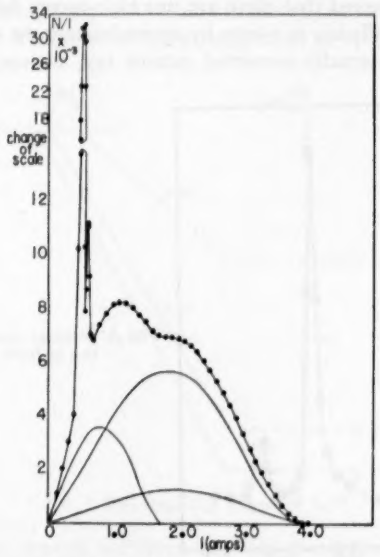

FIG. 1. The beta-ray spectrum of Ba^{139}.

† This work was supported by the joint program of the U. S. Office of Naval Research and the U. S. Atomic Energy Commission.

[1] L. R. Shepperd and J. M. Hill, Nature **162**, 566 (1948).

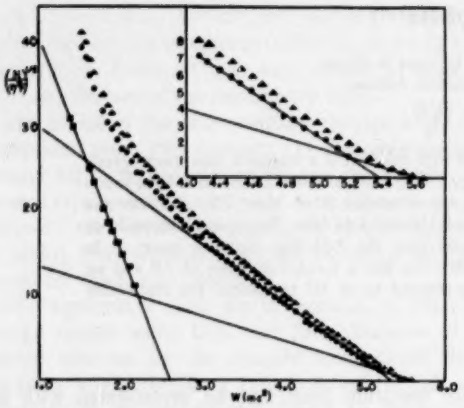

FIG. 2. Fermi plot of the beta rays of Ba^{139}.

determination of the internal conversion coefficient will be discussed in connection with the disintegration scheme.

The energy of the high-energy gamma ray was reinvestigated using a uranium radiator. Weak K and L photolines were found corresponding to a gamma ray of energy 1.43 ± 0.03 Mev.

3. EXPERIMENTS WITH SCINTILLATION COUNTERS; COINCIDENCE EXPERIMENTS

The gamma rays were also measured on a scintillation counter using a NaI(Tl) crystal, a Dumont 6292 photomultiplier tube, and a differential pulse-height analyzer. The pulse-height spectrum showed a high-energy gamma ray and the gamma ray at 0.163 Mev and no other gamma rays between these energies.

In order to check the results of the beta-ray analysis which showed that there are two high-energy beta-ray groups differing in energy by approximately the energy of the internally converted gamma ray, arrangements were made to do beta-gamma coincidence experiments using scintillation counters. The gamma rays were measured with the help of a NaI(Tl) crystal and photomultiplier tube. The beta rays were measured using an anthracene crystal and photomultiplier tube. The scintillation spectrometers were connected as shown in Fig. 4. Each branch of the circuit contained a preamplifier, linear amplifier, and differential pulse-height analyzer. The two branches were then fed to a coincidence circuit which had a resolving time of 0.2 microsecond. Arrangements were made to feed the singles output of either branch or the coincidence output to a fast scalar. The NaI(Tl) crystal used was a cylinder of 1-inch diameter and 1-inch height, and was canned in MgO. The anthracene crystal was a cube 2 cm on an edge.

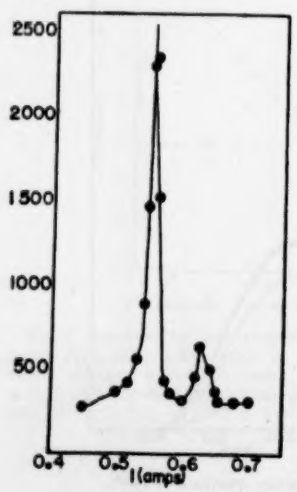

FIG. 3. Internal conversion line in Ba^{139}.

The use of an anthracene scintillation counter as a device for measuring beta-ray distributions was tested by measuring the beta-ray distribution from Cs^{137}. The experiments showed, in addition to the beta-ray spectrum, the internal conversion line corresponding to the gamma ray at 661 kev. The scintillation counter gives the number of particles in a given energy range $N(E)$. Since the resolving power of the scintillation spectrometer goes like $(\epsilon)^{-\frac{1}{2}}$, where ϵ is the dial setting in volts associated with a given energy E, it follows that

$$N(E)=\epsilon^{\frac{1}{2}}N(\epsilon). \quad (1)$$

A Fermi plot can therefore be made from the information obtained from $N(E)$ *vs* E. The energy calibration of the instrument is made from a measurement of the internal conversion line of Cs^{137}. The Fermi plot of the beta-ray distribution of Cs^{137} made in this way shows the well-known forbidden shape.

In order to measure coincidences between the gamma ray at 0.163 Mev and the high-energy beta rays of Ba^{139}, certain additional precautions had to be taken. Since the main interest in the experiment is in the neighborhood of the end point of the beta-ray spectrum (2.3 Mev) enough coincidences had to be obtained between the 0.163-Mev line and the beta rays to give statistically significant results. This entails the possibility that the high-energy end of the beta-ray spectrum may be distorted by pulse pileup from the large number of low-energy beta rays emitted by the source. In order to obviate this effect, an aluminum absorber, thick enough to stop all electrons of energy less than 1.1 Mev, was placed between the source and the anthracene

TABLE I. Beta rays of Ba^{139}.

End point energy Mev	Relative abundance percent	log ft
2.380	15.2	7.60
2.227	65.7	6.81
0.822	19.1	5.67

scintillation spectrometer. In order to carry out the experiment it is necessary to know the number of chance coincidences in a given experiment, i.e., the resolving time of the apparatus. The resolving time was measured both with a double pulse generator and by measuring chance coincidences from a Cs^{137} source.

The experiments on Ba^{139} consisted in placing the source between the two scintillation counters. Channel 1, the NaI(Tl) scintillation spectrometer, was set on the 0.163-Mev line, while the scintillation spectrometer using the anthracene crystal was swept through various pulse-height settings in the neighborhood of the end point of the beta-ray spectrum. The coincidence counting rate was corrected for chance coincidences and the quantity $N_{\beta\gamma}/N_{\gamma}$ was used for making a Fermi plot of the coincidences. The results of the Fermi plot are shown in Fig. 5 together with a Fermi plot for the singles spectrum in the same region. It will be seen that the Fermi plot for the singles counts has a somewhat higher end point than that for the coincidence counts, showing that the 0.163-Mev gamma ray is in coincidence with the lower of the two high-energy groups. The

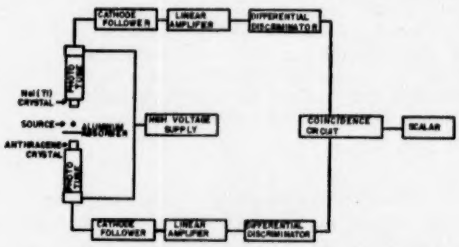

FIG. 4. Block diagram of scintillation spectrometers for beta-gamma coincidence work.

actual end points obtained were 2.195 Mev for the singles and 2.050 Mev for the coincidences, giving a difference of 0.145 Mev. The actual values of the end points obtained are, of course, not as accurate as those obtained in the lens spectrometer, their actual values being dependent on the calibration with Cs^{137}. However, the difference between these two end points is significant. In this paper the more accurate values as determined by the magnetic lens spectrometer will be used.

4. DISCUSSION OF RESULTS

The results of the investigations are embodied in the disintegration scheme of Fig. 6. The experiments showed that the highest-energy beta-ray group has an end point of 2.380 Mev and that the next lower beta-ray group, of energy 2.227 Mev, is in coincidence with the 0.163-Mev gamma ray. The difference in energy between these two beta-ray groups is, within the experimental error, equal to the energy of the 0.163-Mev gamma ray. The third beta-ray group feeds the high-energy gamma ray which presumably leads to the ground state.

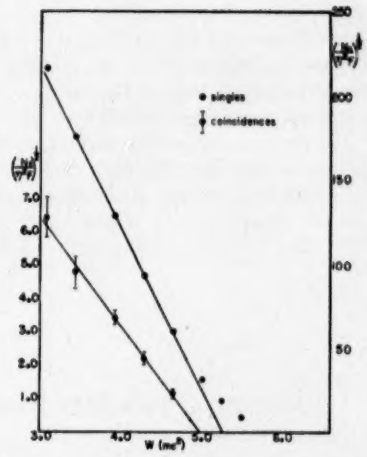

FIG. 5. Fermi plot for beta-gamma coincidences in Ba^{139}.

With the help of the disintegration scheme, it is now possible to calculate the internal conversion coefficient for the 0.163-Mev line. Knowing that the second beta-ray group feeds the line at 0.163 Mev, one can calculate the internal conversion coefficient in the K shell, α_K, from the ratio of the number of K-conversion electrons to the total number of electrons in the second group. The result gives $\alpha_K=0.22$. From the tables of Rose, Goertzel, and Perry[2] one finds that the value of $\beta_1=0.24$ agrees most closely with the measured value. Hence the 0.163-Mev line is magnetic dipole ($M1$). The value of the K/L ratio (7.0) also agrees quite well with that predicted from the empirical curves of Goldhaber and Sunyar[3] for $M1$ radiation ($K/L=7$).

It is now of interest to correlate these findings with what is to be expected from considerations of the shell model. The spin of the ground state of the product

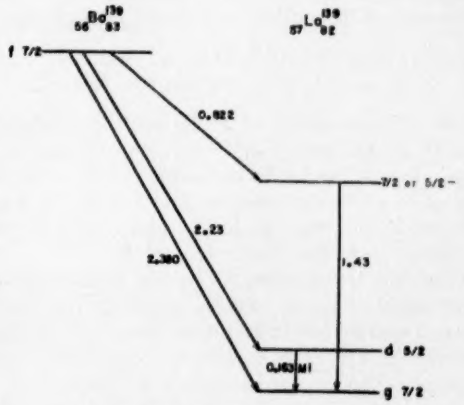

FIG. 6. Disintegration scheme of Ba^{139}.

[2] Rose, Goertzel, and Perry, Oak Ridge National Laboratory Report ORNL-1023, 1951 (unpublished).
[3] M. Goldhaber and A. W. Sunyar, Phys. Rev. 83, 906 (1951).

nucleus La^{139} has been measured and is 7/2, and the state is characterized as $g_{7/2}$. The log ft value for the 2.38-Mev group implies $\Delta I=0$, 1 yes. Taking the first possibility, the ground state of Ba^{139} is $f_{7/2}$. The fact that the internal conversion line at 0.163 Mev is $M1$ and that the log ft value for the second group is 6.8 definitely established that the first excited state of La^{139} is $d_{5/2}$. The beta-ray group of energy 0.822 Mev appears to be allowed, which would imply that the state at 1.43 Mev is odd and has a spin of 5/2 or 7/2. It is interesting to note that in the region of 57 protons the $g_{7/2}$ and $d_{5/2}$ states have nearly the same energy. In the present case the $d_{5/2}$ state lies above the $g_{7/2}$ by 0.163 Mev.

The authors are indebted to Dr. M. B. Sampson and the cyclotron group for making the irradiations and to Mr. A. E. Lessor for making the chemical separations. We are also indebted to Dr. B. D. Kern, Dr. D. J. Zaffarano, Dr. F L. Maienschein, and Dr. J. L. Meem, Jr., who participated in the early experiments in 1948.

PHYSICAL REVIEW VOLUME 95, NUMBER 3 AUGUST 1, 1954

Scattering of 14.1-Mev Neutrons in Helium, Hydrogen, and Nitrogen*

J. R. SMITH†‡
The Rice Institute, Houston, Texas
(Received April 22, 1954)

Cloud-chamber studies have been made of the scattering of 14.1-Mev neutrons in helium, hydrogen, and nitrogen. For each of these gases the angular distribution of the elastically scattered neutrons has been obtained. The angular distribution in helium shows a minimum at about 110° in the center-of-mass system, with a large maximum representing forward scattering and a smaller maximum for backscattering. The hydrogen angular distribution is isotropic. Elastic scattering in nitrogen resembles diffraction scattering, showing a strong forward scattering maximum and smaller maxima at 70° and 180°, with minima close to 60° and 130°. Inelastic scattering in nitrogen does not depart from spherical symmetry by more than a factor of two. The elastic scattering cross section for nitrogen is 0.82 barn and the inelastic scattering cross section is 0.48 barn. Cross sections for two- and three-particle disintegrations are 270 and 16 millibarns, respectively.

I. INTRODUCTION

STUDIES of the scattering of neutrons by nuclei are important for the information they yield relative to the nuclear forces involved. Such studies can be made by observing the recoil nuclei. In the scattering of fast neutrons by light nuclei the recoil nucleus can receive an appreciable part of the energy of the incident neutron. The recoil energy is related to the energy of the incident neutron by the equation

$$E_r=E_n\{2\cos^2\phi+(1+1/M)Q/E_n\pm 2\cos\phi \times[\cos^2\phi+(1+1/M)Q/E_n]^{\frac{1}{2}}\}M/(M+1)^2, \quad (1)$$

where E_n is the energy of the incident neutron and E_r and M are the energy and mass, respectively, of the recoil nucleus, and ϕ is the angle of the recoil with respect to the incident neutron direction. Q is the energy released in the reaction and is negative for inelastic scattering, zero for elastic scattering.

When the target nuclei are contained in the gas of a cloud chamber, the paths of the recoils are made visible as tracks whose length and direction can be measured directly. If the range-energy relation for the recoil nucleus is known, the length of the track gives the energy of the recoil. The remaining unknown in (1) is Q, which is the negative of the excitation energy of the residual nucleus. Thus a cloud-chamber experiment makes possible a study of the inelastic scattering as well as the elastic scattering.

The present work is a cloud-chamber study of the scattering of 14.1-Mev neutrons in helium and hydrogen, where only elastic scattering is possible, and in nitrogen, where there is considerable inelastic scattering at this energy.

II. EXPERIMENTAL ARRANGEMENT

Monoenergetic 14.1-Mev neutrons were obtained from the $H^3(d,n)He^4$ reaction. The unresolved beam of deuterons from the Rice Institute Cockroft-Walton accelerator was used to bombard a target[1] of tritium absorbed in a 300-μg/cm^2 film of zirconium evaporated onto a tungsten disk. The accelerator was operated at about 160 kev. Molecular ions comprised approximately 80 percent of the beam, so that most of the deuterons incident on the target had energies of 80 kev. An aperture 5 mm in diameter was placed over the target to restrict the diameter of the beam and consequently the size of the neutron source. In each experiment the cloud chamber was placed at 90° to the deuteron beam. The energy spread over the angle subtended by the chamber was less than 0.1 Mev.

* Supported by the U. S. Atomic Energy Commission program.
† National Science Foundation predoctoral fellow.
‡ Now at Phillips Petroleum Company, Atomic Energy Division, Idaho Falls, Idaho.

[1] A. B. Lillie and J. P. Conner, Rev. Sci. Instr. **22**, 210 (1951).

For the experiments on helium and nitrogen the same cloud chamber was used. This chamber was of rather heavy construction, as it was designed to operate at either high or low pressures. The body of the chamber was a Pyrex cylinder 23 cm in diameter and 13 cm high, with a wall thickness of 0.9 cm. The outer surface of the cylinder was painted black, except for a window 7.4 cm high and 13 cm wide for admission of the light beam. Illumination was by a 5000-watt incandescent lamp, the light from which was rendered parallel by a lens and cooled by a water cell before it reached the chamber. The chamber was placed with its center 30 cm from the neutron source.

A small chamber of light construction was used for the experiment on hydrogen in an effort to minimize the number of scattered neutrons inside the chamber. The body of this chamber was a Pyrex cylinder having an inside diameter of 15.4 cm and a height of 8.1 cm, with a wall thickness of 0.3 cm. The illuminated portion was 4.3 cm high and 11.3 cm wide. The source of light was a 1000-watt incandescent lamp, the light from which passed through a lens and water cell before reaching the chamber. The center of this chamber was 14 cm from the neutron source.

Stereoscopic pictures of the tracks formed in the chamber were taken through an optical system utilizing one camera and a front surface mirror. The system used with the large chamber for the nitrogen and helium experiments had a stereoscopic angle of about 20°. The stereoscopic angle for the system used with the small chamber for the hydrogen experiment was 15°.

The processed film was reinserted in the camera and the images were projected through the optical system used in taking the pictures. By proper orientation of a white screen, the two images of a track formed thereon could be made to coincide. From the coincident images were measured the true length and orientation in space of the original track. Only tracks making angles of less than 45° to the horizontal were measured. A geometrical correction was applied to the data to allow for tracks excluded by this limitation.

The true length of a track was taken to be its measured length minus its width. Tracks as short as 0.5 mm were measured, although most tracks less than 1 mm long were probably missed. Tracks greater than 2 mm long are considered to have been observed with 100 percent efficiency. Estimated measurement errors are 0.5 mm for length measurements and 2° for angle measurements. For the short tracks of slow nitrogen recoils the errors in angle are closer to 10°.

III. RESULTS

A. Helium

Neutron scattering in helium has been the subject of several experiments[2–4] using proportional counters or ionization chambers. These experiments cover the energy range 0.4 to 14.3 Mev. The data are in substantial agreement with the calculations of Dodder and Gammel,[5] who made phase shift analyses of proton-alpha scattering at energies up to 9.48 Mev. The results they obtained for Li^5 were applied to the mirror nucleus He^5 and neutron-helium scattering. Phase shifts from the theory of Dodder and Gammel are presented by Seagrave[4] for neutron energies up to 20 Mev.

For the present study of neutron scattering in helium the large cloud chamber was filled to approximately 3 atmospheres with 99.9-percent pure helium. The helium was passed through a liquid air trap before it entered the chamber, to remove any vapor that might have been present. Water was used for the vapor in the chamber. The stopping power of the chamber gas was calculated[6] to be 0.56. The alpha-particle tracks ranged up to 15.9 cm in length. Maximum track length component normal to the direction of the neutron was 5 cm at 30°. It is desirable to define a counting volume sufficiently small that all tracks originating in this region would be certain to stop within the illuminated volume of the chamber. The ranges of the alpha recoils encountered in this experiment were too great to allow this practice. Tracks were measured if they began 1.5 cm within the illuminated volume, 3 cm from the wall of the chamber toward the neutron source, and 5 cm from the opposite wall. If a track left the illuminated portion of the chamber, its visible length was recorded as a minimum value.

One thousand tracks were measured. Of these, approximately 35 percent had lengths less than 1.8 cm and were distributed roughly uniformly in angle. This group was compeletely resolved from the remainder of the tracks for recoil angles less than 60°, corresponding to neutron scattering at angles greater than 60° in the center-of-mass system. These tracks were due to neutrons of energies around 1 Mev which had been scattered from the walls of the chamber or the floor. The neutron-helium cross section has a resonance close to 1 Mev, at which energy it reaches a magnitude of 6.7 barns.[7] This is approximately 7 times the cross section at 14 Mev, which has been measured to be 1.02 barns.[8] The observed low-energy background could be produced by a group of 1-Mev neutrons approximately 10 percent of the intensity of the neutrons coming directly from the tritium target. There were some scattered neutrons of other energies incident on the chamber. The recoils from these neutrons were distributed randomly in length and angle and numbered about 5 percent of the total tracks measured. The total intensity of scattered neutrons was thus about 15 percent of that of the 14-Mev neutrons.

The solid angle in the center-of-mass system was

[2] R. K. Adair, Phys. Rev. **86**, 155 (1952).
[3] P. Huber and E. Baldinger, Helv. Phys. Acta **25**, 435 (1952).
[4] J. D. Seagrave, Phys. Rev. **92**, 1222 (1953).
[5] D. C. Dodder and J. L. Gammel, Phys. Rev. **88**, 520 (1952).
[6] C. M. Crenshaw, Phys. Rev. **62**, 54 (1942).
[7] Bashkin, Mooring, and Petree, Phys. Rev. **82**, 378 (1951).
[8] Coon, Graves, and Barschall, Phys. Rev. **88**, 562 (1952).

divided into ten equal parts and the number of neutrons scattered into each interval was plotted at the angle representing the midpoint of the interval. These data include those tracks which left the light beam, and hence had no true length measurements. Accordingly, rather large tolerances were allowed for tracks upon which complete length and angle measurements were made. Tracks were admitted if their length and angle measurements fell within 2 mm and 4° of the calculated values. In the small-angle region, where confusion with the low-energy background exists, an approximate background correction was made by subtracting from the total number of recoils counted the average of the number of low-energy tracks seen in the angular intervals where resolution was complete. This correction was of the order of 20 percent.

The plot of the neutron-helium data is shown in Fig. 1, along with a theoretical curve using phase shifts calculated by Dodder and Gammel for 14 Mev.[4,5] The agreement is good within the limits of the experiment. The discrepancy at small angles can be attributed to the uncertainty in the background corrections for these intervals. The similarity between the scattering of neutrons and protons by helium supports the idea of equivalance of the mirror nuclei He^5 and Li^5.

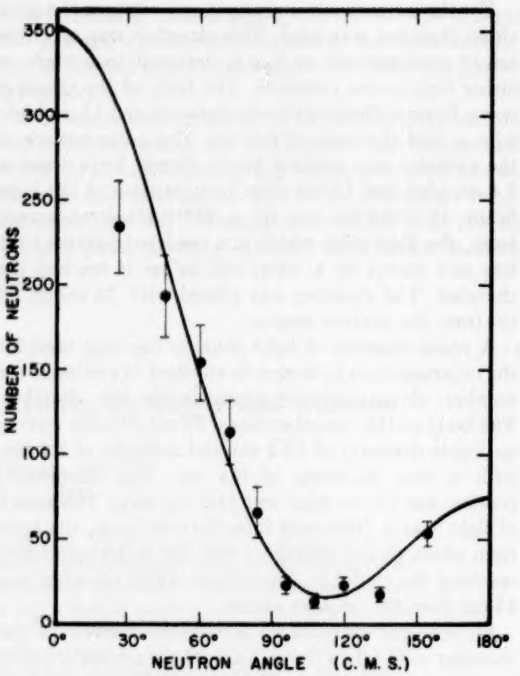

FIG. 1. Angular distribution in the center-of-mass system of 14.1-Mev neutrons scattered in helium. The solid curve is the theoretical distribution according to Dodder and Gammel.

B. Hydrogen

Previous experiments[9–13] on the neutron-proton angular distribution at 14 Mev have indicated isotropy in the center-of-mass system. However, if there were a large peak, such as might be due to diffraction scattering it would probably lie at smaller angles than those covered by the existing data. The small-angle intervals were the principal regions of interest in this cloud-chamber investigation.

Because of the decrease in the total neutron-proton cross section from about 4.5 barns at 1 Mev[14] to 0.689 barn at 14 Mev,[15] one could expect the same type of low-energy background problem as was encountered in the helium experiment. In order to minimize the effect of this low-energy background the chamber of light construction was used. The background appeared roughly isotropic; any very strong anisotropy in the neutron-proton angular distribution could be expected to be evident above the uniform background.

Nine hundred recoil tracks were measured. Measurements of angle only were made, as the stopping power of the chamber gas was not great enough to allow measurements of length. Of the tracks measured, 800 were from pictures taken with the cloud chamber filled to 20 pounds pressure with 99.5 percent pure hydrogen. The other 100 tracks were from pictures taken with the chamber filled to 22 pounds pressure with a mixture of 50 percent hydrogen and 50 percent argon. In each case water was used for the vapor.

The angular distribution obtained is shown in Fig. 2. The points represent the number of neutrons scattered into certain polar angle intervals, divided by the solid angle represented by the interval. The angular intervals were 20° wide for angles greater than 90°, and 10° wide for angles less than 90°. Within statistics the distribution appears to be isotropic. Because of the considerable background present in the experiment it was not thought worth while to improve the statistics by measuring more tracks.

C. Nitrogen

The angular distribution for neutrons scattered in nitrogen has been studied by the counter method at energies between about 1 and 3 Mev.[16,17] At those energies marked anisotropies were found whose form varied as the neutron energy increased across a resonance. The disintegrations produced by 14-Mev neutrons have been studied by Lillie,[18] who used a

[9] C. F. Powell and G. P. S. Occhialini, Rept. Int. Conf. "Fundamental Particles," 1946.
[10] J. S. Laughlin and P. G. Kruger, Phys. Rev. **73**, 197 (1948).
[11] H. H. Barschall and R. F. Taschek, Phys. Rev. **75**, 1819 (1949).
[12] Remley, Jentschke, and Kruger, Phys. Rev. **89**, 1194 (1953).
[13] Allred, Armstrong, and Rosen, Phys. Rev. **91**, 90 (1953).
[14] *Neutron Cross Sections*, Atomic Energy Commission Report AECU-2040 (Technical Information Service, Department of Commerce, Washington, D. C., 1952).
[15] Poss, Salant, Snow, and Yuan, Phys. Rev. **87**, 11 (1952).
[16] Baldinger, Huber, Ricamo, and Zünti, Helv. Phys. Acta **23**, 503 (1950).
[17] Fowler, Johnson, and Risser, Phys. Rev. **91**, 441 (1953).
[18] A. B. Lillie, Phys. Rev. **87**, 716 (1952).

cloud chamber. Lillie also measured the recoil tracks occurring at angles less than 15° to the neutron direction. Those tracks were so short at the pressure of one atmosphere at which he operated his cloud chamber that he was able to conclude only that inelastic scattering is considerably more likely than elastic scattering for recoils projected at small angles.

For the present study the large cloud chamber was filled to approximately 1/5 atmosphere of nitrogen, with water as the vapor. This chamber was the same one used in the helium experiment, so that one could again expect a background due to scattered neutrons having an intensity of about 15 percent of that of the 14-Mev neutrons. While not insignificant, this background does not pose quite so serious a problem in nitrogen as it does in helium and hydrogen. The neutron cross section for nitrogen decreases by about a factor of two from 1 Mev to 14 Mev,[14] compared to the factor of close to seven for the lighter nuclei.

The chamber was flushed and filled with nitrogen of 99.5-percent purity. To determine the stopping power, a polonium alpha-particle source was placed in the chamber. The source was covered with a shield which could be moved aside by means of a magnet from outside the chamber. Five frames of the alpha-particle tracks were photographed at the beginning, middle, and end of each 250-picture roll of film. The stopping power was determined to be 0.187 for the alpha particles, taking the range of plonium alpha particles to be 3.82 cm.[19] For the slower nitrogen recoils the stopping power was somewhat larger than this because of the variation with particle velocity of the stopping power of hydrogen in the water vapor. Values of the stopping power of hydrogen were taken to be 0.35 for the nitrogen nuclei and 0.20 for the alpha particles.[6] The corrected value of the stopping power of the chamber gas for the nitrogen nuclei was 0.191.

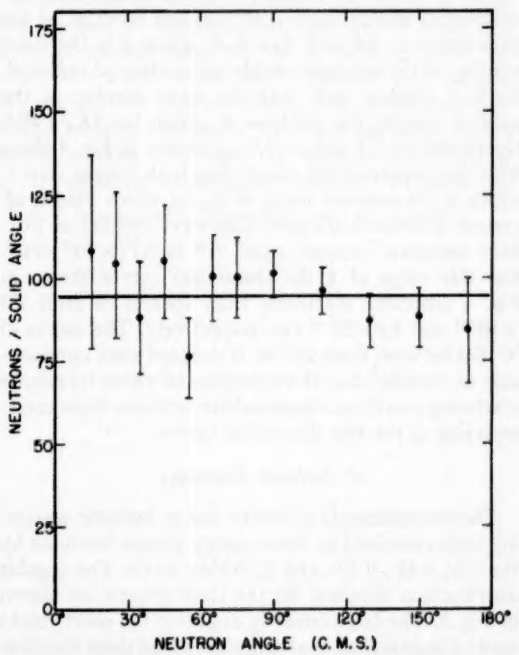

FIG. 2. Angular distribution in the center-of-mass system of 14.1-Mev neutrons scattered in hydrogen. The straight line represents isotropy in the center-of-mass system.

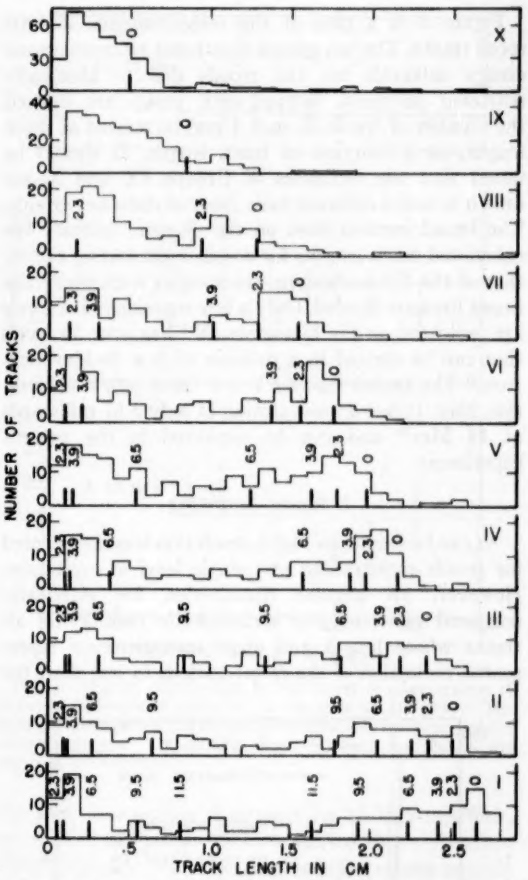

FIG. 3. Plot of number of nitrogen recoil tracks as a function of track length. The ten groups represent equal increments for the cosine of the angle of projection of the recoil nucleus. For the elastically scattered neutrons these groups also represent equal energy intervals. The short, heavy lines represent excitation of the nitrogen nucleus to the energies with which the lines are labeled.

The expected track lengths of the recoils were calculated using the range-velocity data of Blackett and Lees[20] for nitrogen nuclei. It was found that a further correction of 1.6 percent in the stopping power was needed to make the calculated track length agree with the observed value for the group of recoils projected in the forward direction by elastically scattered neutrons. The final stopping power used was 0.194.

[19] H. A. Bethe, Revs. Modern Phys. **22**, 213 (1950).
[20] P. M. S. Blackett and D. S. Lees, Proc. Roy. Soc. (London) **A134**, 658 (1932).

Figure 3 is a plot of the measurements of 1900 recoil tracks. The ten groups illustrated represent equal energy intervals for the recoils due to elastically scattered neutrons. Within each group are plotted the number of tracks in each 1-mm increment of track length, as a function of track length. It should be noted that the ordinates of Groups IX and X are drawn to scales different from those of the other groups. The broad vertical lines on the diagram indicate the calculated track lengths for recoils representing excitation of the N^{14} nucleus to the energies with which the broad lines are labeled. Only a few representative levels are indicated on the histogram. N^{14} has over 30 levels that can be excited in a collision with a 14-Mev neutron.[21] The $(n,2n)$ reaction is not taken into consideration here. It has a cross section of only 5.67 millibarns at 14 Mev[22] and can be neglected in the present experiment.

1. Elastic Scattering

As can be seen from Fig. 3, resolution was not effected for recoils representing any single level of excitation. However, an angular distribution for elastically scattered neutrons was obtained by considering all tracks whose length and angle measurements represented excitation of the recoil nucleus to less than the first excited level of N^{14} at 2.3 Mev. The solid angle in the center-of-mass system was divided into ten equal parts and the expected track lengths for the limits of each division were calculated. The number of tracks in each solid angle division was taken to be the number within the elastically scattered group having track lengths between the values calculated for the limits of the angular interval. Track length was taken to be a more accurate criterion than angle because of large errors present in the angle measurements. These large errors were due to multiple scattering of the slow nuclei as well as to the difficulty of measuring the angles for short tracks.

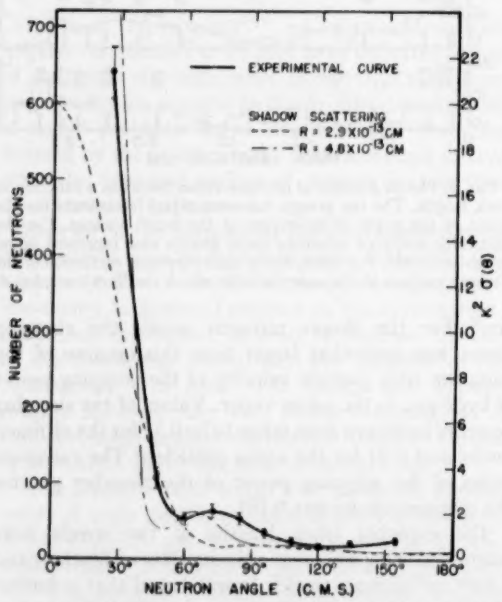

FIG. 4. Angular distribution in the center-of-mass system of 14.1-Mev neutrons elastically scattered in nitrogen. The solid curve is the experimental curve while the dashed curves represent two theoretical curves from the diffraction scattering calculations of Feld *et al.* The ordinate on the right refers to the calculated curves.

The angular distribution of the elastically scattered neutrons thus obtained is shown in Fig. 4. It shows very strong small-angle scattering of the neutrons, with smaller maxima at about 70° and 180° and minima close to 60° and 130°. The latter minimum is very broad, and examination of the data in smaller angular intervals indicates that the curve is essentially flat between 110° and 150°.

The shape of the angular distribution curve is quite similar to that which might be expected from the theory of diffraction scattering. This theory is not intended to apply to such light nuclei, but its characteristic scattering pattern has been observed in the scattering of 14.1-Mev neutrons in oxygen[23] as well as in nitrogen. Feld *et al.*[24] have calculated the angular distributions to be expected of neutrons diffracted by nuclei. They present a series of curves representing the differential scattering cross section as a function of the parameters $x=kR$ and $X_0=K_0R$, where k is the wave number of the neutron outside the nucleus of radius R. K_0 is a number such that the wave number of the neutron inside the nucleus is given by $(K_0^2+k^2)^{\frac{1}{2}}$. Curves for $x=2.2$ and $x=3.7$ are shown in Fig. 4 along with the experimental curve. For both curves $X_0=5$, which is the smallest value of X_0 for which Feld *et al.* present a theoretical curve. The wave number of 14.1-Mev neutrons incident upon N^{14} is 0.77×10^{13} cm^{-1}. For this value of k the theoretical curves shown in Fig. 4 represent scattering from spheres of radii 2.9×10^{-13} and 4.8×10^{-13} cm, respectively. The radius of N^{14} lies between these values. It does not seem unreasonable to consider that the experimental curve represents scattering conditions intermediate between those corresponding to the two theoretical curves.

2. Inelastic Scattering

The measurements of tracks due to inelastic scattering were examined in three energy groups bounded by the 3.9-, 6.45-, 9.49-, and 12.8-Mev levels. The angular distributions obtained for the three groups are shown in Fig. 5. The large errors in angle for the short tracks made it impractical to attempt to extend these distribu-

[21] F. Ajzenberg and T. Lauritsen, Revs. Modern Phys. **24**, 321 (1952).
[22] E. B. Paul and R. L. Clarke, Can. J. Phys. **31**, 267 (1953).
[23] J. P. Conner, Phys. Rev. **89**, 712 (1953).
[24] Feld, Feshbach, Goldberger, Goldstein, and Weisskopf, Atomic Energy Commission Report NYO-636 (unpublished).

tions below 60° in the center-of-mass system. For angles greater than 60° there appears to be no anisotropy greater than a factor of two for any of the three groups. There is some indication of possible anisotropy for the two groups representing lower excitation, but this could be due to statistics and overlapping of measurements of tracks from one group to the next.

From the number of tracks counted in each of the three inelastic scattering groups the relative probability per unit energy interval for excitation to the levels involved can be estimated. This probability appears to be approximately equal for levels around 5 Mev and levels around 8 Mev. However, the probability per unit energy interval for excitation to levels around 11 Mev is less than that for the lower intervals by a factor of three. This is a rather surprising result inasmuch as there are many more levels at higher than at lower energies. Similar results were observed by Conner[23] for the inelastic scattering of 14-Mev neutrons in oxygen. Analyses of the energy distribution of 14-Mev neutrons scattered by several elements[25] indicate that in general the most probable energies for the inelastically scattered neutrons lie below 3 Mev. This corresponds to a greater probability for excitation of the residual nucleus to higher than to lower levels. These analyses did not include oxygen or nitrogen, and it could be that these two elements are exceptions.

3. *Cross Sections*

In addition to the recoil tracks measured, a count was made of all disintegration forks and of recoils too short for measurement. In the pictures on which the count was made, there were observed 1822 recoils, 385 two-particle disintegrations, and 23 three-particle disintegrations. Analysis of the measured recoil tracks yielded a ratio for elastic to inelastic scattering of 1.7:1. Assuming the measured value of 1.59 barns[3] for the total cross section of nitrogen for 14-Mev neutrons, one obtains 270 mb as the cross section for two-particle disintegrations, and 16 mb for the three-particle disintegrations. The elastic scattering cross section is 0.82 barn and the cross section for inelastic scattering exclusive of disintegrations is 0.48 barn.

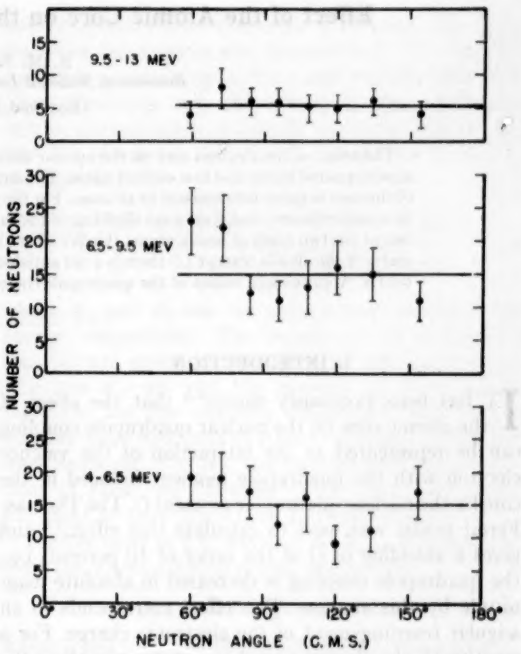

FIG. 5. Angular distribution in the center-of-mass system of neutrons inelastically scattered in nitrogen at 14.1 Mev. The three groups represent three energy intervals for excitation of the nitrogen nucleus. The straight lines represent isotropy in the center-of-mass system.

The author wishes to thank Dr. T. W. Bonner for his interest and counsel throughout the course of this work.

[25] E. R. Graves, and L. Rosen, Phys. Rev. 89, 343 (1953).

Effect of the Atomic Core on the Nuclear Quadrupole Coupling*

R. M. STERNHEIMER
Brookhaven National Laboratory, Upton, New York

(Received April 26, 1954)

The effect of the electron core on the nuclear electric quadrupole coupling has been evaluated for several atomic ground states and first excited states. The antishielding produced by the $np \to p$ and $nd \to d$ excitations of the core is taken into account in all cases. For the ground states, the effect of the angular modes of excitation predominates, and gives a net shielding of the same order as that predicted by the Thomas-Fermi model, except for two cases of heavy atoms (Cs,W) where the antishielding predominates. For the first excited (p) states of the alkalis (except Li) there is a net antishielding which ranges from 10 percent for Na to 24 percent for Cs. Approximate values of the quadrupole correction factor are given for 9 atomic states.

I. INTRODUCTION

IT has been previously shown[1-3] that the effect of the atomic core on the nuclear quadrupole coupling can be represented as the interaction of the valence electron with the quadrupole moment induced in the core by the nuclear quadrupole moment Q. The Thomas-Fermi model was used to calculate this effect,[1,2] and gives a shielding of Q of the order of 10 percent, i.e., the quadrupole coupling is decreased in absolute magnitude by this amount. This effect corresponds to an angular rearrangement of the electronic charge. For a positive Q, the electrons tend to concentrate along the axis of Q where the potential energy is a minimum. This angular rearrangement is due to an excitation of s electrons into higher d states, and of p electrons into f states. It was also shown that, in addition, the perturbation by the nuclear Q gives rise to an excitation of p electrons into higher p states, and a similar effect takes place for d electrons which are excited into higher d states. This effect corresponds to a radial redistribution of the charge of the electron core. If $Q>0$, then along the axis of Q, the electrons tend to be closer to the nucleus than in the unperturbed state, while at right angles to the axis of Q the electrons are on the average farther from the nucleus than without the perturbation. The radial redistribution tends to reinforce the effect of the nuclear Q if the valence electron is sufficiently far outside the core, and for this reason has been referred to as an antishielding. This effect depends sensitively on the principal and azimuthal quantum numbers of the external shells of the core, and cannot be obtained from the Thomas-Fermi model. The effect of the radial modes was shown to be small for the case of Cl previously discussed. However, in a recent investigation of the nuclear quadrupole coupling in polar molecules,[2] it was found that the total induced quadrupole moment due to the antishielding is very large for heavy atoms such as Rb and Cs. Accordingly the effect of the core for the atomic ground states has been calculated for some atoms heavier than those previously investigated. It was found that for Cs and W there is a net antishielding due to the effect of the radial modes, although for light atoms the shielding due to the angular modes generally predominates.

The radial rearrangement of the electron distribution affects most strongly the outer parts of the atomic core, so that the antishielding effect increases rapidly with increasing distance from the nucleus in this region. Thus one may expect that for excited atomic states there will be a net antishielding, even though the shielding due to the angular modes predominates for the ground state. This expectation was borne out by calculations for the first excited (p) states of the alkalis, for which one finds a net antishielding varying from 10 percent for Na to 24 percent for Cs.

In order to check the accuracy of the Thomas-Fermi model, wave function calculations of the shielding due to the angular modes ($ns \to d$, $np \to f$) have been previously carried out[2] for Li, Al, and Cl. It was found that the interaction of the valence electron with the induced moment obtained from the wave-function calculations is $\sim$1.5 times smaller than the interaction with the Thomas-Fermi induced moment. It seemed of interest to check the Thomas-Fermi model for a heavy atom. For this purpose, the perturbed wave functions for the angular modes were calculated for the case of Cs. Similarly to the result for light atoms, it was found that the interaction of a $6p$ electron with the induced moment based on the perturbed wave functions is 1.4 times smaller than the interaction with the Thomas-Fermi induced moment. Thus the Thomas-Fermi values divided by 1.5 should give the order of magnitude of the shielding throughout the range of Z.

The present calculations of the effect of the distortion of the atomic core cannot be checked directly by experimental values. In order to obtain some information on the expected accuracy of the calculations, the same method as used here was applied to calculate the electronic polarizability α of several ions. It was

* Work done under the auspices of the U. S. Atomic Energy Commission.

[1] R. M. Sternheimer, Phys. Rev. **80**, 102 (1950).

[2] R. M. Sternheimer, Phys. Rev. **84**, 244 (1951); **86**, 316 (1952); Foley, Sternheimer, and Tycko, Phys. Rev. **93**, 734 (1954). These papers will be referred to as I, II, and III respectively.

[3] R. M. Sternheimer and H. M. Foley, Phys. Rev. **92**, 1460 (1953). In Eqs. (42) and (43) of this paper, L should be replaced by $\bar{L}$.

found that the calculated values of α lie between 1 and 1.5 times the experimental values in most cases. It may be expected that the accuracy of the calculation of the quadrupole coupling will be of the same order as for α. Thus the values of the quadrupole correction as obtained from the Hartree-Fock wave functions should be accurate, in general, within a factor of 1.5 and may tend to be somewhat larger than the actual values. The calculations of α will be reported in a forthcoming paper.

II. QUADRUPOLE CORRECTION FOR ATOMIC GROUND STATES AND EXCITED STATES

This section is devoted to obtaining values of the quadrupole correction R for several atomic ground states and excited states. Here R is the ratio of minus the interaction energy due to the induced moment to the energy of interaction with the nuclear Q. R is given by

$$R=\frac{\int_0^\infty \gamma v'^2 r^{-3} dr}{\int_0^\infty v'^2 r^{-3} dr}, \tag{1}$$

where r is the distance from the nucleus, v' is the radial part of the valence wave function times r, normalized according to

$$\int_0^\infty v'^2 dr = 1, \tag{1a}$$

and

$$\gamma(r)=(1/Q)\left[\int_0^r Q_i dr' + r^5 \int_r^\infty Q_i r'^{-5} dr'\right], \tag{2}$$

where $Q_i(r)dr$ is the induced quadrupole moment between r and $r+dr$. Q_i consists of two terms, $Q_{i,\mathrm{ang}}$ and $Q_{i,\mathrm{rad}}$ which are, respectively, the induced moment density due to the angular and radial excitations of the core. The angular term will be discussed first. For B, Na, Cl, and Cs, this term was obtained from wave-function calculations. The expression for $Q_{i,\mathrm{ang}}$ is

$$Q_{i,\mathrm{ang}}(r)=Qr^2\left[\frac{8}{5}\sum_n (u_0' u'_{1,0\to 2})_{ns} + \frac{72}{25}\sum_n (u_0' u'_{1,1\to 3})_{np} + \frac{8}{5}\sum_n (u_0' u'_{1,2\to 0})_{nd} + \frac{144}{35}\sum_n (u_0' u'_{1,2\to 4})_{nd}\right]. \tag{3}$$

Here each sum over the principal quantum number n extends over the occupied s, p, d shells, respectively; the u'_0 are the corresponding unperturbed radial functions times r, normalized according to (1a); $u'_{1,l\to l'}$ is r times the radial part of the excitation of nl to l', where l and l' are the azimuthal quantum numbers of the unperturbed function and the perturbation, respectively. The numerical coefficients of Eq. (3) arise from the summation over the magnetic substates of nl and integration over the angle θ between the radius vector of the electron and the axis of Q. The first two coefficients pertaining to the s and p shells have been given previously in I. The remaining ones, which pertain to the excitation of d shells, are derived below (see Sec. IV). As shown in I, the $u'_{1,l\to l'}$ are determined by the equation

$$\left[-\frac{d^2}{dr^2}+\frac{l'(l'+1)}{r^2}+V_0-E_0\right]u'_{1,l\to l'}=\frac{u_0'}{r^3}, \tag{4}$$

where V_0 and E_0 are the unperturbed potential and energy, respectively. The details of the solution of Eq. (4) are given in Sec. III. For the unperturbed functions u'_0 we used the Hartree or Hartree-Fock functions for the elements considered. For B, the Hartree wave functions of Brown, Bartlett, and Dunn[4] were employed. For Na, the Hartree-Fock wave functions of Fock and Petrashen[5] were used. The u'_0 for Cl^- and Cs^+ were taken from Hartree's work.[6,7]

For the cases of Cu, Rb, and W, $Q_{i,\mathrm{ang}}$ was obtained from the Thomas-Fermi model, which gives

$$Q_{i,\mathrm{ang}}=0.2998Q(\chi x)^{\frac{1}{2}}(x/r), \tag{5}$$

where χ and x are the Thomas-Fermi function and variable, respectively; $x=(Z^{\frac{1}{3}}/0.8853)r$, where r is in units a_H (Bohr radius). For large r, the Thomas-Fermi model gives a $1/r$ dependence for $Q_{i,\mathrm{ang}}$ instead of an exponential decrease as required by the wave functions. For this reason, Eq. (5) was modified at large r so as to agree with the total induced moment $Q_{iT,\mathrm{ang}}$ obtained from the wave-function calculations. The values obtained for Cl and Cs (see Sec. III) were interpolated to give $Q_{iT,\mathrm{ang}}(\mathrm{Cu})\cong 2.0Q$, $Q_{iT,\mathrm{ang}}(\mathrm{Rb})\cong 2.2Q$, and Eq. (5) was replaced by an exponential for large x ($x\gtrsim 9$) so adjusted that $\int_0^\infty Q_{i,\mathrm{ang}}dr$ has the appropriate value. For W, a value $Q_{iT,\mathrm{ang}}=3.5Q$ was used. We note that the treatment of $Q_{i,\mathrm{ang}}$ at large r is not critical, because most of the quadrupole coupling takes place near the nucleus.

The term $Q_{i,\mathrm{rad}}$ due to the radial modes is obtained from the corresponding excited wave functions. As shown in I, these functions are determined by the equation

$$\left[-\frac{d^2}{dr^2}+\frac{l(l+1)}{r^2}+V_0-E_0\right]u'_{1,l\to l} = u_0'\left(\frac{1}{r^3}-\left\langle\frac{1}{r^3}\right\rangle_{nl}\right). \tag{6}$$

Here $u'_{1,l\to l}$ is r times the radial part of the perturbation; $\langle 1/r^3\rangle_{nl}$ is the average of $1/r^3$ for the unperturbed function u'_0 whose principal and azimuthal quantum

[4] Brown, Bartlett, and Dunn, Phys. Rev. **44**, 296 (1953).
[5] V. Fock and M. Petrashen, Physik. Z. Sowjetunion **6**, 368 (1934).
[6] D. R. Hartree, Proc. Roy. Soc. (London) **156**, 45 (1936).
[7] D. R. Hartree, Proc. Roy. Soc. (London) **143**, 506 (1934).

numbers are n and l, respectively. That solution of (6) must be chosen which is orthogonal to u'_0. $Q_{i,\mathrm{rad}}$ is given by

$$Q_{i,\mathrm{rad}}(r)=Qr^5\left[\frac{48}{25}\sum_n(u'_0u'_{1,1\to1})_{np}\right.$$

$$\left.+\frac{16}{7}\sum_n(u'_0u'_{1,2\to2})_{nd}+\frac{224}{75}\sum_n(u'_0u'_{1,3\to3})_{nf}\right], \quad (7)$$

where the sums extend over the occupied p, d, and f shells, respectively. The numerical coefficients of (7) are obtained from the summation over the magnetic substates and the integration over θ. The coefficient for $np\to p$ has been derived in I. The coefficients for $nd\to d$ and $nf\to f$ are obtained below.

Except for the case of W, the wave functions $u'_{1,l\to l}$ have been obtained previously, in connection with the work on the quadrupole coupling in polar molecules.[2] The same procedure was employed for W, using the Hartree wave functions obtained by Manning and Millman.[8] The method of calculation will be briefly described. The left-hand side of Eq. (6) involves the function

$$P(r)\equiv[l(l+1)/r^2]+V_0-E_0. \quad (8)$$

In view of the equation satisfied by u'_0, P can be obtained directly from the tabulated Hartree wave functions, as follows,

$$P(r_n)=[u'_0(r_n+\delta)-2u'_0(r_n)+u'_0(r_n-\delta)]/\delta^2u'_0(r_n), \quad (9)$$

where r_n is a selected point, and δ is the interval of integration. The solution is started near $r=0$ by means of a power series, as shown in I. By subtracting a suitable multiple of u'_0 from the resulting function $u'_{1,l\to l}$ one obtains a function orthogonal to u'_0, which is the desired perturbation. The zero-order core wave functions used in these calculations are those mentioned above in connection with $Q_{i,\mathrm{ang}}$, as well as the Hartree-Fock functions[9] for Cu^+ and the Hartree functions for[10] Rb^+.

After $Q_{i,\mathrm{ang}}$ and $Q_{i,\mathrm{rad}}$ are determined, the function $\gamma(r)$ of Eq. (2) can be obtained by numerical integration. In practice, in order to separate the effects of the angular and radial modes, two functions were calculated, $\gamma_{\mathrm{ang}}(r)$ and $\gamma_{\mathrm{rad}}(r)$, defined by

$$\gamma_{\mathrm{ang}}(r)\equiv(1/Q)\left[\int_0^r Q_{i,\mathrm{ang}}dr'+r^5\int_r^\infty Q_{i,\mathrm{ang}}r'^{-5}dr'\right], \quad (10)$$

$$\gamma_{\mathrm{rad}}(r)\equiv(1/Q)\left[\int_0^r Q_{i,\mathrm{rad}}dr'+r^5\int_r^\infty Q_{i,\mathrm{rad}}r'^{-5}dr'\right]. \quad (11)$$

[8] M. F. Manning and J. Millman, Phys. Rev. **49**, 848 (1936).
[9] D. R. Hartree, Proc. Roy. Soc. (London) **157**, 490 (1936).
[10] D. R. Hartree, Proc. Roy. Soc. (London) **151**, 96 (1935).

The corresponding contributions to the quadrupole coupling are proportional to

$$\langle\gamma_{\mathrm{ang}}/r^3\rangle=\int_0^\infty\gamma_{\mathrm{ang}}v'^2r^{-3}dr, \quad (12)$$

$$\langle\gamma_{\mathrm{rad}}/r^3\rangle=\int_0^\infty\gamma_{\mathrm{rad}}v'^2r^{-3}dr. \quad (13)$$

The values of $\langle\gamma_{\mathrm{ang}}/r^3\rangle$, $\langle\gamma_{\mathrm{rad}}/r^3\rangle$, together with their sum $\langle\gamma/r^3\rangle$ are given in Table I. The valence wave functions v' used in the calculations were obtained from the above-mentioned references, except for Rb $5p$ and Cs $6p$. These two functions were obtained by numerical integration of the Schroedinger equation using an appropriate potential V_0. Table I lists the values of the average $\langle1/r^3\rangle$ for the valence wave functions and of the resulting ratio R, as well as $1/(1-R)$. We note that the $4p$ state of Rb, and $5p$ of Cs are filled in the normal state of the atom. The values of R were calculated for these states only because they show the dependence of R on the principal quantum number of v'. A check on the accuracy of the valence wave functions can be obtained by comparing the calculated values of $\langle1/r^3\rangle$ with those obtained by Barnes and Smith[11] from the observed fine structure of these levels. These values are 0.608, 0.244, 7.16, 0.845, $1.29a_{\mathrm{H}}^{-3}$ for B $2p$, Na $3p$, Cl $3p^5$, Rb $5p$, and Cs $6p$, respectively. Comparison with the values of Table I shows that the agreement is reasonably good, the calculated values being somewhat smaller than the fine-structure results, as would be expected since the Hartree wave functions are probably more external than the actual wave functions. It should be stressed that both $\langle\gamma/r^3\rangle$ and $\langle1/r^3\rangle$ are very sensitive to the detailed behavior of the wave functions. A part of this dependence on the wave function is eliminated in the calculation of the ratio R, since $\langle\gamma/r^3\rangle$ and $\langle1/r^3\rangle$ generally vary with the wave function v' in the same manner. Thus if v' is too external, both $\langle1/r^3\rangle$ and $\langle\gamma/r^3\rangle$ are generally decreased.

TABLE I. Values of quadrupole interaction $\langle\gamma/r^3\rangle$ due to induced moment, values of $\langle1/r^3\rangle$, and of correction term R for several atomic ground states and excited states. These values are calculated from the Hartree-Fock wave functions, and disregard the exchange terms. $\langle\gamma_{\mathrm{ang}}/r^3\rangle$ and $\langle\gamma_{\mathrm{rad}}/r^3\rangle$ are the contributions of the angular and radial modes to $\langle\gamma/r^3\rangle\cdot\langle\gamma/r^3\rangle$ and $\langle1/r^3\rangle$ are in units a_{H}^{-3}.

Element	State	$\langle\gamma_{\mathrm{ang}}/r^3\rangle$	$\langle\gamma_{\mathrm{rad}}/r^3\rangle$	$\langle\gamma/r^3\rangle$	$\langle1/r^3\rangle$	R	$1/(1-R)$
B	$2p$	0.0757	0	0.0757	0.535	0.142	1.165
Na	$3p$	0.0151	−0.0291	−0.0140	0.145	−0.097	0.912
Cl	$3p^5$	0.333	0.104	0.437	5.73	0.076	1.081
Cu	$3d^94s^2$	1.95	−0.699	1.25	7.52	0.166	1.20
Rb	$4p$	0.844	−0.229	0.615	19.6	0.031	1.031
Rb	$5p$	0.0341	−0.190	−0.156	0.647	−0.241	0.806
Cs	$5p$	0.58	−0.974	−0.394	22.3	−0.018	0.984
Cs	$6p$	0.0343	−0.304	−0.270	1.11	−0.244	0.804
W	$5d^4$	0.678	−3.10	−2.43	4.76	−0.510	0.663

[11] R. G. Barnes and W. V. Smith, Phys. Rev. **93**, 95 (1954).

Table I shows that for all of the ground states considered, except for W, R is positive, meaning that the shielding due to the angular modes predominates. The preponderance of the antishielding for the case of W is partly due to the fact that the $5p$ shell has a very large total induced moment ($\sim -27Q$). As was pointed out in III, the function γ_{rad} increases very rapidly with increasing r (see Fig. 2 of III). Since the electronic distribution of $5d$ is rather external, the antishielding is quite pronounced and predominates over the effect of the angular modes. It should be mentioned that the detailed vector coupling for W was not calculated, but the contribution of the $5d$ electrons to the radial modes was taken as $\frac{3}{10}$ of that which would be produced by a complete $5d$ shell. This approximation is probably adequate since the $5d \rightarrow d$ term is small compared to the contribution of the core.

For the first excited states of Na, Rb, and Cs, R is in all three cases negative, because the antishielding predominates on account of the external distribution of the excited-state wave functions. The result for the $3p$ state of Na ($R=-0.10$) may be of interest, because the hfs of this state has been recently measured.[12]

The values of R of Table I do not include the exchange terms due to the induced quadrupole moment. The exchange terms have been derived in I for the interaction of a p valence electron with a core of closed s and p shells. This derivation is extended in Sec. IV to d shells of the core. From these results one obtains the following expression for the ratio of minus the exchange energy to the main term in the quadrupole coupling, for an external p electron:

$$\delta R_e = -\frac{1}{\langle r^{-3}\rangle}\left\{\sum_n\left[\frac{4}{3}K(ns\rightarrow d,P_1)\right]_{ns} + \sum_n\left[4K(np\rightarrow p,P_0) + \frac{4}{25}K(np\rightarrow p,P_2) + \frac{36}{25}K(np\rightarrow f,P_2)\right]_{np} + \sum_n\left[\frac{4}{3}K(nd\rightarrow s,P_1) + \frac{4}{3}K(nd\rightarrow d,P_1) + \frac{12}{49}K(nd\rightarrow d,P_3) + \frac{72}{49}K(nd\rightarrow g,P_3)\right]_{nd}\right\}. \quad (14)$$

Here the sums extend over all occupied s, p, and d shells of the core. K is defined by

$$K(nl\rightarrow l',P_L) \equiv \int_0^\infty u'_0 v' f_L dr, \quad (15)$$

where u'_0 is the appropriate unperturbed radial function (nl), and $f_L(r)$ is given by

$$f_L(r) = r^{-L-1}\int_0^r u'_{1,\,l\rightarrow l'} v' r'^L dr' + r^L \int_r^\infty u'_{1,\,l\rightarrow l'} v' r'^{-L-1} dr', \quad (16)$$

where $u'_{1,\,l\rightarrow l'}$ is the perturbation which corresponds to the excitation considered. In the following, the ratio of the induced effects including exchange will be denoted by R_e, so that

$$R_e = R + \delta R_e. \quad (17)$$

The exchange terms of Eq. (14) fall into two classes: (a) the terms of type $-4K(np\rightarrow p,P_0)/\langle r^{-3}\rangle$ whose sum will be denoted by $\delta R_{e,0}$; (b) all other terms, whose sum will be called $\delta R'_e$. Thus

$$\delta R_e = \delta R_{e,0} + \delta R'_e. \quad (18)$$

The reason for this separation will now be shown. The $\delta R_{e,0}$ term arises not only in the quadrupole coupling, but also in the hfs due to the nuclear magnetic moment and in the fine structure. The origin of this term can best be seen by considering the perturbation of the core by the valence electron. As shown in II [see Eqs. (39) and (40)] the exchange between the core and the valence electron gives rise to an excitation of each p shell of the core into higher p states having the same magnetic quantum number m as the valence electron. If $\bar{u}'_1$ denotes the radial wave function (times r) for excitation of the p shell, the quadrupole coupling is given by

$$q' = c\int_0^\infty [v'^2 + 4\sum_n (u'_0 \bar{u}'_1)_{np}] r^{-3} dr, \quad (19)$$

where u'_0 and v' are r times the radial part of the wave function of the core and the valence electron, respectively; $c=-\frac{2}{5}$ for $m=0$, and $+\frac{1}{5}$ for $m=\pm 1$. Equation (19) does not include other first-order induced effects besides the $np\rightarrow p$ exchange terms. $\bar{u}'_1$ is determined by

$$\left(-\frac{d^2}{dr^2} + \frac{2}{r^2} + V_0 - E_0\right)\bar{u}'_1 = \left[r^{-1}\int_0^r u'_0 v' dr' + \int_r^\infty u'_0 v' r'^{-1} dr'\right] v'(r). \quad (20)$$

The appearance of $4\sum_n (u'_0 \bar{u}'_1)_{np}$ along with v'^2 in Eq. (19) is a result of the fact that the induced density has the same m as the valence electron. As shown previously[2,3] the contribution of $4u'_0\bar{u}'_1$ to the quadrupole coupling is equal to the $4K(np\rightarrow p, P_0)$ term obtained above. The fact that the induced density has the same m as the valence electron is also responsible for the appearance of this term in the magnetic hfs and in the fine structure.

It was shown in I that when $\langle 1/r^3\rangle$ is obtained from the magnetic hfs interval a and the nuclear magnetic moment μ, the correction factor C by which a/μ is multiplied is given by

$$C = (1-\delta R_m)/(1-R_e). \quad (21)$$

Here δR_m is defined as minus the interaction energy due to the core for the magnetic hfs divided by the inter-

[12] I. I. Rabi (private communication).

action energy for the valence electron. Thus δR_m corresponds to $-R_m$ as defined in I and II. δR_m is given by

$$\delta R_m = \delta R_{e,0} + \delta R'_m, \tag{22}$$

where $\delta R'_m$ is a term of the same type as $\delta R'_e$. As shown in II [see Eqs. (56) and (56a)], $\delta R'_m$ is a sum of terms containing the integrals $K(nl \to l', P_L)$ $(L>0)$ but with coefficients which differ from those of (14). Moreover, these coefficients are different for the $^2P_{\frac{1}{2}}$ and $^2P_{\frac{3}{2}}$ states of the atom.

In view of (21) and (22) the quadrupole correction factor C is given by

$$C = \frac{1-\delta R_{e,0}-\delta R'_m}{1-R-\delta R_{e,0}-\delta R'_e} = \left[1-\frac{\delta R'_m}{1-\delta R_{e,0}}\right] \Big/ \left[1-\frac{R+\delta R'_e}{1-\delta R_{e,0}}\right]. \tag{23}$$

As will be shown, $\delta R'_m$ and $\delta R'_e$ are generally small compared to $\delta R_{e,0}$. If these terms could be entirely neglected, C would be given by

$$C = 1 \Big/ \left[1-\frac{R}{1-\delta R_{e,0}}\right]. \tag{23a}$$

Since $\delta R_{e,0}<0$, R is effectively decreased. $\delta R_{e,0}$ has been calculated in I for Al $3p$ and Cl $3p^5$; the values are -0.174 and -0.472, respectively. In the present work the calculation of the exchange terms has been extended to B $2p$, Na $3p$, and Cs $6p$. Since B has no filled p shells, $\delta R_{e,0}$ is zero. For Na and Cs, $\delta R_{e,0}$ is -0.180 and -0.152, respectively. Thus the factor $1-\delta R_{e,0}$ in (23a) is of order 1.15–1.5.

The term $\delta R_e'$ in the quadrupole coupling will now be considered. $\delta R_e'$ has been evaluated in I for Li $2p$, Al $3p$, and Cl $3p^5$, and was found to be -0.061, -0.033, and -0.037, respectively, for these states. In the present work, calculations carried out for B $2p$, Na $3p$, and Cs $6p$ gave the values -0.086, -0.015, and -0.009, respectively.

Equation (23) shows that C involves $\delta R'_m$ besides $\delta R_{e,0}$ and $\delta R'_e$. An experimental indication about the values of $\delta R'_m$ is provided by the ratio of the magnetic hfs intervals a for the $^2P_{\frac{1}{2}}$ and $^2P_{\frac{3}{2}}$ states. This ratio is given by

$$\frac{a(^2P_{\frac{1}{2}})}{a(^2P_{\frac{3}{2}})} = \frac{F(3/2)[1-\delta R_m(^2P_{\frac{1}{2}})]}{5F(1/2)[1-\delta R_m(^2P_{\frac{3}{2}})]}, \tag{24}$$

where $F(j)$ is a relativistic correction obtained by Casimir.[13] Equation (24) will be applied to the case of boron-11 for which measurements of a have been carried out recently by Wessel.[14] From the experimental values $a(^2P_{\frac{1}{2}})=73.347$ Mc/sec and $a(^2P_{\frac{3}{2}})=366.2$ Mc/sec, together with[13] $F(3/2)=1.0006$ and $F(1/2)=1.0025$, one obtains $[1-\delta R_m(^2P_{\frac{1}{2}})]/[1-\delta R_m(^2P_{\frac{3}{2}})]=1.0034$. The calculated values[15] of the δR_m are $\delta R_m(^2P_{\frac{1}{2}})=-0.0485$ and $\delta R_m(^2P_{\frac{3}{2}})=-0.0290$, so that $[1-\delta R_m(^2P_{\frac{1}{2}})]/[1-\delta R_m(^2P_{\frac{3}{2}})]=1.0190$. Thus the calculated deviation from 1 is too large by a factor ~ 6. A similar discrepancy[16] was found in II for the $^2P_{\frac{1}{2}}$ and $^2P_{\frac{3}{2}}$ states of Cl. Since the same integrals $K(nl \to l')$ are involved in the quadrupole term $\delta R'_e$ as in $\delta R'_m$, the calculated values of $\delta R'_e$ cannot be considered as completely reliable. However, there seems to be no reason to believe that the actual value of $\delta R'_e$ will be of a larger order of magnitude than is given by the calculations, and it may well be smaller, as is indicated by the magnetic hfs.

Values of C will be given in Sec. V. In obtaining C we will use Eq. (23) except that $\delta R'_m$ will be taken as zero, since $\delta R'_m$ appears to be small (~ 0.01) from the experimental values of the intervals a. This procedure is probably adequate, except perhaps for the heavy atoms Rb, Cs, and W, where the effect of the core on the magnetic hfs is pronounced.[17] Thus C is obtained from

$$C = 1 \Big/ \left[1-\frac{R+\delta R'_e}{1-\delta R_{e,0}}\right]. \tag{25}$$

The uncertainty of the values of $\delta R'_e$ will be taken into account.

Besides the exchange terms, it should be noted that three effects contribute uncertainties of the order 0.01–0.02 in R_e. (1) The second-order quadrupole effect, previously described in III, is evaluated in the Appendix for the ground state of Cl, and adds a term $+0.005$ to R_e. This effect arises from the perturbation of the core wave functions by the external valence electron (or hole) taken in second order. In first order the perturbation gives rise to an added term in the electric field gradient at the nucleus which corresponds to the first-order induced effect described above (angular, radial, and exchange terms).[3] In second order, the perturbation of the core wave functions gives rise to additional terms in the quadrupole coupling. These terms arise both from the square of the first-order perturbed wave functions, and from the overlap of the unperturbed functions with the second-order perturbed

[13] H. B. G. Casimir, *On the Interaction between Atomic Nuclei and Electrons* (Teyler's Tweede Genootschap, Haarlem, 1936).

[14] G. Wessel, Phys. Rev. **92**, 1581 (1953).

[15] As shown in II, besides the excited $nl \to l'$ waves which contribute to the quadrupole coupling, δR_m involves also the excitation of s states of the core into higher s states by virtue of exchange with the valence electron. These $ns \to s$ terms were calculated for B $2p$, and are included in the values of δR_m given here.

[16] The reason for the discrepancy of the magnetic hfs correction factor is difficult to determine. As pointed out in II, a relatively small inaccuracy of the radial wave functions used in the calculations could be responsible for the disagreement. Another possible reason is that the electrostatic correlation of the valence electron with the core electrons of antiparallel spin is not taken into account, whereas the correlation of the core electrons of parallel spin is represented to some extent by the exchange terms which give rise to δR_m. It is possible that inclusion of the correlation for antiparallel spin would being the values of $[1-\delta R_m(^2P_{\frac{1}{2}})]/[1-\delta R_m(^2P_{\frac{3}{2}})]$ closer to 1.

[17] G. F. Koster, Phys. Rev. **86**, 148 (1952).

wave functions obtained by applying twice the perturbation due to the external valence electron.

(2) The Hartree-Fock functions which have been used in the calculations do not give as much binding as the actual wave functions which would be obtained from an exact solution of the Schroedinger equation for the core. As a result, the actual induced quadrupole moment is probably smaller than the Hartree-Fock value because an increase of the binding is expected to lead to a decrease of the polarizability. Such an effect was found in calculating the electronic polarizabilities α of various ions using the Hartree-Fock wave functions. As an example, for K^+, the calculated value of α is $1.26A^3$ as compared to experimental values ranging from $0.87A^3$ to $1.20A^3$. For Cl^-, the calculated $\alpha=5.6A^3$ is a factor 1.7 larger than the experimental value ($\sim 3.3A^3$). From these results it is expected that the calculated values of R tend to be somewhat larger than the actual values, possibly by as much as a factor of 1.5. The quadrupole correction R is probably less sensitive to the exact amount of binding than the polarizability α, since R depends on the behavior of the core wave functions near the nucleus, whereas α is determined mainly by the behavior of the wave functions in the outer parts of the core which is more sensitive to small changes of the binding.

(3) The numerical integrations introduce some error in the results. The possible errors are due to the interpolation necessary to find a suitably well-behaved function, and the finite size of the intervals used. The corresponding uncertainties were generally found to be small. A detailed check was made for the case of Cl. As shown previously,[3] the contribution of a given mode of excitation to $\langle\gamma_{\rm ang}/r^3\rangle$ or $\langle\gamma_{\rm rad}/r^3\rangle$ can be found in two independent ways: (a) by calculating the interaction of the valence electron with the quadrupole moment induced by the nuclear Q which corresponds to the mode of excitation considered (e.g., $1s\rightarrow d$); (b) by finding first the excitation of the same type ($1s\rightarrow d$) produced by the asymmetric potential of the valence electron, and then obtaining the contribution to the quadrupole coupling at the nucleus due to this mode of excitation. In general the contributions calculated by both methods agreed within $\sim$10 percent. Thus for $3s\rightarrow d$ the contribution to $\langle\gamma_{\rm ang}/r^3\rangle/\langle 1/r^3\rangle$ was obtained as 0.00684 from method (a) and 0.00693 from (b). The only exception is the $3p\rightarrow p$ term of $\langle\gamma_{\rm rad}/r^3\rangle$ where the value calculated from (b) was found to be $\sim$1.5 times larger than that given by (a). It is believed that this discrepancy is associated with the external charge distribution of $3p$, and could be resolved by taking a larger number of steps in the numerical integration than was used ($\sim$50 intervals δ). However, in view of the other uncertainties it did not seem worthwhile to carry out this refinement of the calculation.

III. WAVE-FUNCTION CALCULATIONS OF SHIELDING

Calculations of the perturbed wave functions for the angular modes were previously carried out[3] for Li, Al, and Cl, in order to check the prediction of the Thomas-Fermi model. It was found that the perturbed wave functions lead to values of $\langle\gamma_{\rm ang}/r^3\rangle$ which are $\sim$1.5 times smaller than those obtained from the Thomas-Fermi density of the induced moment. This result shows that the statistical model tends to overestimate the shielding for light atoms. In order to check the accuracy of the Thomas-Fermi model for a heavy atom, the excited waves due to the perturbation by the nuclear Q were calculated for the case of Cs^+, using the Hartree functions[7] for the unperturbed functions u'_0.

The angular part of the induced moment $Q_{i,\rm ang}$ is given by Eq. (3). The radial parts $u'_{1,1\rightarrow l'}$ of the excited wave functions are determined by Eq. (4). The function in the square bracket of (4), which will be called P', was calculated as follows,

$$P'\equiv\frac{l'(l'+1)}{r^2}+V_0-E_0=P+\frac{l'(l'+1)-l(l+1)}{r^2}, \quad (26)$$

where P is obtained from u'_0 [see Eq. (9)]. The integrations of Eq. (4) were performed somewhat differently for the different angular modes. For $ns\rightarrow d$, the integration was started near $r=0$, using the power series [see Eq. (10) of I],

$$u'_{1,0\rightarrow 2}=a_0+a_1r+a_2r^2+a_3r^3+a_4r^4+\cdots +b_3r^3\log r+b_4r^4\log r+\cdots, \quad (27)$$

where a_3 is arbitrary and the remaining coefficients a_i and b_i are determined by Eq. (4), as was shown in I. The integrations were carried out for various a_3, until a value of a_3 was found for which the resulting $u'_{1,0\rightarrow 2}$ is well-behaved for large r. In practice, the numerical solutions obtained for two neighboring values of a_3 which enclose the correct value diverge slowly, the one to positive, the other to negative values, for $r\rightarrow\infty$. However, they agree closely (in general, within 10 percent) in the region near the nucleus which is of importance for the quadrupole coupling. For $nd\rightarrow s$, the integration was started at $r=0$ by means of a power series $a_1r+a_2r^2\cdots$. In this case, a_1 is arbitrary, and its value is varied until the resulting $u'_{1,2\rightarrow 0}$ is well-behaved at infinity.

For the $np\rightarrow f$ waves, a method of inward integration was used, starting at a large radius r_1, as follows. Equation (4) can be written

$$-d^2u'_{1,1\rightarrow 3}/dr^2+Nu'_{1,1\rightarrow 3}=0, \quad (28)$$

where

$$N\equiv P'-u'_0/(r^3u'_{1,1\rightarrow 3}), \quad (29)$$

and P' is defined by Eq. (26). Note that for sufficiently large r, N approaches the constant value $-E_0$. For the numerical integration it is assumed that N is constant

for $r>r_1$. For an assumed value of $u'_{l,\,l\to l'}(r_1)$, N is calculated from Eq. (29), and $u'_{l,\,l\to l'}(r_1+\delta)$ is obtained from

$$u'_{l,\,l\to l'}(r_1+\delta)=u'_{l,\,l\to l'}(r_1)\exp(-N^{\frac{1}{2}}\delta). \quad (30)$$

The numerical integration is then carried out starting with the two values $u'_{l,\,l\to l'}(r_1)$ and $u'_{l,\,l\to l'}(r_1+\delta)$. This procedure is repeated for several choices of $u'_{l,\,l\to l'}(r_1)$ until a value is found for which the corresponding $u'_{l,\,l\to l'}$ goes to zero at $r=0$. This requirement is appropriate since the actual solution is proportional to r near $r=0$. For the $nd\to g$ waves the same method of inward integration as for $np\to f$ was employed.

After the functions $u'_{l,\,l\to l'}$ were determined, the distribution of the induced moment $Q_{i,\,\mathrm{ang}}$ was obtained from Eq. (3). This distribution can be compared with the prediction of the Thomas-Fermi model [Eq. (5)]. Both functions $Q_{i,\,\mathrm{ang}}/Q$ are shown in Fig. 1. It is seen that the agreement between the wave-function calculations and the Thomas-Fermi model is reasonably good. Of course the Thomas-Fermi model smoothes over the maxima of $Q_{i,\,\mathrm{ang}}$ as obtained from the wave functions, which correspond to the electronic shells of the ion.

When γ_{ang} is calculated from $Q_{i,\,\mathrm{ang}}$ as obtained from the wave-function calculations, one finds for the $6p$ state, $\langle\gamma_{\mathrm{ang}}/r^3\rangle=0.0343a_{\mathrm{H}}^{-3}$ (see Table I). The Thomas-Fermi values of $Q_{i,\,\mathrm{ang}}$ lead to $\langle\gamma_{\mathrm{ang}}/r^3\rangle=0.0492a_{\mathrm{H}}^{-3}$ which is a factor $\sim$1.4 larger than the value obtained from the wave functions. The result that the Thomas-Fermi model gives an overestimate of $\langle\gamma_{\mathrm{ang}}/r^3\rangle$ can be attributed in part to the fact that the Thomas-Fermi density $Q_{i,\,\mathrm{ang}}$ is too large at small r. As shown in Fig. 1, inside $r=0.7a_{\mathrm{H}}$ $Q_{i,\,\mathrm{ang}}$ as obtained from the Thomas-Fermi model is appreciably larger than the wave function values, except for a small region near $r=0.3a_{\mathrm{H}}$, which corresponds to the maximum of the M shell. These results for Cs together with those for light atoms indicate that the Thomas-Fermi value of $\langle\gamma_{\mathrm{ang}}/r^3\rangle$ divided by 1.5 should give the correct order of magnitude of the shielding throughout the range of Z.

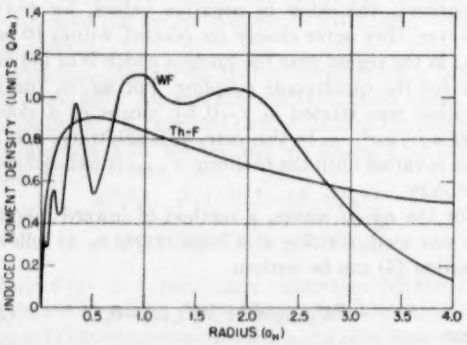

FIG. 1. Distribution of the quadrupole moment induced by the nuclear Q for the Cs^+ ion. Only the angular modes of excitation of the core are included. The curve marked WF is obtained from wave function calculations using the Hartree wave functions for Cs^+. The curve marked Th-F is calculated from the Thomas-Fermi model [see Eq. (5)].

From the excited core wave functions for Cs it is of interest to calculate the total induced moment due to the various perturbed waves, as obtained by integrating the terms of Eq. (3) over r. The total induced moment due to the angular modes is $Q_{iT,\,\mathrm{ang}}=2.95Q$. The largest contributions are made by the $5s\to d$ and $5p\to f$ waves, which give $Q_{iT,\,\mathrm{ang}}(5s\to d)=0.93Q$, and $Q_{iT,\,\mathrm{ang}}(5p\to f)=0.76Q$, corresponding to the large values of $\langle r^2\rangle$ for these shells. The remaining induced moment of $1.26Q$ is made up of contributions 0.012, 0.064, 0.27, and $0.91Q$ from the $n=1$, 2, 3, and 4 shells, respectively. By comparing $Q_{iT,\,\mathrm{ang}}/Q$ for Cs with the values for light atoms (0.62 for Na, 1.06 for Al, 1.41 for Cl) it is seen that $Q_{iT,\,\mathrm{ang}}/Q$ increases slowly with Z.

The present values of $Q_{i,\,\mathrm{ang}}$ for Cs obtained from the perturbed wave functions have been used in the calculation of the values of $\langle\gamma_{\mathrm{ang}}/r^3\rangle$ for the $5p$ and $6p$ states, which are given in Table I. The values of $\langle\gamma_{\mathrm{rad}}/r^3\rangle$ for these states were obtained by means of the function $Q_{i,\,\mathrm{rad}}$ for the radial modes obtained in III. The $5p$ state is, of course, occupied so that the corresponding quadrupole correction is only of theoretical interest. The calculations for this state indicate a weak net antishielding. This result is in contrast to the results for the ground states of the light atoms for which the shielding predominates, although for $3p$ of Al, as shown in I, the effect of the angular modes is only slightly larger than the antishielding due to $2p\to p$. It has also been shown above that for the somewhat external $5d$ electron of W, the antishielding predominates strongly. Nevertheless, the correction $\langle\gamma_{\mathrm{rad}}/r^3\rangle/\langle 1/r^3\rangle$ for the radial modes, which is $-3.10/4.76=-0.65$ (see Table I) is small compared to the total induced moment in units of Q which is ~-50. The reason is that the induced moment due to the radial modes is localized considerably outside the region where most of the quadrupole coupling of the $5d$ electron takes place ($\langle r^{-3}\rangle_{5d}^{-\frac{1}{3}}=0.60a_{\mathrm{H}}$).

On the basis of the two examples of Cs $5p$ and W $5d^4$, it is not possible to conclude that the antishielding generally predominates for heavy atoms. To ascertain this point would require more extensive calculations. However, the fact that the antishielding appears to be relatively more important for heavy atoms than for light atoms can be attributed in part to the somewhat different Z dependence of the effect of the angular and the radial modes. As shown in III, the induced moment due to the radial modes $Q_{iT,\,\mathrm{rad}}$ increases very rapidly with Z, namely from $-2.7Q$ for Na^+ to $-90Q$ for Cs^+. In comparison, $Q_{iT,\,\mathrm{ang}}$ increases less rapidly, i.e., from $0.61Q$ for Na^+ to $2.95Q$ for Cs^+. The tendency for $R>0$ (shielding) for low Z, and $R<0$ for high Z can be correlated with the different Z dependence of the angular and the radial modes.

Besides the calculations for Cs, wave function calculations of the shielding were also carried out for B, Na,

and Cl. The resulting values of $\langle\gamma_{\text{ang}}/r^3\rangle$ are given in Table I.

IV. EXCITATION OF d SHELLS OF THE CORE

In previous work[2] the calculations of induced effects have been restricted to atoms with closed s and p shells. In the present section these results will be extended to d states of the core.

We consider the excitation of d states by the field of the nuclear Q. The perturbation of d states to excited d states will be treated first. For the state $m=0$, we have for the unperturbed wave function (times r),

$$u_0^{(0)}=(5/8)^{\frac{1}{2}}u'_0(3\cos^2\theta-1)=u'_0\Theta_2^0, \tag{31}$$

where u'_0 is r times the radial function normalized according to

$$\int_0^\infty u'^2_0 dr=1. \tag{31a}$$

The angular functions Θ_l^m are normalized according to

$$\int_0^\pi |\Theta_l^m|^2\sin\theta d\theta=1. \tag{31b}$$

In Eq. (31) and in the following a superscript (e.g., for $u_0^{(0)}$) indicates the value of the magnetic quantum number m. The equation for the perturbed wave $u_1^{(0)}$ is

$$(H_0-E_0)u_1^{(0)}=-H_1u_0^{(0)}+E_1u_0^{(0)}, \tag{32}$$

where H_1 is the perturbation of the Hamiltonian, and is given by

$$H_1=-QP_2^0/r^3, \tag{33}$$

where P_l^m is the Legendre polynomial. E_1 is the first-order perturbation of the energy, and has the following value, in view of (31) and (33),

$$E_1=\int_0^\infty\int_0^\pi H_1[u_0^{(0)}]^2 dr\sin\theta d\theta=-(2/7)Q\langle r^{-3}\rangle_{nd}. \tag{34}$$

Upon substituting (31), (33), and (34) in Eq. (32) one obtains

$$(H_0-E_0)u_1^{(0)}=\left(\frac{5}{32}\right)^{\frac{1}{2}}Q(3\cos^2\theta-1)^2\frac{u'_0}{r^3}-(2/7)Q\langle r^{-3}\rangle_{nd}u'_0\Theta_2^0. \tag{35}$$

The factor $(5/32)^{\frac{1}{2}}(3\cos^2\theta-1)^2$ in the first term on the right-hand side must now be written as a sum of s, d, and g functions. From these functions arise the $nd\rightarrow s$, $nd\rightarrow d$, and $nd\rightarrow g$ excited waves, respectively. The d wave part is given by $c_2\Theta_2^0$, where

$$c_2=(5/32)^{\frac{1}{2}}\int_0^\pi(3\cos^2\theta-1)^2\Theta_2^0\sin\theta d\theta=2/7. \tag{36}$$

One thus obtains the following expression for the d wave part of $u_1^{(0)}$ which will be called $u^{(0)}{}_{1,2\rightarrow 2}$,

$$u^{(0)}{}_{1,2\rightarrow 2}=(2/7)(5/8)^{\frac{1}{2}}Qu'_{1,2\rightarrow 2}(3\cos^2\theta-1), \tag{37}$$

where the radial function $u'_{1,2\rightarrow 2}$ is determined by [see Eq. (6)]

$$M_2u'_{1,2\rightarrow 2}=u'_0(r^{-3}-\langle r^{-3}\rangle_{nd}). \tag{38}$$

Here and in the following, M_l is defined by

$$M_l\equiv-\frac{d^2}{dr^2}+\frac{l(l+1)}{r^2}+V_0-E_0. \tag{39}$$

By means of Eqs. (31) and (37), one obtains for the induced moment $Q_{iT}^{(0)}$ due to the $m=0$ electrons,

$$Q_{iT}^{(0)}=4\int_0^\infty\int_0^\pi u_0^{(0)}u^{(0)}{}_{1,2\rightarrow 2}(3\cos^2\theta-1)r^2dr\sin\theta d\theta=\frac{32}{49}Q\int_0^\infty u'_0u'_{1,2\rightarrow 2}r^2dr, \tag{40}$$

where the factor 4 arises from the fact that the first-order density is $2u_0^{(0)}u^{(0)}{}_{1,2\rightarrow 2}$ for each $m=0$ electron.

In the same manner as in the derivation of (37) one finds for the d wave perturbation of the $m=\pm 1$ states,

$$u^{(\pm 1)}{}_{1,2\rightarrow 2}=\frac{Qu'_{1,2\rightarrow 2}\Theta_2^{\pm 1}}{7}=\mp\frac{15^{\frac{1}{2}}}{14}Qu'_{1,2\rightarrow 2}\sin\theta\cos\theta. \tag{41}$$

The $\mp$ sign in the last expression corresponds to the choice of phases of Condon and Shortley,[18] and, of course, does not affect the final result. The induced moment due to the four electrons with $m=\pm 1$ is given by

$$Q_{iT}^{(\pm 1)}=8\int_0^\infty\int_0^\pi u'_0\Theta_2^{\pm 1}u^{(\pm 1)}{}_{1,2\rightarrow 2}(3\cos^2\theta-1)r^2dr\sin\theta d\theta=\frac{16}{49}Q\int_0^\infty u'_0u'_{1,2\rightarrow 2}r^2dr. \tag{42}$$

In a similar manner, one obtains for the d wave perturbation of the $m=\pm 2$ states,

$$u^{(\pm 2)}{}_{1,2\rightarrow 2}=-\frac{2}{7}Qu'_{1,2\rightarrow 2}\Theta_2^{\pm 2}=-\frac{15^{\frac{1}{2}}}{14}Qu'_{1,2\rightarrow 2}\sin^2\theta. \tag{43}$$

The resulting induced moment due to the $m=\pm 2$ electrons is

$$Q_{iT}^{(\pm 2)}=8\int_0^\infty\int_0^\pi u'_0\Theta_2^{\pm 2}u^{(\pm 2)}{}_{1,2\rightarrow 2}(3\cos^2\theta-1)r^2dr\times\sin\theta d\theta=\frac{64}{49}Q\int_0^\infty u'_0u'_{1,2\rightarrow 2}r^2dr. \tag{44}$$

[18] E. U. Condon and G. H. Shortley, *The Theory of Atomic Spectra* (Macmillan Company, New York, 1935), p. 52.

From Eqs. (40), (42), and (44) one obtains for the total induced moment due to $nd \to d$ for the complete d shell,

$$Q_{dT}(nd\to d) = (16/7)Q\int_0^\infty u'_0 u'_{1,2\to 2} r^2 dr. \quad (45)$$

The induced moment due to the $nd \to s$ waves can be found in the same manner. Only the $m=0$ electrons contribute. In Eq. (35) the s wave part of $(5/32)^{\frac{1}{2}} \times (3\cos^2\theta - 1)^2$ can be written $c_0\Theta_0^0$ where

$$c_0 = (5/32)^{\frac{1}{2}}\int_0^\pi (3\cos^2\theta - 1)^2 \Theta_0^0 \sin\theta d\theta = 5^{-\frac{1}{2}}. \quad (46)$$

Therefore one obtains for the s wave part of the perturbation,

$$u^{(0)}{}_{1,2\to 0} = 10^{-\frac{1}{2}} Q u'_{1,2\to 0}, \quad (47)$$

where the radial function $u'_{1,2\to 0}$ is determined by [see Eq. (4)]

$$M_0 u'_{1,2\to 0} = u'_0/r^3. \quad (48)$$

Note that the E_1 term of (32) does not contribute, since it gives only a d function. The resulting term in the induced moment is

$$Q_{dT}(nd\to s) = 4\int_0^\infty\int_0^\pi u'_0 \Theta_2^0 u^{(0)}{}_{1,2\to 0}(3\cos^2\theta - 1) r^2 dr \times \sin\theta d\theta = -\frac{8}{5} Q\int_0^\infty u'_0 u'_{1,2\to 0} r^2 dr. \quad (49)$$

The derivation of the $nd \to g$ wave with $m=0$ will now be briefly outlined. If one subtracts from $(5/32)^{\frac{1}{2}} \times (3\cos^2\theta - 1)^2$ its s and d wave parts, one is left with the g wave part, which in view of Eqs. (36) and (46) is given by

$$A_g = \left(\frac{5}{32}\right)^{\frac{1}{2}}(3\cos^2\theta - 1)^2 - \frac{\Theta_0^0}{5^{\frac{1}{2}}} - \frac{2\Theta_2^0}{7} = \left(\frac{5}{32}\right)^{\frac{1}{2}}\left(9\cos^4\theta - \frac{54}{7}\cos^2\theta + \frac{27}{35}\right). \quad (50)$$

Hence the g wave perturbation $u^{(0)}{}_{1,2\to 4}$ is given by

$$u^{(0)}{}_{1,2\to 4} = -\frac{9}{2}\left(\frac{5}{8}\right)^{\frac{1}{2}} Q u'_{1,2\to 4}\left(\cos^4\theta - \frac{6}{7}\cos^2\theta + \frac{3}{35}\right), \quad (51)$$

where the radial function $u'_{1,2\to 4}$ is determined by

$$M_4 u'_{1,2\to 4} = u'_0/r^3. \quad (52)$$

The $nd \to g$ wave functions for $m = \pm 1$, and ± 2 are given by

$$u^{(\pm 1)}{}_{1,2\to 4} = \mp\frac{3}{2}\left(\frac{15}{4}\right)^{\frac{1}{2}} Q u'_{1,2\to 4} \times (\sin\theta\cos^3\theta - (3/7)\sin\theta\cos\theta), \quad (53)$$

$$u^{(\pm 2)}{}_{1,2\to 4} = \frac{3}{2}\left(\frac{15}{16}\right)^{\frac{1}{2}} Q u'_{1,2\to 4} \times (\sin^2\theta\cos^2\theta - (1/7)\sin^2\theta). \quad (54)$$

For the total induced moment, one finds

$$Q_{dT}(nd\to g) = 4\sum_{m=-2}^{2}\int_0^\infty\int^\pi u_0^{(m)} u_{1,2\to 4}{}^{(m)}(3\cos^2\theta - 1) r^2 dr \times \sin\theta d\theta d\theta = \frac{144}{35} Q\int_0^\infty u'_0 u'_{1,2\to 4} r^2 dr. \quad (55)$$

The exchange terms involving the excitation of the d shell will now be obtained. For this purpose, it will be assumed that the valence electron is in a p state with $m_v = 0$. Here m_v is the magnetic quantum number of the valence electron while m_u will denote the magnetic quantum number of the nd state. Of course, the choice of m_v is immaterial, since the final result is independent of m_v. The $nd \to d$ waves will be treated presently. We consider first the electron with $m_u = 0$. As was shown in I, the exchange energy can be regarded as due to the interaction of an exchange potential V_e with the overlap density $u_0^{(0)} v$ of the unperturbed wave functions of the core and the valence electron. Here v is the wave function (times r) of the valence electron, and is given by

$$v = (3/2)^{\frac{1}{2}} v' \cos\theta, \quad (56)$$

where v' is the radial function, normalized according to (1a). V_e is the potential produced by the overlap of $u_1^{(0)}$ with v. Since $u_1^{(0)}$ and v are a d wave and a p wave, respectively, V_e has both a P_1 and a P_3 part. The P_1 part will be considered first. It arises from the term $2(r_</r_>^2)\sum_{m=-1}^{1} P_1^m(\theta_1) P_1^{-m}(\theta_2)$ of $2/r_{12}$, where r_{12} is the distance between the two electrons, $r_<$ and $r_>$ are the smaller and the larger, respectively, of the distances r_1 and r_2 of the electrons from the nucleus; $\theta_{1,2}$ is the angle between the radius vector and the axis of Q. For $m_u = 0$ we have

$$V_{e,P_1}{}^{(0)} = -4\left[\int_0^\infty\int_0^\pi u^{(0)}{}_{1,2\to 2} v \cos\theta_2 (r_</r_>^2) dr_2 \times \sin\theta_2 d\theta_2\right]\cos\theta_1, \quad (57)$$

where the factor -4 arises from the Rydberg units and from a factor of 2 in the overlap density. Upon inserting Eqs. (37) and (56) in (57), one obtains

$$V_{e,P_1}{}^{(0)} = -[16/7(15)^{\frac{1}{2}}] Q f_1(r_1)\cos\theta_1, \quad (58)$$

where $f_L(r_1)$ is defined by

$$f_L(r_1) = r_1^{-L-1}\int_0^{r_1} u'_{1,1\to 1} v' r_2^L dr_2 + r_1^L\int_{r_1}^\infty u'_{1,1\to 1} v' r_2^{-L-1} dr_2, \quad (59)$$

and $u'_{1,l\to l'}$ is taken as $u'_{1,2\to 2}$. The exchange energy is given by

$$\Delta E_{e,P_1}{}^{(0)}=\int_0^\infty\int_0^\pi V_{e,P_1}{}^{(0)}u_0{}^{(0)}v d\tau_1\sin\theta_1 d\theta_1. \quad (60)$$

Upon inserting (31), (56), and (58) in (60), one obtains

$$\Delta E_{e,P_1}{}^{(0)}=-(32/105)QK(nd\to d,P_1), \quad (61)$$

where $K(nl\to l',P_L)$ is defined by

$$K(nl\to l',P_L)=\int_0^\infty u'_0 v' f_L d\tau, \quad (62)$$

with f_L given by (59). For the $m_u=\pm 1$ states, $V_{e,P_1}{}^{(\pm 1)}$ for the P_1 interaction is given by

$$V_{e,P_1}{}^{(\pm 1)}=-4\left[\int_0^\infty\int_0^\pi u^{(\pm 1)}{}_{1,2\to 2}v\left(\frac{\sin\theta_2}{\sqrt{2}}\right)\frac{r_<}{r_>{}^2}d\tau_2 \times\sin\theta_2 d\theta_2\right]\frac{\sin\theta_1}{\sqrt{2}}. \quad (63)$$

In view of (41) one finds

$$V_{e,P_1}{}^{(\pm 1)}=\pm(4/35)(5/2)^{\frac{1}{2}}Qf_1(r_1)\sin\theta_1. \quad (64)$$

One obtains for the exchange energy for the two electrons with $m_u=\pm 1$ and spin parallel to the valence electron spin,

$$\Delta E_{e,P_1}{}^{(\pm 1)}=2\int_0^\infty\int_0^\pi V_{e,P_1}{}^{(\pm 1)}u_0{}^{(\pm 1)}v d\tau_1\sin\theta_1 d\theta_1 =-\frac{8}{35}QK(nd\to d,P_1). \quad (65)$$

As is easily seen, the $m_u=\pm 2$ electrons do not contribute to the P_1 exchange interaction. Thus Eqs. (61) and (65) give for the total P_1 interaction with $nd\to d$,

$$\sum_{m_u=-2}^{2}\Delta E_{e,P_1}{}^{(m_u)}=-(8/15)QK(nd\to d,P_1). \quad (66)$$

The direct interaction of Q with the valence electron is

$$E_Q=-Q\int_0^\infty\int_0^\pi P_2{}^0 v^2 r^{-3}\sin\theta d\theta d\tau=-(2/5)Q\langle r^{-3}\rangle_v, \quad (67)$$

where $\langle r^{-3}\rangle_v$ is the average of r^{-3} over the valence wave function. Thus one obtains the following contribution to R_e,

$$\delta R_e(nd\to d,P_1)=-(4/3)K(nd\to d,P_1)/\langle r^{-3}\rangle_v, \quad (68)$$

where the $-$ sign indicates that for $K>0$ the effect is a negative shielding.

The P_3 exchange with $nd\to d$ can be obtained in a similar manner, and gives the result

$$\delta R_e(nd\to d,P_3)=-(12/49)K(nd\to d,P_3)/\langle r^{-3}\rangle_v, \quad (69)$$

where the f_L which appears in Eq. (62) for K is given by f_3 of (59) with $u'_{1,l\to l'}$ taken as $u'_{1,2\to 2}$.

The exchange of the valence electron with the $nd\to s$ excitation is obtained as follows. Only the electron with $m_u=0$ (and parallel spin) contributes. In view of Eq. (47) for the perturbation $u^{(0)}{}_{1,2\to 0}$, we have

$$V_e=-4\left[\int_0^\infty\int_0^\pi u_1 v(r_</r_>{}^2)\cos\theta_2 d\tau_2\sin\theta_2 d\theta_2\right]\cos\theta_1 =-\frac{4}{15^{\frac{1}{2}}}Qf_1\cos\theta_1, \quad (70)$$

where f_1 is obtained from Eq. (59), with $u'_{1,l\to l'}$ taken as $u'_{1,2\to 0}$. The resulting energy term is

$$\Delta E_e=\int_0^\infty\int_0^\pi V_e u_0{}^{(0)}v d\tau_1\sin\theta_1 d\theta_1 =-\frac{8}{15}QK(nd\to s,P_1). \quad (71)$$

In view of (67) the contribution to R_e is given by

$$\delta R_e(nd\to s,P_1)=-(4/3)K(nd\to s,P_1)/\langle r^{-3}\rangle_v. \quad (72)$$

The exchange of the valence electron with the $nd\to g$ waves can be treated in the same manner. Since the overlap of the valence function with the excited g wave produces angular terms which vary as P_3 and P_5, while the overlap of p with d produces P_1 and P_3 terms, the interaction involves only the P_3 term of $2/r_{12}$. By summing over the contributions of the m_u states of the d shell, one obtains

$$\delta R_e(nd\to g,P_3)=-(72/49)K(nd\to g,P_3)/\langle r^{-3}\rangle_v, \quad (73)$$

where K is given by (62) with $f_L=f_3$ as obtained from Eq. (59) in which $u'_{1,l\to l'}$ is taken as $u'_{1,2\to 4}$.

Upon combining the preceding results for the d shells [Eqs. (68), (69), (72), and (73)] with those found in I for the exchange with the closed s and p shells, one obtains Eq. (14) for the contribution of exchange to R_e for the case of an external p electron.

The effect of the $nf\to f$ radial modes induced by the nuclear Q has been given in Eq. (7). The derivation follows the same lines as for the $nd\to d$ terms. Here only the expressions for the perturbed wave functions $u^{(m)}{}_{1,3\to 3}$ will be given:

$$u^{(0)}{}_{1,3\to 3}=(4/15)(7/8)^{\frac{1}{2}}Q(5\cos^3\theta-3\cos\theta)u'_{1,3\to 3}, \quad (74)$$

$$u^{(\pm 1)}{}_{1,3\to 3}=\mp(1/5)(21/32)^{\frac{1}{2}} \times Q(5\cos^2\theta\sin\theta-\sin\theta)u'_{1,3\to 3}, \quad (75)$$

$$u^{(\pm 3)}{}_{1,3\to 3}=\mp(1/3)(35/32)^{\frac{1}{2}}Q\sin^3\theta u'_{1,3\to 3}, \quad (76)$$

and $u^{(\pm 2)}{}_{1,3\to 3}=0$. We use the same convention of signs for $\Theta_3{}^{\pm 1}$ and $\Theta_3{}^{\pm 3}$ as in Condon and Shortley.[18] The radial function $u'_{1,3\to 3}$ is determined by Eq. (6). The

resulting induced moment is

$$Q_{iT}(nf\to f)=\sum_{m=-3}^{3}\int_0^\infty\int_0^\pi u_0^{(m)}u^{(m)}{}_{1,3\to3}(3\cos^2\theta-1)r^2dr \times\sin\theta d\theta=\frac{224}{75}Q\int_0^\infty u'_0u'_{1,3\to3}r^2dr, \quad (77)$$

where $u_0^{(m)}$ is the unperturbed f function (times r) for magnetic quantum number m.

V. CONCLUSIONS

The atomic core introduces three types of terms into the quadrupole coupling: (1) shielding terms due to angular modes of excitation of the core; (2) terms due to radial modes which are generally antishielding; (3) exchange terms.

(1) The shielding terms have been considered as due to the interaction of the angular part of the induced quadrupole moment with the valence electron. The effect of the angular modes is generally overestimated by a factor $\sim$1.5 by the Thomas-Fermi model. This conclusion can be drawn from the previous wave-function calculations[2] for Li, Al, and Cl, as well as from the present calculations for Cs. Although the total induced moment due to the angular modes is appreciable (e.g., 1.41Q for Cl), the contribution to the quadrupole coupling is only of order 10 percent of the direct interaction of Q with the valence electron, because only the induced moment near the nucleus contributes appreciably on account of the penetration of the valence electron.

(2) The effect of the radial modes generally produces an antishielding i.e., it reinforces the effect of the nuclear Q, and increases the magnitude of the quadrupole coupling. As was shown in III, the total induced moment due to the radial modes, $Q_{iT,\text{rad}}$, is very large, with values ranging from $-2.7Q$ for Na^+ to $-90Q$ for Cs^+. However, the induced moment distribution is quite external, and for this reason, the antishielding due to the radial modes is, in general, unimportant for the atomic ground states (except for heavy atoms) but becomes rapidly more effective as more external distributions of the valence electron are being considered. Thus for the first excited (p) states of the alkalis the antishielding predominates and gives effects ranging from 10 percent for Na to 24 percent for Cs.

The radial modes vanish for s states, and depend sensitively on the azimuthal quantum number. $Q_{iT,\text{rad}}$ increases very rapidly with increasing principal quantum number n, and is generally larger for the $np\to p$ wave than for the $nd\to d$ wave of the same shell. By far the largest term of $Q_{iT,\text{rad}}$ is due to the outermost shell. The Thomas-Fermi model appears not to include the effect of the radial modes. This result is not surprising in view of the sensitive dependence on l, and the fact that the effect concerns mostly the outermost shell of the core.

(3) The exchange terms are discussed in Secs. II and IV. In the present work values have been obtained for B $2p$, Na $3p$, and Cs $6p$, besides previous calculations[2] for Li $2p$, Al $3p$, and Cl $3p^5$.

For light atoms where the effect of the core on the magnetic hfs is small the correction factor C is given by

$$C=1\Big/\left[1-\frac{R+\delta R'_e}{1-\delta R_{e,0}}\right]. \quad (25)$$

The values of R are listed in Table I. The exchange terms $\delta R_{e,0}$ and $\delta R'_e$ are given in Sec. II. For the cases of Cu, Rb, and W, these terms were obtained by interpolation of the values calculated for the other elements. The resulting values of C are: 1.12$\pm$0.08 for Li $2p$, 1.06$\pm$0.11 for B $2p$, 0.92$\pm$0.02 for Na $3p$, 0.97 $\pm$0.03 for Al $3p$, 1.03$\pm$0.05 for Cl $3p^5$, 1.10$\pm$0.10 for Cu $3d^94s^2$, 0.82$\pm$0.02 for Rb $4p$, 0.83$\pm$0.02 for Cs $6p$, 0.68$\pm$0.10 for W $5d^4$. The upper and lower limits correspond to the uncertainty of $\delta R'_e$. The upper limit of C is obtained by assuming that $\delta R'_e$ is actually zero, while the lower limit corresponds to a value of $\delta R'_e$ which is twice that calculated from the perturbed wave functions. For Cu and W, the uncertainty $\pm$0.10 is somewhat larger than that obtained from $\delta R'_e$ alone. It is seen from Table I that for all cases the values $C=1/(1-R)$ which would be obtained without exchange are inside the range of C given above, so that the inclusion of exchange does not materially affect the results. The contribution of exchange for excited states (Na, Rb, Cs) is very small, so that the values of C are most probably less than 1 for these states (net antishielding), even allowing for a considerable uncertainty of the exchange terms.

The present values of C for B, Al, Cl, and Cu may be compared with those given in Table III of II. The values of II (e.g., $C=1.068$ for Cl) are close to the upper limit of the range of C given above, corresponding to the fact that $\delta R'_e$ was assumed very small in the calculations of II. The calculations for the first excited (p) states of Na, Rb, and Cs have not been previously carried out. The present values for Li $2p$ and Al $3p$ are based on I. We note that since there are no filled p shells for Li, there is no antishielding, and hence C exceeds 1 for all excited states of the valence electron. Calculations for W have not been carried out previously. However, in Table III of II, Thomas-Fermi values of C were given for the neighboring elements Lu and Ta, for which the valence electron is also in the $5d$ state. The present calculations for $5d$ of W show that these values are probably incorrect because of the neglect of antishielding. In general, the values of C given in II cannot be considered as reliable, except for the four cases B, Al, Cl, and Cu which are supported by the present calculations, if one assumes that the exchange term $\delta R'_e$ is, in fact, very small. In order to obtain accurate values of C for the other atomic states

of Table III of II, it would be necessary to carry out a calculation of the antishielding and exchange for each element. However, it may be expected from the present work that the shielding predominates for light atoms, and that the actual correction factors are in many cases close to those given in II. For the ground states of heavy atoms ($Z \gtrsim 55$) there is an indication that the antishielding predominates. For all cases, the correction factors listed in II give a rough upper limit, since both the radial and the exchange terms tend to decrease C.

I would like to thank Professor H. M. Foley for several stimulating and helpful discussions.

APPENDIX. SECOND-ORDER QUADRUPOLE EFFECT

It has been pointed out in III, in connection with the quadrupole coupling in polar molecules, that the quadrupole distortion induced in the core by an external charge gives rise in second order to a further contribution to the quadrupole coupling. In the present case, the external charge corresponds to the valence electron. As has been shown previously,[3] the distortion of the core by the valence electron taken in first order is equivalent to the interaction of the valence electron with the quadrupole moment induced in the core by the nuclear Q. The second-order quadrupole effect involves the perturbation of the core by the external valence electron taken in second order. In as much as the first-order quadrupole correction is small for atoms, (of the order of 10 percent), it was expected that the second-order quadrupole effect would be even smaller, of the order of 1 percent of the main term in the quadrupole coupling. This expectation was borne out by a calculation of the second-order quadrupole effect for the $3p^5$ state of Cl.

In the following we will first give a derivation of the second-order quadrupole effect for s states of the core. The valence electron (or hole) is assumed in a p state with magnetic quantum number $m=1$; the p state will be taken as $3p$ (Cl). The various perturbations which arise in first and second order have been given in Fig. 3 of III. In first order, one obtains a d wave, d_{ns}. In second order, d_{ns} is excited into an s wave, a d wave d'_{ns}, and a g wave. The first-order perturbation Ψ_1 is determined by

$$(H_0-E_0)\Psi_1=[(-2/r_{12})+E_1]\Psi_0, \tag{1A}$$

where $\Psi_0=\psi_{ns}(1)\psi_{3p,1}(2)$ is the zero-order wave function, H_0 and E_0 are the unperturbed Hamiltonian and energy, respectively, E_1 is the first-order perturbation energy, and vanishes for s states. Ψ_1 can be written,

$$\Psi_1=\sum_{mm'} a_{mm'}\psi_{d,m}(1)\psi_{3p,m'}(2), \tag{2A}$$

where $a_{mm'}$ is a coefficient, $\psi_{d,m}$ is the perturbed d wave, $\psi_{3p,m'}$ is a $3p$ function, m and m' are the magnetic quantum numbers of the d wave and of $3p$, respectively. Upon inserting (2A) in (1A) one obtains

$$(H_0-E_0)\sum_{mm'} a_{mm'}\psi_{d,m}(1)\psi_{3p,m'}(2) = [(-2/r_{12})+E_1]\psi_{1s}(1)\psi_{3p,1}(2). \tag{3A}$$

Since we are interested in the P_2 perturbation, the term of $-2/r_{12}$ which will be used is

$$-2(r_<^2/r_>^3)\sum_{m=-2}^{2} P_2^m(\theta_1)P_2^{-m}(\theta_2).$$

The values of $a_{mm'}$ are obtained in the same manner as shown in II for the magnetic hfs. These values depend on the normalization of $\psi_{d,m}$ which will be chosen as follows. $\psi_{d,m}$ will be written

$$\psi_{d,m}=[w_1'(d_{ns})/r]\Theta_2^m, \tag{4A}$$

where Θ_2^m is the normalized angular function [Eq. (31b)], and the radial function $w_1'(d_{ns})$ is determined by

$$M_2 w_1'(d_{ns})=fu'_0, \tag{5A}$$

where u'_0 is r times the radial ns function, M_2 is defined by Eq. (39), and $f(r)$ is given by

$$f(r)=r^{-3}\int_0^r v'^2r'^2dr'+r^2\int_r^\infty v'^2r'^{-3}dr', \tag{6A}$$

with $v'=r$ times the radial $3p$ function, normalized according to (1a). Equation (5A) and the values of $a_{mm'}$ are obtained by multiplying both sides of (3A) by $\Theta_2^{m*}(1)\psi^*_{3p,m'}(2)$ and integrating over $\sin\theta_1 d\theta_1$ and $d\mathbf{r}_2$, where θ_1 is the polar angle of electron 1, and $d\mathbf{r}_2$ denotes the volume element of electron 2. Throughout this discussion we use wave functions normalized to a volume element $\sin\theta_i d\theta_i dr_i$. The resulting equation for $a_{mm'}$ is

$$a_{mm'}=-2\int_0^\pi \Theta_1^1\Theta_1^{m'*}P_2^{m'-1} \times\sin\theta_2 d\theta_2\int_0^\pi P_2^{1-m'}\Theta_2^0\Theta_2^{m*}\sin\theta_1 d\theta_1. \tag{7A}$$

From (2A) and (7A) one obtains

$$\Psi_1=(2/5^{\frac{1}{2}})[\psi_{d,0}(1)\psi_{3p,1}(2)-3^{\frac{1}{2}}\psi_{d,1}(1)\psi_{3p,0}(2) +6^{\frac{1}{2}}\psi_{d,2}(1)\psi_{3p,-1}(2)]. \tag{8A}$$

It will now be verified that the overlap of Ψ_0 and Ψ_1 gives the previous result[3] for the first-order induced effect [Eq. (3)]. The quadrupole coupling q' will be defined by

$$q'=-\int[\rho(3\cos^2\theta-1)/(2r^3)]dV, \tag{9A}$$

where ρ is the electronic probability density and dV is the volume element. The main term of q' which is

due to the valence electron density is given by

$$q'_0 = -\int_0^\infty v'^2 r^{-3} dr \int_0^\pi |\Theta_1^1|^2 P_2^0 \sin\theta d\theta = (1/5)\langle r^{-3}\rangle_v. \quad (10A)$$

The term of q' due to the overlap of Ψ_0 and Ψ_1 is

$$\Delta q' = -4\int \Psi_0 \Psi_1 P_2^0(1) r_1^{-3} dV_1 dV_2$$

$$= -\frac{8}{5^{\frac{1}{2}}} \int_0^\pi \Theta_0^0 \Theta_2^0 P_2^0 \sin\theta_1 d\theta_1 \int_0^\infty \frac{u'_0 w_1'(d_{ns})}{r^3} dr, \quad (11A)$$

where dV_i is the volume element of electron i, and the factor 4 in the first equation arises from the presence of two terms in the overlap for each s electron. Upon evaluating (11A) one finds in view of (10A)

$$\Delta q' = -(8/5)\left[\int_0^\infty u'_0 w_1' r^{-3} dr\right] q'_0/\langle r^{-3}\rangle_v. \quad (12A)$$

Equation (12A) gives the same result as the induced moment density $(8/5)Qu'_0 u'_{1,0\to 2} r^2$ since the radial integral over $u'_0 u'_{1,0\to 2}$ and v'^2 is equal to $\int_0^\infty [u'_0 w'_1/r^3] dr$ of (12A), as shown in reference 3.

The second-order terms arise from two sources. The square of the first-order perturbation Ψ_1^2 contributes a term. We have

$$\Psi_1^2 = (4/125)[\psi^2_{d,0}(1)\psi^2_{3p,1}(2) + 3\psi^2_{d,1}(1)\psi^2_{3p,0}(2) + 6\psi^2_{d,2}(1)\psi^2_{3p,-1}(2) + \cdots], \quad (13A)$$

where cross terms have not been written down since they do not contribute to q'. The contribution to q' is

$$\Delta q'_1 = -2\int \Psi_1^2 P_2^0(1) r_1^{-3} dV_1 dV_2 = -\frac{8}{125}[I_2^0 + 3I_2^1 + 6I_2^2] J(d_{ns}, d_{ns}), \quad (14A)$$

where I_i^m is defined by

$$I_i^m \equiv \int_0^\pi |\Theta_i^m|^2 P_2^0 \sin\theta d\theta, \quad (15A)$$

and

$$J(a,b) \equiv \int_0^\infty w'_i(a) w'_j(b) r^{-3} dr, \quad (16A)$$

where $w'_i(a)$ and $w'_j(b)$ are the radial parts of the perturbed wave functions whose subscript (i, j) indicates the order of the perturbation. One finds $I_2^0 = 2/7$, $I_2^1 = 1/7$, $I_2^2 = -2/7$. Thus Eq. (14A) gives

$$\Delta q'_1/q'_0 = (8/25)J'(d_{ns}, d_{ns}), \quad (17A)$$

where $J'(a,b)$ is defined by

$$J'(a,b) \equiv J(a,b)/\langle r^{-3}\rangle_v. \quad (18A)$$

The other second-order term is contributed by the overlap of Ψ_0 with the second-order perturbation of the wave function, which will be called Ψ_2. Ψ_2 is determined by

$$(H_0 - E_0)\Psi_2 = (-2/r_{12})\Psi_1 + E_2\Psi_0 + E_1\Psi_1, \quad (19A)$$

where E_1 and E_2 are the first- and second-order perturbations of the energy, respectively. Ψ_2 consists of s, d, and g waves, but only the d wave, which will be called d'_{ns}, is of interest since the overlap of ns with excited s or g waves does not contribute to the quadrupole coupling. The term $E_2\Psi_0$ enters only into the equation for the s wave, so that it will not be considered here. Moreover, $E_1 = 0$ for s states. Ψ_2 will be written

$$\Psi_2 = \sum_{mm'} b_{mm'} \chi_{d,m}(1)\psi_{3p,m'}(2), \quad (20A)$$

where $b_{mm'}$ is a coefficient, $\chi_{d,m}$ is the d'_{ns} wave, m and m' are the magnetic quantum numbers of d'_{ns} and $3p$, respectively. Upon inserting (8A) and (20A) into (19A), one obtains

$$(H_0 - E_0)\sum_{mm'} b_{mm'}\chi_{d,m}(1)\psi_{3p,m'}(2) = -\frac{4}{5^{\frac{1}{2}} r_{12}}[\psi_{d,0}(1)\psi_{3p,1}(2) - 3^{\frac{1}{2}}\psi_{d,1}(1)\psi_{3p,0}(2) + 6^{\frac{1}{2}}\psi_{d,2}(1)\psi_{3p,-1}(2)]. \quad (21A)$$

A given $b_{mm'}$ will contain, in general, contributions from more than one term of Ψ_1 on the right-hand side of (21A). The terms of $b_{mm'}$ will be labeled by m_1 and m_2, which are the magnetic quantum numbers of the first-order d wave ψ_{d,m_1} and of ψ_{3p,m_2}, respectively. The contribution of m_1 and m_2 to $b_{mm'}$ will be written $b_{mm'(m_1m_2)}$. By multiplying both sides of (21A) by $\Theta_2^{m*}(1)\psi^*_{3p,m'}(2)$ and integrating over $\sin\theta_1 d\theta_1$ and $d\tau_2$, one obtains

$$b_{mm'(m_1m_2)} = -\frac{4c_{m_1m_2}}{5^{\frac{1}{2}}} \int_0^\pi \Theta_1^{m_2}\Theta_1^{m'*} P_2^{m'-m_2} \times \sin\theta_2 d\theta_2 \int_0^\pi \Theta_2^{m_1}\Theta_2^{m*} P_2^{m_2-m'} \sin\theta_1 d\theta_1, \quad (22A)$$

where $c_{m_1m_2}$ is the coefficient of $\psi_{d,m_1}(1)\psi_{3p,m_2}(2)$ in the square bracket of (21A). In obtaining (22A) it was assumed that $\chi_{d,m}$ is normalized as follows

$$\chi_{d,m} = [w_2'(d'_{ns})/r]\Theta_2^m, \quad (23A)$$

where the radial function $w'_2(d'_{ns})$ is determined by

$$M_2 w'_2(d'_{ns}) = w'_1(d_{ns}) f. \quad (24A)$$

Upon summing (22A) over m_1m_2, and inserting the result in (20A) one obtains

$$\Psi_2=-(4/5^{5/2})[\chi_{d,0}(1)\psi_{3p,1}(2)-3^{\frac{1}{2}}\chi_{d,1}(1)\psi_{3p,0}(2)+6^{\frac{1}{2}}\chi_{d,2}(1)\psi_{3p,-1}(2)]. \quad (25A)$$

Only the overlap of the first term $\chi_{d,0}(1)\psi_{3p,1}(2)$ with Ψ_0 contributes to q'. One finds

$$\Delta q'_2=-4\int\Psi_0\Psi_2P_2^0(1)r_1^{-3}dV_1dV_2=(16/125)J(ns,d_{ns}), \quad (26A)$$

where $J(ns,b)$ is given by

$$J(ns,b)=\int_0^\infty u'_{0,ns}w_2'(b)r^{-3}dr, \quad (27A)$$

and $u'_{0,ns}$ is the unperturbed ns radial function. In analogy with (18A) $J'(ns,b)$ will be defined as $J(ns,b)/\langle r^{-3}\rangle_v$. Thus the total second-order contribution of an s shell is

$$\Delta q'_{ns}/q'_0=(8/25)J'(d_{ns},d_{ns})+(16/25)J'(ns,d'_{ns}). \quad (28A)$$

The excitation of np states can be treated in the same manner as the excitation of ns. As shown in Fig. 3 of III, np is excited in first order to a p wave p_{np} and an f wave f_{np}. In second order, p_{np} is excited to a p wave p'_{np} and an f wave f'_{np}. Similarly, f_{np} is excited to a p wave p''_{np} and an f wave f''_{np}. The second-order quadrupole effect arises from terms containing the square of p_{np} and f_{np}, and from the overlap of u'_0 with the second-order perturbations. We will give only the final result. One obtains for the second-order quadrupole effect of a complete p shell,

$$\frac{\Delta q'_{np}}{q'_0}=\frac{168}{625}J'(p_{np},p_{np})+\frac{336}{625}J'(np,p'_{np})+\frac{288}{625}J'(f_{np},f_{np})+\frac{144}{625}J'(np,p''_{np})+\frac{144}{625}J'(np,f'_{np})+\frac{576}{625}J'(np,f''_{np}), \quad (29A)$$

where the J' are determined by Eqs. (16A), (18A) and

$$J'(np,b)=\left[\int_0^\infty u'_{0,np}w'_2(b)r^{-3}dr\right]/\langle r^{-3}\rangle_v, \quad (30A)$$

in which $u'_{0,np}$ is the unperturbed radial np function of the core. The radial functions appearing in the J' are determined by the following equations

$$M_1w'_1(p_{np})=u'_{0,np}[f-\langle f\rangle_{np}], \quad (31A)$$

$$M_3w'_1(f_{np})=u'_{0,np}f, \quad (32A)$$

$$M_1w'_2(p'_{np})=w'_1(p_{np})[f-\langle f\rangle_{np}]-\left[\int_0^\infty fw'_1(p_{np})u'_{0,np}dr'\right]u'_{0,np}(r), \quad (33A)$$

$$M_3w'_2(f'_{np})=w'_1(p_{np})f, \quad (34A)$$

$$M_1w'_2(p''_{np})=w'_1(f_{np})f-\left[\int_0^\infty fw'_1(f_{np})u'_{0,np}dr'\right]u'_{0,np}(r), \quad (35A)$$

$$M_3w'_2(f''_{np})=w'_1(f_{np})f, \quad (36A)$$

where

$$\langle f\rangle_{np}\equiv\int_0^\infty fu'^2_{0,np}dr. \quad (37A)$$

In Eqs. (33A) and (35A) that function $w'_2(p'_{np})$ or $w'_2(p''_{np})$ must be chosen which is orthogonal to $u'_{0,np}$. It may be noted that the numerical coefficients of Eqs. (28A) and (29A) are proportional to those which appear in the expressions for $\Delta q'_{ns}$ and $\Delta q'_{np}$ for the case of an external point charge, as given by Eqs. (61) and (64) of III; the proportionality factor is 7/10. The contribution of the second-order terms to R_e is $-\sum_n(\Delta q'_{ns}+\Delta q'_{np})/q'_0$ since R_e is defined in terms of minus the interaction energy due to the induced effects.

The radial functions and integrals obtained above were calculated for Cl. Only the $3s$ and $3p$ shells had to be considered since the contribution of the inner shells is negligible. It was found that $-(\Delta q'_{3s}+\Delta q'_{3p})/q'_0$ is $\sim+0.005$ and is thus smaller than the uncertainties in the first-order terms of R_e.

It should be noted that the preceding results do not represent the complete second-order correction. There are additional terms[19] which arise from the simultaneous excitation of a core electron and the valence electron by the perturbation e^2/r_{12}. As an example, let us consider the term

$$e^2(r_</r_>^2)\sum_{m=-1}^{1}P_1^m(1)P_1^{-m}(2)$$

of e^2/r_{12}. Let

$$\Psi_0=s_0(1)p_0(2) \quad (38A)$$

denote the zero-order wave function for a system consisting of a core electron in an s state and a p valence electron. In first order, one obtains the perturbation

$$\Psi_1=p_1(1)s_1(2)+p_1'(1)d_1(2), \quad (39A)$$

where p_1 and p'_1 are p functions which describe the

[19] The existence of these terms was pointed out to the author by Professor H. M. Foley.

excitation of electron 1 into higher p states, while s_1 and d_1 are s and d functions, respectively, which describe the excitation of electron 2. The first-order overlap $\Psi_0\Psi_1$ does not contribute to q' because $s_0(1)$ is orthogonal to $p_1(1)$ and $p'_1(1)$, and similarly $p_0(2)$ is orthogonal to $s_1(2)$ and $d_1(2)$. However, Ψ_1^2 contributes three second-order terms to q' which arise from $[p_1(1)]^2$, $[p'_1(1)]^2$, and $[d_1(2)]^2$. Second-order terms of the type Ψ_1^2 are also obtained from the simultaneous P_1^m excitation of a core electron in a p state and the valence electron. A similar class of terms is obtained using the P_2^m part of e^2/r_{12}. These terms were not evaluated because of the difficulty of determining the functions of type p_1, s_1, p'_1, and d_1. Thus p_1 and s_1 satisfy a set of two simultaneous differential equations. The same applies for p'_1 and d_1. The numerical solution of these sets would be much more complicated than the solution of Eqs. (5A) and (24A) which involve a single unknown function. However, there seems to be no reason to believe that the two-electron terms would be appreciably larger than the one-electron excitation terms which were shown to be very small for the case of Cl.

PHYSICAL REVIEW VOLUME 95, NUMBER 3 AUGUST 1, 1954

Cross Sections for the Reactions $Ti^{48}(d,2n)V^{48}$; $Cr^{52}(d,2n)Mn^{52}$; and $Fe^{56}(d,2n)Co^{56}$†

WARREN H. BURGUS,* GEORGE A. COWAN,* J. W. HADLEY, WILMOT HESS,‡ THEODORE SHULL,*
M. L. STEVENSON,‡ AND H. F. YORK
Radiation Laboratory, Department of Physics, University of California, Livermore, California

(Received March 12, 1954)

Measurements have been made of the $(d,2n)$ cross sections of the nuclear species Ti^{48}, Cr^{52}, and Fe^{56}. Results are given for incident deuterons in the energy region 1–20 Mev.

THE cross sections for the reactions $Ti^{48}(d,2n)V^{48}$, $Cr^{52}(d,2n)Mn^{52}$, and $Fe^{56}(d,2n)Co^{56}$ have been measured as functions of energy of the bombarding deuterons, using the conventional stacked foil method, for energies of 1 to 20 Mev. A beam of deuterons was provided by the 60-inch cyclotron of the Crocker Laboratory of the University of California.

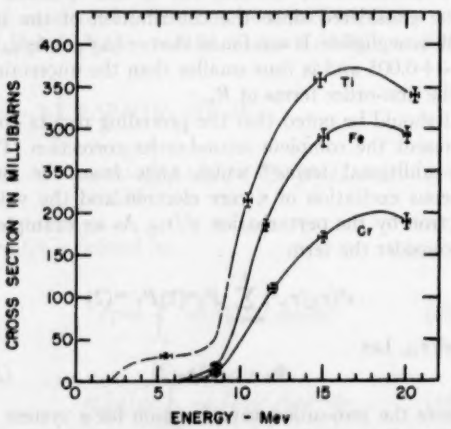

FIG. 1. Cross sections for the reactions $Fe^{56}(d,2n)Co^{56}$, $Cr^{52}(d,2n)Mn^{52}$, and $Ti^{48}(d,2n)V^{48}$.

† This work was performed under the auspices of the U. S. Atomic Energy Commission.

* Los Alamos Scientific Laboratory of the University of California.
‡ University of California Radiation Laboratory, Berkeley, California.

The range distribution of deuterons in the beam, which was collected in a Faraday cup, was measured before each run by placing absorber foils of known thickness of aluminum in the beam and measuring the charge I_f collected on the foils, and the charge I_e passing through the foils and collected by the Faraday cup. These charges were measured by two electrometers and recorded. The ratio $I_e/(I_e+I_f)$ was determined as a function of thickness of aluminum absorber, giving the range distribution of deuterons. The target foils of Ti metal, Fe metal, and stainless steel were then placed in the beam and bombarded. The beam current was monitored by reading both I_e and I_f. The equivalent Al thickness of the target foils was determined by placing Al foils of varying thickness behind the target foil in the beam and again measuring $I_e/(I_e+I_f)$. Comparison of this measurement with that for the Al absorber foils determined the equivalent aluminum thickness of the stack of target foils and thereby the energies of the deuterons that struck each foil in the target stack.

Absolute cross-section measurements were made by chemical separation of the end products, with subsequent absolute β^+ counting. The absolute counting was done using a thin-window methane-flow proportional counter and correcting for scattering and absorption. The results for V^{48} and Mn^{52} were checked by 4π counting of very thin samples, and good agreement was obtained.

The absolute cross-section values depend on the fact that the end products of the bombardment decay

partly by β^+ emission and partly by electron capture. It was assumed for V^{48} that 58 percent of the disintegrations were by β^+ emission and 42 percent by electron capture.[1] For Mn^{52}, 35 percent of the disintegrations were taken to be β^+ emission.[1] No effort was made to measure the 23-minute Mn^{52} isomer. For Co^{56} the disintegration rate was arbitrarily multiplied by four, since it is reported that K capture is at least three times as abundant as positron emission.[2] Thus the Fe cross section is a lower limit.

Corrections were made for the energy spread in the incident beam, as determined from the range distribution. The β^+ activities were corrected for the fact that the momentum of the incident deuteron sometimes carried the resultant struck nucleus out of the target foil.

The excitation functions are shown in Fig. 1. Individual experimental points could not be presented, as their identity was lost in the process of making corrections for the energy distribution of the deuteron beam. This process consisted of an inverse folding operation, carried out numerically on an IBM Card-Programmed Calculator. The vertical errors shown on the excitation function curves were estimated from the reproducibility of the shape of the excitation function. The horizontal errors represent the uncertainty in the energy of the incident deuterons. The uncertainty in the absolute cross-section scale, deriving principally from uncertainties in absolute β^+ counting efficiency, is estimated at ± 10 percent. No estimate is included for the possible errors in the values taken for β^+/K-capture.

The shelf at the low-energy end of the titanium curve is thought to represent a contribution from the $Ti^{47}(d,n)$-V^{48} reaction, which could not be avoided without the use of targets depleted in Ti^{47}.

Half-lives measured during the course of this experiment were:

$$T_{\frac{1}{2}} \text{ of } Mn^{52} = 5.60 \pm 0.01 \text{ days},$$

$$T_{\frac{1}{2}} \text{ of } V^{48} = 16.25 \pm 0.17 \text{ days},$$

$$T_{\frac{1}{2}} \text{ of } Co^{56} = 77.2 \pm 0.80 \text{ days}.$$

Some indications were given by the form of the experimental data that a small dip in the excitation function for the $Ti^{48}(d,2n)V^{48}$ reaction may be present at about 16 Mev. The evidence that has been accumulated is insufficient to settle this point at present, but it is hoped that further work may clear it up. We also plan to carry out a measurement of that part of the $Cr^{52}(d,2n)Mn^{52}$ excitation function leading to the 23-minute Mn^{52} isomer, in order to provide a Cr excitation function that will be more directly comparable to those given for Ti and Fe, which represent the total $(d,2n)$ cross section rather than just part of it.

[1] Good, Peaslee, and Deutsch, Phys. Rev. **69**, 313 (1946).
[2] L. G. Elliott and M. Deutsch, Phys. Rev. **64**, 321 (1943).

PHYSICAL REVIEW VOLUME 95, NUMBER 3 AUGUST 1, 1954

n-γ Coincidences Produced by Inelastic Scattering of Neutrons

P. Shapiro, V. E. Scherrer, B. A. Allison, and W. R. Faust
Naval Research Laboratory, Washington, D. C.

(Received February 18, 1954; revised manuscript received May 5, 1954)

Scintillation spectrometer analysis of the gamma-ray spectrum arising from interaction of 3.2-Mev neutrons with chromium shows several gamma rays including a very pronounced 1.43-Mev line. Coincidence observations indicate that there are a negligible number of gamma rays in cascade with the 1.43-Mev line. Thus the residual nucleus is left in the 1.43-Mev state by emission of a neutron which carries off the remaining portion of the energy. The energy distribution of this group of inelastically scattered neutrons as deduced from the coincidence pulse-height distribution of recoil protons in a stilbene detector has a maximum at 1.5 Mev.

THE particular level structure of chromium is such that inelastic scattering of neutrons yields relatively simple spectra that permit the spectrum of both scattered neutrons and gamma rays to be deduced. Spectral distribution of gamma rays shows several different energy lines and is in agreement with results of Peacock and Deutsch[1] on the decay of Mn^{52}. γ-γ coincidence observations[2] of Cr excited by 3.2-Mev neutron bombardment indicate that few gamma rays are in coincidence with the strong 1.43-Mev line. This indicates that chromium is left in the 1.43-Mev excited state by emission of a group of inelastically scattered neutrons of energy $E_n = [(52/53) \times 3.2 - 1.43] \cong 1.71$ Mev. To verify that this supposition is correct the spectral distribution of neutrons in coincidence with the 1.43-Mev gamma ray have been observed.

[1] W. C. Peacock and M. Deutsch, Phys. Rev. **69**, 306 (1946).
[2] Scherrer, Allison, and Faust, Phys. Rev. **94**, 791 (1954).

DESCRIPTION OF EXPERIMENTS

Figure 1 illustrates the basic experimental arrangement of which various modifications were made by substitution of one type of scintillation detector for

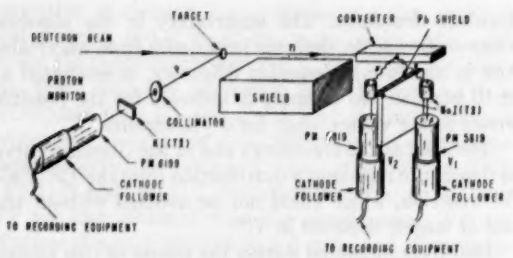

FIG. 1. Schematic arrangement of chromium radiator and detectors.

another or complete removal of one or the other detectors. Neutrons were obtained from the *d-d* reaction which was produced in a Cockcroft-Walton accelerator by 350-kev deuteron bombardment of a thick deuterium target formed by the adsorption of deuterium onto aluminum. The reaction was monitored by counting the protons from the companion reaction, $H^3(d,p)H^4$, in a KI(Tl) scintillation counter. As shown in Fig. 1, a chromium radiator was placed at 0° relative to the deuteron beam and about 25 cm from the target. Detectors used in the inelastic scattering experiments were placed about 10 cm below the chromium radiator and were partially shielded by a 10 cm×10 cm by 20 cm block of tungsten interposed between the accelerator target and detectors. The neutron detector used was a 7.5 cm diameter by 1.25 cm thick crystal of stilbene mounted on a K1197 photomultiplier. A single crystal of NaI(Tl), 12.7 cm in diameter and 5.1 cm thick in conjunction with a K1198 photomultiplier served as a gamma-ray spectrometer. NaI(Tl) crystals used in γ-γ and n-γ coincidence arrangements were 5.0 cm in diameter by 5.1 cm thick mounted on 5819 photomultiplier tubes. All of these detectors were used in conjunction with the usual amplifiers and pulse-height distributions were recorded on a twenty-channel analyzer.

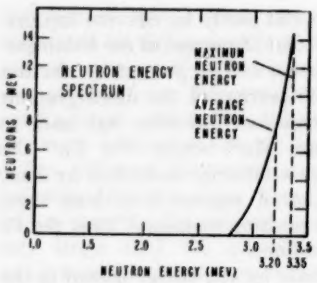

FIG. 3. Energy distribution of accelerator neutrons as deduced from Fig. 2.

The stilbene crystal which was used as a neutron spectrometer will count gamma rays or neutrons with about the same sensitivity. However, the absence of gamma rays in coincidence with the 1.43-Mev gamma ray makes it possible to count only neutrons in the stilbene if one records only those pulses which are in coincidence with the 1.43-Mev gamma ray.

Calibration of the neutron spectrometer was performed by observing the pulse-height distribution produced by neutrons leaving the target at 100°. At this angle the neutrons are nearly monoenergetic and have an energy of 2.46 Mev. Comparison of this distribution was made with that produced by the known electron distribution from gamma-ray sources. Absolute energy calibration was performed by using the calibration point at 2.46 Mev and utilizing data of Taylor *et al.*,[3] to calculate the energy corresponding to any arbitrary given recoil proton pulse height.

The energy distribution of neutrons incident on the radiator was determined from pulse-height distributions taken with the stilbene detector at the nominal position of the radiator. The pulse-height distribution produced by neutrons leaving the accelerator at 0° when the machine is operated at 350 kv is shown in Fig. 2. The pulse-height distribution shown in Fig. 2 was then corrected approximately for the photomultiplier statistics and the finite resolution of the pulse-height

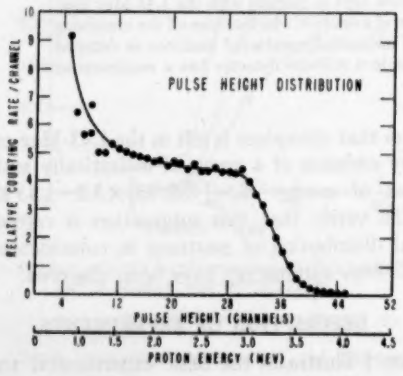

FIG. 2. Pulse-height distribution produced by accelerator neutrons falling on a stilbene crystal.

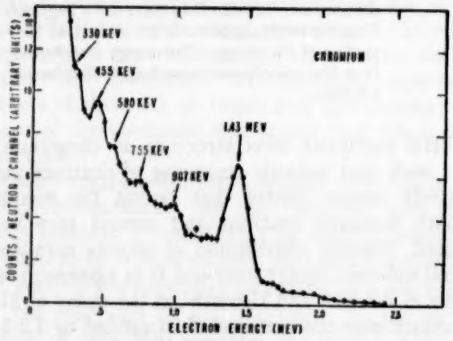

FIG. 4. Pulse-height distribution of gamma rays from chromium radiator.

[3] Taylor, Jentschke, Remley, Eby, and Kruger, Phys. Rev. 84, 1034 (1951).

analyzer using the method of Owen and Primakoff[4,5] assuming a Gaussian response. The half-width of the Gaussian was taken to be proportional to the square root of the pulse height and the constant of proportionality was determined by observing the Compton distribution in the crystal from known gamma-ray lines and correcting this data to the theoretical Compton distribution. The neutron spectrum $N(E)$ was then calculated from the corrected pulse-height distribution $P(E)$ by use of the well-known formula[6]

$$-dP/dE \propto \sigma(E)N(E)/E,$$

and the resulting spectrum is shown in Fig. 3. The end point agrees with that calculated from the known accelerator voltage and Q of the reaction.

Experiments were performed to obtain the pulse-height distribution of chromium gamma rays produced by the inelastic scattering of 3.2-Mev neutrons. The large NaI crystal described above was used as a detector. Because of the size of this crystal all secondary radiation was absorbed and most pulses appeared near the primary gamma-ray energy. Figure 4 shows the pulse-height distribution obtained in this manner. These results indicate chromium gamma rays at 1.43, 0.97, 0.75 Mev, with perhaps other possibilities.

A γ-γ coincidence experiment was performed next. Two NaI(Tl) detectors were placed in the detector positions as indicated in Fig. 1. Pulses from one detector operated a single channel pulse-height analyzer which

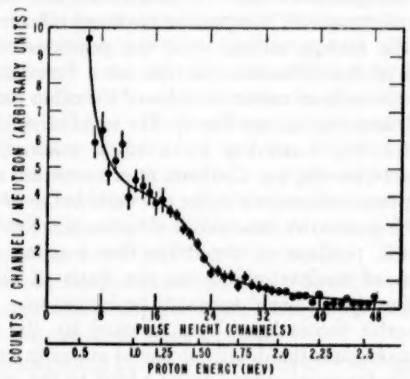

FIG. 5. Pulse-height distribution produced by neutrons from chromium radiator falling on a stilbene crystal.

[4] G. E. Owen and H. Primakoff, Phys. Rev. **74**, 1406 (1948).
[5] G. A. Morton, Advances in Electronics **IV**, 97 (1952).
[6] M. J. Poole, Proc. Phys. Soc. (London) **A65**, 453 (1952).

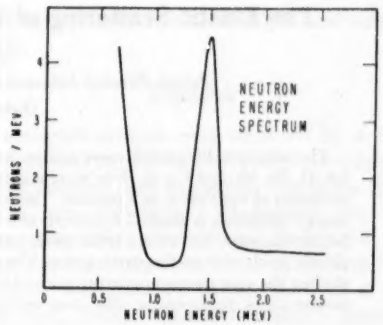

FIG. 6. Energy distribution of neutrons from inelastic scattering of 3.2-Mev neutrons by a chromium radiator.

was adjusted so that only those pulses arising from the strong 1.43-Mev photopeak produced an output. The single channel output pulses operated the gating circuit on the twenty-channel analyzer which recorded the coincidence pulses from the second NaI(Tl) detector. Results of this experiment were essentially null indicating that few gamma rays are in coincidence with the 1.43-Mev line.

n-γ coincidences were observed by the same technique as used for the γ-γ coincidences. Here, however, one of the NaI(Tl) detectors was replaced by the stilbene detector described previously. The NaI(Tl) detector was adjusted so that the photopeak of the 1.43-Mev line was in the single channel, and the "coincidence" pulse-height distribution produced by the stilbene detector was recorded on the twenty-channel analyzer. The pulse-height distribution is shown in Fig. 5, and the neutron energy spectrum calculated from the pulse-height distribution is shown in Fig. 6.

DISCUSSION

The energy spectrum of inelastically scattered neutrons as calculated from data of Taylor *et al.*, has a maximum in the vicinity of 1.5 Mev, which should be compared with the value of 1.7 Mev mentioned previously. This discrepancy is ascribed to an inadequate knowledge of the pulse-height distribution produced by protons below 2 Mev; the error made by extrapolating Taylor's data to zero energy is of the order of 20 percent. The experiment does, however, show a fairly homogeneous group of neutrons near the expected energy and verifies that the strong 1.43-Mev chromium gamma ray arises from inelastic scattering of fast neutrons.

The Elastic Scattering of 18-Mev Protons by Al, Fe, Ni, and Cu†

IRVING E. DAYTON
Palmer Physical Laboratory, Princeton University, Princeton, New Jersey
(Received February 2, 1954)

The absolute differential cross section for the elastic scattering of 18-Mev protons has been measured for Al, Fe, Ni, and Cu at 35 or more angles between 15 degrees and 172 degrees. The estimated standard deviation of each point is 3 percent. The scattered protons are detected by a sodium iodide crystal whose energy resolution is about 2.5 percent, and the resulting pulse spectrum is recorded on a 15-channel pulse-height analyzer. For all materials used, protons scattered inelastically to the lowest known level are completely resolved from the elastic group. The differential cross sections for the four elements are qualitatively similar, showing pronounced structure and low cross sections in the background direction. The experimental results are in disagreement with cross sections predicted by the optical model of the nucleus.

I. INTRODUCTION

THE measurement of the elastic scattering cross section of nucleons by nuclei provides a method for studying several properties of the nucleus. At low nucleon energy the scattering cross sections give information about single levels in the compound nucleus. This resonance scattering cannot be observed if the incident nucleon energy exceeds several Mev, since the levels of the compound nucleus become wide and overlapping. The scattering cross section should then show little variation with the energy of the incident nucleon.

This elastic scattering is often called potential or diffraction scattering because the differential cross sections show great similarity to optical diffraction patterns. This analogy has been used in constructing the optical model[1] of the nucleus. The optical model replaces the field of the nucleus by a complex potential in analogy to a complex refractive index for the scattering of light by a partly opaque body. The imaginary part of the potential is responsible for the absorption of a fraction of the incident beam by the nucleus.

The optical model has been successfully applied in the high energy region to neutron scattering[1,2] and to the analysis of meson reactions.[3,4] It has also been used successfully in predicting the energy and Z dependence of the total neutron cross sections up to 3 Mev.[5] However, these applications constitute a relatively weak test of the theory, since it was only necessary to fit total cross sections. Kessler and Lederman[6] recently report being able to fit total cross sections for high-energy mesons but not the angular dependence of the scattering cross sections.

The optical model was first used in the intermediate energy region by LeLevier and Saxon,[7] who succeeded in fitting the data of Burkig and Wright[8] on the elastic scattering of 18.6-Mev protons by Al. Gugelot[9] performed additional experiments at 18.3 Mev, the results of which were compared with those from optical model calculations by Chase and Rohrlich.[10] They confirmed the agreement between theoretical and experimental cross sections for the scattering of protons by Al. However, they were able to show that for heavier elements the backward scattering cross section was lower than the theoretical values for any square well potential. It now appears that the initial agreement in the case of Al was illusory, for in the earlier experiments[8,9] data were taken at such wide intervals that the sharp structure of the differential cross section was completely missed.[11]

The disagreement between theoretical and experimental results makes it impossible to obtain information about the nuclear radius, since the positions of the maxima of the diffraction pattern are a function not only of the nuclear radius but also of the other parameters of the potential (see Fig. 4). The usual calculations for diffraction scattering by a black nucleus,[12] in addition to leaving out Coulomb effects, contain small angle approximations which are not valid in the present case. The qualitative conclusions of Cohen and Neidigh[11] about the position of the diffraction maxima as a function of nuclear radius on the basis of simple diffraction theory would appear to be fortuitous.

Spin-orbit forces have been invoked by the shell model to explain the details of bound states in nuclei, and these forces may have to be added to the optical model to obtain complete agreement with experiment. The data presented in this paper may help to prove whether or not the interaction between a nucleon and the nucleus can be represented by a single potential independent of angular momentum and energy.

All of this information could also be obtained from neutron scattering data, and the absence of Coulomb

† Supported by the U. S. Atomic Energy Commission and The Higgins Scientific Trust Fund.

[1] Fernbach, Serber, and Taylor, Phys. Rev. **75**, 1352 (1949).
[2] J. DeJuren and N. Knable, Phys. Rev. **77**, 606 (1950).
[3] H. A. Bethe and R. R. Wilson, Phys. Rev. **83**, 690 (1951).
[4] Byfield, Kessler, and Lederman, Phys. Rev. **86**, 17 (1952).
[5] Feshbach, Porter, and Weisskopf, Phys. Rev. **90**, 166 (1953).
[6] J. O. Kessler and L. M. Lederman, Phys. Rev. **94**, 689 (1954).
[7] R. E. LeLevier and D. S. Saxon, Phys. Rev. **87**, 40 (1952).
[8] J. W. Burkig and B. T. Wright, Phys. Rev. **82**, 451 (1951).
[9] P. C. Gugelot, Phys. Rev. **87**, 525 (1952).
[10] D. M. Chase and F. Rohrlich, Phys. Rev. **94**, 81 (1954).
[11] B. L. Cohen and R. V. Neidigh, Phys. Rev. **93**, 282 (1954).
[12] B. T. Feld *et al.*, Atomic Energy Commission Report NYO-636 (unpublished).

effects would make the analysis considerably simpler. However, the experimental problems connected with intensity and energy resolution are formidable, and it may be some time before the neutron data will approach in accuracy what is now easily obtainable with protons.

II. EXPERIMENTAL TECHNIQUE

This experiment was carried out using the 60-in. precision scattering chamber and Faraday cup constructed by Yntema and White.[13] The center of the chamber, where the target was located, was about 8 meters from the cyclotron. The beam was collimated by two $\frac{1}{4}$-in. diameter apertures, one 1.32 meters from the center of the scattering chamber and the other 0.56 meter from the center. Each of these collimators was followed by baffles to remove slit-scattered protons from the beam.

The charge collected in the Faraday cup flowed through a calibrated resistance, developing across it a voltage which was integrated electronically. The integrator circuit could be checked by applying a known voltage to the input. It was found that the drift was less than one percent during running times of the order of five hours. The performance of the integrator circuit has also been checked by substituting for it an electrometer which measures the charge collected on a polystyrene capacitor. Cross sections obtained by the two methods checked to within the counting statistics of 2 percent.

The energy of the beam was determined from the range in Al of protons scattered at 90 degrees from C^{12}. The recent experimental range-energy data of Bichsel and Mozley[14] was used. The theoretical range-energy relation of Smith[15] would increase the quoted energies by about 140 kev. The beam energy was measured at the beginning of each run, and was adjusted so that it was the same for all runs with a given element. Tests have been made which indicate that the beam energy remains constant to ± 50 kev over periods of 24 hours if operating conditions are not changed. The pulse height from the photomultiplier tube would have shown any short time changes in beam energy large enough to affect the measured cross sections.

The scattering foils were at an angle of 45 degrees to the incident beam for data taken between 50 degrees and 135 degrees, and normal to the beam for the other points. The Al foil was about 7 mg/cm^2 thick; for the other materials the thickness varied between 3 and 4 mg/cm^2. In the case of Fe, Ni, and Cu, the counting rate in the backward direction was so low that it was necessary to double the foil thickness there. With two foils it was always possible to repeat to within statistics data taken with a single foil. For this reason it is believed that effects due to multiple scattering were negligible.

Detector

The scattered protons were detected by a NaI(Tl) crystal mounted on the face of a 5819 photomultiplier tube. The counter was located at distances of 30 cm to 50 cm from the target. In general, the counter aperture subtended an angle of about 0.6 degree. However, for data taken on Al at angles less than 90 degrees this was reduced to one-third of a degree. Yntema and White[13] and Brockman[16] have made estimates which show that under these circumstances geometry corrections are quite small.

After amplification, the pulses from the photomultiplier were fed into a 15-channel differential discriminator of the Oak Ridge design.[17] The resolution of the crystal (full width at half-maximum) was generally about 2.5 percent. The gain of the system was adjusted so that the elastic peak was about three or four channels wide at half-maximum. This meant that in addition to the elastic peak the spectrum of all protons scattered inelastically with a loss of up to 1.0 or 1.5 Mev was also recorded. If one restricts his attention to isotopes whose natural abundance is more than a few percent, the lowest reported level in Al is at 0.84 Mev[18]; in Fe at 0.82 Mev[19]; Ni, 1.34 Mev[19,20]; and Cu, 0.96 Mev.[19] In all cases peaks were observed due to inelastic scattering to levels at about these energies, and these peaks were completely resolved from the elastic peak. Any existing unreported energy levels between 0.5 Mev and these levels would have been observed. Levels lower than about 0.25 Mev would have been missed since they would not be resolved from the elastic peak. The importance of the rejection of inelastically scattered protons will be discussed in the section on results.

The cross sections were determined from the area under the elastic scattering peak. The measured cross sections are corrected for the fact that about 1 percent of the beam at the target has an energy at least 300 kev less than the mean beam energy.[21] Because of the energy resolution of the detector, events produced by this low-energy tail will not be recorded.

This energy resolution also eliminated effects due to "slit scattering" from the detector collimator because any proton whose total path length in the brass collimator was more than about 0.0008 in. would be rejected. Calculations by Courant[22] bear out the

[13] J. L. Yntema and M. G. White, Atomic Energy Commission Report NYO-3478 (unpublished).
[14] H. Bichsel and R. F. Mozley, Phys. Rev. **94**, 764 (1954).
[15] J. H. Smith, Phys. Rev. **71**, 32 (1947).
[16] K. W. Brockman, Princeton University thesis, 1954 (unpublished).
[17] A. B. Van Rennes, Nucleonics **10**, No. 10, 50 (1952).
[18] Nuclear Science Abstracts **6**, No. 24*B*, 12–13 (1952).
[19] Hollander, Perlman, and Seaborg, Revs. Modern Phys. **25**, 469 (1953).
[20] Ely, Allen, Arthur, Bender, Hausman, and Reilley, Phys. Rev. **86**, 859 (1952).
[21] R. W. Peelle (unpublished measurements).
[22] E. D. Courant, Rev. Sci. Instr. **22**, 1003 (1951).

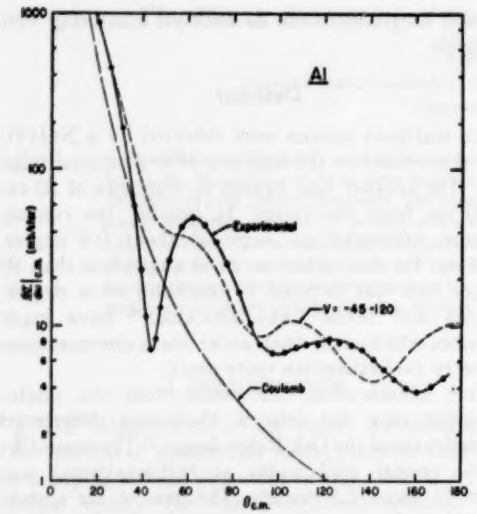

FIG. 1. Measured differential cross section for the elastic scattering of 18.4±0.1-Mev protons by Al. The estimated standard deviation is given by the size of the points. Included for comparison are curves calculated for Coulomb scattering from a point charge and for Coulomb plus a complex square well potential.

conclusion that the increase in effective solid angle in this case is negligible.

Errors

Data were taken every five degrees from 15 degrees to 172 degrees. Additional points were taken near the minima so that their true shape was resolved. At least 2500 counts were taken at each point. In addition to the statistical errors in counting there may also be random errors due to short-time drifts in the integrator (1 percent maximum) and random error in determining the area under the elastic scattering peak (2 percent). Errors in other parameters were negligible compared to these. These are combined to give a conservative estimated standard deviation of 3 percent for each point.

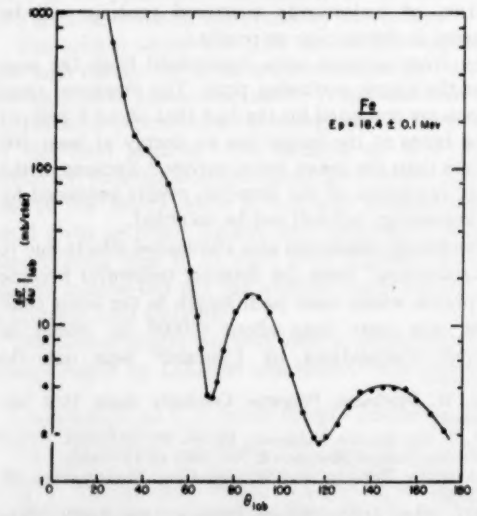

FIG. 2. Measured differential cross section for the elastic scattering of 18.4±0.1-Mev protons by Fe. The estimated standard deviation is given by the size of the points.

III. RESULTS

The measured differential cross sections are plotted in Figs. 1 through 4. The energy of the proton beam was 18.4±0.1 Mev for Al and Fe, 18.1±0.1 Mev for Ni, and 18.7±0.1 Mev for Cu. The estimated standard deviation is given by the size of the points. As a matter of convenience, smooth curves have been drawn through the points. The data for Al have been transformed to the center-of-mass system; for the other materials the correction is at most one degree in angle and 4 percent in solid angle and has not been included.

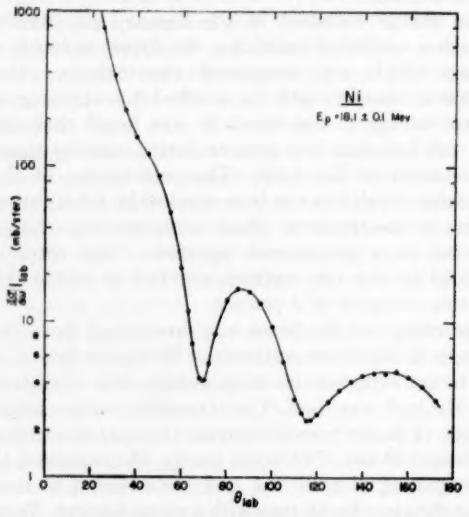

FIG. 3. Measured differential cross section for the elastic scattering of 18.1±0.1-Mev protons by Ni. The estimat ed standard deviation is given by the size of the points.

Inelastic Scattering

As mentioned in the preceding section, it was possible to observe the inelastic scattering to the lowest level in each target material. The angular distribution of the inelastic scattering is strikingly different from that of the elastic scattering, and appears to be smooth and peaked somewhat in the forward direction. Near minima in the elastic cross section the inelastic scattering is comparable with it, and near maxima the inelastic scattering is small compared with the elastic. This effect is most pronounced near the first minimum and smaller in the backward direction.

This fact would lead to serious consequences if one

attempted to measure the differential cross section for elastic scattering with an energy resolution of several Mev. In the nuclei studied here, inelastic scattering from several levels would then be included, and as a result the cross section near the first minimum could be in error anywhere from 50 percent to a factor of three or four. In contrast, measurements in the forward direction and near the second peak would be virtually unchanged. Hence, the effect of poor energy resolution is to smooth out the structure in the curves. The available energy resolution may make it difficult to obtain reliable elastic scattering data for heavier elements, where in general the levels are more closely spaced and nearer to the ground state.

IV. DISCUSSION

Many of the features of the measured cross sections can be explained qualitatively by using the simple model of a plane wave diffracted by a spherical obstacle. The curves for Fe, Ni, and Cu are plotted together in Fig. 5 in order to facilitate comparison. At angles less than 30 degrees, the cross section increases with increasing Z. This fact agrees with expectations, since Coulomb scattering predominates in that region.

Since Cu is the largest nucleus of the three, and since the incident proton energy was highest in this case, its "diffraction pattern" should be the narrowest, which is in fact the case. In Fe and Ni the effects of nuclear size and beam energy go in the opposite direction and apparently approximately compensate each other. In the region around 40 degrees, one can see another minimum starting to form as the size of the nucleus decreases. The "diffraction pattern" argument also shows that the first minimum in the Fe, Ni, and Cu curves corresponds to the second minimum in the Al curve.

The Fe and Ni nuclei have spin 0, Cu has spin 3/2, and Al has spin 5/2. However, it is not possible to observe any qualitative change in the curves which might be ascribed to any spin interaction. It will be necessary to have detailed calculations available in order to decide to what degree the nuclear spin may have an effect on the scattering cross section.

Comparison with Optical Model Calculations

Chase and Rohrlich[10] have made calculations on the elastic scattering of 18.3-Mev protons using the optical model with a square well potential. Some of their curves are compared with the experimental results for Al and Cu in Figs. 1 and 4. The curves labeled "Coulomb" refer to pure Rutherford scattering from a point charge. For Cu the curve $V=-45-31i$ Mev is almost identical with that for $V=-45-20i$ Mev and has not been plotted.

It can be seen that the results of the calculations presented are in disagreement with the experimental results. Over a wide variation in parameters the complex square well potential will not yield both the pronounced

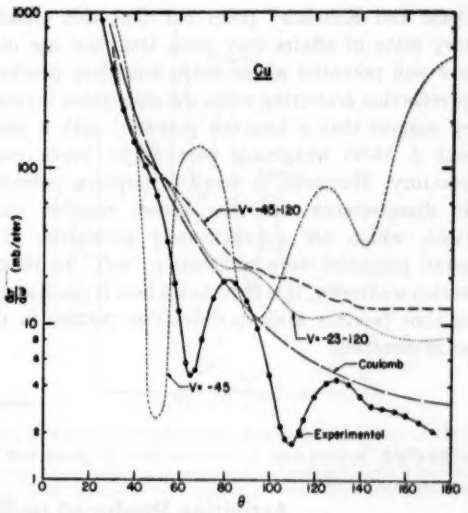

FIG. 4. Measured differential cross section for the elastic scattering of 18.7±0.1-Mev protons by Cu. The estimated standard deviation is given by the size of the points. Included for comparison are curves calculated for Coulomb scattering from a point charge and for Coulomb plus different complex square well potentials.

structure and the low cross section in the backward direction found by experiment. It is possible to decrease the backward cross section somewhat by increasing the imaginary (absorptive) part of the potential. On the other hand, in order to reproduce the structure of the curves, a small absorptive potential is necessary. When the absorption is reduced, the backward cross section increases rapidly due to reflection scattering. All of these features are exhibited in the graphs of Fig. 4.

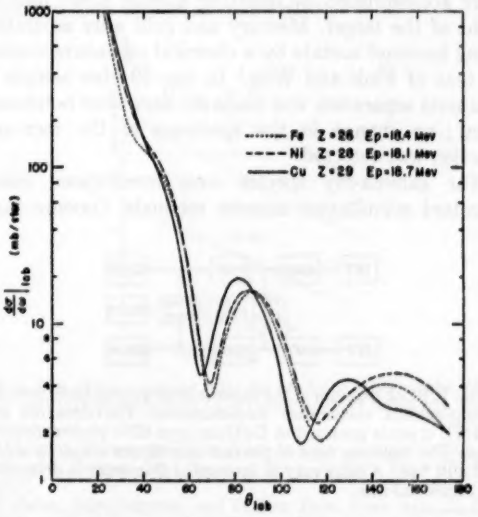

FIG. 5. Comparison of the measured differential cross sections for Fe, Ni, and Cu.

Chase and Rohrlich[10] point out that this unsatisfactory state of affairs may stem from the use of a square well potential whose sharp boundary produces large reflection scattering when the absorption is small. They suggest that a long-tail potential with a small (about 5 Mev) imaginary part might prove more satisfactory. However, a small absorptive potential is in disagreement with the known reaction cross sections, which are approximately geometric. If a long-tail potential were sufficiently "soft" to reduce reflection scattering, it is hard to see how it could at the same time produce a sharp diffraction pattern in the forward direction.

It is important to repeat these experiments with neutrons, for the absence of the Coulomb scattering may reveal whether these discrepancies are due to specific nuclear effects or to the interplay of nuclear and Coulomb scattering.

V. ACKNOWLEDGMENTS

The author wishes to thank Professor P. C. Gugelot for suggesting this experiment and for many helpful discussions during it. Dr. John McIntosh and Dr. W. A. Aron provided illuminating discussions of the theory. The author is deeply indebted to Mr. R. W. Peelle and Mr. J. B. Reynolds for their patient introduction to the lore of the Princeton cyclotron.

PHYSICAL REVIEW VOLUME 95, NUMBER 3 AUGUST 1, 1954

Activities Produced in Gold by Proton Bombardment*

C. H. Braden, L. D. Wyly, and E. T. Patronis, Jr.
School of Physics, Georgia Institute of Technology, Atlanta, Georgia
(Received April 15, 1954)

We have investigated activities produced in gold by bombardment with 12- and 20-Mev protons. Gamma rays of 1.17, 0.81, 0.58, and 0.255 Mev energy are found in the Hg fraction from the target bombarded at 20 Mev. These gamma rays all decay with a half-life of 42±3 hours and we ascribe them to Hg^{195} produced by the Au(p,3n)Hg reaction. Our data concerning the decay of Hg^{197}, Au^{196}, and Au^{195} are, in most cases, consistent with previous work.

INTRODUCTION AND EXPERIMENTAL PROCEDURE

WE have studied the gamma-ray spectra of activities produced by the bombardment of gold with 12- and 20-Mev protons in the Oak Ridge 86-inch cyclotron. Bombardments at about 12 Mev were accomplished by inserting slowing down foils in front of the target. Mercury and gold were separated using iso-amyl acetate by a chemical procedure similar to that of Fink and Wiig.[1] In one 20-Mev sample a platinum separation was made six days after bombardment; no change in the spectrum of the mercury fraction was detected.

The gamma-ray spectra were investigated using standard scintillation counter methods. Gamma rays were detected by use of a 1½-in. diameter by 1 in. NaI(Tl) crystal affixed to a DuMont type 6292 photomultiplier tube. The pulses were amplified by an Atomic Instrument Company amplifier and applied to either an Atomic Instrument or a locally built single-channel pulse-height analyzer. A resolution of about 12 percent was obtained for the Cs^{137} 0.662-Mev gamma line. Some gamma-gamma coincidence work was done using two such gamma-ray counters and a coincidence circuit based on the fast-slow method.[2] The resolving time of our fast-coincidence circuit was limited by the rise time of the amplifier to about 0.25×10^{-6} sec. The coincidence circuits are a modification of one described by Elmore.[3] The associated trigger, delay, and pulse-shaping circuits are modifications of standard designs. A block diagram of the coincidence counting setup is given in Fig. 1. A section of delay line was inserted in one of the fast-coincidence channels in order to determine the accidental counting rate.

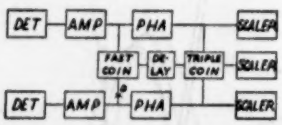

FIG. 1. Block diagram of the experimental arrangement used for gamma-gamma coincidence measurements. The detectors are NaI(Tl) crystals mounted in DuMont type 6292 photomultiplier tubes. The resolving time of the fast coincidence circuit is about 0.25×10^{-6} sec. A delay may be inserted at D in order to determine the accidental rate.

MERCURY DECAY ACTIVITIES

Figure 2 is a gamma-ray spectrum of Hg^{197} produced by the Au(12-Mev$p$,n)Hg reaction. Some gamma rays found by other investigators in conversion electron

* Supported in part by the National Science Foundation.
[1] R. W. Fink and E. O. Wiig, J. Am. Chem. Soc. 74, 2457 (1952).
[2] F. K. McGowan, Phys. Rev. 79, 404 (1950); 93, 163 (1954).
[3] W. C. Elmore, Rev. Sci. Instr. 21, 649 (1950).

spectra[4–7] are not evident here. These missing lines are in all cases either in a weak branch of the decay or are almost wholly converted. The 0.133-Mev line decays with a 24±1 hour half-life which is in agreement with previous work. The 0.279-Mev line decays with a 29±2 hour half-life. It is difficult to decide whether this longer half-life is significant. The half-life determination for the weak 0.279-Mev line is much more subject to a systematic error in procedure than is the case for the 0.133-Mev line. One Hg sample bombarded at 12 Mev shows a slight bump in the gamma-ray spectrum at about 0.58 Mev Therefore, a small contamination of Hg^{195} might be suspected. However, Goldburg and Williamson[8] report an excitation of a 0.55-Mev level in Au^{197} by Coulomb excitation.

Figure 3 is the high-energy region of the gamma-ray spectrum of Hg activities formed by the bombardment of gold with 20-Mev protons. The spectrum was followed over a period of two weeks after which the activity of the weaker lines became impossible to measure effectively. Gamma rays of 1.17±0.02,

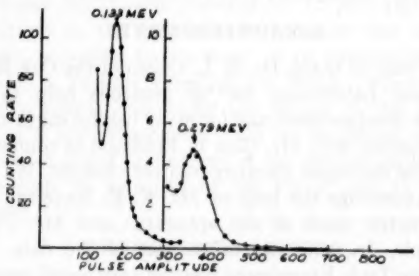

FIG. 2. Plot of the gamma-ray spectrum of the Hg fraction formed by bombardment of gold with 12-Mev protons. Counting rate is plotted against pulse amplitude, both in arbitrary units. This spectrum was obtained two days after bombardment.

0.81±0.02, 0.58±0.02, and 0.255±0.010 Mev energy are clearly seen. The energy values for the 1.17, 0.81, and 0.58 Mev lines are based upon comparison with well-known lines in the decay of Cs^{137}, Co^{60}, and Co^{58}. The energy of the 0.255-Mev line is based upon comparison with the 0.279-Mev line[5] associated with the decay of Hg^{197}.

Figure 4 is a plot of the counting rate due to the 0.81, 0.58, and 0.255 Mev lines *versus* time. Additional data showed that the relative intensities of these lines remained constant over a period of 14 days. We believe the half-lives of these lines are consistent with the single value 42±3 hours. We place these three

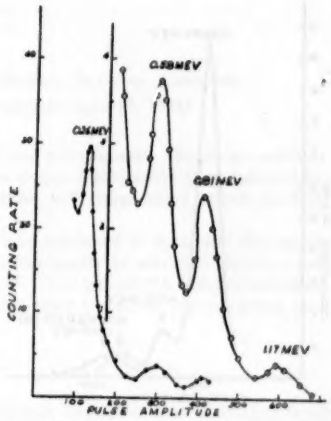

FIG. 3. Plot of the high-energy gamma-ray spectrum of the Hg fraction found by bombardment of gold with 20-Mev protons. Counting rate is plotted against pulse amplitude, both in arbitrary units. This spectrum was obtained three days after the bombardment.

lines in the decay of Hg^{195} formed by the Au^{197}(20 Mev $p,3n$)Hg^{195} reaction. Previous workers have measured the half-life of Hg^{195} as 31,[1] 38,[9] and 40[10] hours. The 1.17-Mev gamma ray is of very weak intensity and precise measurements on it were not possible. Data taken over a period of six days on the relative intensity of the 1.17-Mev line to the lower-energy lines indicate that this line has the same half-life as the other three and is, therefore, probably associated with the decay of Hg^{195}. No 0.5-Mev gamma line due to positron annihilation was detected.

Gamma-gamma coincidence experiments indicate that the 0.81, 0.58, and 0.255 Mev lines are all in coincidence with a line of 0.067 Mev, presumably the Au x-ray following K capture in Hg^{195}. The 0.255- and 0.58-Mev lines are not in coincidence.

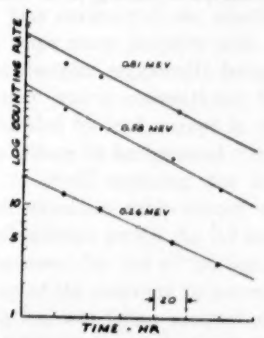

FIG. 4. Plot of the counting rates (in arbitrary units) of the 0.81, 0.58, and 0.26 Mev gamma rays found in Hg^{195} *versus* the time.

[4] Gillon, Gopalakrishnan, de-Shalit, and Mihelich, Phys. Rev. **93**, 124 (1954).
[5] J. W. Mihelich and A. de-Shalit, Phys. Rev. **91**, 78 (1953).
[6] Cork, Martin, Le Blanc, and Branyan, Phys. Rev. **85**, 386 (1952).
[7] Huber, Humbel, Schneider, de-Shalit, and Zunti, Helv. Phys. Acta **24**, 127 (1951).
[8] W. I. Goldburg and R. M. Williamson, Phys. Rev. **94**, 747 (1954).
[9] Douglas, Foster, and Thompson, private communication to Hollander, Perlman, and Seaborg, Revs. Modern Phys. **25**, 469 (1953).
[10] Huber, Joly, Scherrer, and Verster, Helv. Phys. Acta **25**, 621 (1952) and private communication to Hollander, Perlman, and Seaborg, Revs. Modern Phys. **25**, 469 (1953).

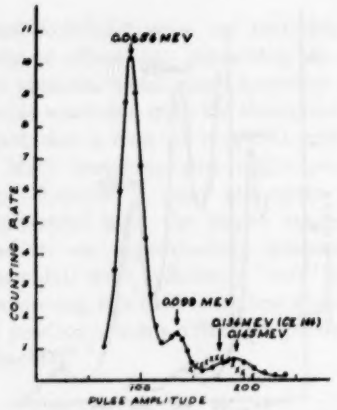

FIG. 5. Plot of the gamma-ray spectrum of Au^{195} resulting from the decay of Hg^{195}. Counting rate is plotted against pulse amplitude, both in arbitrary units. This spectrum was obtained 31 days after the bombardment. The points represented by a cross refer to the gamma-ray spectrum of Ce^{144}.

The gamma ray of 0.255±0.010-Mev energy has been found by several investigators.[4,9,10] A gamma ray of 0.558-Mev energy has been reported in the Hg^{195} activity.[9] A gamma ray of 0.780-Mev energy has been reported in a 9.5-hr Hg^{195} activity.[11] If the 9.5-hr activity of Hg^{195} follows the 38-42 hr metastable state of Hg^{195} as suggested in one decay scheme,[4] the present work would measure no effect of the 9.5-hr period since our measurements were not begun until 35 hours after bombardment.

GOLD ACTIVITIES

The gamma-ray spectra of the separated gold from the targets were also investigated. Activities due to the decay of both Au^{196} and Au^{198} were detected in both the 12- and 20-Mev bombardments. The Au^{196} in the 12-Mev bombardment could be detected only by coincidence techniques. The Au^{198} is atrributed to sufficient neutron flux at the target to produce this activity. The half-lives and gamma spectra were not inconsistent with previously published data.[12]

The Hg^{195} decays into Au^{195}. A plot of the gamma-ray spectrum associated with the decay of Au^{195} obtained 31 days after bombardment is shown in Fig. 5. This activity has been previously studied.[4,12,13] We find a gamma ray of about 0.099-Mev energy in agreement with earlier work. A gamma ray has been previously reported at 0.126–0.130 Mev. All of our data indicate the presence of a higher energy line. We obtain a value of 0.145±0.005 Mev by comparison with the 0.134-Mev gamma ray[12] in the decay of Ce^{144}. A chemical separation of gold from the Hg^{195} source after a period of several weeks shows that these lines are definitely associated with the decay of radioactive gold. We have not measured the half-life of this long-lived activity but our measurements are not inconsistent with the 180-day value previously reported by other workers.

ACKNOWLEDGMENTS

We wish to thank Dr. B. L. Cohen of the Oak Ridge National Laboratory for his generous help in the sample bombardment and for many helpful suggestions. A discussion with Mr. Glen P. Robinson in connection with the electronic circuitry was very helpful. We wish to acknowledge the help of Mr. R. E. Anderson who constructed much of the apparatus and Mr. C. M. Gillespie, Jr., who has taken part of the data. The Georgia Tech Experiment Station purchased some of the isotopes used in this work.

[11] Hollander, Perlman, and Seaborg, Revs. Modern Phys. **25**, 469 (1953).

[12] K. Way *et al.*, *Nuclear Data*, National Bureau of Standards Circular 499 and supplements (U. S. Government Printing Office, Washington, D. C., 1950).

[13] Cork, Le Blanc, Stumpf, and Nester, Phys. Rev. **86**, 414 (1952).

Beta Decay of F^{20}†

CALVIN WONG*
Kellogg Radiation Laboratory, California Institute of Technology, Pasadena, California
(Received February 1, 1954; revised manuscript received April 13, 1954)

The beta decay of F^{20} has been investigated with a magnetic lens spectrometer. The decay proceeds mainly to the first excited state of Ne^{20} by a beta ray of maximum energy 5.419±0.013 Mev, followed by a gamma ray of energy 1.627±0.005 Mev. The excited state transition, with comparative half-life $ft=9.73\times10^4$ seconds, has the allowed shape down to 1 Mev.

A magnetically compensated stilbene scintillation counter has been employed to show that the counts beyond the end point of the intense beta component are due predominantly to scattered electrons and room background. The direct transition to the ground state of Ne^{20} ($Q=7.047\pm0.014$ Mev) is estimated to have a relative intensity of less than $\sim3.2\times10^{-4}$ of the excited state transition, corresponding to a comparative half-life $ft\gtrsim10^9$ seconds.

INTRODUCTION

THE beta decay of F^{20} has been investigated most recently by Alburger[1] who reports that the decay proceeds mainly to the first excited state of Ne^{20} by a beta ray of 5.406±0.017-Mev maximum energy, followed by a gamma ray of energy 1.631±0.006 Mev. The Fermi plot is linear above about 2.5 Mev and direct transitions to the ground state comprise less than 1 percent, according to this work. In the present paper is reported a parallel investigation which confirms Alburger's results concerning the nature of the decay, enables a somewhat lower limit to be placed on the fraction of direct transitions to the ground state, and establishes the linearity of the Fermi plot to lower energies.

EXPERIMENTAL METHOD

Radioactive F^{20} ($\tau_{\frac{1}{2}}=11.4$ sec) was produced by the $F^{19}(d,p)F^{20}$ reaction; CaF_2 targets were bombarded with 2.3-Mev deuterons from the 3-Mev Kellogg Radiation Laboratory electrostatic generator. The deuteron beam was brought directly into the vacuum chamber of the spectrometer to bombard targets at the source position. The beta-ray spectrometer, which is described in an earlier paper,[2] had a resolution of 2 percent, and the effective solid angle was 2.5 percent of a sphere. Helical baffles permit observation of electrons and positrons separately. The momentum calibration was obtained from the average of three independent determinations of the peak position of the internal conversion "X" line of Th-D, $B\rho=9988.4\pm2$ gauss-cm. The compensation for the vertical component of the earth's magnetic field was checked by running the Th-C "I" and "F" lines (222 and 147 kev, respectively), and was found to be satisfactory as evidenced by the fact that the resolution for these lines was the same as that for the high-energy "X" line.

The electron detector was a magnetically compensated stilbene scintillation counter. The stilbene crystal was cylindrical in shape having a diameter and height of one inch. A 57-cm Lucite light pipe was employed to allow operation of the 5819 phototube in a region of comparatively weak magnetic field. The spectrometer field in the region of the phototube was then compensated by employing a suitably designed solenoid connected electrically in parallel with the spectrometer coils. The compensation was checked by placing a gamma-ray source in a fixed position external to the spectrometer proper and observing the counting rate as a function of spectrometer current. Even for the highest currents utilized in the present experiment, the counting rates were constant, showing that the counter sensitivity was not a function of spectrometer current. It was found that the pulse-height output of the counter was directly proportional to the energy of the electrons being focused in the range $E_\beta=0.2$ to 6 Mev. This useful property enables one to distinguish between direct and scattered electrons, since the latter are usually much degraded in energy. One has only to run integral bias curves and see whether or not the integral bias steps move properly with respect to the energy of the electrons supposedly being focused. The monitor counter was a conventional Geiger counter which was shielded by lead, except in the direction of the target, to reduce its background counting rate.

Primarily to avoid counting the intense prompt radiation, the counters were turned off during the 6-second bombardment period. An 0.2-second delay was introduced between the end of the bombardment and the turning on of the counters to insure that only the delayed radiation was being counted and monitored. During the 5.8-second counting period, the deuteron beam was intercepted by a tantalum-backed beam chopper. This cycle was repeated until the monitor counter recorded a fixed number of gamma-ray counts, which indicated that a certain number of beta disintegrations had occurred. The turning on and off of the counters and the operation of the beam chopper

† Assisted by the joint program of the U. S. Office of Naval Research and the U. S. Atomic Energy Commission.
* Present address: University of California Radiation Laboratory, Livermore, California.
[1] D. E. Alburger, Phys. Rev. **88**, 1257 (1952).
[2] Hornyak, Lauritsen, and Rasmussen, Phys. Rev. **76**, 731 (1949).

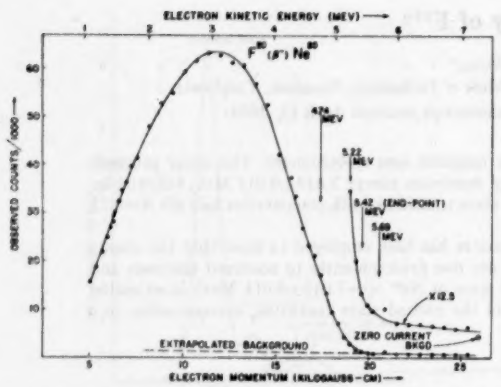

FIG. 1. Electron spectrum from the beta decay of F^{20}. The spectrum was run with a counter bias of 10 volts which corresponds to counting all electrons with energies ≥ 900 kev. The zero current background has not been subtracted from the spectrum.

were accomplished by a system of relays actuated by a synchronous motor.

ELECTRON SPECTRUM

For the beta-spectrum measurements, a thin layer of CaF_2 was evaporated on 0.1-mil nickel foil. This foil was then supported by a 5-mil aluminum foil which had a $\frac{3}{8}$-inch hole in its center. The observed spectrum, displayed in Fig. 1, shows the main component having an end point at about 5.42 Mev and a tail extending to higher energies. The tail eventually runs into the zero current background which represents the sum of room background plus gamma-ray background from the $F^{20}(\beta^-)Ne^{20*}$ reaction. The field-sensitive part of the tail, particularly the broad fillet in the region of 5.69 Mev, is attributed either to scattered electrons or to the ground-state transition ($Q=7.05$ Mev). In order to determine to what extent scattering is present, the energy distribution of the electrons at a spectrometer setting of 5.69 Mev was analyzed by running an integral bias curve with the scintillation counter detector. For

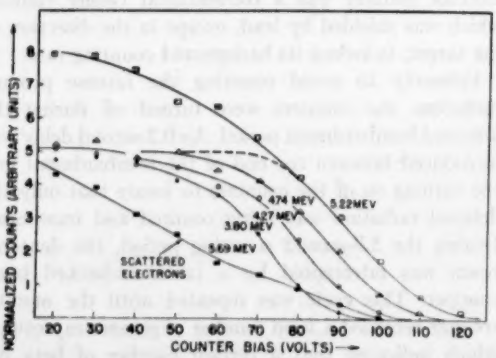

FIG. 2. Integral bias curves of the F^{20} beta spectrum. The dashed portion of the 5.22-Mev curve represents what would be observed if scattered electrons were not present.

purposes of comparison, integral bias curves were also run at spectrometer settings corresponding to 5.22, 4.74, 4.27, and 3.80 Mev. The results are shown in Fig. 2, where the curves have been normalized in accordance with the beta spectrum of Fig. 1. In addition, the curves have been corrected for room background and gamma-ray background from the $F^{20}(\beta^-)Ne^{20*}$ reaction by subtracting the zero current integral bias curve from the observed bias curves. As can be inferred from Fig. 1, the zero current background correction was negligible in the case of the three lower energy curves of Fig. 2 because of the relatively large number of beta counts.

At 4.74 Mev, for example, where it is clear from Fig. 1 that most of the counts are due to focused electrons, the bias curve displays a reasonably flat plateau indicating that the electrons are monoenergetic. The half-value point, 87 volts, agrees with that expected from the energy calibration of the crystal and the

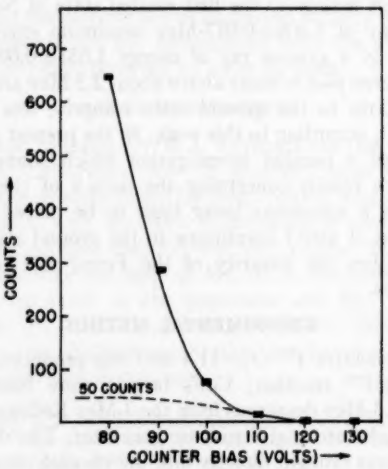

FIG. 3. The 5.69-Mev bias curve plotted on an expanded vertical scale in the region beyond 80 volts.

momentum setting of the spectrometer. At 5.69 Mev, however, it is apparent that focused electrons are almost totally absent since the bias curve does not display the integral bias step expected from 5.69-Mev electrons. Furthermore, since the integral bias curve is a sloping straight line, its differential bias curve is a rectangle which indicates that, below approximately 4 Mev, electrons of all energies are present in equal amounts. This again suggests that the counts recorded at 5.69 Mev, after subtracting the zero current background, are due predominantly to scattered electrons. The 5.22-Mev curve, on the other hand, shows a transition shape consistent with the expectation from extrapolating the fillet of Fig. 1 that about a third of the recorded counts, after subtracting the zero current background, are due to scattered electrons. In order to establish a rough upper limit on the number of true 5.69-Mev electrons that could be present, one may fit a calculated 5.69-Mev

bias step to the observed bias curve at a point where the bias step should reach half-maximum, i.e., at approximately 105 volts. This is depicted in Fig. 3, where the 50 counts represent the maximum admixture of 5.69-Mev electrons allowable on the basis of the observed integral bias curve. Comparing this figure with the 374 000 counts observed at the peak of the excited state component, and assuming an allowed shape for the ground-state transition, a rough upper bound of 3.2×10^{-4} is obtained for the ground-state branching ratio. On the basis of the present experimental evidence, it cannot be said that the branching ratio is equal to 3.2×10^{-4} since the 5.69-Mev curve does not show enough structure to make possible a positive identification.

Since scattering was shown to be present, its effect upon spectrum shape and measured end point was determined experimentally by running the beta spectra of Na^{22} and P^{32}. The Na^{22} Fermi plot, Fig. 4, is linear down to 200 kev, and the 540-kev end point is in agreement with the currently accepted value of 542 ± 5 kev.[3] The P^{32} Fermi plot, not displayed, is linear down to 330 kev, and the 1.714 ± 0.006 Mev end point is in agreement with the 1.707 ± 0.004-Mev value quoted by Li.[4] The effects of scattering upon spectrum shape and measured end point are thus negligible above about 300 kev.

TABLE I. Contributions of various sources of error.

Source of error	Error in end point (Mev)
Background	±0.010
Calibration	±0.006
Error in fitting Kurie plot (above 2.8 Mev)	±0.005
Statistical	±0.004
Total probable error in end point	±0.013

The background correction for the beta spectrum was obtained by a straight line extrapolation of the high-energy tail to lower energies as shown in Fig. 1. This method of background subtraction has no *a priori* justification except that its application to the Na^{22} and P^{32} beta spectra gave end points in good agreement with currently accepted values. From Fig. 1, it is evident that the zero current background accounts for the major part of the extrapolated background. Subtracting the high-energy tail and the extrapolated background and making the usual Fermi plot yielded the straight line of Fig. 5. A straight line fits the data from the end point down to 1 Mev. The values of the Fermi function $f=Fp^2$ were obtained from tables published by the National Bureau of Standards.[5] A least-squares analysis

[3] Macklin, Lidofsky, and Wu, Phys. Rev. **78**, 318 (1950).
[4] C. W. Li, Phys. Rev. **88**, 1038 (1952).
[5] *Tables for the Analysis of Beta Spectra*, National Bureau of Standards; Applied Mathematics Series (U. S. Government Printing Office, Washington, D. C., 1952), Vol. 13.

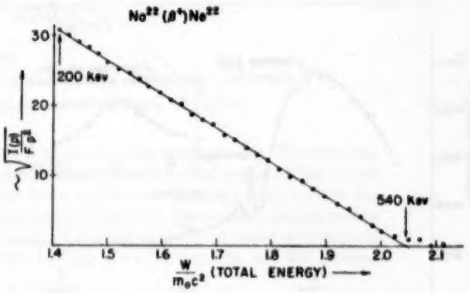

FIG. 4. Fermi-Kurie plot of the Na^{22} positron spectrum.

of four sets of data between 2.8 and 5.4 Mev gave an end-point energy of 5.419 ± 0.013 Mev. The end-point value includes a three kev correction for energy loss in the Ni foil. The data below 2.8 Mev usually displayed more scattering and hence were disregarded in the least-squares solutions for the end point. Table I shows how the various sources of error contribute to the final probable error of ±0.013 Mev.

The principal source of uncertainty in the end-point value lies in the estimate of background: a variation of a factor of two in the background value assumed would not have noticeably affected the straightness of the plot, but would have changed the apparent end point by 14 kev. Due to difficulty in estimating the exact contribution from scattered electrons throughout the spectrum, the background in the present case is uncertain to about ±70 percent, and the resulting uncertainty in the end point is ±10 kev. It may be remarked this source of error seems to have been frequently disregarded in the literature and may account for some of the discrepancies which have appeared in β-ray end point determinations.

GAMMA-RADIATION SPECTRUM

For the delayed gamma-ray measurements, a 40-mil CaF_2 crystal, 150-mil copper absorber, and a 23.2-mg/cm^2 thorium converter were used. The observed

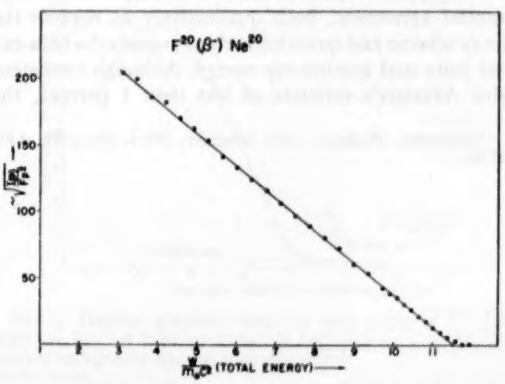

FIG. 5. A typical Fermi-Kurie plot of the F^{20} electron spectrum.

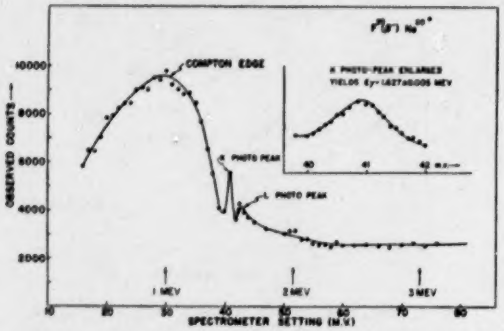

FIG. 6. Gamma radiation from the beta decay of F^{20}. In the upper right-hand corner, the K photopeak is shown enlarged.

spectrum, shown in Fig. 6, shows the Compton edge, K and L photopeaks from a single gamma ray. The gamma-ray energy was obtained by adding the K binding energy of thorium plus a converter shift correction[2] to the measured energy of the K photoelectrons. An average of four independent determinations yielded 1.627 ± 0.005 Mev as the gamma-ray energy. The position of the Compton edge is consistent with a gamma ray of this energy.

As a check on the accuracy of the gamma-ray measurements, the Co^{60} K photoelectric peak was run using the same absorber and converter geometry. An average of two determinations gave 1.332 Mev as the gamma-ray energy, in good agreement with the currently accepted value of 1.3325 ± 0.0003 Mev.[6]

DISCUSSION

The present investigation confirms that the decay proceeds mainly to the first excited state of Ne^{20} by a beta ray of maximum energy 5.419 ± 0.013 Mev, followed by a gamma ray of energy 1.627 ± 0.005 Mev. The Fermi plot is linear down to 1 Mev, and direct transitions to the ground state is estimated to have a relative intensity of less than 3.2×10^{-4} of the excited state transition.

Comparison with the results of Alburger shows substantial agreement, both qualitatively as regards the decay scheme and quantitatively as regards the beta-ray end point and gamma-ray energy. Although consistent with Alburger's estimate of less than 1 percent, the upper limit for the ground-state branching ratio is now a factor of thirty smaller. As regards the Fermi plot, it is not obvious why Alburger's plot deviates from linearity at approximately 2.5 Mev; the target thicknesses were comparable while the source backing was twice as thick in the present experiment.

Adding a 1-kev correction for the Ne^{20} recoil (the calculated correction being 0.92 kev), the $F^{20}-Ne^{20}$ atomic mass difference is 7.047 ± 0.014 Mev. Using, in addition, the Q values for the $F^{19}(d,p)F^{20}$ and $Ne^{20}(d,p)Ne^{21}$ reactions,[4] the predicted Q value for the $Ne^{21}(d,\alpha)F^{19}$ reaction is 6.442 ± 0.019 Mev. This is in agreement with the value determined by Whaling and Mileikowsky: 6.432 ± 0.010 Mev.[7]

Since Alburger's publication, two additional pieces of information affecting the F^{20} beta decay have become available. Seed[8] and Richards[9] report that the Ne^{20} first excited state has the assignment 2+. Bromley *et al.*,[10] applying the Butler stripping theory to the $F^{19}(d,p)F^{20}$ reaction, report that the F^{20} ground state has the assignment 1+. The excited state transition is thus $\Delta J=1$; no parity change, and hence allowed. This agrees with the experimental evidence: the Fermi plot is linear down to 1 Mev and the comparative half-life ft equals 9.73×10^4 seconds ($E_{\beta\,\max}=5.42$ Mev and $\tau_{\frac{1}{2}}=11.4$ seconds). Since the Ne^{20} ground state is 0+, the ground-state transition is also $\Delta J=1$; no parity change, and hence should be allowed. However, the upper limit of 3.2×10^{-4} for the ground-state branching ratio yields a comparative half-life $ft\gtrsim10^9$ seconds. The ground-state transition appears then to be at least first forbidden. A possible explanation for the apparent anomaly is that the transition is l forbidden. Nordheim[11] lists 7 ground-state transitions involving even-A nuclei as l forbidden with logft ranging from 5.0 to 9.0.

The author is grateful to W. Whaling for suggesting the problem and to T. Lauritsen for guidance during the course of the experiment. He is also grateful to C. Mileikowsky, W. A. Fowler, and R. F. Christy for helpful discussion. In particular, he is indebted to D. E. Alburger for communicating his results prior to publication, and for his helpful criticism about experimental technique.

[6] Lindström, Hedgran, and Alburger, Phys. Rev. **89**, 1303 (1953).

[7] C. Mileikowsky and W. Whaling, Phys. Rev. **88**, 1254 (1952).

[8] J. Seed, Phil. Mag. **44**, 921 (1953).

[9] H. T. Richards, Indiana University Conference, 1953 (unpublished).

[10] Bromley, Bruner, and Fulbright, Phys. Rev. **89**, 396 (1953).

[11] L. W. Nordheim, Revs. Modern Phys. **23**, 322 (1951).

Beta Decay of F^{17} and C^{11}†

CALVIN WONG
Kellogg Radiation Laboratory, California Institute of Technology, Pasadena, California
(Received February 1, 1954; revised manuscript received April 13, 1954)

The beta decay of F^{17} and C^{11} has been investigated with a magnetic lens spectrometer. The positron spectrum of F^{17} consists of one component of maximum energy 1.748±0.006 Mev. The ground-state transition, comparative half-life $ft=2420$ sec, has the allowed shape down to 570 kev. Beta-ray branching to the first excited state of O^{17} at 874 kev, if present, has a relative intensity of less than one percent, corresponding to a comparative half-life $ft \gtrsim 2\times10^4$ sec. The positron spectrum of C^{11} consists of one component of maximum energy 968±8 kev. The ground-state transition, comparative half-life $ft=4170$ seconds, has the allowed shape down to 255 kev.

INTRODUCTION

IN the preceding paper (hereafter referred to as I) some results on the beta decay of F^{20} are reported. In this paper, a brief account will be given of the results obtained in investigating two mirror ("superallowed") transitions in the light elements. The beta decay of F^{17} has been investigated most recently by Perez-Mendez and Lindenfeld,[1] who report that the beta spectrum, end-point energy 1.72±0.03 Mev, deviates from linearity around 775 kev. This deviation from linearity is not due to beta-ray branching to the known 874-kev level in O^{17} since Perez-Mendez and Lindenfeld[2] report the absence of gamma radiation in the beta decay of F^{17}. In addition, Meyerhof[3] reports that in the beta decay of F^{17} less than one percent of the beta transitions result in gamma radiation. In the interest of establishing the linearity of the Fermi plot below 800 kev, and of determining more accurately the end point, it was felt that the beta spectrum of F^{17} should be remeasured. The beta spectrum of C^{11} has been measured by Townsend[4] and Siegbahn and Bohr.[5] They find a simple allowed spectrum with end point 0.981±0.005 and 0.993±0.010 Mev, respectively. It was felt that the C^{11} spectrum should be remeasured since the above-reported beta-ray end points are considerably higher than that expected from the $B^{11}(p,n)C^{11}$ threshold measurement. The threshold measurement reported by Richards and Smith[6] indicates a beta-ray end point of 0.958±0.003 Mev; the discrepancies thus lie outside the combined probable errors.

EXPERIMENTAL METHOD

Radioactive F^{17} ($\tau_{\frac{1}{2}}=66$ sec) was produced by the (d,n) reaction on O^{16}. PbO targets, evaporated on 0.15-mil aluminum foils, were bombarded with 2.1-Mev deuterons from the 3-Mev electrostatic generator. Radioactive C^{11} ($\tau_{\frac{1}{2}}=20.4$ min) was produced by the $B^{10}(d,n)C^{11}$ reaction. Thin B_2O_3 targets, having 0.15-mil aluminum backings, were bombarded with 1.77-Mev deuterons. The bombarding energy is below the $O^{16}(d,n)F^{17}$ threshold at 1.836 Mev[7] since F^{17} positrons would interfere with the measurement of the C^{11} spectrum. The spectra were normalized by directly comparing the counts at each point of the spectrum with that observed at a selected reference point. The targets were bombarded for a time comparable with the half-life, at the end of which the accelerator was shut down before the counting interval commenced. During the measurements, the half-life was carefully checked to insure that the positrons counted were from the F^{17} or the C^{11}. For a description of the beta-ray spectrometer and the scintillation counter detector, the reader is referred to I.

EXPERIMENTAL RESULTS

The observed positron spectrum from F^{17} is shown in Fig. 1, while the corresponding Fermi plot is shown in Fig. 2. An average of three independent determinations gave an end-point energy of 1.748±0.006 Mev. The C^{11} positron spectrum is displayed in Fig. 3, while the

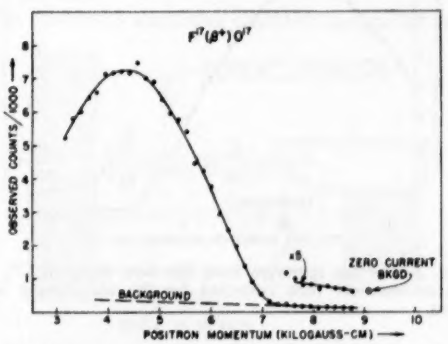

FIG. 1. Positron spectrum from the beta decay of F^{17}. The spectrum has not been corrected for background, i.e., the zero-current background has not been subtracted.

† Assisted by the joint program of the U. S. Office of Naval Research and the U. S. Atomic Energy Commission.

[1] V. Perez-Mendez and P. Lindenfeld, Phys. Rev. **80**, 1097 (1950).

[2] V. Perez-Mendez and P. Lindenfeld, Phys. Rev. **83**, 864 (1951).

[3] W. E. Meyerhof (private communication to F. Ajzenberg and T. Lauritsen).

[4] A. A. Townsend, Proc. Roy. Soc. (London) **177**, 357 (1940, 41).

[5] K. Siegbahn and E. Bohr, Arkiv Mat., Astron. Fysik **30B**, No. 3 (1944).

[6] H. T. Richards and R. V. Smith, Phys. Rev. **77**, 752 (1950).

[7] T. W. Bonner and J. W. Butler, Phys. Rev. **83**, 1091 (1951).

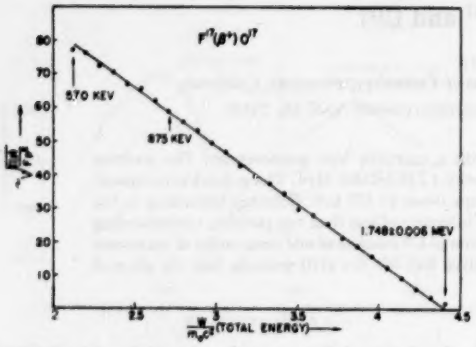

FIG. 2. Fermi-Kurie plot of the F^{17} positron spectrum.

corresponding Fermi plot is shown in Fig. 4. An average of three independent determinations gave an end-point energy of 968±8 kev. For both spectra, the least-squares solutions agree with the graphical ones to within 2 kev. It is of interest to note that the high-energy background tail of Figs. 1 and 3 is very similar to that which is observed with the F^{20} electron spectrum. This suggests, as is shown in I, that the slightly field-sensitive background is instrumental in origin, i.e., is attributed to the small degree of scattering present. However, the major part of the background correction is attributed to the constant zero-current background which has not been subtracted in Figs. 1 and 3. The method of background subtraction and analysis is similar to that described in I.

DISCUSSION

The Fermi plot of Fig. 2 is linear from the end point down to an energy of 570 kev. If the beta spectrum were complex, a deviation from linearity should occur around 875 kev. Since this is not observed experimentally, it is concluded that the spectrum is simple, and that the deviation from linearity observed in reference 1 is presumably due to scattered positrons caused perhaps by excessive source thickness. From an examination of the Fermi plot, an upper limit can be put on the transition to the known 874-kev level in O^{17}. If the excited-state transition does occur, its intensity is less than 1 percent (assuming an allowed shape for the excited-state component). The experimentally determined half-life of 66.0±1.8 sec coupled with the end-point determination gives an *ft* value of 2420 sec for the ground-state transition. The low *ft* value and the straight-line Fermi plot show that the transition is "superallowed." From the upper limit for the branching ratio, the minimum *ft* value for the excited-state transition is approximately 2×10^4 sec. This minimum estimate is reasonable since the assignment of spins and parities[8] predicts a second forbidden transition, *ft* of the order of 10^{13} sec.[9] The 1.748±0.006 Mev end point is in agreement with the 1.745±0.006 Mev expected from the *Q* values for the $O^{16}(d,n)F^{17}$ and $O^{16}(d,p)O^{17}$ reactions.[10]

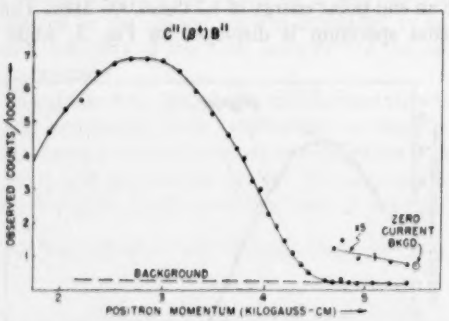

FIG. 3. Positron spectrum from the beta decay of C^{11}. The spectrum has not been corrected for the zero-current background.

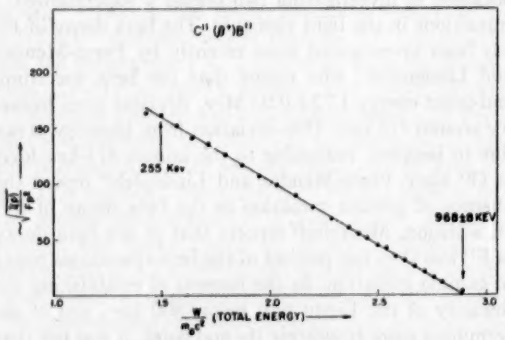

FIG. 4. Fermi-Kurie plot of the C^{11} positron spectrum.

The C^{11} Fermi plot, Fig. 4, is linear from the end-point down to 255 kev. The end-point energy of 968 kev coupled with a half-life of 20.4 min gives an *ft* value of 4170 sec for the ground-state transition. Hence the *ft* value and the allowed shape of the spectrum confirm the "superallowed" nature of the transition (C^{11} and B^{11} are mirror nuclei). The *ft* value lies within the accepted range for mirror transitions: *ft* between 1000–5000 sec. The 968±8 kev end point agrees with that expected from the $B^{11}(p,n)C^{11}$ threshold measurement within the combined probable errors.

[8] F. Ajzenberg and T. Lauritsen, Revs. Modern Phys. **24**, 321 (1952).
[9] Mayer, Moszkowski, and Nordheim, Revs. Modern Phys. **23**, 315 (1951).
[10] C. W. Li, Phys. Rev. **88**, 1038 (1952).

Coulomb Excitation of Ta, W, and Au†

W. I. GOLDBURG AND R. M. WILLIAMSON
Department of Physics, Duke University, Durham, North Carolina

(Received April 20, 1954)

By using protons as bombarding particles, a study has been made of the yields and angular distributions of Coulomb-excited gamma rays in tantalum (137, 166, 303 kev), tungsten (114 kev), and gold (277, 195, 545 kev). Coincidence experiments show that the 277-kev and the previously unreported 545-kev transition go to the ground state and that the Ta 166-kev line represents a cascade from 303 kev. Thin-target yield data for the 277-kev gamma gives an absolute cross section which is in approximate agreement with the theory while the absolute cross section for the 545-kev transition is seven times too large. [*Note added in proof.*—On correcting an arithmetical error the absolute cross section for the 545-kev transition is also found to be in approximate agreement with the theory.] In both cases the experimental cross sections increase more rapidly than the theory. Thick-target yields from the five strongest gamma rays are greater than the theory by factors ranging from 6 to 100 percent between proton energies of 2 and 4 Mev. Agreement with the theory becomes worse with increasing level energy and decreasing proton energy. On the basis of the theory the angular distribution data permit an unambiguous spin assignment of 7/2 to the 545-kev level and give agreement with the previously established spins for the 277 (Au), 137, 303 (Ta), and 114-kev (W) levels. The ratio of $E2$ to $M1$ radiation is $7_{-5}^{+13}/100$ for the 277-kev radiation (Au) and less than 5/100 for the 137-kev radiation (Ta).

INTRODUCTION

THE present investigation was undertaken to examine the quantitative predictions of present theories concerning the yields[1] and angular distributions[2] of gammas resulting from Coulomb excitation of nuclei by incident charged particles. We also wish to compare the observed energy levels with the predictions of the collective model.[3] Since the initial experimental work done by Huus and Zupančič[4] and McClelland and Goodman,[5] a search for Coulomb excited gamma rays has been carried out in many elements using both alpha particles[6,7] and protons. Thick target yield studies[4,6] have been made on Ta and the angular distribution of Ta lines has been studied.[8] We have surveyed spectroscopically pure targets of Ta, W, and Au bombarded by 4-Mev protons, for gammas having energies different than the K and L x-rays. Coincidence measurements were made in order to check decay schemes. The thin target yields of two gold gammas and thick target yields of gammas from all targets are compared with each other and with theory. Angular distributions of the five strongest gammas are reported and compared with theory.

EXPERIMENTAL ARRANGEMENT

The proton source for these experiments was the Duke 4-Mev Van de Graaff accelerator.[9] The proton energy resolution and accuracy were both better than 0.05 percent after 25° deflection in a magnet equipped with a proton-moment fluxmeter. The target and detector area was shielded from the machine by a concrete block wall. Figure 1 shows the setup for the thin-target yield measurements. Since Rutherford scattering of the proton beam by the target foil was considerable, a large-diameter collecting chamber lined with lead was used. (We have verified Goodman's report[5] that protons excite no levels in lead.) Thin Ta lining in the tubing ahead of the target improved the background. When thick targets were mounted at D (Fig. 1), the collector (E) was removed. The target insulation and current integrator[10] input were periodically checked with a megger. The lead diaphragm (A) in Fig. 1 was made larger than the defined beam; it served to stop collimating slit-scattered particles and to absorb gammas. Current integration appeared reproducible to ±1 percent when the beam current was held constant to 10 percent.

The cylindrical scattering chamber used in the angu-

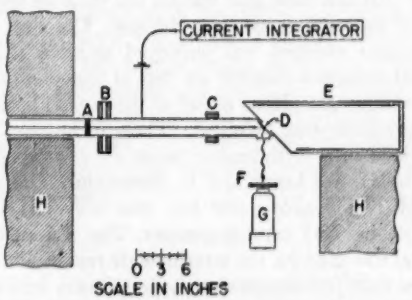

FIG. 1. Thin-target assembly showing: A—lead diaphragm; B—insulated flanges; C—coupling joint; D—thin foil; E—lead-lined beam collector; F—absorbers; G—scintillation counter; H—concrete shielding.

† This work was supported by the U. S. Atomic Energy Commission.

[1] K. A. Ter-Martirosyan, J. Exptl. Theoret. Phys. (U.S.S.R.) **22**, 284 (1952).
[2] K. Alder and A. Winther, Phys. Rev. **91**, 1578 (1953).
[3] A. Bohr and B. R. Mottelson, Kgl. Danske Videnskab. Selskab. Mat.-fys Medd. **27**, No. 16 (1953).
[4] T. Huus and Č. Zupančič, Kgl. Danske Videnskab. Selskab, Mat.-fys Medd. **28**, No. 1 (1953).
[5] C. L. McClelland and C. Goodman, Phys. Rev. **91**, 760 (1953).
[6] N. P. Heydenburg and G. M. Temmer, Phys. Rev. **93**, 351 (1954).
[7] N. P. Heydenburg and G. M. Temmer, Phys. Rev. **93**, 906 (1954).
[8] Class, Cook, and Eisinger, Phys. Rev. **94**, 747 (1954).
[9] Designed and built by the High Voltage Engineering Corporation.
[10] R. C. Mobley (to be published).

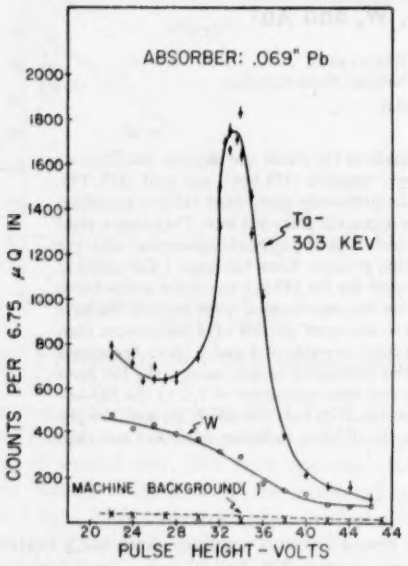

FIG. 2. Pulse-height spectrum from the 1.5-in.×0.5-in. NaI crystal showing the thick Ta 303-kev photopeak, the thick W spectra, and machine background. The proton energy is 4 Mev and the counter distance is 2 in.

lar distribution measurements was 5.25 in. in diameter, 6.0 in. deep, and had 0.12-in. aluminum walls. It was connected at point (*C*) in Fig. 1. The target could be rotated about the axis of symmetry. The chamber was lined with 0.020-in. cadmium in order to prevent the scattered protons from producing gammas in the aluminum walls. It was necessary to use thick (0.004-in.) targets for all angular distribution measurements. An attempt to use thin foils failed because of the size of the background produced when the proton beam struck the chamber wall.

A NaI crystal counter 1.5 in. in diameter and 0.5 in. thick was placed at 4 in. to 6 in. from the target in all angular distribution measurements. The DuMont 6292 photomultiplier tube was magnetically shielded in order that the tube gain remain the same as the direction of the counter axis was changed. The x-ray region of gamma energies was surveyed using a thin NaI crystal mounted directly on top of the phototube; a $\frac{1}{8}$-in. diaphragm placed ahead of the crystal limited the photocathode area involved. (These techniques will be described in a forthcoming paper on *L* x-ray production by H. W. Lewis and E. Bernstein.) The gamma energy region above 600 kev was surveyed using a 2-in.×2-in. NaI crystal counter. The 1.5-in.×0.5-in. crystal was used for the intermediate region. Phototube pulses were fed throgh a cathode follower into an A-1 linear amplifier and then put into a single-channel differential pulse-height analyzer. Care was taken at all times not to exceed maximum equipment counting rates. Gamma-energy calibrations were made relative to the Pb *K* line and 191, 277, 364, 511, and 662-kev gammas from In^{114*}, Hg^{203}, I^{131}, Na^{22}, and Cs^{137}. The coincidence circuit was similar to that published by Burke and Risser.[11] It has pulse-height discrimination in both channels, a resolving time of 0.1 microsecond, and recorded gross and accidental counts simultaneously.

PROCEDURE AND DISCUSSION OF ERRORS

Our ability to locate the background below the NaI scintillator photopeaks was the main factor limiting our determination of relative gamma intensities. We approached the problem two ways. Figure 2 shows the Ta 303-kev gamma photopeak along with the W yield in that region as well as the machine background. The Pb yield (not shown) was found to be very much the same as the W yield. These targets were spectroscopically pure. Curves taken with added absorber in front of the scintillator indicated a hard background, presumably due to gammas from vacuum system impurities, about three times machine background in each target. The remainder of the W and Pb yield is consistent with calculated bremsstrahlung yield from the incident protons.[12] Since Pb and W have no gammas in or above this region, they should be a measure of the Ta background.[4] The shape of the corrected Ta curve is in excellent agreement with the spectrum of 277-kev gammas from a Hg^{203} source placed at the position of the Ta target. The gold 277-kev gamma (Fig. 3) also submitted nicely to this comparison after the gold 545-kev Compton distribution was subtracted from the data. Data taken with varied absorber thicknesses and counter distances indicated that the background could be located within 25 percent. Gamma peaks varied from four to ten times background. Statistical errors were limited to 2 percent. Absolute cross sections quoted are based on calculated scintillator efficiency and are therefore approximate.

Full-proton-energy yield curves were taken on all strong lines in order to verify their nonresonant behavior and similarity to the theoretical yields. Then several repeated yield ratios were taken at the selected

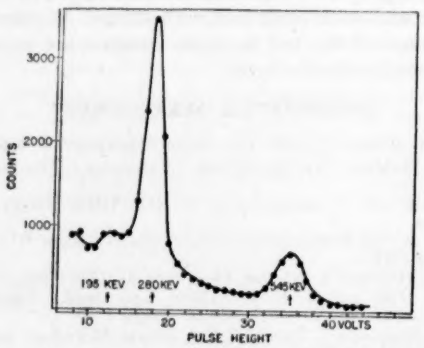

FIG. 3. Gammas from thick gold bombarded by 3.86-Mev protons. 0.5-in.×1.5-in. NaI crystal at 5 in. with 0.069-in. Pb absorber added.

[11] W. H. Burke and J. R. Risser, Phys. Rev. **87**, 294 (1952).
[12] Č. Zupančič and T. Huus. Phys. Rev. **94**, 205 (1954).

proton energies. The proton beam current was held constant within 10 percent for all data. In all cases these ratios agreed with each other within the ±3-percent counting statistics.

The symmetry of the angular distribution setup was checked by observing the Au 545-kev gamma at angles of 0°, 45°, 90°, 135°, 225°, 270°, and 315°. The 0.004-in. target foil was thin for this radiation. Since the rather small anisotropies observed showed nothing other than $\cos^2\theta$ dependence, repeated points were then taken at 270°, 0°, and 90° counter angles. The target angle was set so that gammas always traversed $\sqrt{2}$ times the target thickness. Runs were taken at both 45° target angles when the counter angle was 0° in order to check the target setting.

The effect of Compton scattering of the observed gamma rays both in the target itself and in the material between it and the detector was considered. Placing a 0.010-in. Ta sheet, which was thicker than any of the targets used, behind the gold target had no effect on the anisotropy of the 277-kev line. The change of the Compton cross section, as a function of gamma-ray energy, is not sufficiently great to require our repeating this experiment for all the lines studied. By varying the amount of scattering material near the detector we likewise showed that Compton scattering produced in the chamber wall and in the absorbers was negligible.

RESULTS

A. Observed Energy Levels

Only previously observed 137, 166, and 303-kev gammas were found in pure Ta. There were 1.7±0.1 times as many 166 as 303-kev gammas—in agreement with previous data.[8] Data using both 0.25-in. Cu and 0.069-in. Pb absorbers were analyzed in order to establish this figure. We also established the coincidence of the 137- and 166-kev gammas, but were unable to use this data as a check on the 303-kev level branching ratio. No levels other than the 114 kev, the average of gammas from four isotopes,[13] were observed in W.

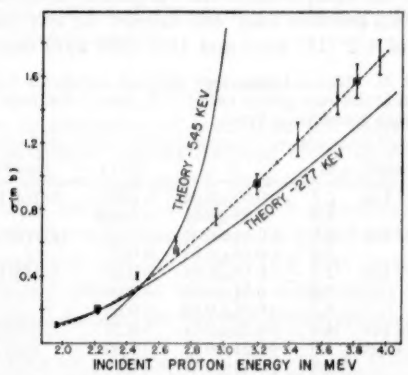

FIG. 4. Yield of 277-kev gammas from 0.0001-in. Au foil mounted at 45° to the incident proton beam. The theoretical cross section has been slightly modified to allow comparison with the 300-kev target. The measured absolute cross section has a possible error of +50 percent. Theoretical curves are drawn for several assumed level energies.

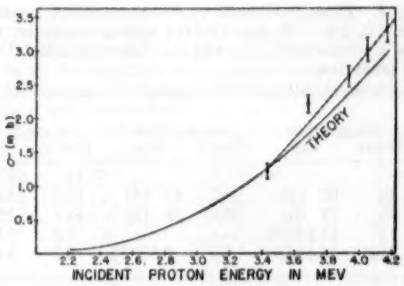

FIG. 5. Yield of 545-kev gammas from 0.0001-in. Au foil mounted at 45° to the incident proton beam. The theoretical cross section has been slightly modified to allow comparison with the 300-kev target thickness. The measured absolute cross section has a possible error of +50 percent. *Note added in proof.*—Cross-section scale should be multiplied by 1.0×10^{-1}.

Previously reported gammas[7,14] of 195±10 and 277 ±5 kev were observed in gold. A new gamma at 545±8 kev is shown in Fig. 3. (This gamma has also been observed by C. M. Class, private communication.) The 195-kev gamma is better defined in data at lower proton energies. The most recent beta decay data[14] give levels at 77, 268, and 279 kev which involve excitation spin changes equal to or less than two. We compared our 277-kev photopeak shape very carefully (at 2- and 4-Mev proton energies) with the 277-kev Hg^{203} gamma and find no evidence of a 268-kev gamma. We also looked for 277–268 kev coincidences and found that the 545-kev level decays by cascade radiation to these levels less than 10 percent of the time. No 545–277 kev or 545–191 kev coincidences were observed. 545–77 kev coincidences could not be checked because of the dominant Au K x-rays. Thus it appears that Au has a 545-kev level decaying directly to the ground state.

Weak high-energy gammas of 840, 1000, 1360, and 1720 kev were observed in each of the three targets and are assumed to be from surface impurities from the vacuum system. These peaks were 2 to 10 percent of the Ta 303-kev peak and were about 10 times machine background. A yield curve run on the 1720-kev/gamma showed thin target resonances. Further, we observed both the K x-ray escape peaks and Ag K x-rays in commercial purity gold and platinum. Pure gold later showed no Ag K x-ray. The $1/Z^{12}$ cross-section dependence of K x-ray production greatly magnifies light element impurities when the low-gamma-energy region is being surveyed.

B. Yields

Figures 4 and 5 show the energy dependences of the thin target yields of the 277- and 545-kev gold gammas compared with the theoretical excitation of levels of those energies. A comparison of the magnitudes of

[13] McClelland, Mark, and Goodman, Phys. Rev. **93**, 904 (1954).
[14] J. W. Mihelich and A. de-Shalit, Phys. Rev. **91**, 78 (1953).

TABLE I. Theoretical and experimental thick-target yield ratios at 4.0, 2.5, 2.25, and 2.0-Mev proton energy for the five strongest gammas in W, Ta, and Au. The experimental error is given in parentheses.

Gamma energy (kev)	$I(4.0)/I(2.0)$ Theory	$I(4.0)/I(2.0)$ Exp.	$I(4.0)/I(2.25)$ Theory	$I(4.0)/I(2.25)$ Exp.	$I(4.0)/I(2.5)$ Theory	$I(4.0)/I(2.5)$ Exp.
545					40	65 (6)*
303	46	97 (12)	20.8	33 (3)	10.7	12.7(0.7)
277	46	79 (6)	20.8	28 (2)	10.7	12.9(0.7)
137	14	13.8(0.8)	...	...	5.2	5.5(0.3)
114	11.2	13.4(0.8)	7.1	7.8(0.5)	5.2	5.1(0.3)

measured cross sections with the theory for the excitation of rotational levels[3] is necessarily approximate because the quadrupole moment of gold has not been measured and our scintillators were not accurately calibrated. We have tried using $Q=0.6\times10^{-24}$ cm^2—obtained by extrapolation from the curve of experimentally measured quadrupole moments.[16] The 277-kev cross section is within a factor of two of the calculated cross section, while the 545-kev cross section is eight times the calculated cross section at a proton energy of 4 Mev.* The size of the 277-kev gamma yield curve at low energies indicates that it is not a transition from a level of much higher energy.

Table I lists thick target yield ratios. The experimental error quoted is the sum of the background uncertainties at the two energies being compared.‡

C. Angular Distributions

The third column of Table II contains the results of our distribution measurements. We have tabulated the anisotropy (C) at various energies for the five gamma rays studied. C is defined as

$$C=[I(E_p,0°)-I(E_p,90°)]/I(E_p,90°).$$

$I(E_p,\theta)$ is the gamma-ray photopeak intensity, corrected for background, at a proton energy E_p and at an angle θ with respect to the proton beam.

The strong energy dependence of the Coulomb excitation cross sections makes the comparison of the experimental thick-target angular distributions and the calculated thin-target values meaningful. With the exception of tungsten, the data support the predicted slow energy dependence of the distribution.[3] Both of these factors, *viz.*, the strong energy dependence of the yield and the weak energy dependence of the anisotropy, make comparison of the magnitude of the thick-target angular distribution and the theoretical thin-target distribution valid. The intensity of the 545-kev gamma was insufficient to measure its angular distribution below 4 Mev.

Only the anisotropies are quoted because all angular distributions measured were indistinguishable from $\cos^2\theta$ distributions. The theoretical values of the anisotropy which best fit the observed distributions appear in the column headed "C_2+C_4." The angular distribution function, whose derivation by Alder and Winther is based on the assumption of pure electric quadrupole excitation, is given by

$$W(\theta)=\frac{8-4B_2a_2+3B_4a_4}{8}\left(1+\left[\frac{12B_2a_2-30B_4a_4}{8-4B_2a_2+3B_4a_4}\right]\times\cos^2\theta+\left[\frac{35B_4a_4}{8-4B_2a_2+3B_4a_4}\right]\cos^4\theta\right).$$

The coefficients of $\cos^2\theta$ and $\cos^4\theta$ are denoted by us as C_2 and C_4, respectively. It is readily seen that the quantity, C_2+C_4 is the theoretical counterpart of the experimental parameter C. B_2 and B_4 are angular correlation coefficients and have been calculated by Biedenharn and Rose.[16] They depend only on the multipolarity of excitation and emission and on the spins of the states involved. The coefficients, a_2 and a_4,[17] the only energy-dependent parameters in the distribution function, are functions of the nuclear matrix elements and are given in reference 2. The last two columns of Table II list the spin of the excited state and the type and multipolarity of radiation that is implied by our choice of C_2+C_4.

The choice of spin and multipolarity from our data is usually unambiguous. This is seen in Table III, which shows values of C_2+C_4 for various assumed spins and multipolarities. The calculations were all made assuming a proton bombarding energy of 4.0 Mev.

The errors quoted in Table II are ±3 percent background uncertainty and ±1 percent statistics for all gammas except those from tungsten. Here, the 0.004-in. target apparently caused more absorption difficulties than in the other cases. Both Ta gamma distributions agree with previous data[3] and support the level assignments of 9/2 (137 kev) and 11/2 (303 kev) made by

TABLE II. Measured anisotropy (C) and calculated (C_2+C_4) are given at different proton energies, E_p(Mev). The most probable gamma transition is listed.

Gamma	E_p	C	C_2+C_4	Transition
Ta, 137 kev	2.7	0.00±0.04	−0.005	9/2(M1)7/2
	3.8	0.00±0.04	−0.005	
Ta, 303 kev	2.7	+0.14±0.04	+0.18	11/2(E2)7/2
	3.8	+0.16±0.04	+0.17	
Au, 277 kev	2.7	−0.17±0.04	−0.06	5/2(M1)3/2
	3.8	−0.14±0.04	−0.06	
	4.1	−0.15±0.04	−0.06	
Au, 545 kev	4.0	+0.25±0.04	+0.23	7/2(E2)3/2
W, 114 kev	2.0	+0.21±0.07	+0.36	2(E2)0
	2.8	+0.18±0.07	+0.31	
	3.6	+0.10±0.07	+0.27	
	4.2	+0.11±0.07	+0.21	

[16] W. C. Gordy, Phys. Rev. **76**, 139 (1949).

* See abstract, note added in proof.

‡ *Note added in proof.*—Alder and Winther have recently improved the theory by taking into account the energy loss of the incident particle. With this correction the calculated relative cross section is brought into agreement with our measurements for both the 277- and 545-kev gold lines over the full range of proton energies studied. We are indebted to A. Bohr and B. Mottelson for the communication of this information.

[16] L. C. Biedenharn and M. E. Rose, Revs. Modern Phys. **25**, 729 (1953).

[17] a_4 is a negative number. C. M. Class (private communication).

Huus and Zupančič.[4] A calculation of mixed $M1$ and $E2$ radiation from the 137-kev level indicates that $E2$ is either more than 90 percent or less than 5 percent of the total radiation. Internal conversion electron data[18] support the latter assumption.

The Au 545-kev gamma anisotropy clearly demands the assumption of a $7/2(E2)3/2$ transition. The Au 277-kev gamma distribution may be fitted by mixed $E2$ and $M1$ radiation using a phase shift of 180° for the interference term.§ The intensity ratio of $E2$ to $M1$ is either $(7_{-5}^{+13})\div 100$ or $(3_{-1.5}^{+2})\div 1$. Beta-decay data support the former assumption.

The tungsten gammas are expected to be predominantly $2(E2)0$ transition in the even isotopes. W^{183} (14 percent abundant) has a ground-state spin of $\frac{1}{2}$ and an observed gamma at 103 kev.[13] The only possible transitions in W^{183} which could decrease the observed anisotropies are $M1$. Further, the internal conversion coefficient for $M1$ is large compared to the $E2$ expected from the even isotopes. The 102-kev conversion electron peak observed by Huus and Bjerregaard[18] is comparable to peaks from the other even isotopes and should, therefore, be mainly due to the 102-kev level in W^{182}.[13] We, therefore, do not think that the low experimental anisotropy can be explained by the radiation from W^{183}. However, if we assume that the intrinsic quadrupole moment (Q_0) of tungsten[4] is 7×10^{-24} cm^2, the lifetime of rotational levels in W is about 10^{-9} sec.[19] We might therefore expect some decrease in anisotropy due to interaction between the quadrupole moment of the nucleus and atomic electric-field gradients.[20] Further study of this possibility is planned.

It was hoped that the W gammas would afford a particularly sensitive check on angular distribution theory, since it had a relatively large anisotropy and rapidly changing energy-dependent coefficients, a_2 and a_4. The order of magnitude of the predicted anisotropy change with energy is observed but the possible effect discussed above may also depend on the recoil velocity of the tungsten nucleus.

CONCLUSIONS

The determination of scintillator line shapes with artificial sources appears the most direct approach to the problem of background. Detection of high-energy gammas is limited by target surface impurities rather than machine background when no special cold baffles are employed near the target. Very pure targets are particularly important when the x-ray energy region is surveyed. Gamma-gamma coincidence counting rates in Ta showed that angular correlations demand better than 0.1-microsecond resolving time.

The identification of the two Ta^{181} levels as pure rotational levels[4] is further supported by our angular distribution and coincidence data. The gold 545-kev level does not fit pure rotational level spacing when related to any of the lower states. Its energy is 2 times that of the 277-kev level, while the calculated figure is 2.5. However, the vibrational distortions discussed by Bohr and Mottelson[3] would tend to lower the energy of the upper level.

The Au 277-kev gamma thin target yield curve departs from theory by about 20 percent between 2- and 4-Mev proton energy. It will be noted that the discrepancy between theory and experiment is much greater for the thick target yield ratio between 2 and 4 Mev. The data also suggest that this gamma is from a level not more than 50 percent above 277 kev. This indicates that the experimental yield is much too low below 2 Mev and rises slightly too rapidly between 2 and 4 Mev. It is also seen (Table I) that the theory is most in error for higher level excitation. This is reasonable in light of the neglect of the change in energy of the incident proton in present theory.[2] The yield ratio errors do not seem to be systematic with excitation spin change. This point needs further data despite the fact that magnetic dipole excitation by incident particles moving slowly, compared to velocities within the nucleus, is expected to be small.‡

We have verified that there is no rapid change in angular distribution of gammas with incident proton energy. The magnitude of the anisotropies is in good agreement for all levels except those in tungsten. Further study of $2(E2)0$ transitions is planned.

We are very grateful for the aid and advice given us by our colleagues, H. W. Newson, H. W. Lewis, S. A. Cox, and E. M. Bernstein, and E. Merzbacher of the University of North Carolina.

TABLE III. Calculated values of the anisotropy C_2+C_4 for various transitions using a proton energy of 4 Mev. Except for the 137-kev Ta line, transitions for which B_2 and B_4 equal zero are not listed. Because of the small change in C_2+C_4 with gamma energy, we have not listed separately the transitions possible for each gamma from one nucleus.

Target	Ground state	Transition	C_2+C_4
Ta^{181}	7/2	7/2($M1$)7/2	−0.09
	7/2	7/2($E2$)7/2	+0.06
	7/2	9/2($M1$)7/2	−0.005
	7/2	9/2($E2$)7/2	+0.015
	7/2	11/2($E2$)7/2	+0.17
Au^{197}	3/2	5/2($M1$)3/2	−0.07
	3/2	5/2($E2$)3/2	+0.04
	3/2	7/2($M1$)5/2	−0.15
	3/2	7/2($E2$)5/2	+0.03
	3/2	7/2($E2$)3/2	+0.23
W^{even}	0	2($E2$)0	+0.38
W^{183}	1/2	3/2($M1$)1/2	−0.20
	1/2	3/2($E2$)1/2	+0.20
	1/2	5/2($E2$)1/2	+0.24

[18] T. Huus and J. H. Bjerregaard, Phys. Rev. **92**, 1579 (1953).

§ For this particular nucleus a phase shift of 180° is predicted by the theory, assuming the transition is rotational. A. Bohr and B. Mottelson (private communication).

[19] A. W. Sunyar, Bull. Am. Phys. Soc. **29**, No. 4, 38 (1954).

[20] Alder, Albers-Schonberg, Heer, and Novey, Helv. Phys. Acta **26**, 761 (1953).

Small-Angle Cross Sections for the Scattering of Protons by Tritons*

MALCOLM E. ENNIS AND ARTHUR HEMMENDINGER
University of California, Los Alamos Scientific Laboratory, Los Alamos, New Mexico
(Received April 5, 1954)

The proton-triton differential scattering cross section has been measured for center-of-mass angles between 20° and 150° and proton energies in the range 1 to 2.55 Mev. Probable errors vary between 3 and 5 percent.

INTRODUCTION

AN analysis by McIntosh, Gluckstern, and Sack[1] of two sets of proton-triton scattering data[2,3] presents two possible sets of phase shifts, one of which implies the existence of a singlet P resonance in He^4, the other of which is nonresonant. To date no differential cross sections have been reported for laboratory angles less than 45 degrees, and it is in this range that the calculated differential cross sections are most sensitive to the choice of phase shifts. These measurements were undertaken with the hope that, even if they do not lead to unique values of phase shifts, they might help answer the question of the existence of a singlet P resonance in He^4.

In both earlier experiments small volume scattering chambers were used, similar to that first described by Taschek[4]; these chambers cannot be used at small angles, and they are difficult to use for tritium because with such a small volume-to-surface ratio rapid changes in isotopic composition occur. The present experiment was undertaken with a large chamber, 14 inches in diameter and 4 inches high, a complete description of which is given by Sherr *et al.*[5]

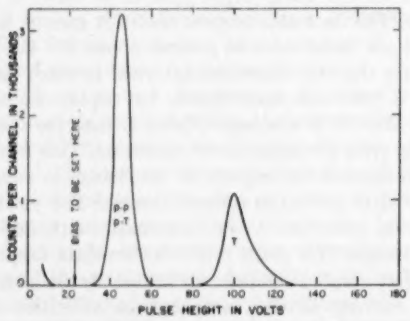

FIG. 1. Pulse-height distribution for the monitor counter showing the bias setting for the integral discriminator.

APPARATUS

The proton beam was provided by the Los Alamos 2.5-Mev electrostatic accelerator A, the same one used in the earlier scattering measurements.[2]

The current collector described by Sherr[5] was modified so that it remained close to ground potential and was isolated from electron currents by a cylindrical barrier electrode at a potential of -250 volts located just in front of the collector.

The target gas was confined by an entrance foil of 0.16-mil aluminum, an exit foil of 0.05-mil nickel, and two counter foils each of 0.05-mil nickel. The pressure of this gas was measured, through a liquid nitrogen trap, by a 0–20-mm Wallace and Tiernan differential pressure gauge used as a null indicator, with an oil manometer to indicate pressure on the static side of the gauge.

The dimensions of the movable-counter collimator were, in the usual notation,[6] $A=1.807\times10^{-2}$ cm², $2b=0.2111$ cm, $h=6.982$ cm, $R=12.893$ cm, from which we find $G=4.242\times10^{-5}$ cm.

The counter fillings were 25 or 50 cm pressure of argon plus 7 percent of carbon dioxide. Counter anodes were 5-mil wires, at a voltage of 1150 or 1450. The energy resolution of the counters, about 15 percent with a new gas filling, deteriorated slowly, so that the counters needed refilling every day.

Tritium, stored in a uranium furnace, was readily pumped into or out of the chamber; each pumping cycle separated hydrogen isotopes from the contaminants that grew slowly in the chamber.

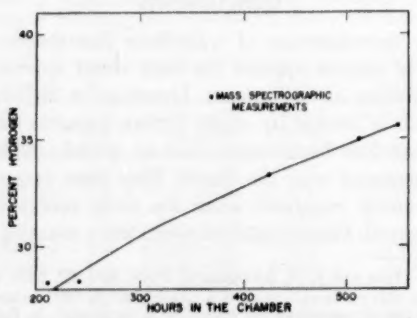

FIG. 2. The growth of hydrogen in the chamber, used for interpolation between mass spectroscopic measurements.

* Work done under the auspices of the U. S. Atomic Energy Commission.

[1] McIntosh, Gluckstern, and Sack, Phys. Rev. **88**, 752 (1952).

[2] Hemmendinger, Jarvis, and Taschek, Phys. Rev. **76**, 1137 (1949).

[3] Claassen, Brown, Freier, and Stratton, Phys. Rev. **82**, 589 (1951).

[4] R. F. Taschek, Rev. Sci. Instr. **19**, 591 (1948).

[5] Sherr, Blair, Kratz, Bailey, and Taschek, Phys. Rev. **72**, 662 (1947).

[6] Breit, Thaxton, and Eisenbud, Phys. Rev. **55**, 1018 (1939).

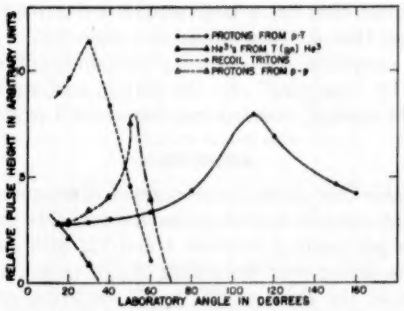

FIG. 3. A representative set of curves, for 50-cm counter pressure (argon) and 2.548-Mev incident proton energy, showing the pulse height due to various scattered and reaction particles as a function of angle.

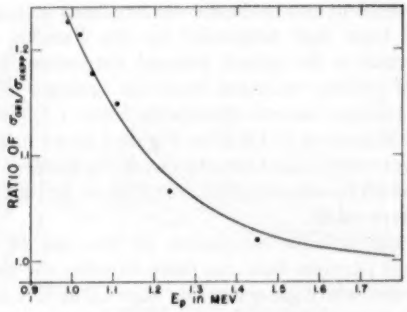

FIG. 4. Measurements of the proton-proton scattering cross section, at various angles, plotted as the ratio to the HKPP measurements as a function of energy. The smooth curve was used to show the ratio of observed Faraday cage current to the actual current that would be observed in the absence of gas scattering.

Electronic circuits were the same as those described by Sherr, with the substitution of a new 18-channel pulse-height analyzer[7] for the older 10-channel analyzer.

EXPERIMENTAL PROCEDURE

The yield in counts per microcoulomb of beam current integral at the angle ϑ as a function of the differential scattering cross section $\sigma(\vartheta)$ is

$$Y = Nn\sigma(\vartheta)G \csc\vartheta, \tag{1}$$

where $N = 6.250 \times 10^{12}$ protons/microcoulomb, n = number of scattering particles per cubic centimeter, and G = the geometry factor ($= 4.242 \times 10^{-5}$ cm).

The thickness of the entrance foil was determined by measuring the $T^3(p,n)$ threshold with a few millimeters pressure of tritium in the chamber, and later with no foil and a zirconium-tritium target, in each case using a long counter to detect neutrons.

The monitor counter at 14 degrees, with the bias set carefully at the minimum shown in Fig. 1 between background and the smallest peak in pulse height, was used instead of a current integrator and was calibrated at a known temperature and pressure of chamber gas in terms of the charge collected in the Faraday cage as measured by a ballistic galvanometer. Frequent calibration was required because the heavy contaminant in the chamber gas grew at the rate of 0.06 percent per hour.

Whenever the tritium was pumped into the uranium trap a background run was made on the residual gas to correct tritium scattering data, especially at small angles. After each two days of running time a mass spectrometric determination of tritium concentration was made. Hydrogen concentration at intermediate times was evaluated from the curve of Fig. 2. The liquid nitrogen trap connected to the chamber was kept full whenever there was a beam through the chamber to minimize the rate of deposition of carbon films on the foils.

[7] C. W. Johnstone, Nucleonics **11**, 36 (1953).

ANALYSIS OF DATA

The various scattered and recoil groups traversing the counter, including at some angles and energies the recoils from the reaction $T^3(p,n)He^3$, produced such a multiplicity of peaks that any one could be identified only after calculation of particle energetics and energy losses in target gas, foil, counter, as shown in Fig. 3. When the peak due to $p-p$ protons overlapped that due to $p-T$ protons at small angles, it was necessary to subtract the calculated $p-p$ yield from the total, using the mass spectrometric hydrogen concentration and the known values for the $p-p$ cross section.[8] Equation (1) for the $p-T$ cross section then becomes

$$\sigma = \frac{Y \sin\theta}{n_1 NGP_T} - \frac{P_H}{P_T}\sigma_1, \tag{2}$$

where n_1 is the number of atoms in a diatomic gas per cubic centimeter at 1 cm of mercury pressure, P_T is the partial pressure of tritium, P_H is the partial pressure of hydrogen, and σ_1 is the $p-p$ scattering cross section. Except for the two points at 120 degrees laboratory angle all of the large angle data are calculated from yields of recoil tritons at small angles. At the higher energies, recoil-triton and scattered-proton data join neatly.

Often a group was superposed on the "tail" of another group—a tail on the low-energy side produced by small-angle secondary scattering in gas or slit edges—in which case the pulse distributions were plotted, tails were drawn by extrapolation, and suitable subtractions were made.

Small counter backgrounds due to recoils from $T(p,n)$ neutrons and possibly from gamma pileup were measured by moving a magnetically operated shutter into the beam entering the counter; these corrections were never greater than a few percent.

At the lower beam energies an appreciable fraction

[8] Herb, Kerst, Parkinson, and Plain, Phys. Rev. **55**, 998 (1939); referred to later as HKPP.

of the incident proton beam was scattered into angles greater than that subtended by the Faraday cage. Corrections to the current integral, determined by the yield of protons scattered from the hydrogen diluent in the tritium, became appreciable below 1.3 Mev and rose to 20 percent at 1.0 Mev. Figure 4 shows a smooth curve for scattering of protons out of the incident beam determined by experimental points, from which corrections were taken.

An approximate calculation of the loss of once-scattered particles from the beam entering the counter due to secondary gas scattering shows that it is largely self compensating in that there will be as many particles scattered into the beam as there are lost to the beam. The correction due to the use of a counter subtending a finite solid angle to measure an angular distribution that has a large second derivative proves to be less than 0.5 percent and was neglected.

The correction due to heavy contaminants, determined by "pumping" out the tritium and scattering from the residual chamber gas, was about 1 percent.

RESULTS

In Table I are shown the averages of all measurements weighted inversely as their probable errors. The number of runs per point is between 1 and 12, with most of the data falling near the middle of this range. A comparison of the three sets of $p-T$ scattering data at energies selected is shown in Fig. 5.

The probable error in the mean energy of the incident protons corrected for energy loss in the entrance foil and target gas is ± 5 kev.

TABLE I. The $p-T$ cross sections in both laboratory and center-of-mass systems.[a]

Lab. angle θ	C.m. angle Ω	$E_p=0.990$ Mev $\sigma\theta$	$\sigma\Omega$	$E_p=1.019$ Mev $\sigma\theta$	$\sigma\Omega$	$E_p=1.049$ Mev $\sigma\theta$	$\sigma\Omega$	$E_p=1.108$ Mev $\sigma\theta$	$\sigma\Omega$	$E_p=1.236$ Mev $\sigma\theta$	$\sigma\Omega$	$E_p=1.450$ Mev $\sigma\theta$	$\sigma\Omega$
15	20	4.043	2.314	3.997	2.287	3.751	2.147	3.364	1.925	2.733	1.564	2.010	1.150
20	26.6	1.300	0.756	1.277	0.742	1.208	0.702	1.016	0.590	0.905	0.526	0.723	0.420
25	33.1	0.627	0.371	0.617	0.366	0.562	0.333	0.489	0.290			0.415	0.246
30	39.6	0.394	0.239	0.378	0.229	0.332	0.201	0.315	0.191	0.291	0.176	0.316	0.192
35	46.0	0.303	0.189	0.305	0.190	0.278	0.173	0.234	0.146			0.263	0.164
40	52 4	0.265	0.171	0.253	0.163	0.239	0.154	0.215	0.138	0.213	0.137	0.236	0.152
45	58.7	0.260	0.173	0.240	0.160	0.215	0.143	0.189	0.126	0.181	0.121	0.217	0.145
50	64.8	0.231	0.160	0.224	0.155	0.193	0.134	0.181	0.125	0.180	0.125	0.199	0.138
55	70.9												
60	76.8			0.205	0.155							0.165	0.125
62.8	80												
71.6	90											0.156	0.133
80.8	100									0.167	0.158	0.152	0.144
90.5	110											0.150	0.160
100.9	120	0.163	0.198	0.161	0.196	0.155	0.188	0.152	0.185	0.158	0.185	0.157	0.191
112.0	130	0.160	0.223	0.151	0.210	0.150	0.209	0.151	0.210			0.157	0.219
120	136.8									0.148	0.227		
123.9	140	0.146	0.234	0.148	0.239	0.144	0.231	0.141	0.226	0.152	0.243	0.157	0.251
136.8	150	0.150	0.274	0.140	0.256	0.137	0.250	0.141	0.258	0.148	0.270	0.157	0.287

Lab. angle θ	C.m. angle Ω	$E_p=1.678$ Mev $\sigma\theta$	$\sigma\Omega$	$E_p=1.900$ Mev $\sigma\theta$	$\sigma\Omega$	$E_p=2.117$ Mev $\sigma\theta$	$\sigma\Omega$	$E_p=2.335$ Mev $\sigma\theta$	$\sigma\Omega$	$E_p=2.548$ Mev $\sigma\theta$	$\sigma\Omega$
15	20	1.458	0.834	1.207	0.691	1.062	0.608	0.958	0.548	1.020	0.584
20	26.6	0.606	0.352	0.565	0.328	0.591	0.343	0.622	0.362	0.697	0.405
25	33.1	0.389	0.230	0.417	0.247	0.477	0.283	0.528	0.313	0.578	0.342
30	39.6	0.353	0.214	0.366	0.222	0.418	0.253	0.447	0.271	0.495	0.300
35	46.0	0.308	0.192	0.333	0.207	0.368	0.229	0.369	0.230	0.421	0.262
40	52.4	0.275	0.177	0.280	0.180	0.310	0.199	0.355	0.228	0.358	0.230
45	58.7	0.237	0.158	0.240	0.160	0.265	0.176			0.320	0.213
50	64.8	0.211	0.146	0.218	0.151			0.242	0.168	0.257	0.178
55	70.9					0.190	0.137				
60	76.8	0.171	0.129	0.157	0.119	0.172	0.130	0.160	0.121	0.186	0.141
62.8	80			0.155	0.121			0.149	0.116	0.161	0.126
71.6	90	0.127	0.108	0.132	0.113	0.128	0.109			0.119	0.102
80.8	100	0.139	0.132	0.130	0.123	0.119	0.113	0.104	0.099	0.101	0.096
90.5	110	0.138	0.147	0.129	0.138	0.118	0.126	0.109	0.116	0.098	0.105
100.9	120	0.147	0.179	0.136	0.165	0.132	0.160	0.113	0.137	0.106	0.129
112.0	130	0.154	0.215	0.145	0.202	0.134	0.187	0.129	0.180	0.112	0.156
120	136.8	0.133	0.204								
123.9	140	0.152	0.243	0.150	0.240	0.143	0.229	0.131	0.210	0.121	0.194
136.8	150	0.147	0.268	0.147	0.268	0.144	0.263	0.134	0.245	0.125	0.228

[a] The probable errors in these cross sections are as follows:

$E_p=0.990$ to 1.108 Mev—5 percent.
$E_p=1.236$ and 1.450 Mev—3 percent.
$E_p=1.678$ to 2.548 Mev—4 percent above the horizontal line and 3 percent below.

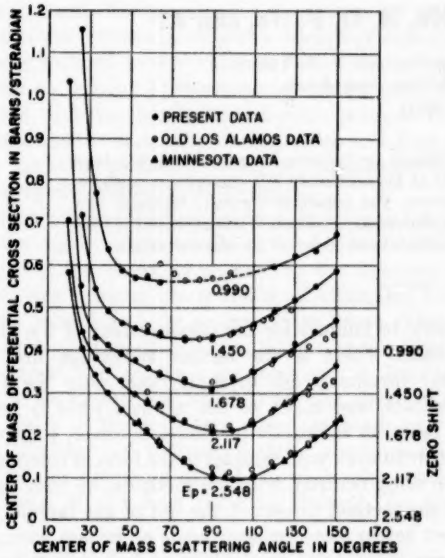

FIG. 5. The $p-T$ cross section as a function of angle (c.m. system) for five energies, including all of the earlier measurements at the energies selected.

Estimates of probable errors in cross sections and their sources are as follows:

Y, 2.5 percent due to statistics;
P_T, 0.5 percent due to pressure measurement, 0.7 percent due to isotopic composition;
P_H, 0.5 percent due to pressure measurement, 2.0 percent due to isotopic composition;
G,* 0.5 percent due to distance measurements.

The errors in cross section approximate 3 percent, except where the subtraction indicated in Eq. (2) must be performed, where they are 5 percent. At the lowest energies there is an additional error, possibly as great as 3 percent, due to the correction of the current integral for scattering out of the beam.

* *Note added in proof.*—Shortly before receiving the galley proofs, one of the authors (A. H.) removed the entrance foil of the movable counter and found that about 1.5 percent of the hole A was covered with wax. The authors will send to anyone requesting it a table of cross sections calculated using a corrected geometry factor.

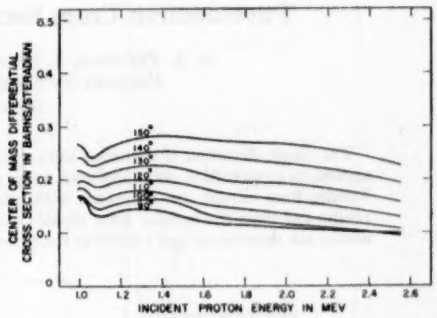

FIG. 6. The $p-T$ cross section as a function of energy (c.m. system) for large angles, showing the minimum near 1-Mev proton energy.

Comparison of the present work with earlier measurements[2] confirms the observation of a minimum in the center-of-mass cross section as a function of energy near the $T(p,n)$ threshold, as predicted in a theory of Wigner.[9] The general trend, more pronounced for large angles, is shown in Fig. 6. This particular feature in the earlier work was somewhat in doubt because of the energy and angle straggling in the Faraday cage foil.

The 20-degree center-of-mass differential cross section calculated from the eight phase-shift "fits" given by McIntosh *et al.* for the 2.5-Mev Minnesota data give two good fits for the small angles, of which one,

$$^1K_0=64°,\quad ^3K_0=64°,\quad ^1K_1=-60°,\quad ^3K_1=3°,\quad \text{(A)}$$

is resonant (large singlet p phase shift) and the other,

$$^1K_0=64°,\quad ^3K_0=64°,\quad ^1K_1=46°,\quad ^3K_1=-16°,\quad \text{(B)}$$

is not. The resonant fit is slightly better than the nonresonant, but each fit might be improved by including a small amount of d wave. Actually the existence of an appreciable d-wave component appears plausible in the light of recent angular distribution measurements for $T^3(p,n)$ by Willard and collaborators,[10] and it is demanded by the angular distributions for $T^3(p,\gamma)$ measured by Perry and Bame.[11]

[9] E. P. Wigner, Phys. Rev. **73**, 1002 (1948).
[10] Willard, Bair, and Kington, Phys. Rev. **90**, 865 (1953).
[11] J. E. Perry and S. J. Bame, Phys. Rev. **90**, 380 (1953).

Photoneutron Cross Sections in He, N, O, F, Ne, and A†

G. A. Ferguson, J. Halpern, R. Nathans, and P. F. Yergin
University of Pennsylvania, Philadelphia, Pennsylvania

(Received April 1, 1954)

The direct detection of neutrons from (γ,n) reactions induced by betatron bremsstrahlung has been applied to cross-section determinations using gaseous targets at approximately 100 atmospheres pressure. Results from oxygen are consistent with other determinations. The remaining elements represent new results and show the familiar giant dipole resonance for the photoneutron process. Parameters of the resonances are determined and related to the systematic behavior previously reported for other elements.

INTRODUCTION

STUDIES of the energy dependence of the photoneutron cross sections for light elements have been a useful tool in exploring the nucleon-nucleon interaction as exemplified by deuterium, and the details of nuclear structure, as illustrated by beryllium. As in the case of medium and heavy elements, the cross sections of other light elements investigated to date show the familiar giant dipole resonance behavior, and in some cases anomalous photon absorption has been reported in the form of "breaks" in the curve of bremsstrahlung yield *vs* maximum bremsstrahlung energy.[1]

Knowledge of the parameters of the giant resonance for light nuclei is, in fact, of importance in understanding the photon absorption mechanism in all nuclei, for the role played by subunits in the photonuclear process can be investigated directly. The photodisintegration of helium is of importance in this respect.

For some light elements, the position of the resonance peak is far removed from the (γ,n) threshold, thus affording an opportunity for studying the photon absorption process over a wide energy region below the resonance. N^{14}, with a (γ,n) threshold at 10.25 Mev and a dipole resonance peak at 22.5 Mev, is such a case.

Just as for other elements,[2,3] the direct detection of neutrons has many practical advantages over radioactivity techniques for the measurement of the above reactions. There is the further advantage that the (γ,pn) thresholds are in some cases near the (γ,n) thresholds, and much of the neutron yield is lost if one relies on radioactivity. Since, however, it is often difficult to work with samples in the form of compounds when using neutron detection methods, we have modified the method to permit the use of gas targets, and report herein measurements made on helium, nitrogen, oxygen, neon, and argon. Fluorine does permit the use of the compound Teflon, since the neutron contribution from carbon can be separated with ease and the gas is somewhat more difficult to handle.

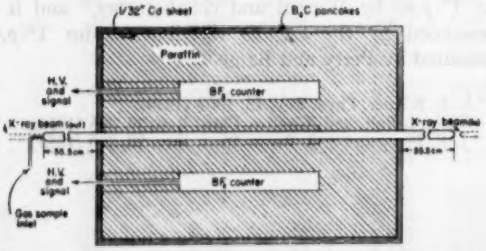

FIG. 1. Arrangement of paraffin block showing stainless steel cylinder to hold gaseous targets. The paraffin shielding (12 inches thick) that surrounds the entire block is not shown.

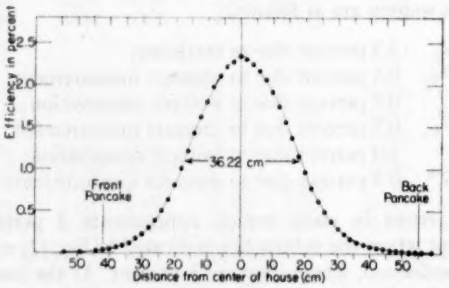

FIG. 2. Efficiency of apparatus for neutron detection as a function of position along beam axis.

APPARATUS

The general arrangement of the apparatus as well as the significant performance data have been presented in previous publications.[2] The only modification for the present study was the introduction of the bomb to hold gases at high pressures, as shown in the diagram (Fig. 1) of the paraffin block used in these studies. The bomb, made from a $1\frac{1}{4}$-in. o.d. stainless steel cylinder with 0.085 in. thick wall, fitted snugly into the beam hole passing through the paraffin house and extended approximately 25 cm beyond the shielding on both ends. The end caps, made from 0.049-in. stainless steel sheet drawn into hemispheres and welded to the tubing, were well outside the house so that (γ,n) reactions in the caps could not contribute appreciably to the background counts. The beam, 1.40 cm in diameter at the center of the house, did not of course strike the walls

† Supported in part by the U. S. Air Research and Development Command and the joint program of the U. S. Office of Naval Research and the U. S. Atomic Energy Commission.

[1] Haslam, Katz, Horsley, Cameron, and Montalbetti, Phys. Rev. **87**, 196 (1952).

[2] R. Nathans and J. Halpern, Phys. Rev. **93**, 437 (1954).

[3] Montalbetti, Katz, and Goldemberg, Phys. Rev. **91**, 659 (1953).

of the bomb. The gases under study were led into the bomb from commercial cylinders through $\frac{3}{16}$-inch copper tubing soldered to the center of the rear cap. Neutron yields at varying bremsstrahlung energy were determined with the bomb flushed with nitrogen at one atmosphere as a standard background, and then with the gas to be measured added to the nitrogen to approximately 2000-lb/sq in. pressure.

With this arrangement neutrons from (γ,n) reactions in the gases originated along the beam for the full length of the house, as opposed to the situation with solid targets where the neutrons all originated from a target localized at the center of the house. Thus the neutron counting efficiency varied along the length of the target and required measurement. A 2-millicurie Ra-Be source was positioned at varying distances from the center of the apparatus along the beam axis, and the efficiency *vs* position thereby determined. The results are presented in Fig. 2, where the combined efficiency of the four counting channels for Ra-Be

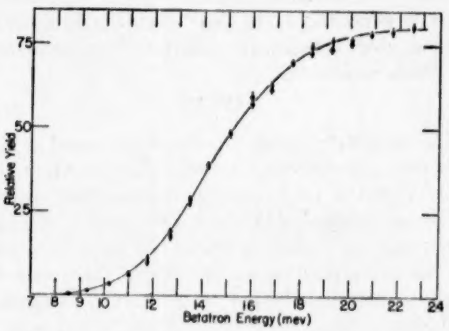

FIG. 3. Photoneutron yield from gold target. ● Gold at center of paraffin house; ▲ gold at end of house; ■ points common to both positions.

neutrons is plotted against distance of source from the center of the house. As indicated, the effective length of the gas targets was 36.22 cm.

Of greater concern than varying efficiency along the length of the targets, which affects only absolute values of (γ,n) cross sections, was the possibility that the detection efficiency for distances far from the center might be dependent on neutron velocity and thereby distort a yield curve since photoneutron velocity distributions change with increasing bremsstrahlung energy. Yield curves were therefore taken for a 498 mg/cm² gold target placed at the center of the house and at 25.1 cm from the center. Normalization of the yields as given by the relative efficiencies at the two positions, according to the results presented in Fig. 2, gave the two essentially identical yield curves of Fig. 3. It was therefore thought safe to assume that the counting efficiency was independent of neutron velocity throughout the length of the targets.

With the stainless steel bomb in the house, one further

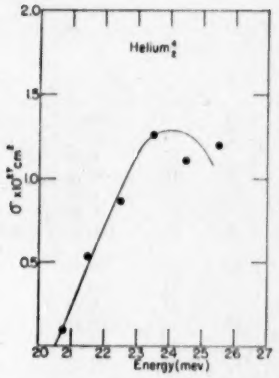

FIG. 4. Photoneutron excitation function for helium.

problem required investigation. Atomic scattering by the gaseous targets could cause a fraction of the scattered beam to strike the walls of the bomb and the resultant (γ,n) reaction in the iron might contribute to the measured net neutron yield attributed to the gaseous targets. Although this scattered radiation is degraded in energy, small-angle scattering is important for the forward portions of the target and the effect is enhanced by the low (γ,n) threshold of iron. This effect was easy to explore, however, for it should contribute a measured neutron yield at a betatron energy below the threshold of the element investigated but above the iron threshold. Helium and oxygen, with thresholds 9.3 Mev and 4.3 Mev, respectively, above the threshold for the 91.6 percent isotope of iron were carefully explored. A positive effect was measured, but it was found too small to influence in any way the cross-section curves derived from the measured yields.

Procedures for taking the photoneutron yield curves and converting to cross sections have been described in previous publications,[2] which also include details of operating conditions of the betatron used to produce the bremsstrahlung beam up to a maximum energy of 26 Mev.

RESULTS

Cross section *versus* energy curves for all the elements investigated exhibited the familiar giant dipole resonance behavior with the possible exception of helium. In the latter element, the curve could not be explored over a sufficient range to be positive of the resonance, but indications are that helium is no exception. The parameters of the giant resonances as taken from the excitation functions are presented in Table I. Here E_m is the energy at the peak of the resonance, σ_m the value of the peak cross section, Γ the width at half-maximum, and $\int \sigma dE$ the integrated cross section from threshold to 25 Mev. The details for each element are discussed below.

HELIUM

The cross-section curve for helium is shown in Fig. 4, with the circles representing the values of the cross

TABLE I. Summary of data.

Element	Z	A	Percent abundance	Pressure lb/sq in.	Thresholds in Mev (γ,n)	(γ,p)	(γ,pn)	$(\gamma,2n)$	E_m (Mev)	Γ (Mev)	σ_m (mb)	$\int\sigma dE$ (Mev-barns)
Helium	2	4	100	2190	20.6	19.8	25.9	28.1	24.0	—	1.3	0.004
Nitrogen	7	14	99.62	1820	10.5	7.6	12.4	31.3	22.5	3.2	15.3	0.061
		15	0.38									
Oxygen	8	16	99.76	2230	15.6	12.1	22.9	28.8	22.5	3.5	7.7	0.031
		17	0.04									
		18	0.20									
Fluorine	9	19	100	4.8 g/cm² Teflon	10.4	7.9	15.9	19.6	22.2	5.6	11.5	0.077
Neon	10	20	90.00	310	16.9	12.9	23.0	28.3	21.5	6.6	7.3	0.052
		21	0.27									
		22	9.73		10.4							
Argon	18	36	0.31									
		38	0.06									
		40	99.63	2100	9.8	11.1	20.0	14.9	20.0	8.5	31.2	0.23

section derived from the (γ,n) yield curve for helium by the method of successive bremsstrahlung subtractions. Since the peak of the resonance occurs at 24 Mev, it is difficult to tell how the curve behaves on the high side of the resonance, and values of Γ and $\int\sigma dE$ are thus not known. The maximum cross section is measured to be 1.3 millibarns.

NITROGEN

Figure 5 represents the cross-section curve for nitrogen, a particularly interesting case both because of the large separation between the threshold (10.5 Mev) and the peak of the resonance (22.5 Mev) and because of the low value of the (γ,pn) threshold (12.4 Mev). The dotted curve represents the (γ,n) cross section as measured by Johns, Horsley, Haslam, and Quinton[4] using radioactivity. The large (γ,pn) contribution is clearly demonstrated, particularly since the $(\gamma,2n)$ threshold is at approximately 31 Mev and cannot contribute to the observed yields. The integrated cross section for total neutron yield is 0.06 Mev barn compared with the value of 0.015 Mev barn for the radioactivity data. The total neutron yield integrated cross section would be expected to include most of the contribution from the (γ,p) as well, for at energies in the vicinity of the rather narrow (3.2-Mev) resonance the emission of a proton is almost certain to be followed by neutron emission. It is clear that the radioactivity method gives erroneous values for the parameters of the dipole resonance.

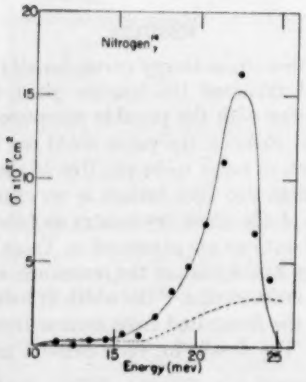

FIG. 5. Photoneutron excitation function for nitrogen.

[4] Johns, Horsley, Haslam, and Quinton, Phys. Rev. 84, 856 (1951).

OXYGEN

The oxygen excitation function is presented in Fig. 6. This does not represent a new result, as Montalbetti *et al.*[3] report a total neutron cross-section curve for oxygen as reproduced by the dotted curve of the figure. Here again the $(\gamma,2n)$ threshold (29 Mev) is far above the resonance position at 22.5 Mev. There may be a small (γ,pn) contribution starting at a threshold of 22.9 Mev.

FLUORINE

Fluorine was bombarded in the form of Teflon, with a composition of 76 percent fluorine and 24 percent carbon by weight. After subtraction of the known carbon yield from the total measured yield and calculation of a cross-section curve, the results are those

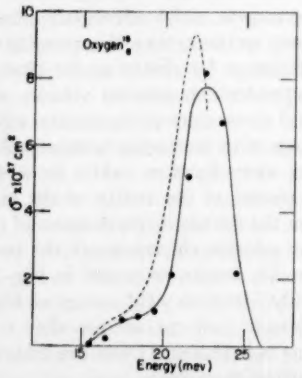

FIG. 6. Photoneutron excitation function for oxygen.

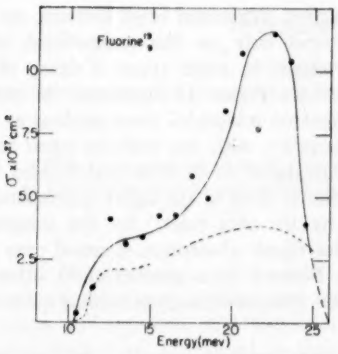

FIG. 7. Photoneutron excitation function for fluorine.

presented in Fig. 7. The dotted curve of the figure is that of Horsley, Haslam, and Johns[5] using radioactivity. The situation with fluorine is somewhat similar to that for oxygen. The (γ,pn) threshold is at 15.9 Mev. There is the one difference that the $(\gamma,2n)$ threshold at 19.6 Mev is below the peak.

NEON

The neon results plotted in Fig. 8 clearly show the two main isotopes, the 90 percent abundant Ne^{20} isotope having a threshold of 16.9 Mev. The $(\gamma,2n)$ and (γ,pn) thresholds are too high to be of any significance. Ne^{20} was considered important because of possible alpha-particle structure. In fact, the results of this paper for helium and oxygen and those for carbon[2] and the Be^8 core[6] of the Be^9 nucleus make interesting comparison with Ne^{20}. This is illustrated in Fig. 9, where the cross section for each element is divided by the number of alpha particles and plotted *vs* energy.

ARGON

The total neutron cross-section curve for argon is shown in Fig. 10. The $(\gamma,2n)$ threshold is at 14.9 Mev

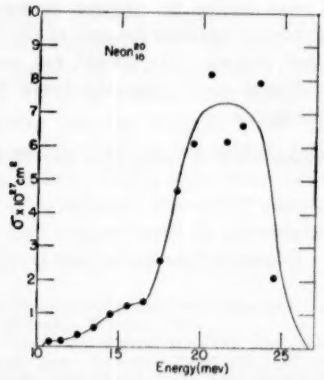

FIG. 8. Photoneutron excitation function for neon.

[5] Horsley, Haslam, and Johns, Phys. Rev. **87**, 756 (1952).
[6] R. Nathans and J. Halpern, Phys. Rev. **92**, 940 (1953).

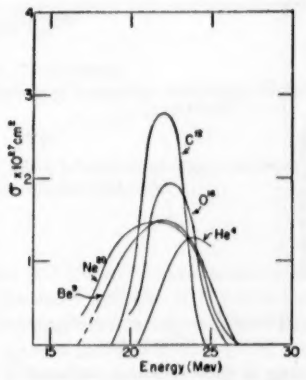

FIG. 9. Cross-section curves for alpha-particle nuclei. The cross-section curves for each element are divided by number of alpha particles and plotted against photon energy.

and the (γ,pn) at 20 Mev. An unambiguous separation cannot of course be made. The resonance width of 8.5 Mev and peak position of 20 Mev are consistent with values for other elements of comparable mass number.

DISCUSSION

It is doubtful that the various collective models proposed[7–9] to account for the giant photon absorption resonance in nuclei are applicable to light elements. Their chief prediction involves the dependence of the energy at the resonance maximum on atomic number. It should therefore be of interest to see how this energy for the elements herein reported compares with that for other elements. Figure 11 shows a plot of all such data from this laboratory. The solid curve drawn through the points represents a dependence of the form

$$E_m = 38.5A^{-0.19},$$

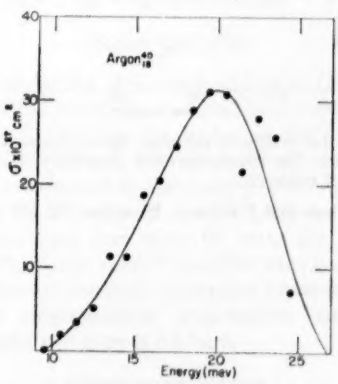

FIG. 10. Photoneutron excitation function for argon.

[7] M. Goldhaber and E. Teller, Phys. Rev. **74**, 1046 (1948).
[8] Steinwedel, Jensen, and Jensen, Z. Naturforsch. **6a**, 218 (1951).
[9] A. Reifman, Z. Naturforsch. **8a**, 505 (1953).

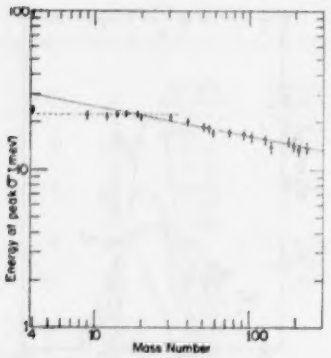

FIG. 11. Energy at giant resonance maximum *vs* mass number. The dots represent data of this paper. The circles are taken from the data of reference 2.

as previously reported.[2] Below an A of 30, E_m assumes a constant value of approximately 22.5 Mev.

Although a nuclear model should predict the width of the resonances as well as the peak energy, such calculations are at present not available. These involve the damping of any modes of oscillation induced by the incident photons. Figure 12 shows the dependence of the half-widths on mass number for all the elements of Fig. 11. Below a mass number of 30 the half-widths drop sharply below the trend for heavier elements as indicated by the solid line of the figure. The four anomalously low values above an A of 30 have been discussed previously.[10]

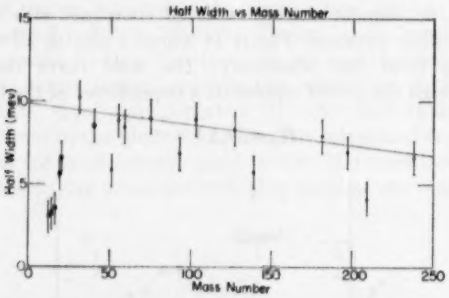

FIG. 12. Half-widths of the giant resonances as a function of mass number. The circles represent the data of this paper, the dots those of reference 2.

[10] R. Nathans and J. Halpern, Phys. Rev. **92**, 207 (1953).

The neutron integrated cross sections, on the other hand, depend only on the competition to neutron emission offered by other types of decay of the compound nucleus. Figure 13 represents the accumulated data on neutron integrated cross sections as a function of mass number, with the ordinate equal to the cross sections integrated to 25 Mev and divided by NZ/A. The horizontal lines of the figure correspond to limits imposed by the sum rules[11] for the integrated cross sections for dipole absorption summed over all partial reactions. Below a mass number of 50, other modes of decay of the compound nucleus become quite important.

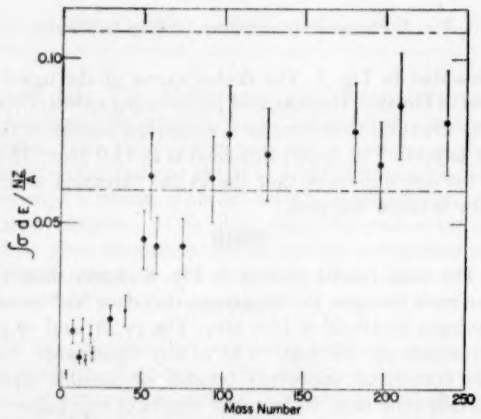

FIG. 13. Total neutron emission cross sections integrated to 25 Mev divided by NZ/A and plotted against mass number. The dots are the data of this paper, the circles those of reference 2.

In fact, as discussed previously for the case of carbon and beryllium,[3] addition of proton yield data will not be sufficient to bring the values into agreement with the sum rules unless one assumes large contributions to the yields by photons above an energy of 25 Mev. Nitrogen is another such example, for the measured integrated cross section for neutron emission includes most of the proton emission because of the importance of the (γ,pn) process. One should not overlook the possibility of large (γ,γ') processes below the particle emission thresholds.

[11] J. S. Levinger and H. A. Bethe, Phys. Rev. **78**, 115 (1950).

Preparation and Half-Life of Cr^{55}

G. A. BAZORGAN,* J. W. IRVINE, JR., AND C. D. CORYELL
Department of Chemistry and Laboratory for Nuclear Science, Massachusetts Institute of Technology, Cambridge, Massachusetts
(Received April 14, 1954)

Cr^{55} has been prepared by $Mn^{55}(d,2p)$ and $Cr^{54}(n,\gamma)$ reactions. A half-life of 3.62 ± 0.15 minutes is observed and the thermal neutron cross section for the production of this nuclide is 0.36 ± 0.04 barn.

THE search for the isotope of chromium of mass number 55 has been carried out by several research groups, and activities with half-lives 1.3, 1.6, and 2.3 hours have been attributed to this isotope.[1] In these experiments the chromium was bombarded with deuterons or slow neutrons and it was assumed that Cr^{55} was synthesized by a (d,p) or (n,γ) reaction.

Nelson and Pool[2] showed that the 1.3–2.3 hour activity attributed to Cr^{55} is not produced by (d,p) reaction on enriched Cr^{54}, nor by an (n,α) reaction on enriched Fe^{58}. Miller[3] found no indication of a two-hour chromium isotope by an (n,p) reaction in bombarding manganese with fast neutrons and concludes that Cr^{55} would have to possess a half-life of less than 15 min or greater than 100 days.

Later, Flammersfeld and Herr[4] reported Cr^{55} with a half-life of 3.52 min by (n,γ) reaction on Cr^{54} or (n,p) reaction on Mn^{55}.

Cr^{55} BY $(d,2p)$ REACTION ON Mn^{55}

An attempt has been made to produce the activity reported by Flammersfeld and Herr for Cr^{55} by a $(d,2p)$ reaction on Mn^{55}. One gram of spectrographically pure manganese powder which showed no lines of vanadium or aluminum in its spectrum was used as target for deuteron beam. This sample was wrapped in gold foil to avoid contamination of the target with 2.3-min Al^{28} from the target holder, and bombarded for 2 min with 15-Mev deuterons at the M.I.T. cyclotron.

The irradiated Mn was dissolved in HCl. The Cr^{55} produced was precipitated by adsorption with a small fraction of the Mn by neutralization with NaOH and addition of 0.2 g of Na_2O_2. The small amount of hydrous MnO_2, carrying virtually all of the Cr, was dissolved in HCl, Cr^{+3} carrier added, and the Mn removed as hydrous MnO_2 with excess NaOH-Na_2O_2, leaving $CrO_4^{=}$ in solution. The $CrO_4^{=}$ was precipitated as $BaCrO_4$ and counted with an end-window Geiger-Mueller tube on the second shelf geometry.

All samples of Cr^{55} were contaminated with 2.59-hr Mn^{56} since the short half-life of the chromium made a thorough decontamination impractical. The corrected decay curve gives a half-life of 3.67 ± 0.25 minutes.

Cr^{55} BY (n,γ) REACTION ON Cr^{54}

An irradiation of high-purity Cr metal showing no lines of vanadium or aluminum in its spectrum was accomplished in the reactor at Brookhaven National Laboratory. Three different samples weighing 2–3 milligrams were irradiated for 5–10 sec by slow neutrons and counted with an end-window Geiger-Mueller tube on the 2nd shelf.

A half-life for these three samples averaged 3.62 ± 0.15 minutes.

RADIATIONS AND ENERGY

Some β ray absorption data were obtained which were consistent with Flammersfeld's β-ray energy of 2.8 Mev.

Gray-wedge pictures were taken of the pulses from a scintillation spectrometer a few minutes after the end of irradiation of the chromium sample in the pile. By comparison with the cesium spectrum a γ ray of energy of 320 kilovolts was found. Since this corresponds to the 27-day Cr^{51}, another picture was again taken some five hours later which verified the fact that this γ ray was due to the long-lived isotope.

CROSS SECTION

To determine the (n,γ) cross section of Cr^{54}, a gold foil of 0.001 in. thickness was irradiated together with one of the Cr samples for 10 sec in the pile. After dissolving the gold foil, 50λ out of 100 ml solution was mounted and counted in the same geometry as for the Cr. From the activities of the Cr^{55} and Au^{198} at the end of irradiation and using 94 barns for the cross section of Au^{197}, the value 0.36 ± 0.04 barn is computed for the thermal neutron absorption cross-section for Cr^{54}. The corresponding cross-section value from Flammersfeld and Herr is 0.4 barn.

ACKNOWLEDGMENT

This work was supported in part by the U. S. Atomic Energy Commission. We wish to acknowledge gratefully the collaboration of Dr. H. L. Finston of Brookhaven National Laboratory in the pile irradiation.

* Ford Foundation Fellow from the Department of Chemistry of Teheran University, Teheran, Iran.

[1] Dickson, Daniel, and Konopinski, Phys. Rev. **57**, 351 (1940); Amaki, Jumori, and Sugimoto, Phys. Rev. **57**, 751 (1940); Seren, Friedlander, and Turkel, Phys. Rev. **72**, 888 (1947).

[2] M. E. Nelson and M. L. Pool, Phys. Rev. **77**, 682 (1950).

[3] D. R. Miller, Phys. Rev. **78**, 808 (1950).

[4] Von A. Flammersfeld and W. Herr, Z. Naturforsch. **7a**, 649 (1952).

Primary Heavy Nuclei*

THOMAS H. STIX†
Princeton University, Princeton, New Jersey
(Received April 16, 1954)

Primary cosmic-ray nuclei of $z \geq 2$ were observed in a balloon-borne cloud chamber. The chamber was triggered by events with ionization loss ≥ 6 minimum in each of three proportional counters, arranged in a telescope. Proportional counter pulse amplitudes were recorded by a neon bulb system.

Two Skyhook daytime balloon flights at geomagnetic latitude 41° maintained average altitudes of 17.6 and 14.3 g/cm². In the 0.77 hour *sensitive* time, in two flights, there were observed in the cloud chamber (charge determined from *both* cloud chamber and proportional counter data) 3–5 Li, 1 Be, 0 B, and 21 $z \geq 6$ nuclei. A primary flux of $10.2_{-3.4}^{+4.8}$ particles per m² sec sterad is found for the $z \geq 6$ nuclei. An unusually large fraction of this group is indicated to be heavier than oxygen. The primary flux of Li, Be, and B nuclei is found to be 5_{-5}^{+25} percent of the primary flux of $z \geq 6$ nuclei, from which we conclude that heavy nuclei have traversed less than 7 g/cm² interstellar hydrogen [$= (4/n) \times 10^9$ light years, where n = number of H atoms per cm³].

The proportional counter data *alone* showed a 14±16 percent decrease in intensity of particles of $z > 8$ from morning to afternoon.

I. INTRODUCTION

THE discovery of heavy primaries among cosmic rays[1] brought about important modifications of thought concerning the origin of cosmic radiation. Because these nuclei of helium through iron are stripped (or mostly stripped), their charge to mass ratio is almost independent of charge, and differs by only a factor of two from that of the protons. If then the protons sweep out orbits in extraterrestrial magnetic fields, the heavies should sweep out roughly similar orbits. Following along the proton paths, the heavies serve as sensitive probes to matter encountered on the way since they are irreversibly destroyed by collision.

Comparison of the number of heavy nuclei coming into the earth's atmosphere with the number of protons and alpha particles can lead to an upper limit on the amount of interstellar matter traversed by the heavy nuclei. For example, in the present experiment, at 41° north geomagnetic latitude, a vertical flux of 10 particles per m² sec sterad was found for nuclei of $z \geq 6$. The total number of vertically incident cosmic ray particles (mostly protons) with energies above 1.65 Bev per nucleon (cutoff energy at 41° for stripped heavy nuclei) is around 1700 per m² sec sterad.[2] Consider the extreme case: that only nuclei of $z \geq 6$ are originally accelerated. The 1700 protons then are the fragments of about 100 original heavy nuclei. If 110 heavies had been present at the start, the fluxes observed at the earth imply that 10 remained intact. The attenuation of 11 to 1 implies 2.4 "annihilation" lengths, or perhaps 4.8 mean free paths for collision with interstellar matter. The geometric mean free path for a nitrogen nucleus in hydrogen (the main constituent of matter in space) is 4.3 g/cm². The maximum amount of traversed interstellar hydrogen is thus about 20 g/cm². The interstellar proton density is, within a factor of 10, about 1 per cm³.[3] For a density of n protons per cm³ in interstellar space, one can state equivalently that the heavy nuclei cannot have traveled more than $13/n$ million light years between the time of their acceleration and their observation at the earth.

The foregoing estimate used the protons and alpha particles as indicators of interstellar fragmentation of heavier nuclei. A more sensitive measure of such fragmentation was discovered by Bradt and Peters.[4] The elements of lithium, beryllium, and boron which are very rare in the universe,[5] may nevertheless appear in the cosmic radiation as breakup fragments of $z \geq 6$ nuclei which have collided with interstellar hydrogen. In fact, Hodgson[6] found, in agreement with Bradt and Peters' surmise, that the probability that a CNO nucleus would produce a Li, Be, or B fragment on collision with a proton was 0.22±0.06.[7] From a measurement of the amount of Li, Be, and B occurring in the primary cosmic-ray flux, one can set an upper limit to the amount of traversed interstellar hydrogen.

The results of different measurements of the primary Li, Be, and B flux have been severely contradictory,[8–10] and are summarized in Table I. The last column of Table I estimates, on the basis of Eq. (12), the amount of traversed interstellar hydrogen. The last line of

* The principal results presented here were reported at the 1953 American Physical Society Washington Meeting: T. H. Stix, Phys. Rev. 91, 431 (1953). The work was supported in part by the U. S. Office of Naval Research, and was submitted by the author to the Graduate School of Princeton University in partial fulfillment of the requirements for the Ph.D. degree.

† U. S. Atomic Energy Commission Predoctoral Fellow.

[1] Freier, Lofgren, Ney, Oppenheimer, Bradt, and Peters, Phys. Rev. 74, 213 (1948).

[2] Winckler, Stix, Dwight, and Sabin, Phys. Rev. 79, 656 (1950).

[3] B. Stromgren, Astrophys. J. 108, 242 (1948).

[4] H. L. Bradt and B. Peters, Phys. Rev. 80, 943 (1950).

[5] L. Spitzer, Jr., Astrophys. J. 109, 548 (1949); J. L. Greenstein and E. Tandberg-Hanssen, Astrophys. J. 119, 113 (1954).

[6] P. E. Hodgson, Phil. Mag. 42, 955 (1951).

[7] Noon, Kaplon, and Ritson, Phys. Rev. 92, 1585 (1953), quote a value of 0.83±0.5 for this probability.

[8] Dainton, Fowler, and Kent, Phil. Mag. 43, 729 (1952).

[9] Kaplon, Peters, Reynolds, and Ritson, Phys. Rev. 85, 295 (1952).

[10] Kaplon, Racette, and Ritson, Phys. Rev. 93, 914 (1954).

TABLE I. Primary cosmic-ray flux of Li, Be, B nuclei.

Group	Technique	Geomagnetic latitude	Results: estimated primary fluxes	Implication: based on Eq. (12) using $\gamma=0.22$
Bradt and Peters,[a] 1950	Nuclear emulsions	30°	$\frac{\text{Li, Be, B}}{\text{C, N, O, F}}<0.1$	$z\geq 6$ nuclei have traversed <1.5 g/cm^2 interstellar hydrogen.
Dainton, Fowler, and Kent,[b] 1952	Nuclear emulsions	55°	$\frac{\text{Li, Be, B}}{\text{C, N, O, F}}\sim 1$	$z\geq 6$ nuclei have traversed >15 g/cm^2 interstellar hydrogen, or Li, Be, B nuclei are abundant in source region.
Kaplon, Peters, Reynolds, and Ritson,[c] 1952	Nuclear emulsions	42°	Be and B rare or absent	Same as first reference.
Kaplon, Racette, and Ritson,[d] 1953	Nuclear emulsions	41°	$0.1\leq\frac{\text{Li, Be, B}}{\text{C, N, O, F, Ne}}\leq 0.5$	$z\geq 6$ nuclei have traversed between 1.5 and 8 g/cm^2 interstellar hydrogen, or Li, Be, B are abundant in source region.
Stix, 1953	Cloud chamber proportional counter telescope	41°	$\frac{\text{Li, Be, B}}{z\geq 6}<0.37$	$z\geq 6$ nuclei have traversed <7 g/cm^2 interstellar hydrogen.

[a] See reference 4. [b] See reference 8. [c] See reference 9. [d] See reference 10.

Table I gives the results from the present experiment. These are statistically compatible with all but the Bristol measurements.

A strong diurnal variation for heavy nuclei would suggest a solar origin for these particles, but observations on this effect have been contradictory. Dwight's[11] calculations point out that charged particles coming directly from the sun can only enter into the earth's atmosphere from certain directions, at certain latitudes and times. For example, particles over a wide range of energies emitted in straight lines from the sun can arrive at the latitude of 41° only in the vertical direction in the middle of the winter, and only between 4 and 8 o'clock in the morning. The calculations thus imply that the heavy nuclei that passed through our vertical telescope in this experiment cannot have come directly from the sun.

Time variation measurements of the heavy nucleus flux are summarized in Table II.[12–18] The present experiment is consistent with a constant isotropic flux.

The present experiment introduces a new technique—the cloud chamber-proportional counter telescope combination—for observation of heavy cosmic-ray primary particles. Skyhook balloons carried 220-lb gondolas above 90 000 ft in two flights at 41° geomagnetic latitude. A gondola contained a cloud chamber which was triggered by a vertical telescope of three proportional counters (Fig. 1). An ionization larger than six times minimum was required in *each* of the three proportional counters in order to trip the discriminator-coincidence circuit. This selection scheme accepts all particles of $z>2$.

At the latitude and altitude of operation, vertically

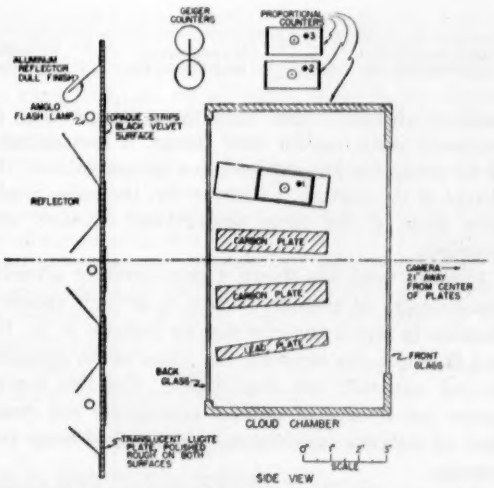

FIG. 1. Schematic drawing of balloon-borne cloud chamber and proportional counter telescope. Bottom counter of telescope is inside cloud chamber. Neon bulbs recorded pulse amplitudes from each proportional counter as variable length streaks above the cloud chamber photograph on the continuously moving 35-mm film. An additional neon bulb indicated events where one or both of the out-of-line Geiger tubes discharged in coincidence with the proportional counter telescope. Also indicated on the drawing is the compact cloud chamber rear illumination scheme.

[11] K. Dwight, Phys. Rev. **78**, 40 (1950).
[12] J. J. Lord and M. Schein, Phys. Rev. **78**, 484 (1950); Phys. Rev. **80**, 304 (1950).
[13] Freier, Ney, Naugle, and Anderson, Phys. Rev. **79**, 206 (1950).
[14] E. P. Ney and D. M. Thon, Phys. Rev. **81**, 1069 (1951).
[15] Freier, Anderson, Naugle, and Ney, Phys. Rev. **84**, 322 (1951).
[16] G. W. McClure and M. A. Pomerantz, Phys. Rev. **84**, 1252 (1951).
[17] Anderson, Freier, and Naugle, Phys. Rev. **91**, 431 (1953).
[18] V. H. Yngve, Phys. Rev. **92**, 428 (1953).

TABLE II. Time variations in the heavy nuclei flux.

Group	Technique	Geomagnetic latitude	Date of flight launching	Altitude in g/cm²	Results
Lord and Schein,[a] 1950	Nuclear emulsions	55°	Oct. 31, 1949	45	$\frac{\text{Night flux}}{\text{Day flux}} = 0.48 \pm 0.14$
		55°	Nov. 30, 1949	87	$\frac{\text{Night flux}}{\text{Day flux}} = 0.33 \pm 0.12$
		55°	May 22, 1950	15	$\frac{\text{Night flux}}{\text{Day flux}} = 0.39 \pm 0.04$
Freier, Ney, Naugle, and Anderson,[b] 1950	Nuclear emulsions	55°	Oct. 26, 1949	23–35	$\frac{\text{Night flux}}{\text{Day flux}} = 0.3$ to 0.5
Ney and Thon,[c] 1951	Scintillation counter	55°	Oct. 4, 1950	10	$\frac{\text{Afternoon flux}}{\text{Morning flux}} = 1.44 \pm 0.18$
Freier, Anderson, Naugle, and Ney,[d] 1951	Nuclear emulsions	55°	April 13, 1950	14	Night flux = day flux
McClure and Pomerantz,[e] 1951	Ionization chamber	55°	Aug. 17, 1951	29	Night flux = day flux ±13%
Anderson, Freier, and Naugle,[f] 1953	Nuclear emulsions	55°	July 31, 1952	18.5	Constant flux ±20% over 20-hr period
		55°	Aug. 28, 1952	30	
Yngve,[g] 1953	Nuclear emulsions	55°	June 4, 1952	17	Flux at 1 P.M. = 125±9% of average of 10:30 A.M. and 3:30 P.M. fluxes
Stix	Cloud chamber-proportional counter telescope	41°	April 26, 1952	17.6	$\frac{\text{Afternoon flux}}{\text{Morning flux}} = 0.86 \pm 0.16$
			May 8, 1952	14.3	

[a] See reference 12. [b] See reference 13. [c] See reference 14. [d] See reference 15. [e] See reference 16. [f] See reference 17. [g] See reference 18.

incident particles have velocities corresponding to minimum ionization for their charge. A measurement of the ionization loss can lead to a unique value of the charge of the particle. Consequently, the pulse height from each of the three proportional counters was recorded.

Previous work has shown a great need for accurate measurement of altitude. A drop in altitude causes a decrease in high-z particles and an increase in Li, Be, and B nuclei. An incorrect flux value or an apparent diurnal variation can thus appear. For this crucial reason the amount of residual atmosphere was measured by mercury manometer, photographed every two minutes.

The proportional counter telescope would be suited to survey measurements. In designing the present experiment, one had in mind that the counter telescope, without the cloud chamber but with additional shower protection from Geiger tubes, could at some time be used in a series of heavy-nuclei observations at different latitudes.

II. INTERPRETATION OF DATA FROM A PROPORTIONAL COUNTER TELESCOPE

In this experiment, heavy nuclei pass through the cloud chamber and their charge can be estimated. For events thus known from their cloud-chamber pictures to be heavy nuclei, the nuclear charge is measured quantitatively by the three proportional counters in the proportional counter telescope. The geomagnetic cutoff at this latitude (41°) for stripped vertically incident nuclei with equal numbers of protons and neutrons is 1.65 Bev per nucleon.[19] Allowed particles are still at minimum ionization at the balloon altitude (~15 g/cm²), consequently a proportional counter measurement of ionization loss can lead to a unique value for the nuclear charge.

The relation between most probable ionization loss and incident particle charge is found using an extension of the theoretical work of Landau[20] and Symon.[21] The

[19] M. S. Vallarta, Phys. Rev. 74, 1837 (1948).
[20] L. Landau, J. Phys. (U.S.S.R.) 4, 201 (1944).
[21] K. R. Symon, Harvard Ph.D. thesis, 1948 (unpublished). I am grateful to Dr. Symon for verifying the validity of this extension.

ionization loss fluctuation treatment developed by both of these authors becomes valid for incident particles of charge ze (rather than charge e) when the energy ξ defined by Landau is simply replaced by the new energy $\xi''=z^2\xi$. For Landau's work, we then have

$$\xi''=1.54\times10^5\mu z^2\frac{\Sigma Z}{\Sigma A}\frac{1}{(v/c)^2}\text{ electron volts,} \quad (1)$$

and the most probable energy loss is now given by Δ_0 as

$$\Delta_0=\xi''\left[\log\left\{\frac{4.62\times10^5\mu z^2\Sigma Z/\Sigma A}{Z^2[1-(v^2/c^2)]}\right\}+1-\frac{v^2}{c^2}\right]$$

$$\text{electron volts,} \quad (2)$$

where μ is the thickness of matter traversed in g/cm², ΣZ is the molecular charge, ΣA is the molecular weight of the traversed matter, and v is the velocity of the incident particle.

In particular, for minimum ionizing particles passing through one of the proportional counters (4.0 mg/cm² of argon), the most probable ionization loss is found to vary approximately as

$$\Delta_0\sim z^{2.16}, \quad (3)$$

in contrast to the z^2 variation for *average* ionization loss.

For a single particle, the proportional counter telescope gives three ionization loss measurements, Δ_1, Δ_2, Δ_3. It is necessary to determine from the three measurements a single equivalent ionization loss, Δ_E. Because the ionization loss distribution has a high positive skew, cosmic-ray workers by rule of thumb choose the smallest of the three measurements to be the equivalent ionization loss. In an effort to improve on this rule of thumb, the following data fitting scheme was used: For the ith counter, we denote the probability that a particle with most probable ionization loss Δ_0 will give rise to an ionization loss Δ_i in the range $d\Delta_i$ by $L(\Delta_i;\Delta_0)d\Delta_i$. By using the method of maximum likelihood, Δ_E for the group is then that value of Δ_0 for which the likelihood

$$L(\Delta_1;\Delta_0)L(\Delta_2;\Delta_0)L(\Delta_3;\Delta_0) \quad (4)$$

is a maximum.[22]

The ionization loss distribution, $L(\Delta_i;\Delta_\mu)$ was determined experimentally at sea level for fast mu mesons passing through one of the proportional counters (Fig. 2). A twofold Geiger tube telescope collimated the beam, and only those events were recorded where the mesons penetrated 4 in. of lead after passing through the proportional counter. The median energy for these mesons is 18 times their rest mass[23] corresponding to a

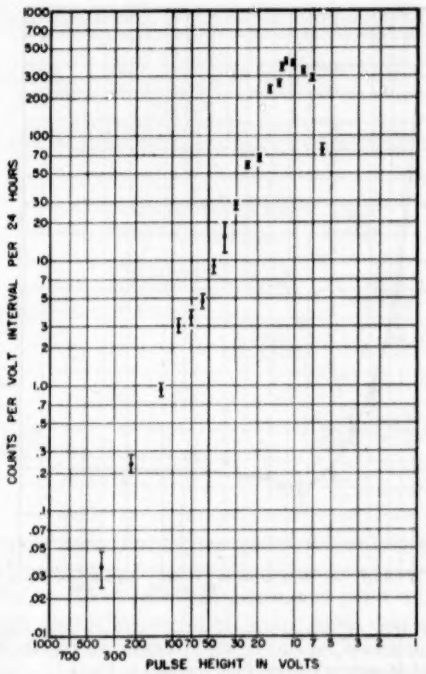

FIG. 2. Ionization loss distribution for fast mu mesons passing through a single proportional counter. Beam was collimated by twofold Geiger tube telescope, and only those events recorded where the mesons penetrated 4 in. of lead after passing through the proportional counter. Pulse-height distribution obtained at sea level using laboratory (not flight) electronics.

most probable ionization, (Δ_μ), according to the Landau formula of 1.19 times that for a minimum ionizing particle. To maximize the expression in (4), one has to know $L(\Delta_i;\Delta_0)$ for all values of Δ_0. In the absence of direct experimental knowledge, we used the scaling relation

$$L(\Delta_i;\Delta_0)=(\Delta_\mu/\Delta_0)L(\Delta_\mu\Delta_i/\Delta_0;\Delta_\mu) \quad (5)$$

to obtain an ionization loss distribution for particles of all values of Δ_0 (thus all values of z) from the experimental mu meson distribution. Equation (5) is an approximation to the Landau formula when ionization is considered a function only of the charge of the incident particle.

By using (5), the condition that (4) be a maximum is found by solving the equation

$$M(\Delta_1/\Delta_0)+M(\Delta_2/\Delta_0)+M(\Delta_3/\Delta_0)=-3 \quad (6)$$

for Δ_0. Here we have defined

$$M\left(\frac{\Delta_i}{\Delta_0}\right)=\frac{\Delta_i}{L(\Delta_i;\Delta_0)}\frac{\partial L(\Delta_i;\Delta_0)}{\partial\Delta_i}. \quad (7)$$

M is the slope of the ionization loss distribution when the latter is plotted on log log paper. A graph of M is shown in Fig. 3.

[22] The method of maximum likelihood assumes a flat *a priori* spectrum. The analysis was also carried through using a $1/\Delta_0$ *a priori* spectrum, but the change in results was completely negligible.

[23] B. Rossi, Revs. Modern Phys. **20**, 537 (1948).

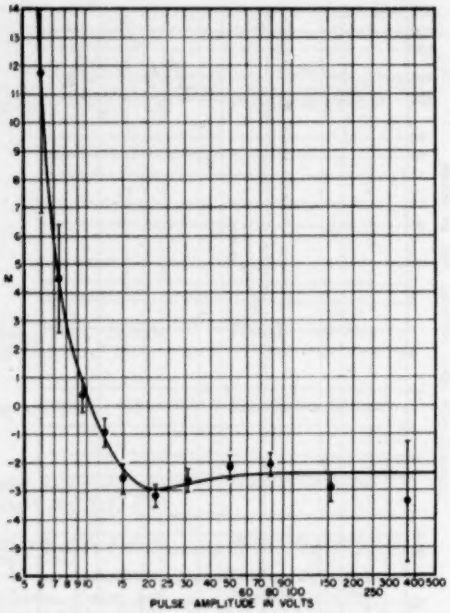

FIG. 3. $M(\Delta_i/\Delta_\mu)$ *versus* ionization loss (Δ_i) for a most probable ionization loss for μ mesons (Δ_μ) of $\Delta_\mu = 10.5$ volts. [See Eq. (7).] Values of M were calculated from the data in Fig. 2.

We denote by α the ratio $\Delta_E/\Delta_{\text{smallest}}$. The approximate solution of Eq. (6), α=constant, would correspond to the rule of thumb mentioned earlier. If one uses the *theoretical* Landau ionization loss distribution in 4.0-mg/cm² argon for $L(\Delta_i; \Delta_0)$, one finds that α always lies between 0.97 and 1.10. By using the *experimental* ionization loss distribution found for fast mu mesons for $L(\Delta_i; \Delta_0)$, the values of α are found to lie between 0.88 and 1.33. While these last values of α were the ones used in the analysis of the experimental data, it is worth noting that the rule of thumb ($\alpha = 1.11$ for all values of Δ_1, Δ_2, Δ_3) would never give values for Δ_E which differed by more than 26 percent from the values of Δ_E arrived at on the basis of the above detailed method. A difference of 26 percent in ionization loss corresponds to a difference of only 12 percent in charge.

In the analysis of the experimental data, one assigns a value Δ_E to the group Δ_1, Δ_2, Δ_3 for each heavy nucleus. The nuclear charge that is assigned to this event is that value, z_E, for which Δ_E is the most probable ionization loss. We use the relation

$$\Delta_E \sim z_E^{2.16}. \tag{8}$$

The calibration technique will be outlined in the next section.

III. THE FLIGHT APPARATUS

The flight apparatus contains a rear-illuminated cloud chamber which is triggered by a threefold proportional counter telescope (Fig. 1). The cloud chambers in this experiment had been used previously for balloon flight work.[24] The distance between the centers of the top and bottom counters of the telescope is $5\frac{1}{8}$ in. The area integral of the telescope solid-angle is 14.0 cm² sterad. With an isotropic flux, the average deviation from the vertical for particles traversing the telescope is 17°.

The rectangular proportional counters have a sensitive volume $4\frac{1}{2}$ in. long, $\frac{7}{8}$ in. high, $1\frac{7}{8}$ in. wide. Top and bottom counter walls are $\frac{1}{32}$-in. bronze, the side walls $\frac{1}{16}$-in. bronze. The counters are filled with 769 mm Hg of tank argon, are operated with approximately 1200 volts on the 0.00135-in.-diameter tungsten center wire, producing a gas amplification of about 200. A field tube termination for the center wire shown in Fig. 4 is used to reduce end effect.[25] Experiments made in the laboratory with collimated polonium alpha particles and collimated gamma rays indicated that the rms fluctuation in a random ionization measurement, due to gas attachment, recombination, and variation of gas amplification in the counter would be about 15 percent. The ionization loss distribution for fast mu mesons (Fig. 2) shows a half-width at half-maximum of about 50 percent. This is in excellent agreement with D. West[26] who beamed relativistic electrons through the central portion of a proportional counter filled with a similar amount of argon, and found a half-width at half-maximum of about 45 percent.

A block diagram of the electronics is given in Fig. 5. Separate channels amplify and record pulses from each of the three proportional counters. At the output of the gate circuits, the durations of the amplified pulses are 50 to 400 μsec and roughly proportional to the logarithms of the original amplitudes, owing to their exponential decay in the early stages of amplification. The linear pulse lengthener (Fig. 6) stretches these pulses to durations between $\frac{1}{4}$ and 2 sec. Neon recording lights

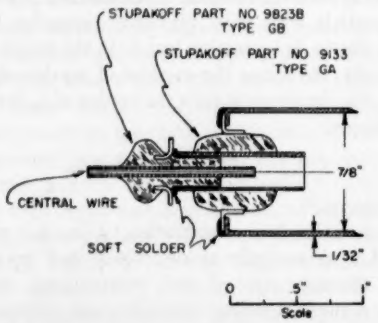

FIG. 4. Wire termination on proportional counters. Co-axially mounted Stupakoff seals provide simple field tube geometry. End of 0.00135 in. tungsten center wire is run through $1\frac{1}{4}$ in. long 0.045 in. o.d. nickel tube (not shown), which is clamped shut with spot-welder and soft-soldered in place inside innermost Stupakoff tube.

[24] R. R. Rau, Rev. Sci. Instr. **23**, 443 (1952).
[25] A. L. Cockcroft and S. C. Curran, Rev. Sci. Instr. **22**, 37 (1951).
[26] D. West, Proc. Phys. Soc. (London) **A66**, 306 (1953).

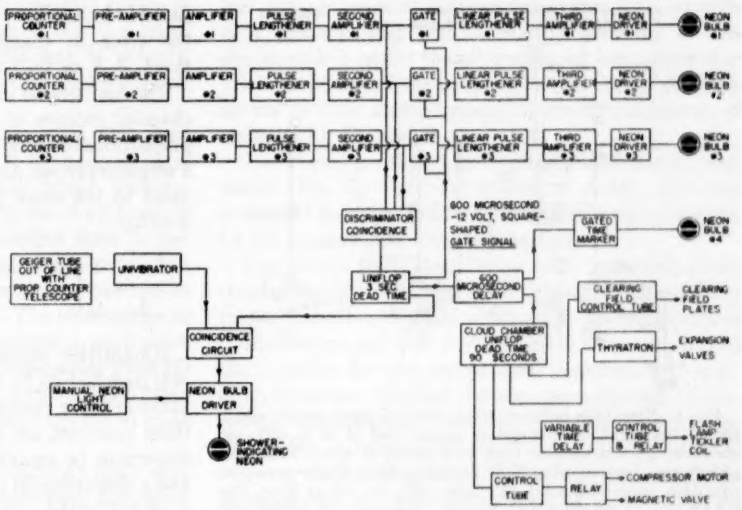

FIG. 5. Block diagram of electronics for balloon-borne cloud chamber and proportional counter telescope. Discriminator-coincidence circuit is triggered when event produces ionization loss greater than 6 times minimum in each proportional counter, and in turn triggers uniflop, which then cannot be retriggered for 3 sec. Gates open for 600 μsec, allowing signals to reach neons. Neon recording lights are energized for lengths of time between ¼ and 2 sec roughly proportional to logarithms of corresponding proportional counter pulse heights. Neon bulb No. 4 oscillates for 3 sec, 10 times per sec, providing time base on film record. Dead time for recording circuit is 3 sec, for cloud chamber, 90 sec.

are energized for these times producing streaks near the edge of the continuously moving 35-mm camera film—the same film used for the cloud-chamber photographs.

The triggering of the cloud chamber is delayed by 600 μsec so that the firing of the expansion valve thyratron and the removal of the cloud chamber clearing field voltage will occur *after* the gates are closed. Pickup from these cloud-chamber operations then can *not* produce spurious contributions to the proportional counter pulse-height record. A uniflop circuit inhibits the triggering of the cloud chamber if less than 90 sec have elapsed since the previous expansion.

The over-all gain of the amplifier up to the discriminator stage is around 3000, and the rise time is 40 μsec, although the rise time of the preamplifier is 6 μsec. The noise level is below 1 percent of the smallest signal that the discriminator will accept. Cross-talk can introduce spurious signals in adjacent channels no larger than 0.005 of the original signal. The ratio between maximum and minimum readable pulses is around 300 to 1, although readability becomes poorer for large pulses. The over-all resolution of the pulse height recording system was approximately 10 percent for the small pulses, 20 percent for the very large pulses.

The equipment was calibrated before flight by applying standard pulses of different amplitudes to the three preamplifiers. The neon bulb output was recorded on the camera film, as in flight. For the second flight, a post-flight calibration was also made. The two calibration curves were constant within a *full width* of 20 to 30 percent at the beginning and the end of the 22-hr period. From this and from similar curves made in the laboratory, we conclude that over the 8-hr period at altitude, the over-all drift in amplification was less than 20 percent in full width, or 10 percent from an average value. For the purpose of this experiment, this drift is small.

By an indirect method, a reference point was established correlating recorded proportional counter pulse output with ionization loss inside the counter. The response of the counters to an external radium source was used as a link. From the fast mu meson curve (Fig. 2), the pulse height P_0 was determined, which corresponded to six times the most probable ionization loss for minimum ionization-singly charged particles. Then, using the same equipment, with a 100 microcurie radium source placed exactly 1 meter away from the counter it was found that 320 pulses per min occurred with amplitude larger than P_0. The final step was to adjust the flight apparatus, before flight, so that with the same radium source at 1 m, 320 pulses per min arrived in each proportional counter channel with an amplitude larger than the discrimination level of the electronic circuitry. The "cutoff" point for small pulses is thus set in each channel at "6 minimum." The requirement that the ionization loss in each of three counters be larger than 6 minimum was approximately equivalent to an equivalent ionization loss, Δ_E, larger than 6.7 times minimum. In Sec. IV, we shall see that the alpha-particle data provides an independent verification of this reference "cutoff" point at 6.7 minimum.

Two units were flown at Pyote, Texas. A General Mills type 871 balloon was used for Flight I, on April 26, 1952, and reached 90 500 ft (17.1 g/cm²) at 0830 CST. In the first 7 hr at altitude, the balloon dropped only 500 ft. In the eighth hour, the balloon lost 2000 ft more. The load was released at 1630 CST from 88 000 ft (19.2 g/cm²). With a General Mills type 1101 balloon, Flight II, on May 8, 1952, reached 98 000 ft (12.0 g/cm²) at 0915 CST, held full altitude 1½ hr, then in 5½ hr gradually lost 7500 ft. The load was released at 1620 CST from 90 500 ft (17.1 g/cm²).

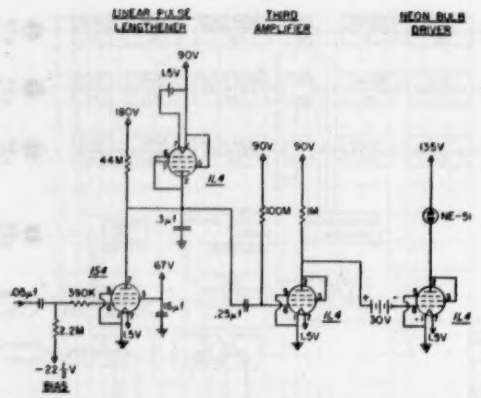

FIG. 6. Neon-bulb pulse recorder. Positive input pulses, which are 35 volts high, approximately square, and of 50 to 400 μsec duration, are stretched in time by a factor of about 5000, amplified, and used to drive Ne51 recording light. Under no-signal condition, diode-connected 1*L*4 holds plate of 1*S*4 at 90 v. The 0.3 mfd condenser discharges linearly when signal is applied and 1*S*4 pentode conducts, and charges linearly afterwards through 44 megohm resistor, as though charging to 180 v. When potential approaches 90 v, current flows in grid circuit of next stage and in 1*L*4 diode, returning voltages quickly to equilibrium. Amplifier stage is dc coupled to neon driver to accommodate repeated signals.

IV. THE FLIGHT DATA

In the course of the two balloon flights, about 7000 events triggering the proportional counter telescope were recorded. Cloud-chamber pictures accompanied approximately 10 percent of these events and 423 readable cloud-chamber pictures were obtained over a 10-hr period corresponding to 0.77 hr sensitive time. The photographs were classified: 68 nuclei of $z\geq 2$, 5 heavy nuclei which broke up before they reached the cloud chamber; 5 heavy nuclei which came very close to the wall of the top or bottom proportional counter and gave misleading proportional counter pulses; 3 heavy nuclei which broke up in the chamber, sending fragments back up through the telescope to trigger it; 57 slow protons stopping in an absorber in the cloud chamber; 76 showers; 63 bursts; and 146 cases identified simply as not due to a heavy nucleus.

Heavy nuclei were identified from the cloud-chamber data alone by the density of ionization along the track, estimated by visual examination, by their ability to penetrate the 4.1-g/cm² brass-jacketed carbon absorbers without an observed change in ionization, by the presence of delta rays, and occasionally by the appearance of an energetic nuclear interaction. With these criteria, it was possible to differentiate slow proton tracks (about 10 percent of the incident protons with energies in the range 50–100 Mev would produce ionizations in the three proportional counters sufficient to trigger the discrimination circuit) from tracks of relativistic particles of $z\geq 2$. Fast nuclei seen in the cloud chamber were classified as $z=1$, 2, 3, or ≥ 4. For $z\geq 4$, the average ionization is greater than 16 minimum and the cloud-chamber track is opaque. One estimates that the error in charge classification for fast particles ($z=1$, 2, 3, or ≥ 4) is one unit.

The histograms in Fig. 7 show the number of cloud-chamber pictures of different types, plotted against the proportional counter telescope charge measurement. For a single traversal, the fractional rms deviation from the mean in the three proportional counter pulse heights is σ/Δ_0:

$$\frac{\sigma}{\Delta_0}=\frac{1}{\Delta_0}\left\{\frac{(\Delta_1-\Delta_{Av})^2+(\Delta_2-\Delta_{Av})^2+(\Delta_3-\Delta_{Av})^2}{3}\right\}^{\frac{1}{2}}. \quad (9)$$

(Quantities defined in Sec. II, and denoting $\Delta_{Av}=\frac{1}{3}[\Delta_1+\Delta_2+\Delta_3]$.) In Fig. 7, narrow histogram bars indicate those events for which $\sigma/\Delta_0\geq 100$ percent. For three counters, an *average* dispersion σ/Δ_0 indicates a dispersion in equivalent pulse heights, Δ_E, of $\sigma/\sqrt{3}\Delta_0$ and a dispersion in the resultant charge measurements, z, of $\sigma/2.16\sqrt{3}\Delta_0$. [See Eq. (8).] In Fig. 7, $\sigma/\Delta_0\geq 100$ percent for only 3 of the 34 alpha particles and for none of the 21 $z\geq 6$ events. Thus, in more than 90 percent of the cases, the indicated deviation from the

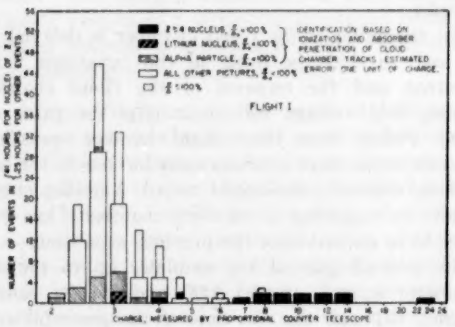

I

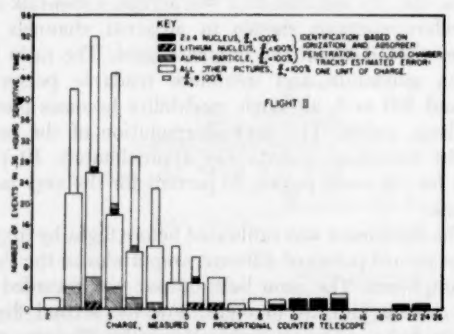

II

FIG. 7. Charge spectrum for events seen in cloud chamber, Flights I and II. Charge estimated visually from density of ionization along track and absorber penetration (indicated by shading) and measured by proportional counter telescope (abscissa). For each event, σ/Δ_0 denotes the fractional rms deviation from the mean of the three proportional counter ionization loss amplitudes.

mean measured value of z was less than $100/2.16\sqrt{3}=27$ percent. Similarly, the *median* value of the dispersion, σ/Δ_0, for the alpha and $z\geq 6$ events was 31 percent, indicating a median deviation from the mean measured value of z of less than 9 percent.

A comment can be made on skewness. The three pulse heights show a positive skew if the average pulse height is larger than the middle pulse height. Twenty-five of the 34 alpha particles and 16 of the 21 $z\geq 6$ events showed such a positive skew. A positive skew is predicted both by the theoretical Landau ionization loss distribution and by the experimental fast mu meson ionization loss distribution (Fig. 2). The observation of positive skew in the flight data provides a qualitative justification for the use of a data fitting scheme (Sec. II) which assigns to an ionization loss group Δ_1, Δ_2, Δ_3 an equivalent ionization loss, Δ_E, smaller than the average ionization loss, $\Delta_M=\frac{1}{3}(\Delta_1+\Delta_2+\Delta_3)$.

The counter telescope and discrimination circuit were adjusted to reject all events with equivalent ionization loss smaller than 6.7 minimum (Sec. III). This cutoff at 6.7 minimum provided the reference point for calibrating the charge measurement scale. An independent check on the accuracy of this scale calibration comes from the alpha-particle data. A fraction of the incident alphas gave ionization losses in each of the three proportional counters sufficiently larger than the most probable loss (4.5 minimum) to trigger the telescope. Knowing the dispersion in the ionization loss and the fraction of alphas that triggered the telescope, we can make an independent estimate of the equivalent ionization loss at the cutoff point.

Based on a primary alpha flux at 41° of 140 particles per m² sec sterad and an absorption length in the atmosphere of 60 g/cm²,[9] the flux of alphas expected to reach the cloud chamber is 103 particles per m² sec sterad. The 34 observed alpha particles correspond to an incident flux of 11.0 particles per m² sec sterad *triggering* the telescope, or 11 percent of the incident alphas. The area under a *Gaussian* curve to the right of center by 1.23 standard deviations (1.23σ) is 11 percent of the total. The median value of the dispersion σ/Δ_0 for the observed alphas was 35 percent, indicating a dispersion in Δ_E of 20 percent. The cutoff point then occurs at an ionization loss of $4.5(1+1.23\times 0.20)=5.6$ minimum. The possible error introduced by calling this point 6.7 minimum, as we do in this experiment, is 20 percent in ionization or 9 percent in charge. However, since the ionization loss distribution is not Gaussian, but skewed positive, the above error is smaller and could be zero.

In summing up, single nuclei are classified from their cloud-chamber photographs into $z=1$, 2, 3, or ≥ 4 with an error estimated to be one unit of charge. For the proportional counter telescope, the dispersion data leads us to expect that in 90 percent of the cases the fractional deviation from the mean measured value of z will be less than 27 percent, and in 50 percent of the cases, less than 9 percent. Furthermore, the alpha-particle data indicate that the calibration accuracy of the charge scale is better than 9 percent for low values of z. These estimates of the accuracy of the charge determination provide useful criteria in the identification of nuclei of Li, Be, and B.

Two events in Flight I gave the appearance of lithium nuclei (Fig. 7). For both events, a charge of 3 was estimated from the cloud chamber picture and measured by the proportional counter telescope.

Five events were identified as $z=3$ from their cloud chamber pictures in Flight II (Fig. 7). However, for two of them, the charges measured by the proportional counter telescope were 5 and 6. Such errors are out of the question for the proportional counters, and similarly, the cloud chamber pictures are completely inconsistent with labeling these particles boron or carbon nuclei. We interpret these two cases as unusual bursts or heavy nucleus fragmentations, and discard them from consideration as valid examples of Li nuclei. For two more of the $z=3$ events in Flight II, dispersions σ/Δ_0 of 162 percent and 175 percent were recorded. The smaller of these dispersions is 5.2 times as large as the median dispersion found for alpha and $z\geq 6$ particles. It is thus probable that these two events also are not valid Li nuclei, but, to be conservative, we do not discard them. The number of Li nuclei observed is then 2 Li in Flight I in 0.41 hr sensitive time, and 1–3 Li in Flight II in 0.36 hr sensitive time.

For Flight I, Fig. 7 shows one beryllium nucleus and one event halfway between beryllium and boron. Figure 7 shows an apparent boron nucleus in Flight II. However, these last two events both showed dispersions σ/Δ_0 larger than 100 percent (3.2 times as large as the median dispersion for alphas and $z\geq 6$ nuclei). More important, the three pulses for both these events showed a large negative skew (one small pulse and two large pulses) which is highly unusual (see above). The small pulse came in both cases from the counter inside the cloud chamber, and the stereographic cloud-chamber photographs show that in each case the particle passed *very* close to the front wall of this proportional counter. This close passage could account for the small pulse. In both events, the density of ionization of the cloud-chamber track, and the pulse amplitudes from the top two proportional counters are consistent with particles of $z\geq 6$. We conclude that these events are $z\geq 6$ nuclei which passed outside the proper solid angle of the proportional counter telescope, and on this basis, we discard them from consideration. The only valid observation is then the first: 1 beryllium and 0 boron nuclei in Flights I and II in 0.77 hr sensitive time.

For all of the $z\geq 6$ nuclei, the dispersions σ/Δ_0 were <100 percent. From Fig. 7, we have 12 nuclei of $z\geq 6$ in Flight I in 0.41 hr sensitive time, and 9 nuclei of $z\geq 6$ in Flight II in 0.36 hr sensitive time.

V. EXPERIMENTAL RESULTS

In this section we present the significant experimental results and interpretations bearing on (a) the mean free path for heavy nuclei in carbon and lead, (b) the time variation in the primary flux of heavy nuclei, (c) the primary flux and relative abundances of nuclei of $z \geq 6$, and (d) the primary flux of nuclei of $z=3$, 4, and 5.

The small numbers of events we have to deal with necessitate a cautious evaluation of the statistics. In assigning limits of error, we follow V. H. Regener.[27] Consider a given measured count n. It is possible to determine a value a_1 for a hypothetical average count which lies so far below n that the total probability (evaluated on the basis of a Poisson distribution) for the actual count to fall anywhere below n assumes a specific value p. Above n, another value a_2 can be determined so that the total probability for the count to fall anywhere above n assumes again the value p. In the data analysis to follow, we make the conservative choice: $p=95$ percent, noting that for a Gaussian distribution the use of limits $a_1=n-\sqrt{n}$, $a_2=n+\sqrt{n}$ corresponds to $p=84$ percent.

(a) Mean Free Paths in Carbon and Lead

By counting the number of traversals of the cloud-chamber absorbers with and without observed interaction, mean free paths can be evaluated for alphas and $z \geq 6$ nuclei. The two top absorber plates were each $\frac{3}{4}$-in. slabs of graphite jacketed with 0.020-in. brass sheeting, totaling 4.1 g/cm² apiece. The third absorber was lead, $\frac{7}{16}$ in. or 12.5 g/cm² thick. The average angular deviation from the vertical for the primary particle passing through the horizontal absorber plates was 17°. In Table III, a collision in an absorber is also counted as half a traversal.

The mean free paths listed in Table III agree within the statistics with similar measurements made in nuclear emulsions.[9,15] Later we will need to know the absorption length in air for $z \geq 6$ nuclei. On the basis of a simple geometrical model, used by Kaplon, Peters, Reynolds, and Ritson[9] to describe the cross section for collision between two heavy nuclei, the calculated mean free path expressed in g/cm² for our carbon-brass absorber is very close to that in air. Therefore we use our measured value of 29 g/cm² for an absorption length for $z \geq 6$ nuclei in air. We note also that the mean free path for the oxygen nucleus in air, calculated from the model, is also 29 g/cm².

TABLE III. Interactions seen in cloud chamber.

	Number of traversals without observed interaction	Number of observed interactions	Mean free path (95% limits) g/cm²
	Alpha particles		
78% Carbon 22% Brass	50	3	70_{-44}^{+198}
Lead	13	3	57_{-40}^{+168}
	$z \geq 6$ particles		
78% Carbon 22% Brass	27	4	29_{-18}^{+80}
Lead	9	0	>32

[27] V. H. Regener, Phys. Rev. 84, 161 (1951).

(b) Variation of Counting Rates with Time

A limited amount of information is obtainable from the proportional counter telescope data alone. The two out-of-line Geiger tubes, shown in Fig. 1, afford insufficient protection to the proportional counter telescope. Without the aid of cloud-chamber pictures, multiple particle events (showers and bursts) produce a large background against which it is not possible to detect the presence or absence of Li, Be, and B, and from which it is not possible to make a clean separation of the heavy ($z \geq 6$) nuclei. (See beginning of Sec. IV; also note white histogram bars on Fig. 7.) It was noticed, however, that multiple particle events gave rise to a pulse-height dispersion σ/Δ_0 which was on the average 4 times as large as the dispersion for single nuclei. Moreover, Fig. 7 shows that in 18 out of 20 events of $z \geq 9$ the proportional counter telescope and cloud chamber agreed. In looking for a time-intensity variation for the heavy nuclei, we choose only counter telescope events where $\sigma/\Delta_0 < 100$ percent, and for which z was measured to be ≥ 9, and which were not accompanied by a time-coincident discharge in the out-of-line Geiger tubes. We expect 90 percent of the events thus selected to be single heavy nuclei.

Figure 8 shows the counting rate, per hour, during the two flights for these events. Also shown, for comparison, is the counting rate for all events triggering the proportional counter telescope. The small steady attenuation in the observed flux during the flight period was evaluated using the method of averages. A correction was made for the small change in altitude of the balloons during flight, using an absorption length in air of 29 g/cm² for the heavy nuclei (see Sec. V-a), and of 195 g/cm² for the total counting rate (based on data taken during ascent of the balloons). Error from possible changes of electronic amplification during flight was estimated and included with the statistical counting rate error. Errors from the two sources were approximately equal.

The attenuation in intensity thus calculated was 4 ± 4 percent per 4 hr for all events triggering the proportional counter telescope, and 14 ± 16 percent per 4 hr for events where $\sigma/\Delta_0 < 100$ percent and $z \geq 9$. The measurement is compatible with no change in the intensity of the heavy nuclei during the flight period, but the observed variation is in the opposite direction from the morning-afternoon intensity variation at 55° reported by Ney and Thon[14] and fails to show the mid-day peak

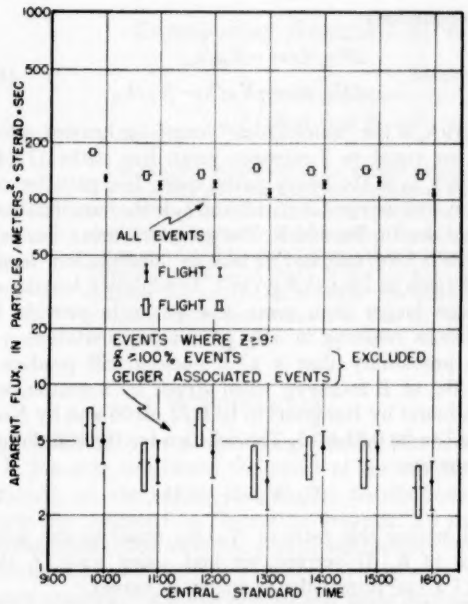

FIG. 8. Variation of event frequency with time. Events comprising upper set of points are predominantly showers and bursts. More than 90 percent of the events comprising the lower set of points are expected to be single heavy nuclei. Indicated errors are standard deviations based only on number of counts.

reported by Yngve,[18] also at 55°. However, recent measurements at 55° by Anderson, Freier, and Naugle[17] also indicated no diurnal intensity variation. Heavy nucleus intensity-time variation data is summarized in Table II.

(c) Primary Flux of Nuclei of $z \geq 6$

For the two flights, in 0.77 hr sensitive time, a total of 21 nuclei were seen in the cloud chamber for which the proportional counter telescope measured nuclear charges of $z \geq 6$. The average path length through the atmosphere and through the 2 g/cm² air-equivalent of material in the gondola above the cloud chamber, at 17° average deviation from the vertical, was 18.5 g/cm². By using an absorption length in air of 29 g/cm² and recalling that the solid-angle area integral of the counter telescope was 14.0 cm² sterad, the primary flux for $z \geq 6$ is $10.2_{-3.4}^{+4.5}$ primary nuclei per m² sec sterad.

The errors quoted are 95 percent limits. The upper error limit here is two standard deviations.

Van Allen[28] made rocket flights at the same latitude with a single cylindrical ionization chamber, and from his data estimated an upper limit for $z \geq 6$ of 13 nuclei per m² sec sterad. With nuclear emulsions also at the same latitude, Kaplon *et al.*[9] found a flux for $z \geq 6$ of 8.3 ± 0.8 nuclei per m² sec sterad.

On the other hand, from measurements at 55° geomagnetic latitude, Dainton *et al.*[8] find the flux of particles with energies greater than 1.5 Bev per nucleon (based on measurement of multiple Coulomb scattering) and $z \geq 6$ (by grain-density and delta-ray counts) to be only 3.2 ± 0.5 nuclei per m² sec sterad. The geomagnetic cutoff at 41° is 1.6 Bev per nucleon for heavy nuclei, so the flux found by the Bristol group is incompatible with both the Rochester flux measurement and our own.

Concerning relative abundances within the $z \geq 6$ classification, Bradt and Peters[29] report a primary flux for $z > 10$ particles about a third that of the $6 \leq z \leq 10$ flux, and other nuclear emulsion data[8,9,13] yield similar ratios. However, in the present experiment, for 12 of the 21 nuclei with $z \geq 6$ shown in Fig. 7, the measured charge was $z > 10$. A high proportion of very heavy nuclei is favored by the telescope's narrow angle of acceptance around the zenith and by the small amount of residual atmosphere. However, we point out that the measurement of the $6 \leq z \leq 10$ nuclei to $z > 10$ nuclei ratio requires an accurate calibration of the charge measurement scale in the neighborhood of $z = 10$. In the present experiment, we have an independent check on the calibration accuracy in the low-z region (Sec. IV) but not in the high-z region.

(d) Primary Flux of Li, Be, B

In the same interval during which 21 nuclei of $z \geq 6$ were seen in the cloud chamber, there were observed 3–5 Li nuclei, 1 Be nucleus, and 0 B nuclei (Sec. IV).

A certain number of Li, Be, and B nuclei are expected to appear in the atmosphere as breakup fragments of heavier nuclei. At the end of 18.5 g/cm² equivalent air path, if one observed N_H nuclei of $z \geq 6$, the expected number N_L of Li, Be, and B nuclei due to breakup is

$$N_L = \eta N_H \int_{x=0}^{x=18.5} \exp\left(\frac{18.5}{\lambda_H} - \frac{x}{\lambda_H} - \frac{18.5-x}{\lambda_L}\right)\frac{dx}{\lambda_H}, \quad (10)$$

where η is the probability that a $z \geq 6$ nucleus, on collision with an air nucleus, will yield a fast Li, Be, or B fragment. Bradt and Peters[4] use a value of $\eta = 0.23$, while Noon, Kaplon, and Ritson[7] report a value of 0.56 ± 0.18 for P_{ML} (Li, Be, and B fragments from $6 \leq z \leq 10$ collisions in air). In our case, $N_H = 21$, and using $\lambda_H = 29$ g/cm² and $\lambda_L = 37$ g/cm² (from an empirical formula[9] based on emulsion measurements), we get $N_L = 2.9$ and 7.0 Li, Be, and B nuclei corresponding to the values $\eta = 0.23$ and 0.56, respectively.

The observed value of N_L was 4–6 in 0.77 hr sensitive time. (The larger figure includes two doubtful events. See Sec. V.) The above calculation shows that it is possible to account for all of the observed Li, Be, and B particles on the basis of the breakup mechanism alone.

From our data, we can calculate the ratio R of the flux of Li, Be, and B to $z \geq 6$ nuclei in the primary cosmic radiation. To be conservative, we choose the smaller value of η, and attribute all Li, Be, and B

[28] J. A. Van Allen, Phys. Rev. **84**, 791 (1951).

[29] H. L. Bradt and B. Peters, Phys. Rev. **77**, 54 (1950).

nuclei in excess of 2.9 particles per 0.77 hr to primary cosmic radiation. To set an upper limit, we use Regener's 95 percent probability calculations[27] and again to be conservative, we include the two doubtful events in N_L observed: if the average total flux of Li, Be, and B nuclei at the end of 18.5-g/cm² equivalent air path were 11.84 particles per 0.77 hr, the probability would be 95 percent for *more than* 6 events to have been observed in this time. We then have

$$R=\frac{\text{Primary Li, Be, B}}{\text{Primary } z\geq 6}$$

$$=\left\{\begin{array}{l}\text{upper limit: } (11.84-2.9)/21\\ \text{observed: } (4-2.9)/21\\ \text{lower limit: } 0\end{array}\right\}\times\exp\left(\frac{18.5}{37}-\frac{18.5}{29}\right)$$

$$=5_{-5}^{+32}\text{ percent},$$

where the exponential factor extrapolates to the top of the atmosphere the fluxes observed at 18.5 g/cm² due to primary nuclei.

Table I shows the values obtained for R by different groups. Within the statistics, our finding is compatible with the various Rochester measurements, but is in disagreement with the measurements made by Bristol.

VI. CONCLUSION

Cosmic rays, between the time of their acceleration and observation at the earth, pass through interstellar space. Even if no Li, Be, B nuclei are originally accelerated, these nuclei will appear at the earth as a result of fragmentation of heavier nuclei against hydrogen nuclei, present in space. If one has an upper limit to the ratio R, one can set an upper limit to the number of g/cm² interstellar hydrogen traversed by the heavy nuclei.

Consider that $N_H(x)$ and $N_L(x)$ are the fluxes of heavy ($z\geq 6$) and light ($z=3, 4, 5$) nuclei as a function of x, the distance along the path from the region of origin measured in g/cm² of interstellar hydrogen. Assume the extreme case: $N_L(0)=0$. We can write the two equations:

$$\begin{aligned}dN_H/dx&=-N_H/\lambda_1,\\ dN_L/dx&=\gamma N_H/\lambda_2-N_L/\lambda_3,\end{aligned}\qquad(11)$$

where λ_1 is the "annihilation" length for heavies, which we set equal to 2 nitrogen mean free paths (2×4.3 g/cm²), λ_2 is the heavy nuclei mean free path for collision, and we use 4.3 g/cm², and λ_3 is the "annihilation" length for Li, Be, and B. The geometric mean free path for Be is 5.8 g/cm², and we take an "annihilation" length half again as long (8.6 g/cm²). Annihilation lengths are chosen longer than mean free paths to provide for collisions resulting in only partial fragmentation. γ is the probability that a $z\geq 6$ nucleus will produce a Li, Be, or B fragment when struck by a proton, and was found by Hodgson[6] to be 0.22 ± 0.06 and by Noon *et al.*[7] to be 0.83 ± 0.5. The solution for the equation is, in our case

$$N_L/N_H=(\gamma/4.3)x,\qquad(12)$$

and setting this ratio of N_L/N_H equal to the upper limit of R, 37 percent, we find, using $\gamma=0.22$, that $x<7$ g/cm² interstellar hydrogen traversed.

The interstellar proton density is, within a factor of 10, around 1 per cm³.[3] For a density of n protons per cm³ in interstellar space, the upper limit on x can be expressed as an upper limit on the effective mean length of path for heavy nuclei in interstellar space, L:

$$L<4\times 10^6/n \text{ light years.}$$

Such a limit on heavy nuclei interstellar path lengths may be imposed by leakage of the particles out of the volume of a containing magnetic field.[4,30] If $\gamma=0.83$ is used, the above upper limits on x and L will be proportionately reduced.

ACKNOWLEDGMENTS

It is a pleasure to acknowledge the help of my advisors, Professor R. Ronald Rau and Professor Geo. T. Reynolds. I also wish to thank Professor John A. Wheeler for valuable suggestions on the presentation of the results, Dr. A. L. Hodson for giving generously of his time in running the fast mu meson experiment, and Dr. S. B. Treiman for helpful discussions on the problem of statistics.

[30] E. Fermi, Astrophys. J. 119, 1 (1954).

Cosmic-Ray Neutrons in Water at an Altitude of 10 600 Feet*†

MARTIN JAY SWETNICK‡
Physics Department, New York University, New York, New York
(Received April 29, 1953; revised manuscript received April 27, 1954)

The neutron component of the cosmic radiation in the first 50-cm layer of water adjacent to the surface of a mountain lake, located at an altitude of 10 600 feet, was studied with the aid of a tray of ten enriched boron trifluoride filled counters connected in parallel. A measure of the thermal neutron intensity was obtained by alternately shielding the tray of counters with tin and cadmium of equal g cm^{-2}. A transition region was found to exist between the surface and the 30-cm level wherein the thermal neutron intensity decreased rapidly with depth. Below the 30-cm level, the thermal neutron intensity was found to be almost constant over an interval of 20 cm. The neutron production rate and thermal neutron flux, just below the transition region, were found to be 4.6×10^{-5} neutrons g^{-1} sec^{-1} and about 4.3×10^{-4} thermal neutrons cm^{-2} sec^{-1}, respectively.

I. INTRODUCTION

A LITTLE over a decade ago Bethe, Korff, and Placzek[1] considered the effect of the surface of the earth on the energy and spatial distributions of cosmic-ray neutrons on theoretical grounds. To show how large the influence of the ground can be, they chose an extended water surface as a special case since the known chemical composition of air and water permitted numerical calculations to be made on the basis of neutron slowing-down theory. The results of the calculations indicate that the influence of the water surface should be felt up to a height equivalent to 1 meter of water in air and only over an interval of about 30 cm of water below the surface.

This paper is only concerned with the distribution of cosmic-ray neutrons below the surface of an extended body of water. The surface of the water, according to Bethe *et al.*, has a marked influence on the spatial distribution of thermal neutrons in the 30-cm layer of water adjacent to the surface. At the 1.5-cm level, the thermal neutron intensity is predicted to be a maximum while in the interval 3 to about 20 cm below the surface the thermal neutron intensity is predicted to decrease rapidly. Below the 30-cm level, however, the thermal neutron intensity is predicted to remain almost constant over an interval of at least 20 cm.

Bethe *et al.* attribute the form of the thermal neutron distribution in the first 30 cm of water to neutrons which are produced in air and enter the water while their energies are between 4 Mev and 0.06 ev. These neutrons, on colliding with hydrogen nuclei, are rapidly slowed down to thermal energies. Since the diffusion length of thermal neutrons in water is about 2 to 3 cm, some of the thermal neutrons within 2 cm of the surface diffuse back into the air where they are captured by nitrogen nuclei. As there are more neutrons available to be slowed down near the surface than at greater depths a greater intensity of thermal neutrons should exist near the surface. At depths greater than 30 cm the thermal neutron distribution should be due only to neutrons produced in water since neutrons produced in air cannot penetrate there.

During the summer of 1950, an experiment was carried out to study the neutron component of the cosmic radiation below the surface of Echo Lake, located at an altitude of 10 600 feet in Colorado. The objectives of the experiment were to determine the form of the thermal neutron intensity variation over the first 50 cm of water from the surface and to obtain quantitative measurements of the production rate and flux of neutrons in water at mountain altitudes. All measurements were made at the center of the lake where the neutron distribution near the surface is least influenced by the surrounding ground.

II. APPARATUS

A block diagram of the experimental setup is shown in Fig. 1. The neutron detector was composed of a tray of ten identical neutron counters positioned side by side in a horizontal plane. The counters were connected in parallel to the input of a cathode follower preamplifier. The counters were filled to a pressure of 25 cm of Hg with enriched BF_3 (96 percent B^{10}). Each counter had a 50 cm long copper cathode of

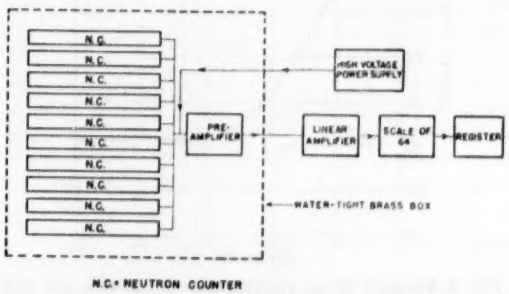

FIG. 1. Block diagram of experimental setup.

* Assisted by the joint program of the U. S. Office of Naval Research and the U. S. Atomic Energy Commission.

† This report is an abridgement of a dissertation submitted in partial fulfillment of the requirements for the degree of Doctor of Philosophy at New York University, 1951.

‡ Now at the Anton Electronic Laboratories, Inc., Brooklyn, New York.

[1] Bethe, Korff, and Placzek, Phys. Rev. **57**, 573 (1940).

2-cm i.d. and 0.2-cm wall thickness. Three-mil tungsten wire served as counter anodes.

The neutron detector and a cathode follower preamplifier were enclosed in a thin-wall, water-tight brass box. The box was equipped with a pair of lever arms that were fastened to the legs of a small wooden platform which had been erected at the center of the lake. The lever arms served to hold the tray of counters parallel to the surface at all depths within the first 50 cm of water from the surface.

The linear amplifier, scaling circuit, and high voltage supply were kept on the small wooden platform. The circuitry was kept in an insulated box to protect them from the elements. Power for the equipment was brought to the platform by means of heavy duty cable that was connected to a transformer on shore.

III. THERMAL NEUTRON DETECTION

To determine the thermal neutron counting rates, a 1-mm thick cadmium shield and a tin shield of equal g cm^{-2} were used in conjunction with the neutron detector. When the detector is shielded with cadmium, the counting rate is due to neutrons having energies greater than 0.4 ev, the cadmium cutoff, to ionizing events produced by cosmic and counter background radiations, and to some star fragments produced in the cadmium shield. When the detector is shielded with tin, the counting rate is due to neutrons having all energies, to cosmic and counter background radiations, and to star fragments produced in the tin shield. The difference between the tin and cadmium counting rates gives an accurate measure of the thermal neutron counting rate. The counting rates due to the cosmic and counter background radiations and to the star fragments produced in the shields cancel out since they are the same for the tin- and cadmium-shielded detector.

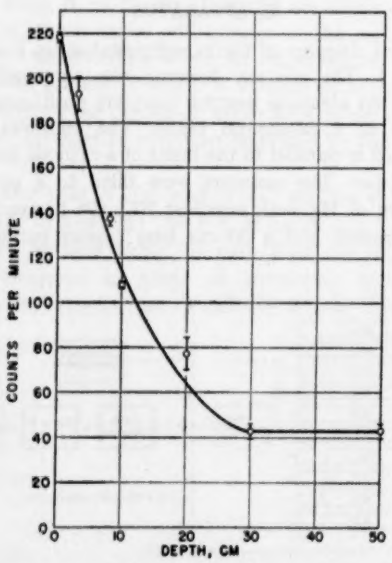

FIG. 2. Variation of the thermal neutron counting rate with depth below the surface of an extended body ofw ater at an altitude of 10 600 feet.

The tin shield is primarily used to compensate for the star fragments that are produced in the cadmium shield, which at the 10 600 foot elevation may be a few percent of the thermal neutron counting rate. As remarked by Yuan,[2] the production rate of stars in the tin and cadmium shields of equal g cm^{-2} should be about equal since the atomic numbers of tin ($Z=50$) and cadmium ($Z=48$) are almost the same.

IV. EXPERIMENTAL PROCEDURE

Measurements of the thermal neutron intensity were made at the surface, and at the 3-cm, 8-cm, 10-cm, 20-cm, 30-cm, and 50-cm depths. At each of these depths the following procedure was followed. First the tin shield was placed over the box containing the detector and the counting rate was determined at 50-volt intervals between 1800 volts and 2550 volts. The tin shield was then replaced by the cadmium shield and the counting rate was once more determined as a function of voltage at the same 50-volt intervals. The time of each run at a particular voltage setting varied between one-half hour and three hours, depending on the counting rate. To check the consistency of the measurements, they were repeated at different depths during the five weeks the experiment was carried out.

There were two reasons for making the tin and cadmium counting rate determinations as a function of voltage instead of at one fixed voltage midway along the neutron detector plateau. The first was that these measurements permitted a continuous check on the operation of the detector. In the event the plateau shifted or changed its length or slope it would be an indication that one or more counters were not operating properly. This situation could then be corrected. If, on the other hand, the detector was operated at one fixed voltage, a change in its operating characteristics would yield ambiguous counting rates. The second reason was that on taking the tin-cadmium difference counting rate a thermal neutron counting rate plateau would be found where the average of the counting rates on the plateau could be taken as the thermal neutron counting rate at the depths investigated.

V. EXPERIMENTAL RESULTS

Tabulated in Table I are the experimental results showing the average thermal-neutron counting rates at the depths investigated. The errors given are the probable errors of the mean. A plot of the mean thermal-neutron counting rate *versus* depth is shown in Fig. 2.

VI. DISCUSSION OF RESULTS

The form of the thermal-neutron intensity variation with depth, as shown in Fig. 2, offers direct experimental

[2] L. C. L. Yuan, Phys. Rev. **81**, 175 (1951).

evidence for the existence of a surface effect on the neutron energy and spatial distributions in water. It is seen that the first 30-cm layer of water adjacent to the surface is a transition region wherein the thermal neutron intensity varies rapidly with depth. The thermal neutron intensity is found to be a maximum at the surface, and not at the 1.5-cm level as theoretically predicted. It is impossible to say, on the basis of the present experiment, whether this discrepancy is real or not. To obtain results which would clearly show the position of the maximum, measurements at 0.5-cm intervals in the first 3 cm of water would have had to be made. Such measurements could not be made with the detector used since its height of 2 cm was almost as large as the layer of water in which the maximum is located. The rapid decrease of the thermal neutron intensity between the 3-cm and 30-cm level is, however, in agreement with theory.

Below the 30-cm level, the thermal neutron intensity is found to remain almost constant over 20 cm of water. In this region there exist three conditions which make it possible to obtain a quantitative determination of the neutron production rate in water. They are (1) the accurate measure of the thermal neutron counting rate by means of the tin-cadmium difference method, (2) the fact that the intensity of the neutron-producing radiation remains almost constant over the 20-cm interval, and (3) the slowing down of about 99.3 percent of the total number of neutrons produced to thermal energies before capture.

These conditions permit the use of an expression, first given by Korff,[3] for finding the neutron production rate in terms of the thermal neutron counting rate of a BF_3 neutron detector: namely,

$$q=n(\sigma_w/\sigma_b)(2.24\times10^4/MVp),$$

where q is the neutron production rate g^{-1} sec^{-1}, n is the thermal neutron counting rate in counts sec^{-1}, M is the molecular weight of water, V is the active volume of the BF_3 detector, p is the gas pressure in atmospheres, σ_w is the capture cross section of water for thermal neutrons, and σ_b is the capture cross section of 96 percent enriched BF_3 for thermal neutrons. With $n=0.72$ neutron sec^{-1}, $M=18.00$, $V=6140$ cm^3, $p=0.33$ atmos, $\sigma_w=0.33$ barn, and $\sigma_b=3384$ barns, the production rate of neutrons just below the transition region in water at an altitude of 10 600 feet is found to be 4.2×10^{-5} neutron g^{-1} sec^{-1}.

The thermal neutron distribution below the 30-cm level also permits a quantitative determination of the thermal neutron flux in water. By flux we mean the product of the thermal neutron density ρ, and the thermal neutron velocity v, since ρv is the number of thermal neutrons incident per unit area per unit time.[4] Since v for thermal neutrons is known to be 27×10^4 cm sec^{-1}, only ρ must be determined. The thermal neutron density is related to the thermal neutron counting rate, n, as follows[5]:

$$n=VLpv\sigma_b\rho,$$

where V is the sensitive volume of the detector, L is Loschmidt's number, p is the pressure in atmospheres, and σ_b is the thermal neutron capture cross section of enriched BF_3. With $n=0.72$ thermal neutrons sec^{-1}, $V=6.10\times10^3$ cm^3, $L=2.7\times10^{19}$ cm^{-3}, $\sigma_b=3.4\times10^{-21}$ cm^2, $p=0.33$ atmos, and $v=27\times10^4$ cm sec^{-1}, the thermal neutron density in water at an altitude of 10 600 feet is found to be about 1.45×10^{-8} thermal neutrons per cc. The thermal neutron flux ρv is then about 3.9×10^{-4} thermal neutron cm^{-2} sec^{-1}.

The values computed above for the neutron production rate and the thermal neutron flux are subject to error because of the fact that they were computed on the basis of the thermal neutron counting rate which itself is in error. This error was introduced by the walls of the brass box and the copper cathodes of the counters. Since the walls have finite slow neutron capture cross sections, they are not "thin" for slow neutrons. Absorption of slow neutrons by the walls reduces the neutron density at the detector and changes the neutron distribution near the detector.

The magnitude of the error may be computed so as to permit appropriate corrections to be made. The percentage absorption of each of the two walls may be readily calculated to be[6]:

$$H=(\sigma Adt/M)\times100,$$

where σ is the boron capture cross section for thermal neutrons, A is Avogadro's number, d is the density of the wall, t is the wall thickness in cm, and M is the mean atomic weight of the wall material. The 0.2-cm brass walls and the 0.2-cm copper walls act to absorb about 8 percent of the incident thermal neutrons. Thus, the thermal neutron density at the detector is only 92 percent of the true thermal neutron density. Applying this correction to our computed values, the true neutron production rate and thermal neutron flux are 4.6×10^{-5} neutrons g^{-1} sec^{-1} and 4.3×10^{-4} thermal neutrons cm^{-2} sec^{-1}, respectively.

TABLE I. Mean thermal-neutron counting rate *versus* depth.

Depth (cm)	Counts per minute
0	218.4±1.5
3	193.0±6.1
8	137.2±2.3
10	108.0±0.9
20	78.0±6.8
30	43.7±2.8
50	43.3±2.7

[3] S. A. Korff, Revs. Modern Phys. **11**, 211 (1939).

[4] J. G. Beckerley, U. S. Atomic Energy Commission Report AECD-2664, 1949 (unpublished).

[5] S. A. Korff, *Electron and Nuclear Counters* (D. Van Nostrand Company, Inc., New York, 1946), p. 53.

[6] *The Science and Engineering of Nuclear Power*, edited by C. Goodman (Addison-Wesley Press Inc., Cambridge, 1947), Vol. I, p. 15.

VII. CONCLUSIONS

The neutron component of the cosmic radiation in water at mountain altitudes has been studied. From an analysis of the experimental results it can be concluded that neutron energy and spatial distributions undergo a transition in the first 30-cm layer of water adjacent to the surface. Below the transition region the thermal neutron intensity remains almost constant over a 20-cm interval of water. The neutron production rate and the thermal neutron flux in water at an altitude of 10 600 feet are 4.6×10^{-5} neutron g^{-1} sec^{-1} and about 4.3×10^{-4} thermal neutron cm^{-2} sec^{-1}, respectively.

VIII. ACKNOWLEDGMENTS

The author wishes to express his sincere appreciation to Professor S. A. Korff for suggesting the problem and for giving helpful suggestions during the course of the investigation. The author is indebted to Mr. A. C. Neuberg for his continued assistance in seeing the experiment through to its completion.

The author wishes to thank Professor Byron Cohn and Professor Mario Iona for their splendid cooperation during his stay at the Inter-University High Altitude Laboratory; and the Department of Mountain Parks of the City of Denver for their permission to use Echo Lake as the site for the experiment.

PHYSICAL REVIEW VOLUME 95, NUMBER 3 AUGUST 1, 1954

High-Energy, Large-Angle Distribution of Pair Electrons Produced by Bremsstrahlung*

R. C. MILLER
Department of Physics, University of Illinois, Urbana, Illinois
(Received February 11, 1954)

The results of a calculation of the number of high-energy pair particles emitted into large angles in a pair production process initiated by bremsstrahlung are tabulated. A very approximate estimate of the effect of nuclear screening is given.

THE considerable amount of work being done at present with high-energy bremsstrahlung from electron synchrotrons and betatrons makes it useful to have some information on pair production at high energies and large angles. The computations below should have some use for estimating background and jamming levels, and may also be of interest in suggesting a test of some details of the pair production theory at high energies.

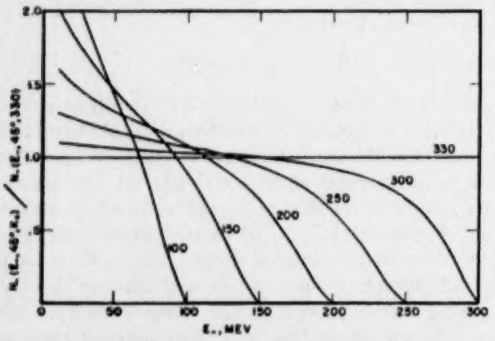

FIG. 1. Curves for extention of data in Table I to other values of k_0. Curves are labeled by k_0 in Mev. These curves were calculated for $\theta_-=45°$, but may be used for other angles between 22.5° and 90° with an accuracy of a few percent.

The expression obtained by Hough[1] for the angular distribution of high-energy electrons (or positrons) emitted into large angles in a pair production process has been integrated over the bremsstrahlung spectrum. The spectrum used is the zero angle formula obtained by Schiff,[2] normalized to 1 erg/cm² beam energy. Our notation is that of Heitler,[3] *viz.*, E_-, p_-, θ_- are, respectively, the electron total energy, momentum $\times c$, and angle relative to the photon. The same symbols with subscript $+$ refer to the positron. μ is the electron rest energy, and k_0 is the maximum energy of the bremsstrahlung spectrum. $N_-(E_-,\theta_-,k_0)$ is the number of electrons per hydrogen nucleus per erg/cm² beam energy per Mev electron energy per steradian.

$$I_-(E_-,\theta_-,k_0)=\int_{E_-}^{k_0} N_-(E_-',\theta_-,k_0)dE_-'$$

is the number of electrons whose energy exceeds E_-, per hydrogen nucleus per erg/cm² beam energy per steradian.

Hough's expression results from an approximate integration of the Bethe-Heitler differential cross section over positron angles, and is valid for energies E_+, $E_-\gg\mu$ and angles $\theta_-\gg\mu/E_-$. Outer screening is neglected. For electron energies near the maximum energy k_0 of the bremsstrahlung spectrum, the number of electrons N_- receives significant contributions from

* Assisted by the joint program of the U. S. Office of Naval Research and the U. S. Atomic Energy Commission, and by a grant from the National Science Foundation.

[1] P. V. C. Hough, Phys. Rev. **74**, 80 (1948), his formula 2.
[2] L. I. Schiff, Phys. Rev. **83**, 252 (1951).
[3] W. Heitler, *Quantum Theory of Radiation* (Oxford University Press, London, 1949), second edition, p. 196.

TABLE I. $N_-(E_-,\theta_-,k_0)$, the number of electrons per hydrogen nucleus per erg/cm² beam energy per Mev electron energy per steradian. $k_0=330$ Mev. N_- is given by $n\times10^{-p}$, where n is the four-digit number at the left of each column and p the two-digit number at the right. The exponent p is given only when it changes. To obtain N_- for other elements, multiply by Z^2.

	θ_-																	
E_- (Mev)	22.5°		30°		37.5°		45°		52.5°		60°		67.5°		75°		82.5°		90°	
	n	p	n	p	n	p	n	p	n	p	n	p	n	p	n	p	n	p	n	p
10.11	0.296	25	0.946	26	0.390	26	0.188	26	0.'01	26	0.587	27	0.362	27	0.234	27	0.156	27	0.108	27
20.11	0.439	26	0.140		0.575	27	0.276	27	0.148	27	0.857	28	0.526	28	0.338	28	0.225	28	0.154	28
30.11	0.135		0.430	27	0.176		0.846	28	0.452	28	0.261		0.160		0.103		0.681	29	0.465	29
40.11	0.568	27	0.181		0.740	28	0.355		0.189		0.109		0.669	29	0.428	29	0.284		0.193	
51.10	0.269		0.855	28	0.350		0.168		0.895	29	0.516	29	0.316		0.202		0.133		0.907	30
61.83	0.146		0.465		0.190		0.912	29	0.487		0.281		0.171		0.109		0.723	30	0.491	
72.55	0.869	28	0.276		0.113		0.541		0.288		0.166		0.102		0.648	30	0.428		0.290	
83.28	0.549		0.175		0.714	29	0.342		0.182		0.105		0.640	30	0.408		0.269		0.183	
94.01	0.364		0.116		0.473		0.226		0.121		0.695	30	0.424		0.270		0.178		0.121	
104.73	0.251		0.797	29	0.326		0.156		0.830	30	0.478		0.291		0.186		0.122		0.827	31
115.46	0.178		0.565		0.231		0.111		0.589		0.339		0.206		0.131		0.865	31	0.585	
126.19	0.129		0.412		0.168		0.804	30	0.428		0.246		0.150		0.954	31	0.628		0.424	
136.92	0.961	29	0.306		0.125		0.597		0.318		0.183		0.111		0.707		0.465		0.314	
147.64	0.726		0.231		0.943	30	0.450		0.240		0.138		0.838	31	0.533		0.350		0.236	
158.37	0.556		0.177		0.722		0.345		0.183		0.105		0.641		0.407		0.267		0.180	
169.10	0.431		0.137		0.559		0.267		0.142		0.814	31	0.495		0.314		0.206		0.139	
179.82	0.337		0.107		0.436		0.208		0.111		0.636		0.386		0.245		0.161		0.108	
190.55	0.265		0.841	30	0.343		0.164		0.870	31	0.499		0.303		0.192		0.126		0.846	32
201.28	0.209		0.664		0.271		0.129		0.686		0.393		0.239		0.151		0.990	32	0.665	
212.00	0.166		0.526		0.214		0.102		0.541		0.310		0.188		0.119		0.780		0.524	
222.73	0.131		0.415		0.169		0.805	31	0.427		0.244		0.148		0.938	32	0.614		0.412	
233.46	0.103		0.327		0.133		0.632		0.335		0.192		0.116		0.735		0.481		0.322	
244.18	0.805	30	0.255		0.103		0.492		0.260		0.149		0.902	32	0.571		0.373		0.250	
254.91	0.619		0.196		0.794	31	0.377		0.200		0.114		0.691		0.437		0.286		0.191	
265.64	0.466		0.147		0.595		0.283		0.150		0.855	32	0.517		0.327		0.214		0.143	
276.37	0.339		0.107		0.432		0.205		0.108		0.619		0.374		0.237		0.155		0.104	
287.09	0.233		0.731	31	0.296		0.140		0.742	32	0.424		0.256		0.162		0.106		0.708	33
297.82	0.146		0.457		0.185		0.876	32	0.463		0.264		0.160		0.101		0.659	33	0.441	
308.55	0.753	31	0.236		0.953	32	0.452		0.239		0.136		0.825	33	0.521	33	0.340		0.227	
319.27	0.233		0.729	32	0.294		0.140		0.737	33	0.421	33	0.254		0.161		0.105		0.701	34

events involving positrons whose energy is too small to satisfy the requirement $E_+\gg\mu$. The error in our estimates from this source is about 5 percent if E_- is less than k_0 by 10 Mev, and decreases steadily as the difference between k_0 and E_- increases.

Table I lists the results for $k_0=330$ Mev, and these are extended to other values of k_0 in Fig. 1. The angular dependence is $(\cot\frac{1}{2}\theta_-/\sin\frac{1}{2}\theta_-)^2$ to within a few percent, and the energy variation is, very roughly, $E_-^{-3.5}$. The error in these estimates from violation of the conditions $E_-\gg\mu$, $\theta_-\gg\mu/E_-$ is less than 3 percent in the most unfavorable case ($E_-=5$ Mev, $\theta_-=22.5°$), and decreases rapidly for larger E_- or θ_-. Table II presents the number of electrons whose energy exceeds a given energy. k_0 is 330 Mev, and Fig. 2 extends the results to other values of k_0. These estimates were obtained by graphical integration of the results in Table I.

Failure of the Born approximation for moderate and high Z elements and the effect of recoil corrections on the pair cross section for light elements,[4] both of which may be noticeable at high energies and large angles, are neglected in these results. A very approximate account of inner screening, which, because of the finite size of the nuclear charge distribution, should begin markedly reducing N_- whenever $[2(p_-/\hbar)$

TABLE II. $I_-(E_-,\theta_-,k_0)=\int_{E_-}^{k_0}N_-(E_-',\theta_-,k_0)dE_-'$, the number of electrons whose energy exceeds E_-, per hydrogen nucleus per erg/cm² beam energy per steradian. k_0 is 330 Mev. I_- is given by $n\times10^{-p}$, where n is the four-digit number at the left of each column and p the two-digit number at the right. The exponent p is given only when it changes. To obtain I_- for other elements, multiply by Z^2.

	θ_-																	
E_- (Mev)	22.5°		30°		37.5°		45°		52.5°		60°		67.5°		75°		82.5°		90°	
	n	p	n	p	n	p	n	p	n	p	n	p	n	p	n	p	n	p	n	p
5.00	0.571	24	0.183	24	0.754	25	0.364	25	0.196	25	0.114	25	0.708	26	0.458	26	0.308	26	0.213	26
7.50	0.277		0.887	25	0.365		0.176		0.945	26	0.549	26	0.338		0.218		0.146		0.100	
10.00	0.168		0.537		0.221		0.106		0.570		0.330		0.203		0.131		0.871	27	0.598	27
12.50	0.111		0.354		0.145		0.698	26	0.374		0.217		0.133		0.855	27	0.569		0.390	
15.00	0.782	25	0.250		0.102		0.492		0.263		0.152		0.935	27	0.600		0.399		0.273	
17.50	0.579		0.185		0.757	26	0.364		0.195		0.113		0.690		0.442		0.294		0.201	
20.00	0.444		0.142		0.580		0.278		0.149		0.860	27	0.527		0.338		0.224		0.153	
22.50	0.350		0.111		0.456		0.219		0.117		0.676		0.414		0.265		0.176		0.120	
25.00	0.282		0.897	26	0.367		0.176		0.942	27	0.544		0.333		0.213		0.141		0.962	28
27.50	0.230		0.733		0.300		0.144		0.769		0.444		0.272		0.174		0.115		0.784	
30.00	0.191		0.609		0.249		0.120		0.638		0.368		0.225		0.144		0.954	28	0.649	
35.00	0.137		0.435		0.178		0.854	27	0.456		0.263		0.161		0.103		0.680		0.462	
40.00	0.102		0.323		0.132		0.634		0.338		0.195		0.119		0.762	28	0.503		0.342	
45.00	0.778	26	0.248		0.101		0.485		0.259		0.149		0.911	28	0.582		0.384		0.261	
50.00	0.610		0.194		0.793	27	0.380		0.203		0.117		0.713		0.455		0.300		0.204	
55.00	0.487		0.155		0.633		0.303		0.162		0.930	28	0.568		0.362		0.239		0.162	
60.00	0.394		0.125		0.513		0.245		0.131		0.753		0.460		0.293		0.193		0.131	
65.00	0.324		0.103		0.421		0.201		0.107		0.618		0.377		0.240		0.159		0.107	
70.00	0.269		0.855	27	0.350		0.167		0.891	28	0.513		0.313		0.199		0.131		0.889	29
80.00	0.190		0.604		0.247		0.118		0.630		0.362		0.221		0.141		0.926	29	0.626	
90.00	0.139		0.440		0.180		0.861	28	0.459		0.264		0.161		0.102		0.673		0.455	
100.00	0.103		0.328		0.134		0.642		0.342		0.196		0.120		0.761	29	0.501		0.338	

[4] S. D. Drell, Phys. Rev. 87, 753 (1952).

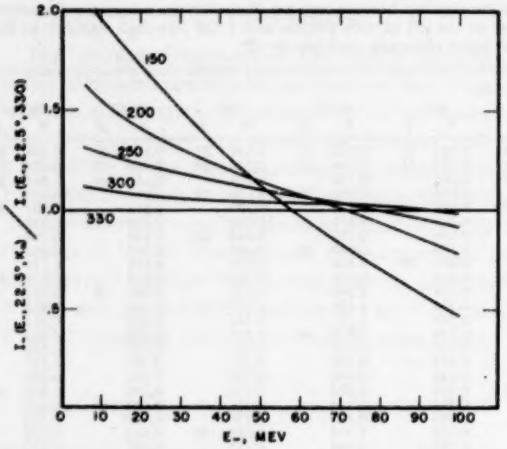

FIG. 2. Curves for extension of data in Table II to other values of k_0. Curves are labeled by k_0 in Mev. These curves were calculated for $\theta_-=22.5°$, but may be used for all angles between 22.5° and 90° with an accuracy of a few percent.

$\times\sin\frac{1}{2}\theta_-]^{-1}$ (cm) is comparable with the nuclear radius, is given below.

For a spherically symmetric charge distribution, the nuclear form factor is, in the first Born approximation, a function only of the magnitude q of the nuclear recoil momentum. The form factor for a uniform charge distribution, assuming monochromatic photons, was calculated in the Born approximation by Hough,[5] who recommends the use of a value of q intermediate between $\bar{q}\equiv 2p_-\sin\frac{1}{2}\theta_-$ and $q_{\min}\equiv(k^2+p_-^2-2kp_-\times\cos\theta_-)^{\frac{1}{2}}-p_+$. ($q_{\min}$ is the smallest nuclear recoil kinematically possible for a given photon momentum k and given electron energy and angle.)

Reference to Fig. 3 shows that if p_+ is small, $\bar{q}\simeq q_{\min}$; on the other hand, if p_+ is large, the bulk of contributions to N_- come from the region $\theta_+\simeq 0$.[6] Since, then, $k-p_+\simeq p_-$, and $q\simeq 2p_-\sin\frac{1}{2}\theta_-=\bar{q}$.[7] Events for which

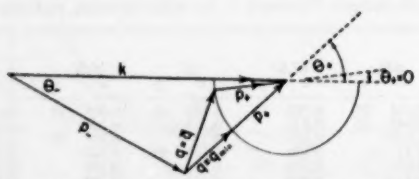

FIG. 3. Momentum diagram for a pair production event in which the electron is emitted with high energy into a large angle θ_-. The nuclear recoil energy is neglected. To illustrate for the case $q=q_{\min}$ (which corresponds to Heitler's $\phi_+=180°$), all vectors should be taken in the plane of the paper.

[5] See reference 1, pp. 84, 85.

[6] L. I. Schiff, Phys. Rev. 87, 750 (1951). The analogous case for bremsstrahlung is discussed.

[7] We have obtained $N_-(E_-,\theta_-,k_0)$ as a function of q for several typical cases, using a dk/k spectrum. The results indicate that around 90 percent of the contribution comes from values of q lying within ±1 percent of $\bar{q}$, the remainder coming more or less equally from q's between $\bar{q}$ and $q_{\min}$.

$q>\bar{q}$ contribute negligibly to N_-. Hence, we may argue that the use of $q\simeq\bar{q}$, which is independent of k, and consequently leaves the inner screening calculation unaffected by integration over the bremsstrahlung spectrum, is sufficiently accurate for rough estimates. This is especially true in view of the fact that the Born approximation itself cannot be taken seriously when applied to moderate and high Z elements, where nuclear screening is of most importance.

The Born approximation correction for screening by a uniform charge distribution is given in Fig. 4 for Cu and Al, assuming a radius $R=1.2\times10^{-13}A^{\frac{1}{3}}$ cm. Yennie's phase shift calculations[8] for electron scattering from a uniform charge distribution show that the diffraction

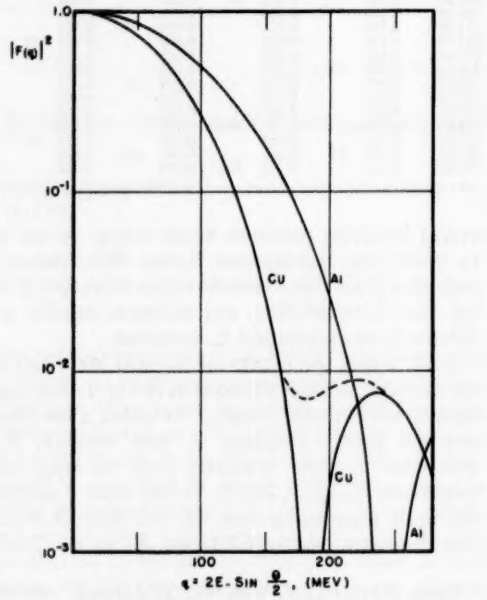

FIG. 4. $|F(q)|^2$, squared form factor for a uniform charge distribution, calculated in the Born approximation. $R=1.2\times10^{-13}A^{\frac{1}{3}}$ cm. The dashed curve is an estimate, based on Yennie's graphs, of the actual shape of $|F(q)|^2$ near the first "zero" in Cu.

"zeros" in Fig. 4 are spurious, but that the Born approximation for Cu agrees fairly well with the exact phase shift calculation, except near these "zeros." The form factor is

$$F(q)=3[\sin(qR)-(qR)\cos(qR)]/(qR)^3,$$

and the correction is obtained by multiplying $|F(q)|^2$ into the results of Table I.

Part of this calculation was made using the Illinois Digital Computer. I wish to thank Professor C. S. Robinson for suggesting and encouraging this work, and to acknowledge support by a General Electric Fellowship.

[8] Yennie, Wilson, and Ravenhall, Phys. Rev. 92, 1325 (1953).

The Sachs Exchange Moment*

R. H. DALITZ†
Laboratory of Nuclear Studies, Cornell University, Ithaca, New York
(Received April 29, 1954)

A derivation of the Sachs exchange moment is given which clearly shows how this exchange moment is uniquely determined by the exchange potential. The relation between this and the treatments of Sachs and of Osborne and Foldy is discussed.

IT has long been recognized[1,2] that the presence of exchange forces between nucleons implies the presence of currents in the space about interacting nucleons, currents which will generally contribute to the magnetic properties of nuclei. In fact, a contribution of this origin has long been recognized[3] in the magnetic moments of H^3 and He^3; these currents appear to play an important role in the *n-d* capture process[4] and their contribution to the *n-p* capture process has recently been established.[5] Physically, these currents are due to the charged mesons which are being exchanged between the nucleons, giving rise to the exchange force between them, and their contributions to the exchange moments have frequently been calculated according to various meson theories.[6] However, as was pointed out, first by Sachs[2] and more recently by Osborne and Foldy,[7,8] one term of this exchange moment has a phenomenological origin, independent of the particular meson theory, but in neither of these discussions does it appear clearly that this term is defined unambiguously. The purpose of the present note is to derive this term again, showing clearly its origin, and to discuss the relationship of these previous treatments.

Consider first two nucleons with position vectors $\mathbf{r}_1$ and $\mathbf{r}_2$ (with respect to an origin O) and denote the current density at the point $\mathbf{r}$ by $\mathbf{J}(\mathbf{r})$. Then from the equation of charge conservation,

$$\operatorname{div}\mathbf{J}=-\frac{1}{c}\frac{\partial\rho}{\partial t}=\frac{i}{\hbar c}[\rho,H], \tag{1}$$

where $\rho(\mathbf{r})$ is the charge density and H the Hamiltonian for the two nucleons. If, as is usual, the nucleons are regarded as point charges, then

$$\rho(\mathbf{r})=\tfrac{1}{2}e\{(1+\tau_3{}^1)\delta(\mathbf{r}-\mathbf{r}_1)+(1+\tau_3{}^2)\delta(\mathbf{r}-\mathbf{r}_2)\}. \tag{2}$$

Lack of commutativity of ρ and H arises first from the kinetic energy terms and from any velocity dependent potentials, and also from the τ-dependent exchange potential. The currents arising from the first of these are those due to the translation of the charge of the nucleon and give the usual orbital contribution to the magnetic moment. The second terms come from the currents which are recognized when the replacement $\mathbf{p}\rightarrow\mathbf{p}-(e/c)\mathbf{A}$ is made in the velocity-dependent potentials. We will denote by $\mathbf{J}_{12}(\mathbf{r})$ the total current excluding these two current contributions, so that if the τ-dependent potential is $\tau^1\cdot\tau^2V_{12}$, then,[7] from (1) and (2),

$$\operatorname{div}\mathbf{J}_{12}=\frac{e}{\hbar c}(\tau^1\times\tau^2)_3V_{12}[\delta(\mathbf{r}-\mathbf{r}_1)-\delta(\mathbf{r}-\mathbf{r}_2)]. \tag{3}$$

The magnetic moment of the two nucleons which arises from $\mathbf{J}_{12}(\mathbf{r})$ may then be broken up in the following way:

$$\int\mathbf{r}\times\mathbf{J}_{12}d\tau=\frac{(\mathbf{r}_1+\mathbf{r}_2)}{2}\times\int\mathbf{J}_{12}(\mathbf{r})d\tau+\int\left(\mathbf{r}-\frac{\mathbf{r}_1+\mathbf{r}_2}{2}\right)\times\mathbf{J}_{12}(\mathbf{r})d\tau. \tag{4}$$

Now, since the current $\mathbf{J}_{12}(P)$ can depend only on the relative positions of P and the two nucleons, the second term of (4) does not depend on the origin O, where as the first term does depend on the choice of O. Using Green's theorem and the physical fact that the currents $\mathbf{J}_{12}$ vanish exponentially at large distances from the nucleons, the integral in the first term of (4) becomes

$$\int\mathbf{J}_{12}(\mathbf{r})d\tau=-\int\mathbf{r}\operatorname{div}\mathbf{J}_{12}(\mathbf{r})d\tau. \tag{5}$$

According to (3), this integral (5) is known uniquely and its contribution to the magnetic moment (4) is unambiguously

$$\frac{(\mathbf{r}_1+\mathbf{r}_2)}{2}\times\left[-(\mathbf{r}_1-\mathbf{r}_2)\frac{e}{\hbar c}(\tau^1\times\tau^2)_3V_{12}\right]=\frac{e}{\hbar c}(\tau^1\times\tau^2)_3(\mathbf{r}_1\times\mathbf{r}_2)V_{12}. \tag{6}$$

* Assisted in part by the U. S. Office of Naval Research.
† On leave of absence from the Department of Mathematical Physics, University of Birmingham, England.
[1] A. J. F. Siegert, Phys. Rev. **52**, 787 (1937).
[2] R. G. Sachs, Phys. Rev. **74**, 433 (1948); R. G. Sachs and N. Austern, Phys. Rev. **81**, 705 (1951).
[3] Blanchard, Avery, and Sachs, Phys. Rev. **78**, 292 (1950).
[4] N. Austern, Phys. Rev. **83**, 672 (1951); **85**, 147 (1952).
[5] N. Austern, Phys. Rev. **92**, 670 (1953).
[6] C. Moller and L. Rosenfeld, Kgl. Danske Videnskab. Selskab, Mat.-fys. Medd. **17**, 8 (1940); S. T. Ma and F. C. Yu, Phys. Rev. **62**, 118 (1942); F. Villars, Helv. Phys. Acta **20**, 476 (1947).
[7] R. K. Osborne and L. L. Foldy, Phys. Rev. **79**, 795 (1950).
[8] L. L. Foldy, Phys. Rev. **92**, 178 (1953).

Therefore the magnetic moment terms which depend on the origin O are uniquely determined, whereas (3) imposes no restrictions on those last terms of (4) which are independent of the origin chosen. The possible forms for these latter terms, allowed after all invariance requirements are met, have been discussed by Osborne and Foldy,[7,8] by Kynch,[9] and by Austern and Sachs[2] and those which are velocity-independent are very limited in number, and all spin-dependent. For a system of nucleons the exchange-moment contributions for each pair of nucleons are to be added, three-particle interaction effects being neglected, and the origin is clearly to be chosen at the mass center of the nucleus.

The exchange-moment term (6) was obtained by Sachs[2] from the interaction

$$U_{12}=\exp\left\{\frac{-ie}{2\hbar c}(\tau_3^1-\tau_3^2)\int_{r_1}^{r_2}\mathbf{A}(\mathbf{r})\cdot d\mathbf{r}\right\}\times V_{12}(1+\tau^1\cdot\tau^2), \quad (7)$$

which is a quite special gauge-invariant generalization of the exchange interaction $V_{12}(1+\tau^1\cdot\tau^2)$, the integration being taken along the straight line joining the nucleons. The term of U_{12} linear in $\mathbf{A}(\mathbf{r})$, which is all that is relevant in the present application, may be written

$$\frac{-ie}{2\hbar c}(\tau_3^1-\tau_3^2)(1+\tau^1\cdot\tau^2)V_{12}\int_{r_1}^{r_2}\mathbf{A}(\mathbf{r})\cdot d\mathbf{r}$$
$$=-\int\frac{e}{\hbar c}(\tau^1\times\tau^2)_3V_{12}\int_0^1 ds\delta(\mathbf{r}-s\mathbf{r}_1-(1-s)\mathbf{r}_2)\times(\mathbf{r}_1-\mathbf{r}_2)\cdot\mathbf{A}(\mathbf{r})d\tau,$$

so that the expression (7) given by Sachs involves the assumption that the current flow between the nucleons occurs only along the straight line joining them, the current density being

$$\mathbf{J}_{12}(\mathbf{r})=-\frac{e}{\hbar c}(\tau^1\times\tau^2)_3(\mathbf{r}_1-\mathbf{r}_2)V_{12}\times\int_0^1 ds\delta(\mathbf{r}-s\mathbf{r}_1-(1-s)\mathbf{r}_2). \quad (8)$$

[9] G. J. Kynch, Phys. Rev. 81, 1060 (1951).

Although this is clearly not the physical situation, this treatment gives the origin-dependent term (6) of the exchange moment correctly since all that is necessary for this is that the space integral of the current density should equal that implied by the Eqs. (5) and (3), and this is so for the current distribution (8). Sachs' treatment gives only the exchange moment (6) since the second term of (4) vanishes, this current flow having zero moment about the midpoint between the nucleons.

In the treatment of Osborne and Foldy,[7] it is proposed to split the current $\mathbf{J}_{12}$ into an irrotational part which is to be determined from (3) and an undetermined solenoidal part. The exchange moment (6) is considered to arise from this irrotational current flow, a paradoxical conclusion since it is well known that any irrotational current flow of finite extent has zero magnetic moment. In fact the integral (4) for this irrotational flow is quite indeterminate since, for large distances, the solenoidal current flow decreases only as $\sim(\mathbf{r}_{12}-3\mathbf{r}\mathbf{r}\cdot\mathbf{r}_{12}/r^2)/r^3$ [compare Eqs. (23) and (25) of Oxborne and Foldy[7]]. Since the physical currents are restricted to a distance of order $\hbar/\mu c$ about the nucleons, it is artificial (and, as we have seen, quite unnecessary) to split this current into irrotational and solenoidal parts each of which decreases only slowly at large distances, though their sum decreases exponentially.

To exemplify explicitly a typical meson-current distribution,[6] we consider finally the adiabatic limit of symmetric scalar meson theory. The exchange-current density due to the meson field is given by

$$\mathbf{J}_{12}(\mathbf{r})=\frac{-ie}{\hbar c}\sum_{\alpha,\beta}\epsilon_{3\alpha\beta}[\phi_\alpha(1)\nabla\phi_\beta(2)-\phi_\beta(2)\nabla\phi_\alpha(1)],$$

where $\phi_\alpha(i)=g\tau_\alpha{}^i\exp(-\kappa|\mathbf{r}-\mathbf{r}_i|)/|\mathbf{r}-\mathbf{r}_i|$, $\kappa=\mu c/\hbar$, and $\epsilon_{\gamma\alpha\beta}$ is the alternating tensor. It may be verified readily that this current distribution satisfies Eq. (3), V_{12} being $-g^2e^{-\kappa r_{12}}/r_{12}$, and that a direct calculation of the magnetic-moment integral (4) gives the result (6). In the adiabatic limit, the scalar meson field and currents do not depend on the nucleon spins, so that there can be no origin-independent exchange-moment term.

Phenomenological Many-Body Exchange Forces

L. E. H. TRAINOR
Department of Physics, Queen's University, Kingston, Ontario, Canada
(Received March 8, 1954)

Phenomenological many-body exchange potentials are defined in group-theoretical analogy with the usual 2-body exchange potentials of Heisenberg, Bartlett, and Majorana. The uniform model of Wigner is then extended to include many-body Wigner and Majorana forces. The theory predicts a symmetry energy between neighboring isobars of even-odd nuclei which depends upon whether the isobar of highest $T_<$ is *OE* or *EO*, where *OE* signifies that the odd number of particles is greater than the even number, and *EO* signifies the reverse. A comparison is made with such energy differences in $T_<=\frac{1}{2}$ and $\frac{3}{2}$ isobars, taken from β-decay data in the range $15\leqq A\leqq 59$. This leads to a rough estimate of the magnitude and sign of the contribution from 3-body potentials. On this basis, the contribution from 3-body potentials is not negligible in comparison with that from 2-body potentials.

I. INTRODUCTION

IT has been customary in the theory of nuclei to talk of nuclear forces in terms of static 2-body potentials, whose variety and form are limited by invariance requirements and by considerations of simplicity. Such potentials can be constructed, for example, in second approximation of a perturbation treatment of the interaction between nucleons and the meson field by a systematic elimination of the field variables, if one neglects the nucleon recoils due to meson emission.[1] Primakoff and Holstein[2] had shown, in the early stages of meson theory, that this approach is equivalent to an expansion in terms of many-body forces, the relative magnitudes of $(m+1)$- and m-body forces being of order v/c, where v is the nucleonic velocity and c is the velocity of light. Since this ratio is of the order of $\frac{1}{3}$ in actual nuclei, neglect of 3- and 4-body forces was expected to be serious. Wentzel[3] and Drell and Huang[4] have used pseudoscalar meson theory to explain the saturation of nuclear forces in terms of many-body potentials. They show that the m-body forces are attractive for m even, repulsive for m odd, at least for the first nonvanishing terms of each variety in their perturbation treatment. However, it is not clear just how significant are the neglected terms in these calculations in so far as quantitative results are concerned. Methods of successive approximations,[5] more reliable than the conventional ones associated with a weak coupling theory, have been developed recently which consistently take into account the effect of each term on the succeeding terms. As a result, pseudoscalar theory is not in disagreement with the experimental results.[6] However, it does not yet provide a convenient quantitative approach to nuclear forces in many-body problems. The detailed calculations in such problems are prohibitive. For this reason it seems useful to eliminate the field variables *ab initio* in the crude sense of a phenomenological approach to many-body forces, just as it has been customary to do for 2-body forces. The obvious advantages are simplicity and manoeuverability.

It is proposed here that the phenomenological approach of Wigner,[7] Heisenberg,[8] and Majorana[9] to nuclear forces in terms of static 2-body exchange and nonexchange potentials, be extended to many-body forces. This is not the only possible generalization of the usual phenomenological approach. One might, for example, introduce short-range repulsive potentials between nucleons and such potentials have achieved considerable success in the nuclear 2-body problem.[10–12] Alternatively, one might introduce velocity-dependent potentials in a variety of forms. Neither approach is likely to be convenient in many-body problems having to do with gross nuclear properties such as binding energy and stability. The forms of the many-body exchange forces (Sec. III) used in the present work, were adopted by making a group-theory analogy with the 2-body case, with a view toward exploiting to advantage the properties of the symmetric group in relation to nuclear structure.

As an example of the use of many-body exchange potentials, the uniform model of Wigner[13,14] is extended to include such exchange forces (Sec. IV). Wigner's model is based on fairly general symmetry arguments and accounts in a general way for nuclear stability and the shape of the binding energy curve in the medium and light nuclei. It makes no attempt to account for detailed nuclear properties which change abruptly from one nuclear species to the next. Rather it is concerned with the general variation with atomic mass number A of those nuclear properties which are expected to be

[1] See for example, G. Wentzel, *Quantum Theory of Fields* (Interscience Publishers, Inc., New York, 1949).
[2] H. Primakoff and T. Holstein, Phys. Rev. **55**, 1218 (1939).
[3] G. Wentzel, Helv. Phys. Acta **15**, 111 (1942); **25**, 569 (1952).
[4] S. Drell and K. Huang, Phys. Rev. **91**, 1527 (1953).
[5] K. Brueckner and K. Watson, Phys. Rev. **90**, 699 (1953).
[6] K. Brueckner and K. Watson, Phys. Rev. **92**, 1023 (1953).
[7] E. Wigner, Phys. Rev. **43**, 252 (1933).
[8] W. Heisenberg, Z. Physik **77**, 1 (1932).
[9] E. Majorana, Z. Physik **82**, 137 (1933).
[10] R. Jastrow, Phys. Rev. **81**, 165 (1951).
[11] M. Levy, Phys. Rev. **88**, 725 (1952).
[12] E. Salpeter, Phys. Rev. **91**, 944 (1953).
[13] E. Wigner, Phys. Rev. **51**, 106, 947 (1937).
[14] E. Wigner, Bicentennial Symposium, University of Pennsylvania, 1940 (unpublished).

strongly symmetry dependent under the assumed force laws, for example, the energy differences in neighboring isobars. Wigner assumed that the forces were predominantly of the Wigner and Majorana types with 2-body forces preponderant. Despite its many obvious limitations, the theory has achieved considerable success in the direction in which it was originally intended. The present work points out that the same type of considerations can be based on the more general assumption of many-body Wigner and Majorana forces. This extended uniform model predicts an energy dependence in even-odd isobars upon whether the odd number of nucleons is greater or less than the even number of nucleons (Sec. VII). A comparison with experiment lends some support to this prediction and enables one to make a rough estimate of the contribution from nuclear 3-body forces.

II. NOTATION

Let $\mathcal{S}_A$ denote the symmetric group of $A!$ permutations on A things.[15,16] The irreducible representations of this group can be completely characterized by all possible symmetry partitions

$$[\alpha]\equiv[\alpha_1+\alpha_2+\alpha_3+\cdots+\alpha_A]$$

of the number A, where some of the α_i may be zero and the sequences are nonincreasing. The base vectors of a particular representation $[\alpha]$ of dimension g_α we denote by ψ_σ^α, with $\sigma=1, 2, \cdots, g_\alpha$. These may be considered functions of A independent variables, which are the things to be permuted. The symmetry properties[17] of the base vectors of an irreducible representation can be expressed descriptively in terms of the Young diagrams[18] corresponding to the symmetry partition, or analytically in terms of the eigenvalues of the Dirac class sums.[16] Let (a) denote that class of $\mathcal{S}_A$ which has a_1 unary cycles, a_2 binary cycles, etc. The corresponding Dirac class sum $\mathbf{C}(a)$ is the sum over all permutation operators which are in class (a) of $\mathcal{S}_A$ divided by $\rho(a)$, the number of elements in the class (a). The symmetry functions ψ_σ^α belonging to representation $[\alpha]$ are eigenfunctions of the Dirac class sums

$$\mathbf{C}(a)\psi_\sigma^\alpha=\kappa^\alpha(a)\psi_\sigma^\alpha, \quad \sigma=1, 2, 3, \cdots g_\alpha, \tag{1}$$

where the eigenvalue $\kappa^\alpha(a)$ is simply related to the primitive character $\chi^\alpha(a)$ of $\mathcal{S}_A$ corresponding to representation $[\alpha]$ and class (a),

$$\kappa^\alpha(a)=\chi^\alpha(a)/g_\alpha. \tag{2}$$

[15] E. Wigner, *Gruppentheorie* (Edward Brothers, Ann Arbor, Michigan, 1944).

[16] E. M. Corson, *Perturbation Methods in Quantum Mechanics* (Blackie and Son, Glasgow, 1951).

[17] See for example P. Hund, Z. Physik **105**, 202 (1937).

[18] F. D. Murnaghan, *The Theory of Group Representations* (Johns Hopkins Press, Baltimore, 1938). Note that Murnaghan uses subscripts for representations and superscripts for classes on the primitive characters of the symmetric group. An alternative notation is used here and in reference 16 above.

The summation convention is not used in this paper. $\kappa^\alpha(a)$, $\rho(a)$, and $\chi^\alpha(a)$ are *class functions*, $\mathbf{C}(a)$ a *class operator*.

Let B be an integer, $B\leqq A$, and let $\mathcal{S}_B$ denote the symmetric group of $B!$ permutations of B things. $\mathcal{S}_B$ is a subgroup of $\mathcal{S}_A$. We denote its irreducible representations by the corresponding partitions $[\beta]$ and its classes by (b). The special class which has a single cycle of length B, we denote simply by (B). That class of $\mathcal{S}_A$ which has the same cyclic structure as (b) of $\mathcal{S}_B$, plus an additional $(A-B)$ unary cycles, is denoted by $(b, 1^{A-B})$.

III. MANY-BODY EXCHANGE FORCES

Let $\langle\omega\rangle$ denote any particular subset containing B of the A nucleons, namely those numbered $\omega_1, \omega_2, \cdots, \omega_B$, and further let R_ω denote the collection of space coordinates of the B particles in set $\langle\omega\rangle$. We denote the B-body Wigner and Majorana potentials by ${}^B\mathbf{W}$ and ${}^B\mathbf{M}$, respectively. The usual 2-body Majorana potential can be written in the form

$${}^2\mathbf{M}=\sum_{i<j}{}^2J(r_{ij})\mathbf{P}_{ij}, \tag{3}$$

where ${}^2J(r_{ij})$ is a function of the relative coordinate r_{ij} for the ith and jth particles, and $\mathbf{P}_{ij}$ is the simple transposition operator on the *space* coordinates of the ith and jth particles. In terms of the above notation, this expression can be written

$${}^2\mathbf{M}=\sum_{\langle\omega\rangle}{}^2J(R_\omega)\mathbf{C}^\omega(2), \tag{4}$$

if R_ω is identified with r_{ij} for the collection $\langle\omega\rangle$ consisting of the ith and jth nucleons and $\mathbf{C}^\omega(2)$ acts on *space* coordinates of the particles in the collection $\langle\omega\rangle$. We now extend this phenomenological definition to *irreducible B-body exchange forces* of the Majorana type

$${}^B\mathbf{M}=\sum_{\langle\omega\rangle}{}^BJ(R_\omega)\mathbf{C}^\omega(B)=\frac{1}{\rho(B)}\sum_{\langle\omega\rangle}{}^BJ(R_\omega)\sum_{s\text{ in }(B)}\mathbf{P}_s{}^\omega, \tag{5}$$

where the first sum is over all possible collections of B particles, and the second sum is over all permutation operators $\mathbf{P}_s{}^\omega$ belonging to class (B) of $\mathcal{S}_B$ and acting upon the space coordinates of the particles in set $\langle\omega\rangle$. Thus, for a particular set $\langle\omega\rangle$ of B particles, the Majorana B-body potential consists of a product of the function ${}^BJ(R_\omega)$ (which is a function of the space coordinates of the particles and describes the "potential shape") with a sum over all those permutation operators on the space coordinates which have a cyclic structure consisting of a single cycle of length B. This is not the only possible extended definition, but is probably the simplest with sufficient generality (see Appendix I). Irreducibility in this sense implies that ${}^B\mathbf{M}$ cannot be expressed linearly in terms of C-body potentials, where

$C<B$, and also in the sense that every particle in the set $\langle\omega\rangle$ of B particles is involved in the exchange $\mathbf{P}_s^{\omega}$. The Wigner B-body force is simply written as

$$^B\mathbf{W}=\sum_{\langle\omega\rangle} {}^BK(R_\omega), \tag{6}$$

where $^BK(R_\omega)$ is the potential function describing the nonexchange interaction of the B particles in set $\langle\omega\rangle$. (The corresponding B-body Heisenberg and Bartlett exchange forces are of the form of (5) with the re-interpretations that the class sums $\mathbf{C}^{\omega}(B)$ act upon the *charge*, respectively *spin* coordinates.)

IV. THE UNIFORM MODEL

In the approximation that the nuclear forces are described in terms of the expressions (5) and (6), the Hamiltonian is independent of spin and charge variables and the unsymmetrized wave function of the system can be written as a product of a space dependent function and a spin and charge dependent function. Actually this separation is more general since one can add to the Hamiltonian any function which is essentially independent of the space variables, for example Heisenberg and Bartlett potentials of long range. Since the Dirac class sums $\mathbf{C}(a)$ of $\mathcal{S}_A$ commute with the potentials (5) and (6), and with each other,[16] the states of the system can be described as simultaneous eigenfunctions of the Hamiltonian and the $\mathbf{C}(a)$. It then follows from (1) that the eigenfunctions of the system are symmetry functions in the spatial coordinates. Since the total wave function must satisfy the Pauli principle, it must be written as

$$\Psi=\sum_{\sigma=1}^{g_\alpha} k_\sigma\psi_\sigma{}^{\alpha}(\mathbf{r}_1,\mathbf{r}_2,\cdots,\mathbf{r}_A)\phi_\sigma{}^{\alpha'}(t_1,t_2,\cdots,t_A), \tag{7}$$

with

$$\sum_{\sigma=1}^{g_\alpha} |k_\sigma|^2=1, \tag{8}$$

where the k_σ are constants, and t_j denotes the set of spin and charge variables of the jth particle. The $\phi_\sigma{}^{\alpha'}$ are symmetry functions (under simultaneous permutations of spin and charge variables) belonging to that irreducible representation $[\alpha']$ of $\mathcal{S}_A$ which is associate to $[\alpha]$ and which is characterized by the primitive characters

$$\chi^{\alpha'}(a)=\pm\chi^{\alpha}(a), \tag{9}$$

with $\pm$ taken as (a) is an even or odd permutation class of $\mathcal{S}_A$.

The expectation value of the Majorana B-body force, $B\leqq A$, is from (5) and (7),

$$\langle{}^B\mathbf{M}\rangle=(\Psi,{}^B\mathbf{M}\Psi)=\sum_{\sigma=1}^{g_\alpha}|k_\sigma|^2(\psi_\sigma{}^{\alpha},{}^B\mathbf{M}\psi_\sigma{}^{\alpha}), \tag{10}$$

where the orthogonality of the $\phi_\sigma{}^{\alpha'}$ has been used. In a similar manner,

$$\langle{}^B\mathbf{W}\rangle=\sum_{\sigma=1}^{g_\alpha}|k_\sigma|^2(\psi_\sigma{}^{\alpha},{}^B\mathbf{W}\psi_\sigma{}^{\alpha}) \tag{11}$$

for the Wigner B-body force. Since $^B\mathbf{W}$ and $^B\mathbf{M}$ are completely symmetric operators, the inner products on the right-hand sides of Eqs. (10) and (11) are independent of the index σ. Hence, from (8)

$$\langle{}^B\mathbf{M}\rangle=(\psi_\lambda{}^{\alpha},{}^B\mathbf{M}\psi_\lambda{}^{\alpha})\sum_{\sigma=1}^{g_\alpha}|k_\sigma|^2=(\psi_\lambda{}^{\alpha},{}^B\mathbf{M}\psi_\lambda{}^{\alpha})$$
$$=\frac{1}{g_\alpha}\sum_{\sigma=1}^{g_\alpha}(\psi_\sigma{}^{\alpha},{}^B\mathbf{M}\psi_\sigma{}^{\alpha}). \tag{12}$$

Similarly,

$$\langle{}^B\mathbf{W}\rangle=\frac{1}{g_\alpha}\sum_{\sigma=1}^{g_\alpha}(\psi_\sigma{}^{\alpha},{}^B\mathbf{W}\psi_\sigma{}^{\alpha}). \tag{13}$$

The same technique which Wigner used for 2-body Majorana forces may now be used to evaluate (12) and (13). Introducing the expression (5) for $^B\mathbf{M}$ into (12) one has

$$\langle{}^B\mathbf{M}\rangle=\frac{1}{g_\alpha}\sum_{\sigma=1}^{g_\alpha}\sum_{\langle\omega\rangle}(\psi_\sigma{}^{\alpha},{}^BJ(R_\omega)\mathbf{C}^{\omega}(B)\psi_\sigma{}^{\alpha}). \tag{14}$$

Let $\mathbf{D}_{\omega\omega'}$ be the operator which interchanges the set $\langle\omega\rangle$ of B particles and the set $\langle\omega'\rangle$ of B particles such that particles ω_1 and ω_1' are interchanged, ω_2 and ω_2', etc. Since the expectation value is invariant under particle permutation,

$$\langle{}^B\mathbf{M}\rangle=\frac{1}{g_\alpha}\sum_{\sigma=1}^{g_\alpha}\sum_{\langle\omega\rangle}(\mathbf{D}_{\omega\omega'}\psi_\sigma{}^{\alpha},\mathbf{D}_{\omega\omega'}{}^BJ(R_\omega)\mathbf{C}^{\omega}(B)\psi_\sigma{}^{\alpha})$$
$$=\frac{1}{g_\alpha}\sum_{\sigma=1}^{g_\alpha}\sum_{\langle\omega\rangle}(\mathbf{D}_{\omega\omega'}\psi_\sigma{}^{\alpha},{}^BJ(R_{\omega'})\mathbf{C}^{\omega'}(B)\mathbf{D}_{\omega\omega'}\psi_\sigma{}^{\alpha})$$
$$=\frac{1}{g_\alpha}\sum_{\sigma,\nu,\mu=1}^{g_\alpha}\sum_{\langle\omega\rangle}D^{\alpha}(\omega,\omega')_{\nu\sigma}{}^*D^{\alpha}(\omega,\omega')_{\mu\sigma}$$
$$\times(\psi_\nu{}^{\alpha},{}^BJ(R_{\omega'})\mathbf{C}^{\omega'}(B)\psi_\mu{}^{\alpha}), \tag{15}$$

where the $D^{\alpha}(\omega,\omega')_{\sigma\nu}$ are the matrix elements of $\mathbf{D}_{\omega\omega'}$ in the irreducible representation $[\alpha]$ of $\mathcal{S}_A$:

$$\mathbf{D}_{\omega\omega'}\psi_\sigma{}^{\alpha}=\sum_{\nu=1}^{g_\alpha}D^{\alpha}(\omega,\omega')_{\nu\sigma}\psi_\nu{}^{\alpha}. \tag{16}$$

Using the unitarity relations for the group representations

$$\sum_{\sigma=1}^{g_\alpha}D^{\alpha}(\omega,\omega')_{\mu\sigma}D^{\alpha}(\omega,\omega')_{\nu\sigma}{}^*=\delta_{\mu\nu}, \tag{17}$$

we obtain

$$\langle {}^B\mathbf{M}\rangle = \frac{1}{g_\alpha}\sum_{(\omega)}\sum_{\nu=1}^{g_\alpha}(\psi_\nu{}^\alpha, {}^BJ(R_{\omega'})\mathbf{C}^{\omega'}(B)\psi_\nu{}^\alpha)$$
$$= \frac{1}{g_\alpha}\binom{A}{B}\sum_{\nu=1}^{g_\alpha}(\psi_\nu{}^\alpha, {}^BJ(R_{\omega'})\mathbf{C}^{\omega'}(B)\psi_\nu{}^\alpha), \quad (18)$$

where $\binom{A}{B}$ is the usual binomial coefficient, and $\langle\omega'\rangle$ is an arbitrary set of B particles.

For given symmetry partition $[\alpha]$ the choice of an orthornormal set of base vectors $\psi_\nu{}^\alpha$ is not unique if $g_\alpha > 1$, and it is advantageous to choose the base vectors $\psi_\nu{}^\alpha$ so that they have definite properties in the subgroup $\mathcal{S}_B$ of $\mathcal{S}_A$. For example, they can be chosen so that they belong to the irreducible representations $[\beta]$ of $\mathcal{S}_B$ with respect to permutations on the space coordinates of the first B nucleons (as discussed briefly in Appendix II). Let $n(\alpha|\beta)$ be the number of $\psi_\nu{}^\alpha$ which have symmetry $[\beta]$ on the first B particles, and $f_\beta{}^\alpha$ be the number of times the irreducible representation $[\alpha]$ of $\mathcal{S}_A$, when considered as a (reducible) representation of the subgroup $\mathcal{S}_B$, contains the irreducible representation $[\beta]$. Then[18]

$$n(\alpha|\beta) = g_\beta f_\beta{}^\alpha = \frac{g_\beta}{B!}\sum_{(b)}\chi^\beta(b)\rho(b)\chi^\alpha(b, 1^{A-B}), \quad (19)$$

where the sum is over the classes (b) of $\mathcal{S}_B$, and one has the dimensionality condition

$$\sum_\beta g_\beta f_\beta{}^\alpha = \sum_\beta n(\alpha|\beta) = g_\alpha, \quad (20)$$

where the sum is over the irreducible representations $[\beta]$ of $\mathcal{S}_B$.

With this choice of base vectors $\psi_\nu{}^{(\alpha|\beta)}$, and with the particular choice of $\langle\omega'\rangle$ in expression (18) as the set of particles numbered 1, 2, 3, $\cdots$, B, we have for the analogous expressions to (1) and (2) in the group $\mathcal{S}_B$,

$$\mathbf{C}^{\omega'}(B)\psi_\lambda{}^{(\alpha|\beta)} = \frac{1}{\rho(B)}\sum_{s\text{ in }(B)}\mathbf{P}_s{}^{\omega'}\psi_\lambda{}^{(\alpha|\beta)} = \kappa^\beta(B)\psi_\lambda{}^{(\alpha|\beta)} \quad \lambda = 1, 2, \cdots, g_\beta, \quad (21)$$

and

$$\kappa^\beta(B) = \chi^\beta(B)/g_\beta, \quad (22)$$

where $\psi_\lambda{}^{(\alpha|\beta)}$ denotes a function $\psi_\nu{}^\alpha$ belonging to representation $[\alpha]$ of $\mathcal{S}_A$ on all particles, and also to $[\beta]$ of $\mathcal{S}_B$ with respect to the first B particles. Using (19), (21), and (22), the expression (18) becomes

$$\langle {}^B\mathbf{M}\rangle = \frac{1}{g_\alpha}\binom{A}{B}\sum_\beta n(\alpha|\beta)\frac{\chi^\beta(B)}{g_\beta}(\psi_\lambda{}^{(\alpha|\beta)}, {}^BJ(R_{\omega'})\psi_\lambda{}^{(\alpha|\beta)})$$
$$= \frac{1}{g_\alpha}\binom{A}{B}\frac{1}{B!}\sum_{(b)}\rho(b)\chi^\alpha(b, 1^{A-B}) \times\sum_\beta\chi^\beta(b)\chi^\beta(B)M^{[\beta]}, \quad (23)$$

where

$$M^{[\beta]} = (\psi_\lambda{}^{(\alpha|\beta)}, {}^BJ(R_{\omega'})\psi_\lambda{}^{(\alpha|\beta)}), \quad (24)$$

independent of λ, is the expectation value of ${}^BJ(R_{\omega'})$ over the g_β states which have symmetry $[\beta]$ on the set $\langle\omega'\rangle$ of the first B particles. It is convenient to write (23) in the form of a sum over the classes (b) of $\mathcal{S}_B$,

$$\langle {}^B\mathbf{M}\rangle = \sum_{(b)}\Omega^\alpha(b)\mathcal{J}(b), \quad (25)$$

where

$$\mathcal{J}(b) = [\rho(b)/B!]\sum_\beta\chi^\beta(b)\chi^\beta(B)M^{[\beta]}, \quad (26)$$

with the sum over irreducible representations of $\mathcal{S}_B$. The constants $\Omega^\alpha(b)$ are given by

$$\Omega^\alpha(b) = \binom{A}{B}\frac{\chi^\alpha(b, 1^{A-B})}{\chi^\alpha(1^A)}, \quad (27)$$

since g_α, the dimension of the representation $[\alpha]$ is given by $\chi^\alpha(1^A)$.

In an entirely similar manner, the expression (6) for the Wigner forces can, in the same approximation, be written as

$$\langle {}^B\mathbf{W}\rangle = \sum_{(b)}\Omega^\alpha(b)\mathcal{K}(b), \quad (28)$$

with

$$\mathcal{K}(b) = [\rho(b)/B!]\sum_\beta\chi^\beta(b)\chi^\beta(1^B)W^{[\beta]}, \quad (29)$$

where

$$W^{[\beta]} = (\psi_\lambda{}^{(\alpha|\beta)}, {}^BK(R_{\omega'})\psi_\lambda{}^{(\alpha|\beta)}) \quad (30)$$

has a definition analogous to (24). An extension of these definitions and expressions is given in appendix I.

Combining (25) and (28) we obtain, finally

$$\langle {}^B\mathbf{M} + {}^B\mathbf{W}\rangle = \sum_{(b)}\Omega^\alpha(b)\mathcal{L}(b), \quad (31)$$

with

$$\mathcal{L}(b) = \mathcal{J}(b) + \mathcal{K}(b). \quad (32)$$

V. 2-, 3-, 4-BODY FORCES AS EXAMPLES

1. 2-Body Forces

Using character tables for the symmetric group,[18] we have

$$\mathcal{L}(1^2) = \tfrac{1}{2}\{W^{[2]} + W^{[1,1]} + M^{[2]} - M^{[1,1]}\}, \quad (33a)$$

$$\mathcal{L}(2) = \tfrac{1}{2}\{W^{[2]} - W^{[1,1]} + M^{[2]} + M^{[1,1]}, \quad (33b)$$

$$\Omega^\alpha(1^2) = \tfrac{1}{2}A(A-1), \quad (33c)$$

$$\Omega^\alpha(2) = \tfrac{1}{2}A(A-1)[\chi^\alpha(2,1^{A-2})/\chi^\alpha(1^A)] = n_+ - n_-, \quad (33d)$$

where n_+, n_- are the numbers of symmetrically and antisymmetrically coupled pairs. Formulas for $\Omega^\alpha(2)$ are given by Murnaghan.[19] These are just the expres-

[19] See reference 18, pp. 140–141.

sions given by Wigner[18] and recorded in many places.[20,21] In reference 21 the corresponding expressions are L' and L given in terms of the above definitions by

$$\mathfrak{L}(1^2)=-L', \quad \mathfrak{L}(2)=-L. \tag{34}$$

2. 3-Body Forces

$$\mathfrak{L}(1^3)=\{W^{[3]}+4W^{[2,1]}+W^{[1,1,1]}+M^{[3]} -2M^{[2,1]}+M^{[1,1,1]}\}, \tag{35a}$$

$$\mathfrak{L}(2,1)=\tfrac{1}{2}\{W^{[3]}-W^{[1,1,1]}+M^{[3]}-M^{[1,1,1]}\}, \tag{35b}$$

$$\mathfrak{L}(3)=\tfrac{1}{3}\{W^{[3]}-2W^{[2,1]}+W^{[1,1,1]}+M^{[3]} +M^{[2,1]}+M^{[1,1,1]}\}. \tag{35c}$$

As before, the $\Omega^a(b)$ are given by Eq. (27) and evaluated by Murnaghan[18] for $(b)=(2,1)$ and (3). For $(b)=(1^3)$ one simply has

$$\Omega^a(1^3)=\tfrac{1}{6}A(A-1)(A-2). \tag{35d}$$

The significance of the expressions $\mathfrak{L}(b)$ in Eqs. (35) is more evident if one makes the reasonable assumptions,

$$W^{[2,1]}\cong\tfrac{1}{2}\{W^{[3]}+W^{[1,1,1]}\},$$

and

$$M^{[2,1]}\cong\tfrac{1}{2}\{M^{[3]}+M^{[1,1,1]}\}, \tag{36}$$

which state that the potential contribution from a nucleon triple of space symmetry $[2,1]$ is equal to the average of the potential contributions in the states of symmetry $[3]$ and $[1^3]$, for Wigner and Majorana forces separately. The expressions (35) become

$$\mathfrak{L}(1^3)=W^{[2,1]}=-G'',$$

$$\mathfrak{L}(2,1)=\tfrac{1}{2}\{W^{[3]}-W^{[1,1,1]}\}+\tfrac{1}{2}\{M^{[3]}-M^{[1,1,1]}\}=-G',$$

$$\mathfrak{L}(3)=M^{[2,1]}=-G, \tag{37}$$

where we have introduced the notation G, G', G'' for convenience. These parameters are positive if the forces are attractive.

3. 4-Body Forces

Similar expressions to (33) and (35) for 4-body forces can easily be evaluated. With the simplifications (suggested by the relative numbers of symmetric and antisymmetric couplings)

$$M^{[4]}-M^{[1,1,1,1]}=3\{M^{[3,1]}-M^{[2,1,1]}\},$$

$$M^{[4]}+M^{[1,1,1,1]}=M^{[3,1]}+M^{[2,1,1]}=2M^{[2,2]}, \tag{38}$$

$$M^{[4]}-M^{[3,1]}=M^{[2,1,1]}-M^{[1,1,1,1]},$$

and similar simplifications for the Wigner forces, we obtain

$$\mathfrak{L}(1^4)=W^{[2,2]},$$

$$\mathfrak{L}(2,1^2)=\tfrac{1}{2}\{W^{[4]}-W^{[1,1,1,1]}\}=\tfrac{3}{2}\{W^{[3,1]}-W^{[2,1,1]}\},$$

$$\mathfrak{L}(2^2)=\tfrac{1}{2}\{M^{[3,1]}-M^{[2,1,1]}\}, \tag{39}$$

$$\mathfrak{L}(3,1)=2\mathfrak{L}(2^2)=M^{[3,1]}-M^{[2,1,1]},$$

$$\mathfrak{L}(4)=M^{[2,2]}.$$

Murnaghan[18] also gives explicit expressions for the $\Omega^a(b)$ for $(b)\equiv(4)$, $(3,1)$ $(2,1^2)$, but not for (2^2). Also,

$$\Omega^a(1^4)=A(A-1)(A-2)(A-3)/(4!).$$

VI. DISCUSSION

To understand what these results may signify about nuclear structure, it is necessary to make some estimate of the behavior of the parameters L, L', G, G', G'', etc. For 2-body forces alone, if the range of nuclear forces is small compared with the nuclear radius, the probability of finding two particles within range of each other is inversely proportional to the total nuclear volume,[22] and hence to the atomic mass number A. One then expects the parameters L and L' in Eq. (34) to vary inversely with A. Since the $\Omega^a(b)$ in (33d) are roughly proportional to A^2, the expectation value of the potential energy for 2-body forces increases linearly with A. To a first approximation, one can assume the kinetic energy also increases linearly with A, so that one does obtain a saturation of the binding energy per nucleon. In a similar manner, if the effective range of the 3-body interaction is small compared to the nuclear radius, the probability of finding three nucleons within this range of each other is inversely proportional to the square of the nuclear volume, and hence to A^2. One then expects the parameters G, G', G'' in (37) to vary inversely to A^2. Since the $\Omega^a(b)$ appropriate to the 3-body case are essentially proportional to A^3, the 3-body forces themselves show saturation, provided that they are attractive forces. This is by no means certain or necessary. There are some indications that the main contribution from 3-body forces is repulsive.[3,4]

Historically, 2-body exchange forces were introduced to explain saturation without collapse. The same effect can be achieved by introducing repulsive core potentials between nucleons, or by introducing repulsive 3-body forces. The saturation nuclear density is in the latter case, pictured as resulting from a balance between attractive 2-body forces and repulsive 3-body forces. However, exchange forces are predicted by meson theory, and have had direct experimental verification.[23] The extra freedom one obtains in taking into account 3-body forces with exchange may allow a consistent

[20] Gamow and Critchfield, *Atomic Nucleus and Nuclear Energy Sources* (Clarendon Press, Oxford, 1949).

[21] Blatt and Weisskopf, *Theoretical Nuclear Physics* (John Wiley and Sons, Inc., New York, 1951), Chap. VII.

[22] See reference 21, Chap. III.

[23] E. Fermi, *Nuclear Physics Lecture Notes* (University of Chicago Press, Chicago, 1950), p. 121.

explanation of the low and high energy scattering data, as well as the general features of nuclear structure.

The Majorana 2-body force has the property that it gives repulsion for antisymmetric pairs if it gives attraction for symmetric pairs. If one assumes the Majorana potential is attractive, the parameters L, L' in (34) are positive quantities. Now $\Omega^a(1^2)$ is always positive, while $\Omega^a(2)$ is positive for states of high symmetry, and negative for states of low symmetry. Since the space symmetry of the wave function decreases with A because of the Pauli principle, one does achieve saturation if the Majorana forces are strong enough.[22] This also follows from Eqs. (31) and (33d). For 3-body exchange forces of the type considered here, let us assume that the Wigner and Majorana potentials are both attractive. Hence, from Eq. (37) G, G', G'' are all positive. Now $\Omega^a(1^3)$ is always positive. It follows from the definitions (27), that $\Omega^a(2,1)$ is positive for partitions of high symmetry and negative for partitions of low symmetry, whereas $\Omega^a(3)$ is positive in both cases, and is negative for partitions of intermediate symmetry. In view of this behavior it is also possible that the usual saturation conditions[22] on the 2-body potentials can be relaxed somewhat, depending upon the magnitudes of G, G', G''. An attempt is made in Sec. VII to estimate the magnitude of G, and also to determine its sign, on the basis of β-decay data.

It must be noted that the range of nuclear forces is not entirely negligible compared to nuclear radii, so that the above arguments can only be considered as approximate.

VII. SYMMETRY ENERGY OF ISOBARS

In order to find the effect of symmetry on the potential energy, it is necessary to evaluate the quantities $\Omega^a(b)$ for a given class (b) as a function of the symmetry partition $[a]$. These quantities are just binomial coefficients times ratios of the group characters. The $\Omega^a(b)$ of interest to us are given by Murnaghan[18] in terms of the coefficients a_j and b_j which may be used to describe the partition. In the Young diagram[18,24] corresponding to $[a]$, a_j is the number of elements in the jth column below the main diagonal, and b_j is the number of elements in the jth row to the right of the main diagonal. As a consequence of the Pauli principle, the Young diagram has but 4 columns, and for $A>16$ we may assume that $b_1=3$, $b_2=2$, $b_3=1$. For convenience in comparing with the literature we introduce the Wigner partition quantum numbers[20,21] P, P', P'', in terms of which

$$\begin{aligned} a_1&=\tfrac{1}{4}A-1+\tfrac{1}{2}(P+P'+P''),\\ a_2&=\tfrac{1}{4}A-2+\tfrac{1}{2}(P-P'-P''),\\ a_3&=\tfrac{1}{4}A-3+\tfrac{1}{2}(-P+P'-P''),\\ a_4&=\tfrac{1}{4}A-4+\tfrac{1}{2}(-P-P'+P''). \end{aligned} \tag{40}$$

[24] H. Weyl, *The Theory of Groups and Quantum Mechanics* Methuen and Company, Ltd., London, 1931), p. 358.

If any coefficient a_j is negative it is defined to be zero. In the present notation, Murnaghan's formulas then become

$$\Omega^a(2,1)=\tfrac{1}{8}(A-2)\Omega^a(2), \tag{41a}$$

$$\Omega^a(2)=-\tfrac{1}{8}A^2+2A+5/2-\xi, \tag{41b}$$

$$\Omega^a(3,1)=\tfrac{1}{4}(A-3)\Omega^a(3), \tag{41c}$$

$$12\Omega^a(3)=(A/2)^3-24(A/2)^2+53(A/2)+60+3(A-8)\xi+3\xi', \tag{41d}$$

where, with the notation of Blatt and Weisskopf,[21]

$$\xi=\tfrac{1}{2}\{(P+2)^2+(P'+1)^2+P''^2\}, \tag{42}$$

and where we define

$$\xi'=2(P+2)(P'+1)P''. \tag{43}$$

Similar expressions can be written for $\Omega^a(4)$, $\Omega^a(3,1)$ and $\Omega^a(2,1^2)$, but we shall not deal with 4-body exchange forces here. The expressions for $\Omega^a(1^2)$ and $\Omega^a(1^3)$ are given by Eqs. (33c) and (35d).

The total contribution to the potential energy from 2- and 3-body forces can now be written in terms of A and the partition quantum numbers P, P', and P'' by means of Eqs. (31), (34), (37), and (41),

$$\langle {}^2\mathbf{M}+{}^2\mathbf{W}\rangle+\langle {}^3\mathbf{M}+{}^3\mathbf{W}\rangle=-\mathfrak{F}+\xi\,\mathfrak{C}/A-\xi'\mathfrak{G}/A^2, \tag{44}$$

where $\mathfrak{F}(A)$ is a function of the atomic mass number A, and of the five parameters L, L', G, G', G''. Further, $\mathfrak{C}$ and $\mathfrak{G}$ (expected to be roughly independent of A) are given by

$$\mathfrak{C}=A\{L-\tfrac{1}{4}(A-8)G-\tfrac{1}{8}(A-2)G'\}, \tag{45}$$

$$\mathfrak{G}=\tfrac{1}{4}A^2G. \tag{46}$$

Following the notation of Blatt and Weisskopf,[21] we now separate the total nuclear energy $U(A,T_\zeta)$ for a particular nucleus into a part which is independent of symmetry and isotopic spin, $U_0(A)$, and a part dependent on these,

$$U(A,T_\zeta)-U_0(A)=\xi\,\mathfrak{C}/A-\xi'\mathfrak{G}/A^2+T_1\mathfrak{n}/A-4u_cT_\zeta(A-1-T_\zeta)/A^{\frac{1}{3}}+(M_n-M_p)c^2T_\zeta, \tag{47}$$

where the last three terms are respectively, the first approximation to the symmetry dependence of the kinetic energy,[21] the Coulomb energy, and the neutron-proton mass difference. The parameter $\mathfrak{n}$ is given by

$$\mathfrak{n}=\tfrac{1}{2}\{P^2+P'^2+P''^2\}. \tag{48}$$

T_ζ is the usual ζ component of the isotopic spin, and T_1 (a constant) is about 60 Mev. Since isobars have the same value of $U_0(A)$, $\mathfrak{C}$, $\mathfrak{G}$, and T_1, the energy difference between neighboring isobars is given by

$$U(A,T_\zeta'')-U(A,T_\zeta')=\Delta\xi\,\mathfrak{C}/A+T_1\Delta\mathfrak{n}/A-\Delta\xi'\mathfrak{G}/A^2-(4u_c/A^{\frac{1}{3}})\Delta T_\zeta(A-1-T_\zeta'-T_\zeta'')+(M_n-M_p)c^2\Delta T_\zeta, \tag{49}$$

where $\Delta T_\xi = T_\xi'' - T_\xi'$, $\Delta\xi = \xi(T_\xi'') - \xi(T_\xi')$, and so forth.

If we now assume that the 2-body forces are considerably more important than the 3-body forces, then $L \gg AG$ or AG', and since the 2-body forces must then be attractive, the lowest energy is obtained when the positive term $\xi \mathfrak{C}/A$ is a minimum (neglecting the Coulomb effect and the neutron-proton mass difference), i.e., when the partition quantum numbers P, P', P'' are as small as possible. If the 3-body Majorana potential is attractive, the quantity $\xi' \mathcal{G}/A^2$ is positive or negative as ξ' is positive or negative, since $\mathcal{G}$ is then positive. We shall assume that the 2-body forces are, in fact, considerably more important. Under these circumstances, the partition quantum numbers are simply related to T_ξ. Table I summarizes the situation for ξ'. In this table we have distinguished between odd-even (OE) nuclei and even-odd (EO) nuclei. OE nuclei have the odd number of particles in excess of the even, and EO the opposite circumstance, without regard to which is N or Z. The corresponding ξ and $\mathfrak{n}$ functions are tabulated by Blatt and Weisskopf.[21] In Table II, we have tabulated the values of ξ, $\mathfrak{n}$, ξ' for EO and OE nuclei for various $|T_\xi|$ values.

TABLE I. Symmetry function ξ' *versus* nuclear type.

Nuclear type	Partition quantum numbers P	P'	P''	ξ'
EE	$\|T_\xi\|$	0	0	0
OO $(N \neq Z)$	$\|T_\xi\|$	1	0	0
OO $(N=Z)$	1	0	0	0
OE	$\|T_\xi\|$	$\frac{1}{2}$	$\frac{1}{2}$	$\frac{1}{2}(\|T_\xi\|+2)$
EO	$\|T_\xi\|$	$\frac{1}{2}$	$-\frac{1}{2}$	$-\frac{1}{2}(\|T_\xi\|+2)$

We shall now confine ourselves to odd-A nuclei. The Coulomb constant u_c is given by the binding energy difference between the mirror nuclei, corrected for the neutron-proton mass difference,

$$B(\tfrac{1}{2}, -\tfrac{1}{2}) = 4u_c(A-1)/A^{\frac{1}{3}}. \tag{50}$$

Hence, one has for the symmetry energy difference for the T_ξ'', T_ξ' isobars:

$$\begin{aligned}\Delta E &= \Delta\xi\, \mathfrak{C}/A + T_1 \Delta\mathfrak{n}/A - \Delta\xi' \mathcal{G}/A^2 \\ &= B(T_\xi', T_\xi'') + \frac{A-1-T_\xi'-T_\xi''}{A-1} B(\tfrac{1}{2}, -\tfrac{1}{2})(\Delta T_\xi),\end{aligned} \tag{51}$$

where $B(T_\xi', T_\xi'')$ is the binding energy difference between the isobars T_ξ' and T_ξ'', corrected for the neutron-proton mass difference. For $T_\xi' = \frac{1}{2}$, $T_\xi'' = \frac{3}{2}$, we have for the symmetry energy difference, using Table II,

$$\begin{aligned}\Delta E &= 3\,\mathfrak{C}/A + T_1/A \pm 9\mathcal{G}/A^2 \\ &= B(\tfrac{1}{2}, \tfrac{3}{2}) + [(A-3)/(A-1)] B(\tfrac{1}{2}, -\tfrac{1}{2}),\end{aligned} \tag{52}$$

TABLE II. Symmetry functions *versus* $|T_\xi|$ for odd-A nuclei.

$\|T_\xi\|$	ξ	$\mathfrak{n}$	ξ' *OE* nuclei	ξ' *EO* nuclei
1/2	35/8	3/8	15/4	−15/4
3/2	59/8	11/8	21/4	−21/4
5/2	91/8	27/8	27/4	−27/4
7/2	131/8	51/8	33/4	−33/4

where the plus sign is to be taken if the $T_\xi'' = \frac{3}{2}$ isobar is of the EO variety (more nucleons in the even set than in the odd), in which case the $T_\xi' = \frac{1}{2}$ isobar is of the OE variety (more nucleons in the odd set than in the even). Conversely, the negative sign is to be taken if $T_\xi'' = \frac{3}{2}$ corresponds to the OE variety and $T_\xi' = \frac{1}{2}$ to the EO variety.

There are two points of interest in Eq. (52). The $OE-EO$ and $EO-OE$ β transitions ought to show the effect of the alternation in the sign of the term proportional to $\mathcal{G}$. Further, since one expects that $\mathfrak{C}$, $\mathcal{G}$, and T_1 are roughly independent of the mass number A, the right hand side of (52) can be expected to vary roughly as $1/A$ if the 3-body contribution is small, i.e., if $3\mathcal{G} \ll \mathfrak{C}A$. In the limit of vanishing 3-body force, $\mathcal{G}$ is zero, and the parameter $\mathfrak{C}$ reduces to the parameter L_1 of Blatt and Weisskopf.[21]

In Fig. 1, the quantity ΔE of Eq. (52) is plotted in Mev units against $1/A$ using the available β-decay data which are recorded in Table III. These data were taken from the latest tables of isotopes[25] and energy level charts for light nuclei.[26] (For isotopic multiplets

TABLE III. Symmetry energy differences from β-decay data (see reference 25).

A	$B(\frac{1}{2}, -\frac{1}{2})$ (Mev)	$B(\frac{1}{2}, \frac{3}{2})$ (Mev)	$A(\Delta E)$ (Mev)
15	3.48	8.02	165
17	3.51	7.9	186
19	4.03	3.7	138
21	4.31		
23	4.79	3.43	179
25	(4.9)[a]	2.92	185
27	5.28	1.86	181
29	5.4	3.02	232
31	5.74	0.69	187
33	6.10	−0.51	172
35	6.20	−0.61	183
37	6.4	(−1.60)[b]	163
39	6.9		
41	6.74		
43	(7.2)[a]	−2.92	169
45		−2.82	184
47		(−3.45)[a]	172
49		(−3.25)[a]	200
51		(−4.0)[a]	181
53		−4.3	184
55		−4.23	206
57		−4.02	237

[a] Not certain that β transitions end on ground states. [See A. M. Feingold, Revs. Modern Phys. 23, 10 (1951).]
[b] Electron capture, data uncertain.

[25] Hollander, Perlman, and Seaborg, Revs. Modern Phys. 25, 469 (1953).
[26] P. Ajzenberg and T. Lauritsen, Revs. Modern Phys. 24, 321 (1952).

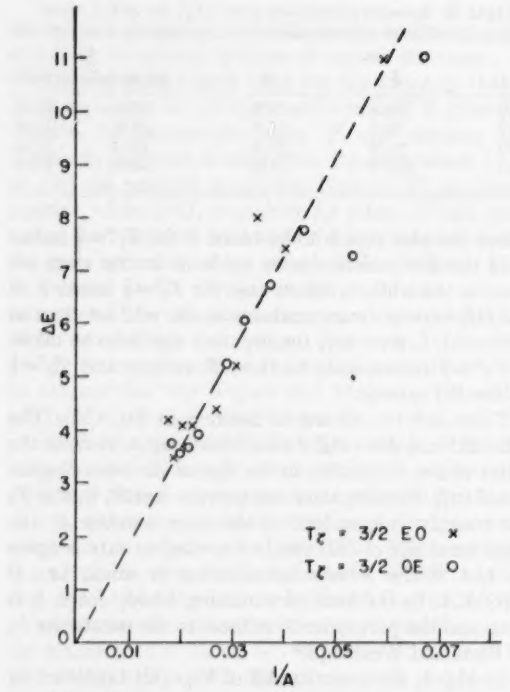

FIG. 1. The symmetry energy differences for $T_\zeta=\frac{3}{2}$ and $T_\zeta=\frac{1}{2}$ isobars as a function of the inverse atomic mass number A^{-1}. The data are taken from the information available on β decay (see references 25 and 26) and are reproduced in Table III. The data corresponding to $T_\zeta=\frac{3}{2}$, *EO* and $T_\zeta=\frac{1}{2}$, *OE* transitions are indicated by crosses; while those corresponding to $T_\zeta=\frac{1}{2}$, *EO* and $T_\zeta=\frac{3}{2}$, *OE* are indicated by circles.

for which no mirror nuclei occur, the Coulomb term was evaluated using $u_e=0.146$ Mev.) As shown in Fig. 1, and also in reference 21, the points do fall roughly along a line. However, Fig. 1 also shows that there is a tendency for the points corresponding to the transitions $T_\zeta''=\frac{3}{2}$, $OE\leftrightarrows T_\zeta'=\frac{1}{2}$, *EO* to lie along a line of smaller slope than the corresponding line for the $T_\zeta''=\frac{3}{2}$, $EO\leftrightarrows T_\zeta'=\frac{1}{2}$, *OE* transitions. The effect is perhaps better illustrated in Fig. 2 where ΔE in Mev times A has been plotted against A. The Wigner theory predicted that these points should fall on a horizontal line. The present extension of Wigner's theory anticipates that the points ought to fall on two curves which are nearly horizontal lines but slowly converge. The actual differences in the two types of β transition shown seem significant. The average value of $A(\Delta E)$ is 194 for the one type and 176 for the other. In Fig. 2, arrows indicate the direction of expected exaggeration for those points which are possibly influenced by shell effects in the experimental results at $N, Z=8, 20, 28$. The theory, of course, has averaged over such effects.

If the differences indicated in Fig. 2 and predicted by the theory are real, it is interesting to note that the constant $\mathcal{G}$ is positive and from (46) and (37) it follows that the Majorana 3-body potential, aside from exchange effects, is attractive. The sign of the exchange part depends upon the symmetry partition, just as for the 2-body potential, as discussed in Sec. VI. Using the value of 18 for the mean difference in $A(\Delta E)$ for the two types of transition we obtain $\mathcal{G}=\bar{A}$ Mev, where $\bar{A}=37$ is the mean value of A in this range. Hence, the average Majorana 3-body potential contribution $G=148/A^2$ Mev. For comparison with the 2-body case, one must compare $AG/4$ (≈ 1.2 Mev for $A=30$) with L (≈ 1.5 Mev[20]). On this basis, the 3-body contribution is by no means negligible. However, we have probably overestimated the difference in symmetry energy for the two types of transition, since the results are greatly affected by the possibly anomalous case of Al^{29} and the shell effects at 28 protons.

Although Wigner's theory predicts a straight horizontal line in Fig. 2 and the present theory two such horizontal lines, the staggering of the experimental points is not surprising. Both theories average over shell effects. However, one might expect that the symmetry differences corresponding to *OE* and *EO* effects should persist. This appears to be the case.

In very light nuclei a somewhat similar effect to that discussed here was accounted for by Phillips and Feenberg[27] in a very different way. For $A\leqq 15$ the binding energy difference $B(\frac{1}{2}, -\frac{1}{2})$ between mirror nuclei was observed to have pronounced fluctuations in addition to the smooth variation with A predicted by Eq. (50). On the basis of Hartree-type calculations for the wave functions, the expectation value of the electrostatic energy has a relatively larger number of exchange terms in even proton as against odd proton nuclei, thus accounting qualitatively for the fluctuations observed. A more general approach by Feenberg and Goertzel[28] explained the fluctuations as a Coulomb symmetry effect by distinguishing between the average electrostatic energy contributed by a symmetric proton pair and that contributed by an antisymmetric proton pair. The fluctuations were expected to decrease rapidly as a function of A, and the experimental results at that time indicated that the effect was negligible beyond $A=20$. An examination of column one in Table III shows that an effect of this type persists beyond $A=20$. A comparison of Eq. (28) of Feenberg and Goertzel with the Coulomb difference term in Eq. (49) here, shows that their constant L_e in the main Coulomb term is given by

$$L_e=8u_e/A^{\frac{1}{3}}.$$

In line with their interpretation, Eq. (49) ought to be modified to include their symmetry term proportional to L_e', where L_e' is the average electrostatic energy of a symmetrical proton pair minus that of an antisymmetrical proton pair. With this modification in Eq.

[27] M. Phillips and E. Feenberg, Phys. Rev. **59**, 400 (1941).
[28] E. Feenberg and G. Goertzel, Phys. Rev. **70**, 598 (1946).

(49), Eq. (52) becomes

$$\Delta E = B(\tfrac{1}{2},\tfrac{3}{2}) + [(A-3)/(A-1)]B(\tfrac{1}{2},-\tfrac{1}{2}) \pm \tfrac{3}{4}L_e', \quad (53)$$

where the plus (minus) sign is to be taken if $T_<'' = \frac{3}{2}$ is of the *EO* (*OE*) variety. Hence, the effect being discussed here is *enhanced* by these considerations. A rough estimate of L_e' based on Eq. (28) of Feenberg and Goertzel and on column one of Table III, yields a value of $L_e' \leqq 0.13$ Mev. Hence, the average difference in the quantity $A(\Delta E)$ for the two types of transitions considered here is modified from 18 to perhaps a maximum of 25 Mev, corresponding to downward translations of the circles in Fig. 2 by 3.5 units and upward translations of the crosses by the same amount.

Since the two varieties of β-decay data correspond, respectively, to transitions between states in which the total numbers of neutron and proton pairs do not change ($T_<=\frac{3}{2}$, *OE* and $T_<=\frac{1}{2}$, *EO*) and to transitions between states in which the total number of neutron pairs increases (decreases) by one and the total number of proton pairs decreases (increases) by one ($T_<=\frac{3}{2}$, *EO* and $T_<=\frac{1}{2}$, *OE*), one might therefore interpret the alternation as due to a difference in the neutron and proton pairing energies. A similar situation in heavy nuclei is discussed by Feather.[29] He interprets the data as evidence that the binding energy of an even-numbered proton exceeds the mean binding energies of the neighboring odd-numbered protons by an amount (1.5 Mev) which is greater than the excess binding of an even-numbered neutron over the mean binding energy of the neighboring odd-numbered neutrons (1.1 Mev). This difference is quite large and is difficult to explain on the basis of charge independence of the nuclear forces, unless one invokes the argument that the neutrons and protons involved belong to different shells. This argument is not valid in the present case of light nuclei. On the other hand, the explanation in terms of 3-body exchange forces is straightforward, since one does expect a different partition for *EO* and *OE* nuclei with $T_<=\frac{1}{2}$, *viz.*, $[4+\cdots+4+3]$ in the former case and $[4+\cdots+4+4+1]$ in the latter. The next higher isobar $T_<=\frac{3}{2}$, has partitions $[4+\cdots+4+3+2]$ and $[4+\cdots+4+2+1]$ in the *EO* and *OE* nuclei, respectively.

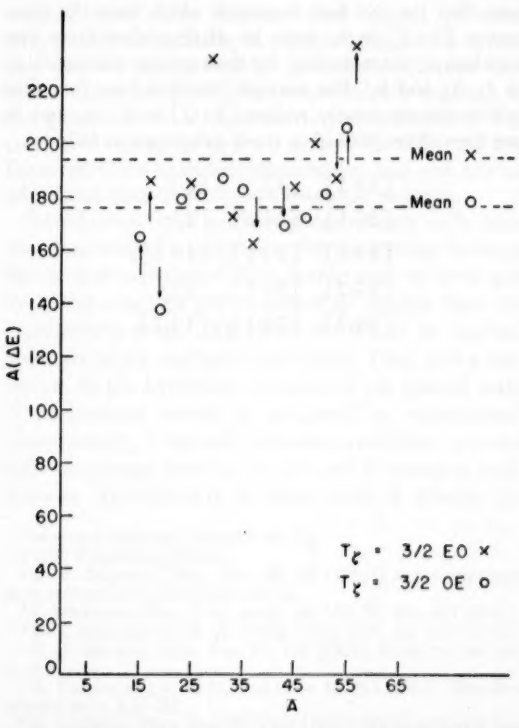

FIG. 2. The product of A and the symmetry energy differences in Mev for $T_<=\frac{3}{2}$ and $T_<=\frac{1}{2}$ isobars as a function of the atomic mass number A. The data are taken from Table III.

This work was initiated while the author held a fellowship with the Summer Research Institute of the Canadian Mathematical Congress at Queen's University, Kingston. The author wishes to express special thanks to the Institute. The author is also indebted to G. E. Tauber of the National Research Council of Canada for an interesting conversation, and to W. R. Dixon of Queen's University for several helpful conversations.

APPENDIX I

Generalized Majorana Exchange Forces

Although we have restricted ourselves here to phenomenological Majorana forces of the type (5) which are irreducible with respect to the exchange part as well as with respect to the form of the potential, as discussed above, we can generalize the definitions by relaxing the first requirement of irreducibility. Thus, if (b') is an arbitrary class of $\mathfrak{S}_B$, one may define the Majorana exchange potential of class (b') by

$$\mathbf{M}(b') = \sum_{(\omega)} J(R_\omega; b')\mathbf{C}^\omega(b'), \quad (54)$$

and obtain quite generally

$$\langle \mathbf{M}(b') \rangle = \sum_{(b)} \Omega^\alpha(b)\mathcal{J}(b,b'), \quad (55)$$

where $\Omega^\alpha(b)$ is again given by (27), and

$$\mathcal{J}(b,b') = \frac{\rho(b)}{B!} \sum_\beta \chi^\beta(b)\chi^\beta(b')M^{[\beta]}(b'). \quad (56)$$

Also,

$$M^{[\beta]}(b') = (\psi^{(\alpha|\beta)}, J(R_{\omega'}; b')\psi^{(\alpha|\beta)}), \quad (57)$$

[29] N. Feather, *Nuclear Stability Rules* (Cambridge University Press, Cambridge, 1952), pp. 118–143. Feather has plotted the energy of β decay so that his curves include the Coulomb energy differences as well as the energy differences arising from specifically nuclear forces.

in analogy with the definition of the expression (24) above. In this more general sense, Wigner forces are just Majorana exchange forces of class $(b')=(1^B)$,with

$$ {}^BK(R_{\omega'}) \approx J(R_{\omega'}; b'=1^B). \tag{58}$$

The total potential contribution from B-body Majorana forces is then

$$ \langle \sum_{(b')} \mathbf{M}(b') \rangle = \sum_{(b)} \sum_{(b')} \Omega^a(b) g(b,b'). \tag{59}$$

APPENDIX II

Classification of the Basis of a Representation of the Symmetric Group

Let $[\alpha]$ denote that irreducible representation of the symmetric group $\mathcal{S}_A$ which has partition $[\alpha_1+\alpha_2+\cdots]$ and dimension g_α. Considered as a representation of the subgroup $\mathcal{S}_{A-1}$, it is reducible, and its reduction in this subgroup yields the direct sum[18]

$$ [\alpha] = \sum_j [\alpha]_j, \tag{60}$$

where $[\alpha]_j$ is that irreducible representation of $\mathcal{S}_{A-1}$ which has partition $[\alpha_1+\alpha_2+\cdots+(\alpha_j-1)+\alpha_{j+1}+\cdots]$, and where the sum is over regular partitions only. (A partition is regular if its summands are nonincreasing.)

Now the representation $[\alpha]$ is characterized by having base vectors which are functions of definite symmetry on the A variables undergoing permutation in $\mathcal{S}_A$. After reduction in $\mathcal{S}_{A-1}$ by a unitary transformation, the new base vectors are also symmetry functions on the $A-1$ variables chosen to undergo permutation in $\mathcal{S}_{A-1}$. Since the representations occurring in the sum (60) occur only once, the number of base vectors having the symmetry characterized by the partition $[\alpha]_j$ is equal to the dimension of the corresponding representation.

Each subrepresentation $[\alpha]_j$ of $[\alpha]$, separately, may now be considered as a (reducible) representation in the subgroup $\mathcal{S}_{A-2}$ of permutations on the coordinates of $A-2$ particles, and each such representation reduced in $\mathcal{S}_{A-3}$. Let the process of reduction be repeated $(A-B)$ times so that $[\alpha]$ is reduced in $\mathcal{S}_B$,

$$ [\alpha] = \sum_\beta [\beta] f_\beta{}^\alpha, \tag{61}$$

where $[\beta]$ denotes the irreducible representations of $\mathcal{S}_B$ and $f_\beta{}^\alpha$ is the number of times each occurs in the representation $[\alpha]$. Relation (20) follows from the fact that the total number of base vectors is invariant in the reduction process. As a result of this process each base vector belongs to some $[\beta]$ as well as to $[\alpha]$, and hence has the symmetry characterized by partition $[\beta]$ on the B particles undergoing permutation in $\mathcal{S}_B$, as well as the symmetry characterized by $[\alpha]$ on the entire A particles undergoing permutation in $\mathcal{S}_A$.

As an example, consider the stepwise reduction of $[3+2]$ of $\mathcal{S}_5$ in $\mathcal{S}_4$, $\mathcal{S}_3$, and $\mathcal{S}_2$, according to Eq. (60) above

$$ \begin{aligned} [3+2] &= [3+1]+[2+2] \\ &= [3]+2[2+1] \\ &= 3[2]+2[1+1]. \end{aligned} \tag{62}$$

Of the five functions forming the basis of $[3+2]$ in $\mathcal{S}_5$, one may be chosen to have symmetry $[3]$ in $\mathcal{S}_3$, while the remaining four have symmetry $[2+1]$ in $\mathcal{S}_3$, since $[2+1]$ is a 2-dimensional representation. It may be seen that the five base functions which have the symmetry $[3+2]$ in $\mathcal{S}_5$, may be distinguished from one another, or characterized, by their generic relationships in $\mathcal{S}_4$, $\mathcal{S}_3$, and $\mathcal{S}_2$. For example, the five base functions which simultaneously reduce $[3+2]$ in $\mathcal{S}_4$, $\mathcal{S}_3$, and $\mathcal{S}_2$ are then characterized in these subgroups as follows:

$$ \begin{array}{lll} [3+1], & [3], & [2]; \\ [3+1], & [2+1], & [2]; \\ [3+1], & [2+1], & [1+1]; \\ [2+2], & [2+1], & [2]; \\ [2+2], & [2+1], & [1+1]. \end{array} $$

Two-Body System in Quantum Electrodynamics. Energy Levels of Positronium

THOMAS FULTON* AND PAUL C. MARTIN†
Harvard University, Cambridge, Massachusetts

(Received February 11, 1954)

Expressions are obtained for all $\alpha^3 Ry$ contributions to the energy levels of the two-fermion system in electrodynamics. These expressions are evaluated from a relativistic two-body equation which takes binding into account in its interaction operator. They are specifically calculated for the $n=2$ levels of the system. Corrections arise from three sources: (1) improved treatment of pair effects of the Coulomb field and of the exchange of transverse photons, (2) self-energy and vacuum polarization terms, and, in positronium, (3) second-order annihilation processes. The energy shifts resulting from (1) and (2) do not depend on the arbitrary masses through a single parameter like reduced mass. In the limit appropriate to hydrogen, the previously calculated two-body corrections of item (1) are confirmed.

The principal new result is the determination of the $n=2$ levels of positronium. In contrast to hydrogen, where the self-energy effect is dominant, here all three items yield roughly equal corrections. Together, they amount to about 3 percent of the $\alpha^3 Ry$ level splitting.

1. INTRODUCTION

ELECTRODYNAMIC corrections to the energy levels of an atomic system consisting of one particle in an external field have been calculated by many authors[1] and yield results in very close agreement with the observed hydrogen spectrum. It was not until the two-body equation was introduced,[2,3] however, that one could handle recoil effects relativistically, and hence accurately calculate energy levels for a two-body system. Several aspects of this problem have been studied since then. Salpeter[4] has treated to order $\alpha^3 Ry(m/M)$ the splitting in the fine structure of hydrogen due to non-self-energy processes; Karplus and Klein[5] have calculated the singlet-triplet splitting in the ground state of positronium; and Arnowitt[6] has computed this splitting for a system in which the two Dirac particles have arbitrary masses and one has an additional phenomenological magnetic moment.

Recoil corrections[4] to the hydrogen Lamb shift have the same order of magnitude as the discrepancy between theory and experiment. The corrections[6] to hydrogen hyperfine structure are considerably smaller than the experimental error. The two-body effects in positronium are larger and more significant. They give a correction to the hyperfine structure of the ground state of positronium which is confirmed by experiment.[7] Consequently, it seemed desirable to calculate to order $\alpha^3 Ry$ the energy levels of the $2S$ and $2P$ states of positronium. The splitting of these levels is affected by several processes contained in the relativistic two-body equation which do not contribute to the hyperfine splitting of the ground state. Measurement of these shifts may therefore provide a more thorough check of the two-body equation than a study of hyperfine structure does. Also, the present problem requires a more precise cut-off technique for low-energy photons.

Our calculation has been performed for a system of two particles with arbitrary masses. This procedure enabled us also to determine the recoil corrections to self-energy terms in hydrogen, and to compare certain parts of our solution with results previously derived from the two-particle equation. Our findings agree,[8] in the appropriate limits, with each of the three calculations mentioned above.[4-6] The general dependence on the two masses does not indicate any method for reducing the problem to one in which a single parameter plays a role similar to the role of reduced mass in nonrelativistic theory.

The use of a two-body formalism, in which binding is taken into account in intermediate states, is an essential theoretical improvement upon previous treatments. One of us[9] has previously derived, in collaboration with Professor R. Karplus, an improved interaction kernel which accomplishes this purpose by selectively resumming certain classes of terms in the expansion of the kernel in free-particle Green's functions.[10] An alternative derivation, presented in the Appendix, yields this effective interaction operator without expansion and resummation. The introduction of binding removes infrared divergences and yields additions to already convergent results less ambiguously than did previous treatments.

---

* Harvard Veterans National Scholar.
† NSF Predoctoral Fellow.
[1] E. E. Salpeter [Phys. Rev. **89**, 92 (1953)] summarizes and gives references to these calculations.
[2] J. Schwinger, Proc. Natl. Acad. Sci. U.S. **37**, 452, 455 (1951).
[3] E. E. Salpeter and H. A. Bethe, Phys. Rev. **84**, 1232 (1951).
[4] E. E. Salpeter, Phys. Rev. **87**, 328 (1952). Hereafter referred to as S.
[5] R. Karplus and A. Klein, Phys. Rev. **87**, 848 (1952). Hereafter referred to as KK–III.
[6] R. Arnowitt, Phys. Rev. **92**, 1002 (1953). We understand that a calculation similar to Arnowitt's has been performed by W. A. Newcomb.
[7] M. Deutsch and S. C. Brown, Phys. Rev. **85**, 1047 (1952).
[8] The purely Coulomb shift [our (3.11) and (35) of S] differs from S by a factor of two. This difference amounts to 0.037 Mc/sec in hydrogen and is not numerically significant for it. The reason for this discrepancy appears to be the use in S of $\Lambda_- \to (E-m)/4E$ instead of $\Lambda_- \to (E-m)/2E$.
[9] T. Fulton and R. Karplus, Phys. Rev. **93**, 1109 (1954). Hereafter referred to as FK.
[10] R. J. Eden, Proc. Roy. Soc. (London) **219**, 516 (1953), has independently suggested such a procedure.

2. WAVE EQUATION, INTERACTION, AND PERTURBATION THEORY

In general, we employ the methods and notation of Schwinger,[2] KK-III, and FK in this paper. A brief recapitulation of the relevant formulas seems in order.

The fully renormalized wave equation for two fermions with arbitrary masses is

$$[\bar{F}_1(11')\bar{F}_2(22')-\bar{I}(12,1'2')]\psi(1'2')=0, \quad (2.1)$$

where

$$\bar{F}_{1,2}=p_{1,2}\gamma_{1,2}+m_{1,2}=(G^0{}_{1,2})^{-1},$$

and m_1 (or m_2) is the experimental mass of particle one (or two). $\bar{I}$ is the renormalized interaction operator.

We introduce center-of-mass and relative coordinates:

$$\eta_1=m_1(m_1+m_2)^{-1}, \quad \eta_2=m_2(m_1+m_2)^{-1},$$
$$\mu=m_1m_2(m_1+m_2)^{-1}, \quad (2.2)$$
$$X=\eta_1x_1+\eta_2x_2, \quad x=x_1-x_2.$$

Every operator, $O(12,1'2')$, which is of interest, depends only on relative coordinates and the difference of center-of-mass coordinates. Hence we define

$$O_K(xx')=\int e^{-iK(X-X')}O(12,1'2')d^4X'. \quad (2.3)$$

The renormalized wave function is

$$\psi(x_1x_2)=(2\pi)^{-3/2}e^{iKX}\varphi_K(x). \quad (2.4)$$

We single out the Coulomb interaction as the part of $\bar{I}$ mainly responsible for the binding and write

$$\bar{I}(12,34)=I^C(12,34)+I'(12,34),$$
$$I^C(xX;x'X')=-ia\delta(X-X')\delta(x-x')\delta(x_0)\gamma_1{}^0\gamma_2{}^0/r. \quad (2.5)$$

This separation serves two purposes. In the first place, we can use perturbation theory[11] with the "unperturbed" equation,

$$[F_{K^C}(xx')-I^C{}_{K^C}(xx')]\varphi_{K^C}(x')=0, \quad (2.6)$$

as a starting point. F_{K^C} is the center-of-mass transform of $\bar{F}_1\bar{F}_2$. To the accuracy of our calculation, the wave function φ_K may be approximated by

$$\varphi_K(x)=-i\int\Lambda_K(xx')\delta(x_0')\varphi_{K^C}(x')d^4x', \quad (2.7)$$

where

$$\Lambda(12,1'2')=G_1{}^0(11')\gamma_1{}^0\delta(22')+\delta(11')G_2{}^0(22')\gamma_2{}^0. \quad (2.8)$$

Energy corrections to order α^3Ry to K^C are given by[4,6,9]

$$\Delta E=K_0-K_0{}^C=i\int\bar{\varphi}_K(x)J_K(xx')\varphi_K(x')d^4xd^4x'$$
$$=-i\int\varphi_{K^C}(\mathbf{r},0)\delta(x_0)\mathcal{K}_K(xx')\delta(x_0')$$
$$\times\varphi_{K^C}(\mathbf{r}',0)d^4xd^4x', \quad (2.9)$$

where

$$K^C=(\mathbf{0},K_0{}^C),$$

$$\mathcal{K}(12,1'2')=\Lambda(12,34)\gamma_1{}^0\gamma_2{}^0J(34,3'4')\Lambda(3'4',1'2'), \quad (2.10)$$

$$J(12,1'2')=I'(12,1'2')+I'(12,34)G^C(34,3'4')\times I'(3'4',1'2').$$

G^C is the Green's function of Eq. (2.6).

Secondly, the separation (2.5) enables us to express I' in a way that takes the Coulomb binding into account. Such a form for the interaction kernel is exhibited to lowest order in the Appendix.[12]

The complete kernel to order α^3Ry including binding, is prohibitively complicated. However, binding is not important everywhere. It need be taken into account only when an interaction term contains significant corrections from intermediate states with low-frequency quanta. Such interaction terms may be easily recognized; when treated by Born approximation, they lead to infrared divergent energy shifts for S states. When this happens, we find that the energy shifts of other states may not be calculated from these Born-approximated kernels either. Though neglect of binding does not produce divergences, it is not sufficiently accurate. On the other hand, kernels which do not yield infrared divergences for S states when calculated by Born approximation describe processes of high-momentum transfer. Low-energy quanta, for which binding is important, give a negligible correction to these kernels. As an initial step of simplification, then, we use Born approximation on those parts of J which, when approximated, yield convergent S-state shifts. Two terms cannot be treated this crudely: one describes the exchange of a single quantum; the other arises from vertex parts. Binding is significant for these two, and the correct kernel must be retained.

We have introduced binding by using, as a first approximation to the two-body system, one in which the instantaneous Coulomb potential is the total interaction. Naturally, this potential is not covariant. As a result, we find that, except in those terms of the renormalized equation which are separately ultraviolet divergent, the noncovariant radiation gauge is more convenient than the Lorentz gauge. The divergent terms, of course, can only be recognized and eliminated unambiguously when expressed in covariant form. We therefore use Lorentz gauge in self-energy, vacuum polarization, and virtual annihilation terms.

With the above remarks in mind, we write down the interaction kernel J correct to order α^3Ry:[13]

$$J=J_C+J_B+J_L+J_V+J_A. \quad (2.11)$$

[11] Alternative approaches to perturbation theory are presented in S and reference 6.

[12] The form is essentially equivalent to those proposed in references 9 and 10.

[13] $\gamma(\xi)=\gamma(\xi,ab)=\gamma_{ab}\delta(x_\xi-x_a)\delta(x_a-x_b)$. The notation, $\gamma(\xi,ab)$ of KK-III is forced upon us by the annihilation interaction. Where the annihilation interaction is not considered, the shorter notation, $\gamma(\xi)$, of reference 2 will be used. The latter employs the standard matrix summation convention for the particle coordinates and spins.

J_C is given by

$$J_C=(4\pi i\alpha)^2\gamma_1^0(\xi)\gamma_2^0(\xi')G_1^0G_2^0\gamma_1^0(\xi') \times\gamma_2^0(\bar{\xi})D_C(\xi\bar{\xi}')D_C(\bar{\xi}\xi'), \quad (2.12)$$

where

$$D_C(\xi\xi')=\frac{1}{(2\pi)^4}\int\frac{e^{ik(\xi-\xi')}}{k^2}d^4k.$$

J_C involves corrections to the energy levels due to pair production by the Coulomb field.[14] It is not included in Eq. (2.6). J_B is defined by

$$J_B=J_{B1}+J_{B2},$$

where

$$J_{B1}=4\pi i\alpha[\gamma_1^T(\xi)F_2G^CF_1\gamma_2^T(\xi') +F_1\gamma_2^T(\xi)G^C\gamma_1^T(\xi')F_2 -\gamma_1^T(\xi)\gamma_2^T(\xi')]D_T(\xi\xi'), \quad (2.13)$$

$$J_{B2}=(4\pi i\alpha)^2[\gamma_1^T(\xi)\gamma_2^T(\bar{\xi}')G_1^0G_2^0\gamma_1^T(\bar{\xi})\gamma_2^T(\xi') +\gamma_1^T(\xi)\gamma_2^T(\xi')G_1^0G_2^0\gamma_1^T(\xi)\gamma_2^T(\bar{\xi}')] \times D_T(\xi\xi')D_T(\bar{\xi}\bar{\xi}'), \quad (2.14)$$

$$\gamma_1^T(\xi)\gamma_2^T(\xi')D_T(\xi\xi') =\frac{1}{(2\pi)^4}\int\frac{e^{ik(\xi-\xi')}}{k_\mu^2}\gamma_1{}^i(\xi)\gamma_2{}^j(\xi')\left(\delta_{ij}-\frac{k_ik_j}{k^2}\right)d^4k.$$

J_{B1} and J_{B2} may be said to represent the exchange by the particles of one and two transverse photons respectively. (The replacement of G^C by $G_1^0G_2^0$ reduces J_{B1} to the more familiar form $4\pi i\alpha\gamma_1^T(\xi)\gamma_2^T(\xi')D_T(\xi\xi')$.) The two parts of J_{B2} are the so-called "crossed" and "uncrossed" terms of the second-order interaction. The kernel J_L, where

$$J_L=-4\pi i\alpha\{\gamma_2(\xi)[F_1(G^C-G_1^0G_2^0)F_1 +4\pi i\alpha G_2^0\gamma_1^T(\bar{\xi})\gamma_2^T(\bar{\xi}')G_2^0D_T(\bar{\xi}\bar{\xi}')]\gamma_2(\xi') +\gamma_1(\xi)[F_2(G^C-G_1^0G_2^0)F_2 +4\pi i\alpha G_1^0\gamma_1^T(\bar{\xi})\gamma_2^T(\bar{\xi}')G_1^0D_T(\bar{\xi}\bar{\xi}')]\gamma_1(\xi') -(\alpha/2\pi)(B_1+B_2)\gamma_1(\xi)\gamma_2(\xi')\}D(\xi\xi'), \quad (2.15)$$

includes the contribution of all vertex parts. (The first square bracket in Eq. (2.15) represents self-energy contributions of the second particle. It would become the more usual $4\pi i\alpha G_2^0\gamma_1(\bar{\xi})\gamma_2(\bar{\xi}')G_2^0D(\bar{\xi}\bar{\xi}')$, if we made the approximation $G^C=G_1^0G_2^0+G_1^0G_2^0I^CG_1^0G_2^0$, and noted the equivalence

$$\gamma_1^T(\xi)\gamma_2^T(\xi')D_T(\xi\xi')-\gamma_1^0(\xi)\gamma_2^0(\xi')D_C(\xi\xi') =\gamma_1(\xi)\gamma_2(\xi')D(\xi\xi').$$

The second square bracket would reduce in similar fashion.) The last group of terms in Eq. (2.15) results from wave-function renormalization corrections to single quantum exchange. They originate in the replacement of $\psi(x_1x_2)$ by $[1-\alpha(B_1+B_2)/4\pi]\psi(x_1x_2)$ and are included in J_L rather than elsewhere to facilitate computation.

[14] J_C corresponds to $G_{CC}^{(2)}$ of S. It is the "crossed Coulomb" term. Note also that $\gamma_1^0(\xi)\gamma_2^0(\xi')D_C(\xi\xi')=I^C$.

The vacuum polarization correction to the exchange of a single quantum is

$$J_{V\mu}=(4\pi i\alpha)\gamma_1{}^\nu(\xi)\gamma_2{}^\mu(\xi')\{(4\pi i\alpha)D(\xi\bar{\xi}) \times[\mathrm{tr}(\gamma_1{}^\nu(\bar{\xi})G_1^0\gamma_1{}^\mu(\bar{\xi}')G_1^0) +\mathrm{tr}(\gamma_2{}^\nu(\bar{\xi})G_2^0\gamma_2{}^\mu(\bar{\xi}')G_2^0)]D(\bar{\xi}'\xi') -(\alpha/2\pi)(A_1+A_2)\delta_{\mu\nu}D(\xi\xi')\}. \quad (2.16)$$

The term containing A_1 and A_2 arises from the already performed charge renormalization and is handled in a fashion analogous to the renormalization term in J_L.

Up to this point, all kernels have the same form, whether m_1 is equal to m_2 or not. However, two modifications must be made in treating positronium. The first concerns J_V. Since there is only a single fermion field in this case, the vacuum is polarized by the emission and absorption of virtual pairs of only one kind of particle. Thus J_V becomes

$$J_{V\,\mathrm{pos}}=(4\pi i\alpha)\gamma_1{}^\nu(\xi)\gamma_2{}^\mu(\xi')\{4\pi i\alpha D(\xi\bar{\xi}) \times\mathrm{tr}[\gamma^\nu(\bar{\xi})G^0\gamma^\mu(\bar{\xi}')G^0]D(\bar{\xi}'\xi') -(\alpha/2\pi)A\delta_{\mu\nu}D(\xi\xi')\}. \quad (2.17)$$

In addition, a new interaction, representing virtual annihilation, arises from the particle-antiparticle relationship of the constituents of the system. The lowest-order contribution of this interaction has been calculated by several authors[15-17] and higher-order corrections have been obtained in KK-III. The complete annihilation kernel is

$$J_A=I_{A1}+J_{A2},$$

$$I_{A1}(12,34)=(4\pi i\alpha)\gamma(\xi,11')C(1'2)D(\xi\xi') \times C^{-1}(43')\gamma(\xi',3'3), \quad (2.18)$$

$$J_{A2}=I_{A2}+I_{A1}G_1^0G_2^0I_{A1}+I_{A1}G_1^0G_2^0I_{B1} +I_{B1}G_1^0G_2^0I_{A1}-(\alpha/\pi)(B+\tfrac{1}{2}A)I_{A1},$$

$$I_{A2}(12,34)=(4\pi i\alpha)^2\gamma(\xi,11')G(1'1'')\gamma(\bar{\xi},1''2') \times C(2'2)D(\xi\bar{\xi}')D(\bar{\xi}\bar{\xi}')[C^{-1}(33')\gamma(\bar{\xi}'3'4') \times G(4'4'')\gamma(\xi',4''4)-C^{-1}(44')\gamma(\bar{\xi}',4'3') \times G(3'3'')\gamma(\xi',3''3), \quad (2.19)$$

$$I_{B1}(12,34)=(4\pi i\alpha)\gamma(\xi,13)\gamma(\xi',24)D(\xi\xi').$$

3. COULOMB CORRECTIONS

In order to calculate energy levels of Eq. (2.1) correct to order α^3Ry, we must first determine the "unperturbed" energy $K_0{}^C$ to that order. For this purpose, we write (2.6) in the form

$$[K_0{}^C-H_1(\mathbf{p})-H_2(-\mathbf{p})]\varphi_K{}^C(\mathbf{r}0) +(2\pi)^{-3}\int e^{i\mathbf{k}\cdot(\mathbf{r}-\mathbf{r}')}[\Lambda_1{}^+(\mathbf{k})\Lambda_2{}^+(-\mathbf{k}) -\Lambda_1{}^-(\mathbf{k})\Lambda_2{}^-(-\mathbf{k})](\alpha/r')\varphi_K{}^C(\mathbf{r}'0)=0, \quad (3.1)$$

[15] V. B. Berestetski and L. D. Landau, J. Exptl. Theoret. Phys. (U.S.S.R.) **19**, 673 (1949).
[16] J. Pirenne, Arch. sci. phys. et nat. **29**, 207 (1947).
[17] R. H. Ferrel, Ph.D. thesis, Princeton, 1951 (unpublished).

where

$$H_{1,2}(\mathbf{p})=\boldsymbol{\alpha}_{1,2}\mathbf{p}+m_{1,2}\gamma_{1,2}{}^0,$$

$$\Lambda_{1,2}{}^+(\mathbf{k})=[E_{1,2}(\mathbf{k})\pm H_{1,2}(\mathbf{k})]/2E_{1,2}(\mathbf{k}),$$

$$\mathbf{p}=-i\nabla, \quad \text{and} \quad E_{1,2}(\mathbf{k})=(m_{1,2}{}^2+k^2)^{\frac{1}{2}}.$$

Equation (3.1) is very similar to the Breit equation without magnetic interaction,

$$[K_0{}'^C-H_1(\mathbf{p})-H_2(-\mathbf{p})+\alpha/r]\varphi_B(\mathbf{r})=0. \quad (3.2)$$

The energy levels of (3.2) may be expressed as power series in α^2 with their leading terms of order Ry;[18] the energy levels of (3.1) may be expanded in powers of α. The corresponding energy levels are equal to order α^2Ry; to the order Ry, they are the reduced mass energy levels of the Schroedinger equation. We compute by perturbation theory the difference, to order α^2Ry, between $K_0{}'^C$ and $K_0{}^C$, the former having no α^2Ry term in its expansion. We rewrite (3.1) as

$$[K_0{}'^C-H_1(\mathbf{p})-H_2(-\mathbf{p})+(\alpha/r)]\varphi_K{}^C(\mathbf{r}0)$$

$$-\int\Omega(\mathbf{r}\mathbf{r}')(\alpha/r')\varphi_K{}^C(\mathbf{r}'0)=0, \quad (3.1a)$$

where

$$\Omega(\mathbf{r}\mathbf{r}')=(2\pi)^{-3}\int e^{i\mathbf{k}\cdot(\mathbf{r}-\mathbf{r}')}[\Lambda_1{}^+(\mathbf{k})\Lambda_2{}^-(-\mathbf{k})$$

$$+\Lambda_1{}^-(\mathbf{k})\Lambda_2{}^+(-\mathbf{k})+2\Lambda_1{}^-(\mathbf{k})\Lambda_2{}^-(-\mathbf{k})].$$

$\Omega(\alpha/r')$ is a small correction to the Hamiltonian of (3.2). By first-order perturbation theory we get

$$\Delta E_{Ca}=K_0{}^C-K_0{}'^C=\int\varphi_B{}^*(\mathbf{r})\Omega(\mathbf{r}\mathbf{r}')(\alpha/r')\varphi_B(\mathbf{r}'). \quad (3.3)$$

Let

$$\varphi_{++}(\mathbf{r})=(2\pi)^{-3}\int e^{i\mathbf{k}\cdot(\mathbf{r}-\mathbf{r}')}\Lambda_1{}^+(\mathbf{k})\Lambda_2{}^+(-\mathbf{k})\varphi_B(\mathbf{r}').$$

The "large component" $[\varphi_{++}{}^*(\mathbf{r})]$ of $\varphi_B{}^*(\mathbf{r})$ is orthogonal to $\Omega(\mathbf{r}\mathbf{r}')$. The small components, correct to the required order, are obtained by iteration. We write (3.2) as an integral equation,

$$\varphi_B(\mathbf{r})=(2\pi)^{-3}\int e^{i\mathbf{k}\cdot(\mathbf{r}-\mathbf{r}')}[H_1(\mathbf{k})+H_2(-\mathbf{k})$$

$$-K_0{}'^C]^{-1}(\alpha/r')\varphi_B(\mathbf{r}'), \quad (3.4)$$

replace $\varphi_B(\mathbf{r}')$ by the Pauli wave function $\varphi_P(\mathbf{r}')$ on the right-hand side of (3.4), and apply the proper projection operators. Using these wave functions for $\varphi_B{}^*(\mathbf{r})$ in (3.3) and also substituting $\varphi_P(\mathbf{r}')$ for $\varphi_B(\mathbf{r}')$ in this equation, we get[4]

$$\Delta E_{Ca}=\frac{\alpha^3}{(2\pi)^3}\int\varphi_P{}^*(\mathbf{r})\frac{1}{r}e^{i\mathbf{k}\cdot(\mathbf{r}-\mathbf{r}')}\frac{[\Lambda_1{}^+(\mathbf{k})\Lambda_2{}^-(-\mathbf{k})+\Lambda_1{}^-(\mathbf{k})\Lambda_2{}^+(-\mathbf{k})+2\Lambda_1{}^-(\mathbf{k})\Lambda_2{}^-(-\mathbf{k})]}{H_1(\mathbf{k})+H_2(-\mathbf{k})-K_0{}'^C}\frac{1}{r'}\varphi_P(\mathbf{r}'). \quad (3.5)$$

Since contributions to the integral come only from large momenta $k\cong m$, φ_P may be replaced by the amplitude of the Pauli wave function at the origin. With these approximations, the energy shift ΔE_{Ca} becomes

$$\Delta E_{Ca}=\frac{\alpha^2|\varphi(0)|^2}{2\pi}\int\frac{d^3k}{k^4}\frac{1}{E_1E_2}\left[\frac{(E_1+m_1)(E_2-m_2)}{(E_1-E_2)-(m_1+m_2)}\right.$$

$$\left.+\frac{(E_1-m_1)(E_2+m_2)}{(E_2-E_1)-(m_1+m_2)}-\frac{2(E_1-m_1)(E_2-m_2)}{E_1+E_2+m_1+m_2}\right];$$

$$E_{1,2}=E_{1,2}(k). \quad (3.6)$$

This integral can be evaluated exactly and yields

$$\Delta E_{Ca}=-\frac{2}{3}\alpha^2|\varphi(0)|^2\left(\frac{2}{m_1{}^2}+\frac{1}{m_1m_2}+\frac{2}{m_2{}^2}\right). \quad (3.7)$$

The kernel J_C gives rise to an integral which is very similar to Eq. (3.6). Because only large photon momenta contribute, we may set

$$\Delta E=-i\int\varphi_K{}^{c*}(\mathbf{r}0)\delta(x_0)\mathcal{K}_K(xx')\delta(x_0')$$

$$\times\varphi_K{}^c(\mathbf{r}'0)d^4xd^4x'\cong-i|\varphi(0)|^2\int J_K(xx')d^4xd^4x'. \quad (3.8)$$

Some simplification yields the integral

$$\Delta E_{Cb}=\frac{i\alpha^2}{\pi^2}|\varphi(0)|^2\int\frac{d^4k}{k^4}\left\langle\frac{\Lambda_1{}^+(\mathbf{k})\Lambda_2{}^-(\mathbf{k})+\Lambda_1{}^-(\mathbf{k})\Lambda_2{}^+(\mathbf{k})}{(k_0-\eta_1K_0{}^C+H_1(\mathbf{k}))(k_0-\eta_2K_0{}^C+H_2(\mathbf{k}))}\right\rangle,$$

$$\cong\frac{\alpha^2}{2\pi}|\varphi(0)|^2\int\frac{d^3k}{k^4}\frac{1}{E_1E_2}\left[\frac{(E_1+m_1)(E_2-m_2)}{(E_1-m_1)+(E_2+m_2)}+\frac{(E_1-m_1)(E_2+m_2)}{(E_1+m_1)+(E_2-m_2)}\right],$$

$$=\frac{2}{3}\alpha^2|\varphi(0)|^2\left(\frac{2}{m_1{}^2}-\frac{1}{m_1m_2}+\frac{2}{m_2{}^2}\right). \quad (3.9)$$

[18] T. Ishidzu, Progr. Theoret. Phys. 6, 154 (1951).

The brackets, $\langle\ \rangle$, denote expectation values between Pauli wave functions. The energy shift of order $\alpha^5 Ry$ arising purely from the Coulomb interaction[8] is

$$(\Delta E_C)_{2S}=-\frac{1}{6\pi}\frac{\alpha^5\mu^2}{m_1+m_2} \quad \text{for } 2S \text{ states}, \tag{3.10a}$$

$$(\Delta E_C)_{2P}=0 \quad \text{for } 2P \text{ states} \tag{3.10b}$$

4. EFFECTS OF TRANSVERSE QUANTA

The kernel $\mathcal{K}_{B1}$, derived from Eqs. (2.8), (2.10), and (2.13) is given in matrix notation by

$$\begin{aligned}\mathcal{K}_{B1}=\{&\alpha_2{}^T(\xi)G^C\gamma_1{}^0\gamma_2{}^0\alpha_1{}^T(\xi')\\&+\gamma_2{}^0\gamma_2{}^T(\xi)[G_1{}^0+G^CI^CG_1{}^0]\gamma_1{}^T(\xi')G_1{}^0\gamma_1{}^0\\&+G_2{}^0\gamma_1{}^0\gamma_2{}^T(\xi)G_2{}^0I^CG^C\gamma_1{}^T(\xi')\gamma_2{}^0\\&+G_2{}^0\gamma_1{}^0\gamma_2{}^T(\xi)G_2{}^0[I^C+I^CG^CI^C]\\&\times G_1{}^0\gamma_1{}^T(\xi')G_1{}^0\gamma_1{}^0+(1\leftrightarrow 2)\}D_T(\xi\xi'),\end{aligned} \tag{4.1}$$

where we have set $\alpha^T=\gamma^0\gamma^T$ and used the relations

$$\begin{aligned}G^C&=G_1{}^0G_2{}^0+G_1{}^0G_2{}^0I^CG^C=G_1{}^0G_2{}^0+G^CI^CG_1{}^0G_2{}^0\\&=G_1{}^0G_2{}^0+G_1{}^0G_2{}^0[I^C+I^CG^CI^C]G_1{}^0G_2{}^0.\end{aligned}$$

Our first step in calculating the energy change due to $\mathcal{K}_{B1}$ is to use Born approximation on the terms of this kernel which involve pair processes, and to neglect processes which require three quanta. Thus we let

$$\begin{aligned}\mathcal{K}_{B1}\rightarrow[&\alpha_2{}^T(\xi)G^C\gamma_1{}^0\gamma_2{}^0\alpha_1{}^T(\xi')\\&+G_1{}^0\gamma_2{}^0\gamma_2{}^T(\xi)\gamma_1{}^T(\xi')G_1{}^0\gamma_1{}^0\\&+G_1{}^0\gamma_2{}^0\gamma_2{}^T(\xi)G_2{}^0I^CG_1{}^C\gamma_1{}^T(\xi')G_1{}^0\gamma_1{}^0\\&+G_2{}^0\gamma_1{}^0\gamma_2{}^T(\xi)G_2{}^0I^CG_1{}^0\gamma_1{}^T(\xi')G_2{}^0\gamma_2{}^0\\&+G_2{}^0\gamma_1{}^0\gamma_2{}^T(\xi)G_2{}^0I^CG_1{}^0\gamma_1{}^T(\xi')G_1{}^0\gamma_1{}^0\\&+(1\leftrightarrow 2)]D_T(\xi\xi').\end{aligned} \tag{4.1a}$$

By substituting $G^C=G_1{}^0G_2{}^0+G_1{}^0G_2{}^0I^CG_1{}^0G_2{}^0$ in (4.1a) and rearranging terms, one may obtain the kernels which give rise to the infrared divergent terms ΔE_B and ΔE_{CT} of S. To avoid these divergences, we treat the first term of (4.1a) more carefully, writing

$$\begin{aligned}\Delta E=4\pi\alpha\int&\varphi_{K^C}{}^*\delta(x_0)\{[\alpha_2{}^T(\xi)G^C\gamma_1{}^0\gamma_2{}^0\alpha_1{}^T(\xi')\\&+(1\leftrightarrow 2)]D_T(\xi\xi')\}_K\delta(x_0')\varphi_{K^C}\\=i\alpha(2\pi)^{-3}\int&\varphi_{K^C}{}^*(\mathbf{r},0)[\alpha_2{}^iG^C{}_{-\mathbf{k},K_0'}(\mathbf{r}0;\mathbf{r}'0)\\&\times\alpha_1{}^ie^{-i\mathbf{k}\cdot(\eta_1\mathbf{r}+\eta_2\mathbf{r}')}+\alpha_1{}^iG^C{}_{-\mathbf{k},K_0'}(\mathbf{r}0;\mathbf{r}'0)\\&\times\alpha_2{}^ie^{i\mathbf{k}\cdot(\eta_2\mathbf{r}+\eta_1\mathbf{r}')}]\exp[i(K_0{}^C-K_0')(X_0-X_0')]\\&\times e^{-a|X_0-X_0'|}k^{-1}(\delta_{ij}-k_ik_j/k^2)\varphi_{K^C}(\mathbf{r}'0)\\&\times d^3\mathbf{r}d^3\mathbf{r}'d^3\mathbf{k}dX_0'dK_0'.\end{aligned} \tag{4.2}$$

For wave functions, we use the approximate form

$$\varphi_{K^C}(\mathbf{r}0)\cong(1+\boldsymbol{\alpha}_1\cdot\mathbf{p}/2m_1)(1-\boldsymbol{\alpha}_2\cdot\mathbf{p}/2m_2)\varphi_P(\mathbf{r}). \tag{4.3}$$

We divide the integration over k into two parts: a region where k is less than and another where k is greater than some given constant. This separation of regions of high and low photon frequencies simultaneously divides G^C into regions of high and low recoil momentum. In the high-frequency, high-recoil-momentum region, G^C can be expanded in terms of free particle Green's functions. In the region of low-frequency quanta and low recoil momenta, large values of $K_0{}^C$ (high-energy intermediate states) do not contribute, and a nonrelativistic approximation to the Green's function may be made. This nonrelativistic approximation involves setting

$$\begin{aligned}G_C(\mathbf{r}0,X;\mathbf{r}'0,X')\cong&-(2\pi)^{-3}\int d^3K''\Sigma_n\varphi\mathbf{K}''{}_{,n}(\mathbf{r}0)\\&\times\varphi^*\mathbf{K}''{}_{,n}(\mathbf{r}'0)e^{iK''(X-X')}, \quad X_0>X_0',\\\cong&0, \quad X_0<X_0',\end{aligned} \tag{4.4}$$

where $K_0''=K_n$ is the energy of the nth state. The $\varphi\mathbf{K}''{}_{,n}(\mathbf{r}0)$ may be taken to satisfy

$$\begin{aligned}[H_1(\eta_1\mathbf{K}''+\mathbf{p})+H_2(\eta_2\mathbf{K}''-\mathbf{p})-\alpha/r]&\varphi\mathbf{K}'',{}_n(\mathbf{r}0)\\&=K_n\varphi\mathbf{K}'',{}_n(\mathbf{r}0).\end{aligned} \tag{4.5}$$

In fact, the approximate solutions

$$\begin{aligned}\varphi\mathbf{K}'',{}_n(\mathbf{r}0)\cong&[1+\boldsymbol{\alpha}_1\cdot(\eta_1\mathbf{K}''+\mathbf{p})/2m_1]\\&\times[1+\boldsymbol{\alpha}_2\cdot(\eta_2\mathbf{K}''-\mathbf{p})/2m_2]\varphi_P(\mathbf{r}),\end{aligned}$$

where

$$K_n\cong E_n+K''{}^2/2(m_1+m_2), \quad E_n=m_1+m_2-\alpha^2\mu/2n^2,$$

are sufficient.

The boundary between the relativistic and nonrelativistic regions is not critical. Thus the constant separating the two regions can be as large as $B\cong\alpha^1\mu$, or as small as $A=\alpha^1\mu$. As indicated in S, the region A to B, in either approximation, yields the same shift.

We are now in a position to outline the details of the calculation. We combine the lowest order, high energy part of the first term in expression (4.1a), $\alpha_1{}^iG_1{}^0G_2{}^0\alpha_2{}^j$, with the second term, and the corresponding terms with the particles interchanged. Employing techniques of KK-III, we then derive to the required order of accuracy a "high-energy, single transverse quantum" contribution,

$$\begin{aligned}\Delta E_{B1}{}^{TH}=\alpha(2\pi^2)^{-1}\int&\phi^*(\mathbf{p}')\delta(\mathbf{p}'-\mathbf{p}''+\mathbf{k})(2k)^{-1}\\&\times R(p'p''k)S(\mathbf{p}'\mathbf{p}''\mathbf{k})\phi(\mathbf{p}'').\end{aligned} \tag{4.6}$$

where

$$R(p'p''k)=\frac{1}{4E_1'E_2''}\frac{(E_1'+m_1)(E_2''+m_2)}{k+E_1'+E_2''-K_0{}^C}$$
$$+\frac{1}{2E_1'E_1''}\frac{m_1{}^2-E_1'E_1''}{k+E_1'+E_1''}+\frac{1}{4E_1'E_2''}$$
$$\times\frac{(m_1-E_1')(m_2-E_2'')}{k+E_1'+E_2''+K_0{}^C}+(1\leftrightarrow 2),$$

$$S(\mathbf{p}'\mathbf{p}''\mathbf{k})\delta(\mathbf{p}'-\mathbf{p}''+\mathbf{k})$$
$$=\left(\delta_{ij}-\frac{k_ik_j}{k^2}\right)\left\langle\left(1+\frac{\boldsymbol{\alpha}_1\cdot\mathbf{p}'}{2m_1}\right)\left(1-\frac{\boldsymbol{\alpha}_2\cdot\mathbf{p}'}{2m_2}\right)\right.$$
$$\left.\times\alpha_1{}^i\alpha_2{}^j\left(1+\frac{\boldsymbol{\alpha}_1\cdot\mathbf{p}''}{2m_1}\right)\left(1-\frac{\boldsymbol{\alpha}_2\cdot\mathbf{p}''}{2m_2}\right)\right\rangle\delta(\mathbf{p}'-\mathbf{p}''+\mathbf{k}),$$

and

$$S(\mathbf{p}'\mathbf{p}''\mathbf{k})=-\frac{1}{4m_1m_2}\left(\delta_{ij}-\frac{k_ik_j}{k^2}\right)$$
$$\times\langle[2\mathbf{p}'-i(\boldsymbol{\sigma}_1\times\mathbf{k})]_i[2\mathbf{p}''-i(\boldsymbol{\sigma}_2\times\mathbf{k})]_j\rangle.$$

The wave function $\phi(\mathbf{p})$ is the Fourier transform of $\varphi_P(\mathbf{r})$. The first approximation to (4.6), obtained by letting $R\to 2k^{-1}$, is the part of the Breit interaction energy which arises from the momentum region $k>B$:

$$\mathcal{E}_{B\infty}=\frac{\alpha}{2\pi^2}\int_{k>B}d^3k\int\varphi_B{}^*(\mathbf{r})\frac{\alpha_1{}^i\alpha_2{}^j}{k^2}$$
$$\times\left(\delta_{ij}-\frac{k_ik_j}{k^2}\right)e^{i\mathbf{k}\cdot\mathbf{r}}\varphi_B(\mathbf{r}). \quad (4.7)$$

In this notation, the total Breit interaction energy is $\mathcal{E}_{0\infty}$.

At energies greater than B, the approximation procedures outlined in KK-III (in the paragraph below Eq. (4.8)) are applicable. Corrections to $\mathcal{E}_{B\infty}$ in this relativistic region ($k>B$) arise only for $p'\gg p''$, or $p''\gg p'$. In these regions we let

$$\delta(\mathbf{p}'-\mathbf{p}''+\mathbf{k})\to\delta(\mathbf{p}'+\mathbf{k}),$$

and

$$\delta(\mathbf{p}'-\mathbf{p}''+\mathbf{k})\to\delta(-\mathbf{p}''+\mathbf{k}),$$

respectively. Consequently, in terms correcting the Breit energy, we can allow

$$S\delta\to(4m_1m_2)^{-1}\langle(\boldsymbol{\sigma}_1\cdot\boldsymbol{\sigma}_2)k^2-(\boldsymbol{\sigma}_1\cdot\mathbf{k})(\boldsymbol{\sigma}_2\cdot\mathbf{k})\rangle\delta. \quad (4.8)$$

Equation (4.6) can then be integrated to give for $\Delta E_{B1}{}^{TH}$ the result of Arnowitt.[6]

$$\Delta E_{B1}{}^{TH}=\mathcal{E}_{B\infty}-\frac{4}{3}\frac{\alpha^2}{m_1m_2}|\varphi(0)|^2\langle\boldsymbol{\sigma}_1\cdot\boldsymbol{\sigma}_2\rangle$$
$$\times\left(2+\eta_2\ln\frac{m_1}{2B}+\eta_1\ln\frac{m_2}{2B}\right). \quad (4.9)$$

Equation (4.6) may also be evaluated for photon momenta lying between A and B. In this region, the methods of KK-III are no longer sufficient; p', p'', and k are now all of comparable magnitude and $k\ll\mu$. Here, we set

$$R(p'p''k)\approx\frac{1}{4E_1'E_2''}\frac{(m_1+E_1')(m_2+E_2'')}{k+E_1'+E_2''-K_0{}^C}+(1\leftrightarrow 2)$$
$$\approx\frac{1}{k}\left(2+\frac{K_0{}^C-E_1'-E_2'}{k}+\frac{K_0{}^C-E_1''-E_2''}{k}\right), \quad (4.10)$$

and obtain

$$\Delta E_{B1}{}^{TH}=\mathcal{E}_{AB}+\frac{\alpha}{(2\pi)^2}\int_{k=A}^{k=B}d^3k\int\phi^*(\mathbf{p}')$$
$$\times\delta(\mathbf{p}'-\mathbf{p}''+\mathbf{k})\frac{1}{k^3}S(\mathbf{p}'\mathbf{p}''\mathbf{k})[(K_0{}^C-E_1'-E_2')$$
$$+(K_0{}^C-E_1''-E_2'')]\phi(\mathbf{p}''). \quad (4.11)$$

The remaining interaction terms of Eq. (4.1a) are relevant only at high energies. Combined with the second part of the expansion of the first term, $\alpha_1{}^iG_1{}^0G_2{}^0I^CG_1{}^0G_2{}^0\alpha_2{}^j$, these comprise the so-called Coulomb-transverse interaction. This kernel gives rise to an energy shift

$$\Delta E_{B1}{}^{CTH}=-i\int\varphi_K{}^{C*}\delta(x_0)\{\Lambda\gamma_1{}^0\gamma_2{}^0$$
$$\times[\gamma_2{}^T(\xi)G_2{}^0I^CG_1{}^0\gamma_1{}^T(\xi')$$
$$+(1\leftrightarrow 2)]D_T(\xi\xi')\Lambda\}_K\delta(x_0')\varphi_K{}^C$$
$$=-\frac{4\alpha^2i}{(2\pi)^2}|\varphi(0)|^2\left\langle\int_{k>B}d^4k\left(\delta_{ij}-\frac{k_ik_j}{k^2}\right)\right.$$
$$\times\frac{1}{k^2k_\mu{}^2}\left[\alpha_2{}^i\frac{1}{H_1(\mathbf{k})-m_1+k_0}\right.$$
$$\left.\left.\times\frac{1}{H_2(\mathbf{k})-m_2+k_0}\alpha_1{}^j+(1\leftrightarrow 2)\right]\right\rangle. \quad (4.12)$$

This shift contains only a spin-spin correction,

$$\Delta E_{B1}{}^{CTH}=\frac{4\alpha^2}{3m_1m_2}\langle\boldsymbol{\sigma}_1\cdot\boldsymbol{\sigma}_2\rangle|\varphi(0)|^2$$
$$\times\left\{2-\ln\frac{2B}{\mu}-\frac{m_1\ln\eta_1-m_2\ln\eta_2}{m_1-m_2}\right\}. \quad (4.13)$$

In the region A to B, the energy shift arises entirely from

$$\alpha_1{}^iG_1{}^0G_2{}^0I^CG_1{}^0G_2{}^0\alpha_2{}^i+(1\leftrightarrow 2),$$

that is, the part of J_{B1} treated in Eq. (4.2). This part yields approximately

$$\Delta E_{B1}{}^{CTH}=\frac{\alpha^2}{(2\pi)^4}\int_{k=A}^{k=B}d^3k\int\phi^*(\mathbf{p}')\times\frac{S(\mathbf{p}'\mathbf{p}''\mathbf{k})+S(\mathbf{p}''\mathbf{p}'\mathbf{k})}{k^3(\mathbf{p}'-\mathbf{p}''+\mathbf{k})^2}\phi(\mathbf{p}''). \quad (4.14)$$

Thus the high-energy result, the sum of (4.9) and (4.13), is

$$\Delta E_{B1}{}^{H}=\mathcal{E}_{B\infty}-\frac{8\alpha^2|\varphi(0)|^2}{3(m_1{}^2-m_2{}^2)}\langle\boldsymbol{\sigma}_1\cdot\boldsymbol{\sigma}_2\rangle\ln\frac{m_1}{m_2}. \quad (4.15)$$

The Fourier transforms of Eqs. (4.11) and (4.14) combine to give, after some manipulation,

$$\Delta E_{B1}{}^{M}=\mathcal{E}_{AB}+\frac{2\alpha}{m_1m_2}\frac{1}{(2\pi)^2}\int_{k=A}^{k=B}\int\left(\delta_{ij}-\frac{k_ik_j}{k^2}\right)\frac{1}{k^3}\times\varphi_P{}^*(\mathbf{r})e^{-i\mathbf{k}\cdot\mathbf{r}}p_i[\mathfrak{IC},p_j]\varphi_P(\mathbf{r}), \quad (4.16)$$

for the intermediate region. $\mathfrak{IC}$ is the Schroedinger Hamiltonian. Equation (4.16) contains an orbit-orbit interaction only; the spin-orbit and spin-spin parts vanish. The equation agrees with (48) of S.

The nonrelativistic contribution of (4.1) may be rewritten, in view of (4.2) and (4.4), in a form which also arises naturally out of three-dimensional perturbation theory:

$$\Delta E=\frac{\alpha}{(2\pi)^2}\int\varphi_K{}^{c*}(\mathbf{r}0)[\alpha_2{}^ie^{-i\mathbf{k}\cdot\boldsymbol{\eta}_1\mathbf{r}}\varphi_{-\mathbf{k},n}(\mathbf{r}0)\times\varphi_{-\mathbf{k},n}{}^*(\mathbf{r}'0)\alpha_1{}^ie^{-i\mathbf{k}\cdot\boldsymbol{\eta}_2\mathbf{r}'}+\alpha_1{}^ie^{i\mathbf{k}\cdot\boldsymbol{\eta}_2\mathbf{r}}\times\varphi_{-\mathbf{k},n}(\mathbf{r}0)\varphi_{-\mathbf{k}n}{}^*(\mathbf{r}'0)\alpha_2{}^ie^{i\mathbf{k}\cdot\boldsymbol{\eta}_1\mathbf{r}'}]\times\frac{1}{k}\sum_n\frac{1}{k+K_n-K_0{}^C}\left(\delta_{ij}-\frac{k_ik_j}{k^2}\right)\varphi_K{}^c(\mathbf{r}'0). \quad (4.17)$$

We first isolate the part of the Breit energy, $\mathcal{E}$, in (4.17), arising from nonrelativistic momenta. The remainder is treated by two approximations. In the region $0\leqslant k\leqslant A$, we may set $k=0$ in the exponents and $\varphi_{-k,n}$, so that

$$\Delta E_{B1}{}^{L}=\mathcal{E}_{0A}-\frac{2\alpha}{(2\pi)^2}\int_{=0}^{k=A}\frac{d^3k}{k^2}\sum_n\frac{(0|\alpha_1{}^i|n)(n|\alpha_2{}^j|0)}{k+K_n-K_0{}^C}\times(K_n-K_0{}^L)\left(\delta_{ij}-\frac{k_ik_j}{k^2}\right)$$

$$=\mathcal{E}_{0A}+\frac{4\alpha}{3\pi m_1m_2}\left\langle(\mathbf{p}\varphi_P(\mathbf{r}))^*\cdot\ln\frac{A}{\mathfrak{IC}-K_0{}^C}\times(\mathfrak{IC}-K_0{}^C)(\mathbf{P}\varphi_P(\mathbf{r}))\right\rangle. \quad (4.18)$$

Again, Eq. (4.18) has no spin-orbit or spin-spin contributions. Because $K_n=E_n$ when k is small, the α^3Ry correction [see S, Eq. (46)] is[19]

$$(\Delta E_{B1}{}^{L})_{2S}=\frac{\alpha^5\mu^2}{3\pi(m_1+m_2)}\ln\left[\frac{A}{k_0(2,0)}\frac{Ry_\infty}{Ry_\mu}\right], \quad (4.19a)$$

and

$$(\Delta E_{B1}{}^{L})_{2P}=(\alpha^5\mu^2/3\pi(m_1+m_2))\ln(Ry_\infty/k_0(2,1)). \quad (4.19b)$$

In $2P$ states, the contribution is independent of A, provided A is large compared to the binding energy. The A we have chosen fulfills this requirement.

Only certain states in the summation over n [in Eq. (4.18)] contribute significantly in the intermediate region to the correction to the Breit energy. In these states, and for this region, $K_n-K_0{}^C$ is much smaller than k. We therefore let

$$\frac{1}{k^2}\frac{K_n-K_0{}^C}{k+K_n-K_0{}^C}\rightarrow\frac{K_n-K_0{}^C}{k^3}. \quad (4.20)$$

Use of the approximation (4.20) yields the expression

$$\Delta E_{B1}{}^{M}=\mathcal{E}_{AB}+\frac{\alpha^2}{(2\pi)^2}\int_{k=A}^{k=B}\frac{d^3k}{k^3}\left(\delta_{ij}-\frac{k_ik_j}{k^2}\right)\times\{(0|\alpha_1{}^ie^{i\mathbf{k}\cdot\boldsymbol{\eta}_1\mathbf{r}}|n,-k)(n,-k|\alpha_2{}^je^{i\mathbf{k}\cdot\boldsymbol{\eta}_2\mathbf{r}}|0)+(0|\alpha_2{}^ie^{-i\mathbf{k}\cdot\boldsymbol{\eta}_2\mathbf{r}}|n,-k)\times(n,-k|\alpha_1{}^ie^{-i\mathbf{k}\cdot\boldsymbol{\eta}_1\mathbf{r}}|0)\}(K_n-K^0). \quad (4.21)$$

Evaluation of Eq. (4.21) shows that spin-spin and spin-orbit terms vanish, while the orbit-orbit part agrees with that in Eq. (4.16). This again confirms[4] the equivalence of the two methods for the intermediate region. The α^3Ry contribution of Eq. (4.16) is like that given in S in Eqs. (48a) and (49a):

$$(\Delta E_{B1}{}^{M})_{2S}=\frac{\alpha^5\mu^2}{3\pi(m_1+m_2)}\left[\frac{25}{12}+\ln\frac{\alpha\mu}{A}\right], \quad (4.22a)$$

and

$$(\Delta E_{B1}{}^{M})_{2P}=-\frac{2\alpha^2}{3\pi m_1m_2}\left\langle\frac{1}{r^3}\right\rangle_{2P}=-\frac{\alpha^5\mu^2}{36\pi(m_1+m_2)}. \quad (4.22b)$$

The energy shift due to J_{B2} is simpler to calculate than that due to J_{B1}. The extremely low energy region does not contribute, and the effects of both the intermediate and relativistic regions can be gotten from the free particle expansions of these interaction terms in-

[19] $k_0(2,0)$ and $k_0(2,1)$ are given by Bethe, Brown, and Stehn, Phys. Rev. **77**, 370 (1950). They are calculated using the electron mass. The factor Ry_∞/Ry_μ serves as the reduced mass correction.

volving two transverse photons. In the relativistic region $k>B$ it is sufficient to set

$$\Delta E_{B2}{}^{H}=-i|\varphi(0)|^2\int(J_{B2})_K(xx')d^4xd^4x'. \quad (4.23)$$

This approximation neglects the relative time dependence of the wave function. It also disregards p' and p'', the momenta of the initial and final states, relative to k and k', the photon momenta. Substituting the explicit form of J_{B2} in Eq. (4.23), we obtain

$$\Delta E_{B2}{}^{H}=\frac{4\alpha^2 i}{(2\pi)^2}|\varphi(0)|^2\int_{k>B}\frac{d^4k}{(k_\mu{}^2)^2}\left(\delta_{ij}-\frac{k_ik_j}{k^2}\right)\left(\delta_{lm}-\frac{k_lk_m}{k^2}\right)\left\langle\frac{\gamma_1{}^i[m_1+\gamma_1{}^0(m_1-k_0)]\gamma_1{}^l}{[E_1{}^2-(m_1-k_0)^2]}\right.$$
$$\left.\times\frac{\gamma_2{}^m[m_2+\gamma_2{}^0(m_2-k_0)]\gamma_2{}^j}{[E_2{}^2-(m_2-k_0)^2]}+\frac{\gamma_1{}^i[m_1+\gamma_1{}^0(m_1-k_0)]\gamma_1{}^l\gamma_2{}^j[m_2+\gamma_2{}^0(m_2+k_0)]\gamma_2{}^m}{[E_1{}^2-(m_1-k_0{}^2][E_2{}^2-(m_2+k_0)^2]}\right\rangle. \quad (4.24)$$

The integral may be evaluated exactly; it has the value

$$\Delta E_{B2}{}^{H}=\frac{2\alpha^2|\varphi(0)|^2}{m_1m_2}\left[\ln\frac{2B}{\mu}+\frac{m_1{}^2\ln\eta_1-m_2{}^2\ln\eta_2}{m_1{}^2-m_2{}^2}\right.$$
$$\left.+\frac{1}{3}\frac{m_1m_2}{m_1{}^2-m_2{}^2}\langle\boldsymbol{\sigma}_1\cdot\boldsymbol{\sigma}_2\rangle\ln\frac{m_1}{m_2}\right]. \quad (4.25)$$

The expression $\ln(2B/\mu)$ arises from two pair terms only. These same terms are the only ones which are significant in the region $A<k<B$. In this region, we still neglect retardation corrections, but no longer omit p' and p'' relative to k and k'. This means that we let

$$\Delta E_{B2}{}^{M}\cong-i\int\varphi_P{}^*(\mathbf{r})\gamma_1{}^0\gamma_2{}^0$$
$$\times(J_{B2}(xx')_{\text{two pair}}\varphi_P(\mathbf{r}'). \quad (4.26)$$

The contribution of (4.26) in the region $0<k<A$ is negligible, and so the integral may be extended from 0 to B. This expression may be simplified to (see S, Sec. VIB)

$$\Delta E_{B2}{}^{M}=-\frac{\alpha^2}{(2\pi)^4m_1m_2}\int\int_0^B d^3k\int_0^\infty d^3k'\varphi_P{}^*(\mathbf{r})$$
$$\times e^{i(\mathbf{k}+\mathbf{k}')\cdot\mathbf{r}}\frac{[1+(\mathbf{k}\cdot\mathbf{k}'/kk')^2]}{kk'(k+k')}\varphi_P(\mathbf{r}). \quad (4.27)$$

Because of the α^2 coefficient, α^2Ry parts of (4.27) will appear only when the initial and final relative momenta are small. Hence k and k' must be roughly equal. In $2S$ states we utilize this fact to make the replacement

$$\int_0^B d^3k\int_0^\infty d^3k'\cdots\cong\int_0^{2B}d^3k\int_0^{2B-k}d^3k'\cdots.$$

In $2P$ states, we merely note that values of k larger than B do not contribute to our order, so that

$$\int_0^B d^3k\int_0^\infty d^3k'\cdots\cong\int_0^\infty d^3k\int_0^\infty d^3k'\cdots.$$

With these changes in the regions of integration, the integrals may be evaluated exactly, although considerable computation is required. The final result is

$$(\Delta E_{B2}{}^{M})_{2S}=\frac{\alpha^5\mu^2}{m_1+m_2}\frac{1}{4\pi}\left[\ln\left(\frac{\mu\alpha}{2B}\right)+\frac{7}{4}+\frac{4}{3}(1-\ln2)\right], \quad (4.28a)$$

and

$$(\Delta E_{B2}{}^{M})_{2P}=-\frac{\alpha^2}{2\pi}\frac{1}{m_1m_2}\left\langle\frac{1}{r^3}\right\rangle_{2P}=-\frac{\alpha^5\mu^2}{48\pi(m_1+m_2)}. \quad (4.28b)$$

The evaluation of $\Delta E_{B2}{}^{M}$ can be briefly outlined as follows. One need only calculate the integral (4.27) for a $1S$ state in order to find the energy shifts for all S states. [This is also true for the S state corrections which arise from J_{B1} and are displayed in Eq. (4.21).] The integral for the nS state may then be determined by parametric differentiations of the result for the $1S$ state. To evaluate $\Delta E_{B2}{}^{M}$ for the ground state, we first perform the integral over $\mathbf{r}$ followed by the integration over the remaining angle variables. After making the transformations $x=(k+k')/\sqrt{2}$ and $xu=(k-k')/\sqrt{2}$, we perform several partial integrations with respect to u and rearrange terms. The integral over x and then the integral over u may be simply evaluated. Confirmation of our method and that of S is provided by the agreement of our result, $(4/3)(1-\ln2)=0.409$, with the answer of S, 0.411, obtained by numerical integration.

To conclude this section, we summarize the total energy correction from J_B:

$$(\Delta E_B)_{2S}=(\mathcal{E}_{0\infty})_{2S}+\frac{\alpha^5\mu^2}{m_1+m_2}\frac{1}{8\pi}\left\{\frac{8}{3}\left[\frac{25}{12}+\ln\frac{2Ry_\infty}{\alpha k_0(2,0)}\right]\right.$$
$$+2\left[\ln\alpha+\frac{7}{4}+\frac{4}{3}(1-\ln2)\right]+\frac{2}{m_1{}^2-m_2{}^2}\left[m_1{}^2\ln\eta_1\right.$$
$$\left.\left.-m_2{}^2\ln\eta_2-\langle\boldsymbol{\sigma}_1\cdot\boldsymbol{\sigma}_2\rangle m_1m_2\ln\frac{m_1}{m_2}\right]\right\}, \quad (4.29a)$$

and

$$(\Delta E_B)_{2P}=(\mathcal{E}_{0\infty})_{2P}+\frac{\alpha^5\mu^2}{m_1+m_2}\frac{1}{8\pi}\left[\frac{8}{3}\ln\left(\frac{Ry_\infty}{k_0(2,1)}\right)-\frac{7}{18}\right]. \quad (4.29b)$$

5. RADIATIVE CORRECTIONS

Radiative corrections arise from self-energy (vertex) and vacuum polarization effects. The change in self-energy of the second particle in the Coulomb field

[first term of Eq. (2.15)] can be approximated by

$$\Delta E_{L2}{}^{C}\cong -4\pi\alpha\int \varphi_K{}^{c*}\delta(x_0)\gamma_2{}^0\gamma_2{}^r \times\{[G^0-G_1{}^0G_2{}^0]D\}_K\gamma_2{}^r\gamma_1{}^0\delta(x_0')\varphi_K{}^c. \quad (5.1)$$

In the above expression we have replaced Λ in Eq. (2.8) by $G_1{}^0\gamma_1{}^0\delta_2$, thereby neglecting the intrinsically higher-order pair terms. After some integrations this becomes

$$\Delta E_{L2}{}^{C}=-i\alpha(2\pi)^{-3}\int \varphi_K{}^{c*}(\mathbf{r}0)\gamma_2{}^0\gamma_2{}^r[G^C{}_{-\mathbf{k},K_0'}(\mathbf{r}0,\mathbf{r}'0) - (G_1{}^0G_2{}^0)_{-\mathbf{k},K_0'}(\mathbf{r}0,\mathbf{r}'0)]e^{-i\eta_1\mathbf{k}\cdot(\mathbf{r}-\mathbf{r}')}\gamma_2{}^r\gamma_1{}^0 \times e^{i(K_0-K_0')(X_0-X_0')}e^{-ik|X_0-X_0'|}k^{-1}\varphi_K{}^c(\mathbf{r}0). \quad (5.2)$$

Once more, the separation of the high- and low-quantum regions is tantamount to a separation of G^C into high- and low-energy parts. In the high-energy region all the terms of (2.15) recombine to yield

$$\Delta E_{L2}{}^{H}=-4\pi\alpha\int \varphi_K{}^{c*}(\mathbf{r}0)e^{-iK(X-X')}\gamma_2{}^0 \times\Big\{4\pi i\alpha\gamma_2{}^rG_2{}^0(x_2x_2')\gamma_1{}^\mu\gamma_2{}^\mu G_2{}^0(x_2'x_4)\gamma_2{}^r\delta(x_1-x_3) \times D(x_2'x_1)\frac{1}{(2\pi)^4}\int_{k>A}d^4k\frac{e^{ik\cdot r}}{k_\mu{}^2}d^4x_2'-\frac{\alpha}{2\pi}B_2\gamma_1{}^\mu\gamma_2{}^\mu \times\delta(x_1-x_3)\delta(x_2-x_4)D(x_1x_2)\Big\} \times\gamma_1{}^0\varphi_K{}^c(\mathbf{r}'0)d^4xd^4x'd^4X'. \quad (5.3)$$

In the foregoing expression, X' and x' are the center-of-mass and relative coordinates associated with x_3 and x_4 in the same way as X and x are related to x_1 and x_2. We have ignored the retardation corrections to the wave function in obtaining (5.3) since, to our accuracy,

$$(G_1{}^0)_K(xx')\delta(x_0)\varphi_K{}^c(\mathbf{r}'0)\cong\varphi_K{}^c(\mathbf{r}0). \quad (5.4)$$

After integration over configuration space, we get

$$\Delta E_{L2}{}^{H}=-2\alpha(2\pi)^{-5}\int \varphi_K{}^{c*}(\mathbf{r}0)e^{ip'\cdot r}\delta(\eta_2K_0{}^C+p_0') \times\delta(\eta_2K_0{}^C+p_0'')\delta(p'-p''+q)(q_\mu{}^2)^{-1}\gamma_2{}^0\gamma_1{}^r \times L_2{}^r(p'p'')\gamma_1{}^0e^{-ip''\cdot r''}\varphi_K{}^c(\mathbf{r}'0), \quad (5.5)$$

where

$$L_2{}^r(p'p'')=\frac{2i\alpha}{(2\pi)^3}\int_{k>A}d^4k \times\frac{\gamma_2{}^\mu[m_2-\gamma_2(p'+k)]\gamma_2{}^r[m_2-\gamma_2(p''+k)]\gamma_2{}^\mu}{k_\mu{}^2[m_2{}^2+(p'+k)^2][m_2{}^2+(p''+k)^2]}-\frac{\alpha}{2\pi}\gamma_2{}^rB_2.$$

The computation follows standard techniques[20,21] from Eq. (5.5) on. We have merely to note that to our order of accuracy, $\eta_2K_C{}^0\cong m_2$, and so we can calculate $L_2{}^r(p'p'')$ as if we were dealing with free particles. In other words, we set

$$(\gamma_2p''+m_2)\gamma_1{}^0\varphi_K{}^c(\mathbf{r}'0)\delta(\eta_2K_0{}^C+p_0'') =\varphi_K{}^{c*}(\mathbf{r}0)\delta(\eta_2K_0{}^C+p_0')\gamma_2{}^0(\gamma_2p'+m_2)=0. \quad (5.6)$$

Computation yields

$$L_2{}^r(p'p'')=\frac{\alpha}{2\pi}\Big\{\gamma_2{}^r\frac{q^2}{m_2{}^2}\Big(\frac{11}{36}+\frac{2}{3}\ln\frac{m_2}{2A}\Big) -\frac{1}{4m_2}q^\mu[\gamma_2{}^\mu,\gamma_2{}^r]\Big\}. \quad (5.7)$$

Using the approximate φ of Eq. (4.3), we obtain

$$\Delta E_{L2}{}^{H}=-\frac{4}{3}\frac{\alpha^2}{m_2{}^2}|\varphi(0)|^2\Big(\frac{5}{6}+\ln\frac{m_2}{2A}\Big)+\langle T\rangle, \quad (5.8)$$

where

$$T=\frac{\alpha}{4}\Big\{\frac{\boldsymbol{\sigma}_2\cdot L}{r^3}\Big[\frac{\alpha}{\pi}\frac{1}{m_2{}^2}+\frac{\alpha}{2\pi}\frac{2}{m_1m_2}\Big] -\frac{\alpha}{2\pi}\Big[\frac{\boldsymbol{\sigma}_1\cdot\boldsymbol{\sigma}_2}{r^3}-\frac{3(\boldsymbol{\sigma}_1\cdot\mathbf{r})(\boldsymbol{\sigma}_2\cdot\mathbf{r})}{r^5}-\frac{8\pi}{3}(\boldsymbol{\sigma}_1\cdot\boldsymbol{\sigma}_2)\delta(\mathbf{r})\Big]\Big\},$$

and $\mathbf{L}=\mathbf{r}\times\mathbf{p}$. The operator T represents the effects of the anomalous magnetic moment of the particles. The correction to the interaction between spin and orbit of the same particle appears as an α/π instead of an $\alpha/2\pi$, because this interaction consists of the purely kinetic Thomas term and a magnetic term. The latter, which is twice as large as the total self spin-orbit effect, is corrected by a factor of $\alpha/2\pi$.[17]

The low energy part is treated by methods analogous to those in Sec. 4. Since renormalization terms have been eliminated, it is convenient to return to a non-covariant form. Low-frequency contributions of the required order *cannot arise* from vertices in which the *self-energy* part is due to the *Coulomb* interaction, since this interaction requires the existence of pairs. Such a process is, therefore, inevitably a high-energy one. Furthermore, non-negligible contributions *only arise* from *Coulomb* interactions *between* the particles. This leaves only one term, which by procedures used in

[20] R. Karplus and N. M. Kroll, Phys. Rev. **77**, 536 (1950), Eq. (27).
[21] F. J. Dyson, "Notes on Advanced Quantum Mechanics," Cornell University lecture notes, 1952 (unpublished).

Sec. 4, reduces to

$$\Delta E_{L2}{}^{L}=-\frac{\alpha}{(2\pi)^2}\int_0^A\frac{d^3k}{k^2}\left(\delta_{ij}-\frac{k_ik_j}{k^2}\right)$$
$$\sum_n\frac{K_n-K_0{}^C}{k+K_n-K_0{}^C}\varphi_K{}^*(\mathbf{r}0)\alpha_2{}^ie^{-i\mathbf{k}\cdot\boldsymbol{\eta}_1\mathbf{r}}\varphi_{-\mathbf{k},n}(\mathbf{r}0)$$
$$\times\varphi^*_{-\mathbf{k},n}(\mathbf{r}'0)\alpha_2{}^je^{i\mathbf{k}\cdot\boldsymbol{\eta}_1\mathbf{r}'}\varphi_K(\mathbf{r}'0). \quad (5.9)$$

Equation (5.9) yields

$$(\Delta E_{L2}{}^{L})_{2S}=\frac{1}{6\pi}\frac{\alpha^5\mu^2}{m_1+m_2}\frac{m_1}{m_2}\ln\left[\frac{A}{k_0(2,0)}\frac{Ry_\infty}{Ry_\mu}\right], \quad (5.10a)$$

and

$$(\Delta E_{L2}{}^{L})_{2P}=\frac{1}{6\pi}\frac{\alpha^5\mu^2}{m_1+m_2}\frac{m_1}{m_2}\ln\frac{Ry_\infty}{k_0(2,1)}. \quad (5.10b)$$

The constant A can be eliminated between Eqs. (5.8) and (5.10a). The first particle can be treated in the same way, to give finally for the contribution of all vertex terms,

$$(\Delta E_L)_{2S}=\frac{\alpha^5\mu^2}{6\pi(m_1+m_2)}\left[\frac{m_1{}^2+m_2{}^2}{m_1m_2}\left(\frac{5}{6}-\ln\frac{\alpha^2k_0(2,0)}{Ry_\infty}\right)\right.$$
$$\left.-\frac{m_1}{m_2}\ln\eta_1-\frac{m_2}{m_1}\ln\eta_2+\frac{1}{2}\langle\boldsymbol{\sigma}_1\cdot\boldsymbol{\sigma}_2\rangle\right], \quad (5.11a)$$

and

$$(\Delta E_L)_{2P}=-\frac{\alpha^5\mu^2}{6\pi(m_1+m_2)}\frac{m_1{}^2+m_2{}^2}{m_1m_2}\ln\frac{k_0(2,1)}{Ry_\infty}$$
$$+\frac{\alpha^2}{2\pi m_1m_2}\left\langle\frac{1}{2}\left(\frac{m_2}{m_1}\boldsymbol{\sigma}_1+\frac{m_1}{m_2}\boldsymbol{\sigma}_2\right)\cdot\frac{\mathbf{L}}{r^3}+\frac{\mathbf{S}\cdot\mathbf{L}}{r^3}\right.$$
$$\left.-\frac{1}{2}\left(\frac{\boldsymbol{\sigma}_1\cdot\boldsymbol{\sigma}_2}{r^3}-\frac{3(\boldsymbol{\sigma}_1\cdot\mathbf{r})(\boldsymbol{\sigma}_2\cdot\mathbf{r})}{r^5}\right)\right\rangle; \quad (5.11b)$$
$$\mathbf{S}=\tfrac{1}{2}(\boldsymbol{\sigma}_1+\boldsymbol{\sigma}_2).$$

The other radiative correction is that arising from the effect of vacuum polarization on the exchange of a single photon between the particles. This term is not altered by the two-body formalism since the correction arises from a change in the photon Green's function and has no direct connection with the two particles. The interaction kernel may be shown to be[5,20]

$$J_{V\mathcal{A}}(12,34)=\frac{2\alpha^2i}{(2\pi)^4}\gamma_1{}^\nu\gamma_2{}^\nu\delta(x_1-x_3)\delta(x_2-x_4)$$
$$\times\int d^4k e^{ik(x_1-x_2)}\int_0^1 dv 2v^2(1-\tfrac{1}{3}v^2)$$
$$\times\{[4m_1{}^2+k^2(1-v^2)]^{-1}+[4m_2{}^2+k^2(1-v^2)]^{-1}\}. \quad (5.12)$$

This kernel will yield no contributions larger than α^3Ry and so it is sufficient to set

$$\Delta E_{V\mathcal{A}}=-i|\varphi(0)|^2\int\gamma_1{}^0\gamma_2{}^2(J_{V\mathcal{A}})_K(xx')d^4xd^4x'$$
$$=-\frac{4}{15}\alpha^2|\varphi(0)|^2\left(\frac{1}{m_1{}^2}+\frac{1}{m_2{}^2}\right). \quad (5.13)$$

For positronium, the result is

$$\Delta E_{\text{pos}}=-\frac{4}{15}\alpha^2|\varphi(0)|^2\frac{1}{m^2}. \quad (5.13a)$$

6. THE ANNIHILATION INTERACTION

The energy contribution of this interaction J_A is calculated in KK-III.[22] We agree with its result, which is

$$(\Delta E_A)_{2S}=\frac{\alpha^5m}{64\pi}\{-4(1-\ln2)$$
$$+\langle S^2\rangle[2(1-\ln2)-4-8/9]\}, \quad (6.1a)$$

and

$$(\Delta E_A)_{2P}=0. \quad (6.1b)$$

7. SUMMARY AND DISCUSSION

The total α^3Ry energy shift for the $2S$ and $2P$ states of positronium is determined by adding the α^3Ry parts of (3.10), (4.29), (5.11), (5.13a), and (6.1). In $2S$ states the result is

$$(\Delta E_B)_{2S}=\frac{\alpha^5m}{64\pi}\left\{-\frac{4}{3}+\frac{8}{3}\left[\frac{25}{12}+\ln\frac{2}{16.646\alpha}\right]\right.$$
$$+2\left[\ln\alpha+\frac{7}{4}+\frac{4}{3}(1-\ln2)\right]$$
$$\left.+(1-2\ln2)-\langle2S^2-3\rangle\right\}$$
$$=\frac{\alpha^5m}{64\pi}(8.784-2\langle S^2\rangle), \quad (\langle S^2\rangle=S(S+1)) \quad (7.1)$$

for the recoil and retardation corrections;

$$(\Delta E_{L,V})_{2S}=\frac{\alpha^5m}{64\pi}\left[\frac{8}{3}\left(\frac{5}{6}-\frac{1}{10}-\ln\frac{16.646\alpha^2}{2}\right)+\frac{2}{3}\langle2\mathbf{S}^2-3\rangle\right]$$
$$=\frac{\alpha^5m}{64\pi}\left(20.546+\frac{4}{3}\langle\mathbf{S}^2\rangle\right) \quad (7.2)$$

for the radiative contributions; and

$$(\Delta E_A)_{2S}=-\frac{\alpha^5m}{64\pi}(1.228+4.275\langle\mathbf{S}^2\rangle) \quad (7.3)$$

[22] There are several typographical errors in Sec. V of KK-III. We agree with the final answer, however.

for the annihilation terms. The total energy shift is

$$(\Delta E)_{2S}=\frac{\alpha^5 m}{64\pi}(28.101-4.942\langle \mathbf{S}^2\rangle). \tag{7.4}$$

The contribution in $2P$ states is

$$(\Delta E_B)_{2P}=-\frac{\alpha^5 m}{64\pi}\left(\frac{7}{18}+\frac{8}{3}\ln 0.9704\right)=-\frac{\alpha^5 m}{64\pi}(0.309) \tag{7.5}$$

for the recoil and retardation corrections, and

$$(\Delta E_{L,V})_{2P}=\frac{\alpha^5 m}{64\pi}\left(-\frac{8}{3}\ln 0.9704+\frac{1}{3}\langle \mathbf{S}\cdot\mathbf{L}\rangle\right)$$
$$-\frac{\alpha^2}{m^2}\frac{1}{4\pi}\left(\frac{\boldsymbol{\sigma}_1\cdot\boldsymbol{\sigma}_2}{r^3}-\frac{3(\boldsymbol{\sigma}_1\cdot\mathbf{r})(\boldsymbol{\sigma}_2\cdot\mathbf{r})}{r^5}\right) \tag{7.6}$$

for the radiative corrections. There are no contributions from the annihilation interaction. Numerically, we find for the total $2P$ energy shift:

$$(\Delta E)_{2P}=\frac{\alpha^5 m}{64\pi}\left[-0.229+\begin{bmatrix}0\\0.300\\-0.167\\-1.000\end{bmatrix}\text{ for }\begin{matrix}{}^1P_1\\{}^3P_2\\{}^3P_1\\{}^3P_0\end{matrix}\right]. \tag{7.7}$$

Our energy unit $(64\pi)^{-1}\alpha^5 m$ is equal to 12.72 Mc/sec.

In positronium, unlike hydrogen, there is no $\alpha^2 Ry$ degeneracy. Hence the $\alpha^3 Ry$ shifts must be added to the much larger $\alpha^2 Ry$ fine and hyperfine structures in order to obtain the level spacing. Table I gives the corrections ascertained by Ferrell,[23] together with the $\alpha^3 Ry$ contributions which we calculated.

A word about the accuracy of this calculation seems in order. We have included all $\alpha^3 Ry$ corrections. There are, of course, $\alpha^4 Ry$ terms with large coefficients; some of these may contain $\ln\alpha$. Such corrections may well amount to several Mc/sec. For example, in the expansion of G^C in (5.1) we have omitted the term, $\alpha_1{}^i G_1{}^0 G_2{}^0 I^C G_1{}^0 G_2{}^0 I^C G_1{}^0 G_2{}^0 \alpha_2{}^i D$, which is known to contribute 7 Mc/sec (an $\alpha^4 Ry$ term with a coefficient of eight) to hydrogen.[24,25] The factor $\frac{1}{4}$ converts the lowest-order Lamb shift correction from hydrogen to positronium. (This number comes from multiplying 2 by $\frac{1}{8}$. The multiplicand 2, comes from the equal contributions of electron and positron self-energies; the multiplier $\frac{1}{8}=(\mu_{pos}/\mu_H)^3$, represents the reduction of the density of the wave function at the origin.) If the same factor applies to the 7-Mc/sec correction to the Lamb shift, then this term alone would amount to about 2 Mc/sec.

TABLE I. Additions to the nonrelativistic $n=2$ level of positronium, Mc/sec.

Order	$^1S_0$	$^3S_1$	$^1P_1$	$^3P_2$	$^3P_1$	$^3P_0$
$\alpha^2 Ry$	−18 135	7413	−3536	−981	−5360	−10 835
$\alpha^3 Ry$	357	232	−3	1	−5	−16
Total	−17 778	7645	−3539	−980	−5365	−10 851

This calculation also determines corrections to the hydrogen Lamb shift. In the terminology of reference 1, and incorporating the change discussed in footnote 8, the theoretical shifts become

$$S_H=[1057.07-22\epsilon_\alpha+S_s^{(3)}+S^{(R)}+\epsilon_{sl}\pm 0.13]\text{ Mc/sec},$$
$$S_D=[1058.43-22\epsilon_\alpha+S_s^{(3)}+S^{(R)}\pm 0.13]\text{ Mc/sec}, \tag{7.8}$$
$$S_D-S_H=[1.371-\epsilon_{sl}\pm 0.035]\text{ Mc/sec}.$$

The theoretical value of the difference S_D-S_H is no longer in such close agreement with experiment, being just at the limit of the experimental error.

We would like to thank Professor R. Karplus for suggesting that the corrections to the fine structure of positronium be calculated, Professor J. Schwinger for valuable advice concerning the material of the Appendix, and Dr. A. Klein and Dr. R. Glauber for helpful conversations. We would also like to thank Harvard University and the National Science Foundation for financial assistance.

APPENDIX

One of us (P.C.M.), with Professor J. Schwinger, has previously derived a method for treating binding which does not involve "selective resummation" of the free-particle expansion of the interacting Green's function. This independent derivation seems sufficiently short and illuminating to merit its inclusion despite articles by FK and by Eden.[10] We employ the variational derivative techniques used by Schwinger[2] in deriving the relativistic two-body equation. To avoid the problems of symmetrization, we use two distinguishable fermion fields. If the particles have masses m_1 and m_2, and charges e_1 and e_2, the Green's function equation is

$$\left(\gamma\pi+m+ie\gamma(\xi)\frac{\delta}{\delta J(\xi)}\right)_1$$
$$\times\left(\gamma\pi+m+ie\gamma(\xi')\frac{\delta}{\delta J(\xi')}\right)_2 G_{12}=1. \tag{A.1}$$

The form of the two-body equation, obtained also by Salpeter and Bethe,[8] is derived by writing Eq. (A.1) as

$$[(\gamma\pi+M)_1(\gamma\pi+M)_2-I_{12}]G_{12}=1, \tag{A.2}$$

[23] R. A. Ferrell, Phys. Rev. **84**, 858 (1951). We have recomputed the numerical results of Dr. Ferrell from his formula for the energy to suit the greater numerical accuracy demanded by the present work.

[24] Karplus, Klein, and Schwinger, Phys. Rev. **86**, 288 (1952).

[25] Baranger, Bethe, and Feynman, Phys. Rev. **92**, 482 (1953).

and using an expansion of I_{12} in powers of e and free-particle Green's functions. A perturbation theory based upon the solution of an equation containing some interaction, is then employed to determine energies, wave functions, and so forth. A more satisfactory and symmetrical approach than this one is to use, in the approximation of I_{12}, the Green's function satisfying the same unperturbed equation (more accurate than the free particle equation) as is subsequently employed for finding the energies and wave functions. Such a procedure is sketched below. It amounts to using a different first approximation in the equation derived by Schwinger for the interaction operator.

Suppose that we employ as a first approximation to G_{12}, the solution to

$$[(\gamma\pi+m)_1(\gamma\pi+m)_2-O_{12}]G_{12}^0=1, \qquad (A.3)$$

where O_{12} is an arbitrary operator which may depend on the external current, J. If we use the relation

$$\left(ie\gamma(\xi)\frac{\delta}{\delta J(\xi)}\right)_1 G_{12}=-ie_1\gamma_1(\xi)G_{12}\frac{\delta G_{12}^{-1}}{\delta J(\xi)}G_{12}, \qquad (A.4)$$

and approximate the right-hand side of (A.4) by

$-ie_1\gamma_1(\xi)G_{12}[\delta(G_{12}^0)^{-1}/\delta J(\xi)]G_{12}$, we obtain

$$\left(ie\gamma(\xi)\frac{\delta G_{12}}{\delta J(\xi)}\right)_1\cong-ie_1\gamma_1(\xi)G_{12}^0\frac{\delta(G_{12}^0)^{-1}}{\delta A(\xi')}\frac{\delta A(\xi')}{\delta J(\xi)}G_{12}$$

$$\cong-ie_1\gamma_1(\xi)G_{12}^0\left\{\frac{\delta}{\delta A(\xi')}[(\gamma\pi+m)_1\right.$$

$$\left.\times(\gamma\pi+m)_2-O_{12}]\right\}\mathcal{G}(\xi\xi')G_{12}. \qquad (A.5)$$

As long as O_{12} is an operator independent on J, insertion of (A.5) into (A.1) yields the "improved" equation for G_{12},

$$\begin{aligned}&[(\gamma\pi+m)_1(\gamma\pi+m)_2\\&+ie_2^2(\gamma\pi+m)_1\gamma_2(\xi)G_{12}^0(\gamma\pi+m)_1\gamma_2(\xi')\mathcal{G}(\xi,\xi')\\&+ie_1^2(\gamma\pi+m)_2\gamma_1(\xi)G_{12}^0(\gamma\pi+m)_2\gamma_1(\xi')\mathcal{G}(\xi\xi')\\&+ie_1e_2(\gamma\pi+m)_1\gamma_2(\xi)G_{12}^0(\gamma\pi+m)_2\gamma_1(\xi')\mathcal{G}(\xi\xi')\\&+ie_1e_2(\gamma\pi+m)_2\gamma_1(\xi)G_{12}^0(\gamma\pi+m)_1\gamma_2(\xi')\mathcal{G}(\xi\xi')\\&-ie_1e_2\gamma_1(\xi)\gamma_2(\xi')\mathcal{G}(\xi\xi')+(ie\gamma(\xi)\delta/\delta J(\xi))_1\\&\times(ie\gamma(\xi')\delta/\delta J(\xi'))_2]G_{12}^1=1. \qquad (A.6)\end{aligned}$$

The procedure of this paper has been to take $O_{12}=I_C$. To the order to which (A.6) is then valid,

$$(ie\gamma(\xi)\delta/\delta J(\xi))_1(ie\gamma(\xi')\delta/\delta J(\xi'))_2$$

does not contribute, and hence has not been evaluated in (A.6). Replacement of G_{12}^0 by $G_1^0G_2^0$ would convert (A.6) into the usual lowest-order two-body equation,

$$[(\gamma\pi+M^1)_1(\gamma\pi+M^1)_2-I^1]G_{12}^1=0. \qquad (A.7)$$

To derive a still better equation, we merely repeat the procedure of Eqs. (A.3)–(A.5), but with an operator given by (A.6). (O_{12} will now depend on J through both $\gamma\pi$ and G_{12}^0.) Needless to say, this iteration gives rise to many terms. However, to the degree of accuracy required by our calculation, G_{12}^0 may be replaced in some of these terms by its Born approximation. This results, for example, in the combination of seven different terms with plus signs and six with minus signs into the one "crossed transverse" term of the usual treatment.

We note in passing that if we knew the solution to (A.3) with $O_{12}=-ie_1e_2\gamma_1(\xi)\gamma_2(\xi')\mathcal{G}(\xi\xi')$, we would only need to proceed as far as (A.6) to include all processes relevant to α^3Ry electrodynamic corrections. In order to have solutions in which the relative time dependence is known, we had to restrict ourselves to an instantaneous interaction. Hence a second approximation to the Green's function equation is necessary to introduce two transverse photons.

Validity of the Born-Oppenheimer Approximation*

S. BLUDMAN† AND P. B. DAITCH
Yale University, New Haven, Connecticut

(Received April 26, 1954)

Solutions of the Schrödinger equation for several simple models in which a light particle, mass m, is bound to a heavy particle, mass M, which in turn is bound to another heavy particle which may be fixed are considered as expansions in the parameter $1/\beta \equiv (m/M)^{\frac{1}{2}}$. A characteristic of such systems is that when the light particle is far from the heavy particle, it centers on the mean position of the heavy particle and when it is close to the heavy particle, it centers on the heavy particle. The classical prediction that the change in centering takes place when the motional frequencies of the light and heavy particles are equal is borne out in quantum mechanics except that here the transition takes place over an extended region as shown by the detailed investigation of models. General arguments are presented which show how low and high momenta of the light particle contribute, respectively, to centering on the mean position and on the changing position of the heavy particle.

The effect of the centering on expectation values of quantities dependent on the density of the light particle at the heavy one is of the order of the ratio of an average radius of the heavy particle motion to an average radius of the light particle motion. Further corrections due to incomplete centering are of the order $1/\beta$ times this ratio.

I. INTRODUCTION

THIS work is concerned with the validity of solutions to certain quantum-mechanical problems based on the Born-Oppenheimer[1] or adiabatic[2] approximation. The situations considered are those in which a light particle is centered either on a slowly moving heavy particle or on the mean position of the heavy particle. A natural expansion parameter for such problems is $1/\beta \equiv (m/M)^{\frac{1}{2}}$ where m and M are the masses of the light and heavy particles, respectively. Classical arguments give $1/\beta$ as the ratio of heavy-particle to light-particle displacement where the centering on the heavy-particle changes to centering on its mean position.

An example obtains in deuterium where Bohr[3,4] attributed a correction to the anomalously large hyperfine splitting to the motion of the proton inside the deuteron. Bohr's explanation, based on the adiabatic approximation, is that as a result of the electron centering on the proton when it is closer to the deuteron than β times the deuteron radius the neutron magnetic moment appears to the electron as a spherically symmetric distribution around the stationary proton and is largely ineffective inside the deuteron. The result is an increase in the hyperfine splitting by 0.018 percent in agreement with experiment.[5]

The Born-Oppenheimer approximation has had its major application in the fields of molecular spectra and solid state physics. The usual expansion in powers of $(m/M)^{\frac{1}{2}}$ is especially designed for the calculation of stationary states of molecules and is not directly applicable in the electron-deuteron problem. The examination of the regions of validity of the adiabatic approximation in relation to Bohr's work appeared appropriate therefore.

In some of the present work simple models suitable for accurate calculation are used. The correction to the wave function is obtained to first order in $1/\beta$ and is then compared with the zero-order centered wave functions. The distance at which centering of the wave function may be said to have changed markedly is determined according to various criteria. Expectation values calculated with corrected wave functions are examined for centering effects for two of the models.

A treatment in momentum space is also presented. The relationship of centering properties of the coordinate wave function to qualitative considerations involving velocities appears in a rather simple form. This method is capable of extension to arbitrary fields.

Notation

Three particles are considered and are nominally called e particle, P particle, and N particle; also, the bound system of P and N particle is called a D particle. The names are suggestive only since the models used do not describe the deuterium atom in detail. The N particle is assumed to be infinitely heavy and the N particle, and hence also the D particle center of mass, is fixed at the coordinate origin; the choice of N particle mass does not, however, affect the essential features of the problem. Occasionally the word "particle" will be omitted, the designations of the particles being then P, N, D, e.

* This research was supported by the United States Air Force, through the Office of Scientific Research of the Air Research and Development Command, and in its earlier stages was assisted by the joint program of the U. S. Office of Naval Research and the U. S. Atomic Energy Commission.

† Now at Radiation Laboratory, University of California, Berkeley, California.

[1] M. Born and J. R. Oppenheimer, Ann. Physik **84**, 457 (1927).
[2] M. Born and V. Fock, Z. Physik **51**, 165 (1928).
[3] A. Bohr, Phys. Rev. **73**, 1109 (1948).
[4] L. Low, Phys. Rev. **77**, 361 (1950), a refined calculation substantiating Bohr's result.
[5] J. E. Nafe and E. B. Nelson, Phys. Rev. **73**, 718 (1948); **75**, 1194 (1949).

The following notation is used.

m = mass of e particle.
M = mass of P particle.
$\beta=(M/m)^{\frac{1}{2}}$.
ξ = coordinate of e particle relative to the center of mass of the D particle.
$\eta/\beta=x_p$ = coordinate of P particle relative to N particle.
$\rho=\xi-(1/\beta)\eta$ = coordinate of e particle relative to P particle.
$\zeta=\eta+(1/\beta)\xi$ = coordinate proportional to distance of the center of mass of the $e-P$ system from the N particle.
P = momentum conjugate to ρ.
$p=(1+1/\beta^2)^{\frac{1}{2}}P$.
p_η = momentum conjugate to η.
$E=-\epsilon^2/2$ = total energy of the system.
$D(x)=[\delta(x-b)+\delta(x+b)]/2$, where x stands for the distance between the e particle and one of the heavy particles and b is a fixed parameter.
$\langle D(x)\rangle$ = the expectation value of $D(x)$ as calculated with exact wave functions.
$\langle D(x)\rangle^0$ = the expectation value of $D(x)$ when calculated with zero-order wave functions obtained from the Schrödinger equation in the variables ξ, η in the limit $1/\beta=0$, i.e., calculated with zero-order D-centered wave functions.
$\epsilon_N=(\langle D(x_{e-N})\rangle-\langle D(\xi)\rangle^0)/\langle D(\xi)\rangle^0$.
$\epsilon_P=(\langle D(\rho)\rangle-\langle D(\xi)\rangle^0)/\langle D(\xi)\rangle^0$.
Ψ, C denote wave functions in coordinate and momentum space, respectively.
u, v are used for the potentials between the P and N particles and between the P and e particles, respectively.

Units are used such that $m=\hbar=c=1$. When numerical values are used, values appropriate for the deuterium atom are taken.

a_0 = atomic radius.
d = deuteron radius.

II. CENTERING AND THE CHANNEL DIAGRAM

The Schrödinger equation for the N, P, e system is used in the following forms:

$$\{-\tfrac{1}{2}[\partial^2/\partial\xi^2+\partial^2/\partial\eta^2]+u(\eta/\beta)+v(\xi-\eta/\beta)-E\}\Psi=0, \quad (1)$$

$$\{-\tfrac{1}{2}[\partial^2/\partial\eta^2-2\partial^2/\beta\partial\eta\partial\rho+(1+1/\beta^2)\partial^2/\partial\rho^2]+u(\eta/\beta)+v(\rho)-E\}\Psi=0, \quad (2)$$

$$\{-\tfrac{1}{2}(1+1/\beta^2)[\partial^2/\partial\rho^2+\partial^2/\partial\zeta^2]+u[(\beta\zeta-\rho)/(1+\beta^2)]+v(\rho)-E\}\Psi=0. \quad (3)$$

The coupling between light- and heavy-particle motion appears in the Schrödinger equation as a term due to the nonzero value of $1/\beta$. If the e particle is very far from the center of mass of D as compared to the heavy particle separation, then η/β may be neglected against ξ and the coordinates are separable in the form (1) of the Schrödinger equation; this is the region of centering on the mean position of the P-particle or D-particle centering. If the e particle is very close to the P particle compared to the distance of the center of mass of the $e-P$ system from the N particle, then ρ may be neglected against $\beta\zeta$ and the Schrödinger equation separates in form (3); this is the P-particle centering region. The neutral set of coordinates, (ρ,η), reduce to (ξ,η) for large e-particle displacements and to (ρ,ζ) for small e-particle displacements; the perturbation term in (2) can easily be shown to be most important for ξ near $\beta\eta$.

In order to simplify the calculation, the three particles are considered constrained to move in one dimension. Such models may be effectively pictured by using the two independent coordinates in the c.m. system as rectangular axes in a plane. Potentials and wave functions may be considered in terms of such a figure which will be called a channel diagram.

To consider a specific one-dimensional model, let the $e-P$ and $N-P$ interactions be represented by square wells of infinite depth and respective widths $2\rho_0$ and $2\eta_0$. Using ρ and η as axes in a channel diagram, the wave function is confined to a rectangle about the origin; such a formulation makes the whole perturbation appear in the kinetic energy operator as in Eq. (2). Referring the problem to the ξ, η (or ρ, ζ) axes, the Schrödinger equation assumes the rather simple form

$$(\partial^2/\partial\xi^2+\partial^2/\partial\eta^2+2E)\Psi=0, \quad (4)$$

and the perturbation is contained in the boundary conditions, that is in the obliqueness of the sides of the parallelogram confining the wave function. The solution is written as

$$\Psi(\xi,\eta)=c_0\cos\omega_0\eta\cosh\kappa_0\xi+\Sigma_{n\ \mathrm{odd}}c_n\sin\omega_n\eta\sinh\kappa_n\xi+\Sigma_{n\ \mathrm{even}}c_n\cos\omega_n\eta\cosh\kappa_n\xi, \quad (5)$$

$$\omega_n=(n+1)\pi/2\eta_0, \quad \kappa_0^2=2E-\omega_0^2, \quad -\kappa_n^2=2E-\omega_n^2.$$

The energy available to the e particle has been made positive only for the ground state of the D particle. The c_n are determined by the condition that Ψ vanish at $\pm\rho_0=\xi-\eta/\beta$. By Fourier analyzing the function of η obtained by evaluating Eq. (5) at $\xi=\rho_0+\eta/\beta$ and then setting each Fourier coefficient to zero, an infinite set of equations results which may be solved for the c_n by successive approximations in $1/\beta$. The wave function so obtained, correct to order $1/\beta$, is

$$\Psi=\cos(\pi\eta/2\eta_0)\cos(\pi\xi/2\rho_0)+(8/\pi)(\eta_0/\beta\rho_0)\Sigma_{n\ \mathrm{even}}[n/(n^2-1)^2]\times\sin(n\pi\eta/2\eta_0)\sinh\kappa_n\xi/\sinh\kappa_n\rho_0. \quad (6)$$

The first-order correction is appreciable only for $\xi \cong \rho_0$, increasing the wave function near the acute angles and decreasing it near the obtuse angles of the parallelogram. This phenomenon is interpretable as a reflection in the angle between adjacent parallelogram sides.

The small quantity $\eta_0/(\beta\rho_0)$ is defined as the ratio of P to e-particle well radius. The ratio also has the significance of the ratio of e- to P-particle momentum when there is no coupling between e- and P-particle motions. Thus parallelograms with the same angles but different ratios of sides may be used to illustrate various momenta. Further, rotating the (ξ,η) axes through an angle $\theta \cong 1/\beta$, the same angle the oblique side makes with the axes, one obtains a description in (ζ,ρ) coordinates more suited to centering on the P particle.

Another example, to be taken up quantitatively in the next section, retains the square well for the heavy particle interaction but the $e-P$ interaction is taken to be a delta function at their coincidence. In the channel diagram, the wave function is confined to a channel with perfectly reflecting walls at $\pm\eta_0$. For the $e-P$ interaction, the equipotential lines are $\xi-\eta/\beta=$ constant. These lines are oblique to $\xi=$ constant, the equipotentials in the limit $1/\beta=0$. The $e-P$ interaction is thus represented by a trough with a deep center at $\xi=\eta/\beta$. Near the origin, the wave function suffers many reflections so that it involves a mixture of many modes tending to align the waves along the $e-P$ equipotentials. Far out in the channel, however, the higher modes brought in by reflections near the origin are attenuated and the wave function tends to be aligned by the channel walls.

The channel diagram shows a formal similarity between the centering problem in deuterium and nuclear resonances as treated by Breit.[6] In the nuclear resonance problem, an incident particle I interacts with a nuclear particle II, which has been singled out for consideration. The binding of II to the remainder of the nucleus is represented by confining II to a channel down which I is coming. The situation differs from the deuterium problem mainly in the value of the mass parameter β.

III. LINE OF INTERACTION IN A CHANNEL

A one-dimensional model is constructed in which the $N-P$ interaction is taken to be a square well and the $e-P$ interaction is taken to be a delta function at their coincidence. This model allows simple quantitative estimates of the attenuation along the channel of higher modes. The Schrödinger equation, Eq. (1), reduces for $\xi \neq \eta/\beta$ to Eq. (4) with the boundary conditions

$$\Psi=0 \quad \text{at} \quad \xi=\pm\infty \quad \text{and at} \quad \eta=\pm\eta_0,$$
$$[\partial\Psi/\Psi\partial\rho]_{\rho=0-}=-[\partial\Psi/\Psi\partial\rho]_{\rho=0+}=v, \tag{7}$$

where η_0 is the range of the square well and v is the strength of the delta-function interaction. The solution satisfying Eq. (7) is written as

$$\Psi=\Sigma_n c_n \exp(-\kappa_n\xi)\sin\omega_n(\eta+\eta_0), \quad \rho\gtrless 0,$$
$$\Psi=\Sigma_n c_n \exp(\kappa_n\xi)\sin\omega_n(\eta+\eta_0), \quad \rho\lesseqgtr 0, \tag{8}$$

with $\omega_n=(n+1)\pi/2\eta_0$, $\kappa_n{}^2=\epsilon^2-\omega_n{}^2$. The c_n are determined by the requirement that Ψ be continuous for $\xi=\eta/\beta$; that is the c_n should satisfy

$$\Sigma_n c_n[\exp(-\kappa_n\eta/\beta)-(-1)^n \times\exp(\kappa_n\eta/\beta)]\sin\omega_n(\eta+\eta_0)=0. \tag{9}$$

This equation is solved to first order in $1/\beta$; since the determinant of the coefficients is zero to this order, the c_n are determined in terms of c_0. The resulting wave function to order $1/\beta$ is

$$\Psi=\exp(-v\xi)\cos\omega_0\eta-(16/\pi^2) \times(v\eta_0/\beta)\Sigma_{n\ \text{odd}}(-1)^{(n+1)/2} \times[(n+1)/n^2(n+2)^2]\exp(-\kappa_n\xi)\sin\omega_n\eta. \tag{10}$$

Equation (10) applies for $\rho\gtrless 0$; for $\rho\lesseqgtr 0$, ξ is replaced by $-\xi$ and the sign in front of the summation is changed. The normalization is arbitrary.

The proton-centered wave function to order $1/\beta$ is found by transforming Eq. (10):

$$\Psi=\exp(-v\rho)\cos\omega_0\zeta+(1/\beta)\Sigma_{n\ \text{odd}}(-1)^{(n+1)/2} \times\{(16\eta_0 v/\pi^2)[(n+1)/n^2(n+2)^2]\sin\omega_n\zeta \times(\exp(-v\rho)-\exp(-\kappa_n\rho))-(4\omega_0\rho/\pi) \times[(n+1)/n(n+2)]\sin\omega_n\zeta\exp(-v\rho)\}. \tag{11}$$

The region of transition from D to P centering can be determined by investigating where the terms in $1/\beta$ in Eqs. (10) and (11) become large. The mass and energy parameters are adjusted to deuterium. In the D-centered wave function, at $\xi=0$ states up to about $n=7$ occur with small amplitudes; the ratio of the correction to the zero-order term being about 1/100 and roughly independent of η for $0.1\eta_0\lesssim\eta\lesssim 0.9\eta_0$. For $\xi\sim\beta d/20$ only the first excited state remains and its contribution is about 0.5 percent of the value of the zero-order term. For $\xi\sim\beta d/2$ the correction term in the deuteron centered wave function is entirely negligible. On the other hand, the proton centered wave function as given by (11) has a vanishing first-order correction for $\zeta=0$ or $\rho=0$. For ζ on the order of $\eta/2$, the correction begins to build up to about one percent coming from the first five or six excited states for $\rho\sim\beta d$. The correction continues to increase linearly with ρ, so within a few units of $\rho=\beta d$ the correction becomes appreciable. The dependence of the correction on position of the P particle as well as on position of the e particle is evident in Eqs. (10) and (11), particularly the relative importance of the correction term when the heavy particle is near the well edge.

[6] G. Breit, Phys. Rev. **58**, 506 (1940). See strip model, Fig. 3, p. 520.

Hence, the comparison of the P- and D-centered wave functions for this model places the transition as taking place in the region $0.1\beta d$ to $1\beta d$.

IV. SIMPLE HARMONIC OSCILLATOR

The oscillator interaction is an unrealistic model for electron-nuclear interactions because it increases as the separation increases. It has the advantage, however, of permitting a simple exact solution in which the role of the motional frequencies is immediately apparent. Each particle has a fixed classical frequency regardless of its position. By varying the ratio of the classical frequencies, the dependence of the centering on relative frequency but not on position can be investigated.

This model is also treated in one dimension. The Schrödinger equation, (1), has the explicit form

$$[\partial^2/\partial\xi^2+\partial^2/\partial\eta^2-\omega_p{}^2\eta^2-\omega_e{}^2(\xi-\eta/\beta)^2+2E]\Psi=0, \quad (12)$$

where the classical frequencies,

$$\omega_p{}^2=u/\beta^2, \quad \omega_e{}^2=v,$$

have been introduced to replace the spring constants, u and v. In the limit $1/\beta=0$, ω_p and ω_e are the independent frequencies of motion of the P particle inside the D particle and the e particle about the P particle.

The variables are separated in Eq. (12) by the transformation

$$\begin{aligned} x_1&=\xi\cos\theta+\eta\sin\theta,\\ x_2&=-\xi\sin\theta+\eta\cos\theta,\\ \theta&=\tfrac{1}{2}\tan^{-1}[(2\omega_e{}^2/\beta)/(\omega_p{}^2-\omega_e{}^2+\omega_e{}^2/\beta^2)]. \end{aligned} \quad (13)$$

The resulting form of Eq. (13) is

$$\begin{aligned} &(\partial^2/\partial x_1{}^2+\partial^2/\partial x_2{}^2+2E-\lambda_1{}^2x_1{}^2-\lambda_2{}^2x_2{}^2)\Psi=0,\\ &\lambda_1{}^2=(\omega_e{}^2-(\omega_p{}^2+\omega_e{}^2/\beta^2)\tan^2\theta)/(1-\tan^2\theta),\\ &\lambda_2{}^2=(\omega_p{}^2+\omega_e{}^2/\beta^2-\omega_e{}^2\tan^2\theta)/(1-\tan^2\theta),\\ &\lambda_1{}^2\lambda_2{}^2=\omega_e{}^2\omega_p{}^2. \end{aligned} \quad (14)$$

Equation (14) has well-known solutions, the ground state being

$$\begin{aligned} \Psi&=(\lambda_1\lambda_2/\pi^2)^{\frac{1}{4}}\exp[-\tfrac{1}{2}\lambda_1x_1{}^2-\tfrac{1}{2}\lambda_2x_2{}^2],\\ E&=(\lambda_1+\lambda_2)/2. \end{aligned} \quad (15)$$

The wave function given by Eq. (15) is in a convenient form to exhibit centering as a function of classical frequency. The ratio ω_e/ω_p determines the angle of rotation to normal coordinates and thus the character of the coordinates in which the problem is separable. When various ω_e/ω_p are considered it is convenient to keep $\omega_e\omega_p$ fixed since then no normalization correction need be introduced.

In the limit $\omega_e/\omega_p=0$:

$$\theta=0, \quad x_1=\xi, \quad x_2=\eta, \quad \lambda_1=\omega_e, \quad \lambda_2=\omega_p,$$
$$\Psi=(\omega_e\omega_p/\pi^2)^{\frac{1}{4}}\exp[-\tfrac{1}{2}\omega_e\xi^2-\tfrac{1}{2}\omega_p\eta^2].$$

In the limit $\omega_e/\omega_p=\infty$:

$$\theta=\tan^{-1}\beta, \quad x_1=\zeta, \quad x_2=-\rho, \quad \lambda_1=\omega_p, \quad \lambda_2=\omega_e,$$
$$\Psi=(\omega_e\omega_p/\pi^2)^{\frac{1}{4}}\exp[-\tfrac{1}{2}\omega_e\rho^2-\tfrac{1}{2}\omega_p\zeta^2].$$

Thus when the e-particle frequency is negligibly small or when the P-particle is too massive to respond to the e-particle motion, centering on the D particle obtains. In the case of $\omega_e/\omega_p\to\infty$, P centering prevails.

As ω_e/ω_p changes from less than unity to greater than unity, the parameter θ changes abruptly. As ω_e/ω_p changes from 0.9 to 1.1, θ changes by about 70 percent of the difference of its extreme values. The change to the limiting value is virtually complete at $\omega_e/\omega_p=2$ and $\omega_e/\omega_p=\frac{1}{2}$.

Different motional frequencies may be associated with different parts of the atom by means of the classical relations:

$$\omega_e=1/\xi^2, \quad \omega_p=1/\eta^2. \quad (16)$$

Then, when the P particle is inside the D particle and the e particle is in the first Bohr orbit $\omega_e/\omega_p=\beta^2(d/a_0)^2=10^{-5}$; when the e particle is inside the D particle. $\omega_e/\omega_p=\beta^2=10^3$. Since $\omega_e/\omega_p=1$ when $\xi=\beta d$ and the change in centering takes place as ω_e/ω_p goes from 2 to $\frac{1}{2}$, this would place the change in centering in the region from $2^{-\frac{1}{2}}\beta d$ to $2^{\frac{1}{2}}\beta d$.

V. CENTERING CONSIDERED BY MEANS OF MOMENTUM SPACE

In treating the centering problem, the momentum representation has the advantage that it expresses the wave function directly in terms of the variables which determine the centering classically. The appearance of perturbing terms in the kinetic rather than the potential energy proves to be an additional convenience.

Since this treatment applies to three dimensions, we replace the lightface coordinate symbols by boldface vector symbols. With the introduction of Fourier transforms, Eq. (2) may be written

$$\begin{aligned} &[P^2+(\mathbf{p}_v-\mathbf{P}/\beta)^2-2E]C(\mathbf{P},\mathbf{p}_v)+2(2\pi)^{-\frac{1}{2}}\\ &\quad\times\int C(\mathbf{P},\mathbf{p}_v-\mathbf{s})U(\mathbf{s})d\mathbf{s}+2(2\pi)^{-\frac{1}{2}}\\ &\quad\times\int C(\mathbf{P}-\mathbf{t},\mathbf{p}_v)V(\mathbf{t})d\mathbf{t}=0, \end{aligned} \quad (17)$$

where

$$C(\mathbf{P},\mathbf{p}_\eta)=(2\pi)^{-3}\int\int\Psi(\boldsymbol{\varrho},\mathbf{n})\times\exp(-i\mathbf{P}\cdot\boldsymbol{\varrho}-i\mathbf{p}_\eta\cdot\mathbf{n})d\boldsymbol{\varrho}d\mathbf{n},$$
$$U(\mathbf{s})=(2\pi)^{-\frac{1}{2}}\int u(\mathbf{n})\exp(-i\mathbf{s}\cdot\mathbf{n})d\mathbf{n}, \quad (18)$$
$$V(\mathbf{t})=(2\pi)^{-\frac{1}{2}}\int v(\boldsymbol{\varrho})\exp(-i\mathbf{t}\cdot\boldsymbol{\varrho})d\boldsymbol{\varrho}.$$

The integral Eq. (17) can be solved in a power series in $1/\beta$ by a perturbation calculation. The zero-order equation has the product eigenfunctions and eigenvalues

$$C_n(\mathbf{P},\mathbf{p}_\eta)=C_i^e(\mathbf{P})C_j^D(\mathbf{p}_\eta), \quad E_n=E_i^e+E_j^D, \quad (19)$$

where

$$(P^2-2E_i^e)C_i^e(\mathbf{P})+2(2\pi)^{-\frac{1}{2}}\times\int C_i^e(\mathbf{P}-\mathbf{s})U(\mathbf{s})d\mathbf{s}=0, \quad (20)$$

$$(p_\eta^2-2E_j^D)C_j^D(\mathbf{p}_\eta)+2(2\pi)^{-\frac{1}{2}}\times\int C_j^D(\mathbf{p}_\eta-\mathbf{t})V(\mathbf{t})d\mathbf{t}=0. \quad (21)$$

If we write $C(\mathbf{P},\mathbf{p}_\eta)=C_0(\mathbf{P},\mathbf{p}_\eta)+\delta C(\mathbf{P},\mathbf{p}_\eta)$ and $E=E_0+\delta E$, the correction to the ground-state wave function to order $1/\beta$ is

$$\delta C=(1/\beta)\Sigma_{n\neq0}\frac{\langle\mathbf{P}\cdot\mathbf{p}_\eta\rangle_{n0}}{E_n-E_0}C_n(\mathbf{P},\mathbf{p}_\eta), \quad (22)$$

where

$$\langle\mathbf{P}\cdot\mathbf{p}_\eta\rangle_{n0}=\int\int C_n^*(\mathbf{P},\mathbf{p}_\eta)\mathbf{P}\cdot\mathbf{p}_\eta C_0(\mathbf{P},\mathbf{p}_\eta)d\mathbf{P}d\mathbf{p}_\eta.$$

There is no distinction between P-and D-particle centering in zero order since the momenta are conjugate to the "neutral" coordinates (ρ,η). It will now be shown that in the first-order correction, low values of P contribute to centering on the D particle and high values to centering on the P particle.

In the states of low e-particle excitation, $E_j^D\gg E_i^e$ so that for these terms

$$\delta C_{\text{low}}=(1/\beta)\Sigma_{j\neq0}\frac{C_j^D(\mathbf{p}_\eta)}{E_j^D-E_0^D}\Sigma_{i\neq0}\langle\mathbf{P}\cdot\mathbf{p}_\eta\rangle_{n0}C_i^e(\mathbf{P}). \quad (23)$$

Since $C_0^eC_0^D$ is of even parity and $\mathbf{P}\cdot\mathbf{p}_\eta$ of odd the summation may be extended to $i=0$ and since the C_i^e form a complete set, the summation over i in Eq. (23) may be written as

$$\Sigma_{i\neq0}\langle\mathbf{P}\cdot\mathbf{p}_\eta\rangle_{n0}C_i^e(\mathbf{P})=\langle\mathbf{p}_\eta\rangle_{j0}\cdot\mathbf{P}C_0^e(\mathbf{P}). \quad (24)$$

Hence

$$\delta C_{\text{low}}=(1/\beta)C_0^e(\mathbf{P})\mathbf{P}\cdot\Sigma_{j\neq0}\frac{\langle\mathbf{p}_\eta\rangle_{j0}}{E_j^D-E_0^D}C_j^D(\mathbf{p}_\eta), \quad (25)$$

so that $C_0+\delta C_{\text{low}}$ is a state in which the e particle is in the eigenstate $C_0^e(\mathbf{P})$ and the P particle is subject to the perturbing term $-(2/\beta)\mathbf{P}\cdot\mathbf{p}_\eta$, or the P-particle state is an eigenfunction of Eq. (21) of argument $\mathbf{p}_\eta-\mathbf{P}/\beta$. Hence,

$$C_0+\delta C=C_0^e(\mathbf{P})C_0^D(\mathbf{p}_\eta-\mathbf{P}/\beta). \quad (26)$$

The coordinate space transform of this equation is

$$\Psi_{\text{low}}(\boldsymbol{\varrho},\mathbf{n})=(2\pi)^{-3}\int\int C_0^e(\mathbf{P})C_0^D(\mathbf{p}_\eta-\mathbf{P}/\beta)\times\exp(i\mathbf{P}\cdot\boldsymbol{\varrho}+i\mathbf{p}_\eta\mathbf{n})d\mathbf{P}d\mathbf{p}_\eta$$
$$=\Psi_0^e(\boldsymbol{\xi})\Psi_0^D(\mathbf{n}). \quad (27)$$

Thus to order $1/\beta$, the states of low e-particle excitation lead to a normal e particle centered on a normal D particle with no interaction between them.

In a similar way, the high momenta contribute to the wave function when $E_i^e\gg E_j^D$ and lead to a wave function centered on the P particle to order $1/\beta$.

VI. LINES OF INTERACTION

This one-dimensional model employs delta-function interactions between the particles. In a channel diagram, the interactions are zero except on the lines

$$\eta=0, \quad \xi-\eta/\beta=0. \quad (28)$$

This model is especially easy to treat in momentum space so the Schrödinger equation is used in the form of the one-dimensional analog of Eq. (17).

$$[p^2+p_\eta^2-(2/\beta)pp_\eta+\epsilon^2]C(p,p_\eta)+v\int C(p,p_\eta)dp+u\int C(p,p_\eta)dp_\eta=0, \quad (29)$$

where $p=(1+1/\beta^2)^{\frac{1}{2}}P$. The change of variable is made so that only one term involves the perturbation. Because of the odd parity of the perturbation, the ratio of the first-order correction to the well-known zero-order solution of (29) can be found by solving (29) algebraically for this ratio. This yields the wave function to order $1/\beta$,

$$C_0+\delta C=N[p^2+(\pi v)^2]^{-1}[p_\eta^2+(\pi u)^2]^{-1}\times[1+(2/\beta)pp_\eta/(\epsilon^2+p^2+p_\eta^2)], \quad (30)$$
$$\epsilon^2=(\pi u)^2+(\pi v)^2.$$

The correction term approaches its asymptotically maximum value for p and p_η equal and both corresponding to energies ϵ^2 or larger.

The region where the centering of the e particle changes is located by considering the symmetry features of the wave function in the channel diagram. As the e particle moves out along the ξ axis, the wave function changes from P particle centering, symmetry about the ρ axis, to D particle centering, symmetry about the ξ axis. Applied at $\eta=0$, this means that the smallness of $(\partial\psi/\partial\eta)_{\eta=0}$ as a function of ξ is a criterion for centering on the D particle. This quantity may be evaluated by taking the derivative under the integral sign of the inverse Fourier transform of the wave function given by Eq. (30) after having transformed (ρ,η) to (ξ,η). By considering the p integration in the complex plane, the result may be written in the form

$$(\partial\psi/\partial\eta)_{\eta=0}=[\pi N/(2\beta\epsilon)](\xi/|\xi|)\times\left\{(4/\pi)\int_1^\infty(t^2-1)^{\frac{1}{2}}\times(t^2-(\pi v/\epsilon)^2)^{-2}\exp(-|\epsilon\xi|t)dt\right\}. \quad (31)$$

The term in brackets can be evaluated numerically as a function of $|\epsilon\xi|=\xi/(\beta d)$. It is equal to unity for $\xi=0$ and has dropped to one-half at $\xi/(\beta d)=0.2$. For $\xi=\beta d$ it has the value 0.1 and for $\xi=2\beta d$ it has the value 0.02. Taking the transition region as being located around the point where the slope has dropped to one-half its value at $\xi=0$, this model changes from P to D particle centering in about one-fifth the distance classically expected.

VII. EXPECTATION VALUES

The direct relationship of expectation values of observables to physical interpretation makes it now desirable to calculate a few quantum-mechanical means. Expectation values are calculated for

$$D(x)=[\delta(x-b)+\delta(x+b)]/2, \quad (32)$$

where the variable x may stand for the distance of the e particle from any of the other particles and b is a constant parameter. Expectation values of D are calculated for the Simple Harmonic Oscillator (S.H.O.) and the Two Lines of Interaction models.

The quantities of interest are

$$\langle D(x_{e-N})\rangle=\langle D(x_{e-\text{c.m.}})\rangle^0(1+\epsilon_N),\qquad \langle D(\rho)\rangle=\langle D(x_{e-\text{c.m.}})\rangle^0(1+\epsilon_P), \quad (33)$$

where x_{e-N} and $x_{e-\text{c.m.}}$ are the distances of the e particle from the N particle and from the center of mass of $P-N$ system, respectively, and where the superscript zero denotes expectation values calculated with the zero order D-centered wave functions. When the N particle mass is taken to be infinite, the relative increments in the expectation values become

$$\epsilon_N=(\langle D(\xi)\rangle-\langle D(\xi)\rangle^0)/\langle D(\xi)\rangle^0,\qquad \epsilon_P=(\langle D(\rho)\rangle-\langle D(\xi)\rangle^0)/\langle D(\xi)\rangle^0. \quad (34)$$

These relative increments owe their existence to the fact that $\beta\neq\infty$, i.e., to the fact that the P particle moves with respect to the center of mass.

The quantities in Eq. (34) can all be exactly evaluated for the S.H.O. but the results are rather involved. The essential features may be brought out by taking the expectation values evaluated for $b=0$, that is at the heavy particles, and considering the contributions to the relative increments when ω_e/ω_p is much less and much greater than unity. For low ω_e/ω_p, to third order in the small quantities $1/\beta$ and ω_e/ω_p,

$$\epsilon_N\cong 0,\quad \epsilon_P\cong-(1/2\beta^2)(\omega_e/\omega_p). \quad (35)$$

Thus, when ω_e/ω_p is low, the e particle density at the heavy particles is accurately given by the D-centered wave function but the average e particle density at the P particle is slightly reduced as a consequence of the P particle's motion. For high ω_e/ω_p to first order in the small quantities $1/\beta$ and ω_p/ω_e,

$$\epsilon_N\cong-[1/(2\beta^2)](\omega_e/\omega_p),\quad \epsilon_P\cong 0. \quad (36)$$

Thus in this case, the density at the N particle is reduced as the e particle follows the P particle; the density at the P particle is what it would be in the absence of P particle motion.

The same quantities are also evaluated for the Two Lines of Interaction model. Here two effects of the nuclear motion are distinguished. First, there is a displacement between the P and N particle so $\langle D(\rho)\rangle^0$ and $\langle D(\xi)\rangle^0$ are not equal. Second, the wave function is not entirely D-centered so that $\delta\langle D(\rho)\rangle^1$ and $\delta\langle D(\xi)\rangle^1$ appear where $\delta\langle D\rangle^1$ denotes a contribution to the expectation values from the first-order correction to the D-centered wave function. Also, renormalization of the wave function gives a contribution to the expectation value and is denoted by $\delta\langle D\rangle^2$.

The expectation value of D can be evaluated using the momentum space wave function, Eq. (30), directly. The result is evaluated for small b and is accurate to second order in $1/\beta$ and in $(\pi v/\pi u)$. The results are written substituting the ratio of the typical lengths of the problem, $\beta d/a_0$, for $\pi v/\pi u$ and similarly substituting $b/(\beta d)$ for $b|\pi u|$.

$$\epsilon_N=-(d/a_0)[\exp(-2b/d)-(1.3/\beta)K(b/\beta d)]+\tfrac{1}{2}(d/a_0)^2,\quad (37)$$

$$\epsilon_P=-\tfrac{1}{2}(d/a_0)^2,$$

where

$$K(b/\beta d)=(15/2)\int_1^\infty(t^2-1)^{\frac{1}{2}}t^{-6}\exp(-|b/\beta d|t)dt$$

is a function which is unity for $b=0$ and decreases somewhat more rapidly than $\exp(-b/\beta d)$ with increasing b. The first term in square brackets in Eq. (37) predominates for b in the nuclear region; for b greater than d, the second term predominates, but both terms are negligibly small beyond the classical critical distance. The relative change in e-particle density about the N particle as given by Eq. (37) then is: (1) of order d/a_0 inside the D particle; (2) of order $d/(\beta a_0)$ outside the D particle but within the distance βd.

Except for the renormalization correction of order $(d/a_0)^2$, the correction ϵ_N is due to the first-order correction to the wave function which takes account of P centering. This correction may be further broken down. The contribution of order d/a_0 is attributed to the displacement between N and P particles since

$$(\langle D(\rho)\rangle^0-\langle D(\xi)\rangle^0)/\langle D(\xi)\rangle^0 = -(d/a_0)\exp(-2b/\beta d)+(d/a_0)^2. \quad (38)$$

This term in ϵ_p, however, is just canceled by the contribution from the first-order correction to the wave function, $\delta\langle D(\rho)\rangle^1/\langle D(\xi)\rangle^0$; i.e., near the P particle the wave function is centered on the P particle and there the density of the e particle is well represented by the density about a stationary particle as given in this case by $\langle D(\xi)\rangle^0$ which represents the density about the stationary center of mass. Besides these terms, there is a contribution to ϵ_N for small b which is due to the wave function not being completely P-centered. This may be seen by considering the wave function expanded in terms of the solutions of the Schrödinger equation in ρ and η variables with $1/\beta=0$. If $\delta\langle D(\xi)\rangle^I$ is the expectation value of $D(\xi)$ arising from the $1/\beta$ correction to this P-centered wave function for small b, then

$$\delta\langle D(\xi)\rangle^1/\langle D(\xi)\rangle^0=1.3(d/\beta a_0)K(b/\beta d). \quad (39)$$

This is the relative change in e-particle density near the N particle due to incomplete centering on the P particle. The remaining terms in Eq. (37), are due to the second-order renormalization correction,

$$\delta\langle D(\xi)\rangle^2/\langle D(\xi)\rangle^0=\delta\langle D(\rho)\rangle^2/\langle D(\xi)\rangle^0=-\tfrac{1}{2}(d/a_0)^2. \quad (40)$$

The relative change in expectation value of an operator dependent on e-particle density at the heavy particles is given by Eq. (37) with $b=0$:

$$\epsilon_N=-0.97(d/a_0)+\tfrac{1}{2}(d/a_0)^2, \qquad \epsilon_P=-\tfrac{1}{2}(d/a_0)^2. \quad (41)$$

Here there is a correction of d/a_0 due to the displacement between N and P particles which changed by about 3 percent owing to the lack of complete P centering.

An estimate of the correction to the wave function to order $1/\beta^2$ applicable to this model is given in Appendix I. No special build up of numerical factors was found to be present in the second order correction.

VIII. CONCLUSIONS

The transition in centering takes place about where it is expected classically, at about βd, but differs from the classical prediction in two respects. The transition is naturally not sharp, as has been demonstrated for several models: the transition takes place over the region from $2^{-\frac{1}{2}}\beta d$ to $2^{\frac{1}{2}}\beta d$ for the S.H.O. model, from $0.1\beta d$ to βd for the Line of Interaction in a Channel model, and over a broad region centered at $0.2\beta d$ for the Two Lines of Interaction model. Also, the transition is not dependent only on e-particle position but is dependent on the position of the P particle as well as may be seen from an inspection of the results for all examples.

The discussion of expectation values shows three different effects: (1) The centering of the wave function on the P particle near the nucleus decreases the density of the e particle at the N particle in the order d/a_0; (2) The lack of complete P-particle centering increases this density in the order $(1/\beta)(d/a_0)$; (3) The renormalization of the wave function decreases expectation values dependent on the distance of the e particle from the N or P particle in order $(d/a_0)^2$. Before renormalization the correction to the wave function was required to be orthogonal to the zero-order function and the coefficient of the zero-order function was kept constant.

The foregoing conclusions are based on simple models used solely to bring out the general features of centering effects and other effects, such as those due to spin and relativity, have been purposely neglected. For these reasons, the results do not apply directly to the physical problem of the deuterium atom.

ACKNOWLEDGMENT

The authors thank Professor Gregory Breit for discussions and access to some preliminary calculations upon which the present work is based. They also thank Mr. J. P. Lazarus for checking some of the calculations.

APPENDIX I

In the case of the Two Lines of Interaction model, the correction to the wave function to order $1/\beta^2$ may be found by perturbation theory. The perturbing term in the Schrödinger equation, Eq. (29), is

$$H'=-(2/\beta)p_\rho p_\eta.$$

Writing

$$C(p,p_\eta)=C_0(p,p_\eta)+(1/\beta)C^{(1)}(p,p_\eta)+(1/\beta^2)C^{(2)}(p,p_\eta)+\cdots,$$

$$E=E_0+(1/\beta)E^{(1)}+(1/\beta^2)E^{(2)}+\cdots,$$

and extending the perturbation theory of Sec. V to

second order, one has

$$E^{(2)}=\Sigma_{n\neq 0}\frac{\langle 2pp_\eta\rangle_{0n}\langle 2pp_\eta\rangle_{n0}}{E_0-E_n},$$

$$C^{(2)}=\Sigma_{n\neq 0}a_nC_n,$$

$$a_n=\Sigma_{m\neq 0}\frac{\langle 2pp_\eta\rangle_{nm}\langle 2pp_\eta\rangle_{m0}}{(E_0-E_m)(E_0-E_m)}-\frac{\langle 2pp_\eta\rangle_{00}\langle 2pp_\eta\rangle_{0n}}{(E_0-E_n)^2}.$$

The normalized unperturbed continuum eigenfunctions are taken as

$$C_p^{+}(p')=2^{-\frac{1}{2}}[1+(\pi v/p)^2]^{-\frac{1}{4}}\times\{[\delta(p+p')+\delta(p-p')]/2-v/(p'^2-p^2)\},$$

$$C_p^{-}(p')=i2^{-\frac{1}{2}}[\delta(p'+p)-\delta(p'-p)],$$

which are, respectively, the even and odd pth eigenfunctions of argument p'.

Using these eigenfunctions in the above expression for $C^{(2)}$, one obtains

$$C^{(2)}(p,p_\eta)=4N\int\int\int\int F(p_1,p_{\eta 1},p_2,p_{\eta 2})\times[\delta(p_2-p_1)-2v/(p_1^2-p_2^2)]\times[\delta(p_2-p)-2v/(p^2-p_2^2)]\times[\delta(p_{\eta 2}-p_{\eta 1})-2u/(p_{\eta 1}^2-p_{\eta 2}^2)]\times[\delta(p_{\eta 2}-p_\eta)-2u/(p_\eta^2-p_{\eta 2}^2)]\times dp_1dp_{\eta 1}dp_2dp_{\eta 2},$$

where

$$F\equiv p_1^2p_{\eta 1}^2p_2^2p_{\eta 2}^2[(\pi v)^2+p_1^2]^{-1}\times[(\pi v)^2+p_2^2]^{-1}[(\pi u)^2+p_{\eta 1}^2]^{-1}[(\pi u)^2+p_{\eta 2}^2]^{-1}\times[\epsilon^2+p_1^2+p_{\eta 1}^2]^{-1}[\epsilon^2+p_2^2+p_{\eta 2}^2]^{-1}.$$

Since the above integration is difficult, the factors $(\epsilon^2+p_1^2+p_{\eta 1}^2)^{-1}$ and $(\epsilon^2+p_2^2+p_{\eta 2}^2)^{-1}$ were replaced by

$$\epsilon^4(\epsilon^2+p_1^2)^{-1}(\epsilon^2+p_{\eta 1}^2)^{-1}(\epsilon^2+p_2^2)^{-1}(\epsilon^2+p_{\eta 2}^2)^{-1},$$

which reduces the quadruple integral to a product of two double integrals. This approximation was checked by comparing the result of exact integration of terms of zero and first order in the potential strengths which appear explicitly in the numerator of the original integrand with the result of the same terms integrated in the above approximation. Over the region where the exact integral is greater than one-half percent of its maximum value, the approximate result is within about a factor 2. After employing the above approximation and further simplifying the coefficients by neglecting πv compared to πu, the result can be written as

$$C^{(2)}/C_0=(1/4)[(\pi v)^4\epsilon^2+3(\pi v)^2\epsilon^2p^2-\epsilon^2p^4+(\pi v/2\epsilon)p^6]\times[3(\pi u)^6-11(\pi u)^4p_\eta^2-15(\pi u)^2p_\eta^4-p_\eta^6]\times[(\pi v)^2+p^2]^{-1}[\epsilon^2+p^2]^{-3}[\epsilon^2+p_\eta^2]^{-3}.$$

Effects of Certain Three-Body Nuclear Interactions in H^3 and He^3†

A. W. SOLBRIG, JR.*
Department of Physics, Vanderbilt University, Nashville, Tennessee
(Received March 17, 1954)

This limited, theoretical study is phenomenological and nonrelativistic. Effects of interactions on wave functions, magnetic dipole moments, and binding energies are obtained by first-order perturbation methods. The interactions satisfy well-known requirements of invariance, contain no power of momentum higher than the first, involve no dependence on charge, and introduce only P state in a first-order calculation. They contain spin-orbit interactions and may give rise to interaction moments. Each interaction contains a scalar radial function of positions f. The unperturbed potential corresponds to pairwise Hooke's law forces between nucleons. The first-order energy perturbation is shown to vanish for all the interactions. It is shown, without further specialization of the f, that no one of fifty-eight of the seventy-five interactions yields observed magnetic moments. No definite conclusion is obtained for eleven of the remaining seventeen interactions, for calculations with plausible f appear difficult. Each of the remaining six interactions yields observed magnetic moments with plausible f.

INTRODUCTION

SEVERAL workers have recently discussed many-body nuclear interactions in connection with the binding energy of He^4, nuclear saturation properties, and the independent-particle model of the nucleus.[1] Although it is not certain that many-body interactions are required in the explanation of nuclear properties, investigation of possible forms of such interactions and of their effects in nuclei is, nevertheless, of interest. The number of possible forms is very great; and the calculation of their effects is likely to be difficult, especially since meson theory in its present state is not well suited to quantitative calculation. The phenomenological and nonrelativistic treatment of the present work is applied only to the comparatively simple nuclei H^3 and He^3.

If the possible existence of three-body forces is ignored and the two-body forces are assumed to be composed of central and tensor parts, the ground states of H^3 and He^3 are mostly mixtures of S and D states.[2] Such ground states combined with the theory of Sachs[3] give the observed value of the sum of the magnetic dipole moments of H^3 and He^3, but they do not give the observed magnetic moments of the individual nuclei. The work of Sachs indicates that a more complicated ground state containing a considerable fraction of P state in addition to the S and D states can yield values for the individual moments which differ only slightly from the observed moments. Avery and Sachs[4] state that relativistic corrections may overcome the difference; but they also conclude, from kinetic energy considerations, that the calculation of the moments by Sachs[3] requires an unreasonably large fraction of P state and that it is more reasonable to invoke interaction moments[5] to obtain agreement. Ross[6] has examined the evidence for nonadditivity of nucleon moments in heavy nuclei. He concludes (a) that the deviations of static moments of heavy nuclei from the Schmidt lines are an unreliable and ambiguous source of information and that they could be ascribed to a nonadditivity effect only if that were a many-body effect and (b) that the observation of certain "forbidden" magnetic dipole transitions in heavy nuclei seems to provide direct evidence for the existence of nonadditivity effects. Although the existence of such effects is fairly well established, the existence of P state attributed to spin-orbit interaction in other very light nuclei is reason to suppose that similar interactions cause P state to appear in the ground state of H^3 and He^3;[7] and the presence of this state can decrease the interaction moment needed to bring agreement with observation. Apparently no calculation of the fraction of P state introduced by plausible nuclear interactions

† Work performed, in part, under U. S. Atomic Energy Commission Predoctoral Fellowship. This report is from a thesis submitted in partial fulfillment of requirements for the Ph.D. degree at Vanderbilt University. Phys. Rev. **92**, 855 (1953).

* Now at Los Alamos Scientific Laboratory, Los Alamos, New Mexico.

[1] For example, J. Irving, Proc. Phys. Soc. (London) **A66**, 17 (1953); S. D. Drell and K. Huang, Phys. Rev. **91**, 1527 (1953); L. I. Schiff, Phys. Rev. **84**, 1 (1951); R. E. Peierls, Proc. Phys. Soc. (London) **A66**, 313 (1953).

[2] R. L. Pease and H. Feshbach, Phys. Rev. **88**, 945 (1952), present references and recent work.

[3] R. G. Sachs, Phys. Rev. **72**, 312 (1947). Sachs assumes that the wave functions of the conjugate, or mirror, nuclei H^3 and He^3 are identical in the sense that "the wave function of the one nucleus can be obtained from that of the conjugate nucleus by identifying those variables in the one wave function which refer to the neutrons as the variables referring to the protons in the other wave function, and by treating the proton variables in a similar manner." R. Avery and E. N. Adams II, Phys. Rev. **75**, 1106 (1949), conclude that the difference between the H^3 and He^3 wave functions resulting from Coulomb forces has completely negligible effect on the calculated magnetic dipole moments of these nuclei.

[4] R. Avery and R. G. Sachs, Phys. Rev. **74**, 1320 (1948).

[5] F. Villars, Helv. Phys. Acta **20**, 476 (1947) and Phys. Rev. **86**, 476 (1952); R. G. Sachs, Phys. Rev. **74**, 433 (1948) and Phys. Rev. **75**, 1605 (1949); Blanchard, Avery, and Sachs, Phys. Rev. **78**, 292 (1950); R. K. Osborne and L. L. Foldy, Phys. Rev. **79**, 795 (1950); N. Austern and R. G. Sachs, Phys. Rev. **81**, 710 (1951); A. Russek and L. Spruch, Phys. Rev. **87**, 1111 (1952); N. Austern, Phys. Rev. **92**, 670 (1953).

[6] M. Ross, Phys. Rev. **88**, 935 (1952).

[7] L. Rosenfeld, *Nuclear Forces* (Interscience Publishers, Inc., New York, 1948), Sec. A2.251, and Physica **17**, 461 (1951); D. R. Inglis, Revs. Modern Phys. **25**, 390 (1953).

which yield observed magnetic moments of H^3 and He^3 has been published.[8] Adams[9] has made a study of certain hyperfine-structure effects in tritium according to several theories of the origin of the triton moment anomaly. He concludes that the effects do not serve as a possible means of distinguishing among the several theoretical accounts of the triton moment anomaly.

The purposes of the present work are (a) to construct certain types of three-body interactions which give rise to interaction moments and which introduce only P state in a first-order calculation and (b) to study, in a very limited and circumscribed manner, the effects of these interactions on the wave functions, magnetic dipole moments, and binding energies of H^3 and He^3. This work may be of use in further investigations in which these interactions are combined with other interactions to describe nuclear properties in a more comprehensive fashion. We assume throughout that the wave functions of the two nuclei are identical.[8] Our interactions turn out to involve spin-orbit interactions, and development of the independent-particle model has focused attention on this sort of interaction.[10] Spin-orbit interactions are also useful in describing high-energy nucleon-nucleon scattering.[11]

INTERACTIONS AND OPERATORS

To limit the possible forms of interaction, we use the eight general invariance requirements listed by Eisenbud and Wigner.[12] In the present study we consider only those three-body interactions which (a) contain no power of momentum higher than the first, (b) introduce only P state in a first-order calculation, (c) involve no dependence on charge, and (d) contain real scalar radial factors of the sort $f(r_{12},r_{23},r_{31})$, where $r_{ij}=\sqrt{(\mathbf{r}_{ij}\cdot\mathbf{r}_{ij})}$ and $\mathbf{r}_{ij}$ gives the position of particle i relative to particle j. Restriction (b) implies that the interaction must transform in ordinary space[13] like an axial vector. Since the interaction must be invariant under rotations in combined spin-ordinary space, any interaction of the sort considered here may be written as a sum of terms of the form $H'=f(r_{12},r_{23},r_{31})$(axial vector operator in spin space)$\cdot$(axial vector operator in ordinary space).

It is not difficult to show that, for a three-nucleon system, there are just twenty linearly independent isotopic operators which satisfy the general conditions of invariance. In spite of the general conditions that the interaction be symmetric under time reversal and under interchange of any pair of particles, the number of products (axial vector operator in spin space)$\cdot$(axial vector operator in ordinary space)(isotopic operator) is large. In order to reduce the number of such products available, we have ignored the isotopic formalism by taking the isotopic operator to be 1. An interaction with this isotopic factor must be symmetric under interchange of any pair of *identical* particles. Two other important simplifications are obtained by omission of the isotopic formalism: (a) We wish to follow Sachs[8] and assume that the wave functions of the nuclei H^3 and He^3 are identical. Some isotopic factors other than 1 lead to perturbed wave functions for the two nuclei which are essentially not identical. (b) The form of interaction includes no space exchange operator; hence only nonexchange interaction moments appear.

In the wave function of $H^3(He^3)$ we designate the proton (neutron) variables by a subscript 1, and we define B_{ij} as $(1+\boldsymbol{\sigma}_i\cdot\boldsymbol{\sigma}_j)/2$. In spin space there are axial vector operators $\boldsymbol{\sigma}_1$, $\boldsymbol{\sigma}_2$, $\boldsymbol{\sigma}_3$, and scalar operators 1, $\boldsymbol{\sigma}_1\cdot\boldsymbol{\sigma}_2$, $\boldsymbol{\sigma}_2\cdot\boldsymbol{\sigma}_3$, $\boldsymbol{\sigma}_3\cdot\boldsymbol{\sigma}_1$; but there are no polar vector or pseudoscalar operators. The axial vector operator in spin space must then be a linear combination containing one or more of the nine linearly independent operators listed in Table I. Any product among these operators is reducible by the commutation relations to a linear combination of the operators listed, and each of the operators is Hermitian. In ordinary space there are useful polar vector, axial vector, scalar, and pseudoscalar operators. Examples are, respectively, $\mathbf{r}_{12}$, $\mathbf{p}_{12}$; $\mathbf{r}_{31}\times\mathbf{r}_{12}$, $\mathbf{r}_{12}\times\mathbf{p}_{12}$; 1, $\mathbf{r}_{12}\cdot\mathbf{p}_{31}$; and $\mathbf{r}_{31}\cdot\mathbf{r}_{12}\times\mathbf{p}_{31}\equiv(\mathbf{r}_{31}\mathbf{r}_{12}\mathbf{p}_{31})$. The axial vector operator in ordinary space must then be a linear combination containing one or more of twenty-one linearly independent operators. The condition that the operator be Hermitian reduces from twenty-one to thirteen the number of linearly independent operators available. The axial vector operator in ordinary space must then be a linear combination containing one or more of the thirteen linearly independent Hermitian axial vector operators in ordinary space listed in Table II.

The general interaction available under restrictions imposed up to this point is a sum of terms of the sort $f_{ij}\mathbf{S}_i\cdot\mathbf{K}_j$, where $\mathbf{S}_i$ is one of the nine spin operators of Table I and $\mathbf{K}_j$ is one of the thirteen ordinary operators of Table II. No loss of generality is implied by the restriction that each of the axial vector operators contain only one of the tabulated operators, for linear com-

TABLE I. Axial vector operators in spin space.

Symbol and operator	Symmetry: Time reversal	Symmetry: Interchange of particles 2 and 3
$\mathbf{S}_1=\boldsymbol{\sigma}_1$	−	+
$\mathbf{S}_2=\boldsymbol{\sigma}_2+\boldsymbol{\sigma}_3$	−	+
$\mathbf{S}_3=\boldsymbol{\sigma}_2-\boldsymbol{\sigma}_3$	−	−
$\mathbf{S}_4=\boldsymbol{\sigma}_2\times\boldsymbol{\sigma}_3$	+	−
$\mathbf{S}_5=\boldsymbol{\sigma}_1\times\boldsymbol{\sigma}_2-\boldsymbol{\sigma}_3\times\boldsymbol{\sigma}_1$	+	+
$\mathbf{S}_6=\boldsymbol{\sigma}_1\times\boldsymbol{\sigma}_2+\boldsymbol{\sigma}_3\times\boldsymbol{\sigma}_1$	+	−
$\mathbf{S}_7=B_{23}\boldsymbol{\sigma}_1$	−	+
$\mathbf{S}_8=B_{12}\boldsymbol{\sigma}_3+B_{31}\boldsymbol{\sigma}_2$	−	+
$\mathbf{S}_9=B_{12}\boldsymbol{\sigma}_3-B_{31}\boldsymbol{\sigma}_2$	−	−

[8] Blanchard, Avery, and Sachs, reference 5, discuss calculations of interaction moments performed with two-body interactions that can introduce P state; but they neglect effects of this P state on calculated magnetic moments.

[9] E. N. Adams II, Phys. Rev. 81, 1 (1951).

[10] I. Bloch has suggested in a private communication (1952) that the special spin-orbit interactions of the shell model may be the result of many-body spin-orbit interactions.

[11] For example, K. M. Case and A. Pais, Phys. Rev. 80, 203 (1950).

[12] L. Eisenbud and E. P. Wigner, Proc. Natl. Acad. Sci. 27, 281 (1941).

[13] By "ordinary space" we mean "ordinary three-space in which transformations are independent of spin space."

binations may be obtained by suitable choice of the f_{ij} in the sum. Since the interaction must be symmetric under time reversal, only $(3\times1)+(6\times12)=75$ permissible products $\mathbf{S}_i\cdot\mathbf{K}_j$ can be formed. Each of these products has a definite symmetry under interchange of identical particles. It follows that the scalar radial functions f_{ij} associated with each product must have a definite symmetry under interchange of identical particles, for the interaction itself must be symmetric under this interchange. In order to simplify further the following discussion, we consider hereinafter only those three-body interactions which are not a sum of terms, but a *single* term of the sort $H_{ij}'=f_{ij}\mathbf{S}_i\cdot\mathbf{K}_j$.

The interaction moment operators $\mathbf{M}_{ij}$ arising from the interactions considered may be written by use of the results of Sachs and Austern.[14] These operators are listed below in units of the nuclear magneton, $eh/2mc$. The F is $mf_{ij}/\hbar$, and $\mathbf{R}_n$ is the coordinate of particle n with respect to the center of mass of the system. The superscript on H^3 and He^3 is omitted for convenience.

$$\mathbf{M}_{i1}(\mathrm{H})=\mathbf{M}_{i1}(\mathrm{He})=0,$$
$$\mathbf{M}_{i2}(\mathrm{H})=F\mathbf{R}_1\times[(\mathbf{r}_{31}-\mathbf{r}_{12})\times\mathbf{S}_i],$$
$$\mathbf{M}_{i2}(\mathrm{He})=F[\mathbf{R}_2\times(\mathbf{r}_{12}\times\mathbf{S}_i)-\mathbf{R}_3\times(\mathbf{r}_{31}\times\mathbf{S}_i)],$$
$$\mathbf{M}_{i3}(\mathrm{H})=F\mathbf{R}_1\times(\mathbf{r}_{23}\times\mathbf{S}_i),$$
$$\mathbf{M}_{i3}(\mathrm{He})=F[\mathbf{R}_2\times(\mathbf{r}_{12}\times\mathbf{S}_i)+\mathbf{R}_3\times(\mathbf{r}_{31}\times\mathbf{S}_i)],$$
$$\mathbf{M}_{i4}(\mathrm{H})=F\mathbf{R}_1\times[(\mathbf{r}_{12}-\mathbf{r}_{31})\times\mathbf{S}_i],$$
$$\mathbf{M}_{i4}(\mathrm{He})=F[\mathbf{R}_2\times(\mathbf{r}_{31}\times\mathbf{S}_i)-\mathbf{R}_3\times(\mathbf{r}_{12}\times\mathbf{S}_i)],$$
$$\mathbf{M}_{i5}(\mathrm{H})=F\mathbf{R}_1\times(\mathbf{r}_{23}\times\mathbf{S}_i),$$
$$\mathbf{M}_{i5}(\mathrm{He})=F[\mathbf{R}_2\times(\mathbf{r}_{31}\times\mathbf{S}_i)+\mathbf{R}_3\times(\mathbf{r}_{12}\times\mathbf{S}_i)],$$
$$\mathbf{M}_{i6}(\mathrm{H})=F[(\mathbf{r}_{31}\times\mathbf{r}_{12})\times\mathbf{R}_1][(\mathbf{r}_{31}-\mathbf{r}_{12})\cdot\mathbf{S}_i],$$
$$\mathbf{M}_{i6}(\mathrm{He})=F(\mathbf{r}_{31}\times\mathbf{r}_{12})\times[\mathbf{R}_2(\mathbf{r}_{12}\cdot\mathbf{S}_i)-\mathbf{R}_3(\mathbf{r}_{31}\cdot\mathbf{S}_i)],$$
$$\mathbf{M}_{i7}(\mathrm{H})=F[(\mathbf{r}_{31}\times\mathbf{r}_{12})\times\mathbf{R}_1](\mathbf{r}_{23}\cdot\mathbf{S}_i),$$
$$\mathbf{M}_{i7}(\mathrm{He})=F(\mathbf{r}_{31}\times\mathbf{r}_{12})\times[\mathbf{R}_2(\mathbf{r}_{12}\cdot\mathbf{S}_i)+\mathbf{R}_3(\mathbf{r}_{31}\cdot\mathbf{S}_i)],$$
$$\mathbf{M}_{i8}(\mathrm{H})=F[(\mathbf{r}_{31}\times\mathbf{r}_{12})\times\mathbf{R}_1][(\mathbf{r}_{12}-\mathbf{r}_{31})\cdot\mathbf{S}_i],$$
$$\mathbf{M}_{i8}(\mathrm{He})=F(\mathbf{r}_{31}\times\mathbf{r}_{12})\times[\mathbf{R}_2(\mathbf{r}_{31}\cdot\mathbf{S}_i)-\mathbf{R}_3(\mathbf{r}_{12}\cdot\mathbf{S}_i)],$$
$$\mathbf{M}_{i9}(\mathrm{H})=F[(\mathbf{r}_{31}\times\mathbf{r}_{12})\times\mathbf{R}_1](\mathbf{r}_{23}\cdot\mathbf{S}_i),$$
$$\mathbf{M}_{i9}(\mathrm{He})=F(\mathbf{r}_{31}\times\mathbf{r}_{12})\times[\mathbf{R}_2(\mathbf{r}_{31}\cdot\mathbf{S}_i)+\mathbf{R}_3(\mathbf{r}_{12}\cdot\mathbf{S}_i)],$$
$$\mathbf{M}_{i10}(\mathrm{H})=\mathbf{M}_{i10}(\mathrm{He})=0,$$
$$\mathbf{M}_{i11}(\mathrm{H})=-\mathbf{M}_{i11}(\mathrm{He})=F(\mathbf{r}_{31}\mathbf{r}_{12}\mathbf{S}_i)(\mathbf{r}_{23}\times\mathbf{R}_1),$$
$$\mathbf{M}_{i12}(\mathrm{H})=\mathbf{M}_{i12}(\mathrm{He})=0,$$
$$\mathbf{M}_{i13}(\mathrm{H})=\tfrac{1}{2}\mathbf{M}_{i13}(\mathrm{He})=\mathbf{M}_{i11}(\mathrm{H}).$$

THE UNPERTURBED SYSTEM

We consider the nucleus H^3 (or He^3) as a system of three particles each of mass m[15] with position vectors $\mathbf{r}_1$, $\mathbf{r}_2$, $\mathbf{r}_3$, where particles 2 and 3 are identical. We take the unperturbed Hamiltonian of the system to be[16] $H=[(p_1^2+p_2^2+p_3^2)/2m]+[k(r_{12}^2+r_{23}^2+r_{31}^2)/2]+D$, where k is a real positive constant and D is a real constant. In order to separate and solve the unperturbed Schrödinger equation, we transform to normal coordinates in which $\boldsymbol{\rho}_i$ has components x_i, y_i, and z_i by the relations

$$x_1=-X_2/\sqrt{2}+X_3/\sqrt{2},$$
$$x_2=2X_1/\sqrt{6}-X_2/\sqrt{6}-X_3/\sqrt{6},$$
$$x_3=X_1/\sqrt{3}+X_2/\sqrt{3}+X_3/\sqrt{3},$$

and by similar relations for y and z components. The space-dependent factor of the wave function is

$$u_{t1,\,t2}=u_{n1}(x_1)u_{p1}(y_1)u_{q1}(z_1)u_{n2}(x_2)u_{p2}(y_2)u_{q2}(z_2)\times u(x_3,y_3,z_3)=u_{n1,\,p1,\,q1,\,n2,\,p2,\,q2}u(x_3,y_3,z_3),$$

where

$$(t1)=(n1)+(p1)+(q1),\quad (t2)=(n2)+(p2)+(q2),$$
$$u(x_3,y_3,z_3)=C\exp(i\mathbf{P}_3\cdot\boldsymbol{\rho}_3/\hbar),$$
$$u_{n1}(x_1)=N_{n1}H_{n1}(x_1/a)\exp(-x_1^2/2a^2),$$
$$(n1)=0,\,1,\,2,\,\cdots,$$
$$N_{n1}=[(n1)!\,2^{n1}a\pi^{\frac{1}{2}}]^{-\frac{1}{2}},\quad a=(\hbar^2/3km)^{\frac{1}{4}},$$

H_{n1} is an Hermite polynomial, and the remaining u's are similar to $u_{n1}(x_1)$. If we assume that the momentum of the center of mass of the nucleus $\mathbf{P}_3$ is zero and that $C=1$, then the space-dependent factor is normalized and the energy eigenvalues are

$$E_{t1,\,t2}=[(t1)+(t2)+3](\hbar^2/ma^2)+D.$$

The spin-dependent factor of the wave function must be a linear combination containing one or more of the eight linearly independent spin functions for three

TABLE II. Axial vector operators in ordinary space.

Symbol and operator	Symmetry: Time reversal	Symmetry: Interchange of particles 2 and 3
$\mathbf{K}_1=\mathbf{r}_{31}\times\mathbf{r}_{12}$	+	−
$\mathbf{K}_2=\mathbf{r}_{12}\times\mathbf{p}_{12}+\mathbf{r}_{31}\times\mathbf{p}_{31}$	−	+
$\mathbf{K}_3=\mathbf{r}_{12}\times\mathbf{p}_{12}-\mathbf{r}_{31}\times\mathbf{p}_{31}$	−	−
$\mathbf{K}_4=\mathbf{r}_{31}\times\mathbf{p}_{12}+\mathbf{r}_{12}\times\mathbf{p}_{31}$	−	+
$\mathbf{K}_5=\mathbf{r}_{31}\times\mathbf{p}_{12}-\mathbf{r}_{12}\times\mathbf{p}_{31}$	−	−
$\mathbf{K}_6=-2\hbar i(\mathbf{r}_{31}\times\mathbf{r}_{12})+\mathbf{r}_{12}(\mathbf{r}_{31}\mathbf{r}_{12}\mathbf{p}_{12})+\mathbf{r}_{31}(\mathbf{r}_{31}\mathbf{r}_{12}\mathbf{p}_{31})$	−	−
$\mathbf{K}_7=\mathbf{r}_{12}(\mathbf{r}_{31}\mathbf{r}_{12}\mathbf{p}_{12})-\mathbf{r}_{31}(\mathbf{r}_{31}\mathbf{r}_{12}\mathbf{p}_{31})$	−	+
$\mathbf{K}_8=\hbar i(\mathbf{r}_{31}\times\mathbf{r}_{12})+\mathbf{r}_{31}(\mathbf{r}_{31}\mathbf{r}_{12}\mathbf{p}_{12})+\mathbf{r}_{12}(\mathbf{r}_{31}\mathbf{r}_{12}\mathbf{p}_{31})$	−	−
$\mathbf{K}_9=\mathbf{r}_{31}(\mathbf{r}_{31}\mathbf{r}_{12}\mathbf{p}_{12})-\mathbf{r}_{12}(\mathbf{r}_{31}\mathbf{r}_{12}\mathbf{p}_{31})$	−	+
$\mathbf{K}_{10}=(\mathbf{r}_{31}\times\mathbf{r}_{12})(-8\hbar i+\mathbf{r}_{12}\cdot\mathbf{p}_{12}+\mathbf{r}_{31}\cdot\mathbf{p}_{31})$	−	−
$\mathbf{K}_{11}=(\mathbf{r}_{31}\times\mathbf{r}_{12})(\mathbf{r}_{12}\cdot\mathbf{p}_{12}-\mathbf{r}_{31}\cdot\mathbf{p}_{31})$	−	+
$\mathbf{K}_{12}=(\mathbf{r}_{31}\times\mathbf{r}_{12})(4\hbar i+\mathbf{r}_{31}\cdot\mathbf{p}_{12}+\mathbf{r}_{12}\cdot\mathbf{p}_{31})$	−	−
$\mathbf{K}_{13}=(\mathbf{r}_{31}\times\mathbf{r}_{12})(\mathbf{r}_{31}\cdot\mathbf{p}_{12}-\mathbf{r}_{12}\cdot\mathbf{p}_{31})$	−	+

[14] R. G. Sachs and N. Austern, Phys. Rev. **81**, 705 (1951), Sec. II. It is not difficult to demonstrate that our three-body interactions satisfy the general consequences of gauge invariance given in Sec. III of this reference.

[15] We assume $m=m_p$, for $|m_n-m_p|/(m_n+m_p)<0.1$ percent.

[16] Although this Hamiltonian is unrealistic, it leads to a fairly reasonable ground-state wave function. Hamiltonians of this type have the advantage of allowing calculation of a set of energy eigenfunctions for any nucleus.

TABLE III. Spin functions for three particles.

Symbol and spin function	Eigenvalues of $S^2/\hbar^2$	Eigenvalues of $S_z/\hbar$	Symmetry under interchange of particles 2 and 3
$s_1=\alpha\alpha\alpha$	15/4	3/2	+
$s_2=\beta\beta\beta$	15/4	−3/2	+
$s_3=(\alpha\alpha\beta+\alpha\beta\alpha+\beta\alpha\alpha)/\sqrt{3}$	15/4	1/2	+
$s_4=(\beta\beta\alpha+\beta\alpha\beta+\alpha\beta\beta)/\sqrt{3}$	15/4	−1/2	+
$s_5=(\alpha\alpha\beta+\alpha\beta\alpha-2\beta\alpha\alpha)/\sqrt{6}$	3/4	1/2	+
$s_6=(\beta\beta\alpha+\beta\alpha\beta-2\alpha\beta\beta)/\sqrt{6}$	3/4	−1/2	+
$s_7=(\alpha\alpha\beta-\alpha\beta\alpha)/\sqrt{2}$	3/4	1/2	−
$s_8=(\beta\beta\alpha-\beta\alpha\beta)/\sqrt{2}$	3/4	−1/2	−

particles: $\alpha\alpha\alpha$, $\alpha\alpha\beta$, $\alpha\beta\alpha$, $\beta\alpha\alpha$, $\beta\beta\alpha$, $\beta\alpha\beta$, $\alpha\beta\beta$, $\beta\beta\beta$.[17] It is convenient to group these functions into combinations that are simultaneous eigenfunctions of $\frac{1}{4}(\sigma_1+\sigma_2+\sigma_3)^2 \equiv \mathbf{S}^2/\hbar^2$ and $\frac{1}{2}(\sigma_{1z}+\sigma_{2z}+\sigma_{3z})\equiv S_z/\hbar$. These combinations may be generated with the aid of a spin raising operator $(\sigma_{1x}+\sigma_{2x}+\sigma_{3x})+i(\sigma_{1y}+\sigma_{2y}+\sigma_{3y})$. In Table III are shown a set of such linearly independent orthonormal spin functions. Now the magnetic moment is conventionally described as the expectation value of the z component of a magnetic moment operator over a state in which the z component of total angular momentum has its maximum value $J_z=J$. Since the total angular momentum of each of the nuclei H^3 and He^3 is $\hbar/2$ and since the common wave function of the nuclei must be antisymmetric under interchange of particles 2 and 3, we write the normalized unperturbed ground-state wave function of the nuclei as $\psi_0=s_7u_{000,\,000}$.

For the sake of simplicity the unperturbed ground-state wave function written just above is used in all calculations in this report, although it is possible to carry out the calculations using a slightly more general unperturbed Hamiltonian.[18] Let us take k_{nn1}, k_{pp1}, k_{np1}, and k_{np3} to be force constants between two neutrons in a relative singlet spin state, two protons in a singlet state, a neutron and a proton in a singlet state, and a neutron and a proton in a triplet state, respectively. If $k_{nn1}=k_{pp1}=k_1$ and $k_{np1}=k_{np3}=k_2\neq k_1$, then the normal coordinates are just those defined above; but the eigenfunctions of the altered Hamiltonian contain two distinct a's: $a_1=(\hbar^2/[(2k_1+k_2)m])^{\frac{1}{2}}$ and $a_2=(\hbar^2/3k_2m)^{\frac{1}{2}}$. This choice of force constants seems unacceptable, for it is believed[19] that, although the singlet forces are nearly equal in strength, the triplet force is about 60 percent stronger than the singlet forces. If we attempt to simulate spin-dependent forces by using $k_{nn1}=k_{pp1}=k_{np1}=k_{np3}/1.6$, then the Hamiltonian is not symmetric under interchange of identical particles and the eigenfunctions of the Hamiltonian are not antisymmetric under interchange of identical particles. From these eigenfunctions we may, however, construct antisymmetric functions which are in a sense approximate eigenfunctions of the Hamiltonian. The spin dependence of the forces is properly taken into account by use of a Hamiltonian which contains spin operators and which is symmetric under interchange of identical particles.

[17] Notation for spin functions and operators is that of L. I. Schiff, *Quantum Mechanics* (McGraw-Hill Book Company, Inc., New York, 1949), Sec. 33, with (+) here replaced by α and (−) by β.

[18] For example, W. V. Houston, Phys. Rev. 47, 942 (1935), treats the case of three different force constants and three different masses.

[19] See L. Rosenfeld, *Nuclear Forces*, reference 7, Sec. 3.3 and Tables 6.432, 7.13, and 8.1.

THE PERTURBED SYSTEM

The Ground-State Wave Function and Binding Energies

The perturbed ground-state wave function may be written $\psi=\psi_0+\psi_{ij}'$, where the perturbing wave function ψ_{ij}' is obtained by the standard first-order method. It is easy to show that $\mathbf{p}_{bc}u_0=hia^{-2}\mathbf{r}_{bc}u_0$,[20] a result which is helpful in writing the products $\mathbf{K}_iu_0$ of u_0 by the ordinary operators of Table II. These products reveal that only thirty-two of our seventy-five permissible interactions may yield a nonvanishing perturbing wave function. These interactions contain either a product of any one of the spin operators $\mathbf{S}_1$, $\mathbf{S}_3$, $\mathbf{S}_7$, $\mathbf{S}_8$, $\mathbf{S}_9$ by any one of the ordinary operators $\mathbf{K}_5$, $\mathbf{K}_6$, $\mathbf{K}_8$, $\mathbf{K}_{10}$, $\mathbf{K}_{11}$, $\mathbf{K}_{12}$ or one of the products $\mathbf{S}_4\cdot\mathbf{K}_1$ or $\mathbf{S}_6\cdot\mathbf{K}_1$. For brevity we list these products as $\mathbf{S}_{1,3,7,8,9}\cdot\mathbf{K}_{5,6,8,10,11,12}$, $\mathbf{S}_{4,6}\cdot\mathbf{K}_1$.

The unperturbed potential leads to an infinite binding energy. The first order-energy perturbation vanishes because ψ_0 is spherically symmetric while H_{ij}' transforms like a P state. The perturbed potential is unsuited to energy calculations because it yields an infinite binding energy in a first-order calculation.[21] In view of this fact we shall not consider the second-order energy perturbation.

Magnetic Dipole Moments

In the following calculations we take the observed magnetic dipole moments in nuclear magnetons to be $\mu_p=2.7928$, $\mu_n=-1.9129$, $\mu(H^3)\equiv\mu_H=2.9789$, and $\mu(He^3)\equiv\mu_{He}=-2.1276$.[22] It is not likely that any of these values is in error by much more than ±0.0002.

Our perturbed wave function contains only $^2\bar{S}$, $^2\bar{P}$, $^2\bar{P}$, and $^4\bar{P}$ states, where $\sim$ or — indicates[23] that the spin-dependent factor is antisymmetric or symmetric, respectively, under interchange of particles 2 and 3. The spin and orbital contribution to the magnetic dipole moment may be written by use of the results of Sachs.[3] If the interaction is one which yields a vanishing perturbing wave function, then from spin and orbital contribution alone $\mu_H(\text{calc})=\mu_p<\mu_H$, $\mu_{He}(\text{calc})=\mu_n>\mu_{He}$, and $\mu_H(\text{calc})+\mu_{He}(\text{calc})=\mu_p+\mu_n>\mu_H+\mu_{He}$. If the interaction is one of the thirty-two which may yield a nonvanishing perturbing wave function, we can reach

[20] This result implies at once that all two-body interactions which satisfy the general requirements of invariance and are of first degree in momenta yield no perturbing wave function on application to our ground state. The same conclusion holds for any ground state with space dependence a function of $r_{12}^2+r_{23}^2+r_{31}^2=3(\rho_1^2+\rho_2^2)$; but it does not hold (a) if the function contains $(x_1x_2+y_1y_2+z_1z_2)/(\rho_1\rho_2)$, which is the q of Avery and Sachs, reference 4, or (b) if, as discussed above, the unperturbed Hamiltonian contains two or more distinct force constants.

[21] H. Margenau and D. T. Warren, Phys. Rev. 52, 790 (1937) and D. T. Warren and H. Margenau, Phys. Rev. 52, 1027 (1937), consider a two-body central perturbing potential designed to remove this difficulty.

[22] N. F. Ramsey, *Experimental Nuclear Physics*, E. Segrè, Editor (John Wiley and Sons, Inc., New York, 1953), Vol. 1, Part III. The sign of μ_{He} is from Fred, Tomkins, Brody, and Hammermesh, Phys. Rev. 82, 406 (1951).

[23] Rosenfeld, *Nuclear Forces*, reference 7.

useful conclusions about spin and orbital contributions by considering the general properties of the space dependence and the details of only the spin dependence of the perturbed wave function. It may be shown[24] that any one of the interactions yields by spin and orbital contribution alone $\mu_H(\text{calc}) \leqslant \mu_p < \mu_H$ and $\mu_{He}(\text{calc}) \geqslant \mu_n > \mu_{He}$, although some interactions may possibly give $\mu_H(\text{calc}) + \mu_{He}(\text{calc}) = \mu_H + \mu_{He}$.

Since any one of our interactions yields by spin and orbital contribution alone $\mu_H(\text{calc}) < \mu_H$ and $\mu_{He}(\text{calc}) > \mu_{He}$, it is necessary for agreement with experiment that the interaction contributions $\langle M_z(\text{H}) \rangle$ and $\langle M_z(\text{He}) \rangle$ be different from zero and of opposite sign. In terms of a normalized perturbed wave function ψ, the interaction contribution is $\langle M_z \rangle = (\psi, M_z\psi) = (\psi_0, M_z\psi_0) + (\psi', M_z\psi') + (\psi', M_z\psi_0) + (\psi_0, M_z\psi')$, where the subscripts ij have been omitted from $M_{ij\varepsilon}$ and ψ_{ij}' for brevity. The $(\psi', M_z\psi')$ is hereinafter ignored, for it is essentially a third-order term comparable with terms like $(\psi'', M_z\psi_0)$ arising from a second-order perturbed wave function. Fairly straightforward manipulations reveal[24] (a) that an interaction not containing one of the twenty-four products $\mathbf{S}_{1,7,8} \cdot \mathbf{K}_{2,3,4,5,7,9,11,13}$ gives $(\psi_0, M_z\psi_0) = 0$ and (b) that an interaction not containing one of the twelve products $\mathbf{S}_{1,7,8,9} \cdot \mathbf{K}_{5,6,8}$ gives $(\psi', M_z\psi_0) + (\psi_0, M_z\psi') = 0$. Clearly, then, only thirty-three interactions may yield a nonvanishing interaction contribution. Closer examination of these thirty-three interactions, with extensive use of symmetry and transformation properties but without specialization of the radial factor f in the interactions, shows[24] that sixteen of them do not yield the observed moments. The seventeen interactions remaining for detailed calculations are those containing one of the products $\mathbf{S}_{1,7,8} \cdot \mathbf{K}_{2,4,6,8,11}$ or $\mathbf{S}_9 \cdot \mathbf{K}_{6,8}$.

In order further to test the remaining interactions, it appears necessary to make some assumption about the radial function. If this function contains factors resembling conventional square, Gaussian, exponential, or Yukawa wells, and if the interaction contains one of the products $\mathbf{S}_{1,7,8} \cdot \mathbf{K}_{6,8,11}$ or $\mathbf{S}_9 \cdot \mathbf{K}_{6,8}$, then the perturbing wave function contains, in general, an infinite number of excited functions, $u_{n1,\,p1,\,q1,\,n2,\,p2,\,q2}$. If the plausible value of $a^2 = 2.8 \times 10^{-26}$ cm^2 is selected,[21] then $E_{t1,\,t2} - E_0 = [(t1) + (t2)]$ (14.8 Mev); so there may be appreciable fractions of excited states with $(t1) + (t2) > 6$ associated with a not unreasonable kinetic energy of the system. The calculations involving a perturbing wave function expressed as an infinite series in the excited functions appear difficult; and it is not evident how to estimate the error committed in performing a calculation with a truncated series. If the radial function f is a polynomial in the coordinates of the particles, then the perturbed wave function contains only a finite number of excited functions. We carried out detailed calculations[24] with the radial function

$$f = \frac{V}{ha^2}\left(1 + w\frac{\rho_1^2}{a^2} + v\frac{\rho_2^2}{a^2}\right) = \frac{V}{ha^2}\left[1 + \frac{w}{3}\left(\frac{r_{12}^2 + r_{31}^2}{a^2}\right) + \left(\frac{w}{2} - \frac{v}{6}\right)\frac{r_{23}^2}{a^2}\right]$$

for interactions containing one of the products $\mathbf{S}_{1,7,8} \cdot \mathbf{K}_{11}$ or $\mathbf{S}_9 \cdot \mathbf{K}_{6,8}$ and with the radial function

$$f = \frac{V}{ha^4}\left(1 + w\frac{\rho_1^2}{a^2} + v\frac{\rho_2^2}{a^2}\right)(\boldsymbol{\rho}_1 \cdot \boldsymbol{\rho}_2) = \frac{V}{ha^4}\left[1 + \frac{w}{3}\left(\frac{r_{12}^2 + r_{31}^2}{a^2}\right) + \left(\frac{w}{2} - \frac{v}{6}\right)\frac{r_{23}^2}{a^2}\right]\left(\frac{r_{12}^2 - r_{31}^2}{2\sqrt{3}}\right)$$

for interactions containing one of the products $\mathbf{S}_{1,7,8} \cdot \mathbf{K}_{6,8}$. For all real values of the parameters V, a^2, w, and v the calculated moments differ from the observed moments by many times the experimental error in the observed moments. Omission of the term unity in the second factor of the f does not alter this result. Since the calculations were carried out with a very specialized form of radial function, and since this form is not very reasonable physically, we have no definite conclusion about agreement between observed moments and moments calculated from interactions containing one of the eleven products $\mathbf{S}_{1,7,8} \cdot \mathbf{K}_{6,8,11}$ or $\mathbf{S}_9 \cdot \mathbf{K}_{6,8}$.

Interactions containing one of the products $\mathbf{S}_{1,7,8} \cdot \mathbf{K}_{2,4}$ lead to no perturbing wave function. A radial function which is fairly reasonable physically is

$$f = \frac{V}{h}\left[1 + w\left(\frac{\rho_1^2 - \rho_2^2}{a^2}\right)\right]\exp\left(-\frac{\rho_1^2 + \rho_2^2}{g^2}\right) = \frac{V}{h}\left[1 + \frac{w}{3}\left(\frac{2r_{23}^2 - r_{12}^2 - r_{31}^2}{a^2}\right)\right] \times \exp\left(-\frac{r_{12}^2 + r_{23}^2 + r_{31}^2}{3g^2}\right).$$

If we require that calculated and observed moments be equal, easy calculations show that for an interaction containing one of the products $\mathbf{S}_{1,7,8} \cdot \mathbf{K}_2$,

$$\mu_{He} - \mu_n = 2(mVa^2/h^2)[g^2/(g^2 + a^2)]^4,$$

$$\frac{(\mu_{He} - \mu_n) - (\mu_H - \mu_p)}{\mu_{He} - \mu_n} = wg^2/(g^2 + a^2);$$

and for an interaction containing one of the products $\mathbf{S}_{1,7,8} \cdot \mathbf{K}_4$,

$$(\mu_{He} - \mu_n) - (\mu_H - \mu_p) = 2(mVa^2/h^2)[g^2/(g^2 + a^2)]^4,$$

$$\frac{\mu_{He} - \mu_n}{(\mu_{He} - \mu_n) - (\mu_H - \mu_p)} = wg^2/(g^2 + a^2).$$

[24] A. W. Solbrig, Jr., thesis, Vanderbilt University, 1953 (unpublished). Available on microfilm from University Microfilms, Inc., Ann Arbor, Michigan.

TABLE IV. Some values of parameters in interactions which yield observed moments of H^3 and He^3. ($a^2 = 2.8 \times 10^{-26}$ cm^2.)

	$f(S_{1,7,8} \cdot K_2)$		$f(S_{1,7,8} \cdot K_4)$	
$3g^2$	V (Mev)	w	V (Mev)	w
∞	− 1.59	1.87	− 2.97	0.54
$30a^2$	− 2.33	2.05	− 4.35	0.59
$9a^2$	− 5.03	2.49	− 9.39	0.71
$6a^2$	− 8.05	2.80	−15.0	0.80
a^2	−25.5	3.73	−47.5	1.07

Values of V and w required by a few different values of the range parameter $3g^2$ are presented in Table IV for $a^2 = 2.8 \times 10^{-26}$ cm^2.[21]

REMARKS

Since no interaction which alters the ground-state wave function accounts for the observed magnetic moments in the above calculations, we are not able to calculate the nonvanishing fraction of P state introduced by an interaction which yields observed magnetic moments.

Several suggestions for further work arise from the present study: (a) The effects of linear combinations of the three-body interactions on the magnetic moments are worth consideration, for these effects are not necessarily additive. Preliminary calculations indicate that the nonadditive effects may lead to better agreement between calculated and observed moments. (b) Study of the properties of interactions containing one or more of the other nineteen permissible three-body isotopic operators remains to be undertaken. (c) Combination of the three-body interactions with well-known two-body interactions may account for nuclear properties in a more comprehensive way. In particular, combination of the three-body interactions with the conventional tensor force can lead to an orbital $^4P^4D$ cross term which may reduce the difference between calculated and observed moments. (d) Use of an unperturbed ground-state wave function which depends on $\rho_1 \cdot \rho_2$ or which is not symmetric under interchange of normal coordinates 1 and 2 would cause significant changes in the calculation.[20] It therefore appears desirable to seek other acceptable forms of the unperturbed Hamiltonian and to examine the altered effects of the three-body interactions.

ACKNOWLEDGMENT

The author wishes to thank Professor Ingram Bloch for encouragement, direction, and assistance without which this work would have been impossible.

Letters to the Editor

PUBLICATION of brief reports of important discoveries in physics may be secured by addressing them to this department. The closing date for this department is five weeks prior to the date of issue. No proof will be sent to the authors. The Board of Editors does not hold itself responsible for the opinions expressed by the correspondents. Communications should not exceed 600 words in length and should be submitted in duplicate.

The Metamict State

WILLIAM PRIMAK
Chemistry Division, Argonne National Laboratory, Lemont, Illinois
(Received May 10, 1954)

IN a preliminary report on the behavior of a number of insulators exposed to energetic neutrons within a nuclear reactor,[1] it was reported that large changes in physical properties had been observed in diamond, silicon carbide, quartz, and vitreous silica. These property changes and their behavior seemed similar to the property changes associated with the metamictization of minerals,[2] which is attributed to the passage of alpha particles emitted from their own radioactive content. The substances previously examined and a number of others have now been exposed simultaneously in a nuclear reactor at a tempertaure believed to be above room temperature but below 100°C. An x-ray examination of these substances has now been completed and suggests a rather different conclusion as to the substances susceptible to metamictization than those suggested by Goldschmidt,[3] Pellas,[4] and others. It therefore seems desirable to report the results.

As a result of the irradiation, the following substances showed no detectable change in powder pattern: beryl, germanium dioxide (α-quartz structure), germanium, silicon, corundum, and rutile; the following substances showed only the small percent increases in lattice constant given in parentheses: magnesium oxide (0.1), spinel (0.12), calcium fluoride (0.08); the following substances showed the large percent changes given in parentheses but did not show any marked diffuseness in their diffraction patterns: diamond (0.9), silicon carbide (a, 0.68; c, 0.68). In the same irradiation were present samples of quartz, tridymite, and cristobalite. Their diffraction patterns became so diffuse that it was no longer possible to measure the positions of any lines. Chrysoberyl and phenacite irradiated under similar conditions but for about half the time showed a noticeable increase in lattice constant as shown by displacement of lines in the back reflection region (θ *ca* 80 deg) of ½ to 1 deg but there was no noticeable line broadening. On the other hand, the diffraction pattern of a sample of tridymite irradiated simultaneously was diffuse even in the forward reflection region, and no lines could be distinguished past θ *ca* 10 degs.

From these results it is clear that the effects associated with metamictization cannot be associated with a particular crystal structure or bond type. Rather, it seems necessary that the substance possess a quasi-stable vitreous (disordered) state under the conditions of irradiation. The susceptibleness to metamictization is not determined by the state present *ab initio*, but by the difficulty of recrystallization of the disordered regions formed by the traverse of energetic atomic particles, and by the difficulty with which the displaced atoms can again form bonds. The former would give rise to large changes in the x-ray diffraction pattern, the latter to large amounts of stored energy.

The x-ray diffraction patterns were taken and measured by Stanley Siegel of this Laboratory.

Notes added in proof: (1) All of the samples which were irradiated simultaneously, were irradiated in the same container for the same time. The significant neutron flux as a function of energy E is not known, but probably does not differ greatly (by more than a factor of two) from the distribution (constant/E). From a combination of theoretical considerations and experiments performed in various reactor facilities, it seems likely that most of the damage was produced by neutrons between 0.01 and 1–2 Mev. Then, if a dosage unit is defined as the damage produced in a standard substance by $(10^{18} \int_{0.01}^{1} d \ln E)$ neutrons/cm², the radiation-damage dosage of these samples was found to be about 120 units and of the chrysoberyl and phenacite about 50 units, to within the precision usually attained in such experiments (20 percent).

(2) The elastic-constant changes reported by Binnie and Liebschutz[5] for silicon irradiated for a shorter dosage than the sample reported here is taken as evidence of the recrystallization hypothesis proposed here.

[1] Primak, Fuchs, and Day, Phys. Rev. **92**, 1064 (1953).
[2] A. Pabst, Am. Mineralogist **37**, 137 (1952).
[3] V. M. Goldschmidt, Skrifter Norske, Videnskaps-Akad. Oslo, I. Mat.-Naturv. Kl. **1**, No. 5, 51–58 (1924).
[4] P. Pellas, Compt. rend. **233**, 369 (1951).
[5] W. P. Binnie and A. M. Liebschutz, Phys. Rev. **91**, 1410 (1954).

Shape of the *F* Band

R. V. HESKETH AND E. E. SCHNEIDER*
King's College, University of Durham, Newcastle upon Tyne, England
(Received June 7, 1954)

PREVIOUS measurements by Mollwo[1] have shown that the F absorption band in additively colored alkali halide crystals has a Lorentzian shape, and it has been generally assumed that this shape is a fundamental property of the F center and independent of the method of coloration. However, several measurements on potassium chloride crystals colored by 200-kv x-rays have shown that the F band thus formed is more nearly Gaussian in shape.

Crystals were colored at both 290°K and 113°K. In the former case a maximum concentration of 10^{17} centers per cc was obtained, while at the lower temperature only 10^{16} centers per cc were formed, though it is probable that this was not a maximum concentration. The concentrations were sensibly uniform through crystals of several millimeters thickness.

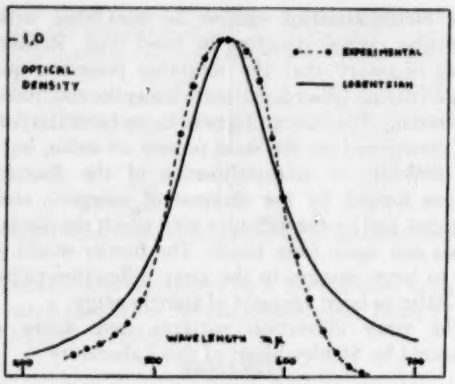

FIG. 1. The F band at 290°K.

X-irradiation creates a well-known subsidiary absorption band in the high-frequency tail of the F band, which distorts its shape at ordinates less than approximately 15 percent of the absorption maximum. At the lower temperature the F' band is also created by x-irradiation, but it can be removed by optical bleaching in F light, an unexpected result in view of the formation of the F' band in additively colored crystals exposed to F light. At room temperature only M secondary centers are created in addition to the F band, and the two absorptions do not overlap. Thus the shape of the whole of the low-frequency side of the F band can be determined at both temperatures, see Figs. 1 and 2.

On the high-frequency side, the F absorption curve is accurately Gaussian down to the 15 percent ordinate, but the equation of the low-frequency side has an index which is not two, and which appears to be temperature-dependent. At room temperature the optical density has the equation, $D=D_{\max}\exp[-(\nu_{\max}-\nu)^{2.5}]$, while at 113°K, after removal of the F' band and the recovery of the F band from bleaching,[2] the index is 2.8.

Measurements have not yet been made on additively colored crystals having a comparable number of centers, nor on x-irradiated crystals containing higher concentrations. Our results on the shape together with those on the half-width[3] of the F-band point to a significant difference between the two types of coloration.

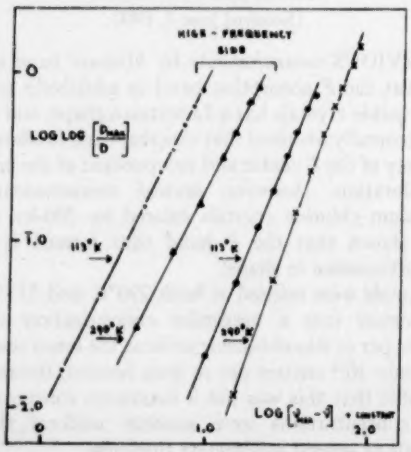

FIG. 2. A Gaussian plot of the F-band absorption.

* At Duke University, Durham, North Carolina, 1953–1954.
[1] E. Mollwo, Z. Physik **85**, 56 (1933).
[2] Markham, Platt, and Mador, Phys. Rev. **92**, 597 (1953).
[3] Mador, Markham, and Platt, Phys. Rev. **91**, 1277 (1953).

Precipitation of Impurities at Dislocations in Heat-Treated Silicon

SUMNER MAYBURG
Sylvania Electric Products, Bayside, New York
(Received June 10, 1954)

WE have conducted a series of heat treatments on silicon which suggest precipitation of impurities at dislocations when the silicon is heated below 900°C. The idea that impurities segregate at dislocations below a certain critical temperature was suggested by the work of Cottrell.[1] The same idea has been applied to the interaction of impurities with dislocations in germanium by Kurtz and Kulin[2] and to the interaction of interstitial germanium with dislocations in germanium by Mayburg.[3]

The single-crystal silicon used was pulled from a quartz boat. Its resistivity before any heat treatment was approximately 8 ohm-cm, p type. The samples are heated by passing current through them in high vacuum, and the effects of the heat treatment are measured by quenching and studying changes in room temperature conductivity. The experimental setup is identical with that previously used for heat treatment studies in germanium.[3]

Any changes in room temperature conductivity σ can be ascribed primarily to changes in the concentration of acceptors N_A or donors N_D. Since the conductivity is

$$\sigma=(N_A-N_D)e\mu_p,$$

where e is the charge of a hole and μ_p is the hole mobility, an irreversible change in σ would correspond to either a continuous increase or decrease with the time of heat treatment in the concentration of either the acceptors or the donors in the sample. Our experimental arrangement is such that it is only possible that impurities are leaving the sample by evaporation. Therefore, any irreversible conductivity change we might observe would result from the loss of either acceptors or donors.

At approximately 1100°C, and also around 1300°C, we observed irreversible increases in the conductivity of an original p-type sample of 100 percent and 25 percent, respectively. The fact that these increases occur at two characteristic temperatures suggest that in this particular p-type crystal there are at least two donor impurities which can be evaporated out of the silicon.

We find that by heating a fresh sample above or below 900°C, we increase or decrease respectively the

room temperature conductivity in an almost reversible way. At low heat-treatment temperatures there is reason to expect that the *n*-type impurities would segregate around edge dislocations because of the strain-energy interaction between edge dislocations and impurity atoms. If we heat treat a sample at a sufficiently high temperature, these impurities are thermally agitated, escape the strain potential energy of the dislocation, and distribute themselves uniformly throughout the crystal. We find that the conductivity of the sample goes down because of the compensation of these *n*-type impurities. The *p*-type impurities, probably substitutional, are considered to be immobile. If we now anneal the crystal at a temperature below 900°C, the thermal energy of the impurities is not sufficient to keep them from being trapped at the dislocations and we find that the conductivity goes back to its original value and slightly above. The aforementioned cycle is not closed because it is not possible to heat the sample to the range close to 1100°C without evaporating some of the impurities. If there were no evaporation of impurities at all, the flow of impurities in and out of edge dislocations would be a completely reversible process.

One of the striking similarities between the condensation of impurities and interstitial germanium at the dislocations in germanium and the condensation of impurities at dislocations in silicon is the fact that the critical temperature for condensation at the dislocation, which is 900°C in silicon, corresponds to the temperature at which plastic deformation can be first observed in silicon. Similarly, the temperature at which interstitial germanium and impurities like copper[4] condense at dislocation lines in germanium is approximately 500°C, which happens to be the temperature at which plastic deformation in germanium becomes noticeable. This correlation points up the possibility mentioned by Seitz[5] that the influence of impurity atoms in locking dislocations in germanium and silicon may have a dominant influence on the plastic properties of these semiconductors.

[1] A. H. Cottrell, *Dislocations and Plastic Flow in Crystals* (Oxford University Press, London, 1953), p. 134.
[2] A. D. Kurtz and S. A. Kulin, Acta Metallurgica **2**, 354 (1954).
[3] S. Mayburg, Phys. Rev. **95**, 38 (1954).
[4] Fuller, Struthers, Ditzenberg, and Wolfstein, Phys. Rev. **93**, 1187 (1954).
[5] G. J. Gallagher, Phys. Rev. **88**, 721 (1952); F. Seitz, Phys. Rev. **88**, 722 (1952).

Electron-Electron Scattering in Alkali Metals*

ELIHU ABRAHAMS
Department of Physics, University of Illinois, Urbana, Illinois
(Received June 7, 1954)

THE calculation of the electron-electron scattering cross section in a degenerate Fermi gas which is reported here was prompted by recent interest in the electron-electron collision mean free path in alkali metals. Reference is made here to recent developments in the interpretation[1] of electron spin resonance line widths,[2] work on electromagnetic absorptivity and anomalous skin effect in metals,[3] and thermal conductivity. In order that electron-electron collisions have an effect in these cases, the mean free path must be comparable to the ordinary electron-phonon mean free path which enters the expression for the resistivity. The result is that this condition is not met.

TABLE I. Electron-electron scattering cross section in sodium.

Energy of relative motion	Total cross section
0.253 rydberg = Fermi energy	$\sigma_F = 17\pi a_0^2$
0	$\sigma_0 = 60\pi a_0^2$

The electron-electron interaction in the metal is of the screened Coulomb type. The character of the electronic interactions in metals has been discussed at length by Pines.[4] We approximate the interaction by a potential of the form $V=(1/r)\exp(-r/r_0)$ (atomic units). Here r_0 is the screening radius for which values for various metals have been given in reference 4, and r is the separation of the interacting particles. We employ the one-electron approximation and use plane waves as the wave functions for the single-particle states. The effect of the periodic potential of the metallic crystal is accounted for by the introduction of an effective mass.

The validity criterion[5] for the Born approximation is not met in the present case since the electron energies are not large. The Born approximation is likely to be invalid for all problems involving the scattering of metallic electrons of a few volts energy unless the effective charge of the potential is very small. In the present case, the Born approximation overestimates the scattering by a factor 5.

The scattering must therefore be calculated by the partial wave method. Only *s*-wave scattering contributes appreciably to the cross section. Overhauser[6] has estimated the *s*-wave phase shift using a somewhat different potential. His result yields a smaller cross section than that obtained here. The calculation of the *s*-wave phase shift is carried out here by numerically integrating the wave equation for the relative motion within the range of the potential. The results for sodium are presented in Table I, where a_0 indicates the Bohr radius.

The mean free path l, for electron-electron collisions, can then be estimated by

$$l \approx (1/N\sigma_F)(E_F/kT)^2,$$

where N is the density of conduction electrons and E_F is the Fermi energy. The two factors of E_F/kT account for the availability of initial and final states which are restricted by the Fermi distribution function in the metal. The mean free path for sodium is then $\sim$4.5 microns at 300°K and $\sim$2.5 cm at 4°K. The electron-electron mean free path is thus longer than the electron-

phonon mean free path throughout this range of temperatures.

At 8°K, the electron-phonon mean free path is about 0.08 cm as determined by the experiments of MacDonald and Mendelssohn.[7] If we extrapolate this result by means of the Bloch-Gruneisen T^5 law, we find that at 4°K, the electron-phonon and electron-electron free paths are comparable. The concept of an electron-phonon free path is used here for purposes of comparison of the importance of the two effects. 4°K is a temperature at which the lattice scattering is negligible compared to the residual resistance. These remarks tend to show that electron-electron scattering effects are less important that lattice or impurity scattering throughout all temperatures.

The author is indebted to Professor D. Pines for valuable discussion.

* Research supported in part by the U. S. Office of Naval Research.

[1] F. J. Dyson (to be published).
[2] G. Feher and T. W. Griswold, Phys. Rev. **93**, 952 (1954).
[3] T. Holstein, Phys. Rev. **91**, 490 (1953).
[4] D. Pines, Phys. Rev. **92**, 626 (1953).
[5] D. Bohm, *Quantum Theory* (Prentice Hall, Inc., New York, 1951), p. 552.
[6] A. W. Overhauser, thesis, University of California, Berkeley, 1951 (unpublished).
[7] D. K. C. MacDonald and K. Mendelssohn, Proc. Roy. Soc. (London) **A202**, 103 (1950).

Two Types of Band Emission Curves of Copper in the Soft X-Ray Region

GUNJI SHINODA, TATSURO SUZUKI, AND SUSUMU KATO
Laboratory for Applied Physics, Faculty of Engineering, Osaka University, Osaka, Japan

(Received June 15, 1954)

EXPERIMENTAL curves showing the energy distribution of the higher electronic levels in solid metals may be obtained from the soft x-ray emission spectra of metals. The methods which have been used may be described as follows: (a) the voltages applied to the anticathode are kept constant and the generally soft x-rays emitted are analyzed by means of a diffraction grating, and (b) the voltages applied to the anticathode are varied gradually, the soft x-rays thus emitted are detected with a photoelectric device, and the resulting voltage *vs* photocurrent curves are differentiated graphically.

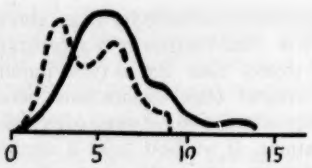

FIG. 2. The full curve shows the typical result obtained by previous investigators and the dotted one shows the theoretical curve of Rudberg and Slater (reference 6).

The former method has recently been improved and used by several investigators,[1] while the latter method has not been used for nearly thirty years.

We have improved this latter method. In our method electronic differentiation devices are used instead of an inaccurate graphical one, and the voltages applied to the anticathode are supplied from the saw-tooth wave oscillator of 100 cps. In this way spectral intensity curves of the soft x-ray may be shown directly on a cathode-ray oscillograph.[2,3] As the period of the repetition of the saw-tooth wave is fairly short, occasional changes due to adhesion and liberation of gas molecules do not cause any harmful effects.

Some of the results obtained for $M_{II,III}$ emission curves of pure copper are shown in Fig. 1. Two types of spectrograms were found. The one shown in (a) resembles those of a number of workers,[4,5] while the one shown in (b) has not been hitherto found. The full curve in Fig. 2 shows the typical result obtained by previous investigators and the dotted one shows the result obtained by Rudberg and Slater[6] theoretically; the latter curve is quite similar to our curve (b).

Usually, a curve like that shown in (a) was observed on the oscillogram. However, the curve frequently changes its shape and after a short transient stage, as

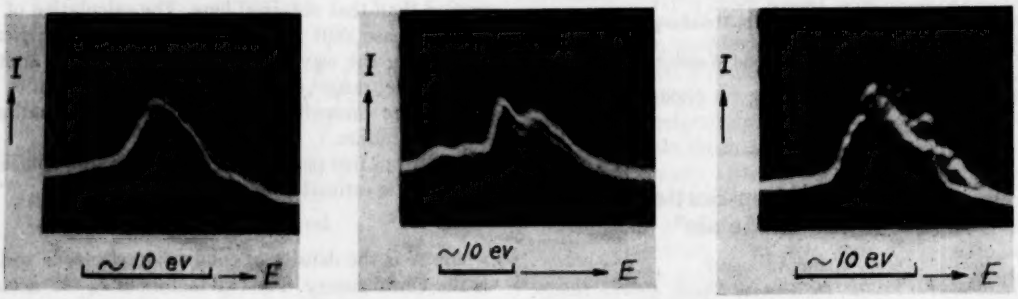

(a) (b) (c)

FIG. 1. Two types of the $M_{II,III}$ band emission curves of pure copper. The curve (a) resembles those of previous investigators, and (b) resembles Rudberg and Slater's theoretical curve. The transient time from (a) to (b) or (b) to (a) was very short. These two curves were observed simultaneously in photograph (c). Exposure: 1/25 sec.

shown in (c), transforms to the type (b). The curve (b) does not persist for a long time and eventually it returns to the curve (a). Therefore, if we take a photograph with long exposure, we will have an oscillogram of type (a). This will be true in the case of diffraction grating spectroscopy. Thus, the curve (b) would not have been found by previous investigators. Perhaps the curve (b) which was predicted by Rudberg and Slater represents the correct energy distribution in a clean metal surface and the type (a) corresponds to a somewhat disturbed state.

[1] E. M. Gyorgy and G. G. Harvey, Phys. Rev. **93**, 365 (1954).
[2] Shinoda, Suzuki, and Kato, J. Phys. Soc. (Japan) **7**, 644 (1952).
[3] Shinoda, Suzuki, and Kato, Technol. Repts. Osaka Univ. **4**, 1 (1954).
[4] F. Seitz, *The Modern Theory of Solids* (McGraw-Hill Book Company, Inc., New York, 1940), Chap. XIII.
[5] E. M. Gyorgy and G. G. Harvey, Phys. Rev. **87**, 861 (1952).
[6] E. Rudberg and J. C. Slater, Phys. Rev. **50**, 150 (1936).

Evaporated Multiple Layers with Semiconductor Properties

J. C. M. Brentano and J. D. Richards*
Northwestern University, Evanston, Illinois
(Received June 3, 1954)

THIN multiple-layer films were deposited on Pyrex in a high vacuum (10^{-6} mm Hg) by alternate evaporations of two metals not likely to form intermetallic compounds or alloys. Successive layers were deposited at intervals of 15 seconds giving about equal increments of conductance with average thicknesses of approximately 2 A. Such films had negative temperature coefficients of resistivity.

Figure 1 refers to a film comprising 210 layers each of iron and lead. The pressure was maintained at 10^{-6} mm Hg for 42 days while measurements *S*1, *S*2, *S*3, and *S*4 were made. The slight increase in conductance and decrease of slope with aging is accentuated by heating indicating some recrystallization.

Thin films of single metals are known to possess negative temperature coefficients[1] which can be interpreted as due to gaps between deposited islands requiring some activation energy to be bridged.[2] This corresponds to a stage of film formation when the increase of conductance is more than proportional to the metal deposited. The multiple layers were at a stage where the conductance increased proportionally with time, indicating a continuous conducting layer.

Films of only iron or lead obtained under conditions similar to those for the composite layers and of similar conductance gave negligibly small or positive temperature coefficients showing that the large negative temperature coefficients of the composite films were not due to impurities or to gross oxidation.

Figure 2 gives the conductance to temperature relation in modified experiments which favored the formation of larger metal agglomerates. At temperatures below that of formation (330°K) the change of conductance with temperature given in Figs. 1 and 2 was

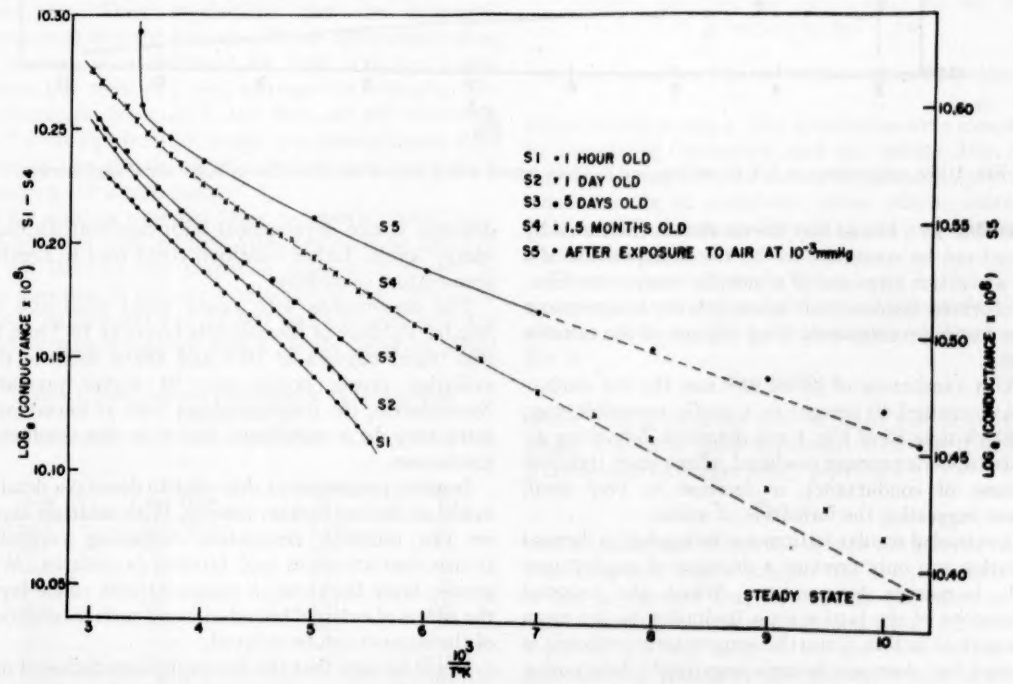

FIG. 1. Log$_e$ conductance *vs* $1/T$ for an alternately evaporated deposit of 210 layers each of iron and lead.

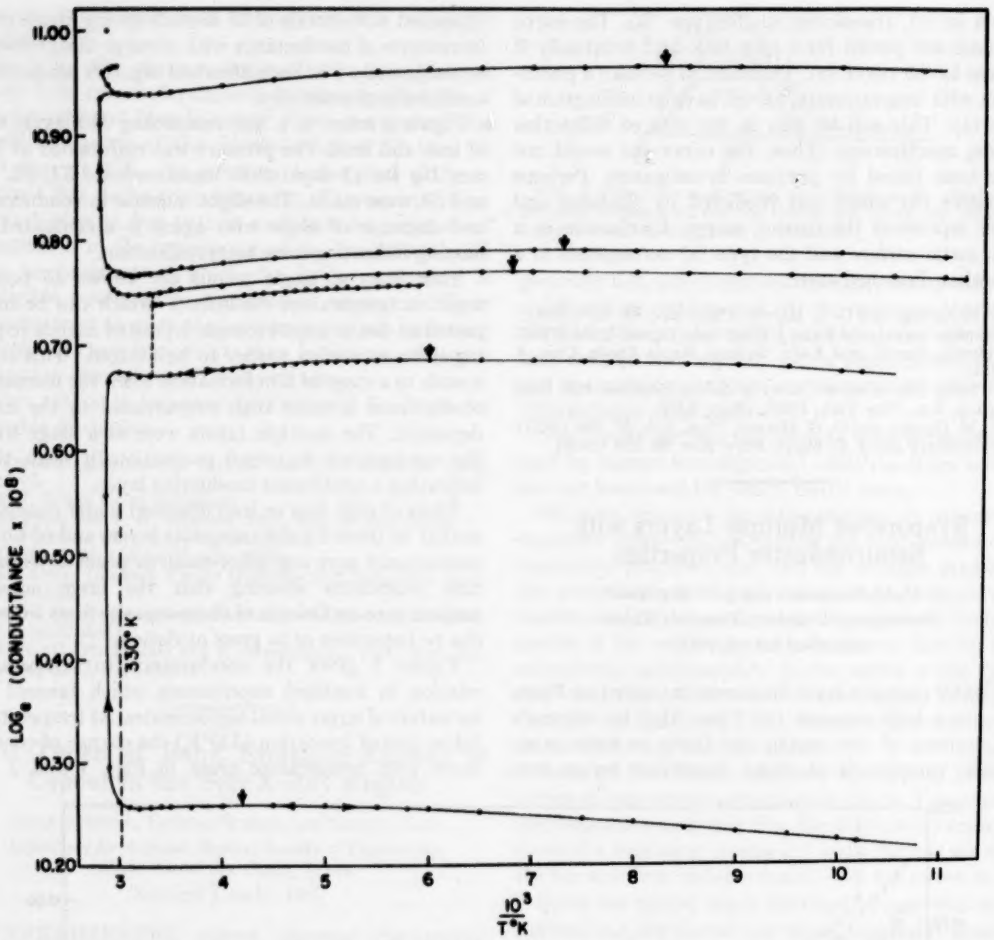

FIG. 2. Log$_e$ conductance *vs* $1/T$ for an iron-lead multiple deposit which favored the formation of larger metal agglomerates.

reversible. In a formal way the maximum (indicated by arrow) can be accounted for by the superposition of a low activation term and of a metallic conduction term. Its observed displacement towards lower temperatures after heating corresponds to an increase of the metallic term.

With admittance of air at 10^{-3} mm Hg the conductance increased 40 percent in a partly reversible way, at which time *S*5 of Fig. 1 was obtained. Admitting air at atmospheric pressure produced, after a short transient increase of conductance, a decrease to very small values suggesting the formation of oxides.

In extended regular lattices scattering due to thermal agitation can only produce a decrease of conductance with increasing temperature. When the external dimensions of the lattice set a limitation to the mean free path as in thin films, the temperature coefficient is reduced but does not become negative.[3,4] Interposing two metals establishes both internal boundaries and deficient lattice development with resultant displaced energy levels. Either condition could lead to negative temperature coefficients.

The experiments with single metal films and the relative stability of the multiple layers at 10^{-6} mm Hg with rapid changes at 10^{-3} and above indicate that oxidation proper occurs only at higher pressures. Nevertheless, the presence of gas even at lowest pressures may be a significant factor in the conduction mechanism.

It seems premature at this stage to develop a detailed model of the conduction process. With multiple layers we can establish conductors containing controlled lattice discontinuities and internal boundaries. With greater layer thickness as compared with single layers the effects of external boundaries and surface conditions of the support can be reduced.

It will be seen that the discontinuities discussed may occur with certain groups of semiconductors by the

way of their formation. Their effects then superpose on the semiconductor properties which would otherwise be observed.

* Milwaukee Gas Specialty Company fellow.

[1] See, for instance, N. Mostovetch and B. Vodar in *Semiconducting Materials* (Butterworths Scientific Publications, Ltd., London, 1951).

[2] C. J. Gorter, Physica **17**, 777 (1951); N. Mostovetch, Compt. rend. **233**, 360 (1951).

[3] E. H. Sondheimer, Advances in Physics **1**, 1 (1952).

[4] F. W. Reynolds and G. R. Stilwell, Phys. Rev. **88**, 418 (1952).

Hall Effect in Ferromagnetics*

CLARENCE KOOI
Department of Physics, University of California, Berkeley, California
(Received June 3, 1954)

THE Hall effect in ferromagnetics is given by[1]

$$E_h = R_0 H + R_1 M, \tag{1}$$

where E_h is the Hall electric field, H is the applied magnetic field, M is the magnetization, and R_0 and R_1 are the ordinary and extraordinary Hall constants, respectively. This letter reports measurements of R_1 as a function of resistivity for iron-silicon alloys of 0 percent to 5 percent silicon.

Karplus and Luttinger,[2] in their theory of the extraordinary Hall effect, have found that in a certain approximation R_1 should depend on the square of the resistivity. Their mechanism uses the spin-orbit interaction of the d electrons. R_1 has been measured as a function of resistivity[3,4] for pure iron and nickel where the resistivity was changed by changing the temperature. Since $\rho \propto T$, this does not tell whether ρ or T is the significant quantity. Our measurements were done on iron-silicon, whose resistivity was changed by changing the silicon content.

Our samples were cut from commercial rolled iron-silicon sheet with no heat treatment and no attempt to cut them at any particular angle with respect to the direction of rolling. A primary current density of about 30 amperes/cm^2 at 600 cps was used and the Hall voltage measured with a narrow band amplifier and a lock-in detector. The resistivities were measured by measuring the current and the voltage drop in a sample. The resistivities do not all agree with previous measurements of resistivity *versus* silicon content.[5] This could be due to special rolling and heat treatment at the rolling mill.

TABLE I. Extraordinary Hall constant R_1 as a function of resistivity ρ.

ρ $\mu\Omega$ cm	R_1 volt cm / amp gauss	Percent Si	Temp. °K
76.5	240×10^{-11}	5.09	300
66.1	200	5.09	77
63.7	202	3.91	298
54.3	159	3.91	77
46.6	120	3.01	299
33.1	66.2	3.01	77
32.5	62.3	1.30	300
21.4	29.5	1.30	77
11.0	8.20		298

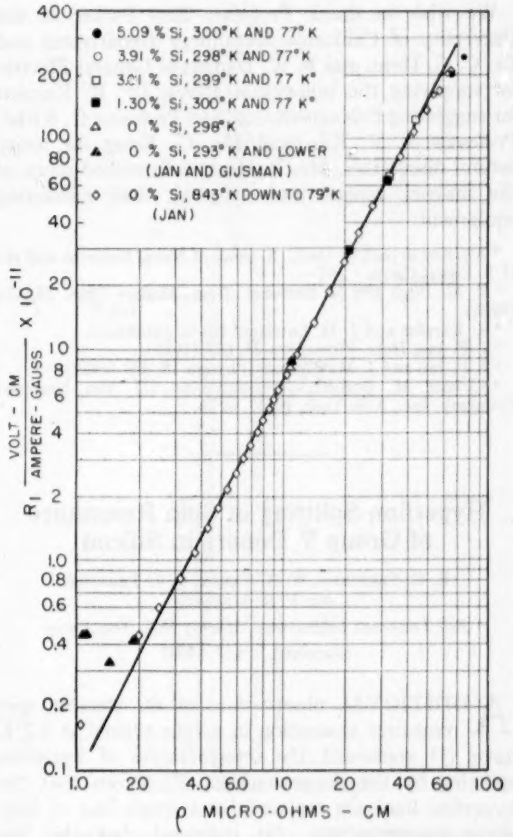

FIG. 1. Extraordinary Hall constant as a function of resistivity.

The results are shown in Table I and in Fig. 1. The measurements of Jan[3] and of Jan and Gijsman[4] for iron are also shown in Fig. 1. The equation of the straight line is

$$R_1 = 0.89\rho^{1.9}, \tag{2}$$

where ρ is in ohm-cm and R_1 is in volt-cm/ampere gauss. This is in good agreement with the theory of Karplus and Luttinger which predicts

$$R_1 \propto \rho^2, \tag{3}$$

with a constant of proportionality of the order of unity. The departure from a straight line at low resistivities is due to the fact that R_1 includes the effect of the magnetization as well as the spin-orbit interaction. Equation (3) was derived for spin-orbit interaction only. At low resistivity the spin-orbit part is of the same order of magnitude as the magnetization part.

We wish to thank Professor Earl Parker of the University of California Metallurgy Department and Dr. C. G. Dunn and F. W. Daniels of General Electric for supplying the iron-silicon alloys, Dr. R. Karplus for suggesting this experiment, and Professor C. Kittel, Professor A. F. Kip, and Mr. G. Feher for many helpful discussions. Mr. R. Hoskins furnished much of the magnet control and magnetic field measuring equipment.

* Assisted in part by the U. S. Office of Naval Research and the U. S. Signal Corps.

[1] E. M. Pugh and N. Rostoker, Revs. Modern Phys. **25**, 151 (1953).
[2] R. Karplus and J. M. Luttinger (to be published).
[3] J.-P. Jan, Helv. Phys. Acta **25**, 677 (1952).
[4] J.-P. Jan and J. M. Gijsman, Physica **18**, 339 (1952).
[5] Richard M. Bozorth, *Ferromagnetism* (D. Van Nostrand Company, Inc., New York, 1951), p. 76.

Hyperfine Splitting in Spin Resonance of Group V Donors in Silicon

R. C. Fletcher, W. A. Yager, G. L. Pearson, and F. R. Merritt
Bell Telephone Laboratories, Murray Hill, New Jersey
(Received June 7, 1954)

ADDITIONAL observations of the electron spin resonance absorption in n-type silicon[1] at 4.2°K have (1) confirmed the interpretation of hyperfine splitting by the donor nucleus, (2) shown that the hyperfine lines are replaced by a single line at high donor concentrations, (3) indicated that the line breadth of the hyperfine lines is of the inhomogeneous type, suggesting residual hyperfine broadening, and (4) revealed the existence of weak satellite lines attributable to forbidden transitions. These observations were made by the same method as described previously[1] on undeformed single crystal bars of silicon.

Fourteen clearly resolved resonance lines (Fig. 1) have been found in antimony-doped silicon (4×10^{71} atoms/cc). These lines naturally fall into two groups, each with lines of about equal intensity and separation. The six lines of the first group have an intensity 1.70 ± 0.05 times and an overall separation 1.32 ± 0.01 times the eight lines of the second group. The number of lines, their relative intensities, and their relative separations appear to be conclusive evidence that the six lines are attributable to interaction with the Sb^{121} nucleus ($I=5/2$, $\mu=3.360$,[2] abundance = 56 percent) and the eight lines to the Sb^{123} nucleus ($I=7/2$, $\mu=2.547$,[2] abundance = 44 percent).

A variety of samples with different concentrations of three donor materials, phosphorus, arsenic, and antimony, have been measured (Fig. 1). With all three it is found that if the concentration exceeds a certain amount (*ca.* 1×10^{18}) the multiplicity of lines disappears, being replaced by a single narrow line (<3 oersteds).

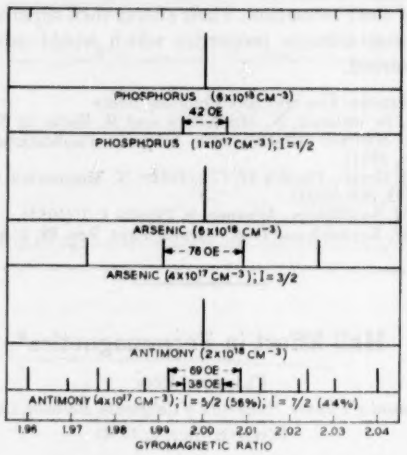

FIG. 1. A schematic representation of the absorption lines observed in silicon doped with various amounts of phosphorus, arsenic, and antimony.

This line has the same g factor and apparently is the same line which Portis *et al.*[3] have attributed to conduction electrons.

In our experiments there is an as yet unexplained shift (≈25 oersteds) in the resonance lines with respect to the calibration line (diphenyl picryl hydrazyl) when the magnetic field is rotated around the cavity containing the sample. This effect accounts for the difference between the g factor of the arsenic-doped silicon of Fig. 1 and the previously quoted value.[1] All the samples of Fig. 1 were taken in the same orientation with the dc magnetic field parallel to the transverse rf magnetic field and along the ⟨100⟩ crystal direction. In this orientation all the lines have the same center of gravity at $g=2.0004\pm0.0005$.

An investigation of the saturation behavior with rf field of the hyperfine lines of an arsenic-doped sample reveals it to be of the inhomogeneous type described by Portis.[4] This suggests that the remaining line breadth of the hyperfine lines is still caused by hyperfine interactions, presumably with the nuclei of Si^{29} (5

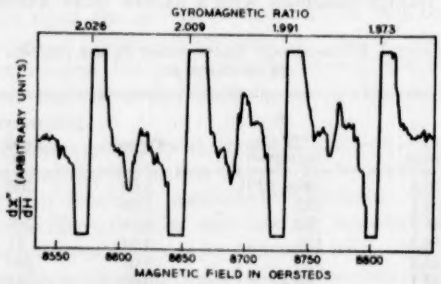

FIG. 2. A reproduction of the observed derivative of the resonance absorption lines of arsenic-doped silicon (4×10^{17} cm^{-3}) showing three satellite lines between the four principal hyperfine lines.

percent relative abundance). All the lines previously reported[1] as well as those in Fig. 1 were measured at rf levels comparable to those which completely saturated the one sample investigated.

As the rf level was decreased, the signal to noise ratio improved enough to show up three satellite lines in the arsenic-doped silicon. A reproduction of the actual trace is shown in Fig. 2. These lines are located midway between the four principal lines with the middle line of the three about 1½ times as large as the side lines. A natural source for such lines is the almost forbidden transitions in which the donor nucleus flips at the same time the electron does. These transitions will produce lines precisely midway between the main lines as observed.

We wish to acknowledge the helpful suggestions of D. A. Kleinman, P. W. Anderson, and C. Kittel, and the experimental assistance of W. F. Flood.

[1] Fletcher, Yager, Pearson, Holden, Read, and Merritt, Phys. Rev. **94**, 1392 (1954).
[2] W. G. Proctor and F. C. Yu, Phys. Rev. **78**, 471 (1950).
[3] Portis, Kip, Kittel, and Brattain, Phys. Rev. **90**, 988 (1953).
[4] A. M. Portis, Phys. Rev. **91**, 1071 (1953).

Phosphorescence of Atoms and Molecules of Solid Nitrogen at 4.2°K

H. P. Broida and J. R. Pellam
National Bureau of Standards, Washington, D. C.
(Received June 11, 1954)

WHILE investigating the possibility of freezing out free radicals at liquid helium temperatures, a phosphorescent glow was observed in the solid products from an electrodeless discharge through nitrogen gas at low pressure. It is possible, therefore, that constituents of the discharge, such as atomic nitrogen, are produced in solid form. This material is observed visually as a thin layer of substance frozen on the inner surface of a single-walled vessel submerged in liquid helium. Presence of an active species on or within the solid is apparent from a visible green glow.

The apparatus is illustrated in Fig. 1. Nitrogen gas is introduced through a control stopcock from a cylinder of nitrogen and traverses the discharge region (*A*) at low pressure, between 0.1 and 3 mm Hg. The discharge is excited by means of a microwave (2450 Mc/sec) voltage induced by antenna (*C*). The single-wall lower extremity (*B*) immersed in liquid helium (*F*) acts as a trap by freezing out all gases, and thus constitutes effectively a high-speed vacuum pump for maintaining the flow of nitrogen. In order to prevent solidification of discharge products at temperatures above 4.2°K, the flow is carried to the cold walls within a passageway kept nearly at room temperature. This relatively high temperature is maintained by forcing warm helium

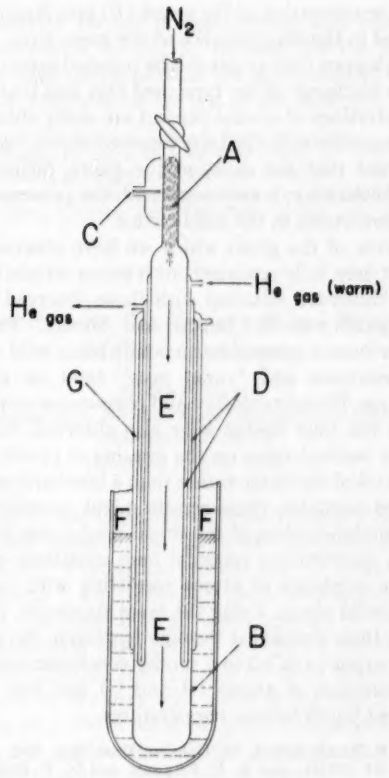

FIG. 1. Diagram of apparatus.

gas between compound walls (*D*) surrounding the channel (*E*) through which the discharge products pass. A vacuum region (*G*) surrounds the entire assembly above chamber (*B*).

While the discharge (*A*) is maintained, the walls of the collecting chamber (*B*) emit a strong green glow. This glow definitely originates from the inner surface where the deposition is occurring; this is verified by observing the interior of the chamber from above. Another characteristic of the surface glow is the random occurrence of local bright spots. After the discharge has been on for several minutes, brilliant flashes of blue appearance are observed spreading as much as two or three centimeters. These flashes are restricted to the surface (not volume effects within the chamber) and appear to be explosive reactions spreading within the deposited material.

After the discharge is extinguished and the flow of nitrogen is stopped, the green glow persists for more than two minutes. During this time the glow intensity diminishes steadily, with no spontaneous flashing. Admission of warm gas (nitrogen or helium) results in increased rate of disappearance and a blue glow before extinction. Removal of the vessel from liquid helium without adding warm gas has a similar result. Once, after the disappearance of both the green and blue

glows, re-immersion of the vessel (B) into liquid helium resulted in the reappearance of the green glow.

It is known that atoms can be pumped some distance from a discharge of the type used here and that atomic concentrations of several percent are easily obtainable.[1] This, together with the facts reported above, leads us to the belief that the cause of the glows, including the phosphorescence, is connected with the presence of free nitrogren atoms in the solid lattice.

Spectra of the glows which we have observed have not yet been fully analyzed but it seems certain that the green bands are identical with those observed in 1924 by Vegard[2] and McClennan and Shrum.[3] These observers found a green glow on bombarding solid nitrogen with electrons and "canal rays" from an electrical discharge. Phosphorescence and phenomena corresponding to the blue flashes were also observed. Since the present method relies on the freezing of products from an electrical discharge rather than a bombardment with charged particles, these results might contribute to a fuller understanding of the actual mechanism involved.

The observations reported here constitute evidence for the existence of atoms coexisting with molecules in the solid phase. Using the same apparatus, products frozen from discharges through hydrogen, oxygen, and water vapor have led to a similar conclusion concerning the collection of atoms (H and O) and free radicals (OH) at liquid helium temperatures.

[1] H. P. Broida and A. G. Gaydon, Proc. Roy. Soc. (London) **A222**, 181 (1954); and R. E. Ferguson and H. P. Broida, Fifth Symposium on Combustion, 1954 (unpublished).
[2] L. Vegard, Nature **113**, 716 (1924), and **114**, 357 (1924).
[3] J. C. McClennan and G. M. Shrum, Proc. Roy. Soc. (London) **A106**, 138 (1924).

Energy Gap of Germanium-Silicon Alloys

A. Levitas, C. C. Wang, and B. H. Alexander
Sylvania Electric Products, Electronics Division, Ipswich, Massachusetts
(Received June 9, 1954)

THE band structure of germanium-silicon alloys has been explored to the extent that the forbidden band width has been determined as a function of composition. A method of preparing homogeneous samples of these alloys was reported at a recent symposium[1] and this will be described more fully in a future publication, together with data on other properties.

In view of the theoretical and practical interest in these alloys, we are reporting here the results of measurements of the forbidden band widths as they were determined from the slopes of logarithmic plots of resistivity *versus* reciprocal temperature in the intrinsic range. The results are shown in Fig. 1 where it can be seen that the energy gap of germanium rises steeply as silicon is added until it is approximately the same as pure silicon at 50 atomic percent. The curve as drawn

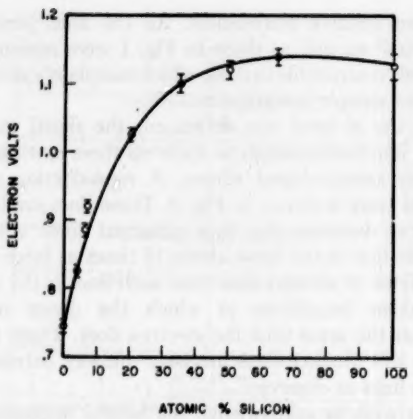

Fig. 1. Energy gap of germanium-silicon alloys against composition.

tends to have a slight maximum at about 75 percent silicon, although the existence of this maximum is uncertain since it is barely detectable within the experimental accuracy.

[1] C. C. Wang and B. H. Alexander, Am. Inst. Mining Met. Engrs. Symposium on Semiconductors, February 15–18, 1954, New York, New York (unpublished).

Paramagnetic Resonance Absorption in a Soft Carbon*

J. G. Castle, Jr.
Department of Physics, University of Buffalo, Buffalo, New York
(Received June 11, 1954)

EXTENSION of our investigation of the magnetic resonance properties of carbons and graphite at room temperature[1,2] has revealed that the width of the electronic spin resonance absorption characteristic of a soft carbon powder varies with heat treatment of the powder. The observed variation suggests the existence of a physical correlation between the width of the spin resonance absorption and the Hall coefficient.

The carbon powder was prepared from a soft coke by milling it to a mean particle size of one to two microns and then heating to the desired temperature Ht. This temperature determines to a large extent the crystallite size. Each series (having several Ht values) was obtained by heat treating a batch of the coke powder to Ht_1, removing a few milligrams of powder to be labeled by Ht_1, heat treating the remainder to Ht_2, removing more powder, etc. Five such series (with interspersed Ht values) were made from the same Texas petroleum coke powder.

Preparation of the microwave samples again[1] included aligning the graphitic planes parallel to each other throughout a given sample. The geometry in the cavity was again such that the plane containing the dc and

rf magnetic field vectors was parallel to most of the graphitic planes in the powder particles.

The derivative of the absorption with respect to dc magnetic field strength was recorded point by point with a microwave spectrometer similar to Yale University's instrument. The crossover values for the observed resonances are reasonably constant, having the mean g value of 2.0056 ± 0.002, based on 2.0036 for powdered picryl hydrazyl. The accuracy of cross-over location is limited by the asymmetry which is quite uniform for all the samples reported here.

The widths, defined for convenience as the separation between points of maximum signal, are given in units of the static magnetic field. The static magnetic field is measured by the proton resonance in USP mineral oil. The modulation amplitude was in each case less than one-third the observed width.

Figure 1 shows what heat treatment of a soft carbon powder does to the width of the spin resonance absorption. The two regions of increased width occur near 1700°C and 2400°C.

According to recent measurements,[3] the Hall coefficient R of a soft carbon solid goes through zero near 1750°C and near 2350°C. The two pairs of Ht values suggest that there is a mechanism of broadening for the spin resonance which produces an increased line width when the densities of electrons and holes are approximately equal. The two cases of heat treatment (near 1700 and 2400) are otherwise quite different with respect to the filling and structure of the electronic energy bands.[4]

Quite recently, resonance absorption in solid carbon samples has been observed with g values of 2.005 ± 0.002. The relation of heat treatment to structure for powders and for solid carbons is being studied.

The author is grateful to Dr. S. Mrozowski for his stimulating interest and helpful advice, to Mr. D. Wobschall for his aid in constructing and operating the spectrometer, to Dr. R. Beringer for the loan of several crucial components of the spectrometer, and to Dr. M. A. Garstens for the gift of the hydrazyl.

* Supported by the U. S. Office of Naval Research.

[1] J. G. Castle, Jr., Phys. Rev. **92**, 1063 (1953).
[2] J. G. Castle, Jr., Phys. Rev. **94**, 1410 (1954).
[3] S. Mrozowski and A. Chaberski, Phys. Rev. **94**, 1427 (1954).
[4] McMichael, Kmetko, and Mrozowski, J. Opt. Soc. Am. **44**, 26 (1954).

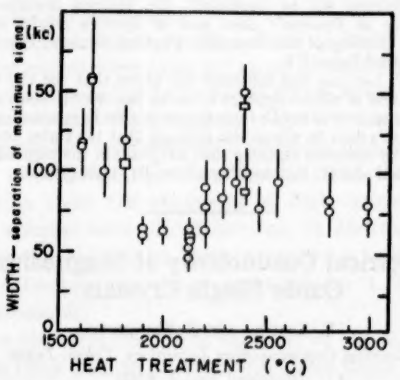

FIG. 1. Paramagnetic resonance absorption in soft carbon powder at 3 cm as a function of the temperature of heat treatment. Circles indicate powder suspended in polystyrene; squares, same powder loose in plastic bag; vertical bars, extreme allowances for error due to bluntness of observed shapes of the first derivative signal.

Speculations on the Energy Band Structure of Ge–Si Alloys

FRANK HERMAN
RCA Laboratories Division, Radio Corporation of America, Princeton, New Jersey
(Received June 14, 1954)

JOHNSON and Christian[1] of these Laboratories have recently reported on some of the properties of Ge-Si alloys. The optical energy gap *vs* composition (see reference 1, Fig. 3) exhibits the following characteristics: In the range 0 to 15 mole percent Si, the gap increases linearly from 0.72 to 0.94 ev. A break then occurs, and the gap continues to increase, reaching 1.2 ev at pure Si. We may ask: What is the energy band structure of a Ge-Si alloy of given composition, and what is the explanation of the break in the curve described above?

Alloys have energy bands with a high density of states and bands with a low density of states.[2] In a Ge-Si alloy, the former should resemble the allowed bands of a perfect germanium or silicon crystal according as the predominant constituent of the alloy is germanium or silicon.

Schematic diagrams of the band structures of perfect germanium and silicon crystals are shown in Figs. 1a and 1b, respectively. Figure 1a was suggested by the preliminary results of a new theoretical investigation of the band structure of the germanium crystal[3] and by the results of cyclotron resonance experiments.[4] The conduction band structure of Fig. 1b was obtained by distorting the conduction bands of Fig. 1a so as to bring the [100] minima below the [111] minima. The conduction band structure of Fig. 1b is consistent with the results of piezoresistance measurements on n-Si by Smith[5] and with unpublished magnetoresistance data on n-Si by Pearson.[6] The valence band structure of Fig. 1b was suggested by recent cyclotron resonance absorption measurements on silicon by Lax and Dexter.[7]

We now make the following assumptions: (1) The addition of silicon to germanium affects the form and relative disposition of all valence and conduction bands. However, the changes produced in the conduction band structure are more radical than those involving the valence band structure. (2) As the silicon content increases, the conduction band having [111] minima is

raised relative to the conduction band having [100] minima. Both of these conduction bands move away from the valence bands, the lowest conduction band at a faster rate than the next-to-the-lowest conduction band. (3) The top of the valence band structure remains at the central point of the reduced zone over the entire range of alloy composition. (4) The optical absorption edge is determined by nonvertical electronic transitions over the entire range.

Referring now to reference 1, Fig. 3 [E_{gap} *vs* mole percent Si], we suggest that electrons occupy states at the [111] minima in the range 0 to about 15 mole percent Si. In the region of the break in the E_{gap} *vs* mole percent Si curve, the [100] and the [111] minima are both populated. These minima are here separated in energy by a quantity of the order of kT. As the silicon content is increased above about 15 mole percent, the [111] minima are pushed above the [100] minima.

The optical absorption edge, i.e., the measured energy gap, is thus determined by electronic transitions from valence band states near $k=(000)$ to the conduction band states near $k=(\frac{1}{2}\frac{1}{2}\frac{1}{2})$ in the range 0 to 15 mole percent Si. The absorption edge in the range above 15 mole percent Si is determined by transitions from the top of the valence band to states at the bottom of the conduction band, which here lie along the [100] axes.

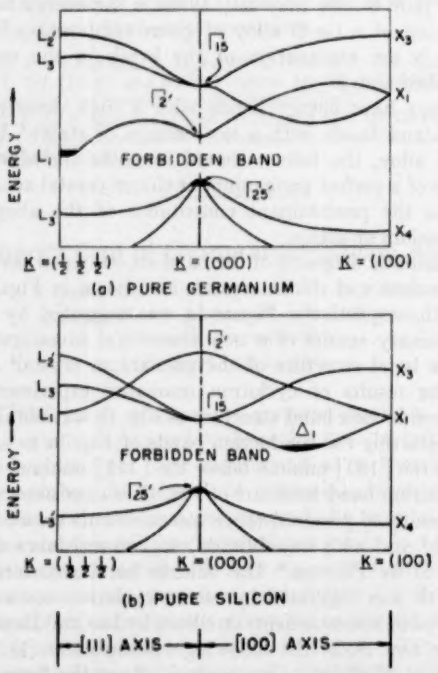

FIG. 1. a and b. Schematic diagrams of energy band contours in perfect germanium and silicon crystals along [111] and [100] axes in the reduced zone. States normally occupied by electrons and holes at room temperature are shown darkened. The symbols give the symmetry classification of the various states in the notation of reference 3. The removal of degeneracy by spin-orbit interaction is not shown.

It is conceivable that these ideas could be verified by performing magnetoresistance or cyclotron resonance measurements on single-crystal suitably-doped Ge-Si alloys of varying compositions. (Johnson and Christian[1] report that single crystals have already been produced in the range 0 to 12.6 mole percent Si.) Magnetoresistance measurements on both *n*- and *p*-type single Ge-Si alloy samples have been initiated at these Laboratories. It is hoped that these experiments will bear out the speculations presented above.

It has occurred independently to Paul and Brooks[8] and to the author that the application of high pressure to perfect single crystals of germanium could raise the [111] minima above the other minima, i.e., above the [100] minima or the (000) minimum. Dr. R. H. Parmenter of these Laboratories is currently engaged in a theoretical study of the modifications in the band structure of germanium produced by changes in lattice constant or addition of silicon atoms.

The author wishes to thank Dr. D. O. North and Dr. R. H. Parmenter of the RCA Laboratories for stimulating conversations. The author is grateful to Dr. B. Lax, Dr. R. N. Dexter, and Dr. H. J. Zeiger of the Lincoln Laboratory, Massachusetts Institute of Technology; Dr. C. Herring and Dr. G. L. Pearson of the Bell Telephone Laboratories; and Professor H. Brooks and Dr. W. Paul of Harvard University for discussing their work with him prior to publication.

[1] E. R. Johnson and S. M. Christian, Phys. Rev. (to be published).
[2] H. M. James and A. S. Ginsbarg, J. Phys. Chem. **57**, 90 (1953); R. Landauer and J. C. Helland, J. Chem. Phys. (to be published).
[3] F. Herman (to be published); see also F. Herman, Phys. Rev. **93**, 1214 (1954).
[4] Dresselhaus, Kip, and Kittel, Phys. Rev. **92**, 827 (1953); Lax, Zeiger, Dexter, and Rosenblum, Phys. Rev. **93**, 1418 (1954); R. N. Dexter *et al.*, Phys. Rev. (to be published).
[5] C. S. Smith, Phys. Rev. **94**, 42 (1954).
[6] G. L. Pearson (private communication); see also G. L. Pearson and C. Herring (to be published). Dr. Herring discussed the significance of Pearson's data and of Smith's results at the Stanford Meeting of the Amercian Physical Society, December, 1953, Invited Paper C1.
[7] Dr. B. Lax has just informed the writer that the top of the valence band in silicon appears to lie at the central point of the reduced zone, and to have a form similar to that in germanium. Lax and Dexter's data on silicon also indicate that the states normally occupied by electrons lie along the [100] axes in the reduced zone.
[8] W. Paul and H. Brooks, Phys. Rev. **94**, 1128 (1954).

Electrical Conductivity of Magnesium Oxide Single Crystals

E. YAMAKA AND K. SAWAMOTO
Electrical Communication Laboratory, Tokyo, Japan
(Received June 4, 1954)

MEASUREMENTS of the electrical conductivity of magnesium oxide have been performed by two or three investigators. Lempicki[1] made measure-

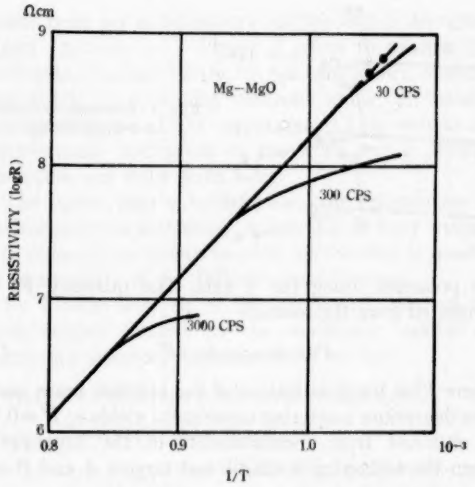

FIG. 1. Plot of resistivity *vs* $1/T$. The frequencies used were 30, 300, and 3000 cps. The solid circles show the values calculated from the resistivities at 30 and 300 cps by using the equivalent circuit shown in Fig. 2.

ments on single crystals by a dc method and concluded that the energy gap between the full band and the conduction band was 4.6 ev by assuming that the conductivity was electronic and intrinsic. Mansfield,[2] on the other hand, deduced that magnesium oxide was a defect-type semiconductor from the positive sign of the thermoelectric power. In addition, he concluded by using Nijboer's theory[3] that the value of E in the expression $\sigma=\sigma_0 \exp(-E/kT)$ was not half the band gap but corresponded to the work function for the impurity level available to holes. Recently Day[4] found from his photoconductivity measurements that the charged carriers released by light from magnesium-excess absorption bands were holes. Therefore it is important to determine whether the 2.3-ev energy level available to the charged carriers originates from excess magnesium or excess oxygen atoms.

In order to eliminate the effects of ionic current, measurements were made by an ac method. However, its frequency had to be as low as about 30 cps because of the effect of shunt capacity. The low conductivity of the samples compelled us to make our measurements in a nitrogen gas flow in order to avoid thermionic emission from the electrodes at high temperatures. The samples were placed between Pt electrodes and heated by an electric furnace around a fused silica tube. Temperatures were measured by a Pt-PtRh thermocouple.

Samples were cleaved on the order of one-half centimeter thick from large clear (uncolored) single crystals supplied by the Norton Company. Coloring with magnesium was obtained by heating the crystals in magnesium vapor at temperatures of about 1300°C for one hour (magnesium colored) and coloring with oxygen was obtained by heating in a dry oxygen gas flow at about 1300°C for two hours (oxygen colored). The measurements of optical absorption indicated: (a) uncolored crystals already have an absorption band in the ultraviolet region due to excess oxygen; (b) oxygen-colored crystals have an intensified band in the ultraviolet region; (c) magnesium-colored crystals reveal broad absorption bands in the visible region caused by excess magnesium, in addition to a weakened band in the ultraviolet region.

The curves of log$R$ *vs* $1/T$ in uncolored, magnesium-colored, and oxygen-colored crystals were the same as the curve shown in Fig. 1. The deviation from the straight line occurred at high resistivity. In order to ascertain whether the deviation was due to different impurity levels or to shunt capacity, the frequency of the oscillator was varied from 30 cps to 300 and 3000 cps, and the results are also shown in Fig. 1. The resistivity of the sample was calculated from the simple equivalent circuit shown in Fig. 2; the value obtained

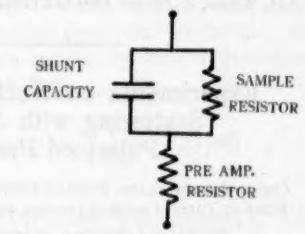

FIG. 2. The equivalent circuit used.

lay on the extrapolated part of the straight line as shown in Fig. 1. This indicated that the deviation was due not to different impurity levels, but to shunt capacity.

The activation energies in uncolored, magnesium-colored, and oxygen-colored crystals were the same, being from 2.2 ev to 2.4 ev. However the specific resistivities of magnesium-colored crystals were lower than those of uncolored and oxygen-colored crystals as shown in Table I. Furthermore it was observed that the resistivity became larger, in contrast with the constant activation energy, when the sample was heated at high temperatures such as 1100°C, especially in magnesium-colored samples. From these experimental facts the following conclusions may be drawn: (a) The 2.3-ev

TABLE I. Specific resistivity at 977°C and activation energy of MgO single crystals.

Sample	Uncolored a	Uncolored b	Uncolored c	O-colored a	O-colored b	Mg-colored a	Mg-colored b	Mg-colored c	Mg-colored d
Specific resistivity[a] (Ω cm)	37	80	15	28	12	4	5.8	1.2	0.5
E (ev)	2.2	2.3	2.3	2.4	2.2	2.3	2.4	2.2	2.3

[a] The values of resistivity are at 977°C.

energy level available to charged carriers originated from excess magnesium and no levels were from excess oxygen. (b) Excess magnesium could move through the lattice comparatively easily so that impurity levels disappeared by heating samples at high temperatures. This conclusion was also reached from the fact that heat treatment destroyed the coloration due to excess magnesium in the visible region. (c) Furthermore, by taking account of Day's results,[4] it was deduced that the charge carriers due to excess magnesium levels were holes, the positive sign of the thermoelectric power obtained by Mansfield[2] being thus explained. These results are not understood by a simple electronic structure model. However, a definite model cannot be established yet.

A full report will be given in the *Journal of the Physical Society of Japan*.

[1] A. Lempicki, Proc. Phys. Soc. (London) **B66**, 281 (1953).
[2] R. Mansfield, Proc. Phys. Soc. (London), **B66**, 614 (1953).
[3] B. R. A. Nijboer, Proc. Phys. Soc. (London) **51**, 575 (1939).
[4] H. R. Day, Phys. Rev. **91**, 822 (1953).
[5] H. Weber, Z. Physik **130**, 392 (1951).

Experiments on Nucleon-Nucleon Scattering with 312-Mev Polarized Protons

OWEN CHAMBERLAIN, ROBERT DONALDSON, EMILIO SEGRÈ, ROBERT TRIPP, CLYDE WIEGAND, AND THOMAS YPSILANTIS
Radiation Laboratory, Department of Physics, University of California, Berkeley, California
(Received June 7, 1954)

IN a previous paper[1] we reported our results on p-p scattering using polarized protons. In the framework of our general program of studying nucleon-nucleon scattering, we would have liked to investigate n-p scattering with polarized neutrons; however, we are still unable to obtain highly polarized neutrons and the next best possibility is to bombard deuterons with highly polarized protons.[2]

Neglecting in first approximation the binding of the deuteron, the processes that occur in p-d bombardment are p-p and p-n scattering in which a p-p or an n-p pair escapes at approximately 90° in the laboratory system. In addition to this there is elastic scattering of the protons. These processes are schematically represented in Fig. 1.

We have detected and measured processes (a) and (b) by coincidence techniques and we have also counted single neutrons and single protons.

In Figs. 2 and 3 we show the asymmetrical part of the cross section, $P\sigma$:

$$P\sigma=\tfrac{1}{2}[\sigma(\theta,0)-\sigma(\theta,\pi)], \tag{1}$$

where $\sigma(\theta,\varphi)$ is the differential cross section for a completely polarized beam scattering on an unpolarized target. The incident protons travel in the z direction and

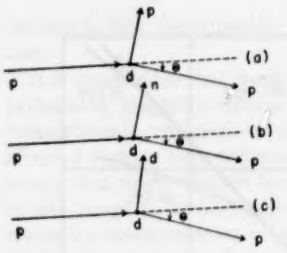

FIG. 1. Processes occurring in p-d scattering.

are polarized along the y axis. The quantity $P\sigma$ is computed from the relation

$$P\sigma=e\sigma_{\text{unpolarized}}/P', \tag{2}$$

where P' is the polarization of the incident beam used. The deuterium scattering experiment yields e; $P'=0.73$ is obtained from measurements of the asymmetry when the scattering is elastic and targets A and B are

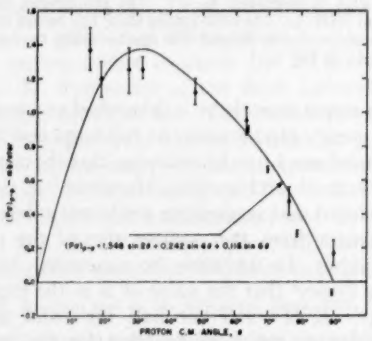

FIG. 2. $P\sigma$ in p-p scattering as a function of θ. Triangles are from reference 1 (290 Mev); dots are from this experiment (312 Mev).

identical; for p-p scattering $\sigma_{\text{unpolarized}}$ is assumed to be 3.75 mb/sterad,[3] and for n-p scattering it is taken from previous work.[4]

Figure 2 refers to the asymmetric part of the p-p scattering with some points taken from previously reported data[1] using a hydrogen target, and some

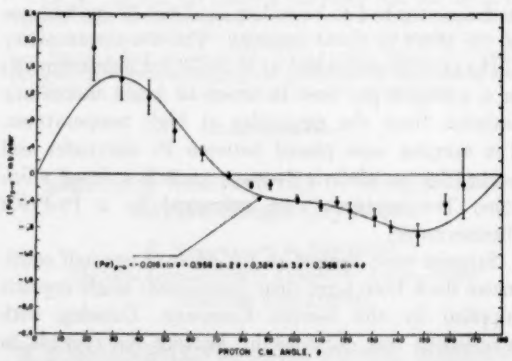

FIG. 3. $P\sigma$ for n-p scattering from d-p scattering measurements, as a function of θ. Energy of incident protons is 312 Mev.

points from p-p coincidence counting with a deuterium target [process (a)]. Figure 3 refers to process (b), with data obtained partly by p-n coincidence counting and partly by counting neutrons alone, all from a deuterium target. Data on process (c), as well as the experimental description of the work and a detailed discussion, are to be given later.

The curves thus obtained give some information on nucleon-nucleon scattering. A first step in their analysis is to obtain from them whatever information is possible on phase shifts of the different partial waves.

By Fourier analysis of the asymmetric part of the cross section limited to the minimum number of harmonics necessary to fit the data, we find

$$(P\sigma)_{p-p}=1.348\sin2\theta+0.242\sin4\theta+0.116\sin6\theta, \quad (3)$$

$$(P\sigma)_{n-p}=-0.016\sin\theta+0.958\sin2\theta +0.324\sin3\theta+0.366\sin4\theta. \quad (4)$$

The solid curves in Figs. 2 and 3 represent these equations. If the sixth harmonic term is omitted from Eq. (3) the fit is still fairly good; however, the fourth harmonic term is necessary in both Eqs. (3) and (4) to fit the data satisfactorily.

From the Fourier analysis it is possible to infer some conclusions on the phase shifts, as is to be shown in the following letter by Dr. B. D. Fried.

This work was performed under the auspices of the U. S. Atomic Energy Commission.

[1] Chamberlain, Segrè, Tripp, Wiegand, and Ypsilantis, Phys. Rev. **93**, 1430 (1954). We use the same notation as in this paper.
[2] Marshall, Marshall, Nagle, and Skolnik have worked on the same subject. We thank them for communicating their results before publication.
[3] Chamberlain, Segrè, and Wiegand, Phys. Rev. **83**, 923 (1951); Chamberlain, Pettengill, Segrè, and Wiegand, Phys. Rev. **93**, 1424 (1954).
[4] Kelly, Leith, Segrè, and Wiegand, Phys. Rev. **79**, 96 (1950).

Phase Shifts for High-Energy Nucleon-Nucleon Scattering

BURTON D. FRIED*
Radiation Laboratory, Department of Physics, University of California, Berkeley, California
(Received June 7, 1954)

SEVERAL attempts have recently been made to fit nucleon-nucleon scattering data using a small number of phase shifts.[1] In particular, Thaler and Bengston have shown that with seven phase shifts—^1S, ^3S, ^1P, ^3P and a single ^3D—it is possible to get a good fit to both the p-p and n-p differential cross sections at an energy of 260 Mev. It is of interest to see whether the recent experiments by Chamberlain *et al.*[2] on the scattering of polarized protons at a similar energy are consistent with the Thaler and Bengston phase shifts.

If partial waves with $L>2$ are excluded and Coulomb effects are neglected, then, for an incident beam of completely polarized protons,

$$(d\sigma/d\Omega)_{p-p}=k^{-2}[A_0P_0(\cos\theta)+A_2P_2(\cos\theta) +A_4P_4(\cos\theta)+B_1\cos\phi\sin\theta P_1(\cos\theta)], \quad (1)$$

where k is the wave number of the relative motion, θ and ϕ are the usual center-of-mass polar angles, and the initial momentum and polarization of the incident protons have been chosen along the z and y axes, respectively. Explicit expressions for A_0, A_2, and A_4 in terms of phase shifts are given by Thaler, Bengston, and Breit.[3] In the same notation,

$$B_1=9S(\delta_{11},\delta_{12})+6S(\delta_{10},\delta_{12}), \quad (2)$$

where $S(x,y)=-S(y,x)=\sin x\sin y\sin(x-y)$, and δ_{1J} are the ^3P phase shifts.

In their analysis, Thaler and Bengston assumed that (a) the nuclear interaction is charge-independent; (b) the triplet phase shifts are all equal,

$$\delta_{21}=\delta_{22}=\delta_{23}\equiv{}^3K_2; \quad (3)$$

(c) the mixing of ^3S and ^3D waves, such as would result from a tensor force or other noncentral interaction, can be neglected. The cross section for polarized protons scattered by neutrons is then

$$(d\sigma/d\Omega)_{p-n}=\tfrac{1}{4}(d\sigma/d\Omega)_{p-p}+\tfrac{1}{4}k^{-2}\Big\{\sum_{n=0}^{4}C_nP_n(\cos\theta) +\cos\phi\sin\theta[D_0P_0(\cos\theta)+D_2P_2(\cos\theta)]\Big\}. \quad (4)$$

Again, the C_n are given by TBB,[3] while

$$D_0=5S(^3K_0,\delta_{12})-3S(^3K_0,\delta_{11})-2S(^3K_0,\delta_{10}),$$
and (5)
$$D_2=5[5S(^3K_2,\delta_{12})-3S(^3K_2,\delta_{11})-2S(^3K_2,\delta_{10})],$$

where $^3K_0$ is the ^3S phase shift.

An examination of the qualitative features of Eqs. (1) and (4) shows that they are incompatible with the data on the scattering of polarized protons as presented in Figs. 2 and 3 of the preceding letter. The following points may be made: (1°) According to Fig. 3, $(P\sigma)_{p-n}$ contains an appreciable amount of fourth harmonic, whereas Eq. (4) allows none; (2°) The amplitudes of the second harmonic components of $(P\sigma)_{p-p}$ and $(P\sigma)_{p-n}$ have a ratio of 1.4 instead of the ratio of 4.00 predicted by Eqs. (1) and (4); (3°) The $(P\sigma)_{p-p}$ data cannot be fitted with a second harmonic term alone.

One obvious conclusion which may be drawn from these observations is that partial waves with $L>2$ are necessary, as is certainly to be expected at this energy ($k^{-1}=5.1\times10^{-14}$ cm). In particular, since only triplet partial waves can contribute to the polarization, the fourth harmonic in $(P\sigma)_{p-p}$ requires at least a ^3F term. However, it may be noted that the discrepancies (1°) and (2°) above could be resolved without using partial waves with $L>2$. The absence of a second harmonic term in $(P\sigma)_{p-n}-\frac{1}{4}(P\sigma)_{p-p}$ and the lack of a fourth

harmonic term in $(P\sigma)_{p\text{-}n}$ are both consequences of the special assumptions (b) and (c) mentioned above. If the requirement (3°) and the assumption that ^3S and ^3D do not mix are dropped, then the missing second and fourth harmonic terms will appear (the former arising from interference effects between the $^3S(Y_0^0)$ and $^3D(Y_2^{\pm 1})$ partial waves, the latter from interference between different ^3D partial waves). Thus, it may be possible to fit the data of Figs. 2 and 3 of the preceding letter and also the ordinary n-p and p-p differential cross sections (for unpolarized protons) by using the most general set of phase shifts consistent with $L \leq 2$, together with a single ^3F phase shift [to give the sin 4θ term in $(P\sigma)_{p\text{-}p}$].

The number of parameters available in this scheme is 13 (12 real phase shifts plus one real "mixing parameter" for the $J=1$; $L=0$, 2 part of the scattering matrix[4]), while a Fourier analysis of the data will provide 18 Fourier coefficients—2 from $(P\sigma)_{p\text{-}p}$, 5 from $(P\sigma)_{p\text{-}n}$, and 4 and 7 from the unpolarized p-p and n-p cross sections, respectively). Of course, even aside from the experimental uncertainties in these Fourier coefficients, it is not likely that a unique set of phase shifts can be found, for as can be seen from Eqs. (2) and (5), the Fourier coefficients are by no means single-valued functions of the phase shifts. Calculations aimed at finding a set of phase shifts consistent with the present knowledge of the cross sections are now in progress.

I am indebted to Drs. Segrè, Chamberlain, and Wiegand and to T. Ypsilantis and R. Tripp for many informative discussions on polarization experiments. This work was performed under the auspices of the Atomic Energy Commission.

* Now at the Ramo-Wooldridge Corporation, Los Angeles, California.

[1] A. Garren, Phys. Rev. **92**, 213, 1587 (1953) and R. M. Thaler and J. Bengston, Phys. Rev. **94**, 679 (1954).
[2] Chamberlain, Donaldson, Segrè, Tripp, Wiegand, and Ypsilantis, preceding letter [Phys. Rev. **95**, 850 (1954).]
[3] Thaler, Bengston, and Breit, Phys. Rev. **94**, 683 (1954).
[4] J. M. Blatt and L. C. Biedenharn, Revs. Modern Phys. **24**, 258 (1953).

π-Meson Production in π-Nucleon Collisions at 1.5 Bev*

W. D. Walker, J. Crussard, and M. Koshiba
University of Rochester, Rochester, New York
(Received June 15, 1954)

As has been pointed out previously,[1] most π^--p collisions at 1.5 Bev lead to the production of a single additional π meson. Since the last note more data have been obtained. (About 150 π^--p interactions have been examined.) In particular, the reaction

$$\pi^- + p \rightarrow \pi^+ + \pi^- + n$$

shows characteristics very similar to those of the production of a single π^0. The neutron usually goes backward in the center-of-mass system with an average momentum of 500 Mev/c. The π^+ and π^- emerge from the reaction with an average angle of 135° between them in the c.m. system. The angular distribution of the $\pi^+ + \pi^-$ is very similar to the angular distribution of the $\pi^- + \pi^0$ from the reaction $\pi^- + p \rightarrow \pi^- + \pi^0 + p$.

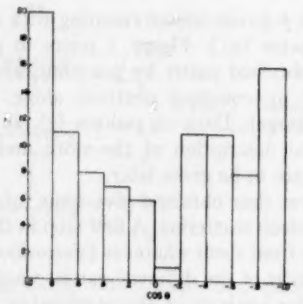

FIG. 1. Angular distribution in the c.m. system of all the π's from the reactions $\pi^- + p \rightarrow \pi^- + p + \pi^0$ and $\pi^- + p \rightarrow \pi^- + n + \pi^+$.

The center-of-mass angular distribution of all the mesons from the above two reactions is given in Fig. 1. There is evidence of peaks in the forward and backward direction in the c.m. system. The forward peak contains mostly fast mesons, and the backward peak relatively slower mesons in the c.m. system, as shown by Fig. 2 which gives the angular distributions of mesons of

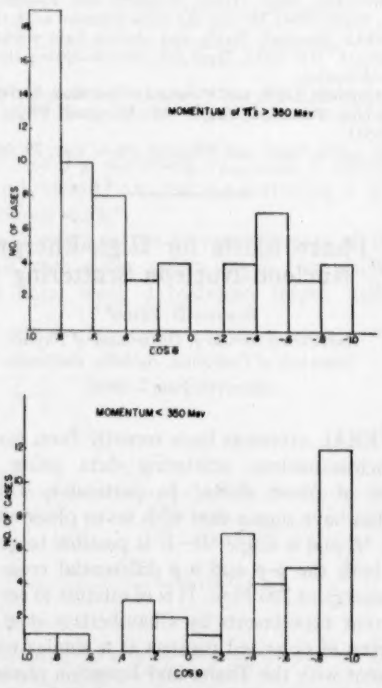

FIG. 2. Angular distributions of mesons of momenta greater than and less than 350 Mev/c in the c.m. system.

momenta greater than and less than 350 Mev/c in the c.m. system. These results suggest that the high-energy meson is the primary meson which sometimes suffers relatively small momentum transfers, while the lower-energy meson is the secondary meson which is usually radiated into the backward hemisphere. If the slower meson is the secondary meson, then these results would be consistent with the results of Yuan[2] and Lindenbaum on the spectrum of π's produced in p-nucleon collisions. In almost 50 percent of the cases of π^0 production, the π^0 is the fast meson; thus it is necessary in this picture that the primary meson have a considerable chance of making a charge exchange in the course of the collision with the nucleon.

In the course of scanning for the hydrogenic interactions, a considerable number of events have been found which appear to be π^- n interactions occurring on the edge of a nucleus.

The following reactions have been found:

$$\begin{aligned} \pi^-+n &\rightarrow \pi^-+n \text{ or } \pi^-+n+\pi^0, && \text{55 cases} \\ &\rightarrow \pi^-+\pi^-+p, && \text{4–6 cases} \\ &\rightarrow \pi^++\pi^-+\pi^-+n, && \text{1 case.} \end{aligned}$$

The events of the first category appear as rather large-angle deflections of the π^-. Sometimes a slow electron emerges from the vertex of the interaction (presumably the β decay of the residual nucleus having lost a neutron). Only deflections of more than 10° have been counted here. There are in addition a great number of cases of deflections of 2°–3° which are mostly diffraction scatterings off nuclei. The c.m. angular distribution of the π^- from this first group is very similar to the angular distribution of the π^- from the two corresponding reactions with protons.

The observed ratio of π^--n and π^+-p interactions is consistent with the following facts:

(1) equal π-p and π-n cross sections at 1.5 Bev as measured by Cool, Madansky, and Piccioni;[3]

(2) about half of the "π-p" interactions observed here occur on free protons, the rest on edge protons.[1]

Recent results of Lindenbaum and Yuan[4] indicate that the $T=\frac{3}{2}$ meson-nucleon state may play an important role in meson production processes in this energy range. If one assumes that all meson production in π-nucleon collisions goes by means of the production of a nucleon excited into a $T=\frac{3}{2}$ state with the subsequent decay into a meson and a nucleon, then one finds by the application of the principle of charge independence that the reaction $\pi^-+p\rightarrow\pi^++\pi^-+n$ predominates over the reaction $\pi^-+p\rightarrow\pi^-+\pi^0+p$ by about a factor of two, and that the reaction $\pi^-+n\rightarrow\pi^-+\pi^0+n$ predominates very much over $\pi^-+n\rightarrow 2\pi^-+p$. The latter statement is consistent with the data presented and the former statement is not. (39 cases of $\pi^-+p\rightarrow\pi^++\pi^-+n$ and 42 cases of $\pi^-+p\rightarrow\pi^-+\pi^0+p$ have been observed.)

An excited nucleon in the $T=\frac{3}{2}$ state would presumably usually decay with a "Q" value of about 150–160 Mev. Figure 3 shows the apparent Q values calculated from the π^--p collisions in which a π^0 or π^+ is produced assuming the slower meson to be the secondary. There is only a slight indication of a peak in the region of 160 Mev. Unfortunately the experimental errors in the energy measurements and the motions of the target nucleon (in the case of edge collisions) could smear any such Q curve almost to the extent observed.

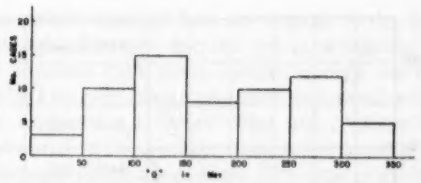

FIG. 3. Distribution of the Q values of an assumed intermediate excited nucleon in the π^--p interactions in which a π^0 or π^+ is produced.

The distribution of angles between the two π mesons in the center-of-mass system[1] seems to be consistent with the excited-nucleon model.

The authors wish to thank H. Fisher, B. Munir, and Mrs. V. Miller for their aid in scanning.

* This work was assisted by the U. S. Atomic Energy Commission.

[1] Crussard, Walker, and Koshiba, Phys. Rev. **94**, 736 (1954).
[2] L. C. L. Yuan and S. J. Lindenbaum, Phys. Rev. **93**, 1431 (1954).
[3] Cool, Madansky, and Piccioni, Phys. Rev. **93**, 249 (1954).
[4] S. J. Lindenbaum and L. C. L. Yuan, Bull. Am. Phys. Soc. **29**, No. 4, 50 (1954).

Nuclear Resonance Fluorescence in Hg^{198} and the Lifetime of the 411-kev Excited State of Hg^{198} *

F. R. METZGER AND W. B. TODD
Bartol Research Foundation of The Franklin Institute, Swarthmore, Pennsylvania

(Received June 1, 1954)

NUCLEAR resonance fluorescence in Hg^{198} has been studied by Moon and co-workers[1–3] and by Malmfors.[4]

Using an ultracentrifuge to provide the necessary Doppler shift to the 411-kev gamma ray, Davey and Moon[3] measured a lifetime of $(3.2\pm0.7)\times10^{-11}$ second for the 411-kev electric quadrupole transition in Hg^{198}.

Malmfors[4] produced an appreciable Doppler broadening of the incident gamma line by heating a source of radioactive Au^{198}. From his measurements of the resulting resonance fluorescence, he deduced a lifetime of 9×10^{-11} second.

Davey and Moon's[3] value for the lifetime agrees with the result of Graham and Bell[5] who determined the same lifetime by the delayed-coincidence method as $(1.5\pm2.4)\times10^{-11}$ second.

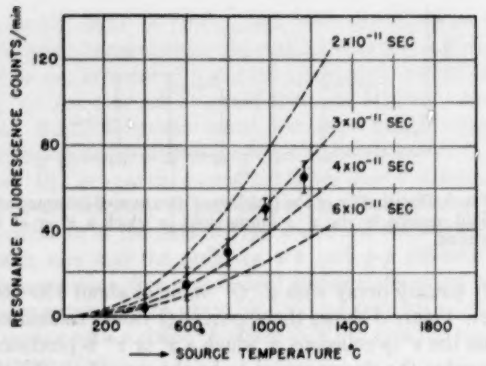

FIG. 1. Resonance fluorescence counting rate as a function of the temperature of the Au^{198} source for a mercury scatterer at room temperature. The dashed lines were calculated for different values of the lifetime τ_γ of the 411-kev gamma-ray transition assuming a pulse-height channel comprising one-third of the 411-kev photopeak and a source strength of eight millicuries.

In view of the large discrepancy between the reported values, Malmfors' experiment was repeated with improved technique. Thanks to the better energy resolution of the scintillation spectrometer and due to the large scattering angle used, the elastically scattered gamma rays could be clearly separated from the much more intense Comption-scattered radiation.

With a 40-millicurie source of Au^{198} the counting rate in the 411-kev photopeak was of the order of twenty thousand counts per minute. It was thus possible to detect small percentage changes in the number of quanta of full energy.

Using a gold source at room temperature, a lead and a mercury scatterer were first matched with respect to the elastic scattering of 411-kev quanta, i.e., the channel of a single-channel pulse-height analyzer was set on the 411-kev photopeak and the mercury scatterer was altered until the two scatterers produced the same counting rate. The temperature of the source was then raised and the counting rates due to the two scatterers were again compared. With increasing temperature the number of resonance scattered gamma rays from Hg^{198} increased. Consequently, the mercury scatterer caused larger counting rates in the full energy peak than did the lead scatterer. At 1175 degrees centigrade the contribution from resonance fluorescence amounted to approximately five percent of the total elastic scattering.

The resonance radiation has the same energy as the primary radiation. The determination of the effective cross section is therefore straightforward and does not involve the knowledge of the detection efficiency of the sodium iodide detector.

Assuming a Maxwellian distribution of the velocities of the emitting and absorbing nuclei, the temperature dependence of the resonance scattering was calculated for the arrangement used. The behavior expected for different values of the lifetime τ_γ of the 411-kev transition is indicated in Fig. 1 by dashed lines. The experimental points follow the expected temperature dependence within the experimental uncertainty. A least-squares fit leads to a value of $(3.3\pm0.3)\times10^{-11}$ second for the lifetime of this fast electric quadrupole transition. Taking into account a value of 0.044 for the total internal conversion coefficient[6] of the 411-kev transition, one finally arrives at a lifetime of $(3.15\pm0.3)\times10^{-11}$ for the first excited state in Hg^{198}. This is in good agreement with Davey and Moon's[3] value and is compatible with Graham and Bell's estimate.

The authors wish to thank Dr. Leonard Eisenbud for informative discussions.

* Assisted by the joint program of the U. S. Office of Naval Research and the U. S. Atomic Energy Commission.

[1] P. B. Moon, Proc. Phys. Soc. (London) **A64**, 76 (1951).
[2] P. B. Moon and A. Storruste, Proc. Phys. Soc. (London) **A66**, 585 (1953).
[3] W. G. Davey and P. B. Moon, Proc. Phys. Soc. (London) **A66**, 956 (1953).
[4] K. G. Malmfors, Arkiv Fysik **6**, 49 (1952).
[5] R. L. Graham and R. E. Bell, Phys. Rev. **84**, 380 (1951).
[6] L. Simons, Phys. Rev. **86**, 570 (1952).

Scattering of 96-Mev Protons from Light Nuclei*

K. STRAUCH AND W. F. TITUS
Harvard University, Cambridge, Massachusetts
(Received June 7, 1954)

WE are investigating the scattering of 96-Mev protons from various nuclei, using the external beam of the Harvard cyclotron. The scattered protons are detected with a range telescope of a type described previously.[1] The primary beam is monitored with an ionization chamber that has been calibrated with a

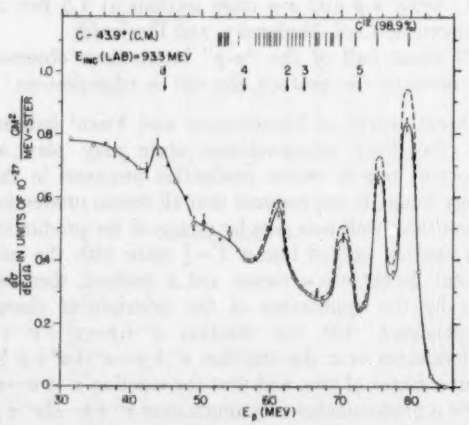

FIG. 1. Energy distribution of protons scattered from a carbon target. The numbered arrows indicate the thresholds for the following reactions: $2(p,pn)$; $3(p,2p)$; $4(p,dp)$; $5(p,\alpha p)$. The arrow labeled d indicates the energy of protons having the same range as pickup deuterons that leave the residual nucleus in its ground state.

Faraday cup.[2] Results obtained with carbon and sulfur targets at 40° in the laboratory system are shown in Figs. 1 and 2. The data are plotted in the c.m. system. The dotted and crossed points represent two sets of data taken one after the other and the full line is drawn through them. The broken line represents the results after a correction for nuclear absorption in the telescope has been applied.

For both carbon and sulfur targets, the highest-energy peak corresponds to elastically scattered protons: the half-width of 3 Mev represents the estimated energy resolution of our experiment at the high-energy end. The lower-energy peaks are due to inelastically scattered protons which leave the residual nucleus in well defined energy states. We have also plotted the known energy levels of C^{12} and S^{32} that are listed in recent compilations,[3,4] and the threshold energies for the simpler reactions. The low-energy peaks (around

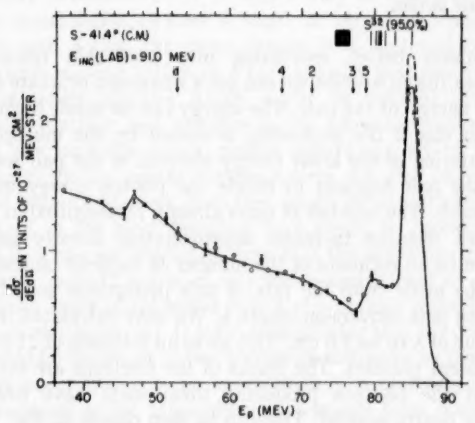

FIG. 2. Energy distribution of protons scattered from a sulfur target.

45 Mev) are believed to represent pickup deuterons whose range corresponds to protons of this energy.

The proton spectrum from carbon suggests that among the first three excited states, only the 4.43-Mev and the 9.61-Mev levels are strongly excited by high-energy protons. Due to our limited energy resolution, it is difficult to estimate any possible small contribution from protons exciting the residual nucleus to the 7.5-Mev level. The 61-Mev peak corresponds to a nuclear excitation of 20.0±1 Mev[5] which could correspond to one or more known levels of C^{12}. The continuum of protons corresponds either to unresolved energy levels of C^{12}, or to breakup of the carbon nucleus, or to both.

The rather broad high-energy inelastic peak obtained with the sulfur target probably corresponds to the unresolved excitation of some if not all of the low-energy levels known in this nucleus. No single peak stands out over the continuum in this case.

The results reported here are typical of the spectra of the light elements that we are investigating. It is quite apparent that many nuclear energy states can be excited by high-energy protons that interact with the target nucleus for a "short" time only; "short," that is, compared to the average time between collisions of the nucleons inside the nucleus. This type of excitation is different from that prevalent at low energies where compound nucleus formation occurs. Experimentally this means that the separation of truly elastic events from inelastic events is often difficult. This fact must be borne in mind in high-energy scattering investigations such as recent diffraction and polarization experiments. However at smaller scattering angles than those reported here, the elastic peak becomes much more prominent compared to inelastic events. Between 40° and 30° (laboratory system) the elastic and first inelastic peaks of C increase by factors of 4.80 and 2.66, respectively. This makes the elastic—inelastic separation easier at small angles.

We are very much indebted to the staff of the Harvard Cyclotron Laboratory for assistance in this investigation.

* Supported by the joint program of the U. S. Office of Naval Research and the U. S. Atomic Energy Commission.

[1] J. A. Hofmann and K. Strauch, Phys. Rev. **90**, 449 (1953).

[2] We are much indebted to Mr. U. Kruse for this calibration.

[3] F. Ajzenberg and T. Lauritsen, Revs. Modern Phys. **24**, 321 (1952).

[4] P. M. Endt and J. C. Kluyver, Revs. Modern Phys. **26**, 95 (1954).

[5] R. Britten [Phys. Rev. **88**, 283 (1952)] studied the scattering of 31.5-Mev protons from carbon. He interpreted as deuterons, particles lying under a peak corresponding to an excitation energy of 18 Mev. In our experiment only protons can produce the 61-Mev peak.

Narrow Shower of Pure Photons at 100 000 Feet*

MARCEL SCHEIN, D. M. HASKIN, AND R. G. GLASSER
Department of Physics, University of Chicago, Chicago, Illinois
(Received June 15, 1954)

A VERY unusual new event consisting of a large number of individual electron pairs has been found in a stack consisting of 18 Ilford G-5 600 μ pellicles flown in a Skyhook balloon from Goodfellow Air Force Base, Texas (41°N geomagnetic latitude). The pellicles were exposed in an aluminum exposure box with walls 0.7 g/cm² and free of other matter. The emulsions were flown for six hours over 100 000 feet. The event entered the side of the stack at a zenith angle of 66° and passed through 14 of the 18 pellicles with a total length of more than 50 000 μ at an angle of 7.5° to the emulsion surface. This makes it possible to carry out accurate measurements on individual tracks. Preliminary results of this analysis will be reported here.

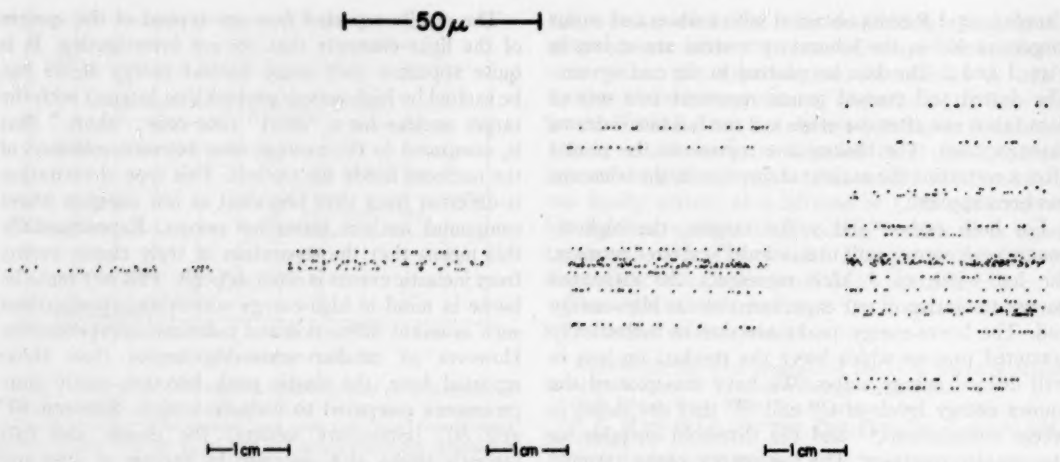

FIG. 1. Narrow shower of pure photons. Sections at arbitrary intervals to show development of shower. Note pair starting in last section.

No incident charged particle can be seen within a radius of 250 μ of the axis of the event with a direction such that it can be considered associated, except for the first of the electron pairs, which had already materialized before entering the sensitive area of the emulsion. Sixteen pairs have been found in the first 33 000 μ, which is just a little less than the mean pair conversion length for high-energy photons in this emulsion. Table I shows the distance of the origin of the first 16 pairs from the start of the event itself. Also shown are the results of multiple scattering measurements on the first five pairs. As already indicated, Pair 1 has already materialized before entering the emulsion. Pairs 6, 7, 8, and 9 are very narrow pairs which go through more than 3500 μ of emulsion before separating into resolvable tracks. From the separation we can get a minimum estimate of the energy of the pair. The energy can be much higher than this if the separation is caused by the multiple scattering of the lower energy electron of the pair and if the pair happens to divide the photon energy unequally. The number of pairs already materialized at a given distance increases approximately linearly and permits an estimate of the number of incident photons to be made from the rate of pair production and the mean pair conversion length λ. We have calculated the value of λ to be 3.6 cm. This gives an estimate of 21 ± 3 incident photons. The tracks of the electrons are such that the photons producing them must have been very nearly parallel. This can be seen clearly in Fig. 1, which represents small sections at arbitrary intervals along the event and shows the very remarkable character of the development of the photon shower in the first radiation unit.

TABLE I. First 16 pairs in narrow photon shower. The radial distance is the distance from the pair origin to the median of the electrons at the pair's point of origin. E_1, E_2 are the measured energies of individual electrons. E is the total energy of the photon. The estimate of E for pairs 6, 7, 8, 9 is made from the distance the pair goes before becoming resolvable into individual tracks.

Pair	Distance to point of conversion (μ)	Radial distance (μ)	E_1 (Mev)	E_2 (Mev)	E (Mev)
1			400±160	100±40	500±165
2	2020	1	350±140	300±120	650±330
3	4440	12	350±140	550±220	900±260
4	13 100	3	100±40	800±320	900±325
5	13 350	23	500±200	150±60	650±210
6	15 750	10			>5000
7	15 770	3			>5000
8	19 900	1			>20 000
9	21 600	2			>20 000
10	27 000	6			
11	27 200	8			
12	29 800	2			
13	30 800	4			
14	31 100	2			
15	31 400	26			
16	33 300	16			

It is quite important to get some idea of the radial spread of the origins of the pairs which corresponds to the radial spread of the photons. For this purpose the distance of each pair origin from the median of the other shower tracks at the point of origin has been computed and is shown in Table I. These values are almost all less than 15 μ while the largest is 23 μ. The total width of the photon burst thus does not exceed 25 μ. Since the shower is observed in the emulsion over a distance of more than 30 000 μ it is evident that for the half-angle θ of the cone enclosing all particles we have

$$\theta \leqq 0.001 \text{ radian},$$

which proves that the shower must be of extremely high energy in accordance with the direct measurements carried out on individual pairs.

From Table I it is evident that several of the pairs have an unusually low energy in comparison with the

very high energy necessary to account for such a narrow collimation.

A more detailed account of this event will be published later when a more careful discussion of possible causes can be undertaken. It should be noted, however, that this event has very remarkable features in that it consists of about 20 photons with no electrons present. Such a phenomenon would appear to be incompatible with the production of these photons by any conventional electromagnetic process. Nuclear collisions can also be ruled out, since even if one had the extreme improbability of no charged particles created in the event, but only neutral pions, the high collimation of the tracks would be totally incompatible with energies of the order of 1 Bev as observed for several of the pairs. No process known to the authors at the present time seems to explain all the features of the event. One possibility, however, which has been considered in an effort to account for it, is that it may be produced by an annihilation process in flight at very high energy. In such a case the event occurs in a center-of-mass system moving with such a high velocity that any very low-energy photons which might be emitted could receive rather high energies in the laboratory system. If the particles which receive practically all of the energy in the center-of-mass system are also neutral, for instance photons, then they might be missed and an event of the kind described here would be produced. It is of special interest to note that the event occurred under only 12 g/cm² of air, which means that at the zenith angle of the event only ⅓ of a nuclear mean free path was traversed. It is thus improbable that the event could be the result of two successive collisions, so that if the event is due to an antiparticle it is probably not produced in the atmosphere, but enters from outside as an extremely high-energy particle ($E>10^{13}$ ev). Production of antiparticles at these energies by cosmic-ray particles outside the atmosphere would be predicted by Fermi's theory.[1]

The authors wish to thank the U. S. Office of Naval Research for arranging the launching of the balloon and Mrs. E. Goodman, who located the event.

* Supported in part by the joint program of the U. S. Office of Naval Research and the U. S. Atomic Energy Commission.

[1] E. Fermi, Progr. Theoret. Phys. (Japan) **5**, 570 (1950).

Photopion *S* Wave Near Threshold and the Pion Nucleon Coupling Constant

G. BERNARDINI AND E. L. GOLDWASSER
Department of Physics, University of Illinois, Urbana, Illinois
(Received June 14, 1954)

IN a previous letter,[1] the authors presented results of investigations of π^+ photoproduction from hydrogen near threshold. New data have been added for a center-of-mass angle of about 90° and all the data for this angle, together with the experimental curve, are presented in Fig. 1. The pellicle data have been corrected for nuclear absorption and scanning efficiency. The maximum correction is 15 percent (for the high-energy point) and the corrections themselves are believed to be accurate to within 30 percent. Errors in the abscissas have been propagated into the indicated errors. Possible errors in the photon flux calibration are not included. They are believed to be less than 3 percent.[2]

In terms of the *S*-matrix formulation, the 90° cross section for photoproduction of positive and negative pions may be expressed, quite generally, as follows:

$$\left(\frac{d\sigma}{d\Omega}\right)^{\pm}_{\text{c.m.}} = \frac{k}{\nu E_i E_f \omega}|\mathfrak{M}^{\pm}|^2\left(1+\frac{\nu}{E_i}\right)^{-1}\left(\frac{1}{\omega}+\frac{1}{E_f}\right)^{-1}. \quad (1)$$

Here k,ω = final meson momentum, energy; ν = photon momentum (or energy); E_i, E_f = initial and final nucleon energies; and $\mathfrak{M}^{\pm}$ are the matrix elements for the production of positive and negative pions. All quantities are in the center-of-mass system and in units $\hbar=c=1$.

The two factors in parentheses represent dynamical corrections to the incident photon flux and final available phase space, respectively, arising from the motion of a nucleon of finite mass. Near threshold $E_i \simeq E_f \simeq M$, the nucleon rest energy (or inverse Compton wavelength of nucleon), and (1) may be written

$$\left(\frac{d\sigma}{d\Omega}\right)^{\pm}_{\text{c.m.}} = \left(\frac{1}{M}\right)^2|\mathfrak{M}^{\pm}|^2\chi;$$
$$\chi=\frac{k}{\nu}\left(1+\frac{\omega}{M}\right)^{-1}\left(1+\frac{\nu}{M}\right)^{-1}. \quad (2)$$

The matrix element $|\mathfrak{M}^{\pm}|$ is not known, but its square can almost certainly be expressed as follows:

$$\left(\frac{1}{M}\right)^2|\mathfrak{M}^{\pm}|^2=\{A_0^{\pm}+A_2^{\pm}\eta^2+\cdots$$
$$\text{higher-order terms}\}, \quad (3)$$

where $\eta=(k/\mu c)$, μ is the meson rest mass, and the A coefficients depend upon the sign of the pion. The absence of the first power term can be shown to follow from the disappearance of interference effects at 90°. Exploring the possibility that the higher-order terms in k may be negligible within the scope and accuracy of this work, the experimental values of $(d\sigma/d\Omega)/\chi$ have been plotted *versus* η^2 (Fig. 2). Within the indicated errors a straight line seems to be a very good fit to the experimental points up to $\eta\simeq 1$ ($E_\gamma\simeq 2.30$ Mev). Three points, which represent the averages of several counter experiments,[3] have been also added to show more clearly the trend of the curve at energies over 200 Mev and the point of deviation from a straight line.

The best least-squares fit straight line has been passed through the experimental points, yielding

$$A_0^+=(1.51\pm0.14)\times10^{-29};\quad A_2^+=(1.12\pm0.31)\times10^{-29}.$$

The errors are determined by a weighted propagation of the errors of the individual observations. Consideration of the external consistency of the points leads to the same estimated errors. The value of A_0^+ gives directly the following total cross section for S-wave photoproduction at threshold:

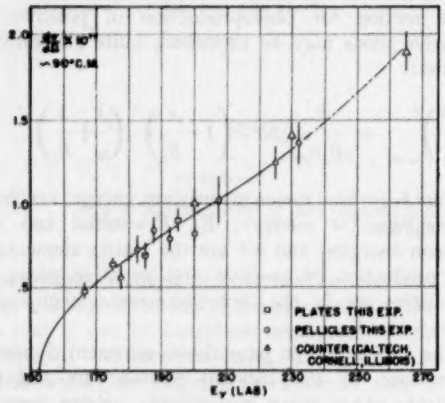

FIG. 1. The 90° c.m. cross section for photoproduction of pions in hydrogen *versus* photon energies in the laboratory frame. The solid curve was obtained by transformation of the straight line of Fig. 2.

$$_{c.m.}\sigma^{+S\text{ wave}}=(1.90\pm0.18)\times10^{-28}\chi. \quad (4)$$

A theorem due to Kroll and Ruderman[4] proves, for a relativistic covariant meson theory, that at threshold,[5]

$$A_0^{\pm}=\frac{e^2g^2}{2M^2}\left\{1\pm\frac{\mu}{M}C+\left(\frac{\mu}{M}\right)^2D\left(\frac{\mu}{M}\right)^{\pm}+\cdots\right\}, \quad (5)$$

where $e^2=1/137$, g is the renormalized symmetric coupling constant, μ/M = ratio of pion mass to nucleon mass, C is a constant, and $D^{\pm}$ are functions of μ/M.

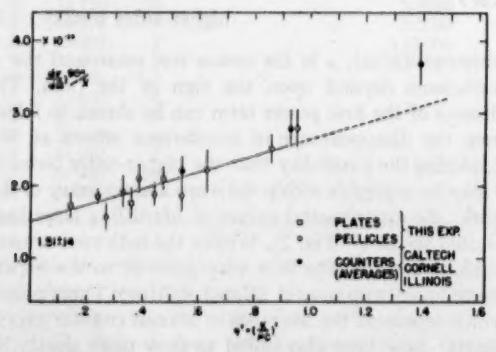

FIG. 2. Plot of $(d\sigma/d\Omega)/\chi$ (see text) *versus* the square of pion momentum in the c.m. frame. The straight line represents the least-squares fit of the points of *this* experiment.

Thus if the assumption is made that $(\mu/M)^2D$ is negligible, it is found that

$$e^2g^2/2M^2=\tfrac{1}{2}(A_0^++A_0^-)=\tfrac{1}{2}A_0^+(1+A_0^-/A_0^+). \quad (6)$$

The ratio A_0^-/A_0^+ is simply the limiting value at threshold of the ratio $d\sigma(\pi^-)/d\sigma(\pi^+)$ from free nucleons. Available experimental data[6] indicate that this ratio in deuterium is 1.51 ± 0.1. This value requires some correction for the effects of the difference of the final states (alternatively two protons or two neutrons for the negative or positive pion case), but it is felt that the corrections will be no larger than the indicated limit of error.

Using this value for A_0^-/A_0^+, it is found that $g^2=11.8\pm0.14$.

Similarly the Chew cut-off theory gives, at threshold,

$$A_0^{\pm}=\frac{2e^2f^2}{\mu^2}\left(1\pm\frac{\mu}{M}C'\right),$$

where f is the coupling constant for this theory. The value obtained is $f^2=0.066\pm0.008$.

We wish to express our deep appreciation to Professor A. O. Hanson for the continuous interest and invaluable help he has lent us throughout this work, and to Professor G. F. Chew and Professor F. Low for numerous enlightening discussions.

[1] G. Bernardini and E. L. Goldwasser, Phys. Rev. **94**, 729 (1954).
[2] P. D. Edwards and D. W. Kerst, Rev. Sci. Instr. **24**, 490 (1953).
[3] Jenkins, Luckey, Palfrey, and Wilson, Phys. Rev. (to be published); J. E. Leiss and C. S. Robinson (private communication); Bacher, Peterson, Tollestrup, and Walker (private communication).
[4] N. M. Kroll and M. A. Ruderman, Phys. Rev. **93**, 239 (1954).
[5] Here the authors have assumed that the kinematical correction factors introduced in (1) are applicable to the Kroll-Ruderman theorem for the case $\mu/M\neq0$.
[6] Beneventano, Lee, and Stoppini, Nuovo cimento (to be published); Sands, Teasdale, and Walker, Phys. Rev. (to be published).

Decay Curve of K Particles*

L. MEZZETTI† AND J. W. KEUFFEL‡
Palmer Physical Laboratory, Princeton University, Princeton, New Jersey
(Received June 14, 1954)

WE have measured the decay curve of stopped unstable cosmic-ray particles with liquid scintillators and directional Čerenkov counters.[1] Auxiliary information is provided by Geiger counters connected to an 80-channel hodoscope. The apparatus is shown in Fig. 1. Each Čerenkov counter is a hollow Lucite box filled with water, painted black on the bottom, and viewed from above by an RCA C7157 photomultiplier. The measured efficiency is 90 percent for fast μ mesons traveling *towards* the photomultiplier end, and 0.4 percent for particles traversing the counter in the

opposite sense. The experimentally verified Čerenkov velocity threshold for water corresponds to $E/mc^2 \geqq 0.52$.

The apparatus was designed to select events of the following type. A charged unstable particle produced in the generating layer of Pb passes through the scintillator S and stops near or inside one of the Čerenkov counters

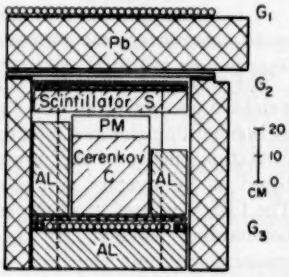

FIG. 1. Experimental arrangement. G_1 and G_3 are trays of GM counters of diameter 1 in. and sensitive length 24 in.; G_2 is a tray of ½-in. GM counters of the same length. All the elements in the array are approximately square except for S, which is 11 in. by 24 in. There are two Čerenkov counters, one behind the other, each 1 ft square by 6 in. thick.

C. There it decays at rest into an upward-going relativistic secondary which is detected in C unobscured by downward-going shower particles. The time delay is measured with a 17-channel chronotron-type timing circuit.[2,3] The triggering requirements included the firing of any two counters in the G_2 bank. We also later rejected, by examining the hodoscope pictures, events where an extension tray and/or tray G_1 indicated an air shower and certain other events discussed below.

Our results are shown in Fig. 2. The time distribution shows a central peak and a well-defined exponential "tail" beginning at about 12.4 mμsec. If the lags greater than 12.4 mμsec are analyzed by the method of Peierls on the basis of a single exponential, the mean life is 8.7 ± 1.0 mμsec. The systematic error is probably no larger than the statistical error quoted. The rate of such events, extrapolated to zero time, is 3.5 hr^{-1}.

Instrumental timing errors were studied in detail by inverting the Čerenkov counters and triggering on fast μ mesons and soft showers. The timing error distributions were consistent with the shape of the central peak in Fig. 2, but could not possibly account for the exponential tail. We found, however, that large pulses in the *scintillator*—as indicated by a high multiplicity in a hodoscoped Geiger tray below it—produced a shift of 3 to 5 mμsec in the direction of apparent lags in the Čerenkov counters.[4] For this reason, we rejected events in the actual run where more than six counters were discharged in trays G_2 or G_3.

Time lags might arise from differences in time of flight of two associated particles. We tested this possibility by displacing the Čerenkov counters 50 cm to one side, but still maintaining similar thicknesses of Pb above and around it. The rate of lags greater than 12.4 mμsec decreased by a factor of 20 under these conditions. (See "KB," Fig. 2.) Such a sharp decoherence cannot be associated with particles from a distant origin. We also verified with a neutron source that the Čerenkov counters had a negligible response to neutrons.

The delayed events are most reasonably interpreted in terms of bona fide decays. Many short-lived unstable particles are known, but we wish to re-emphasize that we detect only those which produce relativistic secondaries. Thus τ mesons can be detected only by the materialization of γ rays from the (relatively infrequent) alternative mode of decay $\tau' \to \pi + 2\pi^0$ while the $\pi \to \mu \to e$ process will be detected only by the decay electrons. These are distributed in time over a 2.2-μsec mean life and are very inefficient in triggering the apparatus compared to long-range μ mesons from K decay. A small number of lags in the microsecond range were indeed observed, but it was not possible in the present experiment to analyze these into 2.2-μsec and flat random noise components; we can only say that the background from such events is at most about 0.5 counts per channel in Fig. 2. (If this background were doubled it would decrease the mean life by only 0.25 mμsec.)

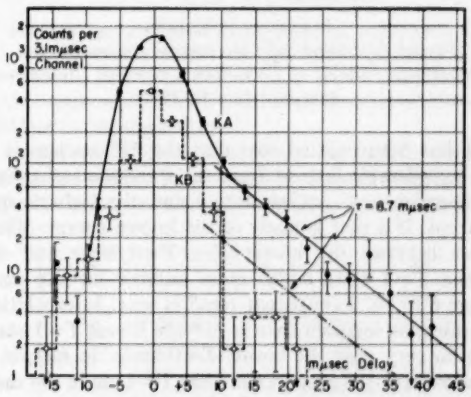

FIG. 2. Time lag distributions. KA: regular run, disposition as in Fig. 1, running time 230.7 hr, total rate 19.8 hr^{-1}. KB: test for lags due to time of flight. Čerenkov counters displaced 50 cm. Normalized to same running time as KA, so that differences in *absolute* rate of lags are significant.

The fact that we considered only lags greater than 12.4 mμsec in the analysis biases us strongly against processes with mean lives less than about 4 mμsec. Our results should be compared particularly with the results of the Paris cloud-chamber group,[5] where the minimum time of flight to the lower chamber is 5 mμsec. These investigators found a predominant K process $K_\mu \to \mu + \nu$, with a unique secondary momentum 223 Mev/c, and it appears likely that we are observing this particle. The Paris group[6] estimates the K_μ mean life as 28 mμsec, but this value is not considered inconsistent with ours because of their small statistical sample. Earlier cloud-chamber mean life estimates gave lower and upper bounds of 4 and 10 mμsec.[7,8] In addition to the K_μ's, these estimates probably involved other

K particles with mean lives short enough not to show up after 12.4 mμsec.

Our rates appear to be consistent with cloud chamber and emulsion rates, but large uncertainties are involved in the comparison.

* Sponsored by the joint program of the U. S. Office of Naval Research and the U. S. Atomic Energy Commission.
† On leave of absence from the University of Rome, Rome, Italy.
‡ Now at University of Utah, Salt Lake City, Utah.
[1] J. Winckler and K. Anderson, Rev. Sci. Instr. **23**, 765 (1952).
[2] J. W. Keuffel, Rev. Sci. Instr. **20**, 197 (1949).
[3] Keuffel, Harrison, Godfrey, and Reynolds, Phys. Rev. **87**, 942 (1952).
[4] Pulse heights could not be measured directly in this experiment because of amplifier saturation.
[5] Gregory, Lagarrigue, Leprince-Ringuet, Muller, and Peyrou, Nuovo cimento **11**, 292 (1954).
[6] B. Gregory, at Padua Conference on Heavy Mesons, April, 1954 (unpublished).
[7] Astbury, Buchanan, Chippindale, Millar, Newth, Page, Rytz, and Sahiar, Phil. Mag. **44**, 242 (1953).
[8] Bridge, Peyrou, Rossi, and Safford, Phys. Rev. **90**, 921 (1953).

Energy Levels of Al^{26}†

CORNELIUS P. BROWNE
Physics Department and Laboratory for Nuclear Science, Massachusetts Institute of Technology, Cambridge, Massachusetts
(Received June 14, 1954)

IT has been pointed out[1] that the Al^{26} nucleus is of considerable interest from the standpoint of charge independence of nuclear forces and the isobaric-spin concept. If a plot is made of the known energy differences between the lowest-lying $T=0$ state and the lowest $T=1$ state *versus* mass number for the mass range 6 to 54, a consistent trend is seen. Interpolation on this plot suggests that in Al^{26} the lowest $T=1$ state will be very near the lowest $T=0$ state. In fact, it is possible that the ground state has $T=1$, as in the case[2] of Cl^{34}. Previous data on Al^{26} are inconsistent and leaves the energy and the isobaric spin of the ground state in doubt.[1]

The reaction $Si^{28}(d,\alpha)Al^{26}$ is suitable for investigating the $T=0$ levels of Al^{26} as it has an estimated Q value of 1 to 2 Mev. The deuteron, the alpha particle, and Si^{28} are all $T=0$ nuclei; therefore, to the degree that isobaric spin-selection rules are valid, levels with $T=1$ will not be observed.

The MIT-ONR electrostatic generator and associated high-resolution magnetic-analysis equipment have been used to study Al^{26} from its ground state to 2-Mev excitation. Fresh targets of natural SiO_2 evaporated on thin Formvar backings were used. Because of low yield from this reaction, the targets used were of such thickness as to give an energy spread in the alpha groups several times the analyzer resolution. The alpha particles were observed at 90 degrees to the incident beam. Assignment of observed alpha groups to Al^{26} was based on observation of the change in alpha energy with a change in bombarding energy.

TABLE I. Reaction energies for the $Si^{28}(d,\alpha)Al^{26}$ reaction.

Q Value in Mev	Excitation of Al^{26} in Mev
1.416 ±0.008	0
0.998 ±0.008	0.418
0.364 ±0.008	1.052
−0.334 ±0.008	1.750
(−0.430)±0.015	(1.846)
−0.648 ±0.008	2.064

The results are given in Table I. Each Q value is the weighted average of at least three measurements made at bombarding energies ranging from 5 to 7 Mev. The excitation energy of Al^{26} given in the last column is based on the average ground-state Q value as shown. The 1.85-Mev level was completely resolved at only one bombarding energy. An accurate "energy shift" measurement was therefore not obtained. Thus, the assignment of this group to Al^{26} is not completely certain.

A region of about 3 Mev below the ground state has been covered with no indication of lower levels. An alpha of 10 percent of the intensity of the ground-state group would have been seen. No group of alphas from this reaction was seen between the listed ground state and the first excited state. At 6.5- and 7-Mev bombarding energy, the limit is about 3 percent of the intensity of the ground-state group.

Figure 1 shows the $T=0$ energy levels of Al^{26} and their relation to reactions that have been studied elsewhere. Recent work of Haslam,[9] using the $Al^{27}(\gamma,n)$ reaction and counting positrons from the Al^{26} decay as well as the neutrons, is in agreement with the presently

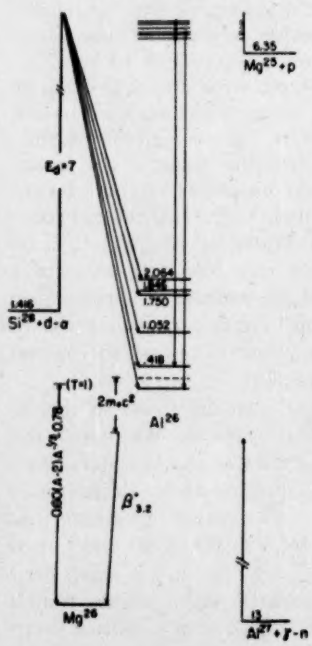

FIG. 1. Energy level scheme for Al^{26}. The levels up to 2 Mev are those observed in the present work. The calculated position of the lowest $T=1$ level is shown. This is seen to coincide with the position given by the observed β^+ decay end point. The $Al^{27}(\gamma,n)$ threshold then agrees with the ground state. The high-lying levels are indicated by the resonances and gamma-ray energies observed by Kluyver *et al.*

determined position of the ground state and suggests that the short-lived level (presumably $T=1$) responsible for the observed positrons lies roughly 200 kev above the ground state. The position of the $T=1$ level relative to the ground state of Mg^{26} may be estimated, using a calculated Coulomb energy difference and the p-n mass difference. The expected position is shown in Fig. 1 and is seen to agree with this suggestion.

Kluyver *et al.*[4] have measured energies of gamma rays from $Mg^{25}(p,\gamma)Al^{26}$. These agree with the ground state and the 0.418-Mev level shown. The conclusion of Kluyver *et al.* that the 0.418-Mev level has $T=1$ is inconsistent with the fact that it is seen here in the $Si^{28}(d,\alpha)$ reaction with intensity comparable to the ground state. The lack of a gamma ray to the $T=1$ level may be the result of a high spin difference between this state and the capturing state.[5]

It would be desirable to study a reaction not involving isobaric spin-selection rules to see both the $T=0$ and $T=1$ levels. Resolution of better than 100 kev may be required, however. Possible reactions are $Si^{29}(p,\alpha)Al^{26}$ and $Mg^{24}(He^3,p)Al^{26}$. The first requires higher bombarding energies than are available at present with the MIT-ONR machine. The second of course entails operation of an ion source with He^3.

† This work has been supported in part by the joint program of the U. S. Office of Naval Research and the U. S. Atomic Energy Commission.

[1] S. A. Moszkowski and D. C. Peaslee, Phys. Rev. **93**, 455 (1954).
[3] W. Arber and P. Stahelin, Helv. Phys. Acta **26**, 433 (1953).
[3] R. N. H. Haslam (private communication).
[4] Kluyver, van der Leun, and Endt, Phys. Rev. **94**, 1795 (1954).
[5] D. C. Peaslee (private communication).

Coulomb Excitation of Energy Levels in Rhodium and Silver

N. P. Heydenburg and G. M. Temmer
Department of Terrestrial Magnetism, Carnegie Institution of Washington, Washington, D. C.
(Received June 10, 1954)

COULOMB excitation has revealed two hitherto unknown energy levels in each of the nuclei Rh^{103}, Ag^{107}, and Ag^{109}; their energies and excitation cross sections (transition probabilities) are quite similar and seen to continue the striking similarity of nuclear properties which have been known to exist in these three nuclei, namely: spin ½ and negative parity ($p_{\frac{1}{2}}$ configuration) in their ground states, and a low-lying isomeric transition of the $E3$ type, coming from a level of spin $7/2^+$ (Rh^{103}: $E=40$ kev, $t_{\frac{1}{2}}=57$ min; Ag^{107}: $E=94$ kev, $t_{\frac{1}{2}}=44$ sec; Ag^{109}: $E=87$ kev, $t_{\frac{1}{2}}=39$ sec).

We have reported the levels in rhodium as lying at 305 and 370 kev;[1] these values are now slightly revised to 295 and 357 kev, respectively. We reported that silver showed no gamma radiation under 3-Mev alpha particle bombardment.[2] A reexamination with 2-Mev protons revealed two lines at around 310 and 410 kev in ordinary silver.

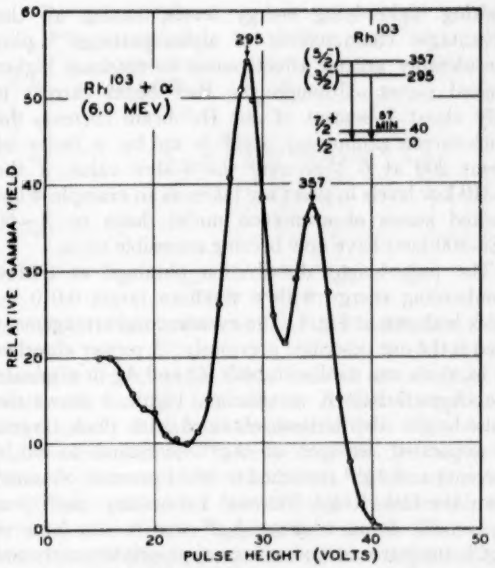

FIG. 1. Pulse-height distribution of gamma radiation from rhodium bombarded with 6-Mev alpha particles.

In the meantime we found that the doubly charged helium-ion current from our rf ion source (~0.3 μa) at *twice* the generator voltage was a very effective tool for

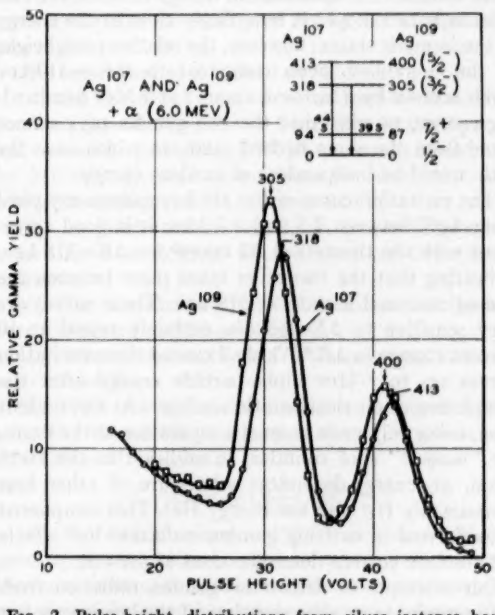

FIG. 2. Pulse-height distributions from silver isotopes bombarded with 6-Mev alpha particles. Circles refer to Ag^{107} (enriched to 90.26 percent, metallic target); squares refer to Ag^{109} (enriched to 99.54 percent, AgCl target corrected for Cl). Relative intensities of all three curves are meaningful.

exciting higher-lying energy levels, having all the advantages characteristic of alpha particles[1-3] plus considerably greater effectiveness in reaching higher excited states. Although the He^{++}-beam current is only about 2 percent of our He^{+}-beam current, the thick-target gamma-ray yield is up by a factor of about 200 at 6 Mev over the 3-Mev value, if the ~310-kev levels in silver are taken as an example. First excited states of even-even nuclei down to $A\sim60$ ($E\sim800$ kev) have now become accessible to us.

The pulse-height distribution obtained at 6-Mev bombarding energy with a rhodium target 0.010 in. thick is shown in Fig. 1. The experimental arrangement used is the one described previously.[4] A copper absorber $\frac{1}{16}$ in. thick was used with both Rh and Ag to eliminate the characteristic K x-radiation. Figure 2 shows the pulse-height distributions obtained with thick targets of separated isotopes of Ag^{107} (enriched to 90.26 percent) and Ag^{109} (enriched to 99.54 percent) obtained from the Oak Ridge National Laboratory. Ag^{107} was in metallic form, whereas Ag^{109} was in the form of AgCl; the latter curve has been appropriately corrected by comparison of ordinary silver with ordinary AgCl. This correction consists merely in multiplying by the constant factor 1.39, since negligible radiation is observed from Cl.[1] Gamma rays of 318 kev and 413 kev are seen to occur with Ag^{107}, whereas lines at 305 kev and 400 kev are observed with Ag^{109}. We assign about ±5 kev uncertainty to their energy values. The relative intensity scales are correct for intercomparison of the three nuclei. The separation in energy between the two lines in both isotopes is temptingly close to the energy of the isomeric states; however, the relative peak height of the ~400-kev levels compared to the ~310-kev levels is down by a factor of about 5 at 3-Mev bombarding energy, proving that the two gamma rays cannot come from the same excited state, in which case the ratio would be independent of incident energy.

The excitation curve of the 318-kev gamma-ray yield from Ag^{107} between 2.5 and 3.3 Mev is in good agreement with the theoretical $E2$ curve[5] for $\Delta E=318$ kev, indicating that the transition takes place between the *ground state* and a state at 318 kev. These curves are very sensitive to ΔE and can certainly reveal at 10 percent change in ΔE.[6] We shall extend these excitation curves up to 7-Mev alpha-particle energy after the completion of an electrostatic analyzer. At the present time, using only gross magnetic separation of the beam, the "mass 2" spot contains, in addition to the He^{++} beam, an energy-dependent admixture of other ions (presumably H_2^+ and low-energy He). This component is ineffectual in exciting gamma radiation but affects the absolute current determinations at present.

Our attempts to detect the gamma radiation from the isomeric states after shutting off the beam were not successful. The direct Coulomb excitation of these levels is of course out of the question because of the $E3$ character of the transition and its long lifetime (small excitation cross section), but formation of the state is possible by cascade from a higher level. The two gamma rays we observe cannot represent cascades to the isomeric state because of our failure to detect the isomeric transition. Huus and Lundén[7] have observed this transition by counting the conversion electrons, after shutting off their 1.75-Mev proton beam. Since the total internal conversion coefficient of the isomeric transitions is of the order of 15, their method was thus much more sensitive to this transition. From a rough excitation function for the yield of conversion electrons they conclude that a level of around 400 kev is responsible for the formation of the isomer. Combining this information with our results they conclude that in about 0.5 percent of the excitations of the (400+413)-kev level an $E1$ cascade occurs to the isomeric state. It is now clear why we were unable to detect gamma radiation from this state. We do not observe the 0.5 percent of 313 (319)-kev cascade radiation because it is buried under the strong 305 (318)-kev line.[8]

TABLE I. Absolute cross sections (in millibarns) for gamma radiations from rhodium and silver bombarded with 6-Mev alpha particles; decoupling parameter a and rotational constant $\hbar^2/2\mathcal{I}$; derived transition probabilities $B_e(2)$ and intrinsic quadrupole moments Q_0.

Nucleus	E_γ (kev)	σ (mb)	a	$\frac{\hbar^2}{2\mathcal{I}}$ (kev)	$B_e(2)$ (10^{-49} cm^4)	Q_0 (10^{-24} cm^2)
Rh^{103}	295	4.1	+0.77	55	1.8	2.1
	357	5.8			3.2	2.3
Ag^{107}	318	2.6	+0.69	62	1.2	1.7
	413	3.1			2.1	1.9
Ag^{109}	305	2.9	+0.68	60	1.3	1.8
	400	3.6			2.3	2.0

The level schemes shown as inserts in Figs. 1 and 2 summarize these results. The spin assignments are made on the basis of the rotational interpretation of these levels, for the anomalous case where $\Omega=\frac{1}{2}$ (component of the odd-proton angular momentum along the nuclear symmetry axis). The expression for the energy levels in this case is given by[9]

$$E_I=\frac{\hbar^2}{2\mathcal{I}}[I(I+1)+a(-1)^{I+\frac{1}{2}}(I+\tfrac{1}{2})];$$

the decoupling parameter a which obtains in these cases turns out to be $\sim2/3$, so that the normal level sequence (1/2, 3/2, 5/2) is maintained ($|a|<1$). The $7/2^+$ isomeric level belongs to a different value of Ω.

The absolute (thin-target) cross sections, calculated from the thick-target yields, for the Coulomb excitation with 6-Mev alphas of the various gamma rays are listed in Table I,[10] together with approximate values for the reduced transition probabilities $B_e(2)$ and intrinsic nuclear quadrupole moments Q_0 derived from the former in the rotational interpretation.[9] No corrections have been made for internal conversion or cascade radiation from the upper level (expected to be small). The large values obtained for the matrix elements are

indicative of $E2$ rotational transitions. It is noteworthy how close the ratios of the quantities $B_e(2)$ for the $(1/2\rightarrow 5/2)$ and $(1/2\rightarrow 3/2)$ transitions come to the value 1.50 predicted from the rotational scheme.

We are indebted to Dr. T. Huus and Dr. A. Lundén for communication of their results prior to publication, and to Dr. A. Bohr and Dr. B. R. Mottelson for informative correspondence.

[1] G. M. Temmer and N. P. Heydenburg, Phys. Rev. **93**, 351 (1954).
[2] N. P. Heydenburg and G. M. Temmer, Phys. Rev. **93**, 906 (1954).
[3] G. M. Temmer and N. P. Heydenburg, Phys. Rev. **94**, 1399 (1954).
[4] N. P. Heydenburg and G. M. Temmer, Phys. Rev. **94**, 1252 (1954).
[5] K. Alder and A. Winther, Phys. Rev. **91**, 1578 (1953).
[6] G. M. Temmer and N. P. Heydenburg, Phys. Rev. (to be published).
[7] T. Huus and A. Lundén, Phil. Mag. (to be published).
[8] T. Huus and A. Lundén see evidence of conversion lines at 306 kev and 321 kev with 1.75-Mev protons on ordinary Ag, in excellent agreement with our values for Ag^{109} and Ag^{107}, respectively.
[9] A. Bohr and B. R. Mottelson, Kgl. Danske Videnskab. Selskab, Mat.-fys. Medd. **27**, No. 16 (1953); also Chapter 17 of a forthcoming book on *Beta and Gamma Ray Spectroscopy*, edited by K. Siegbahn; A. Bohr, dissertation, Copenhagen (1954), and private communication.
[10] The over-all detection efficiency of our system was determined for the 411-kev gamma ray from a Au^{198} source. We are grateful to Miss L. Cavallo and Mr. H. H. Seliger of the National Bureau of Standards for the absolute beta calibration.

Positron Spectrum from the Decay of the μ Meson*

RYOKICHI SAGANE, WALTER F. DUDZIAK, AND JAMES VEDDER
Radiation Laboratory, Department of Physics, University of California, Berkeley, California
(Received June 14, 1954)

THE positron spectrum (Fig. 1) produced by the decay of the μ meson has been studied in detail, and also with much improved accuracy, with a 40-in. (pole base diameter) spiral-orbit spectrometer.

The experimental method that was adopted is similar to the one reported by one of us in 1951.[1] The 340-Mev deflected proton beam was used to produce π^+ mesons in the target. Some of the created π^+ mesons decayed inside the target into μ mesons that in turn disintegrated into positrons. Thus the target mounted coaxially with the symmetric magnetic field was the source of positrons. The energy spectrum of these created positrons was analyzed by means of the spiral-orbit spectrometer.[2]

Positrons were measured with momentum resolutions of $\pm 0.6\sim\pm 1.8$ percent at half intensity. They were detected as quadruple coincidences of signals from four plastic crystals (two of these crystals were $\frac{1}{4}$ by 1.5 by 2.5 in., and the other two $\frac{1}{4}$ by 3 by 3 in.). The counts were taken following a 2-μsec delay relative to the proton pulses and with four consecutive gates each having a 2-μsec width. This enabled us not only to check the half-life but also to reduce background, which usually came in as accidentals.

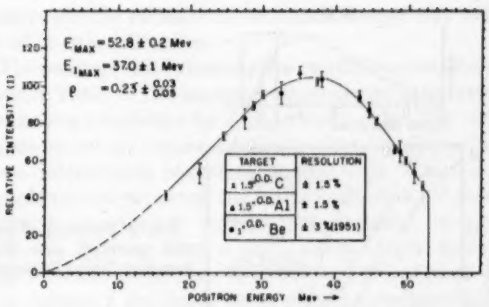

FIG. 1. Positron spectrum from "thick"-target data.

Measurements were made on four thin Be targets of different diameters and thicknesses, as the resolution is directly related to the effective diameter of the cylindrical or tubular targets, and also as the energy absorption of the positrons through the target itself is the other major correction to be applied. In addition to these, two thick targets (C and Al, each $1\frac{1}{2}$ in. outside diameter by 4 in. long) were studied. Each experiment was repeated from 4 to 10 times, and reproducibility of the results was checked.

The accuracy of each magnetic field setting was kept better than 0.1 percent by means of a proton nuclear resonance method during each measurement. As a result, the accuracy of the absolute $H\rho$ value of each measured point is considered to be better than 0.2 percent.

The results are summarized as follows:

(A) All the data (most of which have a reasonably small statistical error) can be fitted best to the theoretical curve with $\rho=0.23_{-0.05}{}^{+0.03}$ (the constant introduced by Michel[3]), if proper corrections for absorption and resolution are applied, as is shown in Fig. 1.

(B) As illustrated in Fig. 2, all thin-target experiments show a definite sharp cutoff at the energy maximum.

(C) The absolute value of this maximum energy has been calculated as 52.8 ± 0.2 Mev.

(D) This corresponds to a μ-meson mass value of $m_\mu=207\pm 0.8m_e$.

(E) With the aid of the fundamental mass ratio,[4] $\pi^+/\mu^+=1.321\pm 0.002$, the mass of the π^+ meson can be established. This value is

$$m_{\pi^+}=273.4\pm 1.1m_e.$$

(F) The data obtained in 1951[1] were found to be in good agreement with the present data. (Unfortunately the mass value of the μ meson at that time was too high, and the results were therefore interpreted to show $\rho=0$.)

(G) Since we have measured directly the cutoff at E_{max} from our experiment, our present results are not dependent on some other mass measurements.

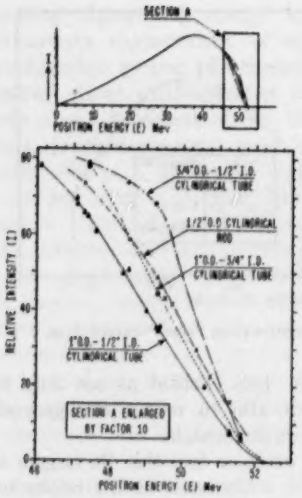
SECTION A
POSITRON ENERGY (E) Mev
5/8"O.D.-1/2" I.D. CYLINDRICAL TUBE
1/2" O.D. CYLINDRICAL ROD
1" O.D.-5/8" I.D. CYLINDRICAL TUBE
1" O.D.-1/2" I.D. CYLINDRICAL TUBE
SECTION A ENLARGED BY FACTOR 10
RELATIVE INTENSITY (I)
POSITRON ENERGY (E) Mev

FIG. 2. Behavior of positron spectrum near E_{max} from four "thin" Be targets.

(*H*) The very good agreement of the mass value of the μ meson obtained with the assumption of the range energy relation[4] gives strong indication that the assumed relation is good for mesons to this order of accuracy.

(*I*) From our present data we are not able to exclude the possibility of the spin values of $\frac{3}{2}$ for the μ meson.

We have been informed of the values $\rho=0.6, 0.5$, and ~ 0, obtained in the recent measurements (each with a different method) at Columbia,[5] Massachusetts Institute of Technology,[6] and Los Alamos.[7] As the discrepancies of the ρ values are quite serious, during the last five months we have made a close examination of the possible systematic errors that we might have overlooked. Our present analysis of our data cannot account for this serious difference in ρ value.

We would like to acknowledge the interest, and particularly the effort in obtaining the funds for the construction of the 40-inch spiral-orbit spectrometer, of Professor E. O. Lawrence and Dr. Walter Barkas.

* This work was performed under the auspices of the U. S. Atomic Energy Commission.

[1] Sagane, Gardner, and Hubbard, Phys. Rev. **82**, 557 (1951).
[3] G. Miyamoto, Proc. Phys.-Math. Soc. Japan **24**, 676 (1942).
[4] L. Michel, Proc. Phys. Soc. (London) **A63**, 514 (1950).
[4] Smith, Birnbaum, and Barkas, Phys. Rev. **91**, 765 (1953).
[5] L. M. Lederman and C. P. Sargent (private communication).
[6] J. H. Vilain and R. W. Williams, Phys. Rev. **94**, 1011 (1954).
[7] Harrison, Cowan, and Reines, Nucleonics **12**, No. 3, 44 (1954).

Gamma Transitions in W^{182}†*

F. BOEHM, P. MARMIER, AND J. W. M. DUMOND
California Institute of Technology, Pasadena, California
(Received June 14, 1954)

A RATHER complicated γ-ray spectrum follows the β^- decay of Ta^{182}.[1] Sixteen transitions have been previously measured here with the curved crystal spectrometer.[2] Recent coincidence work by Mihelich[3] showed the relation between some high-energy lines and the first excited state of W^{182}. Using the precision axial focusing β spectrometer and the curved crystal spectrometer, a new investigation of the decay has been made. The Ta^{182} sources were produced by irradiation of metallic Ta in the Material Testing Reactor[4] (MTR, Arco, Idaho). The β-spectrometer sources were prepared by evaporation of the radioactive Ta (100 $\mu g/cm^2$) on mica. Most of the lines were studied with a momentum resolution of 2.5×10^{-3}. The L_I, L_{II}, and L_{III} conversion lines were resolved for all transitions below 264 kev. Their intensity ratios, together with the absolute conversion probabilities determined from β and γ-spectrometer data allows, in many cases, a unique

TABLE I. γ transitions in W^{182}.

Energy (kev)	Intensity: γ ray	Intensity: Total	Absolute conversion coefficients: α_K	α_{LI}	α_{LII}	α_{LIII}	Multipolarity
33.360±0.010	Weak	Weak	...	...	...	...	(*E*1)
42.710±0.010	Weak	Weak	...	...	...	...	(*E*1)
65.714±0.010	9	40	...	2.8	0.4	0.23	*M*1(+*E*2)
67.736±0.010	100	131	...	0.17	0.07	0.07	*E*1
84.667±0.010	6	53	...	1.85	0.6	0.5	*M*1(+*E*2)
100.092±0.012	46	247	1.5	0.13	1.4	1.35	*E*2
113.656±0.014	9	29	1.75	0.38	0.07	...	*M*1
116.398±0.014	2	(2)	...	...	...	...	...
152.408±0.023	43	46	0.07	...	...	...	*E*1
156.369±0.024	14	(15)	Small	...	...	...	(*E*1)
179.360±0.030	19	31	0.41		0.17	0.05	*M*1+*E*2
198.305±0.036	9	13	0.24	...	0.11	0.07	*E*2
222.051±0.044	45	48	0.06	0.01	...	...	*E*1
229.266±0.046	24	28	0.16	...	0.05	0.03	*E*2
264.086±0.060	27	32	0.11	...	0.04	0.02	*E*2
927 ±1	...	2	...	...	...	...	(*E*3)
960 ±1	...	2	...	...	...	...	(*E*3)
1003 ±1	...	10	...		*K*/*L*=7.0		*E*2
1122 ±1	120	121	0.005		*K*/*L*=6.7		*E*2+*M*1
1155 ±1	8	8	0.004		...		(*M*2)
1189 ±1	56	56	0.006		*K*/*L*=6.5		*E*3+*M*2
1222 ±1	115	115	0.003		*K*/*L*=6.0		*E*2
1231 ±1	58	58	0.003		...		*E*2
1289 ±1	...	(22)	...		*K*/*L*=6.6		(*E*3+*M*2)
1375 ±2	...	(1)	...		...		(*E*3)
1437 ±4	...	(1)	...		...		...
1454 ±4	...	(1)	...		...		(*E*3+*M*2)

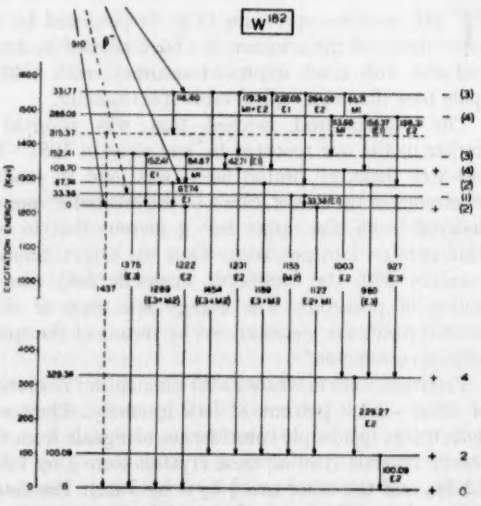

FIG. 1. Proposed energy level scheme for W^{182}. Data in parentheses ( ) are uncertain.

multipolarity assignment.[5] Table I gives a summary of the results.

The β^- spectra cannot be measured accurately because of the large number of internal conversion lines at low energy. The end point of the most energetic group ($\log ft \approx 8$) is at 510 ± 5 kev. We have evidence for at least two more spectra of lower energies ($\log ft \approx 6$–7).

Figure 1 contains the proposed decay scheme. The spin and parity assignment for the higher set of levels is not certain due to the inaccuracy of the multipolarity determination for the high-energy transitions. It is interesting to note that the energy values for the first and second levels are in very good agreement with the predictions of the Bohr-Mottelson theory.[6] We wish to thank Professor R. Christy and Professor R. Feynman for many helpful discussions. We are also indebted to Dr. J. J. Murray and Mr. P. Snelgrove for their help during the measurements.

† During the preparation of the manuscript, a paper on the same subject by C. M. Fowler *et al.*, appeared in Phys. Rev. **94**, 1082 (1954), showing close agreement with the present results.

* Assisted by contracts with the U. S. Atomic Energy Commission and the Office of Ordnance Research.

[1] Cork, Childs, Branyan, Rutledge, and Stoddard, Phys. Rev. **81**, 642 (1951); Beach, Peacock, and Wilkinson, Phys. Rev. **76**, 1585 (1949).
[2] Muller, Hoyt, Klein, and DuMond, Phys. Rev. **88**, 775 (1952).
[3] J. W. Mihelich, Bull. Am. Phys. Soc. **29**, No. 4, 33 (1954).
[4] We are indebted to the Phillips Petroleum Company, and particularly Dr. W. B. Lewis, for their cooperation.
[5] Gellman, Griffith, and Stanley, Phys. Rev. **85**, 944 (1952); Rose, Goertzel, and Swift, privately distributed (1954).
[6] A. Bohr and B. R. Mottelson, Phys. Rev. **90**, 717 (1953).

Two-Body Forces and Nuclear Stability*

DAVID H. FRISCH
Department of Physics and Laboratory for Nuclear Science, Massachusetts Institute of Technology, Cambridge, Massachusetts

(Received June 14, 1954)

RECENT experiments indicate[1] that "nuclear radii" may be as small as $R = 1.1A^{\frac{1}{3}} \times 10^{-13}$ cm. We wish to reexamine whether linear superposition of the central two-body forces observed in p-p and n-p scattering can alone give negative potential energies of sufficient magnitude to account for the observed nuclear binding energies, and at the same time give stability at these small radii.

Rough estimates have previously been made[2] on the uniform model by using a Wigner-Seitz calculation of the average space-symmetric and space-antisymmetric interaction integrals in a Fermi gas. The nucleus was taken to be a finite sphere of nucleons with simple Yukawa potential, $\epsilon V_0 (a/r) e^{-r/a}$, between each pair, where ϵ is the exchange operator, $V_0 = 45.6$ Mev, and $a = 1.185 \times 10^{-13}$ cm. Such a calculation, ascribing the correlation effects solely to the exclusion principle and not at all to the forces between nucleons, may underestimate appreciably the magnitude of the potential energy, and the estimate of the kinetic energy may well be off in either direction.

The results of this calculation for two different radii are given in Table I. The exchange dependences in column 1 include a calculation for S-wave forces only. This was suggested by the remote possibility that higher partial wave interactions observed in two-body scattering experiments might cancel out inside large nuclei, if such interactions originate from a polarizability of the nucleons. This is, then, a particularly simple many-body force derivable from observed two-body forces.

In column 2 the larger value of r_0/a corresponds to $r_0 = 1.54 \times 10^{-13}$ cm, and the smaller to $r_0 = 1.04 \times 10^{-13}$ cm. Column 3 gives the potential energy per particle required to give the observed binding energy (arbitrarily taken the same at the smaller radius as at the observed radius), based on computed kinetic and Coulomb energies: $V = E - K - C$. Column 4 gives the potential energy per particle computed from the superposition of two-body interactions, assuming the various exchange dependences of column 1 and radii of column 2. If the correct model is used, columns 3 and 4 should be equal.

TABLE I. Calculated potential energies for various interactions.

1. ϵ	2. $\frac{r_0}{a}$	3. $\frac{V_{\text{req}}}{A}$ (Mev)	4. $\frac{V_{\text{comp}}}{A}$ (Mev)	5. $\frac{(2K+C)}{V_{\text{req}}}$	6. $\frac{(2K+C)}{V_{\text{comp}}}$	7. $\frac{r_0}{V}\frac{\partial V}{\partial r_0}$
(Majorana)	1.25	−23	−7	1.0	8	0.8
	0.88	−37	−4	1.5	8	−4
(Serber)	1.25	−23	−15	1.0	1.9	2.4
	0.88	−37	−34	1.5	1.6	2.4
(Symmetric)	1.25	−23	−11	1.0	2.7	1.7
	0.88	−37	−16	1.5	3.5	1.5
S wave only	1.25	−23	−13	1.0	2.2	2.2
	0.88	−37	−26	1.5	2.1	1.9

Similarly, stability at r_0 should be expressed by the equality of the logarithmic derivative of potential energy with respect to the radius computed in columns 5, 6, and 7. The values in column 6 are larger than in column 5 because the computed potential is less than that required, so column 5 is probably a better measure of what the values of column 7 should be for stability.

It is seen that near the observed radius the S-wave interaction gives more potential than the symmetric interaction in column 4 (26 *vs* 16 Mev, where 37 Mev is required), but is not exactly at the stable radius as is the symmetric interaction (1.9 *vs* 1.5, where 1.5 is required). Both the Majorana and Serber forces are clearly no better at the small radius than they were at the larger radius, one giving too little attraction and the other giving no stability. But the improvement in both the S wave and the symmetric interactions indicates a possibility that two-body forces, or simply

related many-body forces, even without repulsive cores, might account roughly for nuclear binding energies and radii.

* This work has been supported in part by the joint program of the U. S. Office of Naval Research and the U. S. Atomic Energy Commission.

[1] F. Bitter and H. Feshbach, Phys. Rev. **92**, 837 (1953).
[2] D. Frisch, Phys. Rev. **84**, 1169 (1951).

Charged Pion Production from Carbon by Protons*

WALTER F. DUDZIAK
Radiation Laboratory, Department of Physics, University of California, Berkeley, California
(Received June 8, 1954)

A STUDY has been made with nuclear emulsions of the cross sections for production of positive and negative pions from carbon at 0° and 90° to a 340-Mev proton beam. For the 0° experiment and the 90° π^+ spectrum a uniform magnetic field was used. The 90° π^- spectrum was obtained with the aid of a symmetric heterogeneous magnetic field of a 22-inch spiral orbit spectrometer. The proton source was the external electrically deflected beam of the 184-inch synchrocyclotron. From this study[1] the following conclusions are drawn.

(a) The peak of the cross section for π^- production at these laboratory angles occurs much earlier than the corresponding peak for π^+ production.

(b) The maximum pion energy cutoff for π^- production is smaller than the corresponding pion energy cutoff for π^+ production.

(c) The shapes of the π^- production spectrum disagree with the previously reported spectrum shapes,[2] particularly in the low-pion-energy region.

(d) In the low-energy region the $\pi^\pm$ spectrum shapes when plotted against pion energy qualitatively resemble the corresponding shapes in $\beta^\pm$ decay.

(e) These spectra when integrated over the pion energy give the following results per carbon nucleus:

Laboratory angle θ	$\frac{d\sigma^+}{d\Omega}\times10^{28}$ cm² sterad⁻¹	$\frac{d\sigma^-}{d\Omega}\times10^{28}$ cm² sterad⁻¹	$\frac{\pi^+}{\pi^-}$	$\frac{\pi^+(0°)}{\pi^+(90°)}$	$\frac{\pi^-(0°)}{\pi^-(90°)}$
0°	21.0 ±0.5	0.71±0.02	29.5±1.2	6.3±0.2	1.67±0.09
90°	3.35±0.07	0.43±0.02	7.8±0.04		

(f) An estimate can be made of the total production cross section per carbon nucleus from the following data:

(1) Leonard's 180° results[3] on charged-pion production from carbon, which are $d\sigma^+/d\Omega=(1.77\pm0.40)\times10^{-28}$ cm²/sterad; $d\sigma^-/d\Omega=(1.90\pm0.56)\times10^{-29}$ cm²/sterad;

(2) the preliminary results at 30° on π^+ production which show that the π^+ peak occurs at a pion energy $T_\pi>55$ Mev; and

(3) the assumption that the angular dependence of the π^+ production cross section at each angle when integrated over pion energies can be represented by

$$\frac{d\sigma^+}{d\Omega}(\theta)=A+B\cos\theta+C\cos^2\theta,$$

and the corresponding π^- production cross section by

$$\frac{d\sigma^-}{d\Omega}(\theta)=A'+B'\sin^2\theta+C'\cos\theta.$$

This estimate gives

$$\sigma_T{}^+=(7.6\pm0.7)\times10^{-27}\text{ cm}^2,$$
$$\sigma_T{}^-=(0.55\pm0.09)\times10^{-27}\text{ cm}^2,$$
$$\pi^+/\pi^-=14\pm4.$$

(g) The disagreements between previously published data[2] on π^+ production at 90° can be resolved so that all results on π^+ production at this angle are in good agreement for pion energies above 25 Mev.

(h) For the calculation of the π^- production cross section a more appropriate zero-prong correction that is based on 4883 negative pions in clean C-2 Ilford nuclear emulsions is 1.35.

(i) The spiral-orbit principle[4] is especially suited for the study of charged pion production at 90° to the proton beam.

It is a pleasure to acknowledge the interest and aid of Professor C. Richman and Dr. R. Sagane during these studies.

* This work was done under the auspices of the U. S. Atomic Energy Commission.

[1] W. F. Dudziak, University of California Radiation Laboratory Report UCRL-2564 (unpublished).
[2] C. Richman and H. Wilcox, Phys. Rev. **78**, 496 (1950); Block, Passman, and Havens, *ibid.* **88**, 1243 (1952); Passman, Block, and Havens, *ibid.* **88**, 1247 (1952).
[3] S. Leonard, Phys. Rev. **93**, 1380 (1954).
[4] G. Miyamoto, Proc. Phys.-Math. Soc. (Japan) **24**, 676 (1942).

Natural Radioactivity of Rhenium*

A. D. SUTTLE, JR.,† AND W. F. LIBBY
Department of Chemistry and Institute for Nuclear Studies, University of Chicago, Chicago, Illinois
(Received May 21, 1954)

THE natural radioactivity of rhenium[1] was characterized by an aluminum absorption curve as having an energy of some 43 kilovolts. We have had occasion to attempt a better measurement of the energy and have been surprised to find that the energy is much lower than was originally deduced. In fact an aluminum foil of only 270 micrograms per cm² transmits less than 6 percent of the radiation, whereas the earlier result corresponded to a half-thickness of about 400 micrograms per cm². It seems likely that the earlier result was due either to a small amount of impurity or

to contamination of the foil. In any case it seems quite clear at this point that the radiation emitted by rhenium, which in total intensity is in agreement with the earlier result, 0.14 count per minute per cm² of area of the metal under 2π geometry counting conditions is much less energetic than a 43-kev beta spectrum.

When the screen wall counter was used,[2,3] with a distance of 1.26 cm between the sample cylinder on which the metallic rhenium was mounted and the screen gauze defining the wall of the counter, it was observed that with the wall of the counter negative by any voltage larger than 10 volts with respect to the sample cylinder the rhenium radiation was undetectable with the lowest pressures of gas obtainable. For example, 3 millimeters of Hg pressure of ethylene mixed with 1.1 cm Hg pressure of argon gave less than 3 percent transmission of the rhenium radiation. This would correspond, for an exponential absorption law, to a mean free path of 10 micrograms per cm², or using a ratio of 10 empirically deduced between the range and the mean free path of soft beta radiation,[4] we calculate that the range of the beta radiation from rhenium must be less than 100 micrograms per cm², which according to the relation of Katz and Penfold[5] gives an upper energy limit to the beta radiation from rhenium of 8 kev instead of the 43 kev given earlier.[1]

It is also clear that having reduced the energy of the radiation, the half-life must be recalculated. Whereas the earlier half-life was thought to be about 10^{12} yr, it now is clear that it must be reduced by at least the ratio of the range of 43-kev radiation—about 3 milligrams per cm²—to the new upper limit to the range—0.1 milligram per cm²—or to 10^{11} years or less. It cannot be clear how much less than 10^{11} years the half-life of rhenium 187 is until a successful attempt to measure the radioactivity in a gaseous state has been made. The systematics of the penetrating power of radiations as soft as rhenium is relatively unknown, since there is no other known beta spectrum as soft as this natural radioactivity seems to be.

Several attempts have been made in our laboratory to prepare gaseous compounds of rhenium which could be used in proportional counters to determine not only the half-life, but also the energy of the radiation. The compounds tried were: rhenium trimethyl, which we failed to prepare, and rhenium oxy-chloride and rhenium hexafluoride. The latter two were prepared successfully, but proved to be rather recalcitrant counter gases, and no important data have yet been obtained.

It would seem reasonable to attempt to test for the possibility that the natural radioactivity of rhenium may correspond to a half-life of as short as a few billion years, in which case the accumulation of osmium 187, the daughter isotope, in old rocks should be observable, and use of this observation might produce the first reliable value of the half-life of this most interesting naturally radioactive isotope. The shell model and beta decay systematics[6] say that rhenium 187 should have an *ft* value of about 10^{10} and be only first-forbidden with a spin change of two. This indicates that a one-kev transition should correspond to a half-life of about 10^{11} years, which is in permissive agreement with the facts as stated previously.

* This research was supported by the United States Air Force under a contract monitored by the Office of Scientific Research, Air Research and Development Command.

† Now at Research and Development Division, Humble Oil and Refining Company, Baytown, Texas.

[1] S. N. Naldrett and W. F. Libby, Phys. Rev. **73**, 487 (1948); N. Sugarman and H. Richter, Phys. Rev. **73**, 1411 (1948); B. Gauthe and J. M. Blum, Compt. rend. **236**, 1255 (1953).
[2] W. F. Libby, Phys. Rev. **46**, 496 (1934).
[3] D. D. Lee and W. F. Libby, **55**, 245 (1939).
[4] A. D. Suttle, Jr., thesis, University of Chicago, 1952 (unpublished).
[5] L. Katz and A. S. Penfold, Revs. Modern Phys. **24**, 1 (1952).
[6] M. G. Mayer (private communication).

Fine Structure in U^{233} Fission

E. P. Steinberg, L. E. Glendenin, M. G. Inghram, and R. J. Hayden
Chemistry and Physics Divisions, Argonne National Laboratory, Lemont, Illinois

(Received June 10, 1954)

FINE structure in the light group of the mass distribution for slow-neutron-induced fission of U^{235} was reported in a previous publication.[1] An abnormally high yield was observed at mass 100 suggesting a preference for this mass in the fission act, perhaps as the complement of a preferred 82-neutron

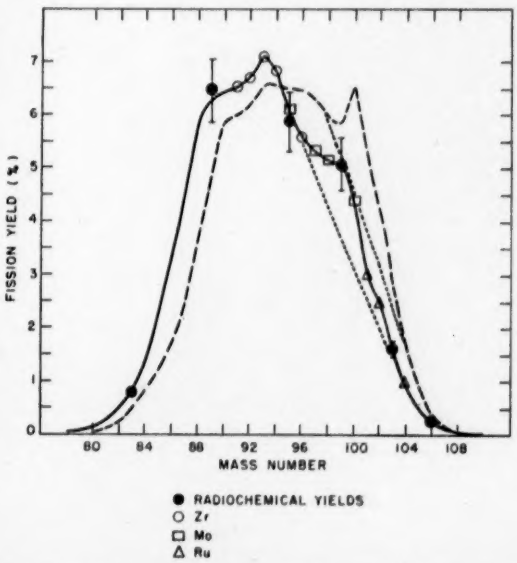

FIG. 1. Yield-mass curves for the light groups in slow neutron-induced fission of U^{233} (solid line) and U^{235} (dashed line).

shell in the heavy fragment at about mass 134. The possibility of such a preference in fission was first suggested by Wiles.[2] Preliminary mass spectrometric determinations of the relative isotopic abundances of fission-produced zirconium, molybdenum, and ruthenium show that this phenomenon also occurs in slow-neutron-induced fission of U^{233}. The relative abundance data for three elements were fitted together with the aid of the radiochemically determined yields[3] of Sr^{90} (6.5 percent), Zr^{95} (5.9 percent), Mo^{99} (5.1 percent), and Ru^{103} (1.6 percent), to give a yield-mass curve for the light group (solid line in Fig. 1). It is seen that, regardless of normalization, fine structure is indicated in the region around mass 99. The corresponding curve for U^{235} fission[1] (dashed line in Fig. 1) is shown for comparison. Hypothetical smooth curves (dotted lines) in the fine structure region serve to show the effect more clearly. A dip in the U^{233} yield-mass curve at masses 91 and 92 is also apparent as in the case of U^{235} fission.

The difference in appearance of the fine structure in U^{233} fission is probably the result of a narrowing of the light group peak and the shift toward lower mass. The maximum of the effect occurs at about mass 99 which is complementary to the heavy fission products containing 82 neutrons (around mass 133), and is consistent with the interpretation in terms of preferential in fission. It is interesting to note that fine structure in the light group for spontaneous fission of Cm^{242} occurs at mass 105,[4] which is again complementary to the 82-neutron shell region, thus providing additional evidence for this interpretation.

A detailed investigation of the mass distribution in neutron-induced fission of U^{235} covering both light and heavy groups is nearing completion and will be reported soon. Mass spectrometry and the isotope dilution technique have been used to obtain absolute fission yields, thus avoiding the difficulties of normalizing relative isotopic abundances of one element to those of another. Similar investigations of U^{233} and Pu^{239} fission will be undertaken.

[1] Glendenin, Steinberg, Inghram, and Hess, Phys. Rev. **84**, 860 (1951).

[2] D. R. Wiles, M.Sc. thesis, Department of Chemistry, McMaster University, Hamilton, Ontario, August, 1950 (unpublished); Wiles, Smith, Horsley, and Thode, Can. J. Phys. **31**, 419 (1953).

[3] Steinberg, Seiler, Goldstein, and Dudley, U. S. Atomic Energy Commission Document MDDC-1632, January, 1948 (unpublished); *Radiochemical Studies: The Fission Products* (McGraw-Hill Book Company, Inc., New York, 1951), National Nuclear Energy Series, Plutonium Project Record, Vol. 9, Div. IV, Appendix B. Revised values to be published.

[4] E. P. Steinberg and L. E. Glendenin, Phys. Rev. **95**, 431 (1954).

CONTENTS—*Continued*

Letters to the Editor:

Metastable States . . . . . William Primak 837

Shape of the *F* Band . . . . . P. V. Heubeck and E. E. Schneider 837

Photoproduction of Impurities at Dislocations in Heat-Treated Silicon . . . . Seymour Mayburg 838

Electron-Electron Scattering in Alkali Metals . . . . . Elihu Abrahams 839

Two Types of Band Emission Curves of Copper in the Soft X-Ray Region . . . . . Genji Shinoda, Tatsuro Suzuki, and Susumu Kato 840

Evaporated Multiple Layers with Semiconductor Properties . . . . . J. C. M. Brentano and J. D. Richards 841

Hall Effect in Ferromagnetics . . . . . Clarence Kooi 843

Hyperfine Splitting in Spin Resonance of Group V Donors in Silicon . . . . . R. C. Fletcher, W. A. Yager, G. L. Pearson, and F. R. Merritt 844

Phosphorescence of Atoms and Molecules of Solid Nitrogen at 4.2°K . . . . . H. P. Broida and J. R. Pellam 845

Energy Gap of Germanium-Silicon Alloys . . . . A. Lawson, C. C. Wang, and B. H. Alexander 846

Paramagnetic Resonance Absorption in a Soft Carbon . . . . . J. G. Castle, Jr. 846

Speculations on the Energy Band Structure of Ge-Si Alloys . . . . . Frank Herman 847

Electrical Conductivity of Magnesium Oxide Single Crystals . . . . R. Yamada and K. Suenmoto 848

Experiments on Nucleon-Nucleon Scattering with 315-Mev Polarized Protons . . . . . Owen Chamberlain, Robert Donaldson, Emilio Segrè, Robert Tripp, Clyde Wiegand, and Thomas Ypsilantis 850

Phase Shifts for High-Energy Nucleon-Nucleon Scattering . . . . . Burton D. Fried 851

π^0-Meson Production in π-Nucleon Collisions at 1.1 Bev . . . . . W. D. Walker, J. Cranzard, and M. Koshiba 852

Nuclear Resonance Fluorescence in Hg^{198} and the Lifetime of the 411-kev Excited State of Hg^{198} . . . . . F. R. Metzger and W. B. Todd 853

Scattering of 96-Mev Protons from Light Nuclei . . . . . K. Strauch and W. F. Titus 854

Narrow Shower of Pure Photons at 160 000 Feet . . . . . Marcel Schein, D. M. Haskin, and R. G. Glasser 855

Photopion β Wave Near Threshold and the Pion-Nucleon Coupling Constant . . . . . G. Bernardini and E. L. Goldwasser 857

Decay Curve of K Particles . . . . . L. Mezzetti and J. W. Keuffel 858

Energy Levels of Al^{28} . . . . . Cornelius P. Browne 860

Coulomb Excitation of Energy Levels in Rhodium and Silver . . . . . N. P. Heydenburg and G. M. Temmer 861

Positron Spectrum from the Decay of the μ Meson . . . . . Ryokichi Sagane, Walter F. Dudziak, and James Vedder 863

Gamma Transitions in W^{180} . . . . . F. Boehm, P. Marmier, and J. W. M. DuMond 864

Two-Body Forces and Nuclear Stability . . . . . David H. Frisch 865

Charged Pion Production from Carbon by Protons . . . . . Walter F. Dudziak 866

Natural Radioactivity of Rhenium . . . . . A. D. Suttle, Jr., and W. F. Libby 866

Fine Structure in U^{235} Fission . . . . . E. P. Steinberg, L. E. Glendenin, M. G. Inghram, and R. J. Hayden 867